

ENERGY SCIENCE AND ENGINEERING:  
RESOURCES, TECHNOLOGY, MANAGEMENT  
An International Series

EDITOR  
JESSE DENTON  
*Belton, Texas*

LARRY L. ANDERSON and DAVID A. TILLMAN (eds.), Fuels from Waste,  
1977

A. J. ELLIS and W. A. J. MAHON, Chemistry and Geothermal Systems,  
1977

FRANCIS G. SHINSKEY, Energy Conservation through Control, 1978

N. BERKOWITZ, An Introduction to Coal Technology, 1979

JAN F. KREIDER, Medium and High Temperature Solar Processes, 1979

STEPHEN J. FONASH, Solar Cell Device Physics

# **Solar Cell Device Physics**

**Stephen J. Fonash**

Engineering Science Program  
The Pennsylvania State University  
University Park, Pennsylvania

1981



**ACADEMIC PRESS**

A Subsidiary of Harcourt Brace Jovanovich, Publishers

New York London Toronto Sydney San Francisco

COPYRIGHT © 1981, BY ACADEMIC PRESS, INC.  
ALL RIGHTS RESERVED.

NO PART OF THIS PUBLICATION MAY BE REPRODUCED OR  
TRANSMITTED IN ANY FORM OR BY ANY MEANS, ELECTRONIC  
OR MECHANICAL, INCLUDING PHOTOCOPY, RECORDING, OR ANY  
INFORMATION STORAGE AND RETRIEVAL SYSTEM, WITHOUT  
PERMISSION IN WRITING FROM THE PUBLISHER.

ACADEMIC PRESS, INC.  
111 Fifth Avenue, New York, New York 10003

*United Kingdom Edition published by*  
ACADEMIC PRESS, INC. (LONDON) LTD.  
24/28 Oval Road, London NW1 7DX

Library of Congress Cataloging in Publication Data

Fonash, S. J.  
Solar cell device physics.

(Energy science and engineering)  
Includes bibliographical references and index.  
1. Solar cells. 2. Solid state physics. I. Title.  
II. Series.  
TK2960.F66 621.31'244 81-14934  
ISBN 0-12-261980-3 AACR2

PRINTED IN THE UNITED STATES OF AMERICA

81 82 83 84 9 8 7 6 5 4 3 2 1

To  
My parents Margaret and Raymond  
for setting me on the path toward intellectual pursuits  
My wife Joyce  
for her continuing support along the way  
My sons Stephen and David  
for making the journey so enjoyable

## Preface

This book is concerned with the physical principles and operating characteristics of solar cell devices. Its approach is to provide a balanced, in-depth qualitative and quantitative treatment. Physical principles and physical insight are stressed throughout the book so that it may be used to understand the operation of the devices of today as well as the devices of the future.

Sections such as "qualitative discussion," "configurations and performance," and "notes for the experimentalist," found in each of the chapters on specific devices, are presented in the belief that a physical "feel" for device operation and a knowledge of the advantages and disadvantages of a specific device are necessities. The more mathematically oriented sections are presented in the belief that the serious student and researcher alike want to know the assumptions behind the mathematical models used to quantify device behavior. Only then can they judge the appropriateness of the assumptions to new devices and new materials.

The level of the book is such that it is appropriate for use as a textbook for graduate students in engineering and the sciences, and as a reference book for those actively involved in solar cell research and development. Since the book has extensive qualitative discussion of physical phenomena and device operation, it can also serve as a textbook for seniors in electrical engineering

and applied physics. When used at this level, the more mathematically oriented sections can be omitted and the emphasis placed on the physical description, the final mathematical model for the operating characteristics of the device, and device performance data. At whatever level the book is used, it will be essential for the reader to have an introductory knowledge of solid state physics and devices as provided in standard texts.

Assuming this background, the book begins, after an introductory chapter, with a review of the physics and materials properties basic to photovoltaic energy conversion (Chapter 2). Careful attention is given in Chapter 2 to the electronic and optical properties of crystalline, polycrystalline, and amorphous materials with both organic and inorganic materials being considered. The manner in which these properties change from one material class to another, and the fundamental reasons for these changes with their implications for photovoltaics, are discussed.

Generation, recombination, and bulk transport are also covered in Chapter 2. The latter is discussed for both transport via delocalized band states and transport via states in the gap. Rather than simply presenting the usual equations of solid state for generation, recombination, and transport phenomena, the origins of the mathematical models are explored. This is done to point out the assumptions on which our models are built. Only with that knowledge can one select the proper model for a particular material and situation. Chapter 2 closes with a discussion of the fundamental origins of photovoltaic action in materials.

Chapter 3 begins with a comparison of the two mechanisms of photo-carrier collection in solar cells: drift and diffusion. The importance of interfaces in the collection process is pointed out, and interface types, interface modeling, and interface transport are discussed. A unified approach, which stresses the roles of thermodynamics, defects created in the act of forming the barrier, intrinsic surface states, and interface or intermediary layers is used in determining interface properties for configurations as diverse as semiconductor-semiconductor heterojunctions and liquid-semiconductor junctions. An extensive tabulation of semiconductor data important to photovoltaics is presented, together with data on work functions which include effective work functions for selected redox couples.

Chapters 4–6 deal with specific solar cell device classes defined in terms of the interface structure employed: Chapter 4 covers homojunctions ( $p-n$ ,  $p-i-n$ ); Chapter 5 covers semiconductor-semiconductor heterojunctions (isotype and anisotype) including S-I-S; and Chapter 6 covers surface-barrier devices (M-S, M-I-S, and liquid-semiconductor). Each of these chapters contains a qualitative discussion of the operation and the design considerations of the device class. Each of these chapters also includes an in-depth quantitative analysis of the device characteristics, which clearly shows the

assumptions and range of validity of the analysis. In the quantitative sections the mathematical development is always given a physical interpretation. The mathematics is viewed as a tool to quantify and catalog the important aspects of device behavior. Each device chapter closes with an extensive survey of specific device configurations and experimental results.

## **Acknowledgments**

The book evolved out of notes used in “solar cell device physics,” a graduate course given at The Pennsylvania State University. That evolution was helped along considerably by the comments of the series of graduate students who took the course over its six-year history. Among them I must especially single out Patricia Wiley and Paul Lester, whose comments and corrections of errors were very helpful. Also, a number of colleagues, including Dr. John Houlihan and Dr. S. Ashok, have contributed comments and suggestions. In particular, I am very grateful to Professor Ashok whose suggestions, stimulating comments, and diligent, critical reading of the manuscript greatly improved the final result.

Lastly, I must mention the three people without whom this book never would have been completed: Stella Updegraff, who typed the manuscript, helped in its editing, and retyped the final manuscript; Dr. John Mentzer, who provided the environment that allowed an undertaking such as this; and my wife Joyce, who greatly assisted and supported the effort.

## List of Basic Symbols

SYMBOL	DEFINITION	UNITS
$a, c$	Lattice parameters	nm
$A^*$	Effective Richardson constant	amp/m <sup>2</sup> /°K <sup>2</sup>
$C$	Capacitance per area	farads/m <sup>2</sup>
$d$	Interfacial layer thickness	m
$D^*$	Ambipolar diffusion coefficient	m <sup>2</sup> /sec
$e$	Magnitude of the charge on an electron = $1.602 \times 10^{-19}$	C or coulomb
$E$	Energy of an electron	joules, eV
$E_c$	Conduction band edge	eV
$E_F$	Fermi level or electrochemical potential	eV
$E_F^i$	Quasi-Fermi level for $i$ th localized state grouping	eV
$E_{F_i}$	Intrinsic Fermi level	eV
$E_{Fn}, E_{Fp}$	Electron and hole quasi-Fermi levels	eV
$E_g$	Forbidden energy gap	eV
$E_{gm}$	Mobility energy gap	eV

SYMBOL	DEFINITION	UNITS
$E_{go}$	Optical energy gap	eV
$E_p$	Energy of phonon	joules, eV
$E_{ph}$	Energy of a photon	joules, eV
$E_{redox}^0$	Standard redox potential measured with respect to the standard hydrogen electrode (obtained for $N_0^{re} = N_0^{ox}$ )	eV
$E_v$	Valence band edge	eV
$E_{VL}$	Vacuum level	eV
$f$	Probability of occupation function	—
$f_0$	Probability of occupation in thermodynamic equilibrium (the Fermi function)	—
$F_e$	Total force on an electron in a solid ( $F_e = -e[\xi + \xi'_n]$ )	N
$F_h$	Total force on a hole in a solid ( $F_h = e[\xi + \xi'_p]$ )	N
FF	Fill factor defined by $(V_{mp}J_{mp})/(V_{oc}J_{sc})$	—
$g$	Generation rate	$\text{sec}^{-1}\text{m}^{-3}$
$g_e(E)$	Density of electron states in energy per volume of the solid	$\text{eV}^{-1}\text{m}^{-3}$
$g_p(E)$	Density of phonon states in energy per volume of the solid	$\text{eV}^{-1}\text{m}^{-3}$
$G_e^c(\mathbf{r}, \mathbf{v})$	Density of conduction-band states per volume of velocity space per volume	$\text{sec}^3\text{m}^{-6}$
$G_e^v(\mathbf{r}, \mathbf{v})$	Density of valence-band states per volume of velocity space per volume	$\text{sec}^3\text{m}^{-6}$
$G_L$	Optical generation rate	$\text{m}^{-3}\text{sec}^{-1}$
$h$	Planck's constant = $6.625 \times 10^{-34}$	joule-sec
$\hbar$	Planck's constant/ $2\pi$ = $1.054 \times 10^{-34}$	joule-sec
$J$	Current density	amp/m <sup>2</sup>
$J_{bk}$	Bucking current $J_{bk} = J_{bk}(\Phi_0, V)$ ; in general, goes to zero as $V \rightarrow 0$	amp/m <sup>2</sup>
$J_{fe}$	Field emission current density	amp/m <sup>2</sup>
$J_{ir}$	Interface recombination current density	amp/m <sup>2</sup>
$J_{mp}$	Current density at the maximum power point	amp/m <sup>2</sup>

SYMBOL	DEFINITION	UNITS
$J_{\text{ob}}$	Thermionic emission current density	amp/m <sup>2</sup>
$J_{\text{ph}}$	Photocurrent $J_{\text{ph}} = J_{\text{ph}}(\Phi_0, V)$ ; in general, goes to zero as $\Phi_0 \rightarrow 0$ .	amp/m <sup>2</sup>
$J_{\text{sc}}$	Short-circuit current density	amp/m <sup>2</sup>
$J_{\text{tf}}$	Thermionic field emission current density	amp/m <sup>2</sup>
$\mathbf{k}$	Wave vector	m <sup>-1</sup>
$L^*$	Ambipolar diffusion length	m
$L_{D_n}$ or $L_n$ & $L_{D_p}$ or $L_p$	Diffusion length for electrons or holes	m
$L_{\xi n}, L_{\xi p}$	Drift length for electrons or holes	m
$m$	Mass	kg
$m_e$	Mass of a free electron = $9.108 \times 10^{-31}$	kg
$m_e^*$	Effective mass of electron	kg
$m_h^*$	Effective mass of hole	kg
$n$	Conduction-band number density; Diode quality factor	m <sup>-3</sup>
$n_i$	Intrinsic number density	m <sup>-3</sup>
$N_c$	Conduction-band effective density of states	m <sup>-3</sup>
$N_0^{\text{oX}}$	Concentration of oxidized species of a redox couple when system is in thermodynamic equilibrium	m <sup>-3</sup>
$N_0^{\text{re}}$	Concentration of reduced species of a redox couple when system is in thermodynamic equilibrium	m <sup>-3</sup>
$N_v$	Valence-band effective density of states	m <sup>-3</sup>
$p$	Valence-band number density	m <sup>-3</sup>
$P_{\text{in}}$	Power per area impinging on cell structure	Watts/m <sup>2</sup> or W/m <sup>2</sup>
$Q$	Collection efficiency	—
$Q_b^-$ or $Q_b^+$	Charge/area developed in a semiconductor space charge region	coulombs/m <sup>2</sup>
$Q_e$	Charge/area developed in electrolyte (Helmholtz and Gouy layers)	coulombs/m <sup>2</sup>

SYMBOL	DEFINITION	UNITS
$Q_{\text{fix}}$	Fixed charge/area	coulombs/m <sup>2</sup>
$Q_s^-$ or $Q_s^+$	Charge/area developed at an interface or surface	coulombs/m <sup>2</sup>
$r$	Recombination rate	sec <sup>-1</sup> m <sup>-3</sup>
$\mathcal{R}$	Net recombination rate	sec <sup>-1</sup> m <sup>-3</sup>
$S$	Seebeck coefficient	eV/°K
$t$	Time	sec
$T$	Temperature	°K
$\langle v \rangle$	Thermal speed	m/sec
$V$	Voltage	volts
$V_{\text{bi}}$	That part of the total electrostatic potential which is developed in a semiconductor	eV
$V_j$	Change in the band bending across a junction	V or eV
$V_{\text{mp}}$	Voltage at maximum power point	amp/m <sup>2</sup>
$V_n(\mathbf{r})$	Defined by $V_n(\mathbf{r}) = E_c(\mathbf{r}) - E_{F_n}(\mathbf{r})$	eV
$V_0$	Total electrostatic potential energy developed across an interface in thermodynamic equilibrium	eV
$V_{\text{oc}}$	Open-circuit voltage	volts
$V_p(\mathbf{r})$	Defined by $V_p(\mathbf{r}) = E_{F_p}(\mathbf{r}) - E_v(\mathbf{r})$	eV
$W$	Activation energy for hopping; Space charge layer width	eV m
$\alpha$	Absorption coefficient	m <sup>-1</sup> , cm <sup>-1</sup>
$\Delta, \Delta_I$	Potential energy developed across an interfacial layer or developed by a surface dipole	eV
$\Delta E$	Bandwidth; activation energy	eV
$\epsilon$	Permittivity of a material	farad/m
$\mu$	Mobility	m <sup>2</sup> /(V-sec)
$\eta$	Thermodynamic efficiency defined by $V_{\text{mp}} J_{\text{mp}} / P_{\text{in}}$	—
$\xi$	Electrostatic field	V/m
$\xi'_n$	Electron effective force field arising from varying material properties	V/m
$\xi'_p$	Hole effective force field arising from varying material properties	V/m
$\Xi$	Transmission probability	—
$\rho$	Resistivity	Ω-m
$\sigma$	Conductivity	Ω/m

SYMBOL	DEFINITION	UNITS
$\sigma_n, \sigma_p$	Electron and hole conductivities	$\Omega/m$
$\tau_n$	Minority-carrier lifetime (electrons)	sec
$\tau_p$	Minority-carrier lifetime (holes)	sec
$\phi$	Defined such that $\Phi_0 = \phi \Delta \lambda$	$m^{-3} sec^{-1}$
$\phi_B$	Schottky barrier height	eV
$\phi_M$	Metal work function	eV
$\phi_{n,p}$	Semiconductor work function	eV
$\phi_0$	Short-range neutrality energy	V or eV
$\phi_{redox}$	Redox couple work function	eV
$\Phi_0$	Number of photons of wavelength $\lambda$ to $\lambda + d\lambda$ per area per second at some reference point $x_0$	$m^{-2} sec^{-1}$
$\chi$	Electron affinity	eV
$\omega$	Angular frequency of vibrational mode in solid; angular frequency of incident electromagnetic radiation	$sec^{-1}$
$\Omega_n$	Capture cross section for electrons	$m^2$
$\Omega_p$	Capture cross section for holes	$m^2$

## CHAPTER 1

# Introduction

### 1.1 PHOTOVOLTAIC ENERGY CONVERSION

As used in this book photovoltaic energy conversion refers to the direct conversion of the energy in light into usable electrical energy which may be employed immediately or stored. The basic ingredients for photovoltaic energy conversion are presented schematically in Fig. 1.1. These are seen to be a light-induced transition from ground state to excited state, a transport mechanism which conveys away the resulting excited electrons and holes, and a "check valve" of some sort which prevents these photogenerated electrons and holes from flowing backwards and recombining. In such a system the electrons, whose energy has been pumped up by the incoming photons, must go through some external path in order to lose their energy and recombine with the holes. This external path may involve an electrical load or some storage mechanism such as chemical storage.

The generalized schematic representation of photovoltaic action shown in Fig. 1.1 may be contrasted with a similar schematic, Fig. 1.2, illustrating the mechanism of natural photosynthesis. Again there is a light-induced transition from ground state to excited state (actually two are seen) and a transport mechanism with a check valve. In the energy conversion system

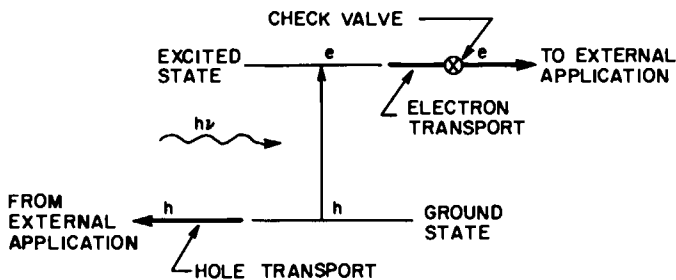


Fig. 1.1 Basic features of photovoltaic energy conversion. The check valve prevents backflow of the excited electrons.

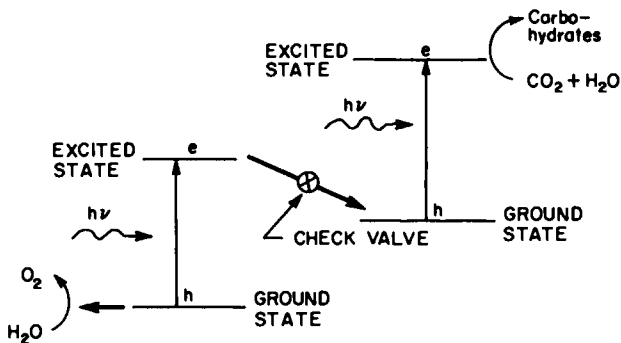


Fig. 1.2 Process of natural photosynthesis. Two photosystems are seen to be involved. Again, a check valve is involved to stop backflow.

devised by nature, the excited electrons and holes are used directly to store energy in chemical bonding.

This text explores the workings of the various man-made photovoltaic devices represented by Fig. 1.1. We shall find that there are a number of materials systems that can function as indicated in the figure. Our specific interest will be in those systems which can efficiently convert the energy in sunlight into usable electrical energy.

## 1.2 SOLAR CELLS AND SOLAR ENERGY CONVERSION

When one of the various man-made photovoltaic energy conversion systems represented by Fig. 1.1 is used to convert sunlight into electrical energy, it is termed a solar cell. The basic energy supply for a solar cell is photons of the solar spectrum and the basic product is usable electrical energy.

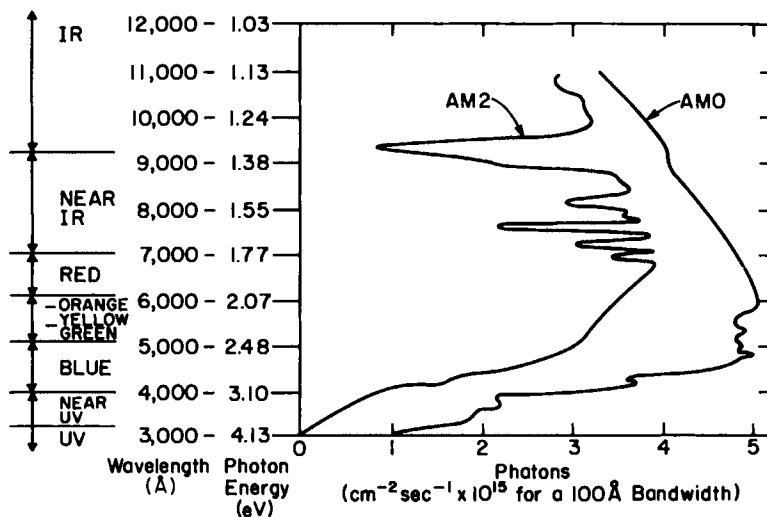


Fig. 1.3 The solar energy spectrum. Shown are air mass zero (AM0) and air mass two (AM2) spectra (based on Hovel [1]; used with permission).

Figure 1.3 shows two examples of solar spectra, air mass zero (AM0) and air mass two (AM2). The AM0 spectrum is the solar energy distribution available just outside the earth's atmosphere. The AM2 spectrum can be considered to be the solar energy distribution available at the earth's surface for average weather conditions [1, 2]. In general the designation AMX for  $x > 0$  is defined formally by  $x = [\cos \theta]^{-1}$  with  $\theta$  being the angle between the sun and the zenith. When the term "light" is used in the text, it refers to these AMX solar energy spectra.

### 1.3 SOLAR CELL APPLICATIONS

Photovoltaic energy conversion is used today for both space and terrestrial solar energy conversion. The success of solar cells in space applications is well known (communications satellites, manned space laboratories), and the need for the increased use of solar cells in terrestrial applications becomes clearer with the growing, widespread demand for a renewable and environmentally acceptable terrestrial energy resource.

As Hill [3] has pointed out, it is interesting to note that this coming, important terrestrial role for photovoltaic solar energy conversion was envisioned as early as 100 years ago by some of the first workers in photovoltaics. For example, writing in 1891, Appleyard [4] foresaw "the blessed vision of the Sun, no longer pouring his energies unrequited into

space, but, by means of photo-electric cells and thermo-piles, these powers gathered into electrical storehouses to the total extinction of steam engines, and the utter repression of smoke."

The effort to develop terrestrial photovoltaics as an important energy resource is not without its critics. Generally, they maintain that terrestrial photovoltaic solar energy conversion will not be successful commercially and financially because of basic technical and economic problems. They argue that these may take hundreds of years to solve, if indeed they are ever solved. Such criticism is valuable since it forces constant assessment and reevaluation, but, it must be kept in proper perspective. In 1926 the man whose invention ultimately led to the development of the TV tube said: "commercially and financially I consider (television) an impossibility, a development of which we need waste little time dreaming [5]." In 1948 a respected science magazine said "Landing and moving around the moon offers so many serious problems for human beings that it may take science another two hundred years to lick them [5]."

#### 1.4 GENERAL OUTLINE

This book is an examination of the physics and materials systems involved in solar photovoltaic energy conversion devices. The examination is divided into two sections. The first section (Chapters 1-3) encompasses the introduction and a résumé of the basic physical principles and materials properties which are the foundations of photovoltaic energy conversion. The second section deals with specific photovoltaic configurations: Chapter 4 covers *p-n* homojunction solar cells; Chapter 5 treats semiconductor-semiconductor heterostructure solar cells (including semiconductor-insulator-semiconductor cells); and Chapter 6 covers surface-barrier solar cells (metal-semiconductor, metal-insulator-semiconductor, and liquid-semiconductor heterostructures). Each of the device chapters consists of a brief background to establish the historical development of that particular device class, an in-depth development of the physical principles operative for that device class, and a survey of experimental work from the literature pertaining to the class.

#### 1.5 SOME COMMENTS

The units in this book are typical of those employed in solid state electronics usage. Energies are measured in electron volts or volts, charge in coulombs, lengths in microns ( $10^{-6}$  m) or nanometers ( $10^{-9}$  m), etc. Every attempt has been made to carefully define symbols as they appear. A

summary of many of the symbols used in this book, together with definitions and units, appears at the beginning of this book.

There may be some conventions used in this book that are not familiar to all readers and these will be pointed out when they first appear. For example, the measure of thermal energy ( $kT$ , Boltzmann's constant times absolute temperature) is in units of electron volts throughout. Consequently, in expressions such as  $\exp(E_F/kT)$  both the numerator and denominator of the argument are in electron volts.

### REFERENCES

1. H. J. Hovel, in "Semiconductors and Semimetals" (R. K. Willardson and A. C. Beer, eds.), Vol. 11, Solar Cells, Academic Press, New York, 1976.
2. A. Rothwarf and K. W. Böer, *Prog. Solid State Chem.* **10**, 71 (1975).
3. R. Hill, Thin Film Solar Cells in "Active and Passive Thin Film Devices" (T. J. Coutts, ed.), Academic Press, New York, 1978.
4. R. Appleyard, *Telegraphic J. and Electr. Rev.* **28**, 124 (1891).
5. "Planting Seeds for the Future." Champion International Corp., Stamford, Connecticut, 1979.

## CHAPTER 2

# Physics and Materials Properties Basic to Photovoltaic Energy Conversion

### 2.1 INTRODUCTION

In order to conceive new photovoltaic energy conversion schemes, to improve existing configurations, to choose materials, and to understand the origins of the technical and economic problems of solar cells, one must have more than an "idea" of how these devices work. One must understand the fundamentals of their operation. To achieve this fundamental understanding, certain concepts must be firmly established. With that goal in mind, a résumé of the physical principles and materials properties basic to photovoltaic energy conversion is presented in this chapter.

The mathematical models for phenomena which are fundamental to solar cell operation such as recombination, drift, and diffusion will be developed. Rather than simply presenting these models in the forms normally used in solid state, an outline of their derivation is presented. This is done because of a firm conviction that, by seeing the assumptions behind the various forms of these equations, one is better able to judge their appropriateness when used with materials under concentration, amorphous materials, organic materials, etc.

## 2.2 STRUCTURE OF SOLIDS

Solids can be broadly classified as being crystalline, polycrystalline, or amorphous. Crystalline refers to single-crystal materials; polycrystalline refers to materials with crystallites (crystals or grains) separated by disordered regions (grain boundaries); and amorphous refers to materials which totally lack long-range order.

### 2.2.1 Crystalline and Polycrystalline Solids

The distinguishing feature of crystalline and polycrystalline solids is the presence of a lattice. These materials possess long-range order (represented by the mathematical construct termed the lattice) and a basic building block (the unit cell) which defines the structure of the lattice of a given crystal. By translating the unit cell, the lattice is generated. By situating the constitutive atoms or molecules of the solid with respect to the lattice, the structure of these solids is determined. Every point in the lattice can be located by a vector  $\mathbf{R}$  drawn from some reference lattice point where any  $\mathbf{R}$  is given by [1]

$$\mathbf{R} = l\mathbf{a} + m\mathbf{b} + n\mathbf{c} \quad (2.1)$$

with  $l$ ,  $m$ , and  $n$  being integers. The vectors  $\mathbf{a}$ ,  $\mathbf{b}$ , and  $\mathbf{c}$  are three primitive basis vectors defining the lattice. Amorphous solids lack this long-range order found in crystalline and polycrystalline materials.

Polycrystalline solids differ from single-crystal solids in that they are composed of many single crystals. It is these single-crystal regions (grains) which exhibit the long-range order in a polycrystalline solid. The various grains comprising a polycrystalline solid may or may not have their lattices randomly oriented with respect to one another. If there is a correlation in the orientations of the grains, the situation is referred to as oriented polycrystalline material. The transition regions in a polycrystalline solid existing between the various single crystals are termed grain boundaries. These are regions of structural and bonding defects which are perhaps tens of angstroms or more in extent [2, 3] and which may contain voids. The influence of these grain boundaries on physical properties can be significant. As we shall see, electric field regions generally exist at grain boundaries and these regions can impede intergrain transport. Since the electric fields can extend into the grain, grain boundaries can also affect intragrain transport.

The grain boundaries of polycrystalline materials can be broadly classified as being either open or closed. An open boundary is easily accessible to gas molecules; a closed boundary is not. However, a closed boundary is expected to be an excellent conduit for solid state diffusion. Diffusion coefficients are generally an order of magnitude larger along such boundaries than those observed in bulk, single-crystal material [2, 3]. It is also

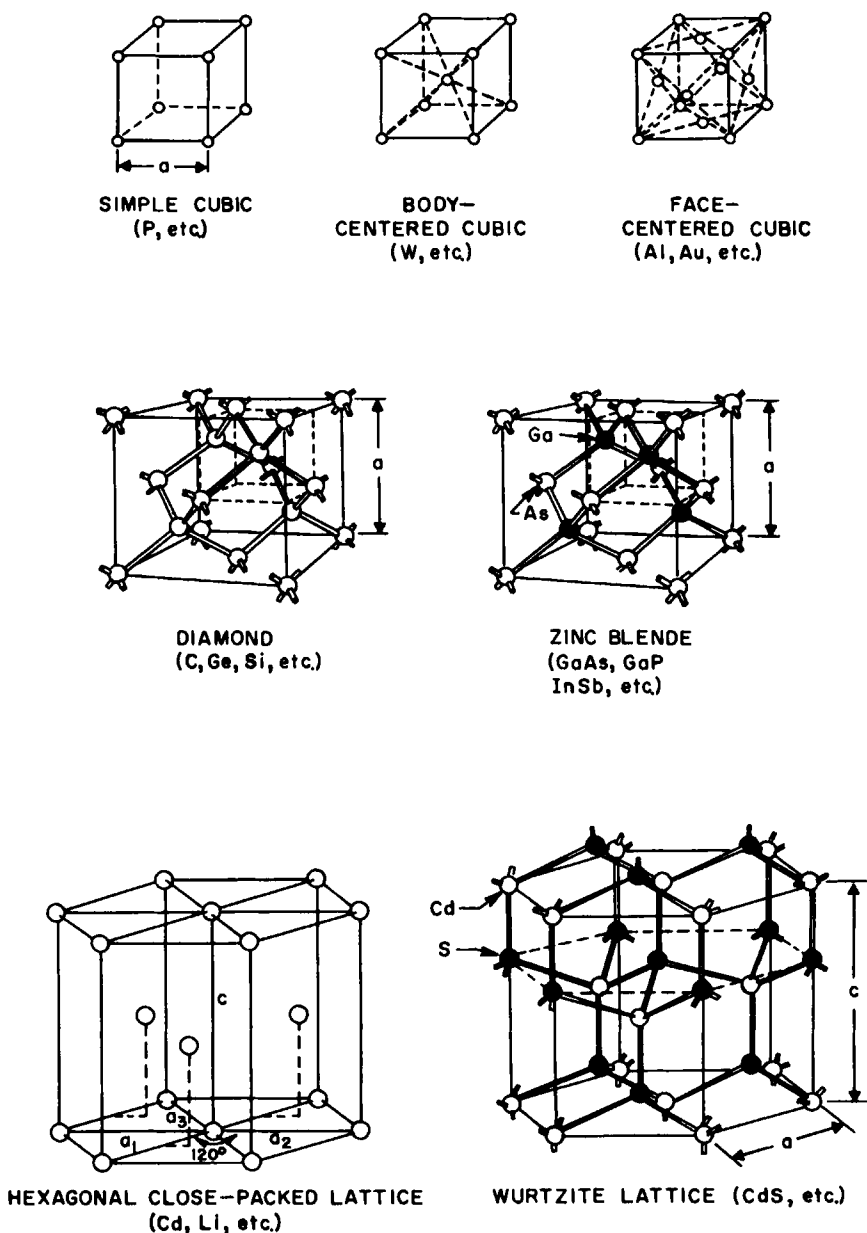


Fig. 2.1 Some important unit cells characterizing crystalline solids.

not surprising, given their physical and chemical structure, that grain boundaries in polycrystalline material can serve as sinks for impurities located in grains [4, 5].

Some of the more important unit cells characterizing the long-range order found in polycrystalline materials (in the grains) and in single-crystal materials (everywhere) are seen in Fig. 2.1 together with examples of materials which have those unit cells. Also shown are the definitions of conventional lattice parameters (e.g.,  $a$  for cubic structures;  $a$  and  $c$  for hexagonal closepacked) used to characterize these unit cells [1, 6].

One of the examples given in Fig. 2.1 is the semiconductor CdS which is seen to have the wurtzite lattice (two interpenetrating hexagonal close-packed lattices). It is interesting to note from the figure that certain planes of crystalline CdS are composed only of Cd atoms while certain others are composed only of S atoms. Obviously these planes have different physical and chemical properties (e.g., they etch differently). This example reminds us of the general need for some scheme to label crystallographic planes and directions. Such a labeling scheme is provided by Miller indices [1, 6].

### 2.2.2 Amorphous Solids

Amorphous solids<sup>†</sup> are disordered materials which contain large numbers of structural and bonding defects. They possess no long-range structural configuration which means there is no unit cell and no lattice. Rather, the solid is composed everywhere of a random arrangement of ion cores which displays only short-range order. However, amorphous materials can exhibit a high degree of short-range order. For example, x-ray and electron diffraction results show that the nearest-neighbor environments, at least for some<sup>‡</sup> amorphous Si and Ge, are almost exactly those found in single-crystal Si and Ge. On the other hand, beyond about fifth-nearest neighbors, these results show that the atoms of the amorphous Si and Ge samples are distributed nearly randomly [7–9].

Figure 2.2a shows radial distribution curves for a particular amorphous silicon and for crystalline silicon as obtained by a Fourier analysis of electron diffraction data [9, 10]. These data show that Si is tetrahedrally coordinated in the crystal and also in this amorphous Si sample. Further, the nearest-neighbor separation in this amorphous Si is unchanged from the

<sup>†</sup>Glasses are a subset of amorphous materials which have the property that they can be formed directly from the melt.

<sup>‡</sup>There is no one amorphous Si, Ge, etc. In the case of silicon, for example, the term amorphous silicon refers to an amorphous material which can be alloyed to varying degrees with hydrogen, fluorine, etc.

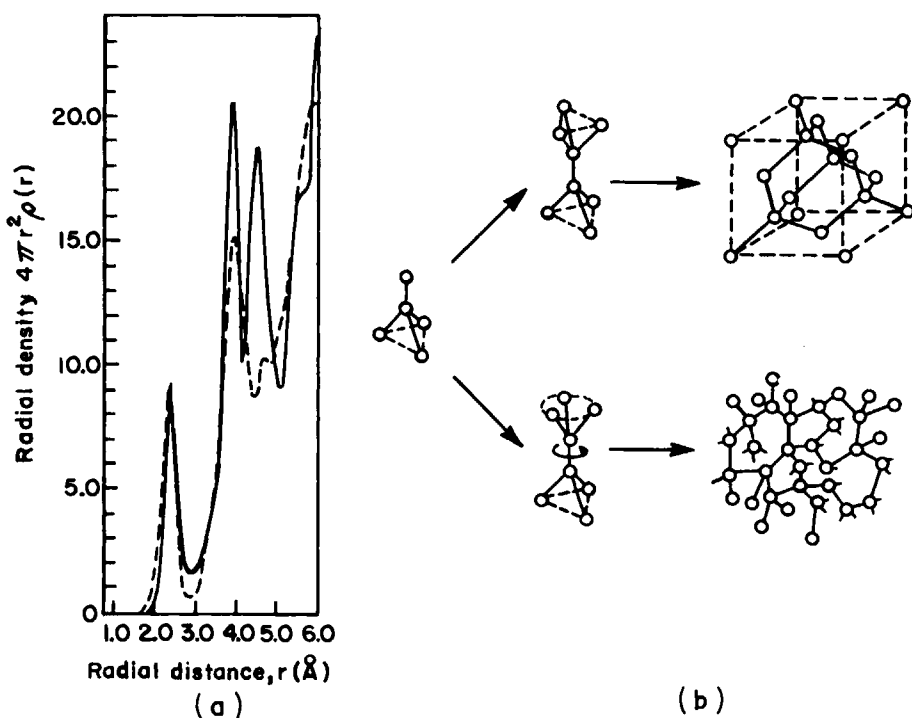


Fig. 2.2 (a) Radial distribution curves for an amorphous Si (----) and crystalline Si (—) as determined from electron diffraction data. (b) The manner in which the basic tetrahedral unit can lead to a crystal or to an amorphous, random network material (from a compilation in [33], Davis, with permission).

crystalline case to within 1 or 2% [9, 10]. Figure 2.2b shows how tetrahedral coordination leads to the fcc unit cell of crystalline Si (see Fig. 2.1) and how tetrahedral structure can be preserved in the network model (see Fig. 2.2) of amorphous Si [11, 12]. Bonding defects as well as voids can be seen in this network model of amorphous silicon.

It should be noted that some materials can exist in a form that contains almost equal regions of crystalline and amorphous phases as seen in Fig. 2.3. In this organic solid, amorphous domains containing disordered polymer chains are joined to crystalline regions where the chains form an ordered array. The possible existence for some organic and inorganic materials, under certain fabrication conditions, of such a mixed phase containing amorphous and microcrystalline regions is a practical consideration which can complicate the study of amorphous solids.

To study theoretically the vibrational bands or the electron energy bands

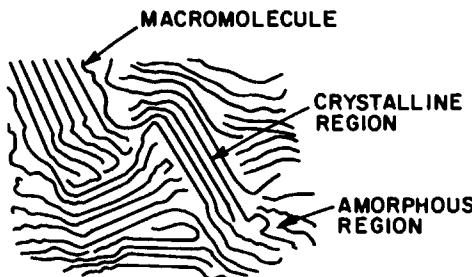


Fig. 2.3 Organic solid containing crystalline and amorphous domains. Some macromolecules of this solid are found in both types of regions.

in a crystal, one need only consider a unit cell and apply the appropriate boundary conditions at the cell boundary since this cell repeats in orientation and structure over and over again throughout the crystal. This mathematical approach (using Bloch functions) is not possible for amorphous materials. Consequently, theoretical understanding of the vibrational, electrical, and optical properties of amorphous materials is not nearly as advanced as it is for crystalline solids [9]. Because of this, the following discussions of physical properties and phenomena are done first in terms of crystalline solids. Then the necessary extensions or qualifications required for amorphous materials are made. Comments concerning polycrystalline materials are generally included in the discussion of crystalline solids.

### 2.3 PHONON SPECTRA OF SOLIDS

In solids, atoms find themselves in a force field resulting from their interaction with the rest of the nuclei and with all electrons of the solid. As a consequence of this force field, there is an equilibrium position for each particular atom. Because of the mutual interaction of atoms, the solid has certain vibrational modes. This mechanical vibration field is quantized with the quantum of vibrational energy being termed the phonon. At a given temperature  $T$ , atoms of a solid are oscillating about their equilibrium sites and therefore there are phonons present in the solid. In thermodynamic equilibrium the distribution of phonons among allowed modes of vibration (energy levels) is dictated by Bose-Einstein statistics [1, 6].

When an electron in a solid interacts with a vibrational mode, the event may be viewed as an interaction between two particles, an electron and a phonon. Phonons affect the optical characteristics of solids. They also affect electrical current transport and they are involved in energy transport.

### 2.3.1 Crystalline Solids

In crystalline solids there is a dispersion relationship  $\omega = \omega(\mathbf{k})$  which relates the angular frequency  $\omega$  of a vibrational mode permitted in a crystal to the wave vector  $\mathbf{k}$  of the mode. Alternatively [1, 6], this dispersion relation may be written as  $E_p = E_p(\mathbf{k})$ , since  $E_p = \hbar\omega$ . Here  $E_p$  is the energy of a phonon with momentum  $\hbar\mathbf{k}$ . For interactions between electrons and phonons in crystals, changes in  $\mathbf{k}$ -vector values must conserve total momentum as well as energy.

In crystalline solids the phonon energy bands  $E_p = E_p(\mathbf{k})$  are conveniently depicted in reciprocal space. In this space, distances have the dimensions of reciprocal length, and directions correspond to directions in the real crystal. Reciprocal space has a lattice defined by the three primitive basis vectors  $\mathbf{a}^*$ ,  $\mathbf{b}^*$ , and  $\mathbf{c}^*$ , where these are related to the three primitive basis vectors of the direct lattice by [1, 6]

$$a^* \equiv 2\pi \frac{\mathbf{b} \times \mathbf{c}}{\mathbf{a} \cdot \mathbf{b} \times \mathbf{c}}, \quad b^* \equiv 2\pi \frac{\mathbf{c} \times \mathbf{a}}{\mathbf{a} \cdot \mathbf{b} \times \mathbf{c}}, \quad c^* \equiv 2\pi \frac{\mathbf{a} \times \mathbf{b}}{\mathbf{a} \cdot \mathbf{b} \times \mathbf{c}} \quad (2.2)$$

Just as all the information on the structure of a crystalline solid is contained in the unit cell of the direct lattice, all the information on the dispersion relation  $E_p = E_p(\mathbf{k})$  is contained in the unit cell of the reciprocal lattice. The unit cell in reciprocal space is termed the first Brillouin zone or simply the Brillouin zone. The rest of reciprocal space (also called  $\mathbf{k}$  space) repeats this  $E_p = E_p(\mathbf{k})$  information. Figure 2.4 shows the Brillouin zones corresponding to fcc and bcc direct lattices. The notation is standard and denotes symmetry points and axes [1, 6].

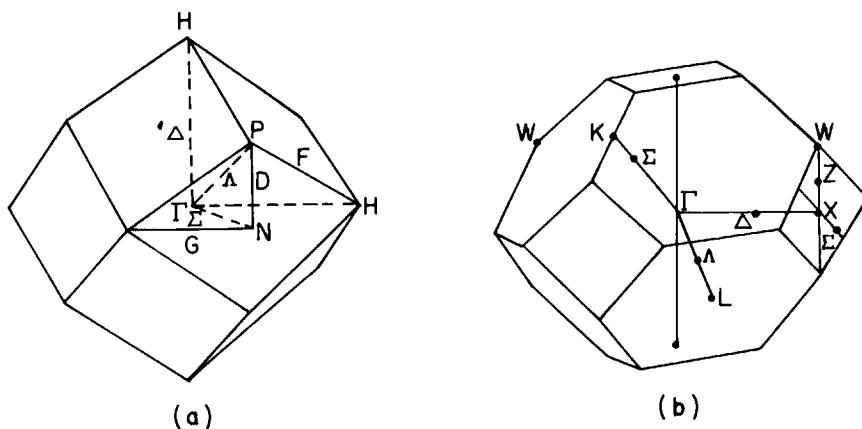


Fig. 2.4 Brillouin zones for (a) a bcc and (b) a fcc crystal structure.

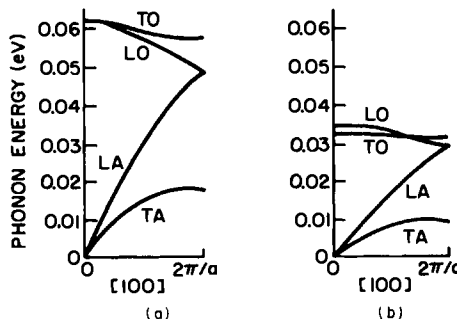


Fig. 2.5 Phonon bands in two crystalline solids, (a) Si, and (b) GaAs, for the [100] directions in the Brillouin zone. (From Ref. [6].)

Information on the dispersion relations  $E_p = E_p(\mathbf{k})$  for the lattice vibrations of two materials of interest to solar cell applications, crystalline silicon and gallium arsenide, is presented as an example in Fig. 2.5. Here the function  $E_p = E_p(\mathbf{k})$  is depicted for the [100] direction in the zone. The Brillouin zone for both of these semiconductors is that shown in Fig. 2.4 for fcc direct lattices. Thus the data of Fig. 2.5 give the phonon energies or bands (the functions are multivalued) found in these crystalline materials for  $\mathbf{k}$  vectors varying from  $\Gamma$  ( $|\mathbf{k}| = 0$ ) to  $X$  ( $|\mathbf{k}| = 2\pi/a$ ) in the Brillouin zone. In the figure the notation O refers to optical branches (in polar materials these modes can be strongly involved in optical properties); the notation A refers to acoustic branches (frequencies audible to the human ear are on these branches at the origin in Fig. 2.5). The notations T and L refer to the transverse and longitudinal modes, respectively. The largest values of  $|\mathbf{k}|$  in the Brillouin zone will depend on the lattice constant of the semiconductor; however,  $|\mathbf{k}|_{\max}$  is of the order of  $10^8 \text{ cm}^{-1}$ . From Fig. 2.5 it may be inferred that phonon energies in solids are of the order of  $10^{-2} \text{ eV}$  to perhaps  $10^{-1} \text{ eV}$ .

It must be remembered that the function  $E_p = E_p(\mathbf{k})$  is not really continuous, since only certain modes ( $\mathbf{k}$  vectors) are allowed in a given crystal. Consequently, there is a density of phonon states in  $\mathbf{k}$  space which can be expressed as a density of phonon states in energy  $g_p(E)$  by using  $E_p = E_p(\mathbf{k})$  [1, 6].

### 2.3.2 Amorphous Solids

In a perfect crystalline solid, a vibrational mode is the property of the whole crystal. The phonons associated with these vibrational modes are not localized; hence, through  $\Delta x \Delta k = \theta(2\pi)$ ,<sup>†</sup> it is seen that they can have a

<sup>†</sup> The notation  $\theta(2\pi)$  means of the order of  $2\pi$ .

well-defined wave vector  $\mathbf{k}$  and we plot the phonon energies allowed for these  $\mathbf{k}$  vectors in the Brillouin zone. In amorphous solids a vibrational mode may extend over only a few tens of angstroms. From  $\Delta x \Delta k = \theta(2\pi)$  it is clear that phonons in disordered materials are not characterized by a well-defined wave vector  $\mathbf{k}$ . In amorphous solids there is no Brillouin zone because there is no unit cell in the real crystal. Also, in these materials it becomes difficult to distinguish between acoustic and optical phonons. An additional complication is that changes in  $\mathbf{k}$  (or more precisely in  $\hbar\mathbf{k}$ ), occurring in phonon interactions with other particles, can no longer be predicted by overall momentum conservation. The quantity  $\mathbf{k}$  is no longer a "good quantum number." However, phonons still play the same role in electron transport, heat conduction, etc. in amorphous materials as they do in crystalline solids.

It follows that the concept of density of  $\mathbf{k}$  states in reciprocal space is not valid for disordered materials. However, the concept of a density of phonon states in energy  $g_p(E)$  is still valid. In fact, this  $g_p(E)$  of an amorphous solid will conform to that of the crystalline material to a degree depending on the importance of second nearest-neighbor, third nearest-neighbor, etc. forces [9].

#### 2.4 ELECTRON ENERGY LEVELS IN SOLIDS

A very helpful assumption which is usually valid for many solids is the Born–Oppenheimer or adiabatic principle. This asserts that, if one is solving the Schrödinger equation for the collection of the ion cores and valence electrons which make up a crystalline, polycrystalline, or amorphous solid, then one can separate the ion core motion from that of the valence electrons [13]. If the ion core motion (phonons) is of concern, then the overall effects of the valence electrons are described in suitable cohesive forces. If we are interested in characterizing the state of valence electrons in the solid, ion core positions are merely parameters and a single electron sees an effective potential resulting from the ion cores and the other valence electrons. In the context of this approach we have already considered the phonon spectra of solids. In this section we examine the resulting single-electron energy levels.

However, as we shall note in this section, it is not always possible to separate the Schrödinger equation for a solid into one problem dealing with phonons and into another dealing with electrons treated as single particles. We can have phonon–electron interactions giving rise to solutions to the overall Schrödinger equation of the solid, which are termed polarons, or we can have electron–electron interactions giving rise to solutions which are termed excitons. These are examples of multiparticle states.

### 2.4.1 Crystalline Solids—Single-Particle States

Because the unit cell of the direct lattice of a crystal completely specifies the structure of these materials, it completely determines the environment of an electron in a crystal. Essentially the Schrödinger equation for single electrons in a crystal, if applicable, need be solved for only one unit cell subject to boundary conditions which represent the periodicity of the structure. A dispersion relation  $E = E(\mathbf{k})$  comes out of this solution which specifies the energy  $E$  available to an electron in a single-particle state with wave vector  $\mathbf{k}$ . This wave vector  $\mathbf{k}$ , when multiplied by  $\hbar$ , may be viewed as the momentum of the electron, just as a phonon of wave vector  $\mathbf{k}$  could be viewed as having the momentum  $\hbar\mathbf{k}$ . As in the case of the phonon dispersion relation for a crystal, the periodicity of the direct lattice ensures that the electron dispersion relation  $E = E(\mathbf{k})$  is periodic in reciprocal space. Hence,  $E = E(\mathbf{k})$  can be completely displayed in the first Brillouin zone appropriate to the crystal.

A one-electron Schrödinger equation can be written for the valence electrons in silicon and gallium arsenide and both have the Brillouin zone of the fcc lattice seen in Fig. 2.4; consequently, the appropriate single electron  $E = E(\mathbf{k})$  functions for these materials can be plotted in this Brillouin zone [14, 15]. The information for certain directions in this first zone is presented in Fig. 2.6. From the dispersion relationships for these two example materials, it can be seen that both have a lower band of allowed electron energy levels (actually two bands), then a gap of forbidden energies of width  $E_g$ , and finally a band (or more precisely overlapping bands) of allowed energy levels. This type of band structure with allowed levels in a band, an energy gap with  $0 < E_g \lesssim 2.5$  eV, and then allowed levels in a band typifies an ideal semiconductor. In the ideal semiconductor the lower band (valence band) would be filled with valence electrons at absolute zero; the upper band (conduction band) would be empty at absolute zero. The energy levels in these bands belong to single-particle states which are delocalized and extend throughout the crystal.

Electrons in these delocalized band states react to an external force  $\mathbf{F}$  with an inertia that is dictated by the electronic configuration and physical structure of the crystal. The measure of this inertia of an electron in a given  $\mathbf{k}$  state is termed [6] its effective mass  $m^*$ . Since crystal bonding and structure will be different in different directions, it is not surprising that effective mass is actually a second-rank tensor. By definition, the effective mass—or rather its inverse—allows us to write [6, 16]

$$d\mathbf{V}/dt = (1/m^*) \cdot \mathbf{F} \quad (2.3)$$

where  $\mathbf{V}$  is the group velocity of an electron in a given  $\mathbf{k}$  state, and  $\mathbf{F}$  is the externally applied force. The second-rank tensor is the reciprocal effective

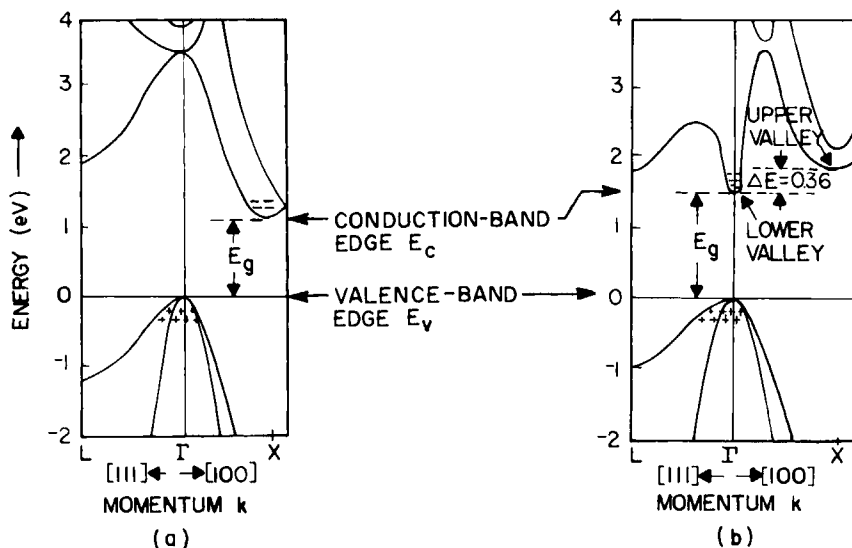


Fig. 2.6 Allowed energies versus  $\mathbf{k}$  vectors (wave vectors) for two crystalline, inorganic semiconductors, (a) Si, and (b) GaAs. Silicon is indirect gap; GaAs is direct gap. The valence band edges are aligned here for convenience only. (After Refs. [14] and [15], with permission.)

mass tensor. This tensor, for an electron in a given  $\mathbf{k}$  state, is given by [6, 16]

$$\left( \frac{1}{\mathbf{m}^*} \right) = \hbar^{-2} \begin{pmatrix} \frac{\partial^2 E}{\partial k_x^2} & \frac{\partial^2 E}{\partial k_x \partial k_y} & \frac{\partial^2 E}{\partial k_x \partial k_z} \\ \frac{\partial^2 E}{\partial k_y \partial k_x} & \frac{\partial^2 E}{\partial k_y^2} & \frac{\partial^2 E}{\partial k_y \partial k_z} \\ \frac{\partial^2 E}{\partial k_z \partial k_x} & \frac{\partial^2 E}{\partial k_z \partial k_y} & \frac{\partial^2 E}{\partial k_z^2} \end{pmatrix} \quad (2.4)$$

If the effective mass values in a given band are large, electrons in those states are tightly bound to the ion cores of the crystal. For such a situation the bandwidth  $\Delta E$  will be narrow.<sup>†</sup> If the effective mass tensor were equal to free electron mass times the unit tensor for a band, then electrons in such states would behave as free electrons.

The group velocity  $V$  referred to in Eq. (2.3) is the actual physical velocity of an electron in a given  $\mathbf{k}$  state. It can be obtained from the dispersion relation by [6, 16]

$$V = (1/\hbar) \nabla_{\mathbf{k}} E(\mathbf{k}) \quad (2.5)$$

<sup>†</sup> The bandwidth  $\Delta E$  is defined by  $\Delta E \equiv E_{\max} - E_{\min}$ , where  $E_{\max}$  is the highest energy in a band and  $E_{\min}$  is the lowest energy in a band.

where the operator  $\nabla_{\mathbf{k}}$  is the gradient operator in  $\mathbf{k}$  space. Thus, knowing the  $\mathbf{k}$  state that an electron in a crystal occupies allows the determination of its energy through  $E = E(\mathbf{k})$ , the determination of its effective mass through Eq. (2.4), and the determination of its group velocity in the crystal through Eq. (2.5). These statements apply to crystalline semiconductors, metals, and insulators.

As in the case of phonons, only certain  $\mathbf{k}$  vectors in  $\mathbf{k}$  space are permitted to electrons in a crystal [6]. Consequently, there is a density of permitted electron states in  $\mathbf{k}$  space. Through the dispersion relationship, this can be transformed into a density of states in energy, per unit volume of the crystal. We shall term this density of allowed electron single-particle states  $g_e(E)$ .

Plots of  $E = E(\mathbf{k})$  surfaces in the Brillouin zone or plots of  $E = E(\mathbf{k})$  for certain directions in the Brillouin zone (as in Fig. 2.6) represent detailed energy, effective mass, and momentum information for the delocalized (extended) states available to electrons in a given crystal. Frequently such detailed information is not required. In many applications it is necessary only to know the location in energy of the conduction band edge  $E_c$ , the location of the valence band edge  $E_v$ , and the bandwidths as functions of position  $x$ . In that case one plots, as a function of position  $x$  in the crystal and with respect to an arbitrarily chosen reference energy, the  $E_c$  and  $E_v$  seen in our examples of Fig. 2.6. Formally, bands such as those seen in Fig. 2.6 (and thus the locations in energy of  $E_c$ ,  $E_v$ , etc.) are representative of a region in the crystal which is large compared to a unit cell but small compared to the characteristic length over which material composition or some external potential varies. As an imposed potential varies or as the material composition varies,  $E_c$ ,  $E_v$ , etc. can move up or down in energy with respect to a fixed reference [6, 16].

Figure 2.7 shows one of these spatial energy band diagrams for an arbitrary, uniform semiconductor. The reference energy is the vacuum (or escape) level  $E_{VL}$  of the crystal. The energy required to go from the bottom of the conduction band to the vacuum level as it exists at some position  $x$  is the electron affinity  $\chi$ . The energy required to go from the top of the valence band to the vacuum level as it exists at some position  $x$  is the hole affinity  $E_g + \chi$ , where  $E_g$  is the width of the forbidden energy gap.

An ideal insulator differs from the ideal semiconductor of Fig. 2.7 only in that  $E_g \gtrsim 2.5$  eV, where the lower bound of 2.5 eV is really arbitrary. The point is that the gap in the ideal insulator is too wide to give any significant intrinsic carrier population at 300°K. A metal arises either when the gap  $E_g$  is zero or when the valence electrons only partially fill the lowest band at  $T = 0$  [1, 6].

Figure 2.7 represents the electron energy band scheme in a uniform

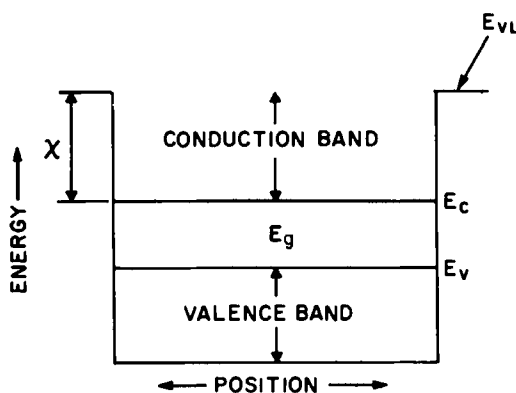


Fig. 2.7 Schematic showing the energy bands available in a semiconductor as a function of position. Reference energy is the vacuum energy  $E_{VL}$ .

composition, ideal crystal. This material is ideal in that only delocalized (extended) states in the valence and conduction bands are available to the valence electrons of the solid. However, real crystals have surfaces and these surfaces introduce localized states (physically localized at the surfaces), which may be populated by the electrons of the solid [6, 16, 17]. In addition, the bulk of a real crystal is not perfect since in the bulk there will be impurities and defects which will also introduce localized, atomic-like states at the positions of these impurities and defects [6, 16, 18]. Further, if a solid is polycrystalline, the structural and bonding defects of the grain boundaries cause localized states to exist in the grain boundary regions. A localized state is represented in energy band diagrams such as Fig. 2.7 by using a short horizontal line drawn at its position in energy and space.

Localized states found in crystalline and polycrystalline solids (and in amorphous solids, as we shall see) may be broadly classified as being either acceptorlike or donorlike in nature. These terms are defined by the following [6]:

(1) *Acceptor states* Neutral when unoccupied by an electron and, therefore, negative when occupied by an electron (ionized).

(2) *Donor states* Neutral when occupied by an electron and, therefore, positive when unoccupied by an electron (ionized).

Localized states are very important in semiconductors and insulators since they can serve as sources (doping) or sinks (recombination centers, trapping sites) for electrons and holes in the bands. Since they can be charged, they are very important in developing electric field regions (barriers) in semiconductors and insulators. The particular localized states which are important in semiconductors and insulators are those which lie,

in energy, in the forbidden gap. Localized states which do not lie in this gap would have their electrons delocalized due to the overlap with the delocalized states of the same energy in the bands. For this reason localized states (such as surface states) in metals are not of technological importance and are neglected in our discussions.

We have just outlined the essential features of the Bloch one-electron energy band picture of crystalline solids which has been extremely successful in describing the electrical properties of crystalline inorganic solids and which was applied as early as 1954 to crystalline organic solids [19]. In summary, this picture presents a crystalline solid as having energy bands (conduction and valence bands) of single-electron, delocalized (extended) states, which may be separated by a forbidden energy gap  $E_g$ . Single-electron localized states, which arise from defects and impurities, can exist in the gap.

When the band theory of single-electron states is applied to organic crystals, there are two approaches that may be taken: one may use the Bloch picture either to describe intermolecular single-electron states or to describe intramolecular single-electron states corresponding to a given macromolecule. Which of these approaches is more valid depends on the particular material under consideration; specifically, the larger the overlap integral for electron wave functions on two adjacent molecules the more valid is the approach of treating the solid as a whole [19–21].

When organic solids are treated as a whole, it is found that the interactions which bind the molecules into crystals are weak compared to inorganic crystals and that the bandwidths of organic crystalline solids are generally about  $10^{-2}$  to  $10^{-1}$  eV. This is about an order of magnitude less than the bandwidths generally found in inorganic crystalline solids and is of the order of magnitude of phonon energies (see Section 2.3.1) and estimated polaron binding energies (see Section 2.4.3). As a consequence, it may not be totally appropriate to describe the electrical properties of some organic crystals in terms of single-electron states [20]. It may be necessary to describe these solids in terms of multiparticle states. Such states are found to be important in some inorganic crystalline materials, also.

The Bloch picture of energy bands of delocalized single-electron states with well-defined  $\mathbf{k}$  vectors was developed by relying on the mathematical expediency provided by the presence of long-range order. It has been recently realized that long-range order is not as physically important to the existence of bands of single-electron states as once thought [22, 23]. In fact, from the standpoint of the tight-binding approximation of band theory [24], electronic energy levels in a solid depend primarily on the nature of the atom from which an electron originates and on the nature and position of its nearest neighbors. This near environment can be very similar in

crystalline and amorphous solids as we have mentioned. The effect of the presence in crystalline solids or of the absence in amorphous solids of long-range order can then be viewed as a perturbation on a basic scheme of single-electron levels determined by the near environment [23]. We can now adopt a more general view of delocalized single-electron energy bands in solids, which allows for the possibility that such bands may exist in amorphous solids. As was the case for phonons, we do not expect  $\mathbf{k}$  vectors to be "good quantum numbers" for band states in disordered solids.

#### 2.4.2 Amorphous Solids—Single-Particle States

From the preceding comments it follows that our generalized band picture can be used to describe amorphous solids. However, the discussion can only be in terms of diagrams such as Fig. 2.7, since diagrams such as Fig. 2.6 are not applicable. From this it also follows that the formal definition given by Eq. (2.4) for effective mass is not valid for amorphous solids nor is the definition given by Eq. (2.5) for group velocity. The concept of density of electron states (states available per energy per volume) is still valid in amorphous materials. Figure 2.8a shows a schematic representation of this density of states function  $g_e(E)$  for an amorphous solid. This may be contrasted with Fig. 2.8b showing  $g_e(E)$  for a crystalline solid which happens to have a donor level present.

From Fig. 2.8 it is clear that amorphous materials can contain large numbers of localized gap states. These are essentially of two types [25]: intrinsic and extrinsic. The intrinsic localized states are defined [25] as those arising from the distribution of bond angles and interatomic distances statistically occurring in an amorphous solid, and the extrinsic localized states are defined [25] as those arising from defects (broken chemical bonds) and impurities (as in crystalline solids). Intrinsic localized states are expected to be the principal contribution to the localized states occurring near the band edges (see Fig. 2.8a); defect states are believed to be the source of the large density of localized states typically seen over the remainder of the gap in many amorphous materials [25]. As long as the density of these defect states is large, doping will have little effect on dislodging the Fermi level position in the gap.

Since the localized state density is so large in many amorphous materials, transport via these gap states is possible; i.e., an electron can move from one localized site to another. We shall discuss this in detail later. It suffices to note at this point that transport via these localized states would give rise to small mobilities compared to transport involving the delocalized states. Hence, there is a mobility gap seen in Fig. 2.8a rather than a true gap, and this mobility gap is expected to have sharp boundaries  $E_c$  and  $E_v$ , which serve as the demarcation between localized and delocalized states [9, 25].

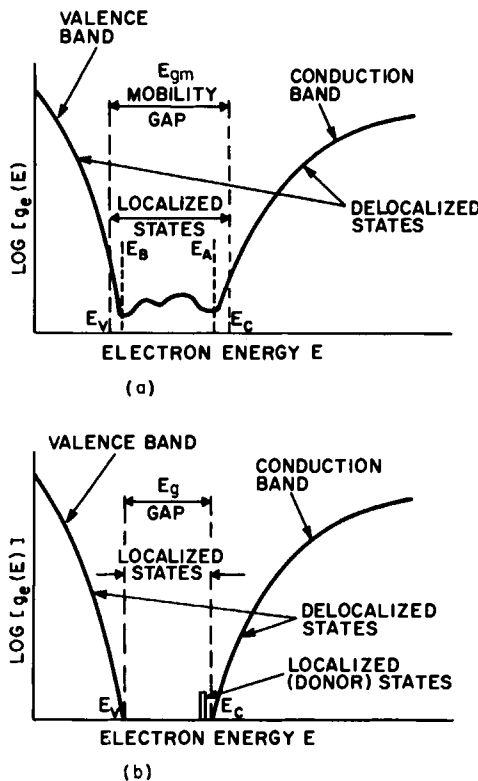


Fig. 2.8 Schematic showing the density of states function  $g_e(E)$  for an amorphous (a) and for a crystalline (b) solid.

### 2.4.3 Crystalline Solids—Multiparticle States

Up to this point we have considered only single particle electron states in crystalline and noncrystalline solids. However, in some materials, multiparticle states, resulting from electron-electron interactions or electron-phonon interactions, could be important.

Generally, we tend to think of some excitation, such as light, as being capable of exciting an electron from the single-electron states of the valence band to the single-electron states of the conduction band in a solid with the resulting hole and electron being free particles. However, if the attraction between an electron and hole is considered, one must admit the possibility that such an excitation could produce an electron bound to a hole,<sup>†</sup> and this bound pair could then wander throughout the solid as a unit. The unit resulting from the electron-hole interaction is termed an exciton [26]. An

<sup>†</sup> Of course, it is also possible that the electron could recombine almost immediately with the hole from which it came. This is referred to as geminate recombination.

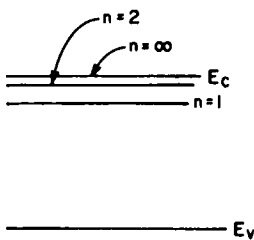


Fig. 2.9 Energy levels for the electron-hole bound pair (the exciton) and several excited levels. The conduction band edge  $E_c$  is the reference and it represents dissociation. Excitons have the kinetic energy of their centers of mass in addition to these energies.

exciton can be viewed as being an excited state of an atom [27] or molecule [28] in a solid which is passed on through the material by quantum mechanical resonance. The motion of an exciton does not give rise to charge transport.

Depicting an allowed exciton energy level in a figure such as Fig. 2.7 does present some difficulties since this figure shows allowed single-particle energy levels. However, by referring the exciton energy levels to the edge of the conduction band as seen in Fig. 2.9, exciton levels may be represented on these diagrams. If the electron bound to the hole can be thought of as a generalized hydrogen atom, then the exciton energies  $E$  labeled by  $n = 1, 2$ , etc. are given by [26]

$$E = -(m_{ex}^* e^4 / 2h^2 \epsilon^2)(1/n)^2 \quad (2.6)$$

with respect to the conduction band edge. Here the effective mass of the exciton  $m_{ex}^*$  is given by  $[1/m_e^* + 1/m_h^*]^{-1}$ . The lowest bound state for the exciton corresponds to  $n = 1$  and is  $(m_{ex}^* e^4) / (2h^2 \epsilon^2)$  below the conduction band edge  $E_c$ . The state  $n = \infty$  corresponds to dissociation (ionization) of the exciton into an electron in a single-particle state at the bottom of the conduction band and a hole in a single-particle state at the top of the valence band.

In addition to the energy of Eq. (2.6), an exciton can have kinetic energy; it can wander throughout the crystal as a mobile pair. To convey this fact, the exciton levels in Fig. 2.9 are not shown dashed but rather as continuous lines. If an exciton is formed in a solid, it may decay by phonon or photon emission. Alternatively, an exciton may result in a free electron and a free hole. This dissociation can take place at a defect, at a surface, in an electric field region, or due to photoionization.

Another multiparticle interaction possible in solids is that between electron and lattice; i.e., electron-phonon interaction. This may be viewed as a distortion of a lattice due to the presence of the charge of an electron (or hole). The electron and its associated lattice distortion (polarization) cloud are termed a polaron [29, 30]. A polaron may also be viewed as a self-trapped carrier—a carrier trapped in a potential well created by its own distortion of the lattice. Polarons can produce charge transport by hopping

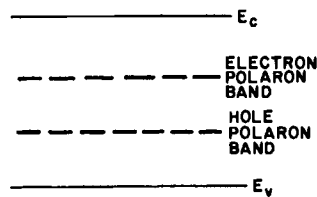


Fig. 2.10 Schematic representation of polaron energy levels.

from one such trapped position to another. An energy level scheme depicting polaron energy levels which is compatible with single-electron levels is presented in Fig. 2.10. Both "electron" and "hole" polaron levels are shown for the hypothetical material of Fig. 2.10.

Polarons populating these levels could be formed in a number of ways. As an example of one possibility, we can suppose that light with photon energies  $\geq E_c - E_v$  creates free electrons and free holes in single-particle states in the conduction and valence bands, respectively. If the material is conducive to polaron formation (generally materials with high dielectric constants are expected to be more conducive), the adjustment of the lattice to the presence of these electrons and holes will self-trap the carriers. This results in the coupled carrier-lattice energy levels seen in Fig. 2.10 being populated by polarons. As mentioned, these can then move about the solid by hopping, a transport mechanism to be discussed in detail in Section 2.7.

#### 2.4.4 Amorphous Solids—Multiparticle States

In general, the disorder in amorphous solids is expected to make them more conducive than crystalline solids to exciton and polaron formation. This can be argued simply from the point of view that disorder tends to constrain the motion of a carrier, making exciton or polaron formation easier in these materials than in their crystalline counterparts. The presence of polarons has been used to explain the transport properties of chalcogenide glasses [31] and excitons have been used to model transport phenomena in amorphous merocyanine films [32].

### 2.5 OPTICAL PROPERTIES OF SOLIDS

Figure 2.11 schematically shows the various processes which absorb electromagnetic radiation in solids and their range of influence. Process 1 is free-carrier absorption (characterized by the absorption coefficient  $\alpha$ ); it arises from electron (or hole) transitions within a band from one single-particle state to another. These intraband transitions are important in metals and semiconductors whenever there is a significant density of carriers in a band; transitions of the type seen in Fig. 2.12a would be

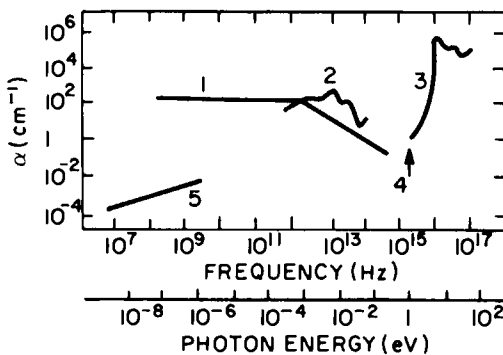


Fig. 2.11 Schematic representation of optical absorption processes. See text for descriptions. (Based on Davis [33]; with permission.)

forbidden in crystalline solids (due to  $\mathbf{k}$  conservation), if it were not for the presence of the scattering processes (defects, impurities, phonons) which give rise to dc conductivity [33]. Process 1 transitions seen in Figs. 2.12a and 2.12b are for the case of a crystalline solid.

Process 2 of Fig. 2.11 is phonon absorption. This normally occurs in the infrared region of the spectrum and three phonon-caused absorption processes can be distinguished [33]:

(a) The “reststrahl” process occurring due to the coupling of the radiation to the oscillating dipole moments in the solid. This takes place in ionic crystals by the creation of optical phonons with  $\mathbf{k} \approx 0$  (see Fig. 2.5).

(b) Multiple-phonon processes, occurring in ionic and covalent materials, due to one vibrational mode inducing instantaneous charges on the lattice sites, and another mode simultaneously vibrating these induced charges. The resultant oscillating moment couples to the radiation field.

(c) Single-phonon processes, in covalent materials, which cause a change in the dipole moment if there are three or more atoms per unit cell. Also, defects and impurities can allow one-phonon absorption processes to take place since they destroy periodicity.

Process 2, phonon-caused absorption, occurs in crystalline and amorphous materials, but the fine structure present in crystalline materials is usually lost in their amorphous counterparts. One-phonon processes may become more favorable in amorphous solids due to the disorder present.

Processes 3–5 of Fig. 2.11 involve electrons in a solid. Process 3 labels the electron interband transitions seen schematically in Fig. 2.12c. In these transitions, electrons move from single-particle states in the valance band into single-particle states in the conduction band; however, the onset of these transitions may be marked by exciton formation.

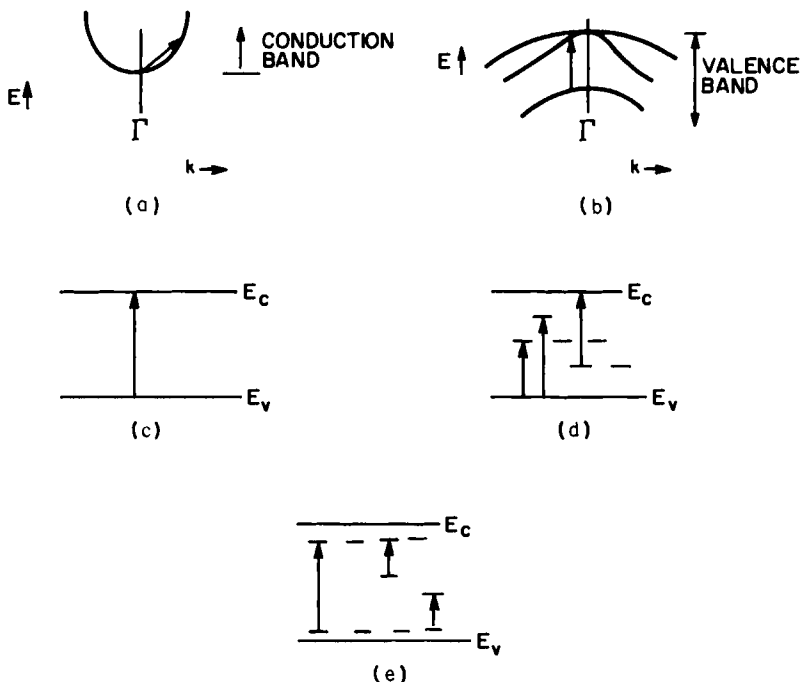


Fig. 2.12 Electron transitions between single-particle states giving rise to optical absorption. (a, b) Free-carrier (intraband) transitions give rise to process 1 of Fig. 2.11. (c) Band-to-band transitions give rise to process 3. (d) Band-localized-state transitions can be the source of process 4, as can (e) localized-state-localized-state transitions.

This brings us to the absorption process, labeled process 4 in Fig. 2.11. Process 4 could involve exciton formation, it could involve electron transitions to or from localized gap states and a band, or could involve transitions between localized band gap states. The latter two possibilities are seen schematically in Figs. 2.12d and 2.12e. Process 5 is an ac loss observed in some amorphous materials; it probably arises due to electrons hopping from localized site to localized site [33].

In crystalline semiconductors and insulators, the transition from process 4 to process 3 is marked by a sharp increase in the absorption coefficient  $\alpha$  at the fundamental absorption edge which occurs for  $h\nu = E_g$ . In some crystalline materials, exciton formation can be important, leading to discrete line spectra at energies just below the fundamental edge [33]; in crystalline solids the functional form of  $\alpha = \alpha(\lambda)$  at and above the fundamental absorption edge will depend on whether the solid has a direct or indirect gap. The  $\alpha = \alpha(\lambda)$  of process 3 is a very important material property for solar cells since process 3 creates free carriers in delocalized states.

To discuss  $\alpha = \alpha(\lambda)$  above the fundamental absorption edge in crystalline solids, we turn to Fig. 2.6. We recall that this figure depicts single-particle electron states available, as a function of  $k$ , in a direct gap (GaAs) and in an indirect gap (Si) crystalline semiconductor. For the case of the direct gap material, it is seen that an electron can be excited from the top of the valence band to the bottom of the conduction band in such a material with essentially no change in  $k$  vector required. Even though a photon would have  $k \approx 0$  on the scale of Fig. 2.6, there is no difficulty in  $k$ -vector conservation in electron-photon interactions which result in an electron being excited across a direct gap. This is not the case for an indirect gap material as Fig. 2.6 also shows. An electron excited across an indirect gap must change its  $k$  vector. The photon simply cannot supply the momentum; hence phonon involvement is required. As seen in Fig. 2.5, phonons can supply the necessary momentum but conservation of total energy and total momentum for the three particles (electron, photon, and phonon) must now apply. This necessity of a three-body interaction in indirect gap materials tends to lessen the magnitude and crispness of  $\alpha = \alpha(\lambda)$  at and above the fundamental absorption edge as may be seen in Figs. 2.13 and 2.14. Presented here are  $\alpha = \alpha(\lambda)$  at and above the fundamental absorption edge

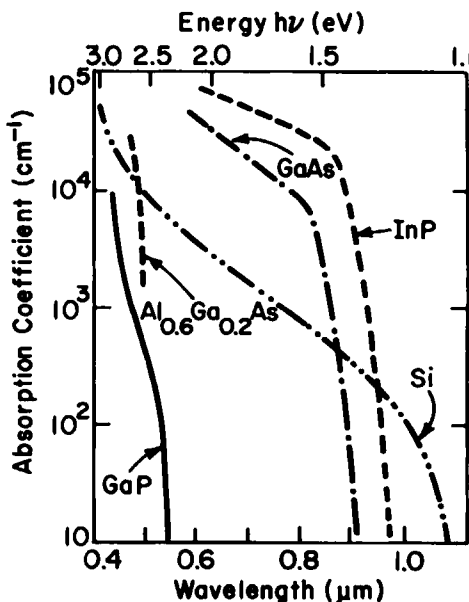


Fig. 2.13 Absorption coefficient  $\alpha$  as a function of wavelength for the elemental semiconductor silicon and several III-V compound semiconductors. The Si is indirect gap and the III-V's shown are direct gap. (Compiled from Refs. [34-37].)

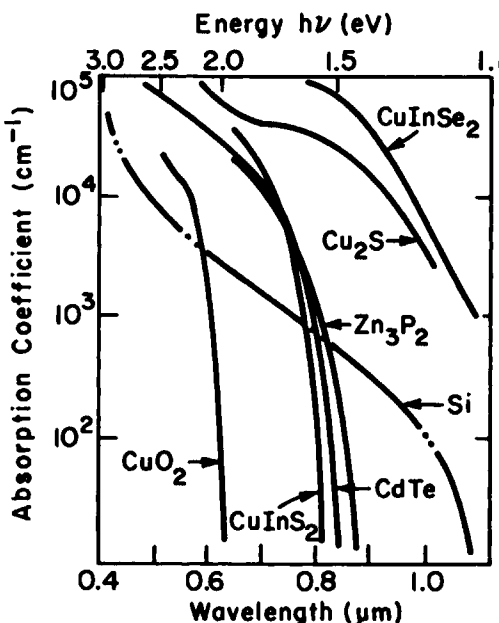


Fig. 2.14 Absorption coefficient  $\alpha$  as a function of wavelength for the elemental semiconductor silicon and several compound semiconductors. The indirect gap material silicon is given again as a basis of comparison. All the other materials shown have direct gaps except possibly  $\text{Cu}_2\text{S}$ : the nature of its interband transitions is not firmly established. (Compiled from Refs. [34-37].)

for silicon (shown in both figures for comparison) and several other crystalline semiconductors of interest to photovoltaics.

The distinction between processes 3 and 4 of Fig. 2.11 generally becomes difficult to discern in amorphous solids. The basic reason for this is that, as seen in Fig. 2.8, amorphous solids can contain large densities of localized gap states. These can be intrinsic-gap states arising from the distribution of bond angles and interatomic distances, and extrinsic-gap states arising from defects and impurities (see Section 2.4.2). As a result, the absorption edge in amorphous materials often is broad [25, 33]. Three regions of behavior of the function  $\alpha = \alpha(\omega)$  near the absorption edge sometimes can be seen [25]. These are depicted in Fig. 2.15.

Region A of Fig. 2.15 is the strong absorption range and in this range  $\alpha = \alpha(\omega)$  often has the form [25]

$$\omega\alpha(\omega) \sim (\hbar\omega - E_{go})^r \quad (2.7)$$

where  $r$  is a constant of the order of one. The physical origin of this behavior has been proposed to lie in band-to-band (delocalized state) transitions with a relaxation of the  $\mathbf{k}$ -vector conservation constraint, or it

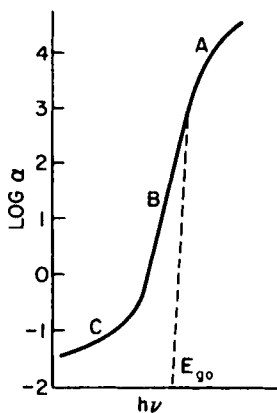


Fig. 2.15 General shape of the absorption edge seen in some amorphous solids. Regions A, B, and C are discussed in the text. (Based on Ref. [25])

has been proposed to lie in transitions involving intrinsic, localized states near the valence (conduction) band and delocalized conduction (valence) band states [25, 33]. An optical energy gap  $E_{go}$  can be extracted from a fit to Eq. (2.7). Depending on the amorphous material and the physical processes involved, this may represent a true gap in the density of states, the mobility gap, or something related to these energies [33].

A number of mechanisms have been proposed for behavior which is depicted by regions B and C of Fig. 2.15. These regions, variously seen in some amorphous materials, have been explained in terms of localized-state-localized-state transitions, transitions involving extrinsic localized states and the bands, and a broadened exciton response [25, 33].

Overall, due to the relaxation of the  $\mathbf{k}$ -vector conservation rules, absorption at and above the fundamental absorption edge can be stronger for amorphous materials than for corresponding crystalline material. Figure 2.16 compares  $\alpha = \alpha(\lambda)$  for several amorphous silicon alloys with crystalline Si. Also shown in the figure are data for the polycrystalline organic dye hydroxy squarylium. Many organic materials such as this example have very high absorption coefficients [35, 36]; however, they also have high densities of gap states.

Since charge-separating electric fields are fundamental to the devices we shall be considering, it is important to bear in mind that strong electric fields can shift the fundamental absorption edge in solids. This phenomenon is known as the Franz-Keldysh effect [38, 39] and its explanation lies in Fig. 2.17. As seen in the presence of an electric field, a delocalized valence-band wave function leaks into the forbidden gap. The same is true for the wave function of a delocalized state in the conduction band. Therefore, the states at the band edges are extended into the gap such that the probability

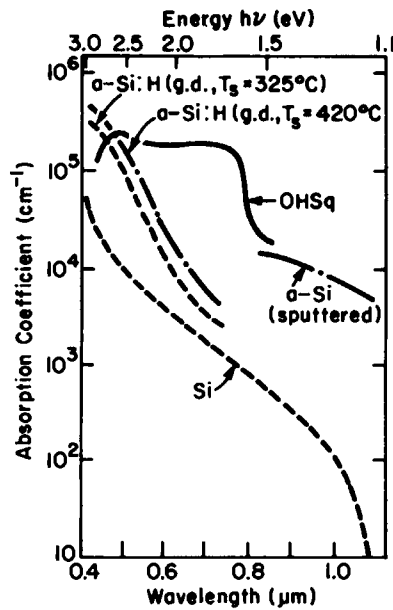


Fig. 2.16 Absorption coefficient  $\alpha$  as a function of wavelength for single-crystal silicon, several amorphous silicon alloys, and polycrystalline hydroxy squarylium. Single-crystal Si has been shown again for comparison. For the amorphous silicon alloys, g.d. refers to glow discharge and  $T_g$  to the substrate temperature during film growth. (Compiled from Refs. [34–37].)

$P$  of finding an electron in one of these state decreases in the band gap according to [40]

$$P \sim \exp - (E'/\Delta E) \quad (2.8)$$

where in this case we are using  $\Delta E$  to mean

$$\Delta E = \frac{3}{2}(m^*)^{-1/3}(e\hbar\xi)^{2/3} \quad (2.9)$$

Here the energy  $E'$  is defined in Fig. 2.17 and  $\xi$  is the electric field. It is seen in Fig. 2.17 that an electron in the valence band can make the transition into such a tail from the conduction band with the absorption of a photon  $h\nu < E_g$ . This gives rise to the shift in the fundamental absorption edge. In amorphous materials one would expect such tails could extend further into the gap due to overlapping with localized gap states.

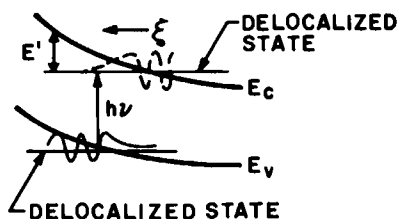


Fig. 2.17 Franz-Keldysh effect allows photon absorption for  $h\nu < E_g$ . As seen, the process involves tunneling and photon absorption in the presence of an electric field  $\xi$ .

As we survey the various absorption processes outlined in Fig. 2.11, we see that process 3 is a useful absorption process from the point of view of photovoltaics, since it can produce free electrons and free holes (and mobile polarons). At the transition from process 4 to process 3 (i.e., near the fundamental absorption edge) absorption may result in the creation of excitons. These can be useful to photovoltaics if they are mobile and can be torn apart in the presence of a high field giving charge carriers. Process 4 can also be directly useful, even if it produces electrons and holes in localized states, provided these carriers in localized states can hop from site to site giving rise to transport. Process 4 can be indirectly useful in that any resulting photoconductivity can decrease series resistance in photovoltaic devices. We return to these points in subsequent sections. From Figs. 2.11 and 1.3 it is seen that processes 3 and 4 couple well to the solar spectrum, which is fortunate for photovoltaic solar energy conversion.

## 2.6 RECOMBINATION, TRAPPING, AND GENERATION IN SOLIDS

### 2.6.1 Recombination and Trapping

Once electrons are excited to higher energy levels in a solid, they can return to a low-energy configuration by one of several recombination processes: (a) an electron can give up its energy through radiative recombination which involves emission of a photon (this may or may not also involve phonons); (b) an electron can give up its energy through Auger recombination, which involves the transfer of its energy to another electron or hole; or (c) an electron can give up its energy by emission of a phonon or phonons. Generally, this latter process will involve localized states existing in the bulk of a material, at surfaces, and at grain boundaries. Multiparticle states also have similar mechanisms for relaxing back to the ground state; for example, excitons can decay by radiation. The principle of detailed balance tells us that in thermodynamic equilibrium all of these recombination processes are exactly offset by corresponding thermal generation processes.

#### 2.6.1.1 Radiative Recombination

Considering the radiative recombination  $r^R$  (number per time per volume) of electrons in the delocalized states of the conduction band to the delocalized states of the valence band, we note that the corresponding generation process  $g^R$  (number per time per volume) produces electrons in the conduction band and holes in the valence band. In thermodynamic

equilibrium this  $g^R$  has the value  $g_{th}^R$  which is governed by the number of photons present in the solid at the temperature  $T$ , and by the rate these photons are absorbed by valence-band electrons causing a transition to the conduction band. The number of inherent photons present in thermodynamic equilibrium is given by Planck's distribution [1]. The mean lifetime of the photons is  $(\alpha v_g)^{-1}$ , where  $v_g$  is the photon group velocity and  $\alpha$  is the absorption coefficient<sup>†</sup> for wavelength  $\lambda$ . Hence  $g_{th}^R$  can be shown to be given by [41]

$$g_{th}^R = \frac{8\pi c^2 k^4 T^4}{h^4} \int_0^\infty \frac{\alpha(x)[\eta(x)]^2 x^3 dx}{e^x - 1} \quad (2.10)$$

where  $x = h\nu/kT$ ,  $c$  is the speed of light, and  $\eta$  is the refractive index. In thermodynamic equilibrium  $r^R = g_{th}^R$ .

When the solid is not in thermodynamic equilibrium, there is a net recombination rate  $\mathcal{R}^R$  defined by

$$\mathcal{R}^R = r^R - g^R \quad (2.11)$$

In this situation, if the photons inherent to the material can still be characterized by a temperature  $T$ , then  $g^R = g_{th}^R$ . Also, we would expect  $r^R$  to be proportional to the product of the conduction-band electron number density  $n$  and valence-band hole number density  $p$ . Consequently, Eq. (2.11) becomes

$$\mathcal{R}^R = (g_{th}^R/n_i^2)(pn - n_i^2) \quad (2.12)$$

where  $n_i^2 = n_0 p_0$  (the subscript zero refers to thermodynamic equilibrium values) is the square of intrinsic number density. Equation (2.12) is the mathematical model for band-to-band radiative recombination.

A time  $\tau^R$  which characterizes this net recombination process can be defined by  $\mathcal{R}^R = \Delta p/\tau^R = \Delta n/\tau^R$ , where  $\Delta p$  and  $\Delta n$  are the deviations<sup>‡</sup> of the hole and electron number densities from their thermodynamic equilibrium values  $p_0$  and  $n_0$ . Since  $p = p_0 + \Delta p$  and  $n = n_0 + \Delta n$ , Eq. (2.12) becomes

$$\mathcal{R}^R = (g_{th}^R/n_i^2)(\Delta p + n_0 + p_0) \Delta p$$

which allows us to write

$$\tau^R = (n_i^2/g_{th}^R)(\Delta p + n_0 + p_0)^{-1} \quad (2.13)$$

Equation (2.13) indicates that the lifetime  $\tau^R$  associated with band-to-band radiative recombination is expected to decrease with increasing doping and

<sup>†</sup> Whether the solid is amorphous (no  $k$  conservation) or crystalline (direct or indirect gap) is accounted for by  $\alpha$ .

<sup>‡</sup> We assume space-charge neutrality at this point for simplicity; i.e.,  $\Delta n \approx \Delta p$ .

with increasing deviations in the number densities away from their thermodynamic equilibrium values. We note that, if a material is *n*-type, for example, and one has a situation where  $\Delta p \ll n_0$ , then Eq. (2.13) simplifies to

$$\tau_p^R = (n_i^2/g_R^{\text{th}})[1/N_D] \quad (2.14)$$

for a doping density of  $N_D$ .

### 2.6.1.2 Auger Recombination

A second process by which electrons relax to lower energies is Auger transitions. Figure 2.18 indicates some Auger recombination processes possible in solids. Considering the band-to-band process seen in Fig. 2.18a,

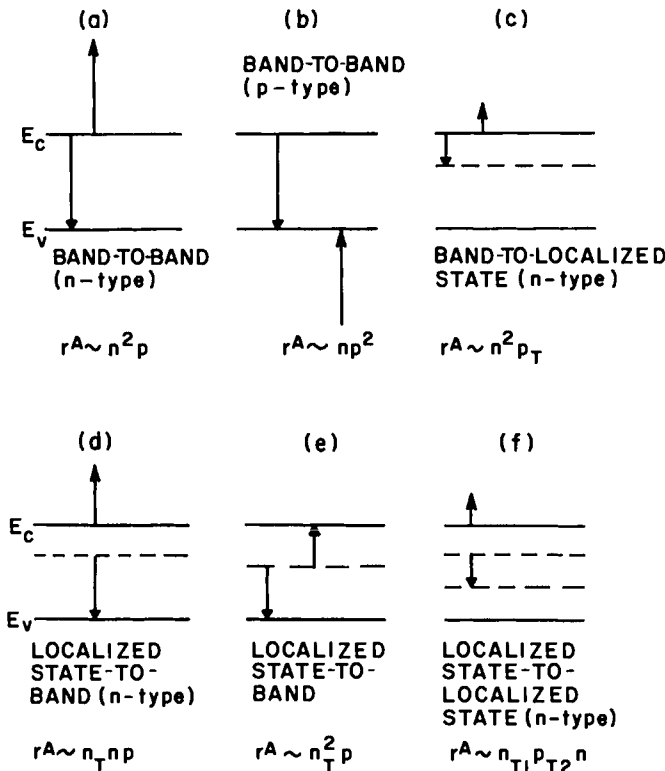


Fig. 2.18 Some possible Auger transition processes in solids. The dependence of  $r^A$  on the various number densities involved is indicated. Here  $p_T$  gives the number of empty localized states per volume and  $n_T$  gives the number of occupied localized states per volume. (Adapted from Ref. [42].)

we expect the Auger recombination rate  $r_A^A$  for this path to obey [42]

$$r_A^A = A_{1A}^A n^2 p \quad (2.15)$$

and we expect the corresponding generation process  $g_A^A$  to obey

$$g_A^A = A_{2A}^A n \quad (2.16)$$

where  $A_{1A}^A$  and  $A_{2A}^A$  depend on the material under consideration. Again we examine the thermodynamic equilibrium situation which allows us to note that  $A_{1A}^A n_0 p_0 = A_{2A}^A$ . Since the net Auger band-to-band recombination rate  $\mathcal{R}_A^A$  may be written as

$$\mathcal{R}_A^A = r_A^A - g_A^A \quad (2.17)$$

it follows that

$$\mathcal{R}_A^A = A_{2A}^A [(n^2 p / n_0 p_0) - n] \quad (2.18)$$

A time  $\tau_A^A$  which characterizes net Auger recombination by process  $A$  can be defined by  $\mathcal{R}_A^A = \Delta p / \tau_A^A = \Delta n / \tau_A^A$ . Since  $p = p_0 + \Delta p$  and  $n = n_0 + \Delta n$ , Eq. (2.18) may be written as

$$\mathcal{R}_A^A = A_{2A}^A \left[ 1 + \frac{n_0}{p_0} + \frac{\Delta p}{n_0} + \frac{2}{p_0} \Delta p + \frac{(\Delta p)^2}{n_0 p_0} \right] \Delta p$$

which yields

$$\tau_A^A = \frac{1}{A_{2A}^A} \frac{n_i^2}{n_i^2 + n_0^2 + p_0 \Delta p + 2n_0 \Delta p + (\Delta p)^2} \quad (2.19a)$$

It follows that the time characterizing process  $B$  of Fig. 2.18, by which energy is given by a hole to another valence-band hole in a band-to-band transition, is

$$\tau_B^A = \frac{1}{A_{2B}^A} \frac{n_i^2}{n_i^2 + p_0^2 + n_0 \Delta p + 2p_0 \Delta p + (\Delta p)^2} \quad (2.19b)$$

Equations (2.19a) and (2.19b) show that the direct band-to-band Auger recombination times decrease with increasing deviations from thermodynamic equilibrium and they decrease with increasing doping. These equations also show that  $\tau_A^A \ll \tau_B^A$  for  $n$ -type material, unless  $\Delta p \gtrsim N_D$ ; hence, we expect Auger recombination by process  $A$  to dominate over Auger recombination by process  $B$  in  $n$ -type material unless the deviation from the thermodynamic equilibrium number densities is extremely large. Such large deviations could occur in solar cells under concentrated light. For  $n$ -type material with  $\Delta p < N_D$ , it follows from Eq. (2.19a) that the band-to-band Auger recombination time simplifies to

$$\tau_p^A = [A_{2A}^A N_D^2]^{-1} \quad (2.20)$$

indicating that  $\tau_p^A$  decreases as one over the square of the doping density in this case [43]. Statements corresponding to these may be made for *p*-type material.

Models such as Eq. (2.18) and characteristic time expressions such as Eqs. (2.19a), (2.19b), and (2.20) can be developed for other Auger processes [42, 43]. The processes of Eq. (2.19) are believed to be important in some photovoltaic structures [44] and depending on the materials involved, other Auger processes seen in Fig. 2.18 could also play a role in solar cell devices.

### 2.6.1.3 Shockley-Read-Hall Recombination

The third process by which electrons can relax to lower energies is phonon emission. As may be seen from Fig. 2.5, phonons are expected to have energies  $\lesssim 0.1$  eV and consequently band-to-band recombination strictly by simple phonon emission would involve essentially simultaneous multiple-phonon emission which is believed to be unlikely. However, the situation changes if localized states present in the material are involved. Charge carriers can give up their energy in collisions with the physical entity that gives rise to this localized level, and become trapped by it. The energy may be released in this collision (trapping) event as phonons or photons or both. The trapping of an electron, for example, and then the trapping of a hole completes the recombination. We shall call the net recombination rate from such trapping processes  $\mathcal{R}^L$  independent of the details of the mechanism of energy release. The superscript emphasizes the role played by localized gap states.

The rate of transition of electrons in the conduction band to localized states in the gap is the  $r_n^L$  seen in Fig. 2.19. A single localized state energy level  $E_T$  is assumed in the figure. We would expect  $r_n^L$  to be proportional to the product of  $n$ , the electron number density in the conduction band, and  $p_T$ , the number of empty localized state levels per volume; i.e.,

$$r_n^L = A_{1n}^L n p_T \quad (2.21)$$

We would expect the corresponding generation path  $g_n^L$  to be proportional to  $n_T$ , the number of occupied localized state levels per volume; i.e.,

$$g_n^L = A_{2n}^L n_T \quad (2.22)$$

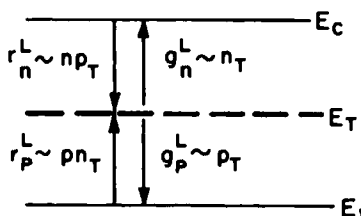


Fig. 2.19 Recombination process whereby electrons relax to a localized state by phonon-photon emission step. The electron can then relax to valence band by another phonon-photon emission step. Corresponding generation processes are also shown. Communication with valence band can be thought of as hole generation and recombination.

Using the fact that these two rates [Eqs. (2.21) and (2.22)] must be equal in thermodynamic equilibrium allows the net trapping rate from the conduction band

$$\mathcal{R}_n^L = r_L^n - g_L^n \quad (2.23)$$

to be written as

$$\mathcal{R}_n^L = A_{1n}^L (n p_T - n_1 n_T) \quad (2.24)$$

where the definition<sup>†</sup>

$$n_1 \equiv n_0 p_{T0} / n_{T0} \quad (2.25a)$$

has been used. In the Shockley–Read–Hall formalism for this type of recombination,  $A_{1n}^L = \langle v_n \rangle \Omega_n$ , where  $\langle v_n \rangle$  is the thermal speed of electrons in the conduction band and  $\Omega_n$  is the localized-state capture cross section for these electrons.

The transition of an electron from the localized state of energy  $E_T$  in Fig. 2.19 to the valence band may be viewed as hole trapping, and the corresponding generation process may then be thought of as hole emission to the valence band. Consequently, the net trapping rate of holes from the valence band to this localized level is given by the hole analog of Eq. (2.24); i.e.,

$$\mathcal{R}_p^L = A_{1p}^L (p n_T - p_1 p_T) \quad (2.26)$$

Here the definition<sup>†</sup>

$$p_1 \equiv p_0 n_{T0} / p_{T0} \quad (2.27a)$$

has been used. In the Shockley–Read–Hall formalism [45],  $A_{1p}^L = \langle v_p \rangle \Omega_p$  with  $\langle v_p \rangle$  and  $\Omega_p$  playing roles analogous to  $\langle v_n \rangle$  and  $\Omega_n$ .

If a material is not in thermodynamic equilibrium but is in steady state,  $\mathcal{R}_n^L$  must equal  $\mathcal{R}_p^L$ . In this special situation we may define a net recombination rate  $\mathcal{R}^L = \mathcal{R}_n^L = \mathcal{R}_p^L$  for band-to-band transitions through these localized states. Using the fact that  $N_T$ , the total number of these localized

<sup>†</sup> Using Eqs. (2.39) and (2.40) of the next section, it is easily shown that we may also write

$$n_1 = N_c \exp[-(E_c - E_T)/kT] \quad (2.25b)$$

and

$$p_1 = N_v \exp[-(E_T - E_v)/kT] \quad (2.27b)$$

Here  $N_c$  and  $N_v$  are the conduction-band and valence-band effective densities of states, respectively; these are introduced in Eqs. (2.41) and (2.42). The quantity  $E_c - E_T$  is the energy difference between the conduction-band edge and the trap level, whereas  $E_T - E_v$  is the energy difference between the trap level and the valence-band edge.

levels of energy  $E_T$  per volume, is such that  $N_T = p_T + n_T$  and using Eqs. (2.24) and (2.26), we obtain [45]

$$\mathcal{R}^L = \frac{A_{1p}^L A_{1n}^L N_T}{A_{1p}^L p + A_{1p}^L p_1 + A_{1n}^L n + A_{1n}^L n_1} [np - n_i^2] \quad (2.28)$$

As was the case with radiative and Auger recombination, a carrier lifetime may be defined according to  $\tau^L = \Delta p/\tau^L = \Delta n/\tau^L$ .<sup>†</sup> From Eq. (2.28) this lifetime is seen to be<sup>‡</sup>

$$\tau^L = \frac{1}{A_{1n}^L N_T} \left[ \frac{p_0 + p_1 + \Delta p}{p_0 + n_0 + \Delta p} \right] + \frac{1}{A_{1p}^L N_T} \left[ \frac{n_0 + n_1 + \Delta p}{p_0 + n_0 + \Delta p} \right] \quad (2.29)$$

Equation (2.29) shows that  $\tau^L$  decreases with increasing trap density  $N_T$ ; but unlike  $\tau^R$  and  $\tau^A$ , it is difficult to discern, in general, the dependence of  $\tau^L$  on the deviation from thermodynamic equilibrium  $\Delta p$  and on the doping density without numerical evaluation for particular values of  $E_T$ ,  $N_T$ ,  $N_c$ ,  $N_v$ ,  $\Delta p$ , etc. [45]. However, certain specific situations may be examined. For example, for  $n$ -type material with  $n_0 \gg p_0$ ,  $n_0 \gg n_1$ , and  $n_0 \gg p_1$ , Eq. (2.29) reduces to

$$\tau^L = \frac{1}{A_{1n}^L N_T} \left[ \frac{p_0 + p_1 + \Delta p}{n_0 + \Delta p} \right] + \frac{1}{A_{1p}^L N_T} \quad (2.30)$$

which says that  $\tau^L$  decreases with increasing doping but increases for increasing deviation from thermodynamic equilibrium.

#### 2.6.1.4 Trapping

Localized states may act as recombination centers or as traps. If they serve as a conduit for recombination from band states higher in energy to band states lower in energy, they are recombination centers. Such states are seen in Fig. 2.19. However, if a given set of localized states only communicates with energy levels above it, or only communicates with energy levels below it, it may be classified as a trap level. Electron traps localize electrons relaxing in energy from higher energies. Hole traps localize holes relaxing in energy from higher hole energies (lower electron energies).

<sup>†</sup> We note that again  $\Delta p \approx \Delta n$  (space-charge neutrally) for simplicity.

<sup>‡</sup> We may ask the following question: If trap levels are located across the gap, which levels are more effective as recombination centers assuming they all have comparable capture cross sections and densities? The answer lies in evaluating  $d\mathcal{R}^L/dE_T$  and looking for a relative maximum. If one allows  $N_c = N_v$  and  $A_{1p} = A_{1n}$ , it is found that Eq. (2.28) is maximum for states in the middle of the forbidden energy gap.

### 2.6.2 Photogeneration

Equation (2.10) gives the rate of production of electrons in the conduction band due to absorption of thermal photons by process 3 of Fig. 2.11. When a solid is subject to an external source of illumination, a new photogeneration rate for conduction-band electrons  $G_n^S$  due to process 3 or 4 develops parallel to  $g_{th}^R$ . Defining  $G_n^S$  as the optical generation rate for conduction-band electrons for the wavelength  $\lambda$ , and using the definition of the absorption coefficient  $\alpha(x, \lambda)$ , we obtain [40]

$$G_n^S(x, \lambda) = K(x, \lambda) \exp \left[ - \int_{x_0}^x \alpha(x', \lambda) dx' \right] \quad (2.31)$$

This is a very general statement for  $G_n^S$  which allows  $\alpha$  to be a function of position. There are expressions analogous to Eq. (2.31) for the valence band and for every localized gap state level. In Eq. (2.31),  $K(x, \lambda)$  is the product of  $\Phi_0$ , number of photons of wavelength  $\lambda$  per area per second at  $x = x_0$ , times  $\alpha(x, \lambda)$ .

## 2.7 TRANSPORT PROCESSES IN SOLIDS

### 2.7.1 Electric Current Transport in Crystalline Materials

#### 2.7.1.1 General Concepts

We now turn our attention to the transport mechanisms in solids which give rise to electric currents, and we begin by considering crystalline solids in which electric current is carried by the motion of electrons in delocalized band states. Specifically, we begin by considering materials where electric current is due to the motion of electrons in the conduction band and holes in the valance band. To examine this motion of electrons in delocalized states, it is convenient to construct a six-dimensional position–velocity space in which there is a probability function  $f(x, y, z, v_x, v_y, v_z)$  for each band. For the conduction band, the  $f^c$  function is defined such that

$$f^c G_e^c(\mathbf{r}, \mathbf{v}) d\mathbf{v} d\mathbf{r}$$

gives the number of electrons in the six-dimensional volume  $d\mathbf{v} d\mathbf{r}$ . Here  $G_e^c(\mathbf{r}, \mathbf{v})$  is the density of conduction-band states, at a position  $\mathbf{r}$  and with velocity  $\mathbf{v}$ , per volume of the solid per volume of velocity space. The velocity  $\mathbf{v}$  of this formulation is the quantum mechanical group velocity [see Eq. (2.5)] associated with a delocalized state.

Using the function  $f^c$  it follows that  $n$ , the total number of electrons in the conduction band per volume, is given at some point  $\mathbf{r}$  by [46–48]

$$n = \iiint_{\text{velocity space}} f^c G_e^c(\mathbf{r}, \mathbf{v}) d\mathbf{v} \quad (2.32)$$

whereas the current density  $J_n$ , in the  $x$  direction, for example, is given at some point  $\mathbf{r}$  by [46–48]

$$J_n = -e \iiint_{\text{velocity space}} v_x f^c G_e^c(\mathbf{r}, \mathbf{v}) d\mathbf{v} \quad (2.33)$$

The analogous expressions for the valence-band hole number density  $p$  and  $x$  component of hole current density  $J_p$  are [46–48]

$$p = \iiint_{\text{velocity space}} (1 - f^v) G_e^v(\mathbf{r}, \mathbf{v}) d\mathbf{v} \quad (2.34)$$

and

$$J_p = e \iiint_{\text{velocity space}} v_x (1 - f^v) G_e^v(\mathbf{r}, \mathbf{v}) d\mathbf{v} \quad (2.35)$$

where the probability function  $f^v$  is such that

$$f^v G_e^v(\mathbf{r}, \mathbf{v}) d\mathbf{v} d\mathbf{r}$$

gives the number of valence-band electrons in the six-dimensional volume  $d\mathbf{v} d\mathbf{r}$ .

In thermodynamic equilibrium the functions  $f^c$  and  $f^v$  are identical and given by  $f_0$ , where  $f_0$  is the Fermi function; viz. [6, 48],

$$f_0 = [1 + \exp(E - E_F)/kT]^{-1} \quad (2.36)$$

Here  $E_F$  and  $T$  are thermodynamic parameters:  $E_F$  is the Fermi level or electrochemical potential and  $T$  is the temperature. In the conduction band,  $E$  may be written as

$$E = E_c + \frac{1}{2}(m_1^* v_1^2 + m_2^* v_2^2 + m_3^* v_3^2) \quad (2.37)$$

where the  $m^*$  values are the diagonalized components of the electron effective mass tensor [6, 48], and for the valence band,  $E$  may be written as

$$E = E_v - \frac{1}{2}(m_1^* v_1^2 + m_2^* v_2^2 + m_3^* v_3^2) \quad (2.38)$$

where the  $m^*$  are the magnitudes of the diagonalized hole effective mass tensor. Equation (2.37) is valid for  $E$  close to  $E_c$ ; Eq. (2.38) is valid for  $E$  close to  $E_v$  [6, 48].

Using  $f_0$  in Eqs. (2.32) and (2.34), we can obtain the thermodynamic equilibrium values of  $n$  and  $p$  at a point. Since  $f_0$  depends on  $E$  only, it is possible to evaluate two of the integrations in velocity space called for by Eqs. (2.32) and (2.34) with the aid of Eqs. (2.37) and (2.38). The remaining integration can be expressed in terms of  $E$ . The result is that Eqs. (2.32) and (2.34) become [6, 48]

$$n = \int_{E_c}^{\infty} [1 + \exp(E - E_F)/kT]^{-1} A_c (E - E_c)^{1/2} dE \quad (2.39)$$

and

$$p = \int_{-\infty}^{E_v} [1 + \exp(E_F - E)/kT]^{-1} A_v (E_v - E)^{1/2} dE \quad (2.40)$$

in thermodynamic equilibrium. Here the material property  $A_c$  depends on the band structure and is a function of the components of the conduction-band effective mass tensor. The material property  $A_v$  depends on the band structure and is a function of the components of the valence-band effective mass tensor [6, 48]. Both  $A_c$  and  $A_v^\dagger$  may vary with  $\mathbf{r}$  but are independent of  $E$ .

For nondegenerate materials the integrations of Eqs. (2.39) and (2.40) may be carried out analytically by using the Boltzmann approximation to the Fermi function; viz.,

$$[1 + \exp(E - E_F)/kT]^{-1} \simeq \exp -(E - E_F)/kT \quad \text{for } E - E_F > kT$$

and

$$[1 + \exp(E_F - E)/kT]^{-1} \simeq \exp -(E_F - E)/kT \quad \text{for } E_F - E > kT$$

With these approximations Eqs. (2.39) and (2.40) integrate in the nondegenerate case to [6, 48]

$$n = N_c e^{-(E_c - E_F)/kT} \quad (2.41)$$

and

$$p = N_v e^{-(E_F - E_v)/kT} \quad (2.42)$$

where  $N_c$  and  $N_v$  are temperature-dependent material properties called the conduction- and valence-band effective densities of states, respectively.<sup>†</sup> It

<sup>†</sup> If there are multiple minima (at  $E_c$ ) or multiple maxima (at  $E_v$ ), these are accounted for in  $A_c$  and  $A_v$  [6, 48].

<sup>‡</sup> For Eq. (2.41) to be valid,  $E_F$  must lie several  $kT$  below  $E_c$ . For Eq. (2.42) to be valid,  $E_F$  must be several  $kT$  above  $E_v$ .

follows that these  $N_e$  and  $N_v$  may be functions of position in some materials of interest to energy conversion. For degenerate materials the integrals given in Eqs. (2.39) and (2.40) must be evaluated numerically since the Boltzmann approximation is not valid; results are available in tabular form [49]. Of course, it follows from Eqs. (2.33) and (2.35)–(2.38) that  $J_n$  and  $J_p$  are zero in thermodynamic equilibrium.

We shall be needing expressions for  $n$ ,  $J_n$ ,  $p$ , and  $J_p$  for situations of interest to solar cell operation; i.e., for situations when crystalline solids are out of thermodynamic equilibrium. We now examine how these expressions are obtained. Considering the conduction band, it is seen from Eqs. (2.32) and (2.33) that what is needed is the function  $f^c$ . As electrons in the conduction band undergo their motion, as they are scattered by intraband collisions, and as they undergo transitions to and from the valence band or localized gap states, the number in some  $d\mathbf{v} d\mathbf{r}$  can change. The result is that the function  $f^c(\mathbf{r}, \mathbf{v})$  for the conduction band must obey the generalized Boltzmann transport equation [46–48]:

$$\frac{\partial f^c}{\partial t} + \frac{d\mathbf{v}}{dt} \cdot \nabla_{\mathbf{v}} f^c + \mathbf{v} \cdot \nabla_{\mathbf{r}} f^c = \left( \frac{df^c}{dt} \right)_s + \left( \frac{df^c}{dt} \right)_{R-G, T-E} \quad (2.43)$$

where  $\partial f^c / \partial t$  is the partial derivative of  $f^c$  with respect to time  $t$ ,  $(df^c / dt)_s$  accounts for the change in time of  $f^c$  due to intraband scattering, and  $(df^c / dt)_{R-G, T-E}$  accounts for the change in time of  $f^c$  due to recombination and trapping [46, 48]. The other terms in Eq. (2.43) account for the fact that conservative external forces, temperature variations, or material properties variations can cause  $f^c$  to change [46–48].

Transport theory in crystalline solids is essentially based on the assumption that the solution to Eq. (2.43), in steady state, can be written as [48]

$$f^c = f'_0 + \Delta f \quad (2.44)$$

where  $f'_0$  differs from  $f_0$  of Eq. (2.36) in that  $T$  is now the effective electron temperature  $T_e$  at a point  $\mathbf{r}$  in the solid, and  $E_F$  is replaced by the electron quasi-Fermi level  $E_{F,n}$  appropriate at that point in the solid.<sup>†</sup> The quantity  $\Delta f$  is assumed small. The idea expressed by Eq. (2.44) is that  $f^c$  is expected to be close to the thermodynamic equilibrium function  $f_0$ , if we define a local temperature  $T_e(x)$  and a local electrochemical potential  $E_{F,n}(x)$  for electrons, even though the solid has been disturbed away from thermodynamic equilibrium.

<sup>†</sup> Out of thermodynamic equilibrium there is clearly a hole quasi-Fermi level  $E_{F,p}$  appropriate for the valence band. There may even be a different effective temperature for the holes in valence band which we may call  $T_h$ . In a very general situation  $T_e \neq T_h \neq T_L$ , where  $T_L$  is the lattice temperature.

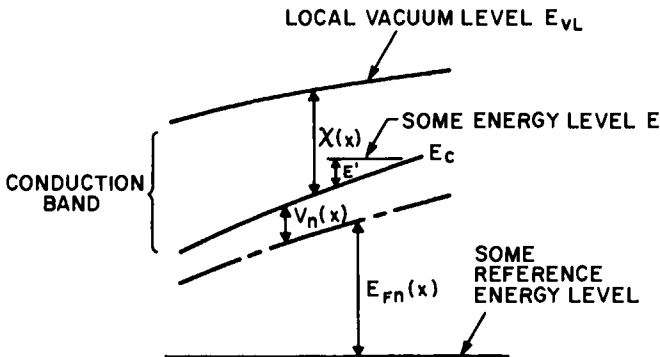


Fig. 2.20 A very general semiconductor conduction band with an electron affinity  $\chi$  which is a function of position. Such a situation could arise in an alloy semiconductor whose composition varies with position. The top of the conduction band is termed the local vacuum level. This is common, but somewhat misleading, terminology. A constant, reference energy is shown.

To continue to explore the basis of transport theory in crystalline solids, we shall assume our material has the very general conduction band seen in Fig. 2.20. An electrostatic field is present as may be seen by the spatial variation of the top of the conduction band  $E_{VL}$ . That is, the gradient of the local vacuum level<sup>†</sup>  $E_{VL}$  gives the electrostatic field  $\xi$  [34]. A variable electron affinity is also assumed present since this can occur in the variable-composition alloy semiconductors used in a number of solar cell structures. For completeness, a gradient in electron temperature  $T_e$  will also be assumed to be present.

Using Eq. (2.37) and Fig. 2.20 we note that, for this very general situation, the energy  $E$  of an electron in the conduction band changes in time according to

$$\begin{aligned} \frac{dE}{dt} = & \frac{dE_c}{dx} v_x + m_1^* v_1 \frac{dv_1}{dt} + m_2^* v_2 \frac{dv_2}{dt} + m_3^* v_3 \frac{dv_3}{dt} \\ & + \frac{1}{2} \left( v_1^2 \frac{dm_1^*}{dx} + v_2^2 \frac{dm_2^*}{dx} + v_3^2 \frac{dm_3^*}{dx} \right) v_x \end{aligned} \quad (2.45)$$

assuming the electron is not scattered and does not undergo recombination or trapping. Also, we note from the preceding equations that

$$\frac{\partial f^e}{\partial v_i} \simeq \frac{f'_0(f'_0 - 1)}{kT_e} m_i^* v_i \quad (2.46)$$

<sup>†</sup> Common usage is to term the top of the conduction band at some point  $r$  the local vacuum level even though this is somewhat misleading.

(where the index  $i$  can be 1–3, the directions which diagonalize the effective mass tensor for the conduction band) [6, 48] and

$$\begin{aligned} \frac{\partial f^c}{\partial x} \simeq & \frac{f'_0(f'_0 - 1)}{kT_e} \left[ \frac{1}{2} \left( v_1^2 \frac{dm_1^*}{dx} + v_2^2 \frac{dm_2^*}{dx} + v_3^2 \frac{dm_3^*}{dx} \right) + \frac{dE_c}{dx} \right. \\ & \left. - \frac{dE_{Fn}}{dx} - \frac{E' + V_n}{T_e} \frac{dT_e}{dx} \right] \end{aligned} \quad (2.47)$$

Here  $E'$  is defined by  $E = E_c + E'$  [see Eq. (2.37) and Fig. 2.20] and  $V_n$  is defined by  $V_n = E_c - E_{Fn}$  at every point.

We are now in a position where we can begin to piece together a solution to Eq. (2.43). For crystalline solids a simplifying assumption is usually made [46]; viz.,

$$(df^c/dt)_s \gg (df^c/dt)_{R-G, T-E} \quad (2.48)$$

This is equivalent to saying that the characteristic time associated with scattering  $\tau_s$  (intraband transitions) is much smaller than the characteristic times associated with any recombination-generation or trapping processes (see Section 2.6). We shall return to question this assumption when dealing with solar cell materials that contain large densities of imperfections and defects.

In addition to Eq. (2.48) it is further assumed that the model<sup>†</sup>

$$(df^c/dt)_s = -(f^c - f'_0/\tau_s) \quad (2.49)$$

is valid. This can be rigorously justified in some cases [50].

Using Eqs. (2.45) and (2.46), we see that in our general case (variations in the  $x$  direction only)

$$\frac{d\mathbf{v}}{dt} \cdot \nabla_{\mathbf{v}} f^c \simeq \frac{f'_0(f'_0 - 1)}{kT_e} \left[ -\frac{dE_c}{dx} - \frac{1}{2} \left( v_1^2 \frac{dm_1^*}{dx} + v_2^2 \frac{dm_2^*}{dx} + v_3^2 \frac{dm_3^*}{dx} \right) \right] v_x \quad (2.50)$$

In evaluating this term of Eq. (2.43), we note that it refers to conservative motion; i.e.,  $dE/dt$  in Eq. (2.45) is zero. Using Eq. (2.47), we can evaluate the next term in Eq. (2.43); viz.,

$$\begin{aligned} \mathbf{v} \cdot \nabla_{\mathbf{r}} f^c \simeq & \frac{f'_0(f'_0 - 1)}{kT_e} \left[ \frac{1}{2} \left( v_1^2 \frac{dm_1^*}{dx} + v_2^2 \frac{dm_2^*}{dx} + v_3^2 \frac{dm_3^*}{dx} \right) + \frac{dE_c}{dx} - \frac{dE_{Fn}}{dx} \right. \\ & \left. - \left( \frac{E' + V_n}{T_e} \right) \frac{dT_e}{dx} \right] v_x \end{aligned} \quad (2.51)$$

<sup>†</sup> Obviously, if there are  $i$  scattering mechanisms present, then  $1/\tau_s = \sum_i (1/\tau_{si})$  where  $\tau_{si}$  characterizes the  $i$ th mechanism.

Making use of Eqs. (2.48)–(2.51) in Eq. (2.43), we finally obtain [6, 48]

$$f^c = f'_0 - \left[ \frac{\tau_s v_x f'_0 (1 - f'_0)}{k T_e} \right] \left[ \frac{dE_{Fn}}{dx} + \left( \frac{E' + V_n}{T_e} \right) \frac{dT_e}{dx} \right] \quad (2.52)$$

We are now in a position to evaluate  $n$  and  $J_n$ . Equation (2.52) may be substituted into Eq. (2.32) to give an expression for the number density  $n$  in terms of the electron quasi-Fermi level  $E_{Fn}$  and the effective electron temperature  $T_e$  occurring in a nonequilibrium situation.<sup>†</sup> The result is seen to be

$$n = \int_{E_c}^{\infty} [1 + \exp(E - E_{Fn})/k T_e]^{-1} A_c (E - E_c)^{1/2} dE \quad (2.53)$$

which may be further simplified to

$$n = N_c \exp[-(E_c - E_{Fn})/k T_e] = N_c \exp[-V_n/k T_e] \quad (2.54)$$

if the quasi-Fermi level  $E_{Fn}$  lies at least several  $k T_e$  below  $E_c$ . Of course, as in the thermodynamic equilibrium case, Eq. (2.53) must be evaluated numerically if the conduction band is degenerate [49].

The expression for  $f^c$  given by Eq. (2.52) may be substituted into Eq. (2.33) to obtain the current density  $J_n$ . Consequently, we find that

$$\begin{aligned} J_n = e & \left[ \iiint_{\text{velocity space}} \frac{\tau_s v_x^2 f_0 (1 - f'_0)}{k T_e} G_e^c(\mathbf{r}, \mathbf{v}) d\mathbf{v} \right] \frac{dE_{Fn}}{dx} \\ & + e \left[ \iiint_{\text{velocity space}} \left( \frac{\tau_s v_x^2 f'_0 (1 - f'_0)}{k T_e} \right) \left( \frac{E' + V_n}{T_e} \right) G_e^c(\mathbf{r}, \mathbf{v}) d\mathbf{v} \right] \frac{dT_e}{dx} \end{aligned} \quad (2.55)$$

which applies to the very general situation seen in Fig. 2.20 in which the material has a variable electron affinity, an electric field present, and an electron temperature gradient (all assumed to occur in the  $x$  direction). The material may be degenerately or nondegenerately doped. Equation (2.55) says the electric current density  $J_n$ , arising from the motion of electrons in the conduction band of this generalized crystalline solid, is driven by gradients in the two thermodynamic quantities  $E_{Fn}$  and  $T_e$ . That is, the current is driven by the gradient in the electron quasi-Fermi level and by the gradient in the effective electron temperature existing in a nonthermodynamic equilibrium situation [46–48].

<sup>†</sup> In many cases it is a good approximation to set  $T_e = T_L$ , where  $T_L$  is the lattice temperature; however, this approximation is questionable in regions of strong electric fields, for example [50].

### 2.7.1.2 Electric Current Transport Equations

(1) *The Conduction Band* The quantities in brackets in Eq. (2.55) are known as transport integrals. These integrals can be expressed in terms of two measurable transport properties, the mobility  $\mu_n$  and the Seebeck coefficient  $S_n$ . The mobility for our very general crystalline solid of Fig. 2.20 is defined by

$$\mu_n = \left( \iiint_{\text{velocity space}} \frac{\tau_s v_x^2 f'_0 (1 - f'_0)}{k T_e} G_e^c(\mathbf{r}, \mathbf{v}) d\mathbf{v} \right) / n \quad (2.56a)$$

which rigorously reduces to

$$\mu_n = e \langle \tau_s \rangle / m^* \quad (2.56b)$$

for spherical energy surfaces in  $\mathbf{k}$  space with effective mass  $m^*$ . Here the average collision time  $\langle \tau_s \rangle$  is defined by

$$\langle \tau_s \rangle \equiv \frac{\int \tau_s(E') (E')^{3/2} f'_0 (1 - f'_0) dE'}{\int (E')^{3/2} f'_0 (1 - f'_0) dE'}$$

Equation (2.56b) is useful for estimating  $\mu$ , even when it is not rigorously applicable.

In a corresponding manner the Seebeck coefficient<sup>†</sup> for our very general crystalline solid of Fig. 2.20 is defined by

$$S_n \equiv \left[ \iiint_{\text{velocity space}} \left( \frac{\tau_s v_x^2 f'_0 (f'_0 - 1)}{k T_e} \right) \left( \frac{E + V_n}{T_e} \right) G_e^c(\mathbf{r}, \mathbf{v}) d\mathbf{v} / n \mu_n \right] \quad (2.57a)$$

which rigorously reduces to

$$S_n = -k \left[ \frac{\langle (\tau_s E') / k T_e \rangle}{\langle \tau_s \rangle} + \frac{V_n}{k T_e} \right] \quad (2.57b)$$

for spherical energy surfaces. To estimate the magnitude of  $S_n$  we note that Boltzmann's constant is  $k = 86 \mu\text{eV}/^\circ\text{K}$ . The averaging process implied by  $\langle (\tau_s E') / (k T_e) \rangle$  is analogous to that for  $\langle \tau_s \rangle$ .

By using Eqs. (2.56a) and (2.57a), Eq. (2.55) may be rewritten in the standard form [46–48, 51]

$$J_n = e \mu_n n dE_{Fn} / dx - e n \mu_n S_n dT_e / dx \quad (2.58)$$

valid for the general situation of Fig. 2.20. We emphasize that Eq. (2.58) is valid for current transport by electrons in the conduction band in the presence of electrostatic fields, variable material properties, and a gradient in the effective electron temperature. Equation (2.58) demonstrates that,

<sup>†</sup> The Seebeck coefficient is also called the thermoelectric power.

even in this most general situation, the electron current density is simply being driven by a gradient in the electron quasi-Fermi level (electrochemical potential for electrons) and by a gradient in the electron effective temperature.

There are a number of alternative ways of writing Eq. (2.58). One particularly useful form replaces  $dE_{Fn}/dx$  with an electrostatic field term, an effective force field term, and a concentration gradient term. This is accomplished by noting from Fig. 2.20 that

$$E_{VL}(x) = \chi(x) + V_n(x) + E_{Fn}(x) \quad (2.59)$$

Substituting this into the expression for  $J_n$  given by Eq. (2.58), we get

$$J_n = e\mu_n n \left( \xi - \frac{d\chi}{dx} - \frac{dV_n}{dx} \right) - en\mu_n S_n \frac{dT_e}{dx} \quad (2.60)$$

which, with the aid of Eq. (2.54), becomes

$$\begin{aligned} J_n = & e\mu_n n \left( \xi - \frac{d\chi}{dx} - kT_e \frac{d \ln N_c}{dx} \right) \\ & + ekT_e \mu_n \frac{dn}{dx} - \left( \frac{eV_n \mu_n n}{T_e} + e\mu_n n S_n \right) \frac{dT_e}{dx} \end{aligned} \quad (2.61)$$

The conduction-band current density  $J_n$  can now be expressed as [51, 53]

$$J_n = e\mu_n n \left( \xi - \frac{d\chi}{dx} - kT_e \frac{d \ln N_c}{dx} \right) + eD_n \frac{dn}{dx} + eD_n^T \frac{dT_e}{dx} \quad (2.62a)$$

or alternatively as

$$J_n = e\mu_n n \xi + e\mu_n n \xi'_n + eD_n \frac{dn}{dx} + eD_n^T \frac{dT_e}{dx} \quad (2.62b)$$

where  $\xi$  is the electrostatic field and  $\xi'_n$  is the effective force field ( $\xi'_n \equiv -d\chi/dx - kT_e d \ln N_c / dx$ ) acting on an electron. In this standard form for  $J_n$  the electron diffusion coefficient  $D_n$  and the electron thermal diffusion coefficient (or Soret coefficient)  $D_n^T$  have been introduced where<sup>†</sup>

$$D_n = kT_e \mu_n \quad (2.63)$$

and

$$D_n^T = -[\mu_n n (V_n + S_n T_e) / T_e] \quad (2.64)$$

As expressed in Eq. (2.62) the electron current density  $J_n$  is now viewed as being driven by a total force [53]  $F_e = -e[\xi - d\chi/dx - kT_e d \ln N_c / dx]$

<sup>†</sup> By using Eq. (2.54) to obtain Eq. (2.61) we have limited ourselves to nondegenerate bands at this stage. More general discussions can be found in the literature on this subject [46–48, 51–53].

acting on electrons (drift term), by an electron concentration gradient (diffusion term), and by a temperature gradient (thermal diffusion term). The total force  $F_e$  is simply the electrostatic force  $-e\xi$  except for those materials that have properties (affinity, density of states) that vary with position [34, 53].

Equations (2.58) and (2.62) are equivalent expressions for the current density  $J_n$ ; however, one sometimes proves to be more convenient than the other when analyzing solar cell structures. For example, we will see that when we need to determine the spatial variation of the electron-electrochemical potential (electron quasi-Fermi level) through a cell, Eq. (2.58) will prove very helpful. On the other hand, when we wish to see the role of electric fields, electron affinity variation, and carrier concentration gradients on electron current flow, Eq. (2.62) will prove very useful.

(2) *The Valence Band* We have reviewed this subject of electric current transport in crystalline solids by focusing on the conduction band. However, we note that expressions analogous to Eq. (2.58) or Eq. (2.62) exist for  $J_p$ , the current density carried by holes in the valence band. Assuming  $J_p$  is in the  $x$  direction only, the expression [46–48, 51–53]

$$J_p = e\mu_p p \frac{dE_{Fp}}{dx} - ep\mu_p S_p \frac{dT_h}{dx} \quad (2.65)$$

is the standard formulation for  $J_p$  in terms of the hole quasi-Fermi level  $E_{Fp}$  and the hole effective temperature  $T_h$ . For the standard formulation<sup>†</sup> in terms of the electrostatic field  $\xi$ , the effective hole force field  $\xi'_p$  ( $\xi'_p \equiv -d(\chi + E_g)/dx + kT_h d \ln N_v / dx$ ) and the concentration gradient  $dp/dx$ , the expression is [46–48, 51–53]

$$\begin{aligned} J_p = & e\mu_p p \left( \xi - \frac{d}{dx}(\chi + E_g) + kT_h \frac{d}{dx} \ln N_v \right) \\ & - ekT_h \mu_p \frac{dp}{dx} + \left( \frac{eV_p \mu_p p}{T_h} - e\mu_p p S_p \right) \frac{dT_h}{dx} \end{aligned}$$

which becomes

$$J_p = e\mu_p p \left( \xi - \frac{d}{dx}(\chi + E_g) + kT_h \frac{d}{dx} \ln N_v \right) - eD_p \frac{dp}{dx} - eD_p^T \frac{dT_h}{dx} \quad (2.66a)$$

or

$$J_p = e\mu_p p \xi + e\mu_p p \xi'_p - eD_p \frac{dp}{dx} - eD_p^T \frac{dT_h}{dx} \quad (2.66b)$$

<sup>†</sup> Eq. (2.65) is valid for degenerate or nondegenerate doping but Eq. (2.66) applies only to nondegenerate doping since  $p = N_v \exp(-V_p/kT_h)$  has been used. More general formulations of Eq. (2.66) may be found in the literature cited.

The coefficients in Eq. (2.66) have the same meaning as the analogous conduction-band coefficients. Use has been made in Eq. (2.66) of

$$p = N_v e^{-(E_{Fp} - E_v)/kT_h} = N_v e^{-V_p/kT_h}$$

which is the valence-band counterpart of Eq. (2.54). It can be seen from Eq. (2.66) that the total force  $F_h$  acting on a hole (where  $F_h = e[\xi - d(\chi + E_g)/dx + kT_h d \ln N_v/dx]$ ) is just the electrostatic force  $e\xi$  except for those materials that have properties (hole affinity, density of states) that vary with position [34, 35].

### 2.7.1.3 Comments

Having established very general expressions for the current densities  $J_n$  and  $J_p$ , we now need to relate these quantities to population changes in the bands due to recombination and generation. The expressions which show the relation are the electron- and hole-continuity equations; viz.,

$$\frac{1}{e} \frac{dJ_n}{dx} = \mathcal{R}_n - \int G_n^S(x, \lambda) d\lambda \quad (2.67a)$$

and

$$\frac{1}{e} \frac{dJ_p}{dx} = -\mathcal{R}_p + \int G_p^S(x, \lambda) d\lambda \quad (2.67b)$$

where  $\mathcal{R}_n = \mathcal{R}_n^R + \mathcal{R}_n^A + \mathcal{R}_n^L$  and  $\mathcal{R}_p = \mathcal{R}_p^R + \mathcal{R}_p^A + \mathcal{R}_p^L$  and the integrations are over the spectrum of any illumination present. If localized gap states are not important in the absorption of light,  $\mathcal{R}_n = \mathcal{R}_p$  and  $G_n^S = G_p^S$ . Equations (2.67a) and (2.67b) can be rigorously derived from Eq. (2.43) for electrons and holes in delocalized band states [48].

The result of our review in this section is that we have established the basic equations governing the number densities  $n$  and  $p$  and current densities  $J_n$  and  $J_p$  in crystalline solids. In so doing we have examined the fundamental assumptions behind the transport models. These fundamental assumptions seem quite reasonable when one is dealing with nearly perfect, crystalline materials, but we have come to realize that, as one employs less expensive, less perfect materials for solar cell structures, use of these expressions for  $\mu_n$ ,  $\mu_p$ , etc. must be constantly scrutinized in light of the assumptions behind them. As we shall see, in disordered materials there are other transport mechanisms in parallel with band conduction that have considerably different formulations for  $\mu_n$ ,  $\mu_p$ , etc.

### 2.7.2 Electric Current Transport in Amorphous Materials

#### 2.7.2.1 General Concepts

Transport in amorphous solids is much more complex than it is in crystalline solids. This is basically because electric current can be carried by electrons and holes in localized as well as delocalized states in these materials. For amorphous solids the current density  $J$  must be written, in general, as

$$J = J_n + J_p + \sum_i J_{Li} \quad (2.68)$$

Here  $J_n$  is the conduction-band contribution (from the delocalized states above  $E_c$  in Fig. 2.8),  $J_p$  is the valence-band contribution (from delocalized states below  $E_v$  in Fig. 2.8), and  $J_{Li}$  is the  $i$ th localized level contribution (states in the mobility gap seen in Fig. 2.8) to the total current density  $J$ .

The motion of the electrons in the delocalized states is expected to be describable [23, 54] in terms of the Boltzmann transport theory discussed in Section 2.7.1. That is, in the presence of a drift field  $\xi$

$$J_n = en\mu_n\xi \quad (2.69)$$

and

$$J_p = ep\mu_p\xi \quad (2.70)$$

for a uniform material in the absence of concentration and thermal gradients. These follow from Eqs. (2.62) and (2.66). Since Boltzmann transport theory applies,  $\mu_n$  is given by Eq. (2.56);  $\mu_p$  is given by the corresponding integral over the valence band. The number density  $n$  is given by Eq. (2.54) and the number density  $p$  is given by the corresponding expression for the valence band. Consequently, the conduction-band contribution to conductivity  $\sigma_n$  and the valence-band contribution to the conductivity  $\sigma_p$  are expected to have the same functional form as that of crystalline solids; i.e., both are products of a nontemperature-activated<sup>†</sup> mobility, determined by the scattering of electrons from one delocalized state to another, and a temperature-activated<sup>†</sup> number density:

$$\sigma = e\mu_{dL}(T)N(T)e^{-\Delta E/kT} \quad (2.71)$$

where  $\Delta E = E_c - E_F$  or  $\Delta E = E_F - E_v$  and  $N$  is a band effective density of states. The quantity  $E_F$  can be a function of  $T$  due to the shift of the Fermi level possible with temperature [55]. In amorphous solids the mobility  $\mu_{dL}$  in Eq. (2.71) is expected to be bound by [54, 56]

$$\mu_{dL} \gtrsim 0.1 - 1.0 \text{ cm}^2/(\text{V}\cdot\text{sec}) \quad (2.72)$$

<sup>†</sup> The term "temperature-activated" is used to denote a dependence of the form  $\exp -\Delta E/kT$  where  $\Delta E$  is the activation energy.

with mobilities in the lower portion of this range more probable, due to the enhanced scattering caused by the disorder.

This brings us to a point that was alluded to in Section 2.7.1. The equation we are using for  $\mu_{dL}$  is Eq. (2.56), and it is on the strength of that equation that we say  $\mu_{dL}$  is not temperature-activated. As we saw in the preceding section, this equation is based on assuming that the time characterizing a scattering process  $\tau_s$  is much smaller than any time characterizing a recombination-generation or trapping process (see Eq. 2.48). The assumption deserves some examination for disordered solids [46]. In crystalline solids  $\langle \tau_s \rangle \approx 10^{-12}\text{--}10^{-13}$  sec for a mobility of about  $1500\text{ cm}^2/(\text{V}\cdot\text{sec})$ , whereas times characterizing recombination-generation or trapping processes in crystalline solids are generally much longer than this value. On the other hand, for amorphous materials the times characterizing trapping and recombination-generation processes can be [46] of the order of  $10^{-12}$  sec due to the large number of localized states in the gap (as discussed in Chapter 3, steps are taken in photovoltaic applications to try to increase this time). However, we apparently are in luck. Because of increased scattering arising from the disorder,  $\tau_s$  is expected to be of the order of  $10^{-15}$  sec in amorphous solids [54]. The conclusion of our examination is that Eq. (2.56) still appears to be a valid basis for the delocalized state mobility  $\mu_{dL}$  in many amorphous solids, but this point should be reassessed for every specific amorphous solar cell material.

Now let us turn to the localized states in the mobility gap of Fig. 2.8. Under the influence of the drift field  $\xi$ , the current density contribution  $dJ_L$  from the localized gap states with energies between  $E$  and  $E + dE$  is [54]

$$dJ_L = [\mu_L(E)f(E)g(E) dE]\xi \quad (2.73)$$

where  $\mu_L(E)$  is the mobility characterizing the movement of localized electrons at energy  $E$  and  $g(E)$  is the density of localized states of energy  $E$  per volume per energy. The concept of a velocity space has no meaning for electrons in these localized states and Boltzmann transport theory is not applicable. The motion of an electron in localized states must be viewed as hopping from one localized site to another. That is, the electron tunnels from one localized site to another. In all probability these sites are not at the same energy. Consequently, hopping is a phonon-assisted tunneling process. Every time the localized electron moves, it emits or absorbs a phonon and the steps which necessitate absorption of a phonon are rate limiting. This makes hopping a thermally activated process.

It follows that a hopping mobility  $\mu_L$  is expected to be of the form

$$\mu_L(E) = \mu_0(E)e^{-W(E)/kT} \quad (2.74)$$

where the quantity  $W$  is the activation energy. It can be argued that  $\mu_L$  is such that [54, 56]

$$\mu_L < 0.1\text{--}1.0 \text{ cm}^2/(\text{V}\cdot\text{sec}) \quad (2.75)$$

A variation of Eq. (2.74) is expected at low temperatures for those localized states near  $E_F$ ; viz. [54],

$$\mu_L(E) = \mu_0(E)e^{-C/T^{1/4}} \quad (2.76)$$

This temperature dependence arises since electrons are forced to tunnel longer distances to sites with energies closer to their initial energy due to the lack of phonons at low temperatures.

From Eqs. (2.73) and (2.74) it is seen that the conductivity contribution  $\sigma_i$  from electrons in the  $i$ th group of localized states located at energy  $E_i$  in the gap may be written as [54]

$$\sigma_i = \sigma_{0i}e^{-W_i/kT}e^{-(E_i - E_F)/kT} \quad (2.77)$$

assuming the Boltzmann approximation [6] to  $f(E)$  can be made ( $E_i$  is several  $kT$  away from  $E_F$ ). Clearly,  $\sigma_i$  contains two activation energies:  $W_i$  characterizes the hopping process and  $(E_i - E_F)$  characterizes the populating of this  $i$ th group of states. The Fermi level  $E_F$  itself may be a function of temperature in Eq. (2.77).

Alternatively, if the  $i$ th group of localized states lies at or very near  $E_F$ , then [54]

$$\sigma_i = \sigma_{0i}e^{-W_i/kT} \quad (2.78)$$

In this case there is only one activation energy expected and  $\exp[-AT^{-1/4}]$  dependence (Eq. 2.76) is predicted at low temperatures [54].

It is clear that the conductivity  $\sigma$  of an amorphous material can contain several components; viz.,

$$\sigma = \sigma_n + \sigma_p + \sum_i \sigma_i \quad (2.79)$$

Since the mobilities of the delocalized states are expected to be orders of magnitude larger than those of localized states (the mobility gap), and since, among the localized states, mobilities can vary by orders of magnitude due to  $\exp(-W_i/kT)$ , the conductivity  $\sigma$  of Eq. (2.79) can be tremendously affected by shifts in populations. For example, if light appreciably shifts the carrier population into localized states with large hopping mobilities or into band states, then large changes in the conductivity will result and, in fact, many amorphous semiconductors, both organic [20] and inorganic [57, 58], are strong photoconductors.

### 2.7.2.2 Poole and Poole-Frenkel Effects

The various components of the total conductivity  $\sigma$  given by Eq. (2.79) can also be affected by high electric fields. The effects basically result from changes in populations caused by the field. To discuss this, we limit ourselves to states in the upper half of the mobility gap and to the conduction band. We must also specify the nature of the localized gap states; that is, whether they are donorlike or acceptorlike. Up to this point we have not been forced to make this distinction. We note that those states which are donorlike have a long-range coulombic attraction for electrons whereas acceptor states in the top part of the gap are electron traps with a short-range attraction for electrons.

Figure 2.21 singles out one particular localized gap state, which is a donor level, and depicts it with respect to the mobility shoulder  $E_c$  of Fig. 2.8 in the presence of a strong electric field  $\xi$ . It is seen that the superposition of the coulomb potential of the donor site and the potential of the electric field  $\xi$  results in a lowering of the ionization energy  $\phi_i$  of the donor by an amount  $\phi_m$ . If the donor sites are far enough apart that their coulomb potentials do not overlap (as pictured in Fig. 2.21), then [59]

$$\phi_m = \beta \xi^{1/2} \quad (2.80)$$

where ideally  $\beta = [e/(\pi\epsilon)]^{1/2}$ . If the donor coulomb potentials do overlap, then [59]

$$\phi_m = S\xi \quad (2.81)$$

where  $2S$  is the distance between donors.

In either case, the population of the conduction band is enhanced due to the presence of the electric field; however, the functional form of the

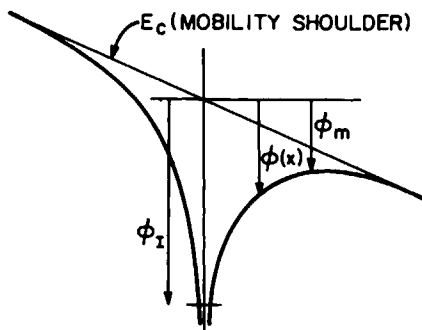


Fig. 2.21 The potential of a coulombic center in the presence of an electric field  $\xi$ .

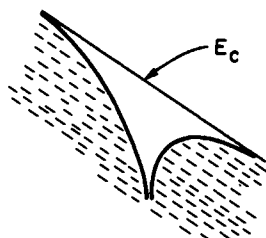


Fig. 2.22 Poole-Frenkel effect involving donor and trap levels in an amorphous material. Interaction of coulombic potential and that of external electric field results in an enhancement of trap level populations.

enhancement is not the same. In the case of Eq. (2.80) the conductivity of the conduction band is enhanced by the factor

$$e^{\beta \xi^{1/2}/kT} \quad (2.82)$$

which is known as the Poole-Frenkel effect, whereas in the case of Eq. (2.81) the conductivity of the conduction band is enhanced by

$$e^{S\xi/kT} \quad (2.83)$$

which is known as the Poole effect. The enhancement in both cases is based on the assumption that the donor level in question is not fully ionized. Thus  $\sigma_n$  or  $\sigma_p$  of Eq. (2.79) can be field dependent for high fields in amorphous solids.

Any localized-state hopping contributions to  $\sigma$  in Eq. (2.79) may also be affected by the presence of a high electric field. Just as in the case of the donor level-band situation of Fig. 2.21, a high electric field can also allow electrons to be more easily ionized from a donor to trap levels enhancing the trap level populations by factors such as Eq. (2.82) or (2.83). The hopping conductivities for these levels would then be correspondingly modified [59] as is the situation seen in Fig. 2.22. A final possible case which does not involve donors, but simply results from the band diagram being tilted is seen in Fig. 2.23. The bands are tilted so much by the field in the figure that the selection of states available to electrons hopping in trap levels is affected. Generally, this case has been found difficult to model [59].

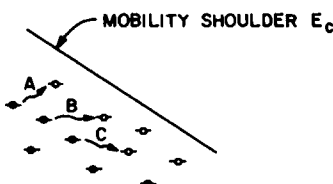


Fig. 2.23 Electronic transitions in a high electric field between full and empty traps, involving a slight gain of energy from (A) phonons, (B) conservation of energy, and (C) a slight loss of energy to the lattice.

### 2.7.2.3 Comments

Up to now we have only considered that there is a drift electrostatic field present in our discussion of transport in amorphous solids. But in solar cell applications there can be present an electric field, effective fields, concentration gradients, and temperature gradients. Since the band contributions  $J_n$  and  $J_p$  should be describable in terms of Boltzmann transport theory, it follows from the preceding section that the general conduction-band contribution  $J_n$  in an amorphous material is given by the same expressions valid for crystalline solids; i.e., Eq. (2.58) or its equivalent, Eq. (2.62). Correspondingly, it follows that the general valence-band contribution  $J_p$  in an amorphous material may be described by Eq. (2.65) or (2.66). The continuity equations given by Eqs. (2.67a) and (2.67b) also apply here to  $J_n$  and  $J_p$ .

Turning now to the localized gap levels, we can define a quasi-Fermi level  $E_F^i$  and an effective temperature  $T_e^i$  for carriers in the  $i$ th group of localized states in the mobility gap seen in Fig. 2.8 which generalize Eq. (2.58) to

$$J_{Li} = \sigma_i dE_F^i/dx - \sigma_i S_i dT_e^i/dx \quad (2.84)$$

However, Boltzmann transport theory is not applicable; therefore,  $\sigma_i$  is given by Eq. (2.77) or (2.78). The Seebeck coefficient  $S_i$  is given by [54]

$$S_i = -k \left( \frac{E_i - E_F^i}{kT_e^i} + A \right) \quad (2.85)$$

where  $E_i$  and  $E_F^i$  are measured from some arbitrary reference energy,  $k = 86 \mu\text{eV}/^\circ\text{K}$  and  $A \lesssim 1.0$  or by [54]

$$S_i = -\frac{\pi^2 k^2 T}{3 e} \left( \frac{\partial \ln \sigma}{\partial E} \right) \Big|_{E=E_F^i} \quad (2.86)$$

if  $E_i$  lies at or near  $E_F^i$ .

Written in terms of the field, the population per volume of the  $i$ th level,  $n_i$ , and the temperature gradient,  $J_{Li}$  becomes

$$J_{Li} = \sigma_i \left( \xi - kT_e^i \frac{d \ln G_i}{dx} \right) + eD_i \frac{dn_i}{dx} + eD_i^T \frac{dT_e^i}{dx} \quad (2.87)$$

where  $D_i$  is the diffusion coefficient of electrons in this  $i$ th group of localized states and  $D_i^T$  is their Soret or thermal diffusion coefficient. If the Boltzmann approximation to Fermi-Dirac statistics holds (nondegenerate case), then  $D_i$  is simply related to  $\mu_i$  by [54]

$$D_i = (kT_e^i)\mu_i \quad (2.88)$$

There is also a continuity equation for carriers in this  $i$ th group of localized states; viz.,

$$dJ_{Li}/dx = e\mathcal{R}_{Li} - e \int G_{Li}^S(x, \lambda) d\lambda \quad (2.89)$$

which is written assuming the charge carriers are electrons.

In addition to single-electron motion, transport in amorphous solids can also involve excitons and polarons. It has been argued that excitons should be prevalent in amorphous materials due to the small diffusion coefficients in these solids. Because of these small diffusion coefficients, carriers (newly created electron-hole pairs) should be more prone to becoming bound in their mutual coulombic potential before they have the opportunity to diffuse away from one another, and the resulting excitons in disordered materials would probably be bound to various defects and move by hopping. Of course, exciton movement does not constitute an electric current, but excitons can give rise to an electric current if they decompose at an interface or are torn apart in an electric field region.

On the other hand, the movement of polarons does constitute an electric current. When present, these, too, are believed to move in amorphous materials by hopping. In fact, their presence is generally suspected when experimental data for the activation energy  $W$  in Eq. (2.74) gives high values ( $W \gtrsim 0.2$  eV or so) [54].

### 2.7.3 Energy Transport in Solids

#### 2.7.3.1 Thermal Conduction

Thermal conduction in solids, whether crystalline, polycrystalline, or amorphous, is due both to lattice vibrations (phonons) and valence electrons. The heat flux carried by phonons  $H_L$  is given by

$$H_L = -K_L dT_L/dx \quad (2.90)$$

where  $K_L = K_L(T_L)$  is the lattice thermal conductivity and  $T_L$  is the lattice temperature, whereas the heat flux carried by electrons, for example, is given by

$$H_n = -K_n(T_e)(dT_e/dx) - \langle E' \rangle J_n \quad (2.91)$$

Here  $K_n$  is the electron thermal conductivity and  $\langle E' \rangle$  is the average kinetic energy transported per electron comprising the electron current density  $J_n$ . The additional term appearing in Eq. (2.91), when compared to Eq. (2.90), arises from the fact that a charge carrier in motion not only gives rise to an electric current but it also carries energy. Equation (2.91) may be derived

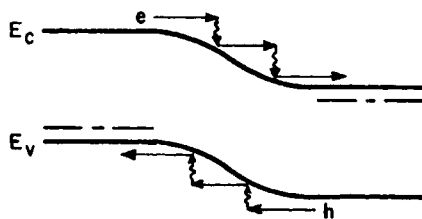


Fig. 2.24 Thermalization of hot photogenerated carriers crossing a  $p-n$  junction.

rigorously from the Boltzmann transport equation for electrons<sup>†</sup> in a band by using Eq. (2.52) and the basic definition of  $H_n$ , viz.,

$$H_n = \iiint_{\text{velocity space}} E' v_x f^c G_e^c(\mathbf{r}, \mathbf{v}) d\mathbf{v}$$

#### 2.7.3.2 Hot Carrier Effects

It will be established in Section 2.8 that built-in electric field regions<sup>‡</sup> in materials, which we term barriers or junctions, are usually the principal source of photovoltaic action in solar cells or, in other words, these regions are usually the principal contributor to the check valve required in Fig. 1.1. Since a barrier electric field is used to sweep out photogenerated charge carriers, in this check valve application, it follows that photogenerated charge carriers cross such regions in the direction of dropping band edges as seen in Fig. 2.24 for the case of a  $p-n$  junction. From the figure it can be noted that photogenerated carriers must lose energy as they cross the electric field region if their distribution in energy is to approach that expected for a lattice temperature  $T_L$ ; i.e., the carriers are "hot" and they must lose energy as they thermalize toward  $T_L$ .

From the preceding discussion it is seen that the potential for hot-carrier effects is intrinsic to solar cell operation due to the direction of current flow through electric field or effective field regions in these devices. Hot-carrier effects can be enhanced in solar cell applications which use concentrated sunlight due to device heating and due to the high current densities present. The possibility that hot-carrier effects might be important in some solar cell structures was anticipated in Sections 2.7.1 and 2.7.2, since it was assumed that electrons may have a temperature  $T_e = T_e(x)$  and holes a temperature  $T_h = T_h(x)$  where, in general,  $T_e \neq T_h \neq T_L$ .

<sup>†</sup>The corresponding equation for holes may be derived rigorously from the Boltzmann transport equation for holes in the valence band.

<sup>‡</sup>We shall also see that effective field regions can play the same role as actual electrostatic field regions as follows from Eqs. (2.62) and 2.66.

Focusing on electrons, for example, we can write an energy balance equation which establishes the value of  $T_e$  at a point; viz.,

$$J_n \xi + J_n \xi' = dH_n/dx + nB(T_e) + e\langle E' \rangle \mathcal{R}_n - e\langle E'' \rangle G_n^S \quad (2.92)$$

Here  $\xi'$  is the effective force acting on electrons introduced in Section 2.7;  $B(T_e)$  is the rate at which electrons lose energy to the lattice in collisions;  $\langle E' \rangle$  is the average kinetic energy of the net electrons recombining per second per volume (where  $\mathcal{R}_n = \mathcal{R}_n^R + \mathcal{R}_n^A + \mathcal{R}_n^L$ ); and  $\langle E'' \rangle$  is the average kinetic energy of photogenerated electrons. Equation (2.92) can be developed rigorously from Eq. (2.43) for electrons in a band and, based on this approach, models for the function  $B(T_e)$  have been obtained for electron scattering by acoustic and (polar and nonpolar) optical modes of lattice vibration [50].

Equations (2.91) and (2.92) may be solved for  $T_e$  provided  $J_n$ ,  $n$ , and  $\mathcal{R}_n$  are known. Unfortunately,  $J_n$ ,  $n$ , and  $\mathcal{R}_n$  themselves depend on  $T_e$  either explicitly or through transport properties such as mobility and, consequently, solving the complete mathematical system is a formidable task in barrier regions. Numerical solutions are necessary in general [50]; however, some observations on hot-carrier effects can be made [60]: The drift velocity  $\mu_n \xi$  is found to have an upper bound  $V_{SL}$  termed the scattering-limited velocity, where  $V_{SL} = \theta (10^7) \text{cm/sec}$  for Si; carrier temperatures significantly different from the lattice temperature can exist; and hot-carrier effects can be significant enough to modify device current-voltage characteristics.

## 2.8 ORIGINS OF PHOTOVOLTAIC ACTION

Having reviewed the physics basic to solar cell device operation, we are now at a point where we can inquire into the origins of photovoltaic action. We ask a fundamental question: What are the sources of photovoltaic behavior? The question can be answered on two levels.

On one level we argue quite simply: Light impinging on a materials system can be absorbed and, as we saw in Section 2.5, some absorption processes result in mobile particles (electrons, holes, excitons, and polarons) which can move about the solid by transport in bands or by hopping. If mobile photogenerated charge carriers are created in or diffuse to a built-in electrostatic field region in a solid, this built-in electric field can separate these carriers according to charge and sweep them out, setting up a current density  $J$ .<sup>†</sup> Under short-circuit conditions this current density  $J$  would have the value  $J_{sc}$ . Under open circuit conditions the structure would have to

<sup>†</sup> In the case of excitons, the field must tear apart the electron-hole pair and then sweep out the charge carriers.

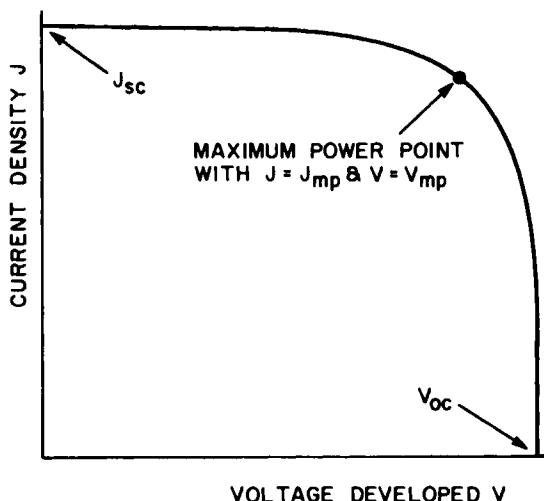


Fig. 2.25 The current-voltage ( $J$ - $V$ ) characteristic of a photovoltaic structure under illumination. Maximum power point (largest  $J$ - $V$  product) is shown. Device efficiency  $\eta$  is defined as  $\eta = (J_{mp} V_{mp}) / P_{in}$  where  $P_{in}$  is the incoming power per area.

bias itself to some voltage  $V_{oc}$  necessary to develop a bucking current just able to counter the light-caused current. The current density  $J$ , the short-circuit current density  $J_{sc}$ , and open-circuit voltage  $V_{oc}$  are obviously the result of the built-in electric field present in the materials system. An optimistic sketch of what this current density  $J$  versus voltage  $V$  curve could look like is seen in Fig. 2.25.

Is a built-in electrostatic field the only source of photovoltaic action operative in materials systems? To answer this question we explore the problem on another level and turn to a mathematical examination of a general materials system to see if such an approach will uncover other sources of photovoltaic action. This general materials system is seen in Fig. 2.26. To keep our exploration as general as possible, we shall allow the semiconductor-electron affinity  $\chi$ , band gap  $E_g$ , and band effective densities of states  $N_c$  and  $N_v$  to be functions of position as can occur in alloy semiconductors with variable composition. A built-in electrostatic field  $\xi_0$  (electrostatic field existing in thermodynamic equilibrium) is present, but its precise dependence on position will not be specified for generality. Further, there will be no specification as to whether the semiconductor is *n*-type, *p*-type, or varies from one to the other. It will be assumed, however, that there are no temperature gradients present and all carriers will be taken to be at the lattice temperature  $T$ . Ohmic contacts (discussed in Chapter 3) exist at both ends of this materials system. Thus the difference in the Fermi-level

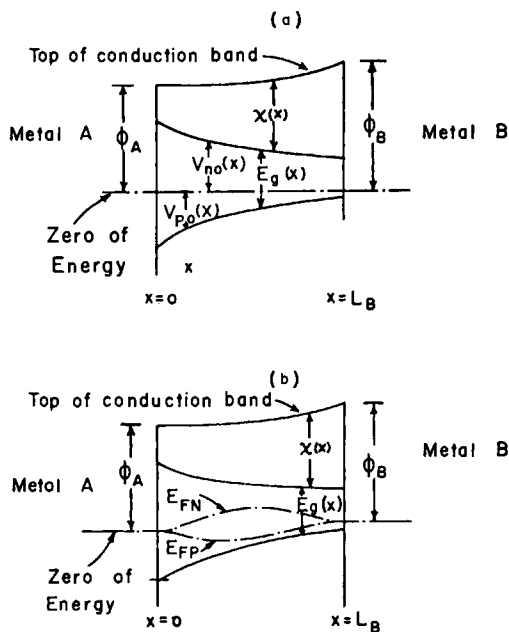


Fig. 2.26 A very general semiconductor material located between two ohmic contacts. (a) depicts thermodynamic equilibrium; (b) The material under illumination. The quasi-Fermi levels are measured here from the Fermi-level position in Metal A; i.e., from what is labeled the zero of energy.

positions of metals *A* and *B* of Fig. 2.26, under illumination with the structure open-circuited, will give  $V_{oc}$ .

We now compute  $V_{oc}$  for this general configuration to determine if we have uncovered all the possible sources of photovoltage. To begin, we shall assume that any electron and hole transport present in this structure shown in Fig. 2.26 takes place in the valence and conduction bands only and, consequently, we are interested in expressions for  $J_n$  and  $J_p$ . Fortunately we have already established very general expression for  $J_n$  and  $J_p$ , Eqs. (2.62) and (2.66), which are applicable to Fig. 2.26. On rewriting Eq. (2.62),  $J_n$  is given by

$$J_n = e\mu_n n \left[ \xi - \frac{d\chi}{dx} - kT \frac{d}{dx} \ln N_c \right] + eD_n \frac{dn}{dx} \quad (2.93)$$

whereas, from Eq. (2.66),  $J_p$  is given by

$$J_p = e\mu_p p \left[ \xi - \frac{d}{dx} (\chi + E_g) + kT \frac{d}{dx} \ln N_v \right] - eD_p \frac{dp}{dx} \quad (2.94)$$

Written in terms of the quasi-Fermi level  $E_{Fn}$  for electrons and the quasi-Fermi level  $E_{Fp}$  for holes, these become

$$J_n = e\mu_n n(dE_{Fn}/dx) \quad (2.93a)$$

and

$$J_p = e\mu_p p(dE_{Fp}/dx) \quad (2.94a)$$

which follows from Eqs. (2.58) and (2.65).

In the case of thermodynamic equilibrium (Fig. 2.26a),  $J_n = J_p = 0$  and  $E_{Fn} = E_{Fp} = E_F$ . These all result from the principle of detailed balance [61]. From Section 2.7 we note that

$$n_0 = N_c e^{-V_{n0}/kT} \quad (2.95)$$

and

$$p_0 = N_v e^{-V_{p0}/kT} \quad (2.96)$$

using the notation<sup>†</sup> of Fig. 2.26a. From Eqs. (2.93)–(2.96) and the fact that  $J_n = J_p = 0$  in thermodynamic equilibrium, we may obtain the built-in electrostatic field  $\xi_0 = \xi_0(x)$ ; viz. [34, 62],

$$\xi_0 = \frac{d\chi}{dx} + \frac{dV_{n0}}{dx} = -\frac{dV_{p0}}{dx} + \frac{dE_g}{dx} + \frac{d\chi}{dx} \quad (2.97)$$

This is the derivative, with position, of the local vacuum level seen in Fig. 2.26a.

When light impinges on this structure, it is driven out of thermodynamic equilibrium and Figure 2.26b applies. The electrostatic field will no longer be  $\xi_0 = \xi_0(x)$  but will be some new  $\xi = \xi(x)$ . In fact,  $V_{oc}$  can be computed from [34, 61]

$$V_{oc} = \int_0^L (\xi - \xi_0) dx \quad (2.98)$$

where  $\xi$  is the electrostatic field present in the structure under open-circuit conditions. If we can evaluate this integral, we shall have a catalog displaying the various sources of photovoltaic action. We note from Eq. (2.98) that, if  $V_{oc}$  is positive, the Fermi level of metal *B* is raised above that of metal *A*.

Using the general statement that

$$\xi = \frac{d}{dx}(E_{Fn} + V_n + \chi) = \frac{d}{dx}(E_{Fp} - V_p + E_g + \chi), \quad (2.99)$$

<sup>†</sup> Here and throughout the book, the subscript zero denotes a thermodynamic equilibrium value.

which follows from Fig. 2.26b, and using the constraint that  $J_n = -J_p \neq 0$  in the open-circuit condition, we can obtain an expression for  $(\xi - \xi_0)$  from the preceding equations. When this expression for  $(\xi - \xi_0)$  is substituted into Eq. (2.98), the result is [34, 62]

$$\begin{aligned} V_{oc} = & - \int_0^L \left( \frac{e\mu_n \Delta n + e\mu_p \Delta p}{\sigma} \right) \xi_0 dx \\ & + \int_0^L \left( \frac{e\mu_n \Delta n}{\sigma} \right) \frac{d\chi}{dx} dx + \int_0^L \left( \frac{e\mu_p \Delta p}{\sigma} \right) \left( \frac{d\chi}{dx} + \frac{dE_g}{dx} \right) dx \\ & - kT \int_0^L \left( \frac{e\mu_p \Delta p}{\sigma} \frac{d}{dx} \ln N_v - \frac{e\mu_n \Delta n}{\sigma} \frac{d}{dx} \ln N_c \right) dx \\ & + kT \int_0^L \frac{1}{\sigma} \left( e\mu_p \frac{d}{dx} \Delta p - e\mu_n \frac{d}{dx} \Delta n \right) dx \end{aligned} \quad (2.100a)$$

which has the alternative form

$$\begin{aligned} V_{oc} = & - \int_0^L \left( \frac{e\mu_n \Delta n}{\sigma} \right) \frac{dE_c}{dx} dx - \int_0^L \left( \frac{e\mu_p \Delta p}{\sigma} \right) \frac{dE_v}{dx} dx \\ & - kT \int_0^L \left( \frac{e\mu_p \Delta p}{\sigma} \frac{d}{dx} \ln N_v - \frac{e\mu_n \Delta n}{\sigma} \frac{d}{dx} \ln N_c \right) dx \\ & + kT \int_0^L \frac{1}{\sigma} \left( e\mu_p \frac{d}{dx} \Delta p - e\mu_n \frac{d}{dx} \Delta n \right) dx \end{aligned} \quad (2.100b)$$

The alternative form of Eq. (2.100) uses the expressions

$$dE_c/dx = \xi_0 - d\chi/dx \quad (2.101)$$

and

$$dE_v/dx = \xi_0 - d(E_g + \chi)/dx \quad (2.102)$$

which relate the derivatives of the band edges to the electrostatic field and to the gradients in the electron affinity  $\chi$  and the hole affinity  $E_g + \chi$ . Equations (2.101) and (2.102) follow from the fact that the top of the conduction band is reached either by adding  $\chi$  to  $E_c$  or by adding  $\chi + E_g$  to  $E_v$  at any point in a semiconductor. Equations (2.100) also use  $n = \Delta n + n_0$  and  $p = \Delta p + p_0$  as well as  $\sigma = \Delta\sigma + \sigma_0$ . The  $\Delta n$  and  $\Delta p$  are light-induced changes in population; and the quantity  $\sigma$ , the total conductivity in the presence of light, is larger than the thermodynamic equilibrium value  $\sigma_0$  by the light-induced change  $\Delta\sigma$ . In establishing Eq. (2.100) we have assumed

that  $\mu_n$  and  $\mu_p$  do not change under illumination; however, the incorporation of mobility variations into the algebra that leads to Eq. (2.100) is straightforward.

Equation (2.100), in either form, is an equation which usually does not prove useful in actual computation but which does prove useful as a catalog of possible sources of photovoltaic action in solar cells. Examination of these statements shows that our initial answer to the question of "what are the sources of photovoltaic action" was too simplistic. Focusing on Eq. (2.100a) we see that the built-in electrostatic field  $\xi_0$  is, indeed, a source of photovoltage, but we also clearly see that effective forces arising from electron and hole affinity variations and band effective density of state variations are also sources of photovoltage [34, 53]. In addition, there is a contribution of the form

$$kT \int_0^L \frac{1}{\sigma} \left( e\mu_p \frac{d}{dx} \Delta p - e\mu_n \frac{d}{dx} \Delta n \right) dx$$

which has been uncovered as a result of our exploration. This component of the photovoltage is termed the Dember potential [63].

Equation (2.100a) shows that the photovoltaic action in a solar cell structure can arise from the presence of (1) an electrostatic field, (2) effective force fields due to material property variations, and (3) the Dember potential. In its alternative form, Eq. (2.100b), it says that photovoltaic action in a cell can be thought of as arising from conduction-band edge variation with position (barriers in the conduction band), valence-band edge variation with position (barriers in the valence band), band density of states variations, and the Dember potential. Comparison of Eqs. (2.100a) and (2.100b) allows us to note that barriers in the bands need not arise just from electrostatic origins, but can also arise from affinity variations with position. Equations (2.100) also emphasize the point that photovoltaic action depends on photoconductivity existing somewhere in a solar cell structure.

Equations (2.100) are useful because they point out the fundamental sources of photovoltaic action. These equations are also useful for estimating the magnitude of the various contributions to  $V_{oc}$  in different structures. For example, assuming effective forces are not present in a particular solar cell configuration, we see from Eq. (2.100a) or (2.100b) that the contribution to  $V_{oc}$  from any built-in electrostatic field must always be less than or equal to the total band bending through the structure since<sup>†</sup>

$$(e\mu_n \Delta n + e\mu_p \Delta p)/\sigma \leq 1$$

However, the total band bending in such a situation can be as large as the

<sup>†</sup> Note that if there are no effective forces present  $dE_c/dx = dE_v/dx = \xi_0$  as follows from Eqs. (2.101) and (2.102).

band gap, which allows us to conclude that the electrostatic field contribution to  $V_{oc}$  can be  $\lesssim E_g$ . We can immediately see why depleted, built-in electric field regions in semiconductors play an important role in solar cell structures: Such regions have the charge separating electrostatic field; they are depleted of carriers in thermodynamic equilibrium, and hence can show significant photoconductivity under illumination; and their contribution to  $V_{oc}$  can be of the order of  $E_g$ .

Equations (2.100) also show us that contributions to  $V_{oc}$  arising from effective forces can be important, if there is appreciable photoconductivity in the effective force regions. As an example, we note that, if the electron affinity changes in magnitude by an amount  $|\Delta\chi|$  in a region of a solar cell structure where  $\Delta\sigma_n = \sigma$ , then the contribution to  $V_{oc}$  from this source would be  $\Delta\chi$  (plus or minus depending on the structure). The presence of such photovoltages caused by compositional grading has been demonstrated experimentally and, as pointed out by Eq. (2.100), they can be significant [64].

We can also estimate the importance of the Dember contribution to  $V_{oc}$  in Eq. (2.100). Generally, it has been argued that this term should be small compared to the built-in electrostatic field term. The basis of this argument has been to assume  $\Delta n = \Delta p$ . Then from expressions (2.100) it is seen that the Dember term is zero unless  $\mu_n \neq \mu_p$ . However, in many materials, such as amorphous solids and organics, it is not true that  $\Delta n = \Delta p$  [34]. Moreover, the hole and electron mobilities in such materials can differ by orders of magnitude; i.e., one carrier could move by hopping and the other by motion in delocalized band states.<sup>†</sup> We conclude that the Dember contribution to  $V_{oc}$  can be significant.<sup>‡</sup> We especially look for strong contributions in amorphous solids and organics [62].

We now examine more closely the physical origins of the contributions to  $V_{oc}$  seen in Eq. (2.100). We use the formulation of Eq. (2.100a) which stresses the role of electrostatic and effective force fields for the discussion. In the case of the electrostatic field, the source of the contribution to  $V_{oc}$  rests in the charge-separating action of the electric field. In the open-circuit condition a solar cell structure must counter this action by modifying the

<sup>†</sup> Although we have established Eq. (2.100) by assuming transport takes place in two bands of delocalized states, it is clear from Eq. (2.84) or (2.87) that we could have just as well assumed, for example, a band and a group of localized gap states as giving rise to the current. An equation such as (2.100) would again result.

<sup>‡</sup> Photovoltages many times the gap energies have been reported in the literature. A summary is found in Ref. [65]. From the foregoing analysis it follows that these must arise from the Dember term or from some fortuitous combination of the other sources [65], when they are true photovoltages. Often these high  $V_{oc}$  values have been observed for materials deposited on an angle [40, 65].

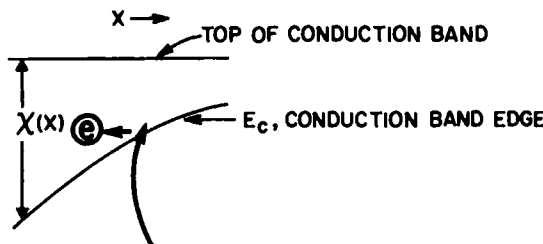


Fig. 2.27 Conduction band of a semiconductor with varying electron affinity  $\chi$ . To concentrate on the effect of  $d\chi/dx$ , a case where there is no built-in electrostatic field is shown. As depicted, photogenerated electrons excited at some point to the conduction-band edge would move to the left since no states exist to the right. In the coordinate system of Fig. 2.26, this would give a negative contribution to  $V_{oc}$ .

electric field from that present in thermodynamic equilibrium. This generates a contribution to  $V_{oc}$  through Eq. (2.98).

In the case of the effective terms, the contribution arising from the variation in the electron affinity may be discussed with the aid of Fig. 2.27 which depicts a situation where there is no built-in electrostatic field so we can focus on the effect of  $d\chi/dx$ . From this figure, it is seen that photogenerated electrons excited across the gap to the conduction band edge will tend to move to the left in their thermal motion due to the absence of available states at their energy to the right. In open circuit, a cell structure sets up an electric field to counter this tendency. Through Eq. (2.98), this field contributes to  $V_{oc}$  and, due to the choice of coordinate system in the figure, the contribution is negative for  $d\chi/dx < 0$ .

The physical origin of the term in Eq. (2.100) caused by the variation in hole affinity ( $\chi + E_g$ ) is, of course, the same as that driven by  $d\chi/dx$ . The terms driven by variations in the effective densities of states may also be viewed in the same manner as the  $d\chi/dx$  and the  $d(\chi + E_g)/dx$  contributions to  $V_{oc}$ , in that their physical origin lies in the unavailability of states in one direction. For example, if photogenerated holes find the effective density of states in the valence band decreasing towards the right, the holes have a tendency to move to the left in their thermal motion. In the coordinate system of Eq. (2.100), this gives a positive contribution to  $V_{oc}$ .

The Dember potential seen in Eq. (2.100) also has a simple physical explanation: When the change in the diffusion current of holes, which occurs between thermodynamic equilibrium and the open-circuit condition, does not equal the change in the diffusion current of electrons, which occurs between thermodynamic equilibrium and the open-circuit condition, an electric field is set up by a cell structure to counter this net current. This contribution to the electric field present under open-circuit conditions, through Eq. (2.98), produces a component of  $V_{oc}$ .

### 2.9 CONCLUDING REMARKS

Manipulation similar to that which produced Eq. (2.100) can be used to obtain a general expression for the  $J$ - $V$  characteristic seen in Fig. 2.25 for a solar cell. This general expression for the current density  $J$  produced under illumination by a cell developing a voltage  $V$  (where  $0 \leq V \leq V_{oc}$ ) is most easily written in the form  $V = V(J)$ ; viz. [34],

$$\begin{aligned} V = & - \int_0^{L_B} \left( \frac{e\mu_n \Delta n + e\mu_p \Delta p}{\sigma} \right) \xi_0 dx + kT \int_0^{L_B} \frac{1}{\sigma} \left( e\mu_p \frac{d}{dx} \Delta p - e\mu_n \frac{d}{dx} \Delta n \right) dx \\ & + \int_0^{L_B} \left( \frac{e\mu_n \Delta n}{\sigma} \right) d\chi dx + \int_0^{L_B} \left( \frac{e\mu_p \Delta p}{\sigma} \right) \left( \frac{d\chi}{dx} + \frac{dE_g}{dx} \right) dx \\ & - kT \int_0^{L_B} \left[ \frac{e\mu_p \Delta p}{\sigma} \frac{d}{dx} \ln N_v - \frac{e\mu_n \Delta n}{\sigma} \frac{d}{dx} \ln N_c \right] dx + J \int_0^{L_B} \frac{dx}{\sigma} \end{aligned} \quad (2.103)$$

As was the case for Eq. (2.100), the expression uses the sign conventions for  $J$  and  $V$  of Fig. 2.26. Consequently, the last term in Eq. (2.103) is a voltage-loss term arising from the resistance inherent in a cell structure (see Section 3.2). Equation (2.103) usually is not actually used to compute the  $J$ - $V$  characteristic of a cell; however, it is useful for visualizing the complexity of the problem we are up against. As can be seen, it explicitly points out that determining the  $J$ - $V$  characteristic of a cell necessitates knowing  $\Delta n = \Delta n(x)$  and  $\Delta p = \Delta p(x)$ . These functions  $\Delta n$  and  $\Delta p$  are themselves functions of  $V$  and the level of illumination.

In the preceding section we have established equations necessary for determining  $\Delta n = \Delta n(x)$  and  $\Delta p = \Delta p(x)$ ; however, to close the mathematical system, one additional equation is required. This additional relation is Poisson's equation, viz.,

$$\frac{d}{dx} (\varepsilon \xi) = e(p - n - n_i + \dots) \quad (2.104)$$

Here, for definitiveness, an assumed  $i$ th group of localized states is taken as being acceptorlike, and implied terms allow for any additional charge residing in localized states. In completed form, the mathematical system describing solar cell operation consists of the equations developed in the preceding sections, Poisson's equation, and appropriate boundary conditions.

When this set of equations plus boundary conditions is solved for the carrier number densities, carrier effective temperatures, and the electrostatic field for a specific level of illumination, the  $J$ - $V$  characteristic can be determined from equations such as Eqs. (2.62), (2.66), and (2.98), or alternatively

from Eq. (2.103). However, this mathematical system describing photovoltaic device operation is seen to be quite formidable. It is a set of coupled, nonlinear differential equations.

In attempting to solve the mathematical system, a number of assumptions are frequently made in solar cell device analysis. These include (1) linearizing the net recombination models of Section 2.6, (2) ignoring the possibility that expression (2.48) and Eq. (2.49) may not be valid in some materials, and for high levels of illumination, (3) ignoring hot-carrier effects, (4) assuming superposition is valid, and (5) assuming the existence of quasi-neutral regions in solar cell structures. We have already discussed the first three of these effects in the course of our review of the basic physics.

The validity of invoking superposition depends on the ability to linearize the full system of equations and boundary conditions [66, 67]. For many photovoltaic configurations, not just the recombination models, but the full mathematical system can be reasonably linearized, and for others it cannot. We shall discuss this further when we analyze actual device structures. Related to this question of linearization is the often-made assumption of the existence of quasi-neutral regions even in the presence of current flow in

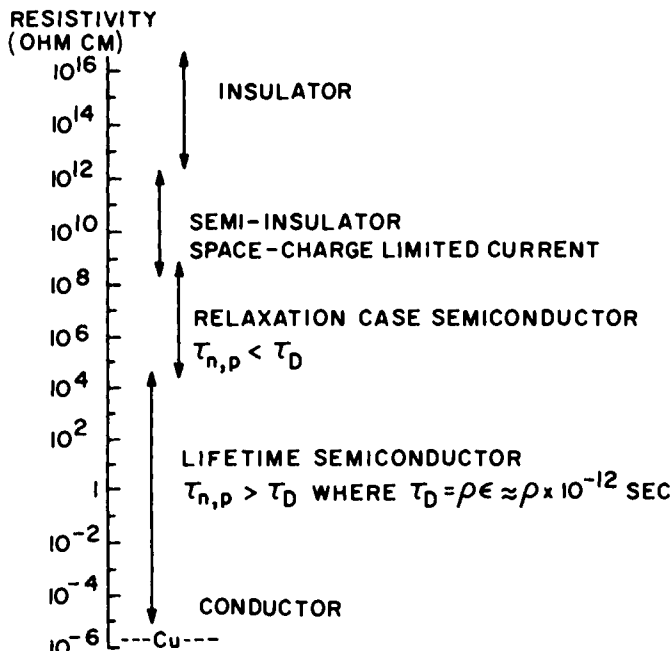


Fig. 2.28 Classification of materials by electrical resistivities. The minority carrier lifetime is  $\tau_{n,p}$  and the dielectric relaxation time is  $\tau_D$  with  $\tau_D = \rho \epsilon$ . Here  $\rho$  is the resistivity in the units of ohm cm and  $\epsilon$  is the material permittivity which is assumed to have the value  $10^{-12}$  F/cm.

photovoltaic structures. As we shall see in succeeding chapters, this assumption, when valid, greatly facilitates the mathematical analysis.

The assumption that there are quasi-neutral regions outside of the barrier region, even in the presence of current flow, is predicated upon carrier lifetimes  $\tau_{n,p}$  (see Section 2.6) being much larger than the dielectric relaxation time  $\tau_D$ . The dielectric relaxation time is defined by [1, 6]

$$\tau_D = \varepsilon/\sigma = \varepsilon\rho \quad (2.105)$$

If  $\tau_{n,p} > \tau_D$ , then mobile carriers (in bands or in localized states) can exist long enough to enable them to neutralize charge; hence, quasi-neutral regions are possible in this case even in the presence of current flow. Figure 2.28 shows the ranges  $\tau_{n,p} > \tau_D$  (lifetime semiconductor) and  $\tau_{n,p} < \tau_D$  (relaxation semiconductor) for a hypothetical material whose permittivity  $\varepsilon$  is such that  $\tau_D = \rho \times 10^{-12}$  sec ( $\rho$  in ohm cm) and whose carrier lifetime  $\tau_{n,p} \approx 10^{-8}$  sec. In the relaxation semiconductor regime [68], quasi-neutrality is not a justifiable a priori assumption. In the extreme case of the space-charge limited regime seen in Fig. 2.28, electric fields, arising from the space charge, control currents. As we mentioned in previous sections, carrier lifetimes less than  $10^{-8}$  sec exist in solids such as amorphous and organic materials. For lifetimes less than  $10^{-8}$  sec, the various regimes seen in Fig. 2.28 would shift appropriately to higher conductivities.

## REFERENCES

1. See, e.g., C. Kittel, "Introduction to Solid State Physics," 5th ed. Wiley, New York, 1976; R. H. Bube, "Electronic Properties of Crystalline Solids." Academic Press, New York, 1974.
2. H. F. Mataré, "Defect Electronics in Semiconductors." Wiley (Interscience), New York, 1971.
3. J. Friedel, "Dislocations." Pergamon, Elmsford, New York, 1964.
4. A. L. Fripp, *J. Appl. Phys.* **46**, 1240 (1975).
5. M. E. Cower and T. O. Sedgwick, *J. Electrochem. Soc.* **119**, 1565 (1972).
6. S. Sze, "Physics of Semiconductor Devices." Wiley (Interscience), New York, 1969; A. S. Grove, "Physics and Technology of Semiconductor Devices." Wiley, New York, 1976; S. Wong, "Solid State Electronics." McGraw-Hill, New York, 1966; R. J. Elliott and A. F. Gibson, "An Introduction to Solid State Physics and Its Applications." Macmillan, New York, 1974; A. Bar-Lev, "Semiconductors and Electronic Devices." Prentice-Hall, New York, Englewood Cliffs, New Jersey, 1979.
7. H. Richter and O. Furst, *Z. Naturforsch.* **6a**, 38 (1951).
8. S. C. Moss and J. F. Graczyk, *Phys. Rev. Lett.* **23**, 1167 (1969).
9. P. G. Le Comber and J. Mort, eds., "Electronic and Structural Properties of Amorphous Semiconductors." Academic Press, New York, 1973.
10. S. C. Moss and J. F. Graczyk, *Proc. Int. Conf. Phys. Semicond.*, 10th, Cambridge, Massachusetts (Keller, Hensel, and Stern, eds.). U.S. Atomic Energy Commission, 1970.
11. E. A. Davis, *Endeavour* **30**, 55 (1971).

12. D. E. Polk, *J. Non-Cryst. Solids* **5**, 365 (1971).
13. R. F. Peierls, "Quantum Theory of Solids." Oxford Univ. Press, London and New York, 1955.
14. M. L. Cohen and T. K. Bergstresser, *Phys. Rev.* **141**, 789 (1966).
15. F. Herman and W. E. Spicer, *Phys. Rev.* **174**, 906 (1968).
16. R. A. Smith, "Semiconductors," 2nd ed. Cambridge Univ. Press, London and New York, 1978.
17. A. Many, Y. Goldstein, and N. B. Grover, "Semiconductor Surfaces." North-Holland Publ., Amsterdam, 1965.
18. A. M. Stoneham, "Theory of Defects in Solids." Oxford Univ. Press (Clarendon), London and New York, 1975; J. H. Crawford and L. M. Slifkin, eds., "Point Defects in Solids." Plenum, New York, 1975.
19. H. Meier, "Organic Semiconductors." Verlag Chemie, Weinheim, 1974.
20. C. B. Duke and L. B. Schein, *Phys. Today* pp. 43-48 (Feb. 1980).
21. See, e.g., O. H. LeBlanc, *J. Chem. Phys.* **35**, 1275 (1961); **36**, 1082 (1962); J. Katz, S. A. Rice, S. Choi, and J. Jortner, *ibid.* **39**, 1683 (1963); W. L. McCubbin and R. Manne, *Chem. Phys. Lett.* **2**, 230 (1968); K. Moorjani and C. Feldmann, *Rev. Mod. Phys.* **36**, 1042 (1964); J. M. André, J. Delhalles, G. Kapsoménos, and G. Leroy, *Chem. Phys. Lett.* **14**, 485 (1972).
22. See, e.g., P. W. Anderson, *Phys. Rev.* **109**, 1492 (1958); M. H. Cohen, H. Fritzsché, and S. R. Ovshinsky, *Phys. Rev. Lett.* **22**, 1065 (1969).
23. D. Adler, "Amorphous Semiconductors." CRC Press, Cleveland, Ohio, 1971.
24. See, e.g., N. F. Mott and H. Jones, "Theory of the Properties of Metals and Alloys." Dover, New York, 1958.
25. J. Tauc, ed., "Amorphous and Liquid Semiconductors." Plenum, New York, 1974.
26. R. S. Knox, *Solid State Phys. Suppl.* **5** (1963).
27. G. Wannier, *Phys. Rev.* **52**, 191 (1937).
28. A. S. Davydov, "Theory of Molecular Exitons." McGraw-Hill, New York, 1962.
29. T. Holstein, *Ann. Phys. N.Y.* **8**, 343 (1959); J. Yamashita, T. Kurosawa, *Phys. Chem. Solids* **5**, 34 (1958).
30. J. T. Devreese, ed., "Polarons in Ionic Crystals and Polar Semiconductors." North-Holland Publ., Amsterdam, 1972.
31. C. H. Seager, D. Emin, and R. K. Quinn, *Phys. Rev. B: Solid State* **8**, 4746 (1973).
32. A. K. Ghosh and T. Feng, *J. Appl. Phys.* **49**, 5982 (1978).
33. E. A. Davis, in "Electronic and Structural Properties of Amorphous Semiconductors" (P. G. LeComber and J. Mort, eds.). Academic Press, New York, 1973.
34. S. J. Fonash, *CRC Crit. Rev. Solid State Mater. Sci.* **9**, 107 (1980).
35. V. Y. Merritt and H. J. Hovel, *Appl. Phys. Lett.* **29**, 414 (1976).
36. C. K. Chaing, S. C. Gau, C. R. Fincher, Jr., Y. Park, A. MacDiarmid, and A. Heeger, *Appl. Phys. Lett.* **33**, 18 (1978).
37. A. Barnett and A. Rothwarf, *IEEE Trans. Electron Devices*, **ED-27**, 615 (1980).
38. W. Franz, *Z. Naturforsch.* **13a**, 484 (1958).
39. L. V. Keldysh, *Sov. Phys.-JETP (Engl. Transl.)* **7**, 788 (1958).
40. J. I. Pankove, "Optical Processes in Semiconductors." Prentice-Hall, Englewood Cliffs, New Jersey, 1971.
41. W. van Roosbroek and W. Shockley, *Phys. Rev.* **94**, 1558 (1954).
42. P. T. Landsberg, *Phys. Status Solidi* **41**, 457 (1970).
43. J. L. Moll, "Physics of Semiconductors." McGraw-Hill, New York, 1964.
44. C. R. Fang and J. R. Hauser, *Conf. Rec. IEEE Photovoltaic Spec. Conf.*, 13th p. 1318. IEEE, New York, 1978; D. Redfield, *Conf. Rec. IEEE Photovoltaic Spec. Conf.* 14th. p. 580. IEEE, New York, 1980.
45. W. Shockley and W. T. Read, *Phys. Rev.* **87**, 835 (1952); R. N. Hall, *ibid.* **87**, 387 (1952).

46. C. T. Sah and F. A. Lindholm, *Solid-State Electron.* **16**, 1447 (1973).
47. A. H. Marshak and K. M. van Vliet, *Solid-State Electron.* **21**, 417 (1978); K. M. van Vliet and A. H. Marshak, *Solid-State Electron.* **23**, 49 (1980).
48. See, e.g., B. R. Nag, "Theory of Electrical Transport in Semiconductors." Pergamon, Elmsford, N.Y., 1972; A. van der Ziel, "Solid State Physical Electronics." Prentice-Hall, Englewood Cliffs, New Jersey, 1976; A. C. Smith, J. F. Janak, and R. B. Adler, "Electronic Conduction in Solids." McGraw-Hill, New York, 1967; J. S. Blakemore, "Semiconductor Statistics." Pergamon, Oxford, 1962.
49. V. I. Fistul, "Heavily Doped Semiconductors." Plenum, New York, 1969.
50. C. Herring, *Bell Syst. Tech. J.* **34**, 237 (1955); R. Stratton, *Phys. Rev.* **126**, 2002 (1962); *J. Appl. Phys.* **40**, 4582 (1969).
51. J. Bardeen, in "Handbook, of Physics" (E. V. Condon, ed.). McGraw-Hill, New York, 1967.
52. P. T. Landsberg and S. A. Hope, *Solid-State Electron.* **20**, 421 (1977).
53. See, e.g., H. Kromer, *RCA Rev.* **18**, 332 (1957); J. Tauc, *Rev. Mod. Phys.* **29**, 308 (1957); P. R. Emtage, *J. Appl. Phys.* **33**, 1950 (1962); L. J. Van Ryuven and F. E. Williams, *Am. J. Phys.* **35**, 705 (1967); Y. Marfaing and J. Chevallier, *IEEE Trans. Electron. Devices* **ED-18**, 465 (1971).
54. N. F. Mott and E. A. Davis, "Electronic Processes in Non-Crystalline Materials." Oxford Univ. Press, London and New York, 1971.
55. W. Beyer and H. Overhof, *Solid State Commun.* **31**, 1 (1979).
56. L. Friedman, *Phys. Rev. A* **133**, 1668 (1964).
57. P. G. LeComber, D. I. Jones, and W. E. Spear, *Philos. Mag.* **35**, 1173 (1977).
58. D. I. Jones, W. E. Spear, P. G. LeComber, S. Li, and R. Martins, *Philos. Mag.* **39**, 147 (1979).
59. A. K. Jonscher, in "Electronic and Structural Properties of Amorphous Semiconductors" (P. G. LeComber and J. Mort, eds.), pp. 329-361. Academic Press, New York and London, 1973.
60. A. L. Fahrenbruch and J. Aranovich, in "Solar Energy Conversion" (B. O. Seraphin, ed.). Springer-Verlag, Berlin and New York, 1979.
61. S. R. DeGroot and P. Mazur, "Non-Equilibrium Thermodynamics." North-Holland Publ., Amsterdam, 1962.
62. S. J. Fonash and S. Ashok, *Appl. Phys. Lett.* **35**, 535 (1979).
63. H. Dember, *Phys. Z.* **32**, 554, 856 (1931); *Naturwissenschaften* **20**, 758 (1932).
64. A. N. Imenkov, N. Nazarov, B. S. Suleimenov, B. V. Tsarenkov, and Yu. P. Yakovlev, *Sov. Phys.—Semicond. (Engl. Transl.)* **12**, 1413 (1978).
65. J. Tauc, "Photovoltaic and Thermoelectric Effects in Semiconductors." Pergamon, Elmsford, New York, 1962; V. M. Fridkin, "Photo-ferroelectrics." Springer-Verlag, Berlin and New York, 1979.
66. A. Rothwarf, *Conf. Rec. IEEE Photovoltaic Spec. Conf.*, 13th p. 1312. IEEE, New York, 1978.
67. F. Lindholm, J. S. Fossum, E. L. Burgess, *Conf. Rec. IEEE Photovoltaic Spec. Conf.*, 12th p. 33. IEEE, New York, 1976.
68. W. van Roosbroeck and H. C. Casey, Jr., *Phys. Rev. B: Solid State* **5**, 2154 (1972).

## CHAPTER 3

# Solar Cell Materials and Structures

### 3.1 INTRODUCTION

We are now ready to explore materials systems which will function as solar cells by using our knowledge of the physical properties of materials (Chapter 2) and our understanding of the origins of photovoltaic action (Section 2.8). We shall find that the materials that are involved in solar cell configurations are quite varied and are perhaps best classified according to their function as absorber materials, window materials, antireflection (AR) coatings, contact materials, and encapsulant materials.

The most important constituent of a solar cell is the absorber in which light-induced transitions produce mobile charge carriers<sup>†</sup> by processes 3 and 4 in Fig. 2.11. Materials which serve as absorbers must have optical gaps  $E_g$  which lie in a range permitting efficient coupling to the spectra of Fig. 1.3. Window materials are large gap materials (roughly with  $E_g \gtrsim 2.5$  eV) which do not appreciably absorb sunlight. They are used to form junctions (transparent part of a heterojunction, for example) or to prevent photocarrier creation near a high recombination surface, and in some configurations they serve both purposes.

<sup>†</sup> For the case of exciton photogeneration, absorption can produce mobile excitons in an absorber which can dissociate into electrons and holes.

Antireflection materials are used for optical impedance matching; they couple light efficiently into the solar cell structure [1]. Contact materials provide the ohmic contacts and grids needed for carrying the current developed by the cell. Contact materials must produce negligible electrical loss and negligible optical loss. Finally, protection of the overall device, while not hindering optical coupling, is the function of encapsulating materials found in solar cell structures.

In contemplating the selection of a materials system for a solar cell, a number of questions immediately come to mind: How thick should the absorber material be; what absorber resistivities can be tolerated; what is the optimum energy gap for an absorber; which of the sources of photovoltaic action [(a) Dember effect, (b) built-in effective force fields arising from the variation of material properties, (c) built-in electrostatic fields] should the solar cell structure be designed to employ; and what specific material configurations will be needed? In this chapter we shall endeavor to answer these questions in general terms. In later chapters we shall examine specific types of materials systems.

### 3.2 ABSORBER MATERIALS

From Figs. 2.13, 2.14, and 2.16 it can be seen that a great variety of materials types (inorganic and organic materials; crystalline, polycrystalline, and amorphous materials) can serve as the absorber in a solar cell. The required thickness of the absorber layer in a device depends on the absorption coefficient  $\alpha = \alpha(\lambda)$  of the material used. For example, it is necessary to have about a 100- $\mu\text{m}$  layer of crystalline Si to absorb most of the photons available to crystalline silicon in the AM2 spectrum, yet approximately a 1- $\mu\text{m}$  layer of crystalline GaAs or less than a 1- $\mu\text{m}$  layer of amorphous Si will absorb the same fraction of photons available to these materials in the AM2 spectrum. The reason for this difference in effective absorption lengths is seen in Figs. 2.13 and 2.16: crystalline GaAs and amorphous Si are much stronger absorbers than crystalline Si. The repercussions of the difference in the effective absorption lengths of crystalline GaAs and crystalline Si are seen graphically in Fig. 3.1 which shows photocurrent  $J_{sc}$  versus absorber thickness.

Once light is absorbed, the photogenerated currents produced must traverse the absorber region of the cell. Since the absorber material is characterized by some electrical resistivity, the absorber contributes to an internal resistance inherent to the solar cell.<sup>†</sup> As a practical matter it is generally found that this internal or series resistance  $R_s$  in a cell should be

<sup>†</sup> See the discussion pertaining to Eq. (2.103).

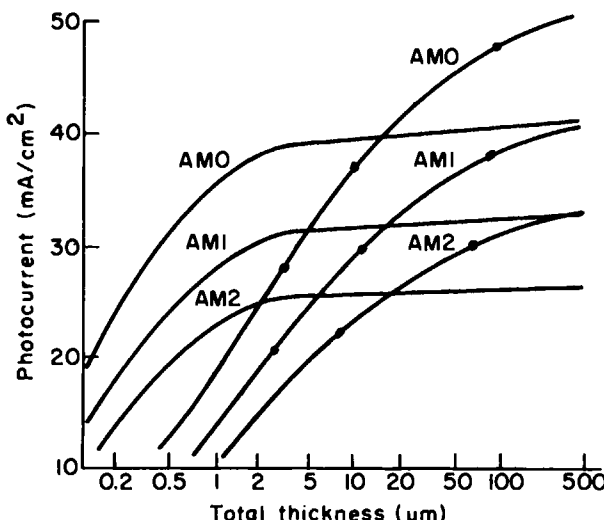


Fig. 3.1 The short-circuit current density  $J_{sc}$  available from crystalline Si (●) and crystalline GaAs (—) as a function of absorber thickness for AM0, AM1, and AM2. Calculation assumes every absorbed photon produces a collected electron-hole pair (After Hovel [1]; with permission).

no more than a few tenths of an ohm for each square centimeter of illuminated cell area under one sun conditions.<sup>†</sup> If this is exceeded the cell loads itself down with internal resistance. The implication is that absorber materials with effective absorption lengths of 1 μm can have resistivities as high as  $10^3 \Omega \text{ cm}$  but absorber materials with effective absorption lengths of 100 μm must have resistivities of 10 Ω cm or less. A plot of the range of absorber resistivities that can be tolerated in a solar cell under one sun conditions as a function of effective absorption length is given in Fig. 3.2.

Being a strong absorber by virtue of processes 3 and 4 of Fig. 2.11 and having a resistivity range consistent with its absorption length as given in Fig. 3.2 are not sufficient to ensure that a material will be an effective absorber in a solar cell structure. An important additional property of a solar cell absorber is that photogenerated carriers must have lifetimes (Section 2.6.1) which are long enough to allow these carriers to exit from the absorber region.

To translate this restriction on  $\tau$  into a length, we specifically discuss electrons and use Eqs. (2.62) and (2.67). We consider the two limiting cases: (1) photogenerated electrons exit the absorber region principally by diffusion, or (2) photogenerated electrons exit the absorber principally by drift. The objective is to develop a feel for the distance [ $L_{Dn}$  for case (1) and  $L_{\zeta n}$

<sup>†</sup> One sun conditions means there is no concentration of the illumination.

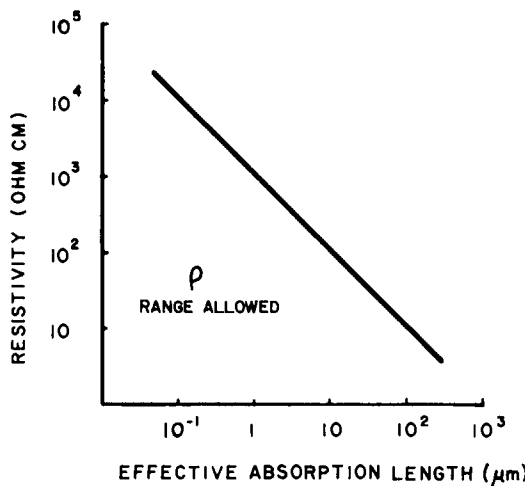


Fig. 3.2 Range of absorber resistivities that can be tolerated in a solar cell under one sun conditions as a function of the effective absorption length. Allowed values are to the left of the boundary.

for case (2)] over which a photogenerated carrier density  $\Delta n$  will decay as it moves subject to recombination characterized by a lifetime  $\tau_n$ . In this spirit, photogeneration and any temperature variations will be neglected in the region of decay.

For case (1), substitution of Eq. (2.62) into Eq. (2.67) yields

$$D_n d^2n/dx^2 = \Delta n/\tau_n$$

which, in this quest for a measure of the length  $L_{Dn}$  over which the photogenerated electrons will diffuse, becomes

$$D_n \Delta n/L_{Dn}^2 = \Delta n/\tau_n$$

This may be rearranged to give a diffusion length defined by

$$L_{Dn} = (\tau_n D_n)^{1/2} \quad (3.1)$$

which may be viewed as the distance over which  $\Delta n$  will decrease by  $e^{-1}$  as the carriers move by diffusion. The diffusion length is a material parameter for which there is a value at every point in the absorber.

For case (2), substitution of Eq. (2.62) into Eq. (2.67) yields

$$\mu_n \xi dn/dx = \Delta n/\tau_n$$

which, in our quest now for a measure of the length  $L_{\xi n}$  over which photogenerated electrons will drift as they undergo recombination, becomes

$$\mu_n \xi \Delta n/L_{\xi n} = \Delta n/\tau_n$$

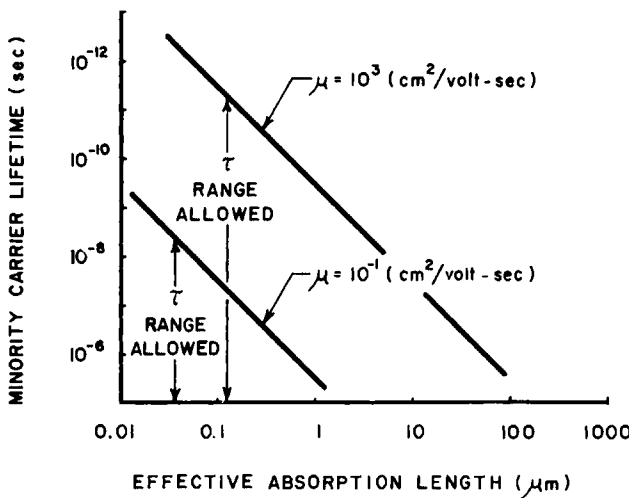


Fig. 3.3 Extraction by diffusion: If minority carriers exit the absorber material by diffusion, then the diffusion length must be of the order of the effective absorption length for efficient use of photogenerated carriers. The resulting relationship between the range of allowable  $\tau$  values and the effective absorption length is indicated graphically for  $\mu = 10^3$  and  $\mu = 10^{-1} \text{ cm}^2/\text{V-sec}$ . The value  $\mu = 10^3 \text{ cm}^2/\text{V-sec}$  corresponds to some of the better values found in crystalline absorbers as may be seen from Table 3.1.

This may be rearranged to give the "schubweg" or drift length defined by

$$L_{\xi n} = \tau_n \mu_n \xi \quad (3.2)$$

which may be viewed as the distance over which  $\Delta n$  will decrease by  $e^{-1}$  as the carriers move by drift. This length may be considered characteristic of a material at a given field strength.

Equations (3.1) and (3.2) provide additional criteria that a solar cell absorber material must fulfill. If a solar cell structure is designed such that photogenerated minority carriers exit the absorber principally by diffusion,<sup>†</sup> the diffusion length  $L_D$  must be at least equal to the effective absorption length. If a solar cell structure is such that photogenerated carriers exit the absorber layer by drift in a strong effective field or strong electrostatic field, the drift length  $L_\xi$  must be at least equal to the effective absorption length. It follows that in absorber materials with poor lifetimes and poor mobilities one wants short effective absorption lengths. It also follows that in materials with poor lifetimes and mobilities, the best approach may be to build

<sup>†</sup> If diffusion is the dominant transport mechanism for minority carriers, it does not follow that it is the dominant mechanism for majority carriers. The situation is not clear-cut for majority carriers since even small fields can give an important drift term for these carriers which are present in a high concentration.

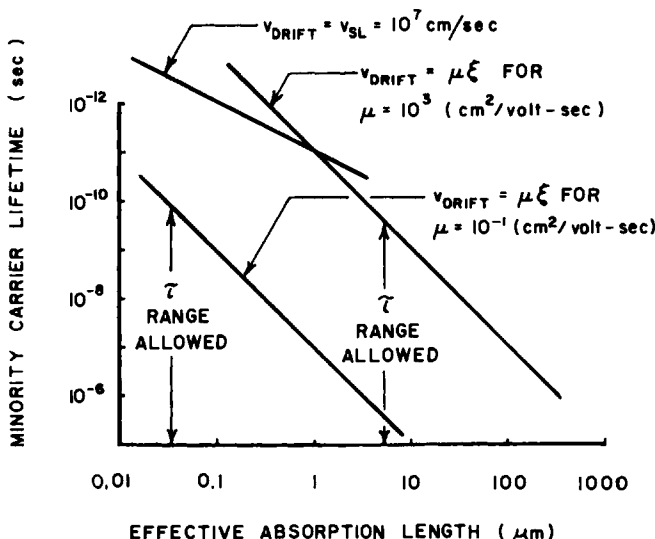


Fig. 3.4 Extraction by drift. If carriers exit the absorber material by drift, the drift length, or Schubweg, must be of the order of the effective absorption length for efficient use of the photo-generated carriers. The resulting relationship between the range of allowed  $\tau$  values and the effective absorption length is indicated graphically for  $\mu = 10^3$  and  $\mu = 10^{-1}$  ( $\text{cm}^2/\text{V-sec}$ ). A limiting drift velocity (the scattering-limited velocity introduced in Chapter 2) of  $10^7 \text{ cm/sec}$  has been assumed for both mobility values. A total band bending of 1 eV has been assumed to be developed across the effective absorption length.

in strong effective fields or strong electrostatic fields rather than to rely on diffusion to collect photocarriers, as a comparison of Eqs. (3.2) and (3.1) indicates.

Figure 3.3 expresses graphically that the diffusion length must be of the order of the absorption length when diffusion is being used for the transport of photogenerated minority carriers out of the absorber region. The resulting boundaries permit an estimation of the range of allowed carrier lifetimes. The boundaries seen in Fig. 3.3 result from Eq. (3.1). They are estimated for two cases, one of which represents mobility values typical of "good" crystalline materials.

Figure 3.4 graphically presents the constraint that the drift length must be of the order of the absorption length when drift is employed for the transport of photogenerated carriers out of the absorber region. The resulting boundaries permit an estimation of the range of allowed carrier lifetimes when drift is used. These boundaries are presented for the same two values of mobility used in Fig. 3.3. The boundaries shown result from Eq. (3.2) where the field is given by assuming 1 eV of band bending (the order of magnitude of  $E_g$  for absorber materials) developed across the absorber. The boundary

of the crystalline example becomes limited by the scattering-limited velocity (see Section 2.7.3.2) for high fields.

It is clear that a rather wide range of materials can function as absorbers and, when classifying these materials, one could go solely on the basis of their band gaps and simply declare them all to be semiconductors. However, a preferable approach is to use the scheme seen in Fig. 2.28 which accounts for the presence of localized states and accounts for transport properties. From this figure it is seen, for example, that a material with a 1- $\mu\text{m}$  effective absorption length and a resistivity of the order  $10^5 \Omega\text{ cm}$  would be classified as a semiinsulator if it has carrier lifetimes  $\tau_{n,p} < 10^{-11} \text{ sec}$ ; as a relaxation semiconductor if  $10^{-11} \lesssim \tau_{n,p} \lesssim 10^{-7} \text{ sec}$ ; and as a lifetime semiconductor if  $\tau_{n,p} \geq 10^{-7} \text{ sec}$ . As pointed out in Section 2.9, the position occupied by a material in this classification scheme has consequences in terms of which transport processes are important.

Table 3.1 presents some selected physical properties for a number of materials useful in solar cell structures as absorbers. Many of these substances may be alloyed to form new absorber materials. Examples are the full range of  $\text{Si}_x\text{Ge}_{1-x}$  alloys, the amorphous  $\text{SiH}_x$  alloys, and the  $\text{Ga}_x\text{Al}_{1-x}\text{As}$  alloys. Wide gap materials which may serve as window materials are also listed.

### 3.3 INTERFACES

If diffusion is used to draw photogenerated minority carriers from the absorber, a minority-carrier collector (sink) must be established to set up the required gradient in carrier number density. Such minority-carrier sinks are created by establishing an electrostatic field (or an effective field) region adjacent to or in the absorber. The field in this limited region is oriented to sweep minority carriers out of the absorber. These minority-carrier sink regions, which serve as the check valve of Fig. 1.1, must be relatively free of recombination centers; otherwise, the photogenerated carriers will simply recombine before entering the external circuit.

The establishment of an electrostatic field region, which serves as a minority-carrier sink and the source of charge carrier separation, necessitates the creation of an interface between dissimilar materials. To establish the alternative of an effective field region for the same purpose requires the creation of a region of varying material properties as was noted in Chapter 2. A region of varying material properties may be viewed as a series of interfaces between dissimilar materials.

Electrostatic field, or effective field, regions must extend into the absorber if drift is used to draw photogenerated carriers from across the absorber region. The result is that interfaces between dissimilar materials will again be required to create these drift-field regions.

TABLE 3.1

Material at 300°K	$E_g$ (eV)	$\chi$ (eV)	$\mu_e$	$\mu_h$	Effective masses		Crystal structure
			(cm <sup>2</sup> /V-sec)		$m_n = m_e^*/m_e$	$m_p = m_e^*/m_e$	
<b>Group IV elemental semiconductors</b>							
Ge	0.66I	4.13	3600	1800	$m_{nl} = 1.6$ $m_{nt} = 0.082$	$m_{pl} = 0.04$ $m_{ph} = 0.3$	Diamond
Si	1.11I	4.01	1350	480	$m_{nl} = 0.97$ $m_{nt} = 0.19$	$m_{pl} = 0.16$ $m_{ph} = 0.5$	Diamond
<b>Group VI (chalcogenide) elemental semiconductors</b>							
Se	1.77	4.23			0.14		Hexagonal
Te	0.32	4.44				0.135	Hexagonal
<b>Some III-V binary compounds and examples of III-V ternary alloys</b>							
AlP	2.45I		80				Zinc blende
AlAs	2.16I		280				Zinc blende
AlSb	1.65I	~3.65	200	420	0.390	0.40	Zinc blende
GaP	2.26I	4.30	130	80	0.350	0.50	Zinc blende
GaAs	1.42D	4.07	8500	420	0.072	0.68	Zinc blende
GaSb	0.72D	4.06	4000	1400	0.042	0.50	Zinc blende
InP	1.35D	4.40	4600	150	0.073	0.40	Zinc blende
InAs	0.36D	4.90	33,000	460	0.025	0.40	Zinc blende
$Al_{0.8}Ga_{0.2}As^a$	2.00I <sup>b</sup>	3.52					Zinc blende
$GaAs_{0.7}P_{0.3}^a$	1.77D <sup>c</sup>	4.15					Zinc blende
<b>Some V-VI binary compounds</b>							
$As_2Se_3$	1.30-		15	45			
	1.60						
$As_2Te_3$	1.00		170	80	0.36		
$Sb_2Se_3$	1.20		15	45			
<b>Some II-V binary compounds</b>							
$Zn_3As_2$	0.90			10			
$Zn_3P_2$	1.50D	3.8(?)		20			Tetragonal
<b>Some III-VI binary compounds</b>							
$In_2Se_3$	1.30-		30				
	2.50						
$In_2Te_3$	1.00		340		0.70	1.23	
<b>Some II-VI binary compounds and examples of II-VI ternary alloys</b>							
ZnS	3.58-	3.90-	120	5	0.25	0.50- 1.00	Sphalerite (fcc)
	3.70D	4.50					Wurtzite
ZnSe	2.67D	4.09	530	16	0.15- 0.17	0.60	Wurtzite <sup>d</sup>

*Properties of Selected Semiconductor Materials (D, direct gap; I, indirect gap)*

Lattice parameters (Å)	Coeff of linear expansion ( $10^{-6}/^{\circ}\text{K}$ )	Density (g/cm <sup>3</sup> )	Melting temperature (°C)	Dielectric constant	Conductivity types prepared	References
$a = 5.66$	5.75	5.33	958	16.0	<i>n, p</i>	2-4
$a = 5.43$	2.33	2.32	1410	11.8	<i>n, p</i>	4, 5
$a = 4.36$	7.4 $\perp$ to C		217		<i>p</i>	6
$c = 4.96$	17.0 $\parallel$ to C					
$a = 4.46$	27.2 $\perp$ to C		450		<i>p</i>	6
$c = 5.93$	16.0 $\parallel$ to C					
$a = 5.46$		2.77	2000	11.6		2-4
$a = 5.66$	3.5	3.79	1600	8.5	<i>n, p</i>	3, 4
$a = 6.14$	3.7	4.15	1050	10.3	<i>n, p</i>	3, 4
$a = 5.45$	5.3	4.14	1465	8.5	<i>n, p</i>	3, 5
$a = 5.65$	5.8	5.40	1238	10.9	<i>n, p</i>	3, 5
$a = 6.095$	6.9	5.65	712	14.0	<i>n, p</i>	3, 4
$a = 5.87$	4.5	4.74	1070	10.3	<i>n, p</i>	3, 5
$a = 6.06$	5.3	5.68	943	11.7	<i>n, p</i>	3, 4
$a = 5.66$	5.3				<i>n, p</i>	3, 5
$a = 5.59$	5.6				<i>n, p</i>	3, 5
		4.75	608			2, 7
		6.00	360			2
		5.81	612			2
$a = 8.1$	13.0	5.59	1015		<i>p</i>	2
$c = 11.4$		4.56			<i>n, p</i>	13
		5.67	890		<i>n</i>	2, 7
		5.78	667		<i>n</i>	2
$a = 5.41$		4.09	1830	8.00	<i>n, p</i>	2, 3, 5
$a = 3.82$	6.2	4.10				
$c = 6.26$						
$a = 4.00$	6.2-	5.26	1100?	8.10	<i>n, p</i>	2, 3, 5
$c = 6.54$	6.5					

*(continued)*

TABLE 3.1

Material at 300°K	$E_g$ (eV)	$\chi$ (eV)	$\mu_e$	$\mu_h$	Effective masses		Crystal structure
			(cm <sup>2</sup> /V-sec)		$m_n = m_e^*/m_e$	$m_p = m_e^*/m_e$	
ZnTe	2.26D	3.53	530	900	0.20	0.10- 0.30	Wurtzite <sup>d</sup>
CdS	2.42	4.50	~400	15	0.15- 0.17	0.80	Wurtzite <sup>d</sup>
CdSe	1.70D	4.95	600		0.13	0.45	Wurtzite <sup>d</sup>
CdTe	1.44D	4.30	300	65	0.14	0.37	Wurtzite <sup>d</sup>
HgS	2.00D		>250				Sphalerite (fcc)
HgSe	0.60D		20,000		0.05	0.02- 0.08	Sphalerite (fcc)
$\text{Cd}_{0.57}\text{Zn}_{0.43}\text{S}^a$	2.92D	4.20	~60				Wurtzite
$\text{ZnS}_{0.08}\text{Te}_{0.92}^a$	2.15D	3.55					Wurtzite
Some Group I-VI binary compounds							
$\text{Cu}_2\text{S}$	1.20D?	4.25- 4.31		25		0.58 1.4-1.5 <sup>e</sup>	Orthorhombic
$\text{Cu}_2\text{Se}$	1.20D?			2-5 <sup>f</sup> 8-15 <sup>f</sup>			Fluorite (fcc)
$\text{Cu}_2\text{Te}$	1.10- 1.40D?						Hexagonal
Some group I-III-VI (chalcopyrite) ternary compounds							
$\text{CuAlS}_2$	3.50D			<2			Chalcopyrite
$\text{CuAlSe}_2$	2.40- 2.70D			~1			Chalcopyrite
$\text{CuAlTe}_2$	2.06D						Chalcopyrite
$\text{CuInS}_2$	1.55D		200	15			Chalcopyrite
$\text{CuInSe}_2$	1.04D	~4.15	320	10			Chalcopyrite
$\text{CuInTe}_2$	0.95D		200	12 <sup>f</sup>			Chalcopyrite
$\text{CuGaS}_2$	2.42D			15			Chalcopyrite
$\text{CuGaSe}_2$	1.60- 1.70D			20			Chalcopyrite
$\text{CuGaTe}_2$	1.00D						Chalcopyrite
$\text{AgInS}_2$	1.94D		150				Chalcopyrite

(Continued)

Lattice parameters (Å)	Coeff of linear expansion ( $10^{-6}/^{\circ}\text{K}$ )	Density (g/cm <sup>3</sup> )	Melting temperature (°C)	Dielectric constant	Conductivity types prepared	References
$a = 4.27$	8.2	5.70	1295	10.10	<i>p</i>	2, 3, 5
$c = 6.99$						
$a = 4.14$	4.0	4.82	1750?	8.28– 8.64	<i>n</i>	2, 5, 8
$c = 6.72$						
$a = 4.30$	4.8	5.81	1350?	9.70– 10.70	<i>n</i>	2, 3, 5
$c = 7.01$						
$a = 4.57$	5.9	5.90	1098	11.0	<i>n, p</i>	2, 3, 5
$c = 7.47$						
$a = 5.85$		7.73	1450	30.70		3
$a = 6.08$		8.26	800	25.60		3
	4.4				<i>n</i>	5, 9
	8.0					5
$a = 11.88$						
$b = 27.33$					<i>p</i>	5, 8
$c = 13.49$					<i>p</i>	11, 12
$a = 5.75$						
$a = 12.50$					<i>p</i>	12
$c = 21.70$						
$a = 5.31$			~1300		<i>p</i>	7, 10
$c = 10.41$						
$a = 5.60$			~1200		<i>p</i>	7, 10
$c = 10.86$						
$a = 5.96$						7, 10
$c = 11.74$						
$a = 5.52$			~1050		<i>n, p</i>	7, 10
$c = 11.12$						
$a = 5.78$			990		<i>n, p</i>	7, 14
$c = 11.62$						
$a = 6.18$			780		<i>n, p</i>	7, 12
$c = 12.36$						
$a = 5.35$			1280		<i>p</i>	7, 10
$c = 10.48$						
$a = 5.60$			1040		<i>p</i>	7, 10
$c = 10.98$						
$a = 5.99$			870			7, 10
$c = 11.92$					<i>n</i>	7, 10
$a = 5.81$						
$c = 11.19$						

(continued)

TABLE 3.1

Material at 300°K	$E_g$ (eV)	$\chi$ (eV)	$\mu_e$	$\mu_h$	Effective masses		Crystal structure
			(cm <sup>2</sup> /V-sec)		$m_n = m_e^*/m_e$	$m_p = m_e^*/m_e$	
AgInSe <sub>2</sub>	1.24D		600	750			Chalcopyrite
AgInTe <sub>2</sub>	0.96D						Chalcopyrite
AgGaS <sub>2</sub>	2.62– 2.70D						Chalcopyrite
AgGaSe <sub>2</sub>	1.72– 1.80D						Chalcopyrite
AgGaTe <sub>2</sub>	1.10D						Chalcopyrite
Some group II–IV–V (chalcopyrite) ternary compounds							
ZnSiP <sub>2</sub>	2.17– 2.20D		100		0.070– 0.130		Chalcopyrite
ZnSiAs <sub>2</sub>	1.70 2.12D			140		0.07	Chalcopyrite
ZnGeP <sub>2</sub>	1.81– 2.25D			20		0.50	Chalcopyrite
ZnGeAs <sub>2</sub>	1.20D			23		0.40– 0.70	Chalcopyrite
ZnSnP <sub>2</sub>	1.70– 2.10D			55			Chalcopyrite
CdSiP <sub>2</sub>	2.16– 2.40D		150		0.090		Chalcopyrite
CdSiAs <sub>2</sub>	1.55D				300– 500		Chalcopyrite
CdGeP <sub>2</sub>	1.72D		100	25			Chalcopyrite
CdSnP <sub>2</sub>	1.17D		2000		0.040		Chalcopyrite
Some oxide semiconductors							
Cu <sub>2</sub> O	1.96– 2.10D				50– 100		Tetrahedral
TiO <sub>2</sub>	3.00		0.2		20		Tetragonal
In <sub>2</sub> O <sub>3</sub>	3.00– 3.60	4.30– 4.40					Cubic
SnO <sub>2</sub>	~3.50I	4.80– 4.90					Tetragonal
“ITO” (In <sub>2</sub> O <sub>3</sub> + SnO <sub>2</sub> alloys)	~3.60	~4.10– 4.60					Cubic?
ZnO	~3.20	4.20					Hexagonal
CdO	~2.70	~4.50?					Cubic

(Continued)

Lattice parameters (Å)	Coeff of linear expansion ( $10^{-6}/^{\circ}\text{K}$ )	Density (g/cm <sup>3</sup> )	Melting temperature (°C)	Dielectric constant	Conductivity types prepared	References
$a = 6.09$			773		<i>n, p</i>	7, 10
$c = 11.69$						
$a = 6.40$			680		<i>n</i>	7, 10, 12
$c = 12.54$						
$a = 5.74$			1040			7, 10
$c = 10.27$						
$a = 5.97$			850			7, 10
$c = 10.87$						
$a = 6.29$			720			7, 10
$c = 11.95$						
$a = 5.40$			1370		<i>n</i>	7, 10
$c = 10.44$						
$a = 5.60$			1096		<i>n, p</i>	7, 10, 12
$c = 10.89$						
$a = 5.46$			1025		<i>p</i>	7, 10
$c = 10.76$						
$a = 5.67$			850		<i>p</i>	7, 10
$c = 11.15$						
$a = 5.65$			930		<i>n, p</i>	7, 10, 12
$c = 11.30$						
$a = 5.67$			< 1200		<i>n</i>	7, 10
$c = 10.43$						
$a = 5.88$			> 850		<i>n, p</i>	7, 10, 12
$c = 10.88$						
$a = 5.73$			776		<i>n, p</i>	7, 10
$c = 10.77$						
$a = 5.90$			570		<i>n, p</i>	7, 10
$c = 11.51$						
$a = 4.28$		6.00	1500		<i>p</i>	2, 12
$a = 4.59$		4.26	2120		<i>n</i>	7, 14
$c = 2.96$						
$a = 10.12$	10.2				<i>n<sup>g</sup></i>	12, 14
$a = 4.74$	4.0					
$c = 3.19$						
$a = 10.12$	~10.2				<i>n<sup>g</sup></i>	14
$a = 3.25$	7.2					14
$c = 5.21$						
$a = 4.69$						14

TABLE 3.1

Material at 300°K	$E_g$ (eV)	$\chi$ (eV)	$\mu_e$	$\mu_h$	Effective masses		Crystal structure
			(cm <sup>2</sup> /V-sec)		$m_n = m_e^*/m_e$	$m_p = m_e^*/m_e$	
Tl <sub>2</sub> O <sub>3</sub>	~2.30	~4.20?					Cubic
Bi <sub>2</sub> O <sub>3</sub>	~2.90	~4.50?					Cubic
Cd <sub>2</sub> SnO <sub>4</sub>	~2.90	~4.50?					Orthorhombic
Some organic semiconductors							
Mg-							
phtallocyanine	~2.00			~0.1			
polyacetylene	1.35 (excitonic?)						
	1.48 (single particle)						

<sup>a</sup> Example of one of a complete series of alloys.

<sup>b</sup> Al<sub>x</sub>Ga<sub>1-x</sub>As has a direct gap for  $x < 0.31$  and an indirect gap for  $x > 0.31$ . At  $x = 0.31$ ,  $E_g = 1.90$  eV.

<sup>c</sup> GaAs<sub>1-x</sub>P<sub>x</sub> has a direct gap for  $x < 0.46$  and an indirect gap for  $x > 0.46$ . At  $x = 0.46$ ,  $E_g = 1.99$  eV.

<sup>d</sup> Also known to exist in zinc-blende form.

How are interfaces between dissimilar materials related to field regions? The answer is clear for the case of effective fields: We saw in Chapter 2 that variations in electron affinity, hole affinity, and densities of states cause the effective fields. In the case of electrostatic fields, more explanation is necessary. We begin by noting that there is an exchange of particles and energy whenever dissimilar materials are placed in intimate contact, which continues until thermodynamic equilibrium is established. This means that when materials are placed in contact to form a system, a flow of electrons, holes, and energy occurs across the interface until there is one electron-electrochemical potential (Fermi level) and one temperature established for the system in thermodynamic equilibrium. Because Fermi levels generally lie at different energies in different materials, something must occur at the interfaces between dissimilar materials to shift the individual Fermi levels until they coincide in energy. What occurs is the development of a space charge (barrier or junction) region which gives rise to an electrostatic potential energy contribution across the interface, and hence gives rise to an electrostatic field across the interface. This potential energy developed across the space-charge region at the interface shifts the energy levels of the constituent materials until their Fermi levels coincide, as required in thermodynamic equilibrium (no bias, no light, and no temperature gradient present).

Since Fermi levels (electrochemical potentials) of different materials generally lie at different energies, some scheme is needed for assessing the

(Continued)

Lattice parameters (Å)	Coeff of linear expansion ( $10^{-6}/^{\circ}\text{K}$ )	Density (g/cm <sup>3</sup> )	Melting temperature (°C)	Dielectric constant	Conductivity types prepared	References
$a = 10.54$						14
$a = 10.25$						14
$a = 5.57$						14
$b = 9.89$						
$c = 3.90$						
					$n, p$	12, 15 16

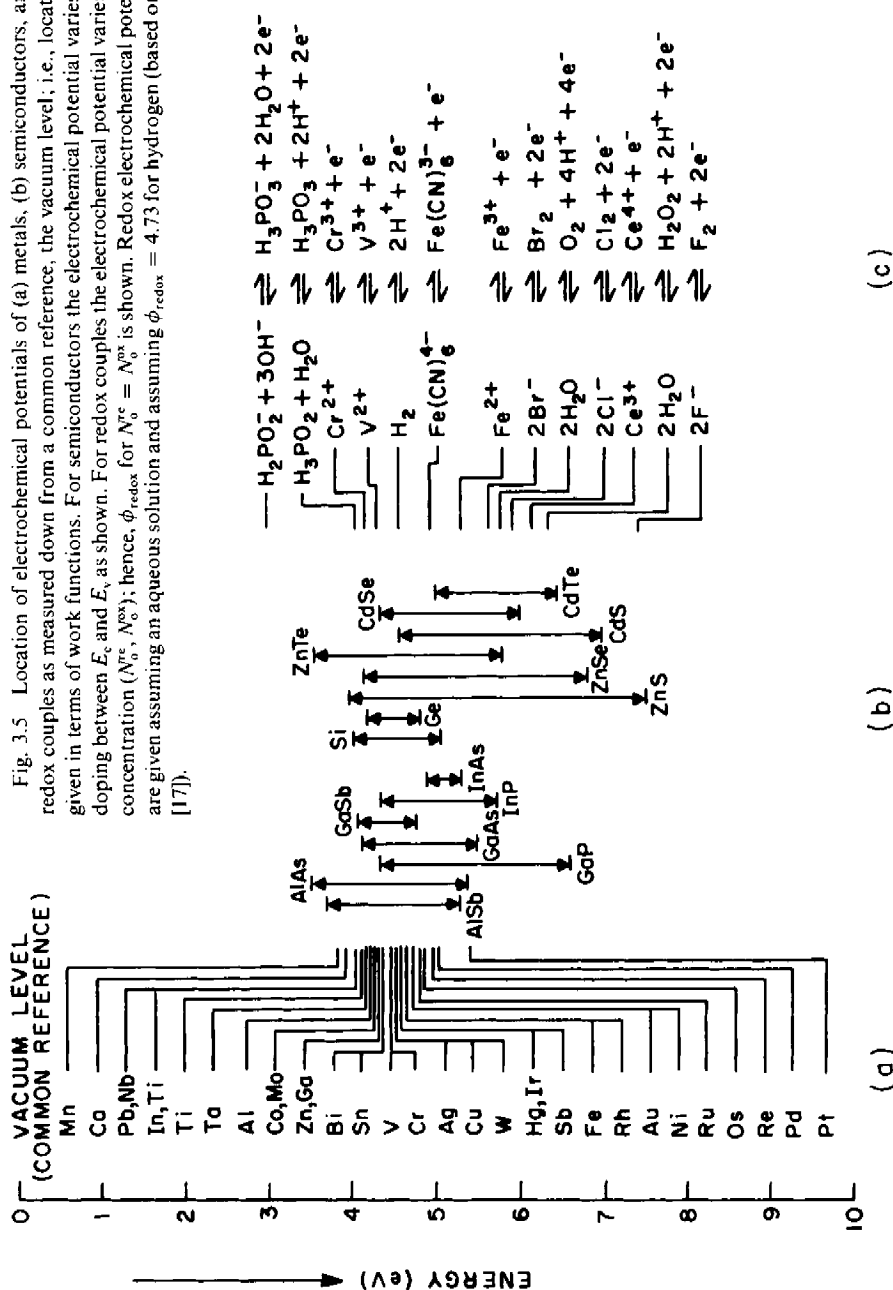
<sup>e</sup> Cast polycrystalline material.<sup>f</sup> Measured in a thin film.<sup>g</sup> Has been made degenerate.

relative positions in energy of electrochemical potentials. Such a scheme is provided by locating the Fermi level with respect to the vacuum-level reference energy. The amount, in energy, that an electrochemical potential of a material lies below this vacuum level is the work function of the material. Figure 3.5 locates the Fermi levels (electrochemical potentials) of a number of different materials with respect to the vacuum level by giving their work functions [17].<sup>f</sup> It can be seen from Fig. 3.5 that the dissimilar materials we shall be considering in interface structures can be as varied as metals, semiconductors, and oxidation-reduction (redox) couples in solution.

The total electrostatic potential energy  $V_0$  developed across an interface is equal to the difference of the work functions of the two constituents because  $V_0$  develops to equate the electrochemical potentials. Note that  $V_0$  is potential energy for an electron and we express it in electron volts. The electrostatic field  $\xi_0$  giving rise to  $V_0$  must always equal the gradient of the top of the conduction band (local vacuum level) as discussed in Chapter 2. As shown by Eqs. (2.101) and (2.102),  $\xi_0$  is also (a) equal to the gradient of the conduction edge  $E_c$ , if the electron affinity is constant in a material, and (b) equal to the gradient of the valence-band edge  $E_v$ , if the hole affinity is constant in a material.

<sup>f</sup> The work function is very useful conceptually, but as a practical matter, it is difficult to measure. Considerable variation in experimental data is found in the literature.

Fig. 3.5 Location of electrochemical potentials of (a) metals, (b) semiconductors, and (c) redox couples as measured down from a common reference, the vacuum level, i.e., location is given in terms of work functions. For semiconductors the electrochemical potential varies with doping between  $E_c$  and  $E_v$  as shown. For redox couples the electrochemical potential varies with concentration ( $N_{o^+}^{red}$ ,  $N_{o^-}^{red}$ ); hence,  $\phi_{redox}$  for  $N_{o^+}^{red} = N_{o^-}^{red}$  is shown. Redox electrochemical potentials are given assuming an aqueous solution and assuming  $\phi_{redox} = 4.73$  for hydrogen (based on Ref. [17]).



The total built-in electrostatic potential energy  $V_0$  is related by simple electrostatics to the electrostatic field  $\xi_0$  existing in thermodynamic equilibrium according to

$$V_0 = \int_{\text{interface region}} \xi_0 dx \quad (3.3)$$

The form of  $\xi_0 = \xi_0(x)$  appearing in the integrand of Eq. (3.3) (i.e., the shape of the electrostatic field region) will depend on how the charge giving rise to  $\xi_0$  is developed. That is, the form of  $\xi_0(x)$  is such that it must obey Eq. (2.104); viz.,

$$\frac{d}{dx}(\varepsilon \xi_0) = \rho \quad (3.4)$$

where  $\rho$  is charge density. Charge developed in delocalized band states and charge developed in localized gap states all contribute to  $\rho$  and, therefore, participate in shaping the electrostatic field region at an interface.

In summary, interfaces between dissimilar materials are important to solar cell devices because they can give rise to effective fields, electrostatic fields, or both, and these fields can be used to separate photogenerated charge carriers. This sets up the photocurrent and agrees with our observations based on Eq. (2.100): Field regions are basic to solar cell structures and are a fundamental source of photovoltaic action. We adopt the view that they are the principal sources of photovoltaic action in solar cells based on our estimate in Section 2.8 of their contributions to  $V_{oc}$ . The Dember contribution, the remaining possible source of photovoltaic action, is viewed as an additional source which may add to, or subtract from, these principal sources.

A natural classification scheme then presents itself for solar cells: We can classify cells according to the type of interface structure used to develop the principal field region. This classification scheme is the subject of Section 3.6. However, we must not get the impression that all interfaces in solar cell structures are primary sources of photovoltaic action. As we shall see, interface structures can also function as reflectors of minority carriers and as ohmic contacts.

### 3.4 INTERFACE TYPES

In this section interfaces are explored in general terms. We examine eight different semiconductor interfaces beginning with semiconductor-vacuum barriers. Semiconductor-vacuum barriers do not really involve dissimilar materials and are not used in solar cell structures. They are, however, a

TABLE 3.2  
*Types of Semiconductor Interfaces*

Interface structure	General features
Semiconductor-vacuum	A surface barrier dominated by surface states, physisorbed, and chemisorbed species. A relatively simple materials system for basic studies.
Semiconductor-semiconductor homojunction	Same semiconductor on either side of junction. Doping changes at interface either from $n$ to $p$ or from $n^+$ to $n$ ( $p^+$ to $p$ ).
Semiconductor-semiconductor heterojunction	Different semiconductor on either side of junction. If the doping changes type at the interface, the structure is referred to as being anisotype; if the doping does not change type, the structure is referred to as being isotype. Band bending is quite often dominated by interface states.
Semiconductor-metal interface	Barrier (electric field) region essentially in semiconductor due to very short Thomas-Fermi screening lengths of metals. In its rectifying form (barrier depletes majority-carrier density), it is referred to as a Schottky barrier. Nonrectifying forms (barrier accumulates majority carriers or very thin barrier transparent to tunneling) often serve as ohmic contacts. Structure quite often dominated by interface states.
Semiconductor-insulator interface	By proper selection of insulator, can passivate semiconductor surface states by chemically tying up the dangling bonds and rendering them electrically inactive. Insulator can protect semiconductor. Generally electrical current transport does not occur across interface.
Semiconductor-ultrathin film insulator-metal and Semiconductor-ultrathin film insulator-semiconductor interfaces	One interface system, since ultrathin insulator film thickness generally $\leq 30 \text{ \AA}$ . The ultrathin 1 layer is used to modify the barrier and transport properties of the junction. This is a conducting structure. Interface states can be important.
Semiconductor-electrolyte interface	Barrier exists in semiconductor and in electrolyte (Helmholtz and Gouy layers). Interface states, physisorbed species, and chemisorbed species can be important.
Semiconductor grain-semiconductor grain-boundary interface	Interface between a given crystal and its grain boundary in polycrystalline material. Can control intergrain transport.

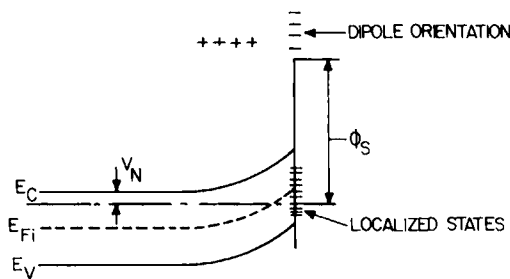


Fig. 3.6 Semiconductor–vacuum interface in thermodynamic equilibrium. In the example shown, acceptorlike surface states develop negative charge which is shielded by positive charge developed in the semiconductor barrier region. To the right of where the intrinsic Fermi level  $E_{Fi}$  passes above the Fermi level, the semiconductor has been (weakly) inverted.

good place to introduce some fundamental ideas. The eight types of semiconductor interfaces to be examined are listed in Table 3.2.

### 3.4.1 Semiconductor–Vacuum Interfaces

Figure 3.6 shows an interface between a crystalline semiconductor and vacuum in the thermodynamic equilibrium. As seen in the figure there can be a space-charge region, even at this simple interface, and an electric field which in the example is oriented from the semiconductor toward the vacuum. There are no effective forces due to variations in  $\chi$ ,  $E_g + \chi$ , etc. present in this example.

Surface states (localized gap states at a surface which are also termed interface states) are seen to cause the electrostatic field region. The surface states have been assumed acceptorlike with those occupied in thermodynamic equilibrium giving rise to a negative sheet charge at the surface. This is shielded by a positive charge developed in the space-charge region in the semiconductor. If these charged acceptor surface states were not present at the semiconductor–vacuum interface, there would be no need for a space-charge region in the semiconductor. There is no interface here between dissimilar materials in the sense that there is no necessity of equating two electrochemical potentials; hence, there is no restriction on  $V_0$ . This built-in electrostatic potential energy reaches whatever value is necessary to develop charge in the bulk semiconductor to balance the charge in the surface states.

The negative charge per area  $Q_s^-$  residing in acceptorlike surface states is given by

$$Q_s^- = \left( -e \int_{\text{gap}} f(E) g_s(E) dE \right) \quad (3.5)$$

where  $f(E)$  is the Fermi function and  $g_s(E)$  is the density of surface states (number per area per energy). This charge  $Q_s^-$  must be balanced by a positive space charge  $Q_b^+$  developed in the semiconductor. That the semiconductor bands must bend up as shown in Fig. 3.6 to develop this positive charge follows from Eqs. (3.4), (2.101), and (2.102). Alternatively, we can understand why the bands must bend up in this case by using the basic fact that the charge density  $\rho$  is given by  $\rho = e(p - n + N_D)$  together with Eqs. (2.41) and (2.42). We note that  $\rho = 0$  in the bulk of the semiconductor; hence,  $p$  must increase and  $n$  decrease as one enters into the interface region of the example of Fig. 3.6. From Eqs. (2.41) and (2.42) it is seen that this means  $E_c$  must move away from  $E_F$  and  $E_v$  must move toward  $E_F$  in the space-charge region as shown. For the example of Fig. 3.6 this has occurred to the degree that the Fermi level moves below the intrinsic Fermi level<sup>†</sup>  $E_{Fi}$  near the surface. Thus the electrons have been depleted and the holes enhanced to such an extent that this *n*-type semiconductor has been inverted<sup>‡</sup> at and near its surface. In this example the band bending developed at the interface is a barrier to the depleted, majority-carrier electrons.

If the surface states had been donorlike, positive charge would have been developed at the surface in the localized states of the *n*-type semiconductor of our example. The positive charge per area  $Q_s^+$  caused by such donorlike surface states is computed from

$$Q_s^+ = e \int_{\text{gap}} [1 - f(E)] g_s(E) dE \quad (3.6)$$

It follows that the corresponding shielding charge  $Q_b^-$  developed in the semiconductor would cause the bands to bend down as the interface is approached in this case. If the semiconductor is *n*-type, accumulation (rather than depletion) of majority carriers results. In this case a barrier is set up which hinders minority carriers and not majority carriers.

We note that in the case of accumulation, a given charge can be developed in the semiconductor over a much smaller width since majority carriers are giving rise to the charge. In depletion the same magnitude of charge requires a much wider space-charge region since charge is coming from fixed donors. In the case of depletion, if inversion occurs, charge is

<sup>†</sup> The intrinsic Fermi level  $E_{Fi}$  is used here as a parameter such that if  $E_F$  were to equal  $E_{Fi}$  at a point, then  $n = p = n_i$ , where  $n_i$  is the intrinsic number density.

<sup>‡</sup> In the bulk of this semiconductor,  $n \gg p$ . Because of the band bending at the surface, there is a point in this example in the barrier where  $n = p = n_i$ , where  $n_i$  is the intrinsic number density. At this point  $E_F = E_{Fi}$ . Closer to the surface the material is inverted, which means  $p \gg n$  and  $E_F$  lies below  $E_{Fi}$ .

also being developed in the semiconductor by minority carriers. In strong inversion this becomes the principal source of charge in the semiconductor.

Analogous to the bulk localized gap states discussed in Chapter 2, surface localized gap (interface) states are of two basic origins [18]: (1) those arising out of unsatisfied chemical bands, and (2) those arising out of structural defects and impurities. The first type (intrinsic) owes its origin to the so-called dangling bonds inherent at semiconductor surfaces due to the termination of the material. The second type [18, 19] is caused by structural defects and by impurities which diffuse into or are adsorbed at semiconductor interfaces.

### 3.4.2 Semiconductor–Semiconductor Homojunctions

#### 3.4.2.1 Semiconductor *p*–*n* Homojunctions

Figure 3.7 depicts an *n*–*p* homojunction in thermodynamic equilibrium. The built-in electrostatic potential energy  $V_0$  is equal to the difference between the work functions. Introducing the notation  $V_{bi}$  for that portion of  $V_0$  which is developed in a semiconductor, it follows that  $V_{bi} = \phi_p - \phi_n$  for a *p*–*n* homojunction. The width of the space-charge region in a *p*–*n* homojunction is  $W = l_1 + l_2$ , where  $l_1$  is the extent in the *n*-type material and  $l_2$  is the extent in the *p*-type material. By definition of a homojunction, there are no effective forces present.

The quantities  $W$ ,  $l_1$ ,  $l_2$ , and  $\xi = \xi(x)$  may be obtained by applying Poisson's equation to the interface region. There are no interface states<sup>†</sup> at the metallurgical junction, since *p*–*n* homojunctions are made by diffusing or implanting one dopant into oppositely doped material.<sup>‡</sup> Consequently, if the depletion assumption (neglect of all mobile charge in the depletion

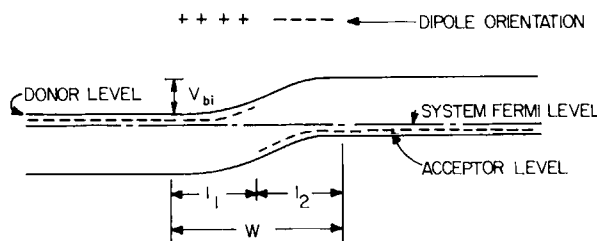


Fig. 3.7 An *n*–*p* homojunction in thermodynamic equilibrium.

<sup>†</sup> “Interface states” is usually the term used to denote surface states at a material–material interface. However, these localized states are sometimes also referred to as surface states.

<sup>‡</sup> When a junction is found in a material, it is termed a buried junction.

regions) is made for the depletion layer seen in Fig. 3.7, an analysis based on Poisson's equation yields [2, 4]

$$\xi_0 = eN_D(x + l_1)/\epsilon_s \quad (3.7)$$

for  $-l_1 \leq x \leq 0$  and

$$\xi_0 = eN_A(l_2 - x)/\epsilon_s \quad (3.8)$$

for  $l_2 \geq x \geq 0$ . These equations are based on  $x = 0$  being the metallurgical junction. The positive part of the interface dipole  $Q_b^+$  arises in the *n* side and the negative part  $Q_b^-$  rises in the *p* side of Fig. 3.7 with  $Q_b^+ = |Q_b^-|$  in the absence of interface states. With the depletion assumption,  $Q_b^+ = eN_D l_1$  and  $|Q_b^-| = eN_A l^2$ . Since  $\epsilon_s \xi_0(0) = Q_b^+ = |Q_b^-|$ , it follows on using Eqs. (3.7) and (3.8) in Eq. (3.3) that

$$l_1 = \left( \frac{2N_A \epsilon_s V_{bi}}{N_D(N_A + N_D)e} \right)^{1/2} \quad (3.9)$$

and

$$l_2 = \left( \frac{2N_D \epsilon_s V_{bi}}{N_A(N_A + N_D)e} \right)^{1/2} \quad (3.10)$$

In these equations  $N_D$  is the donor doping density ( $m^{-3}$ ) and  $N_A$  is the acceptor doping density ( $m^{-3}$ ).

For a homojunction  $\xi_0 = dE_c/dx = dE_v/dx = dE_{Fi}/dx$ ; therefore, the band bending developed across the space-charge region is easily determined as a function of position from Eqs. (3.7) and (3.8). The resulting dependence of the intrinsic Fermi level on position is [2, 4]

$$E_{Fi} = \frac{eN_D x^2}{2\epsilon_s} + \left( \frac{2N_D N_A e}{(N_A + N_D)\epsilon_s} V_{bi} \right)^{1/2} x + \frac{N_A}{N_A + N_D} V_{bi} \quad (3.11)$$

for  $-l_1 \leq x \leq 0$  and

$$E_{Fi} = \frac{-eN_A x^2}{2\epsilon_s} + \left( \frac{2N_D N_A e}{(N_A + N_D)\epsilon_s} V_{bi} \right)^{1/2} x + \frac{N_A}{N_A + N_D} V_{bi} \quad (3.12)$$

for  $l_2 \geq x \geq 0$ . These follow from the above and the condition that the total band bending is  $V_{bi}$  with  $E_{Fi}(x = -l_1) = 0$ .

Equations (3.7)–(3.12) characterize a *p*–*n* homojunction within the framework of the depletion assumption. To avoid this assumption, a solution of Poisson's equation which considers the contributions of charge carriers in the bands may be undertaken to characterize the junction in thermodynamic equilibrium.

If the materials system of Fig. 3.7 is driven out of thermodynamic equilibrium by bias, by light, by a temperature gradient, etc., then  $V_{bi}$

becomes  $(V_{bi} - V)$ , where  $V$  is the change in the band bending across the junction. If the equations resulting from the depletion assumption are used in this situation (they are valid in so far as the depletion assumption remains valid, then  $V_{bi}$  in Eqs. (3.9)–(3.12) is replaced by  $(V_{bi} - V)$  [2, 4].

From the discussion of Section 3.3 it follows that a  $p-n$  homojunction in an absorber can serve as a sink for photogenerated electrons diffusing out of the  $p$  side and for photogenerated holes diffusing out of the  $n$  side, permitting current collection by diffusion. Alternatively, an intrinsic ( $i$ ) layer which develops little charge can be inserted between  $Q_b^+$  of the  $n$  region and  $Q_b^-$  of the  $p$  region giving an extensive region where photogenerated carriers can be separated by drift. This variation is known as a  $p-i-n$  homojunction. In either case it follows from Section 2.8 that the depleted  $p-n$  or the  $p-i-n$  structure provides an excellent vehicle for developing a photovoltage. Hence, it is not surprising that the homojunction structure has been the subject of extensive solar cell research and development work. The  $p-n$  junction solar cell is discussed in Chapter 4.

#### 3.4.2.2 Semiconductor $n^+ - n$ ( $p^+ - p$ ) Homojunctions

Figure 3.8 depicts an  $n^+ - n$  homojunction. Poisson's equation may be used to characterize the space-charge region of this interface structure; however, since the doping in the  $n^+$  region is large and since the  $n$  region is accumulated, we note that the total charge region will be of limited extent spatially. It follows from Section 2.8 that the photovoltage developed by such a junction is limited, due to lack of band bending (both sides are  $n$ -type) and due to lack of a substantial region over which conductivity can be modulated by light.

From Fig. 3.8, it is seen that the  $n^+ - n$  high-low junction forms a barrier which impedes minority carrier flow from the  $n$  to  $n^+$  regions [20]. In solar cell structures this has been used to reflect photogenerated minority carriers away from the high-low junction and toward some depleted barrier region where a large photovoltage can be developed.

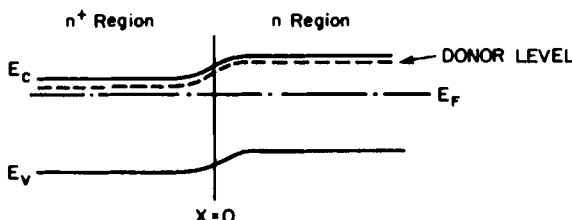


Fig. 3.8 A high-low junction in thermodynamic equilibrium.

### 3.4.3 Semiconductor–Semiconductor Heterojunctions

#### 3.4.3.1 Anisotype Heterojunctions

Figure 3.9 presents an ideal  $n-p$  (anisotype) heterojunction structure in thermodynamic equilibrium. It is assumed that there are no interface states present and that the changes in electron and hole affinities take place abruptly. Such a situation is termed the Anderson model [4]. The  $n$ -type material has an electron affinity  $\chi_1$  and a hole affinity  $\chi_1 + E_{g1}$ ; the  $p$ -type material has an electron affinity  $\chi_2$  and a hole affinity  $\chi_2 + E_{g2}$ . The work function of material 1 is  $\phi_{n1} = \chi_1 + V_{n1}$  and the work function of material 2 is  $\phi_{p2} = \chi_2 + E_{g2} - V_{p1}$ . It is assumed that  $\phi_{p2} > \phi_{n1}$  in the figure. There are no effective forces (due to variations in  $\chi$ ,  $\chi + E_g$ , etc.) present except at the metallurgical junction  $x = 0$  in the Anderson model. At  $x = 0$  the effective forces give rise to the step barriers seen.

The band bending  $V_{bi1}$  in material 1 and the band bending  $V_{bi2}$  in material 2 represent the electrostatic potential energy required to equate the Fermi levels across this interface; i.e.,  $V_0 = V_{bi1} + V_{bi2}$ . As such they must obey

$$V_{bi1} + V_{bi2} = \phi_{p2} - \phi_{n1} \quad (3.13)$$

The discontinuity in the conduction band edge  $\Delta_c$  and the discontinuity in the valence band edge  $\Delta_v$  are easily seen from the figure to be given by the difference in electron affinities,

$$\Delta_c = -(\chi_2 - \chi_1) \quad (3.14)$$

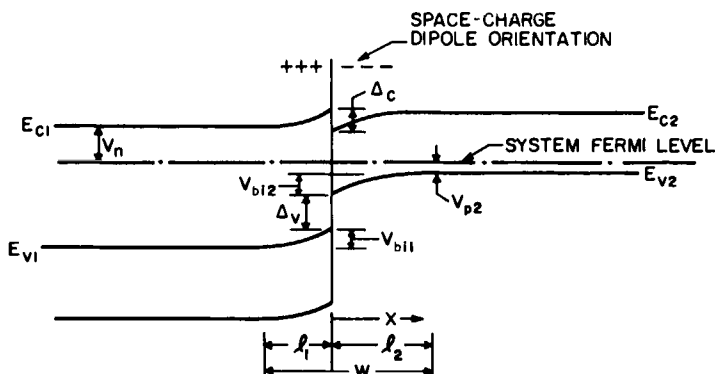


Fig. 3.9 An  $n-p$  heterojunction in thermodynamic equilibrium. In this example it is assumed that there are no interface states at  $x = 0$ , the metallurgical junction, and that the junction is abrupt. Such an idealized structure is termed the Anderson model.

and by the difference in hole affinities,

$$\Delta_v = \chi_2 + E_{g2} - (\chi_1 + E_{g1}) \quad (3.15)$$

respectively. It may be noted from these expression that  $\Delta_c$  and  $\Delta_v$  must be zero for homojunctions, as was shown in Fig. 3.7.

To further characterize this junction, the extent of the charge regions and the electrostatic field, and band bending as a function of position should be determined. If the depletion assumption (neglect of mobile charge) is valid (as it should be for both depletion regions seen in Fig. 3.9), then Poisson's equation is easily solved in each region of this structure. In more general situations other approaches, including numerical solutions, would have to be employed (see Section 3.4.4 for an example). However, for Fig. 3.9, Poisson's equation is integrated easily with the depletion assumption giving the result [1, 5, 6]

$$E_{Fi1} = \frac{e}{2\epsilon_{s1}} N_D x^2 + \frac{e}{\epsilon_{s1}} N_D l_1 x + \frac{eN_D l_1^2}{2\epsilon_{s1}} \quad (3.16)$$

for  $-l_1 \leq x \leq 0$  and

$$E_{Fi2} = \frac{-e}{2\epsilon_{s2}} N_A x^2 + \frac{eN_A l_2 x}{\epsilon_{s2}} \quad (3.17)$$

for  $l_2 \geq x \geq 0$ . These equations use the intrinsic Fermi level to express the electrostatic potential energy or band bending variation as a function of position for each material. Those boundary conditions which led to Eqs. (3.7)–(3.12) have been applied here; i.e.,  $Q_b^+ = |Q_b^-|$  and  $\xi_0(-l_1) = \xi_0(l_2) = 0$ . In addition,  $E_{Fi1}$  has been set equal to zero at  $x = -l_1$  and thus it equals  $V_{bi1}$  at  $x = 0$ . Correspondingly,  $E_{Fi2}$  has been set equal to zero at  $x = 0$  and thus it equals  $V_{bi2}$  at  $x = l_2$ . In these expressions  $\epsilon_{s1}$  is the permittivity of material 1 and  $\epsilon_{s2}$  is the permittivity of material 2. The electrostatic field  $\xi_0$  present in thermodynamic equilibrium is just the derivative of Eqs. (3.16) and (3.17).

In determining the preceding relations, it is found that [4, 6]

$$l_1 = \left( \frac{2\epsilon_{s1}\epsilon_{s2}N_A(\phi_{p2} - \phi_{n1})}{eN_D(\epsilon_{s2}N_A + \epsilon_{s1}N_D)} \right)^{1/2} \quad (3.18)$$

and that

$$l_2 = \left( \frac{2\epsilon_{s1}\epsilon_{s2}N_D(\phi_{p2} - \phi_{n1})}{eN_A(\epsilon_{s2}N_A + \epsilon_{s1}N_D)} \right)^{1/2} \quad (3.19)$$

where the sum of  $l_1$  and  $l_2$  gives  $W$ . Also, from Eqs. (3.16) and (3.17) it follows that [4, 6]

$$V_{bi} = eN_D l_1^2 / 2\epsilon_{s1} \quad (3.20)$$

and

$$V_{bi1} = eN_A l_2^2 / 2\epsilon_{s2} \quad (3.21)$$

The maximum electric field existing in the interface region is seen to occur at  $x = 0$  and is the greater of

$$\xi_{\max} = \frac{e}{\epsilon_{s1}} N_D l_1 = \left( \frac{2eN_D V_{bi1}}{\epsilon_{s1}} \right)^{1/2} \quad (3.22)$$

or

$$\xi_{\max} = \frac{e}{\epsilon_{s2}} N_A l_2 = \left( \frac{2eN_A V_{bi2}}{\epsilon_{s2}} \right)^{1/2} \quad (3.23)$$

Since continuity of electric flux density at  $x = 0$  forces  $N_D l_1 = N_A l_2$ , the maximum electric field occurs in whichever semiconductor has the smaller permittivity.

Equations (3.16)–(3.23) characterize an ideal (Anderson) heterojunction in thermodynamic equilibrium if the depletion assumption is valid. If the junction is driven out of thermodynamic equilibrium by bias, by light, or by a temperature gradient, then the band bending in material 1 becomes  $V_{bi1} - V_1$  and that in material 2 becomes  $V_{bi2} - V_2$ . These quantities replace  $V_{bi1}$  and  $V_{bi2}$  in Eqs. (3.16)–(3.23). Since  $N_D l_1 = N_A l_2$  for this case of no interface states, it follows from Eqs. (3.20) and (3.21) that [2, 4, 6]

$$[N_D \epsilon_{s1} (V_{bi1} - V_1)]^{1/2} = [N_A \epsilon_{s2} (V_{bi2} - V_2)]^{1/2} \quad (3.24)$$

Also, the total change in the band bending  $V$  is

$$V = V_1 + V_2 \quad (3.25)$$

Hence, with Eqs. (3.24) and (3.25)  $V_1$  and  $V_2$  can be expressed simply in terms of  $V$ , the bias developed or impressed on the junction.

We note that the junction shown in Fig. 3.9 has what is referred to as a spike in the conduction band. This can affect electron transport. For example, if the junction were employed as a solar cell, electrons photo-generated in  $l_2$ , and to the right, would tend to pile up at  $x = 0$  and then recombine at this plane, due to the spike. This would reduce the current-generating effectiveness of the device. Note that there is no spike for this particular junction in the valence band; however, it is possible to have a heterojunction which has a spike in both the conduction and valence bands.

For real heterojunctions it is quite possible that interface states will play a significant role in determining the junction configuration and it is quite possible that the change from one material to another will not be abrupt. In addition, there can be cross diffusion of chemical species from one semiconductor to the other which can modify doping. All of these possibilities mean that there is a great variety of heterojunction band bending configurations that can occur and all of these possibilities mean that the Anderson model

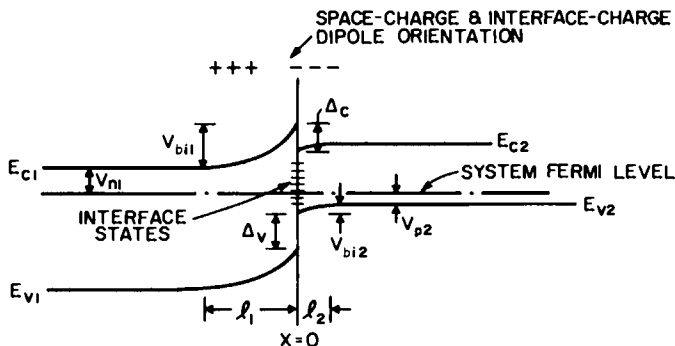


Fig. 3.10 The  $n-p$  heterojunction of Fig. 3.9 but with interface states present. Junction is shown in thermodynamic equilibrium.

is a very idealized situation. This is discussed in considerable detail in Chapter 5 which deals with applications of heterojunctions in solar cell structures.

At this point we shall look at one of these complicating factors in real heterojunctions by considering Fig. 3.10. This heterojunction is ideal except for the presence of interface states. That is, Fig. 3.10 is the same junction as Fig. 3.9 except for the presence of localized states, which are acceptorlike in nature and located at  $x = 0$ . They begin, in energy, at the band edge  $E_{v2}$  at  $x = 0$  and the total charge per area  $Q_s$  in these states in thermodynamic equilibrium is given by

$$Q_s = -e \int_0^{E_{v2}} g_s(E) [1 + \exp(E - V_{bi2} - V_{p2})/kT]^{-1} dE \quad (3.26)$$

where  $g_s(E)$  is the density of the interface states ( $\text{m}^{-2} \text{ eV}^{-1}$ ). Here all energies have been measured from the position of  $E_{v2}$  at  $x = 0$  for convenience.

Equation (3.17) is still valid; i.e., from the figure it is seen that the depletion assumption ( $\rho = -eN_A$ ) is still appropriate for the depletion region in the  $p$ -type material. We shall assume that Eq. (3.16) is also still valid for the depleted region on the  $n$  side. However, it is seen that mobile holes on the  $n$  side are more important in Fig. 3.10 than they were in Fig. 3.9. In fact, if  $E_{F11}$  were to pass above  $E_F$  to an extent that  $p \gtrsim N_D$  in such a region, then the mobile holes must be considered as a component of  $\rho$  in at least part of the space-charge region in the  $n$ -type material [2, 4]. This would invalidate the depletion assumption and strong inversion would be present.

In using Eqs. (3.16) and (3.17) in the presence of interface states, it is necessary to modify one boundary condition:  $Q_b^+$  is no longer equal to  $|Q_b^-|$

or, equivalently, the electric flux density is no longer continuous at  $x = 0$ , but rather

$$\varepsilon_{s2}\xi_2(0) = Q_s + \varepsilon_{s1}\xi_1(0) \quad (3.27)$$

This results in the previous expression for  $l_1$ , Eq. (3.18), being replaced by

$$l_1 = \left\{ -\frac{N_A}{N_D} \frac{Q_s}{\varepsilon_{s2}} + \frac{N_A}{N_D} \left( \frac{N_A^2}{N_D^2} \frac{Q_s^2}{\varepsilon_{s1}^2} + 4 \left( \frac{eN_A^2}{2N_D\varepsilon_{s1}} + \frac{eN_A^2}{2N_A\varepsilon_{s2}} \right) \times \left( \phi_{p2} - \phi_{n1} - \frac{Q_s}{2eN_D\varepsilon_{s1}} \right) \right)^{1/2} \right\} / \left\{ 2 \left( \frac{eN_A^2}{2N_D\varepsilon_{s1}} + \frac{eN_A^2}{2N_A\varepsilon_{s2}} \right) \right\} \quad (3.28)$$

Correspondingly,  $l_2$  becomes

$$l_2 = \left\{ \frac{N_A}{N_D} \frac{Q_s}{\varepsilon_{s1}} + \left( \frac{N_A^2}{N_D^2} \frac{Q_s^2}{\varepsilon_{s1}^2} + 4 \left( \frac{eN_A^2}{2N_D\varepsilon_{s1}} + \frac{eN_A^2}{2N_A\varepsilon_{s2}} \right) \times \left( \phi_{p2} - \phi_{n1} - \frac{Q_s}{2eN_D\varepsilon_{s1}} \right) \right)^{1/2} \right\} / \left\{ 2 \left( \frac{eN_A^2}{2N_D\varepsilon_{s1}} + \frac{eN_A^2}{2N_A\varepsilon_{s2}} \right) \right\} \quad (3.29)$$

Thus the presence of  $Q_s$  causes the size of the space-charge regions in each semiconductor to change. Equations (3.20) and (3.21) remain valid. However, since Eqs. (3.28) and (3.29) are now employed for  $l_1$  and  $l_2$ ,  $V_{bi1}$  and  $V_{bi2}$  are modified subject to the condition that their sum must remain  $\phi_{p2} - \phi_{n1}$ .

If the density of interface states giving rise to  $Q_s$  is large enough, it is possible to have situations where the presence of  $Q_s$  acts to shield the semiconductors from one another. Essentially the interface states in these situations can develop any charge necessary with a very small displacement of the Fermi level position at  $x = 0$  of Fig. 3.10. This pinning of the Fermi level at  $x = 0$  has the result that if one changes  $\phi_{p2}$  in Fig. 3.10, for example, then it is only  $V_{bi2}$  which adjusts. We shall discuss the phenomenon of Fermi level pinning more extensively in the section on metal-semiconductor structures.

The electric field  $\xi_0(x)$  in the presence of interface states is still given by the derivative of Eqs. (3.16) and (3.17), for  $-l_1 \leq x \leq 0$  and for  $l_2 \leq x \leq 0$ , respectively, but now the  $l_1$  and  $l_2$  in these expressions are given by Eqs. (3.28) and (3.29). The maximum electrostatic field is still at  $x = 0$  as it was for Fig. 3.9; again its value is the maximum of Eqs. (3.22) and (3.23). Because of Eq. (3.27) this maximum no longer simply depends on the relative values of  $\varepsilon_{s1}$  and  $\varepsilon_{s2}$ .

These preceding equations form a complete set for determining  $l_1$ ,  $l_2$ ,  $W$ ,  $Q_s$ , etc., for this heterojunction in thermodynamic equilibrium. In this case,

if the structure is driven out of thermodynamic equilibrium,  $V_{bi1}$  must be replaced everywhere by  $(V_{bi1} - V_1)$  and  $V_{bi2}$  must be replaced everywhere by  $(V_{bi2} - V_2)$ . Equation (3.25) is still valid, but Eq. (3.24) is not. Hence, to obtain  $V_1 = V_1(V)$  or  $V_2 = V_2(V)$ , Eqs. (3.25) and (3.27) must be used. Stated simply, with interface states present, a given  $V$  is distributed differently than it would be if there were no interface states.

It is clear that localized gap states at the interface (arising from disrupted bonding, defects, or impurities) can have a major influence on junction parameters in heterojunctions. When we add to this the possibility that the junction may not be abrupt in reality and that cross diffusion can occur, it becomes clear that barrier formation in heterojunctions can be complex. We will return to these points in Chapter 5.

#### 3.4.3.2 Isotype Heterojunctions

There are a number of isotype (same type doping) heterojunctions possible [2, 4, 6]. Again their space-charge regions are analyzed using Poisson's equation and the principles previously discussed. Figure 3.11 depicts an example which is an  $n-n$  isotype heterojunction. This example has no space-charge region since both materials are assumed to have the same work function and there are no interface states present; however, there is an effective force acting on holes at the metallurgical junction due to the step in the hole affinity (i.e., there is a step barrier for holes at the metallurgical junction). Electrostatic fields (oriented oppositely in each of these semiconductors) would be present if there were interface states, developing charge, at the interface.

This particular example of an ideal isotype structure seen in the figure can be used to reflect minority carriers and, as will be discussed later in the chapter, such junctions can be used in solar cells to direct minority carriers to the principal, photovoltage-producing region of a cell.

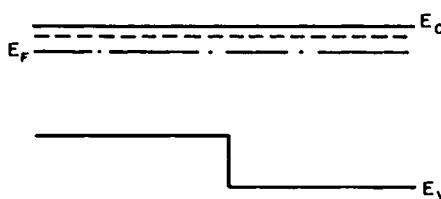


Fig. 3.11 An isotype heterojunction in thermodynamic equilibrium. This particular example has no space-charge region associated with it since both materials have the same work function and there are no interface states present. Since there is no space-charge region, there is no electrostatic force field. There is, however, an effective hole force present which is confined to the plane of the junction in the idealized abrupt structure.

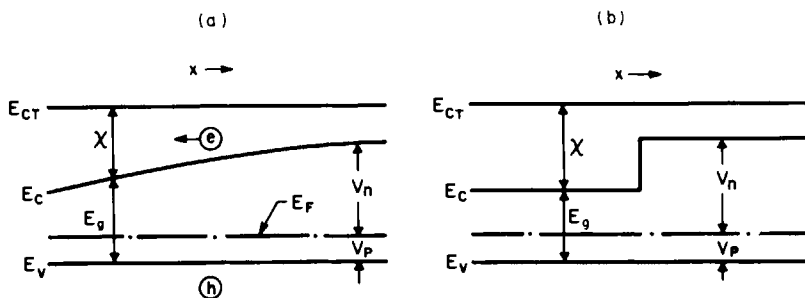


Fig. 3.12 (a) An example of gradually graded gap material. Such a material can be viewed as a series of heterojunctions. For the case shown there is no electrostatic force field present but there is an effective force acting on electrons. (b) The same change in electron affinity as seen in (a); however, in this case the change occurs abruptly. Again there is no electrostatic field present in this example. In both figures,  $F_e = -e[-d\chi/dx]$  and  $F_h = e[0]$ .

### 3.4.3.3 Graded Gap Heterojunctions

As was noted earlier, a material region in which electron affinity, band gap, hole affinity, and band effective densities of states vary with position can be viewed as a series of heterojunctions. Figure 3.12a is an example which can be viewed as a series of *p*-type materials with the same work function and same hole affinity but with a varying electron affinity. Figure 3.12a can be contrasted with Fig. 3.12b which also is made up of materials with the same work function and hole affinity, but in this case the change in electron affinity occurs abruptly.

For the particular example of a continuous heterojunction seen in Fig. 3.12a, there is no electrostatic field present, nor is there any present in Fig. 3.12b. The effective forces present are discussed in the figure caption.

### 3.4.4 Semiconductor-Metal Interfaces

Two metal-semiconductor (M-S) junctions are seen in Fig. 3.13. In both cases the semiconductor is the same *n*-type material; however, in Fig. 3.13a the metal is chosen such that  $\phi_M > \phi_n$  whereas in Fig. 3.13b the metal is chosen such that  $\phi_M < \phi_n$ . In Fig. 3.13a the semiconductor is depleted and inverted just at the surface; in Fig. 3.13b the semiconductor is accumulated. These are ideal metal-semiconductor structures with no interface states or surface dipoles present.

In each case it is seen that the electrostatic potential, and consequently the electric field region, exists in the semiconductor side of the interface. This is due to the extremely short Thomas-Fermi screening length ( $\approx 0.5 \text{ \AA}$ )

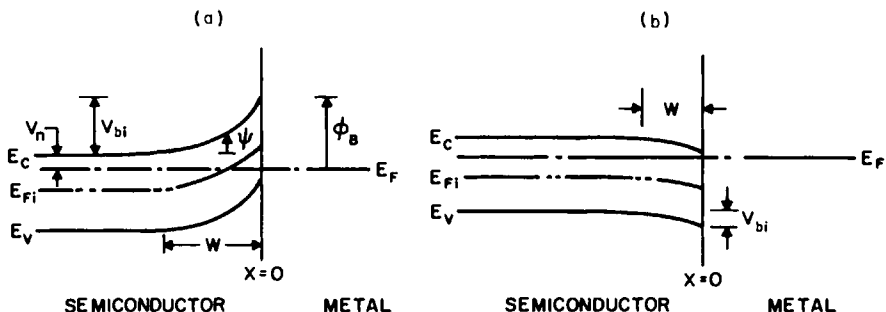


Fig. 3.13 Metal-semiconductor junctions in thermodynamic equilibrium. (a)  $\phi_M > \phi_n$ ; (b)  $\phi_M < \phi_n$ . There are no interface states nor surface dipoles present.

of metals; i.e., the metal develops its part of the space-charge dipole in essentially a sheet layer. For case (a) the band bending  $V_{bi}$  is given by

$$V_{bi} = \phi_M - \phi_n \quad (3.30a)$$

whereas for case (b)

$$V_{bi} = \phi_n - \phi_M \quad (3.30b)$$

Case (a) presents a barrier to the majority carriers; hence this type of interface can be a rectifying contact with a  $J-V$  characteristic similar to that of a  $p-n$  junction (see Section 3.6). The barrier height is characterized by  $\phi_B$ , the Schottky barrier height, given by

$$\phi_B = \phi_M - r \quad (3.31)$$

and seen in Fig. 3.13a. Case (b) presents no barrier to majority carriers; hence, this type of interface structure can be an ohmic contact (see Section 3.6). For  $p$ -type material it follows that the case of  $\phi_M < \phi_p$  gives a barrier to majority carriers whereas the case of  $\phi_M > \phi_p$  gives no barrier to majority carriers [21, 22]. We reiterate that these comments apply to ideal Schottky barriers with no surface states or surface dipoles.

As we have noted before in other interface structures, the majority carriers are depleted in regions in which there is a barrier for majority-carrier motion. This is the situation in Fig. 3.13a. In analyzing depletion regions thus far we have made the depletion assumption when appropriate. However, Fig. 3.13a is a case where material parameters are such that this approximation is not valid. Holes are seen to make a substantial contribution to the space charge near the surface (inversion layer). This gives us the opportunity to see how we can obtain a solution from Poisson's equation in such a situation. Obviously the approach we shall develop can be applied to other interfaces under corresponding conditions.

Since the space-charge region of Fig. 3.13a is depleted of majority carriers, the charge density  $\rho$  must be developed by the fixed donor sites of density  $N_D$  and also, in this case, by holes. However, for the sake of completeness let us also include the contribution of the mobile electrons in formulating  $\rho$  as it exists in thermodynamic equilibrium; viz.,

$$\rho = e[N_D + N_v e^{-(E_F - E_v(X))/kT} - N_c e^{-(E_c(X) - E_F)/kT}] \quad (3.32)$$

which follows from Eqs. (2.41) and (2.42). Expressing Eq. (3.32) in terms of the quantity  $\psi$  defined in Fig. 3.13a and using it in Poisson's equation, we obtain [2, 4, 6]

$$\frac{d^2\psi}{dx^2} = \left[ \frac{en_{n0}}{\epsilon_s} \left( 1 + \frac{p_{n0}}{n_{n0}} e^{\psi/kT} - e^{-\psi/kT} \right) \right] \quad (3.33)$$

where the bulk, thermodynamic equilibrium number densities  $n_{n0}$  and  $p_{n0}$  are related to the doping density  $N_D$  and intrinsic number density  $n_i$  by [2, 4, 6]

$$n_{n0} = N_D \quad (3.34)$$

and

$$p_{n0} = n_i^2/N_D \quad (3.35)$$

Equation (3.33) may be integrated once using  $d\psi/dx$  as an integrating factor. Using the conditions  $\psi(-W) = 0$  and  $\xi(-W) = d\psi/dx|_{-W} = 0$ , we get  $\xi_0$ , the electrostatic field present in thermodynamic equilibrium [2, 4, 6],

$$\xi_0 = \frac{2kT}{L_D} \left[ \left( \frac{\psi}{kT} - 1 + e^{-\psi/kT} \right) + \frac{p_{n0}}{n_{n0}} (e^{\psi/kT} - 1) \right]^{1/2} \quad (3.36)$$

where the extrinsic Debye length  $L_D$  is defined by

$$L_D \equiv [2\epsilon_s kT/(en_{n0})]^{1/2} \quad (3.37)$$

Finding  $\psi(x)$ , which is equivalent to finding  $E_c(x)$ ,  $E_v(x)$ , or  $E_{Fi}(x)$ , necessitates one more integration; viz.,

$$\left( \frac{2kT}{L_D} \right) (x + W) = \int_0^\psi \left[ \left( \frac{\psi'}{kT} - 1 + e^{-\psi'/kT} \right) + \frac{p_{n0}}{n_{n0}} (e^{\psi'/kT} - 1) \right]^{-1/2} d\psi' \quad (3.38)$$

The function  $\psi = \psi(x)$  is obtained by a numerical evaluation of Eq. (3.38). This gives the band bending as a function of position at the interface in thermodynamic equilibrium.

The width  $W$  of the space-charge region can be obtained from Eq. (3.38) by setting  $x = 0$  and  $\psi = V_{bi}$ . The maximum electric field at this interface occurs at  $x = 0$ ; it is

$$\xi_{\max} = \frac{2kT}{L_D} \left[ \left( \frac{V_{bi}}{kT} - 1 + e^{-V_{bi}/kT} \right) + \frac{p_{n0}}{n_{n0}} \left( e^{V_{bi}/kT} - 1 \right) \right]^{1/2} \quad (3.39)$$

in thermodynamic equilibrium. The total space charge developed in the semiconductor  $Q_b$  in thermodynamic equilibrium is

$$Q_b = \frac{2\varepsilon_s kT}{L_d} \left[ \left( \frac{V_{bi}}{kT} - 1 + e^{-V_{bi}/kT} \right) + \frac{p_{n0}}{n_{n0}} \left( e^{V_{bi}/kT} - 1 \right) \right]^{1/2} \quad (3.40)$$

These statements for  $\xi_{\max}$  and  $Q_b$  follow from Eq. (3.36).

If a given metal–semiconductor junction is such that

$$p_{n0} e^{V_{bi}/kT} < n_{n0} \quad (3.41)$$

then holes do not make a significant contribution anywhere in the semiconductor space-charge region. In this case it is seen that Eqs. (3.39) and (3.40), for example, reduce to

$$\xi_{\max} = (2en_{n0}/\varepsilon_s)^{1/2}(V_{bi} - kT)^{1/2} \quad (3.42)$$

and

$$Q_b = (2en_{n0}\varepsilon_s)^{1/2}(V_{bi} - kT)^{1/2} \quad (3.43)$$

By comparing these with Eqs. (3.22) and (3.23), it is seen that expressions (3.42) and (3.43) are what would be expected from the depletion approximation. There is a slight difference:  $V_{bi}$  is replaced by  $(V_{bi} - kT)$  since this analysis did not neglect the mobile majority carriers. They do contribute to the space charge until the bands bend  $\sim kT$ . Frequently, when the depletion approximation is made in analyses of various interface structures,  $(V_{bi} - kT)$  is used in place of  $V_{bi}$  to correct for this contribution of majority carriers near the barrier edge. This correction appears wherever  $V_{bi}$  would be used.

If a given metal–semiconductor junction is such that expression (3.41) is valid, then Eq. (3.38) can be integrated analytically and it gives a  $\psi(x)$  that depends quadratically on  $x$ . In fact, it follows that this  $\psi(x)$  must have the same form as Eq. (3.16). A barrier of this latter form at a metal–semiconductor junction is termed a Schottky barrier (although the term Schottky barrier has also come to be applied to any rectifying M–S structure even when  $\psi(x)$  is given by Eq. (3.38) [21]).

Thus far we have used the Mott–Schottky model [22] of metal–semiconductor interface which neglects any effects of interface states or

surface dipoles. From Eq. (3.31) it predicts that  $d\phi_B/d\phi_M = 1.0$ . Experimentally it is found that [23]

$$d\phi_B/d\phi_M = a \quad (3.44)$$

where  $0.1 \lesssim a \lesssim 0.7$  depending on the semiconductor and the preparation of the semiconductor surface. Phenomenologically this is explained in terms of a model introduced by Bardeen which includes the effects of interface states and surface dipoles [24].

To explore the Bardeen model we admit that it seems very reasonable to accept the possibility that interface states may exist at the semiconductor-metal interface due to dangling bonds (intrinsic interface states) and due to defects and impurities (extrinsic interface states). However, their existence alone is not sufficient to explain Eq. (3.44). In heterojunctions we saw that the presence of interface states alone was sufficient to explain deviations of the barrier shape and built-in potential values from ideal behavior. This can not happen in a metal-semiconductor junction because simple electrostatics tells us that the image of any surface charge held in interface states will appear in the immediately adjacent metal surface as may be seen from Fig. 3.13. The space-charge region in the semiconductor does not have to adjust to the presence of charge in interface states in this case.

The situation is changed, however, if there is a thin interfacial layer—perhaps an oxide, perhaps a chemically modified layer—present. If charge in interface states is separated from the metal by  $d$  where  $d \gtrsim 4-10 \text{ \AA}$ , then part of the charge in the interface states is reflected into the semiconductor. Flux lines originating in the interface states, plus flux lines from the semiconductor space-charge region, cross  $d$  developing a potential  $\Delta$ . Now, in thermodynamic equilibrium,

$$V_{bi} + \Delta = \phi_M - \phi_n \quad (3.45)$$

The barrier has been modified due to the presence of the interface states and an ultrathin interfacial layer. The Schottky barrier height is not that predicted by Eq. (3.31) but instead  $\phi_B$  is given by

$$\phi_B = \phi_M - \chi - \Delta \quad (3.46)$$

Alternatively this same expression results if surface dipoles are present, developing a potential energy  $\Delta$  [22].

For a Schottky barrier structure on an *n*-type semiconductor, with interface states and an interfacial layer present, Eq. (3.46) may be rewritten<sup>†</sup> with the aid of Fig. 3.14 as [22]

$$\phi_B = \phi_M - \chi - (eN_{ss}d/\epsilon_i)(\phi_B - E_g + \phi_0) - Q_b^+d/\epsilon_i \quad (3.47)$$

<sup>†</sup> The occupancy of the interface states has been estimated using the  $T = 0$  form of  $f(E)$ ; i.e., a step function  $f(E)$ .

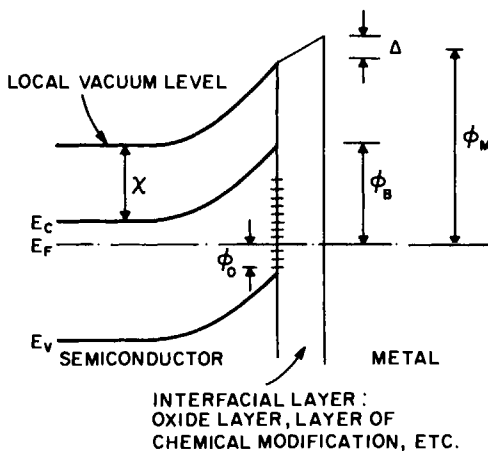


Fig. 3.14 Metal-semiconductor junction with an interfacial layer present. For simplicity the interface states are assumed to reside at the semiconductor-interfacial layer boundary. The quantity  $\phi_0$  labels the short-range neutrality energy level.

where  $\epsilon_i$  is the permittivity of the interfacial layer and  $g_s(E) = N_{ss}$  (a constant density of states has been assumed). We have introduced a new idea here through the quantity  $\phi_0$ . It is an energy, measured from the valence-band edge, such that, if the interface states are filled to this level, the interface is neutral on a local, short-range scale [22]. If  $E_F$  lies above  $\phi_0$ , the interface states are developing negative charge; if  $E_F$  lies below  $\phi_0$ , the interface states are developing positive charge.<sup>†</sup>

With a large interface state density  $N_{ss}$  Eq. (3.47) is seen to reduce to

$$\phi_B = E_g - \phi_0 \quad (3.48)$$

In this Bardeen limit [22], the Fermi level is pinned at  $\phi_0$  at the surface no matter what metal forms the interface structure. The interior of the semiconductor is shielded from "knowing" about the presence of the metal by the high density of localized gap states at the semiconductor-interfacial layer boundary.

From Eq. (3.44) and the fact that  $0.1 \lesssim a \lesssim 0.7$ , it follows that interface states arising from dangling bonds (intrinsic) and from defects and impurities (extrinsic) play a significant role in Schottky barrier formation. From the values of  $a$  found experimentally, it follows that actual metal-semiconductor junctions fall somewhere between the Mott-Schottky and Bardeen limits. As a final comment we also note that the formation of the M-S structure is further complicated by chemical reactions that can take place at the interfaces of some materials systems [23].

<sup>†</sup>The existence of  $\phi_0$  seems plausible. Its introduction here is also convenient since it allows us to avoid specifying whether the interface states are acceptorlike or donorlike.

### 3.4.5 Semiconductor–Insulator Interfaces

Semiconductor–insulator interfaces are generally formed to passivate and protect semiconductors, although we shall see that they can also be used to create space-charge regions in semiconductors [25]. They can passivate since their formation can tie up at least some unsatisfied bonds at the semiconductor surface thereby rendering electrically inactive the otherwise large numbers of surface states which can serve as very effective recombination centers (see Section 2.6). In photovoltaic applications such boundaries of high recombination act as a sink and a loss mechanism for photo-generated carriers.

There are always some interface states which remain after the formation of a semiconductor–insulator interface. According to their response in time, these are classified as being either fast states or fixed charge. Fast states fill and empty as the Fermi level (or quasi-Fermi levels) is moved up and down. Sites giving rise to the so-called fixed charge do not communicate well and, hence, do not change their population as the Fermi level is moved. Apparently, these lie in the insulator adjacent to the interface [25].

In analyzing the barrier regions formed in a semiconductor in these structures, one would proceed as was done for the other interface configurations. For example, for a semiconductor–insulator interface where there is  $Q_{\text{fix}}$  charge in the fixed-charge states, the bands in the semiconductor bend until  $Q_b$  is developed where  $|Q_b| = |Q_{\text{fix}}|$ . For Si/SiO<sub>2</sub> interfaces, this fixed charge is found in the SiO<sub>2</sub> adjacent to the interface. It is always positive [25] and has been used advantageously in M–I–S inversion layer solar cells which are discussed in Chapter 6.

### 3.4.6 Metal–Insulator–Semiconductor and Semiconductor–Insulator–Semiconductor Junctions

Metal–insulator–semiconductor (M–I–S) and semiconductor–insulator–semiconductor (S–I–S) junctions refer to a class of structures in which an ultrathin insulator (I) layer is purposefully inserted between a semiconductor and a metal or between a semiconductor and a semiconductor. As would be anticipated from our discussion of semiconductor–metal and semiconductor–insulator interfaces, the presence of the I layer can modify the barrier regions. Such an I layer can affect interface states and can contain fixed charge. It can affect transport across the interface. It can also induce or inhibit interfacial chemical reactions [26]. The thin I layer M–I–S and S–I–S structures of interest to solar cell applications are conducting, as opposed to the nonconducting thick insulator gate M–I–S structures of

microelectronics; consequently, these M-I-S and S-I-S configurations used in solar cells can serve as charge separating electric field regions in cells.

### 3.4.6.1 Metal–Insulator–Semiconductor Interfaces

In conducting M-I-S structures, an ultrathin I layer is purposefully grown or deposited on the semiconductor before the metal deposition. The layer is of a thickness  $15 \text{ \AA} \lesssim d \lesssim 50 \text{ \AA}$ , although layers as thick as  $200 \text{ \AA}$  have been reported to give conducting configurations [27]. Electron and hole transport between the semiconductor and metal takes place across the insulator layer by direct tunneling or hopping [28].

To examine the M-I-S configuration we consider Fig. 3.15. The total electrostatic potential energy  $V_0$ , developed in this structure to equate the electrochemical potentials of the semiconductor and metal, must be the sum of the built-in potential  $V_{bi}$  in the semiconductor and the electrostatic potential energy  $\Delta_I$  existing across the interfacial layer i.e.,

$$V_{bi} + \Delta_I = \phi_M - \phi_n \quad (3.49a)$$

which, in terms of the Schottky barrier height  $\phi_B$ , may be expressed as

$$\phi_B = \phi_M - \chi - \Delta_I \quad (3.49b)$$

Equations (3.49) point out that the amount of band bending in the semiconductor  $V_{bi}$ , or equivalently, the barrier height presented to majority carriers in the semiconductor  $\phi_B$ , can be adjusted in the M-I-S configurations through the presence of  $\Delta_I$ . For example, to make  $\phi_B$  larger,  $\Delta_I$  can be made negative as seen in Fig. 3.15.

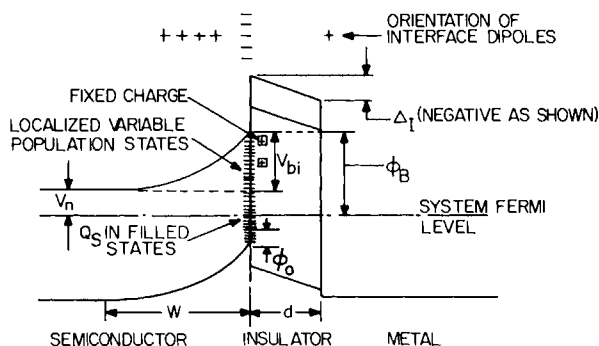


Fig. 3.15 In a conducting M-I-S interface structure the space-charge region can be significantly altered from that of an ideal Schottky barrier due to the presence of interface states and fixed charge. The Schottky barrier height has been substantially increased in this example.

We can express Equation (3.49b) in terms of the bulk charge in the semiconductor  $Q_b$ , the charge in interface states  $Q_s$ , and any fixed charge  $Q_{\text{fix}}$  in the insulator layer; viz.,

$$\phi_B = \phi_M - \chi - d/\epsilon_i(Q_b + Q_{\text{fix}} + Q_s) \quad (3.50)$$

which assumes  $Q_{\text{fix}}$  is located at the semiconductor-insulator boundary. The quantity  $Q_b$  is computed as at other interfaces; i.e., by solving Poisson's equation in the semiconductor subject to boundary conditions similar to those we have seen for other interface structures. The quantity  $Q_s$  is given by

$$Q_s = -e \left[ \int_0^{E_g} f(E) g_s(E) dE - \int_0^{\phi_0} g_s(E) dE \right] \quad (3.51)$$

where we have again used  $\phi_0$ , the short-range-neutrality energy level introduced in Section 3.4.4.

It is seen from Eq. (3.50) that there are three contributions to  $\Delta_I$ . The first of these, the term  $(d/\epsilon_i)Q_b$ , only changes  $\phi_B$  from the value expected in an ideal Schottky barrier (i.e.,  $\phi_B = \phi_M - \chi$ ) by hundredths of an electron volt.<sup>†</sup> This assumes  $15 \lesssim d \lesssim 30 \text{ \AA}$ ; these are values of  $d$  usually encountered in the M-I-S configuration in solar cell applications [28]. However, the terms  $(d/\epsilon_i)Q_s$  and  $(d/\epsilon_i)Q_{\text{fix}}$  can change  $\phi_B$  by tenths of an electron volt for reasonable values of interface state densities and fixed charge [28].

It is clear from Eq. (3.50) that the influence of the I layer becomes negligible as  $d \rightarrow 0$ . Also the equation stresses that the Schottky barrier height can be manipulated in the M-I-S configuration by manipulating  $Q_s$  and  $Q_{\text{fix}}$ . In actuality one is manipulating defects and the chemical state of the interface.

#### 3.4.6.2 Semiconductor-Insulator-Semiconductor Interfaces

As in the M-I-S structure, the S-I-S interface incorporates an ultrathin deposited or grown insulator layer. This I layer modifies the semiconductor interface state densities, perhaps introduces fixed charge, and presents an additional barrier to transport. These first two effects modify the space-charge regions in the semiconductors and thus can affect transport. The last can affect transport directly. Analysis of this interface structure in terms of extent of space-charge region, electric fields, etc., follows that outlined previously for other interface structures.

<sup>†</sup> This is larger if inversion is present.

### 3.4.7 Liquid-Semiconductor Interfaces

Whenever dissimilar materials are placed in contact, space-charge regions, with their associated electrostatic fields, can develop in thermodynamic equilibrium. Liquid-semiconductor interfaces are no exception [29]. The liquid we shall be considering in these junctions is an electrolyte consisting of a solvent and an oxidation-reduction couple. An oxidation-reduction couple is some species whose oxidized form ( $A^{2+}$  in Fig. 3.16) can accept an electron (rendering it reduced) and whose reduced form ( $A^+$  in Fig. 3.16) can give up an electron (rendering it oxidized). At the liquid-semiconductor junction, this redox couple can exchange electrons back and forth with the semiconductor; in thermodynamic equilibrium the net exchange is zero and the electrochemical potentials of the redox couple and semiconductor are the same.

Figure 3.16a shows an *n*-type semiconductor and an electrolyte before contact. The energy levels and electrochemical potentials of these two materials before contact are depicted with respect to the vacuum-level reference energy of solid state. The energy level  $E_{ox}$  seen in the figure is the most probable value for the energy of the unoccupied electron state localized on the oxidized species. Once an additional electron comes to an oxidized species, this oxidized species is reduced and there is a rearrangement of the polarized solvent molecules about it. As a consequence, the energy level  $E_{re}$ , the most probable value for the energy of occupied

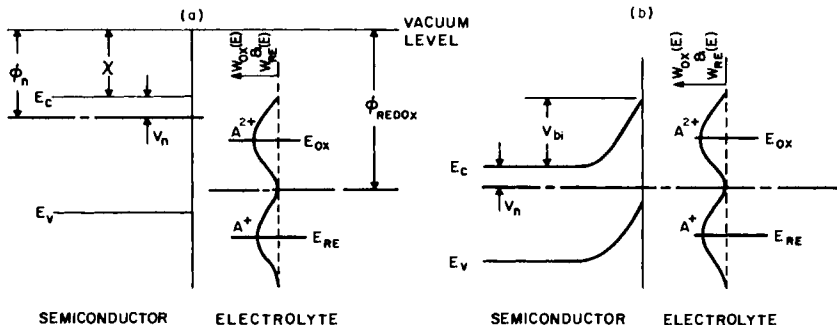


Fig. 3.16 (a) A semiconductor and redox couple before contact. The electrochemical potentials are positioned with respect to a common reference, the vacuum level. (b) The semiconductor and redox couple of (a) in contact and in thermodynamic equilibrium. In this situation the materials system has one electrochemical potential as seen.

The most probable energy for the empty electron state localized on the oxidized species is  $E_{ox}$ ; however, the energy of this empty state fluctuates about  $E_{ox}$  according to the distribution  $W_{ox}$  shown. The most probable energy for the occupied electron state localized on the reduced species is  $E_{re}$ ; however, the energy of this filled state fluctuates about  $E_{re}$  according to the distribution  $W_{re}$  shown.

electron state localized on the reduced species, lies below  $E_{\text{ox}}$  by an energy  $2\lambda$ , where  $\lambda$  is termed the rearrangement or reorganization energy.

Due to the thermal motion of the system composed of an oxidized species and the surrounding solvent molecules, the energy of the unoccupied electron state localized on the oxidized species fluctuates about  $E_{\text{ox}}$  according to [30]

$$W_{\text{ox}} = (4\pi\lambda kT)^{-1/2} \exp[-(E - E_{\text{ox}})^2/(4\lambda kT)] \quad (3.52a)$$

where  $W_{\text{ox}}$  gives the probability,<sup>†</sup> at a given time, that the energy of this unoccupied, available state has the value  $E$ . In a similar manner the energy of the occupied electron state localized on the reduced species fluctuates about  $E_{\text{re}}$  according to [30]

$$W_{\text{re}} = (4\pi\lambda kT)^{-1/2} \exp[-(E - E_{\text{re}})^2/(4\lambda kT)] \quad (3.52b)$$

where  $W_{\text{re}}$  gives the probability,<sup>†</sup> at a given time, that the energy of this occupied state has the value  $E$ . The functions  $W_{\text{ox}}(E)$  and  $W_{\text{re}}(E)$  are shown schematically in the figure. We note that the possible oxidized levels [whose distribution in energy is given by  $W_{\text{ox}}(E)$  and which are labeled  $A^{2+}$  in Fig. 3.16] are not analogous to a conduction band, simply because they can never be partially occupied by electrons. These levels are unoccupied; when they become occupied, the species has become reduced and the levels labeled  $A^+$  apply. It follows that the  $A^+$  levels [whose distribution in energy is given by  $W_{\text{re}}(E)$ ] are not analogous to a valence band. However, these redox couple levels are analogous to solid state polaron levels discussed in Chapter 2.

The quantity which locates the semiconductor electrochemical potential is, of course, the work function  $\phi_n$ , where  $\phi_n$  is measured positively down from the vacuum level. In electrochemistry it is customary to locate the redox couple, electrochemical potential with respect to the electrochemical potential of the standard hydrogen electrode by giving the standard redox potential  $E_{\text{redox}}^0$ . For our work it would be more convenient to locate redox-couple electrochemical potentials with respect to the same reference as that used for metal and semiconductor electrochemical potentials; i.e., the vacuum level.

To do this we can define the "work function"  $\phi_{\text{redox}}$  for a redox couple according to

$$\phi_{\text{redox}} = E_{\text{redox}}^0 + \Delta E_{\text{ref}} \quad (3.53a)$$

where  $E_{\text{redox}}^0$ , the standard redox potential, will be a positive number if the electrochemical potential lies below that of hydrogen in Fig. 3.5, and  $\Delta E_{\text{ref}}$

<sup>†</sup>The prefactors in Eqs. (3.52a) and (3.52b) ensure that  $\int_{\text{energy}} W_{\text{ox}} dE = 1$  and  $\int_{\text{energy}} W_{\text{re}} dE = 1$ .

locates the electrochemical potential of the standard hydrogen electrode with respect to the vacuum level. Unfortunately there is difficulty in pinning down the value of  $\Delta E_{\text{ref}}$ , but it lies in the range [29, 31]  $4.3 \lesssim \Delta E_{\text{ref}} \lesssim 4.73$  eV. Values for  $\phi_{\text{redox}}$  for a number of redox couples are shown in Fig. 3.5 assuming the preferred value of  $\Delta E_{\text{ref}} = 4.73$  eV.

Equation (3.53a) and hence the data of Fig. 3.5 locates the electrochemical potential of a redox couple with respect to the vacuum level assuming the concentration of reduced species  $N_0^{\text{re}}$  equals the concentration of oxidized species  $N_0^{\text{ox}}$ , since the standard redox potential value  $E_{\text{redox}}^0$  of electrochemistry is based on  $N_0^{\text{ox}} = N_0^{\text{re}}$ . For unequal concentrations Eq. (3.53a) becomes

$$\phi_{\text{redox}} = E_{\text{redox}}^0 + \Delta E_{\text{ref}} - kT \ln(N_0^{\text{re}}/N_0^{\text{ox}}) \quad (3.53b)$$

The “work function” of the redox couple varies with  $N_0^{\text{ox}}$  and  $N_0^{\text{re}}$  in a manner analogous to the variation of a semiconductor work function with  $n$  and  $p$ .

When the semiconductor and redox couple of Fig. 3.16a are placed into contact and allowed to come into thermodynamic equilibrium, the system must have one electrochemical potential as seen in Fig. 3.16b. Part of the electrostatic potential energy that is developed to equate the different electrochemical potentials seen in Fig. 3.16a will exist in the semiconductor (the built-in potential  $V_{\text{bi}}$ ), part will exist across any interfacial layer present ( $\Delta_I$ ), part will exist across a very compact layer of ions (Helmholtz layer) at the interphase boundary ( $\Delta_H$ ), and part will exist across a diffuse layer of variable ionic charge (Gouy layer) extending from the Helmholtz layer into the interior of the electrolyte ( $\Delta_G$ ).

As with all the other interface structures we have explored, this total electrostatic potential energy developed in thermodynamic equilibrium must equal the difference in the electrochemical potentials before contact; viz.,

$$V_{\text{bi}} + \Delta_I + \Delta_H + \Delta_G = \phi_{\text{redox}} - \phi_n \quad (3.54a)$$

or

$$V_{\text{bi}} + \Delta_I + \Delta_H + \Delta_G = E_{\text{redox}}^0 + \Delta E_{\text{ref}} - kT \ln(N_0^{\text{re}}/N_0^{\text{ox}}) - \phi_n \quad (3.54b)$$

Both of these are general expressions valid for any concentration of the redox couple. For the semiconductor to have the depleted region necessary for photovoltaics, we should have  $\phi_{\text{redox}} > \phi_n$  for an *n*-type semiconductor. The converse applies to a *p*-type semiconductor.

From a table such as that presented in Fig. 3.5 one can estimate the semiconductor built-in potential for a liquid–semiconductor junction. For example, for an *n*-type semiconductor,  $V_{\text{bi}} \approx \phi_{\text{redox}} - \phi_n$ . (When using this

table it must be recalled that  $\phi_n$  will vary with doping for a given semiconductor and  $\phi_{\text{redox}}$  will vary with concentration for a given redox couple.) However,  $V_{\text{bi}} \approx \phi_{\text{redox}} - \phi_n$  is only a very rough estimate as can be seen from Eq. (3.54). Appreciable electrostatic potential can be developed across an interfacial region ( $\Delta_I$  and  $\Delta_H$ ) due to charge in interface states at the semiconductor surface. In fact, this charge can be so large that it effectively shields the interior of the semiconductor from any changes occurring in the liquid giving  $dV_{\text{bi}}/d\phi_{\text{redox}} \simeq 0$  for some systems [32, 33]. This is the same phenomenon of Fermi-level pinning that we have already seen possible in semiconductor heterojunctions and metal–semiconductor junctions. As with these other types of junctions, the interface states giving rise to the phenomenon can be present intrinsically (due to the termination of the semiconductor lattice), or can be present as a result of the act of forming the junction (i.e., defects due to vacancies, cross diffusion, decomposition).

### 3.4.8 Semiconductor–Grain-Boundary Interfaces

All the interfaces discussed to this point have been junctions that will prove to be useful for photovoltaic action or for ohmic contacts. They have all been purposefully constructed interfaces. Semiconductor grain-boundary interfaces are different.

As we discussed in Section 2.2.1 grain boundaries are the disordered, transition regions between the crystallites (grains) of polycrystalline material. They are tens of angstroms or more in width. Since polycrystalline materials have some distribution of grain sizes, semiconductor grain boundaries are a statistically occurring structure. This is seen in Fig. 3.17, which shows a cross section through a thin-film photovoltaic material. To reduce materials costs and consumption, such thin films are attractive, but film growth kinetics generally produces polycrystalline films. In the figure, several small grains (B and C) are seen, as are several large grains (A and D).

Due to the crystallographic misorientation of adjacent grains of Fig. 3.17, one would expect that there is a distribution of bond angles and interatomic

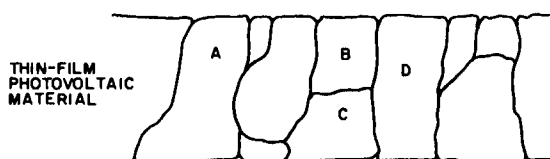


Fig. 3.17 A polycrystalline semiconductor material. A distribution of grain sizes is seen. The grain (crystallite) D is referred to as being columnar.

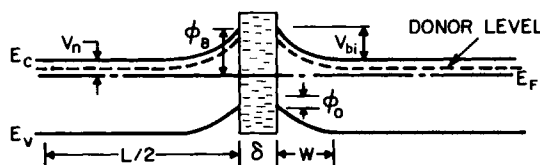


Fig. 3.18 A semiconductor grain-boundary interface in thermodynamic equilibrium. In general, the gap in the grain boundary may be different than that of the adjacent single-crystal material. The energy  $\phi_0$  denotes the level for local neutrality. The doping has been assumed to be uniform in the grain.

distances statistically occurring in the intergrain transition region which is the grain boundary. As is the case for amorphous materials, we would expect these to give rise to localized gap states which we term intrinsic (see Section 2.4.2). As in the case for amorphous materials, we expect that grain boundaries will also contain extrinsic localized gap states arising out of defects (broken chemical bonds) and impurities.

From a band diagram point of view the intragrain (crystalline) region of a polycrystalline material is depicted by Fig. 2.8b; and the grain boundary itself is depicted by Fig. 2.8a. As a result of the large number of localized states possible in the grain boundary, carriers can be trapped there giving rise to a charge per area  $Q_s$ . This charge must be shielded by adjacent regions in the grains. Consequently, barriers (electric field regions) generally are present at semiconductor grain-boundary interfaces. This is seen in Fig. 3.18 which shows an *n*-type polycrystalline material in thermodynamic equilibrium (no bias, no light, no temperature gradients, etc.). In this example, depleted regions have formed in the grains at the interfaces.

We can analyze the electric field regions existing in thermodynamic equilibrium at grain boundaries with the same approach that was used for other interfaces: We use Poisson's equation with appropriate boundary conditions to determine the net charge per area  $Q_b$  developed in grain space-charge regions adjacent to a grain boundary and note that this must equal the charge per area  $Q_s$  developed in the grain boundary where the grain-boundary charge per area is given by

$$Q_s = -e \int_0^{E_g} f(E) g_{gb}(E) dE + e \int_0^{\phi_0} g_{gb}(E) dE$$

Here  $g_{gb}(E)$  is the density of localized grain-boundary states and once again we have used  $\phi_0$ , the short-range-neutrality energy level.<sup>†</sup>

The general features of barrier formation at grain boundaries can be established by examining several cases of grain doping and grain-boundary

<sup>†</sup> We again note that there is no need to specify whether the states are donor- or acceptorlike in this approach.

localized state distributions. To do this we ask ourselves the question: Where would the system Fermi level lie with respect to  $\phi_0$ , if the bands did not bend? We recall that  $\phi_0$  is an energy such that, if the localized gap states of the grain boundary are filled to  $\phi_0$ , then there is no net charge developed in these states. Now if  $E_F$  were to lie above  $\phi_0$ , assuming the bands did not bend, then negative charge would reside in the grain boundary. But because of this, the bands will bend in the semiconductor to develop charge to shield this negative charge and simultaneously to move  $E_F$  closer to  $\phi_0$  to reduce its magnitude. In this case, *n*-type grains will deplete adjacent to the grain boundary to develop a positive  $Q_b$  as seen in Fig. 3.18. From our previous analyses of depleted regions, it follows that<sup>†</sup>  $Q_b = 2[2e\epsilon_s N_D(\phi_B - V_n)]^{1/2}$ , if the depletion assumption is valid. Consequently,

$$2[2e\epsilon_s N_D(\phi_B - V_n)]^{1/2} = eN_{ss}(E_g - \phi_B - \phi_0) \quad (3.55)$$

which results by using a step function ( $T = 0$ ) approximation to  $f(E)$  and  $g_{eb}(E) = N_{ss}$ . Solving Eq. (3.55) for  $\phi_B$  determines the barrier height in Fig. 3.18. If  $eN_{ss}/(8e\epsilon_s N_D)^{1/2} \gg 1$ , Eq. (3.55) predicts that the system Fermi level is pinned at  $\phi_0$ .

If the grains are doped *n*-type, and if  $E_F$  were to lie below  $\phi_0$ , assuming the bands did not bend, then positive charge would reside in the grain boundary. But because of this, the bands will bend in the semiconductor to develop charge to shield this positive grain-boundary charge and simultaneously to move  $E_F$  closer to  $\phi_0$  to reduce its magnitude. If the density of states is very large at  $\phi_0$ ,  $E_F$  would be pinned to  $\phi_0$  at the interface. The need for a negative shielding charge in the bulk will force the *n*-type grains to accumulate adjacent to the grain boundary. As we know from our examination of other interface structures, Eq. (3.55) is not valid in this case since mobile electrons must be considered in setting up and solving Poisson's equation; however, the modifications necessary are straightforward.

For *p*-type material we again consider two situations. If the grains are doped such that  $E_F$  would lie below  $\phi_0$ , assuming the bands did not bend, then positive charge would be developed in the grain boundary. To counter this the bands will bend in the grains adjacent to the grain boundary to develop charge for shielding this positive charge in the localized grain-boundary states. The bending will simultaneously move  $E_F$  closer to  $\phi_0$  to reduce the magnitude of the grain-boundary charge. Hence the grains will contain depleted regions adjacent to the grain boundaries. If the density of localized grain-boundary states near  $\phi_0$  is large [ $eN_{ss}/(8e\epsilon_s N_A)^{1/2} \gg 1$ ], it follows that the system Fermi level will be pinned at  $\phi_0$ . In the second case,

<sup>†</sup> Here  $(\phi_B - V_n)$  should actually be replaced by  $(\phi_B - V_n - kT)$ .

the grains would be doped such that  $E_F$  would lie above  $\phi_0$  before the bands bent. In this situation the *p*-type grains would accumulate adjacent to the grain boundaries, and pinning occurs if the density of interface states is large at  $\phi_0$ .

The picture we have developed for the statistically occurring grain-boundary interfaces of polycrystalline semiconductors is as follows: They can give rise to internal electric field regions such as those seen in Fig. 3.18. Added to this, as discussed in Section 2.2.1, is the evidence that the grain boundary itself can serve as an excellent conduit for atomic and ion transport and, perhaps, impurity segregation.

Figure 3.19 shows how these effects of grain boundaries can influence a very basic materials property; i.e., the resistivity  $\rho$  of a semiconductor. The figure presents measured resistivity data as a function of doping concentration for single-crystal and polycrystalline silicon. These data are for *p*-type materials, but the behavior shown is typical of that observed for both doping types [34–40]. Two models have been proposed to explain this dependence of polycrystalline sample resistivity on doping density. One model, put forth by Kamins [36] and developed by others [35, 38], postulates that the dopant atoms are uniformly distributed throughout the material and that conductivity is limited by transport at the semiconductor

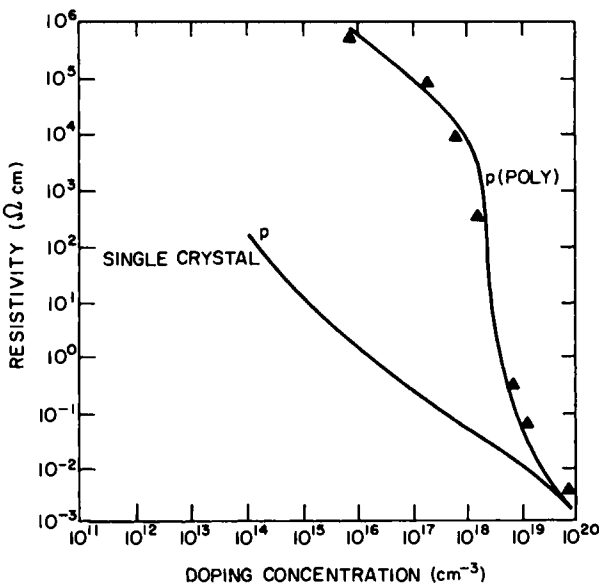


Fig. 3.19 Measured resistivity data for single-crystal and polycrystalline silicon. These data are for *p*-type material; however, the behavior shown is typical (based on Ref. [34]).

grain-boundary interfaces; i.e., by barrier regions, such as those seen in Fig. 3.18, formed by carrier trapping in the grain boundary. A second explanation has been proposed by Cowher and Sedgwick [41]. This postulates that the conductivity is controlled by the segregation of dopant atoms at grain boundaries. In this model it is the dopant atoms that are trapped in the disorder of the grain boundary. There they are rendered electrically inactive producing the behavior seen in Fig. 3.19.

In a given polycrystalline material, both mechanisms probably influence the resistivity to some degree. In the case of polycrystalline silicon, it is generally accepted that semiconductor grain-boundary barriers are the dominant factor controlling resistivity [34–40]. However, even for this material there is some evidence that atomic trapping of the dopant by grain boundaries can be noticeable [40].

When the semiconductor grain-boundary barriers control the resistivity, they do so because transport across the interface barriers becomes the rate-limiting step in carrier motion. With the passage of current, most of the voltage is dropped across the semiconductor grain-boundary interfaces. In general, the relationship between  $J$ , current density, and  $V_{gb}$ , the voltage dropped across a given semiconductor grain-boundary interface, would not be linear. A differential conductivity  $\sigma_{gb}$  must be defined according to [35]

$$\sigma_{gb} \equiv L dJ/dV_{gb} \quad (3.56)$$

where  $L$  is the average grain size. In this case  $\sigma_{gb}$  is such that

$$\sigma_{gb} \ll (e\mu_n n + e\mu_p p) \quad (3.57)$$

where  $n$  and  $p$  are the populations of carriers in a grain. The actual physical mechanisms which can give rise to carrier transport across grain-boundary regions will be discussed in a general treatment of interface transport in Section 3.5. At this point we note that they can be temperature activated; i.e.,

$$\sigma_{gb} \sim e^{-W/kT} \quad (3.58)$$

It is clear that the high density of localized gap states existing in grain boundaries can significantly influence the properties of polycrystalline material. They give rise to interfacial barrier (electric field) regions that can control the transport of electrons and holes. They can also significantly affect the response of a material to light. For example, in photovoltaic devices fabricated using polycrystalline material, the short-circuit current can be substantially reduced due to recombination occurring through these localized states in grain boundaries [34, 35]. The effect is enhanced in the

example of Fig. 3.18. Here the fields, set up by the charge trapped in localized grain-boundary states, are seen to direct photogenerated minority carriers into the high recombination grain-boundary region. Carriers recombining in grain boundaries are obviously lost and cannot add to the photovoltaic response of a solar cell structure.

An important question to ask is: Can these localized grain-boundary states be modified to improve the properties of polycrystalline materials? Specifically, can the density of localized grain-boundary states be reduced and can the neutrality energy  $\phi_0$  be shifted? Figure 3.20 presents experimental data which answer these questions. These results were obtained by subjecting a sample of polycrystalline silicon (doped by neutron transmutation doping) to various chemical treatments [42]. The figure shows how the conductivity of polycrystalline Si, which is controlled by grain-boundary barriers, can be affected. These changes occur because the chemical treatments modify the localized grain-boundary states. In similar work on GaAs, chemisorption of Ru in grain-boundary regions has been shown to decrease photogenerated minority carrier loss arising from grain-boundary localized states acting as recombination centers [43].

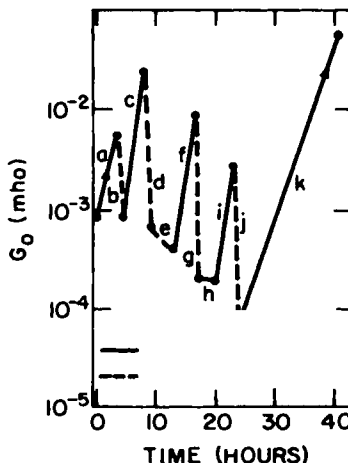


Fig. 3.20 The zero bias conductance  $G_0$  at 300°K of one grain-boundary barrier in polycrystalline silicon sample doped at  $10^{16}$  phosphorus atoms/cm<sup>3</sup>. - hydrogen plasma; ---, other treatments. The letters refer to a series of gas treatments: (a) H plasma at  $6 \times 10^{-2}$  Torr and 322°C, (b) vacuum at  $4 \times 10^{-6}$  Torr and 625°C, (c) H plasma at  $6 \times 10^{-2}$  Torr and 334°C, (d) vacuum at  $3 \times 10^{-6}$  Torr and 620°C, (e) H<sub>2</sub> at  $6 \times 10^{-2}$  Torr and 337°C, (f) H plasma at 1 Torr and 335°C, (g) vacuum at  $2 \times 10^{-5}$  Torr and 655°C, (h) plasma at  $10^{-2}$  Torr and 337°C, (i) H plasma at  $10^{-1}$  Torr and 415°C, (j) O<sub>2</sub> at  $5 \times 10^{-4}$  Torr and 625°C, and (k) H plasma at  $10^{-1}$  and 395°C. (After Ref. [42], with permission.)

### 3.5 INTERFACE TRANSPORT MECHANISMS

Although we never stated a concise definition of the term interface in Section 3.4, it should be clear from that section that we are using the term to mean the metallurgical junction where material properties vary, and any surrounding electric field regions resulting from the presence of the metallurgical junction. Current transport in the electric field regions surrounding a metallurgical junction is by the drift and diffusion processes discussed in detail in Section 2.7. However, there are a number of processes unique to interfaces which can allow carriers to cross the actual metallurgical junction. In this section we focus on those transport mechanisms unique to interfaces.

A metal-semiconductor structure in forward bias is used in Fig. 3.21 to illustrate the various transport mechanisms possible at interfaces. From the figure it is seen that mechanisms a-e involve the majority carriers. Mechanism f involves both majority and minority carriers, whereas mechanism g involves only minority carriers.

The Schottky barrier of Fig. 3.21 is being used to show the general features of these various, interface transport mechanisms. Although their overall features will be preserved, these processes may be slightly modified in other interface structures. For example, for the M-I-S configuration, all of the processes enumerated in Fig. 3.21 would involve the carriers tunneling or hopping across the ultrathin I layer to complete their transport across the interface structure. As we examine various photovoltaic devices in detail in subsequent chapters, we shall discuss these points further. For now our objective is to examine the broad features of the various interface transport mechanisms.

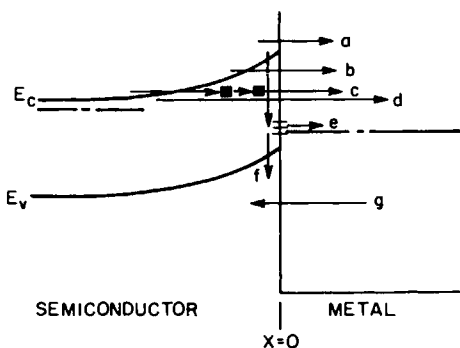


Fig. 3.21 Interface transport mechanisms illustrated using a forward biased, metal-semiconductor junction. Path a is thermionic emission, path b is thermally enhanced field emission, path c is a multistep tunneling process, path d is field emission, path e involves trapping and subsequent emission, path f is recombination, and path g is minority-carrier injection.

### 3.5.1 Thermionic Emission

Thermionic emission in its most general sense is a classical process (no tunneling) by which a carrier transfers from an allowed state in one material to an allowed state in another material with ideally no change in total energy. The thermionic emission of majority carriers from the semiconductor conduction band to the metal seen in Fig. 3.21 (path a) results from the net flux of electrons able to cross over the barrier. This will be a temperature-activated process, as may be inferred from Eq. (2.54), since it will depend on the number of electrons at  $x = 0$  in the figure.

If we consider the general situation of an interface between two materials (material L on the left and material R on the right), the current of carriers (let us assume electrons) thermionically emitted from material R to material L increases as the carrier quasi-Fermi level just to the right of the interface ( $x = 0^+$ ) moves toward the band edge at  $x = 0^+$ . If the quasi-Fermi level just to the right of the interface were to rise above its bulk value by  $E_{Fn}(0^+)$  and if the band bending on the right side were to change such that the bulk value moves closer to the band edge at  $x = 0^+$  by  $V_R$ , then this current of carriers moving right to left goes as  $A^*T^2e^{-\phi_B/kT}e^{V_R/kT}e^{E_{Fn}(0^+)/kT}$ . This dependence arises since the quasi-Fermi level at  $x = 0^+$  has moved closer to the band edge by  $V_R + E_{Fn}(0^+)$ . Similarly, if the quasi-Fermi level of these carriers just to the left of the interface were to rise above its bulk value in the left material by  $E_{Fn}(0^-)/kT$  and if the band bending on the left side were to decrease by  $V_L$ , then the current of carriers moving left to right obeys  $A^*T^2e^{-\phi_B/kT}e^{V_L/kT}e^{E_{Fn}(0^-)/kT}$ .

As a consequence of the preceding discussion it can be seen that the general model for the net current density coming over the barrier at an interface may be written as [44–46].

$$J_{ob} = A^*T^2e^{-\phi_B/kT}[e^{V_R/kT}e^{E_{Fn}(0^+)/kT} - e^{V_L/kT}e^{E_{Fn}(0^-)/kT}] \quad (3.59)$$

For the particular interface of Fig. 3.21 this simplifies to

$$J_{ob} = -A^*T^2e^{-\phi_B/kT}[e^{V/kT}e^{E_{Fn}(0^-)/kT} - 1] \quad (3.60)$$

The minus sign here arises by taking net electron emission to the right as a negative conventional current. The quantity  $V_R = 0$ , since the voltage is developed across the semiconductor; also  $E_{Fn}(0^+) = 0$ , because the high population of carriers in the metal is not disturbed by the flow of current.

In these expressions,  $A^*$  is the effective Richardson constant [22, 44]; it is a function of the materials involved in the interface [44, 47]. For example, in crystalline and polycrystalline materials, electrons crossing the interface in conservative processes must preserve their total energy as well as  $k_{||}$ , the component of their  $k$  vector which lies in the plane of the junction. The

number of electrons in a materials system which are able to do this will depend on the  $E = E(\mathbf{k})$  functions of the materials involved, and this is reflected in the value of  $A^*$ . One can imagine that there may be crystalline and polycrystalline materials systems where it is impossible for electrons coming over the barrier to conserve both energy and  $k_{\parallel}$  (momentum in the plane of the junction [47]). In such cases the electrons must interact with phonons to adjust their  $k$  vectors so they can fit into the  $E = E(\mathbf{k})$  of their new host. In so doing, their energy is changed. For amorphous materials this  $k_{\parallel}$  conservation is relaxed, since  $\mathbf{k}$  is not a “good quantum number”. The effective  $A^*$  must incorporate these variations from materials system to materials system [47].

### 3.5.2 Thermally Enhanced Field Emission

Process b of Fig. 3.21 is thermally enhanced field emission or thermionic field emission. Thermally enhanced field emission is a direct tunneling process by which an electron is transferred from an allowed state in one material to an allowed state in another [48]. It differs from field emission, which is also a direct tunneling process, in that field emission (path d) is not thermally assisted. Put succinctly, the term field emission is applied to the transfer of those electrons which directly tunnel through the bottom of the barrier, where it is at its thickest; and the term thermally enhanced field emission is applied to the transfer of those electrons whose thermal energies allow them to directly tunnel through the barrier at higher energies, where the barrier is thinner. Since the probability of tunneling through a barrier such as that seen in Fig. 3.21 has an exponentiallike dependence on barrier height and width [48], the tunneling probability decreases very rapidly as one examines energies that lie progressively lower than the top of the barrier. Clearly, temperature affects the flow of carriers through the thermally enhanced field emission path, since its increase moves more electrons to the higher energy levels which have higher tunneling probabilities. Which levels contribute the most to  $J_{tf}$ , the thermionic field emission current density, will depend on temperature and doping (barrier height and width) [49]. Except for the higher semiconductor doping levels and, at lower temperatures, thermionic field emission is not expected to dominate over the parallel path of thermionic emission at semiconductor interfaces [22].

### 3.5.3 Multistep Tunneling

Process c of Fig. 3.21 is referred to as multistep tunneling. Such processes involve indirect tunneling and may or may not be conservative although the particular example shown is. Multistep tunneling may be thought of as the

interface analog of the bulk transport process of hopping discussed in Chapter 2. Since this path does not involve direct tunneling but rather tunneling from one defect to another in the barrier region, it can occur for a range of barrier thicknesses and doping levels. If the quasi-Fermi level  $E_{Fn}$  to the left in Fig. 3.21 has the same position in the gap when current is flowing as it does in thermodynamic equilibrium (i.e., it lies above its thermodynamic equilibrium position by  $V$ ), then this transport process has been proposed to have a forward characteristic of the form [50–52]

$$J_{ms} = J'_0 e^{BT} e^{AV} \quad (3.61)$$

where  $A$  and  $B$  are constants. Here  $V$  is the band-bending change in the semiconductor barrier region in the forward bias direction. The quantity  $J_0 = J'_0 e^{BT}$  multiplying the voltage term in Eq. (3.61) is seen to be such that  $\ln J_0$  versus  $T$  gives a linear dependence on  $T$ . This is quite different from the temperature-activated form of  $J_0 = A^* T^2 \exp[-\phi_B/kT]$  seen in Eq. (3.60) for thermionic emission. In these expressions  $J_0$  is the saturation current density. Other functional forms should be possible for  $J_{ms}$  (see the discussion on hopping in Chapter 2).

### 3.5.4 Field Emission

Process d of Fig. 3.21 is pure field emission; i.e., direct tunneling through the semiconductor barrier by majority carriers from the bottom of the band. If the electron quasi-Fermi level  $E_{Fn}$  has the same position in the semiconductor gap as its thermodynamic equilibrium value  $E_F$  and if the semiconductor is such that  $n = N_d$  (i.e.,  $E_F = E_c - kT \ln N_c/N_d$ ), then the supply of carriers available for tunneling is a constant, independent of current and temperature. In that case, the field emission current will be independent of temperature. However, the field emission current density  $J_{fe}$  has a very strong dependence on any changes that take place in the semiconductor band bending since this modifies the barrier shape and, hence, the tunneling probability. Since path d necessitates direct tunneling through the semiconductor barrier at its widest, it is appreciable only for very high doping levels [22, 44].

### 3.5.5 Trapping and Subsequent Emission

Path e requires that an electron in the conduction band at  $x = 0$  in Fig. 3.21 be trapped by a localized state at or near the interface; subsequently, the electron is emitted into the metal. In general, such processes depend on the population of carriers in the initial states, on the population of carriers in the intermediary states, and on the population of carriers in the final states, as well as on capture cross sections.

### 3.5.6 Interface Recombination

For the interface recombination path (path f) seen in Fig. 3.21, the current density  $J_{sr}$  flowing in the conduction band at  $x = 0^-$  due to this process is [36]

$$J_{sr} = \left( \frac{e A_{1p}^L A_{1n}^L N_i}{A_{1p}^L p(0^-) + A_{1p}^L p_1 + A_{1n}^L n(0^-) + A_{1n}^L n_1} \right) (n(0^-)p(0^-) - n_i^2) \quad (3.62)$$

where  $N_i$  is the density, per area of interface, of the intermediary states at energy  $E$ . Equation (3.62) follows from Eq. (2.28). This expression assumes path f and path e exist independent of one another. If this is not so, these processes become coupled, which is a situation that has been discussed in the literature [53].

### 3.5.7 Minority Carrier Injection

Process g seen in the forward biased Schottky barrier of Fig. 3.21 is minority carrier injection. In the case of this figure, holes are generated in the valence band (by electrons moving to the right into the metal) at the metallurgical junction  $x = 0$ . These holes supply path f and any remaining holes move to the left into the bulk of the semiconductor by drift and diffusion. In many interfaces, path g is able to provide as many holes as are required by path f and by the bulk. In such a situation  $E_{FP}(0^-)$  must equal  $E_{FP}(0^+)$ . If path g were not able to supply the holes required by path f and the bulk, then  $E_{FP}(0^-)$  would lie above  $E_{FP}(0^+)$ .

## 3.6 INTERFACE CONFIGURATIONS USED IN SOLAR CELLS

Various interface configurations are used in solar cell devices to achieve different objectives. As we have seen, effective fields and electrostatic fields caused by the presence of interfaces can serve as collectors for photo-generated minority carriers diffusing out of an absorber. These fields can also be designed to extend over an appreciable part of an absorber to collect photogenerated carriers directly by drift. However, we also know from our discussions that field regions do more than just affect transport. We know they are principal sources of photovoltage in solar cells. Interface structures can play another role in solar cells: There are combinations of materials whose interfaces can serve as ohmic contacts. These ideally are resistanceless paths of electrical access into a device. Ohmic contacts allow the currents produced internally in a cell structure to be introduced into an external circuit.

### 3.6.1 Photovoltaic Structures

All solar cells use an interface structure as the principal source of the photovoltage, and the interface structures used are some variation of the six interfaces seen in Fig. 3.22. These include the  $p-n$  junction or its variant the  $p-i-n$  junction, heterojunctions including graded gap structures, metal-semiconductor (M-S) junctions (which can be generalized to M-S-M structures when the built-in electric field extends over the entire absorber), metal-insulator-semiconductor junctions, semiconductor-insulator-semiconductor junctions, and semiconductor-liquid junctions. Effective forces

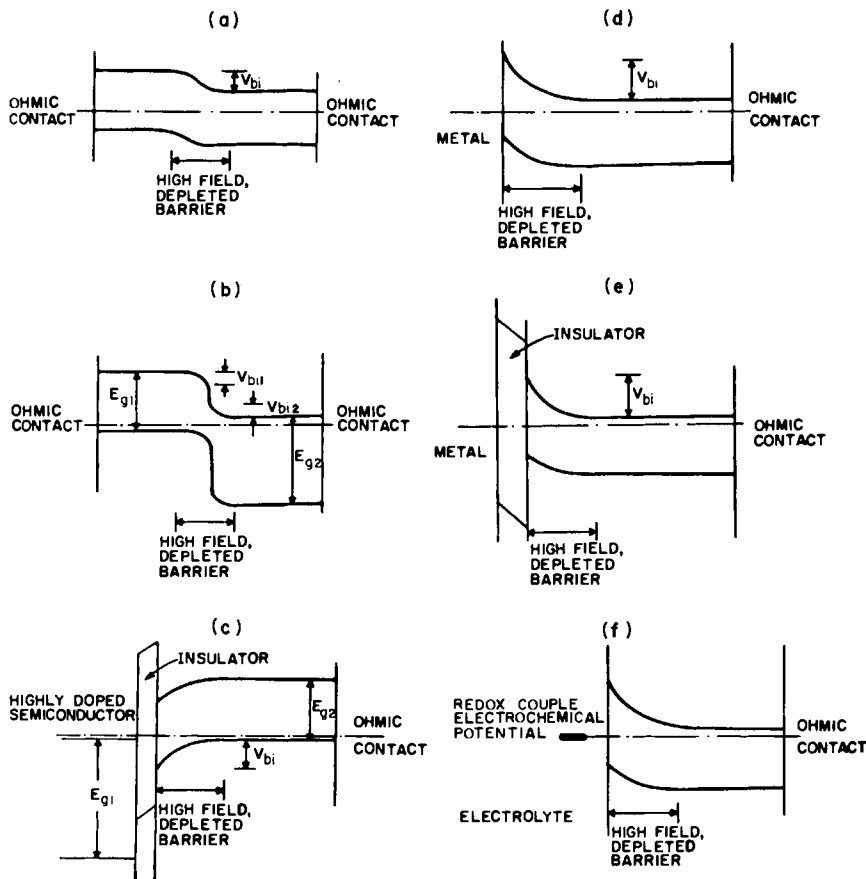


Fig. 3.22 Classification of solar cell types according to the general features of the principal photovoltage-producing region. All structures are shown in thermodynamic equilibrium. (a) homojunction cell, (b) heterojunction cell, (c) semiconductor-insulator-semiconductor cell, (d) metal-semiconductor cell, (e) metal-insulator-semiconductor cell, and (+) semiconductor-electrolyte cell.

are present in graded and abrupt heterostructures, but, in general these interface configurations rely on built-in electrostatic fields as the principal source of photovoltage. For solar cells these electrostatic fields are developed at least partially in depleted regions of semiconductors since such regions can have their conductivity significantly modified by the presence of light regardless of whether or not the bulk semiconductor is a photoconductor [54]. Depleted regions are barriers to majority-carrier flow; hence, solar cells can be expected to have rectifying dark  $J$ - $V$  characteristics.

The general features of the junctions seen in Fig. 3.22 give rise to the classification of solar cell types. The homojunction solar cell configuration ( $p$ - $n$  and  $p$ - $i$ - $n$ ), which is the subject of Chapter 4, is seen in Fig. 3.22a. The semiconductor-semiconductor heterojunction solar cell, which is examined in detail in Chapter 5, is seen in Fig. 3.22b. The semiconductor-insulator-semiconductor solar cell, also examined in Chapter 5, is depicted in Fig. 3.22c. Surface barrier solar cells, the subject of Chapter 6, use interface structures that involve just one semiconductor. These are seen in Figs 3.22d-3.22f. They include the metal-semiconductor (M-S or Schottky barrier) solar cell of Fig. 3.22d, the metal-insulator-semiconductor (M-I-S) solar cell of Fig. 3.22e, and the semiconductor-liquid (electrochemical photovoltaic cell) solar cell of Fig. 3.22f.

### 3.6.2 Ohmic Contacts

Ideally an ohmic contact is one which does not disturb carrier number densities in a semiconductor when it passes current. Equivalently it passes any current demanded with essentially no voltage drop. Ohmic contacts between semiconductors and metals can be formed basically in two ways: One is to form an accumulation layer in the semiconductor adjacent to the metallurgical interface, and the other is to allow a barrier to majority carriers to form, but to dope so heavily as to make the barrier transparent to tunneling. A great deal of practical information on ohmic contacts can be found in Refs. [4] and [55].

Careful attention must be given to the ohmic contacts used in solar cells. As can be seen in Fig. 3.22, ohmic contacts in solar cells must allow majority carriers to leave the absorber easily, yet they must not provide competition (a sink) for minority carriers. Ohmic contacts that are formed by accumulation of majority carriers have an electric field region in the semiconductor which tends to direct minority carriers away from the ohmic contact interface. Ohmic contacts that function by the tunneling of majority carriers through a thin barrier have an electric field region in the semiconductor which tends to direct minority carriers toward the ohmic contact interface. The latter situation is detrimental, since photogenerated minority

carriers will recombine at the ohmic contact (ideally, the number densities do not vary from their thermodynamic equilibrium values) and be lost.

Phenomenologically, the minority-carrier current at an ohmic contact is expressed as [1]

$$J_p = eS(p - p_{n0}) \quad (3.63)$$

where holes have been assumed to be the minority carriers. The so-called surface recombination speed  $S$  characterizes the minority-carrier current at the contact. If the ohmic contact does force  $p$  to  $p_{n0}$ , the thermodynamic equilibrium value, then  $S \rightarrow \infty$  in this formulation. In reality,  $S$  may be large because the contact readily siphons off any holes as well as electrons arriving there or because of interface recombination. The former case is equivalent to recombination because minority carriers attracted to the ohmic contact are moving in the same direction as the majority carriers in solar cell structures (see Fig. 3.22).

When S-R-H recombination<sup>†</sup> is causing  $J_p$  at a contact, then Eq. (3.63) can be established from Eq. (3.62). With the appropriate definition for  $S$ , Eq. (3.62) may be written in the form

$$J_p = (eS/n_{n0})[n(x_c^-)p(x_c^-) - n_{n0}p_{n0}]$$

which assumes the contact is at  $x = x_c$  and the semiconductor is  $n$ -type. Since  $n(x_c^-) \simeq n_{n0}$ , this equation simplifies to Eq. (3.63).

Whatever the physical origin, if  $S$  is large, the result is detrimental to solar cell performance since photogenerated minority carriers will be attracted to the ohmic contact rather than to the depleted barrier region and minority carriers attracted to the ohmic contact will be lost. Ideally, we want ohmic contacts that readily pass majority carriers but block minority carriers for optimum solar cell performance.

### 3.6.3 Selective-Ohmic Contacts

In photovoltaic devices, for optimization of performance, we want  $S \rightarrow 0$  for the minority carriers and  $S \rightarrow \infty$  for majority carriers. This will allow photogenerated minority carriers to be directed to the depleted barrier region which generally is the core of photovoltaic response. We term contacts which block minority carriers but which are ohmic to majority carriers selective-ohmic contacts. Figure 3.23 shows several selective-ohmic contacts for which the effective  $S$  for minority carriers can be very small; i.e.,  $S \lesssim 10^2$  cm/sec.

<sup>†</sup> Shockley-Read-Hall recombination.

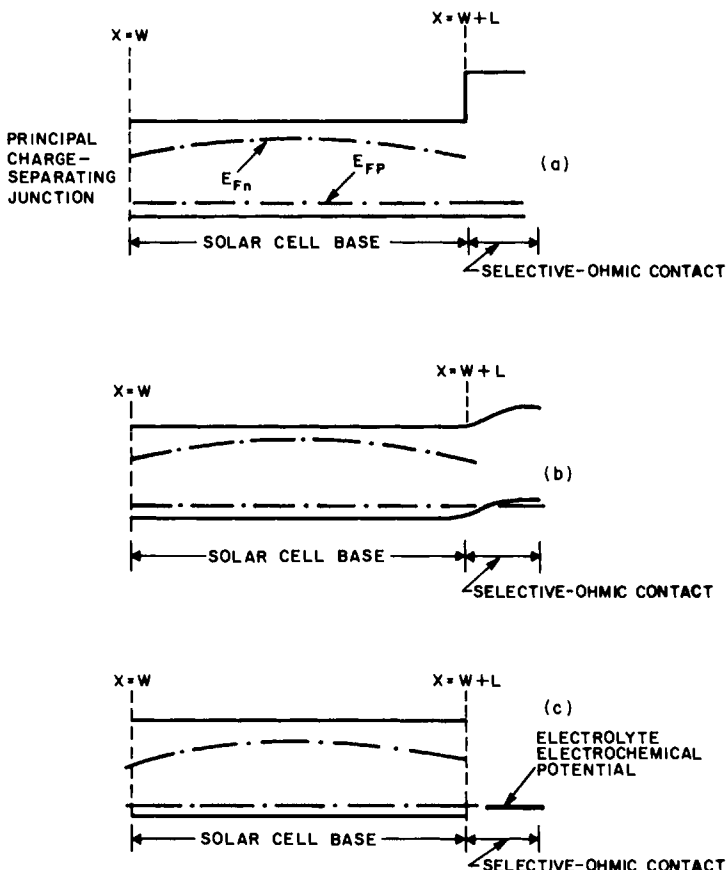


Fig. 3.23 Several selective-ohmic contact structures. The principal charge-separating junction is to the left in the figure and not shown. In each case the semiconductor materials are *p*-type; hence, the driving of the electron quasi-Fermi level away from the majority-carrier quasi-Fermi level is caused by the photogeneration of carriers. Note that in each case the electrons are blocked at  $x = W + L$ . Consequently they will move toward the charge-separating junction and be swept on to the left. Holes swept to the right at the charge-separating junction easily cross  $x = W + L$  since this interface is ohmic to them. (a) Step in conduction-band blocks photogenerated electrons at  $x = W + L$ . No electric field at selective-ohmic contact, but effective field is present. (b) Low-high junction blocks photogenerated electrons at  $x = W + L$ . Electric field present at selective-ohmic contact. (c) Absence of surface states and redox levels in electrolyte near conduction-band blocks photogenerated electrons at  $x = W + L$ . Redox level near valence-band edge carries majority-carrier current.

### 3.7 BARRIER FORMATION—LOCALIZED STATES AND DOPING

We now face a practical but crucial question: How do we form the depleted barrier regions of Fig. 3.22? If the depleted barrier is the interface region of a homojunction, then an absorber material is needed which can be doped both *n*- and *p*-type, and the interface between the *n*- and *p*-type regions will give the depleted barrier region which develops the photovoltage and serves as the check valve of Fig. 1.1. If the absorber can be doped only *n*-type or only *p*-type, depleted barrier regions still can be formed by using semiconductor-semiconductor heterojunctions, S-I-S, M-S, M-I-S, or electrochemical cell configurations. In principle, one need only consult Fig. 3.5 to determine the work function combination needed to obtain the depletion region in the absorber semiconductor.

Unfortunately, as we have seen, barrier formation is not quite that simple. In structures where interface states are present, we know these states can have an important and even overriding influence on barrier formation. In succeeding chapters we shall examine in detail the role of interface states in barrier formation in heterojunctions, S-I-S, M-S, M-I-S, and semiconductor-liquid solar cells.

At this point we focus on barrier formation, for all classes of solar cells, in devices where amorphous solids are being used. In these devices we are dealing with materials that can have very high densities of localized gap states, not just at the interface but throughout the solid. Consequently, such materials can develop their charge contribution to an interface double layer in a very short distance (short Debye lengths) and with very small displacements of the Fermi level through the gap state distribution; i.e., the Fermi level is pinned by the very large density of localized states. In interfaces involving these materials, barriers will be set up (they must be to equate Fermi levels), but they can be very narrow regions through which charge carriers readily pass in either direction via interface transport mechanisms such as direct tunneling. These thin barriers will not effectively encourage carriers to move in one direction; hence, they will not be able to provide the check value action needed in a solar cell structure.

Until almost 1970 the techniques used to fabricate amorphous materials always resulted in materials with very high densities of gap states. The densities had been so high that it was impossible to form an effective barrier in the materials. Because of the high densities of localized gap states, amorphous materials could not be effectively doped (high density of states pinned the Fermi level) and, further, their diffusion lengths were extremely poor. Even though they might have large absorption coefficients, with no substantial built-in field regions and no effective diffusion, there was essentially no barrier photovoltaic response.

However, in 1969, there was a breakthrough when a group reported fabricating amorphous silicon, using radio-frequency glow discharge decomposition of  $\text{SiH}_4$ , that could be doped *n*-type; i.e., the Fermi level could be moved in the gap [56]. Subsequently, another group [57] showed glow discharge *a*-Si could be doped *n*- or *p*-type and that its conductivity could be changed by 10 orders of magnitude. Barrier formation was now possible. Unlike previously produced amorphous silicon materials, this material prepared by a glow discharge decomposition of  $\text{SiH}_4$  had a reduced density of localized gap states which allowed the formation of an effective barrier region and doping; it also displayed a relatively large photoconductivity [the  $\Delta\sigma/\sigma$  type terms in Eq. (2.100) show this is advantageous].

We now know that these glow discharge *a*-Si materials owe their remarkable and desirable properties to a reduced number of defects and, most importantly, to the presence of hydrogen [58, 59]. They have been found to contain hydrogen at atomic percent levels (as high as 35%). This is about 100 times larger than the maximum number of dangling bonds observed, by the concentration of unpaired spins, in conventional *a*-Si [60]. Consequently, the hydrogen must not just play an important role in satisfying dangling bonds but apparently it modifies the whole structure of the film. In this regard it has been found that voids, usually present in conventional *a*-Si, tend to be absent in *a*- $\text{SiH}_x$  [59].

Since that original work, a number of different Si alloys [61] have been explored. The effects of the presence of various chemical species on the density of localized states is presented in Fig. 3.24. These effects seen in the

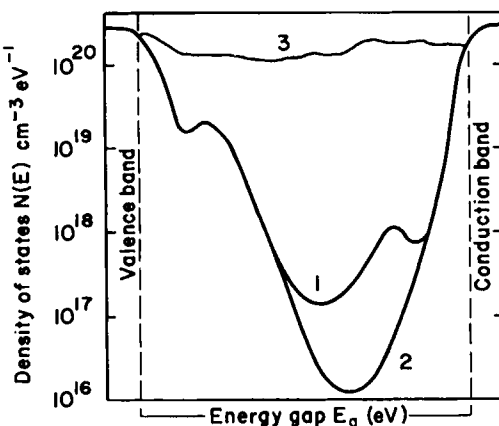


Fig. 3.24 Densities of states in the gap for three amorphous silicon materials. (This first appeared in *New Scientist, London, the weekly review of science and technology* [61].) Curve 1, *a*-Si:H ( $E_g = 1.55$ ); Curve 2, *a*-Si:F:H ( $E_c = 1.65$ ); and Curve 3, *a*-Si ( $E_g = 1.20$ ).

figure are reminiscent of the effects seen in Fig. 3.20, which presents data showing the modification of grain-boundary properties in polycrystalline material. Clearly this alloying approach can be used to reduce localized states and to allow doping and barrier formation for other amorphous materials.

### 3.8 OPTIMUM BAND GAP SELECTION FOR THE ABSORBER

We are able to deduce from Fig. 1.1 that we are looking for absorber materials (crystalline, polycrystalline, or amorphous) with band gaps somewhere in the vicinity of 1 or 2 eV in solar cell applications since  $J_{sc}$  depends on the number of available photons and we expect  $V_{oc} \lesssim E_g$ . At this point we would like to try to refine that estimate. To do so will necessitate making assumptions about the transport mechanisms operative in the cell. As a result this refined estimate of the optimum energy gaps is still only an approximation but a very useful one.

We begin by noting that when light impinges on the various solar cell structures seen in Fig. 3.22, current densities  $J_{sc}$  are developed in short circuit. This current is produced by the sweeping out of photogenerated carriers by the barrier region. At open circuit the various devices bias themselves to the values of  $V_{oc}$  necessary to generate a bucking current density  $J_{bk}$  which just cancels out the photogenerated current density. At some intermediate voltage  $0 \leq V \leq V_{oc}$ , the bucking current is less than the photogenerated current. As we discussed, this causes the general characteristic seen in Fig. 2.25. Assuming superposition is valid, we may express the current density  $J$  produced by a cell when it is developing a voltage  $V$  as

$$J = J_{sc} - J_{bk}(V) \quad (3.64)$$

The value of  $J_{sc}$ , for an incoming spectrum, will depend on the solar cell structure. We assume here that it is independent of voltage developed by the cell. The function  $J_{bk}(V)$  will depend on the solar cell structure. In some cells it may be controlled by bulk transport; in others it will be controlled by interface transport. If superposition is valid, then  $J_{bk}(V)$  would be the same function as the dark, forward bias current-voltage characteristic of each cell structure since solar cells, when producing power, are in a forward bias configuration.

We now ask the following question: On the basis of Eq. (3.64), can we predict the optimum energy band gap a semiconductor should have for matching to a spectrum? The answer is yes—provided we make a number of further assumptions. These assumptions are rather reasonable and they will save us from having to consider the detailed physics of each of the configurations of Fig. 3.22. This we postpone to Chapters 4–6. As a result

of the analysis we are about to undertake, we shall get a better feel for the range of energy gaps of interest to photovoltaics.

Since the barrier regions of Fig. 3.22 all present depleted barriers to majority carriers, we expect they will all display rectifying dark  $J-V$  characteristics. We assume this dark  $J-V$  characteristic is of the form

$$J_{\text{bk}} = J_0(e^{V/nkT} - 1) \quad (3.65)$$

Here  $V$  is the applied bias,  $J_0$  the saturation current density, and  $n$  the diode quality factor or  $n$  factor. We further assume  $J_0$  is of the form

$$J_0 = K e^{-E_g/\gamma kT} \quad (3.66)$$

These assumptions are certainly valid, if the bucking current is rate-limited by bulk diffusion [62]; from Eq. (3.60) it is seen that they are also certainly valid if the bucking current is rate-limited by interface thermionic emission.

At this point we introduce  $Q$ , the overall collection efficiency. It is defined as the ratio of the short-circuit current to the total number of photocarriers created per second per area in the cell by a given spectrum; viz.,

$$Q \equiv J_{\text{sc}}/[eN_{\text{ph}}(E_g)] \quad (3.67)$$

where  $N_{\text{ph}}(E_g)$  is that part of the total photons in the spectrum  $N_{\text{ph}}$  which have energies  $\geq E_g$ .

Our criterion for looking for the optimum band gap is simply to look for the best performance for a given incoming spectrum; i.e., the best efficiency  $\eta$ . Hence, we are looking for  $V_{\text{mp}}$ , the voltage developed at the maximum power point, and  $I_{\text{mp}}$ , the current developed at the maximum power point. This maximum power point is indicated in Fig. 2.25. Using Eqs. (3.64)–(3.67) and the definition of the maximum power point [i.e.,  $d(JV)/dV = 0$ ] gives

$$e^{V_{\text{mp}}/nkT} \left( 1 + \frac{V_{\text{mp}}}{nkT} \right) = e \left( \frac{Q N_{\text{ph}}(E_g)}{K} \right) e^{E_g/\gamma kT} \quad (3.68)$$

The current at the maximum power point  $I_{\text{mp}}$  must obey

$$I_{\text{mp}} = Q e N_{\text{ph}}(E_g) - K \exp[-E_g/\gamma kT] (\exp[V_{\text{mp}}/nkT] - 1) \quad (3.69)$$

By using Eqs. (3.68) and (3.69), the efficiency

$$\eta = I_{\text{mp}} V_{\text{mp}} / e E_{\text{av}} N_{\text{ph}} \quad (3.70)$$

can be written as [62]

$$\eta = \frac{Q N_{\text{ph}}(E_g)}{N_{\text{ph}} E_{\text{av}}} \frac{(V_{\text{mp}}^2/nkT)}{1 + (V_{\text{mp}}/nkT)} \simeq Q \frac{N_{\text{ph}}(E_g)}{N_{\text{ph}}} \frac{V_{\text{mp}}}{E_{\text{av}}} \quad (3.71)$$

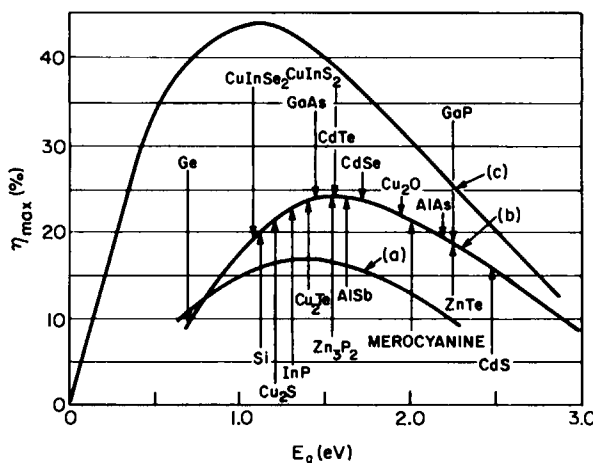


Fig. 3.25 Efficiency versus band gap assuming superposition and the bucking current model of Eqs. (3.65) and (3.66). (Based on Ref. [62]; used with permission).

with  $V_{mp}$  given by Eq. (3.68). The approximate expression is valid for  $V_{mp} \gg nkT$  (which we certainly hope is the case) and the quantity  $E_{av}$  is the average photon energy in the incoming spectrum which contains the total of  $N_{ph}$  photons (per area per second).

Plots of Eq. (3.71) for AM0 efficiency versus  $E_g$  are presented in Fig. 3.25. To simplify the calculation,  $Q$  has been set equal to one. Both curves (a) and (b) from Ref. [62] assume the diode ideality or quality factor  $n$  appearing in Eq. (3.65) is unity. Curve (a) is for  $\gamma = 2$ , whereas curve (b) is for  $\gamma = 1$  in the dark  $J-V$  characteristic. These curves are also useful for the case where  $\gamma$  is fixed and  $n$  is varied. If one assumes a fixed saturation current [i.e., fixed  $K$ ,  $\gamma$  and temperature in the model of Eq. (3.66)], and varies the ideality factor, it is seen from Eqs. (3.68) and (3.71) that the efficiency at a value of  $E_g$  increases linearly with  $n$ . Thus curves (a) and (b) in Fig. 3.25 can be appropriately scaled for such a variation in the model.

The general features seen in Fig. 3.25 are easily explained: with a higher band gap, fewer photons are utilized; however, bucking currents generally decrease with a wider band gap; hence,  $\eta$  has a maximum for some  $E_g$ . Since the actual mechanism giving rise to the bucking current can vary with material (i.e., with  $E_g$ ) and configuration, Fig. 3.25 and similar work by others [63–65] serve only to indicate the  $E_g$  values of interest in solar cells. For example, one can select a photovoltaic material on the basis that its energy gap  $E_g$  lies at the peak at curve (b) in Fig. 3.25. However, in using it in a specific configuration, it can be found that the bucking current model of Eq. (3.66) is not appropriate or that superposition is not valid. If the gap  $E_g$  of

this material were an adjustable parameter, it follows that a higher or lower  $E_g$  would actually be optimum.

The curves shown in Fig. 3.25 are a useful guide to the range of energy gaps to consider. Some materials in this range are noted in Fig. 3.25. Curves (a) and (b) are two of the many functions  $\eta = \eta(E_g)$  which can result by assuming different models for  $J_{bk}$ . However, all of these curves must fit under the limit of the ultimate efficiency curve developed in Ref. [65]. This is curve (c) of Fig. 3.25. It assumes  $V_{oc}$  is bounded by the limit on the built-in field contribution of Eq. (2.100); i.e., for curve (c):

$$\eta = [N_{ph}(E_g)/N_{ph}][E_g/E_{av}] \quad (3.72)$$

since  $V_{oc} \leq V_{bi} \leq E_g$  for the built-in field contribution.

### 3.9 CONCLUDING REMARKS

Although a number of materials can be involved in solar cell devices, the most important is the absorber. We determined that photocarriers can be collected from the absorber region by one of two approaches: by relying on diffusion to cause photogenerated minority carriers to exit the absorber or by relying on drift to cause photogenerated carriers to exit the absorber. In either case, effective field or electric field regions are required. These fields provide the check valve that prevents carriers from returning to the absorber to recombine; they give rise to a photovoltage wherever the conductivity of the field region is modified by the presence of light. Since the photovoltage developed in an electric field region can be of the order of the gap, solar cells are generally designed with a depleted barrier region as the core of the cell.

We noted that interfaces are critical to solar cell structures because they are used to form depleted barrier regions and because they are needed to form ohmic contacts and selective-ohmic contacts. They can also be inadvertently present because of the nature of the absorber material; i.e., polycrystalline materials.

The need for interface structures presents some difficulties. Because dissimilar materials are involved in interfaces, there can be chemical and mechanical potentials present, which can drive electrochemical and chemical reactions, as well as defect and impurity diffusion. As a result, some interface structures can be difficult to form in an optimum configuration and some can be difficult to stabilize. From this point of view one would suspect homojunctions would be the easiest to employ in solar cell structures and, indeed, they are.

## REFERENCES

1. H. J. Hovel, in "Semiconductors and Semimetals" (R. K. Willardson and A. C. Beer, eds.), Vol. 11, Solar Cells. Academic Press, New York, 1976.
2. H. F. Wolf, "Semiconductors." Wiley (Interscience), New York, 1971.
3. C. J. Nuese, *J. Educational Mod. Mat. Sci. Engr.* **2**, 113 (1980).
4. A. G. Milnes and D. L. Feucht, "Heterojunctions and Metal-Semiconductor Junctions." Academic Press, New York, 1972.
5. D. L. Feucht, *J. Vac. Sci. Technol.* **14**, 57 (1977).
6. B. L. Sharma and R. K. Purohit, "Semiconductor Heterojunctions." Pergamon, Elmsford, New York, 1974; R. A. Smith, "Semiconductors." Cambridge Univ. Press, London/New York, 1978.
7. F. F. Y. Wang, "Introduction to Solid State Electronics." North-Holland Publ., Amsterdam, 1980.
8. M. Savelli and J. Bougnot, Problems of the Cu<sub>2</sub>S/CdS Cell, in "Solar Energy, Solid State Physics Aspects" (B. O. Seraphin, ed.). Vol. 31, Topics in Applied Physics, p. 213. Springer-Verlag, Berlin and New York, 1979.
9. N. Romeo, G. Sberveglieri, and L. Tarricone, *Appl. Phys. Lett.* **32**, 807 (1978); Y. Sakurai, Y. Kokubun, H. Watanabe, and M. Wada, *Jpn. J. Appl. Phys.* **16**, 2115 (1977).
10. J. L. Shay and J. H. Wernick, "Ternary Chalcopyrite Semiconductors: Growth, Electronic Properties, and Applications." Pergamon, Oxford, 1975.
11. H. Okimura, T. Matsumae, and R. Makabe, *Thin Solid Films* **71**, 53 (1980).
12. E. Bucher, *Appl. Phys.* **17**, 1 (1978).
13. A. Catalano, M. Bhushan, and N. Convers-Wyeth, *Conf. Rec. IEEE Photovoltaic Spec. Conf. 14th* p. 641. IEEE, New York, 1980; A. Catalano, private communication.
14. R. Singh, K. Rajkanav, D. Brodie, and J. H. Morgan, *IEEE Trans. Electron Devices* **ED-27**, 656 (1980).
15. A. K. Ghosh, D. L. Morel, T. Feng, R. F. Shaw, and C. A. Rowe, Jr., *J. Appl. Phys.* **45**, 230 (1974).
16. T. Tani, P. Grant, W. Gill, G. Street, T. Clarke, *Solid State Commun.* **33**, 499 (1980).
17. K. J. Bachman, Materials Aspects of Solar Cells, in "Current Topics in Materials Sciences" (E. Kaldis, ed.), Vol. III. North-Holland Publ., Amsterdam, 1979.
18. S. G. Davison and J. D. Levine, *Solid State Phys.* **25**, 1 (1970).
19. R. L. Bell, "Negative Electron Affinity Devices." Oxford Univ. Press (Clarendon), New York, 1973.
20. A. K. Jonscher, "Principles of Semiconductor Device Operation." Bell, London, 1960.
21. J. Joffe, *Electron. Communun.* **22**, 217 (1945).
22. E. H. Rohderick, "Metal-Semiconductor Contacts." Oxford Univ. Press, London and New York (1978).
23. J. C. Phillips, *Proc. Symp. Thin Film Phenom.-Interfaces Interact.* Electrochemical Society, Princeton, New Jersey, 1978; I. Lindan, P. W. Chye, C. M. Garner, P. Pianetta, C. Y. Su, W. E. Spicer, *J. Vac. Sci. Technol.* **15**, 1332 (1978).
24. J. Bardeen, *Phys. Rev.* **71**, 717 (1947).
25. A. Goetzberger, E. K. Lausmann, and M. J. Schulz, *CRC Crit. Rev. Solid State Sci.* **6**, 1 (1976).
26. L. L. Tongson, B. E. Knox, T. E. Sullivan, and S. J. Fonash, *J. Appl. Phys.* **50**, 1535 (1979).
27. R. J. Stirn, High Efficiency Thin Film GaAs Solar Cells, Second Interm. Rep. (5030-255), Contract ERDA/NASA EG-77-A-29-1074 (Sept. 1978).
28. S. J. Fonash, *J. Appl. Phys.* **46**, 1286 (1975); **47**, 3597 (1976).
29. H. Gerischer, *J. Vac. Sci. Technol.* **15**, 1422 (1978).

30. R. Memming, "Electroanalytical Chemistry" (A. J. Bard, ed.), Vol. 11, p. 2. Dekker, New York, 1979.
31. A. Heller and B. Miller, *Electrochim. Acta* **25**, 29 (1980).
32. F. R. F. Fan and A. J. Bard, *J. Am. Chem. Soc.* **102**, 3677 (1980).
33. A. B. Bocarsly, D. C. Bookbinder, R. N. Dominey, N. S. Lewis, and M. S. Wrighton, *J. Am. Chem. Soc.* **102**, 3683 (1980).
34. A. Ghosh, T. Feng, H. P. Marnska, and C. Fishman, Thin Film Polycrystalline Si Solar Cells, Quart. Rep. I, DOE Contract DE-AC03-79ET23047 (1979).
35. C. H. Seager and T. G. Castner, *J. Appl. Phys.* **49**, 3879 (1978).
36. T. I. Kamins, *J. Appl. Phys.* **42**, 4357 (1971).
37. A. L. Fripp, *J. Appl. Phys.* **46**, 1240 (1975).
38. J. Y. W. Seto, *J. Appl. Phys.* **46**, 5247 (1975).
39. T. Tsuchimoto, I. Yudasaka, and T. Shirasu, in "Ion Implantation in Semiconductors" (S. Namba, ed.). Plenum, New York, 1974.
40. M. M. Mandurah, K. C. Saraswat, and T. I. Kamins, *Ext. Abstr. Meet.-Int. Soc. Electrochem., Los Angeles*, No. 571. Electrochemical Society, Princeton, New Jersey, 1979.
41. M. E. Cowher and T. O. Sedgwick, *J. Electrochem. Soc.* **119**, 1565 (1972).
42. C. H. Seager and D. S. Ginley, *Appl. Phys. Lett.* **34**, 337 (1979).
43. H. J. Leamy, W. D. Johnston, Jr., B. A. Parkinson, S. S. Chu, A. Heller, and B. Miller, *Ext. Abstr. Meet.-Int. Soc. Electrochem., Los Angeles*, No. 579. Electrochemical Society, Princeton, New Jersey, 1979.
44. S. Sze, "Physics of Semiconductor Devices." Wiley, New York, 1969.
45. S. J. Fonash, *J. Appl. Phys.* **46**, 1286 (1975).
46. S. J. Fonash, *J. Appl. Phys.* **51**, 2115 (1980).
47. S. J. Fonash, *Solid-State Electron.* **22**, 907 (1980).
48. E. Burstein and S. Lundqvist, eds., "Tunneling Phenomena in Solids." Plenum, New York, 1969.
49. F. A. Padovani, in "Semiconductors and Semimetals," (R. K. Willardson and A. C. Beer, eds.), Vol. 7A. Academic Press, New York, 1971.
50. J. P. Donnelly and A. G. Milnes, *Proc. IEEE* **113**, 1468 (1966).
51. A. R. Riben and D. L. Feucht, *Int. J. Electron.* **20**, 583 (1966).
52. A. R. Riben and D. L. Feucht, *Solid-State Electron.* **9**, 1055 (1966).
53. H. J. Pauwels and P. de Visschere, *Solid-State Electron.* **21**, 693 (1978).
54. S. J. Fonash and S. Ashok, *Appl. Phys. Lett.* **35**, 535 (1979).
55. B. Schwartz, ed., *Ohmic Contacts Semicond. Symp. Pap. 1968*. Electrochemical Society, Princeton, New Jersey, 1969.
56. R. G. Chittick, J. H. Alexander, and H. F. Sterling, *J. Electrochem. Soc.* **116**, 77 (1969).
57. W. E. Spear and P. G. LeComber, *Solid State Commun.* **17**, 1193 (1975); *Philos. Mag.* **33**, 935 (1976).
58. D. E. Carlson, J. I. Pankove, C. R. Wronski, and P. J. Zanyucchi, *Thin Solid Films* **45**, 43 (1977).
59. A. Barna, P. B. Barna, G. Radnoci, L. Toth, and P. Thomas, *Phys. Status Solidi A* **41**, 81 (1977).
60. H. Fritzsche, C. C. Tsai, and P. Persans, *Solid State Technol.* pp. 55-60 (Jan. 1978).
61. S. Ovshinsky, *New Sci.*, p. 674 (30 Nov. 1978).
62. J. J. Loferski, *J. Appl. Phys.* **27**, 777 (1956).
63. M. B. Prince, *J. Appl. Phys.* **26**, 534 (1955).
64. E. S. Rittner, *Phys. Rev.* **96**, 1708 (1954).
65. P. Rappaport, *RCA Rev.* **20**, 373 (1959).
66. W. Shockley and H. J. Queisser, *J. Appl. Phys.* **32**, 510 (1961).

## CHAPTER 4

# Homojunction Solar Cells

### 4.1 INTRODUCTION

We now begin our detailed examination of specific photovoltaic structures. The first photovoltaic device to be explored is the  $p$ - $n$  homojunction solar cell. A general  $p$ - $n$  homojunction solar cell band diagram is seen in Fig. 4.1; its variant, the  $p$ - $i$ - $n$  homojunction solar cell configuration, is seen in Fig. 4.2. The lineage of this solar cell structure can be traced back to the work by Ohl [1] in 1941, demonstrating a grown Si  $p$ - $n$  junction photovoltaic device. About 12 years later a 6% efficient, diffusion-formed Si  $p$ - $n$  junction device was demonstrated [2] and by 1958, 14% efficient silicon devices were available using this technology. Subsequently,  $p$ - $n$  homojunctions were explored using other semiconductors such as GaAs [3]. During this period (late 1950s–early 1970s)  $p$ - $n$  homojunction solar cells fabricated using other semiconductors were not able to seriously challenge silicon in efficiency or cost. For the silicon  $p$ - $n$  solar cell itself, efforts over these years focused on space power applications and, hence, on improving reliability and resistance to radiation as well as reducing costs.

In the 1970s  $p$ - $n$  homojunction solar cell devices again entered into a period of dramatic development. The advances in the case of Si  $p$ - $n$  cells led

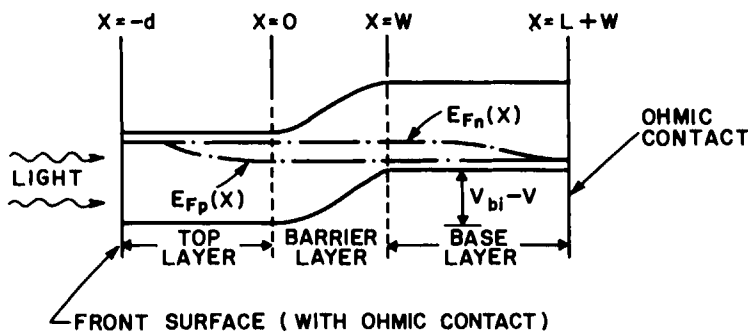


Fig. 4.1 An  $n$  on  $p$  ( $n-p$ ) homojunction solar cell structure shown developing power. Quasi-Fermi levels actually must have "humps" as seen exaggerated in Fig. 4.7. Regions are not to scale.

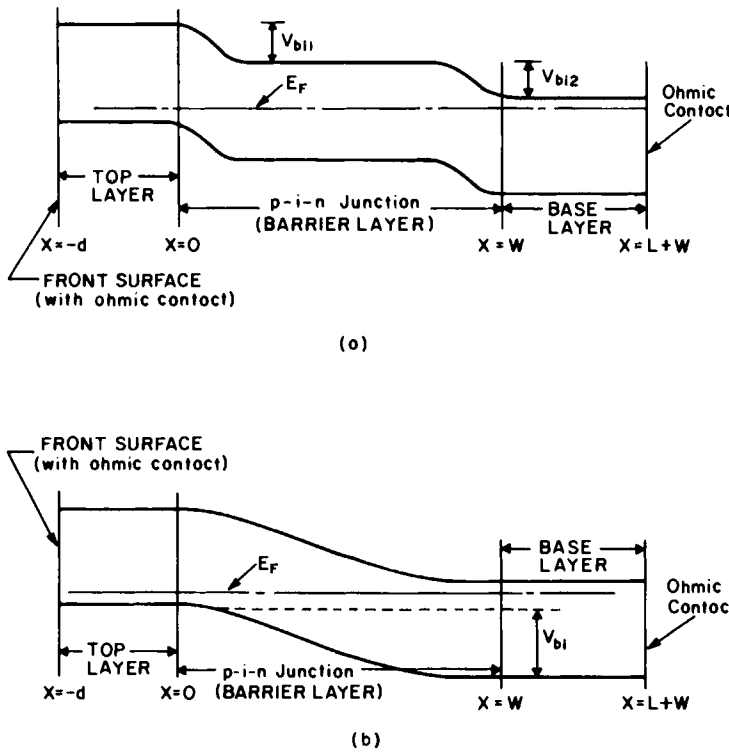


Fig. 4.2 Two  $p-i-n$  homojunction solar cell structures in thermodynamic equilibrium. Shown are cases where the electric field (a) does not and (b) does extend across the whole  $i$  layer. Which situation prevails essentially depends on the ratio of the Debye length  $L_D$  to the width  $w$  of the  $i$  layer. Case (a) occurs when  $L_D < w$ . Regions are not to scale.

to AM1 efficiencies approaching  $\sim 20\%$  and AM0 efficiencies of  $\sim 16\%$  [4, 5]. These efficiencies were achieved using devices fabricated from single-crystal material. In 1972 two major independent events occurred which substantially improved the  $p-n$  junction solar cell and thereby began this period of advancement: The development of the so-called "violet" Si  $p-n$  cell was announced [6] and the back-surface field (BSF) cell was demonstrated [7].

The violet cell employed a shallow, diffused junction which resulted in the depleted barrier region being closer to the top surface where light enters the device and which also resulted in a narrower, heavily doped diffused layer. As a consequence, better use is made of the higher energy photons absorbed near the top surface. Further, the violet cell employed more sophisticated grid patterns than had been previously employed (needed to compensate for the larger lateral resistance offered by the narrower top layer), and a more transparent AR coating, which provided better optical impedance matching. These various components are seen in the generalization of Fig. 4.3. This cell design, which also employed improved encapsulation, resulted in a gain of 15 to 20% in power output. The other advance, the back-surface field (BSF) cell, introduced the concept of shielding photogenerated minority carriers from the high recombination plane of the back surface by employing the electric field of a low-high junction (a selective-ohmic contact; see Section 3.6.3). Within two years both advances were appearing in some commercial cells.

In 1974 another innovation occurred in  $p-n$  homojunctions: the Comsat Laboratories' "black" cell [8]. This device added to the advances of the violet cell the idea of texturing the top of a Si surface to aid in coupling light into a  $p-n$  structure and to increase the optical path length in the

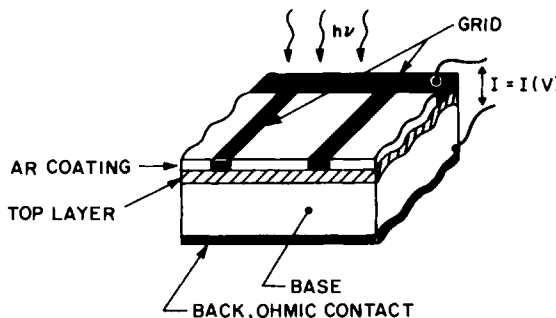


Fig. 4.3 A common  $p-n$  homojunction solar cell configuration. The top (emitter) layer is either  $p$ - or  $n$ -type with a corresponding  $n$ - or  $p$ -type base layer. The grid fingers make ohmic contact to the front of the cell; an ohmic contact covers the back of the device. The antireflection (AR) coating is for optical impedance matching. Encapsulation is not shown.

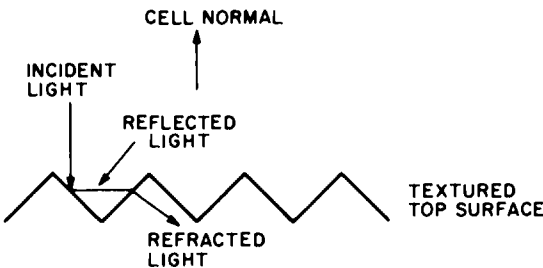


Fig. 4.4 Textured front surface causes multiple reflections increasing the probability that light will enter the cell structure. On entering the cell, refracted light has longer optical path length than light entering the nontextured surface due to the angle with the cell normal. Texturing can be used with an antireflection (AR) coating for increased coupling of light into the cell absorber.

absorber. These effects of texturing are seen in Fig. 4.4. With the advent of designs that effectively increased the optical path length and with the advent of the BSF selective-ohmic contact, it was realized that Si solar cell thickness could be reduced. Additional impetus was given in this direction with the proposal of a back-surface reflector [9]—a thin layer of metal such as gold, copper, or aluminum at the back surface to reflect photons back through the Si. The dramatic result of incorporating these concepts into *p-n* homojunction solar cell design is seen in Fig. 4.5 which compares the *I-V* characteristic, under illumination, of a 350- $\mu$  thick Si *p-n* homojunction of

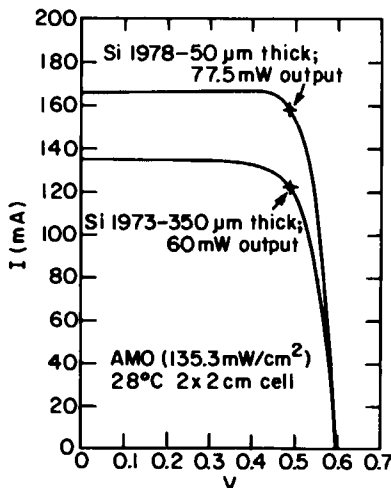


Fig. 4.5 Current-voltage (*I-V*) characteristics under light for a 1973 and a 1978 *p-n* Si solar cell. These experimental data indicate the rapid evolution which occurred in single-crystal Si *p-n* cells during this period. (After Ref. [10], with permission © IEEE 1978.)

1973 with a  $50\text{-}\mu$  thick device of 1978. The utilization of a shallow junction, texturing, and the BSF selective back-ohmic contact has led to increased efficiency from a considerably thinner structure.

During the same time that single-crystal Si  $p\text{-}n$  solar cells were entering into this period of innovation, great strides were taken in developing the homojunction configuration in other semiconductors and in thin film polycrystalline and amorphous materials. A shallow junction GaAs homojunction device with  $\eta = 22\%$  (under one sun conditions) was demonstrated [11], as was a  $(p)\text{Ga}_y\text{Al}_{1-y}\text{As}/(p)\text{GaAs}/(n)\text{GaAs}$  device with  $\eta = 22\%$  (under essentially one sun conditions) [12]. In this latter structure the wide gap  $(p)\text{Ga}_y\text{Al}_{1-y}\text{As}$  layer serves as a window significantly preventing photo-generation of carriers near the high-recombination front surface, and the  $(p)\text{Ga}_y\text{Al}_{1-y}\text{As}/(p)\text{GaAs}$  interface serves as a selective-ohmic contact. Completely thin film,  $p\text{-}n$  homojunction structures using semiconductors such as polycrystalline  $\text{CuInS}_2$  [13],  $\text{CuInSe}_2$  [14], and amorphous  $\text{SiH}_x$  [15] were also demonstrated. Today,  $p\text{-}n$  and  $p\text{-}i\text{-}n$  junction devices using organic and inorganic materials in crystalline, polycrystalline, and amorphous forms are under extensive exploration and development.

## 4.2 HOMOJUNCTION SOLAR CELL DEVICE PHYSICS

### 4.2.1 Qualitative Discussion

#### 4.2.1.1 General Features

We begin our examination of  $p\text{-}n$  homojunctions by considering the simple structures seen in Figs. 4.1 and 4.2. The materials shown are assumed to be single-crystal lifetime semiconductors (see Section 2.9) for simplicity for which the delocalized levels of the valence band constitute the ground state, and the delocalized levels of the conduction band constitute the excited state of Fig. 1.1. Light ( $h\nu \geq E_g$ ) excites electrons from the ground state to the excited state and photogenerated electron-hole pairs are created in the top (emitter<sup>†</sup>) layer, in the barrier (high electric field) region, and in the base layer of the absorbers of these structures. In each of the simple structures shown in these figures, there are high electrostatic fields in the barrier regions of the absorber but no electrostatic fields outside of the barrier region in thermodynamic equilibrium. With electric currents flowing, there will also be electrostatic fields set up in both the top and base layers, but the top and base layer electric fields, arising from the flow of

<sup>†</sup> The top layer is also commonly referred to as the emitter layer; however, there is no physical reason for this, since the bucking current developed in that region often dominates the total bucking current.

current, are usually expected to be small compared to the built-in barrier electric field. This point is discussed in some detail in Section 4.2.2.2. There are no effective fields (as defined in Chapter 2) present in a homojunction barrier region.

The structures seen in Figs. 4.1 and 4.2b represent extremes in the approaches to homojunction solar cell design. In the case of Fig. 4.1, we rely on diffusion to collect photogenerated minority carriers from the emitter and base regions, and the barrier layer is relatively narrow. In Fig. 4.2 the emitter and base regions can be made narrow compared to the barrier region. In Fig. 4.2b we rely directly on drift in the barrier region to collect photogenerated carriers created in that layer. Obviously, combinations of these approaches can be employed in general. We note that these two extreme approaches to photocurrent collection were discussed in broad terms in Section 3.2.

The homojunction structure of Fig. 4.1 is suitable for absorber materials that have diffusion lengths  $L_{n,p}$  which are of the order of, or greater than, the absorption length  $1/\alpha$ . In this homojunction configuration, the electric field of the barrier region acts as a sink which draws photogenerated holes

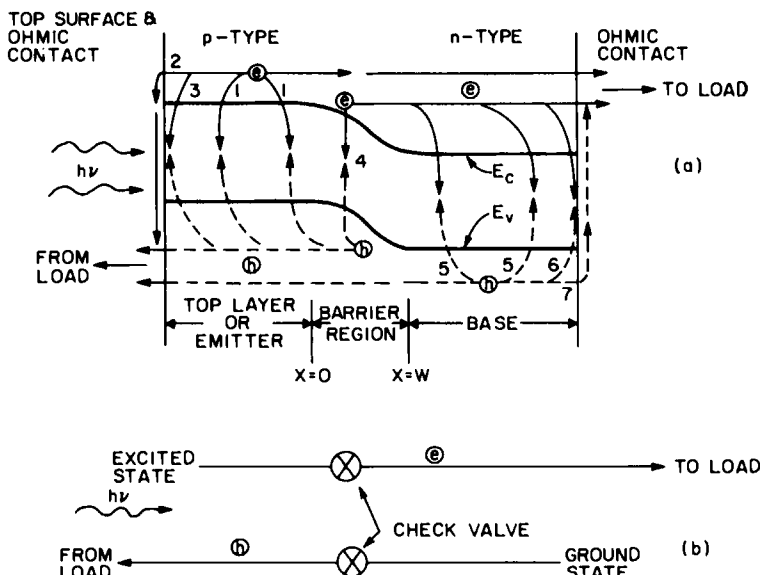


Fig. 4.6 (a) A simple  $p$  on  $n$  ( $p-n$ ) homojunction solar cell structure under illumination; (b) the device in terms of the generalized representation of Chapter 1. Processes 1-7 are all loss mechanisms: processes 1, 4, and 5 are bulk recombination, whereas processes 2, 3, 6, and 7 are losses at the top-surface/ohmic contact and base-layer ohmic contact. The check valve is the high-field barrier region.

from the *n*-type top layer and photogenerated electrons from the *p*-type base layer. That is, under illumination the minority-carrier populations are increased in the emitter and base regions, but minority carriers are swept out in the barrier region. Resultant population gradients drive minority-carrier diffusion (particle) currents toward the junction, setting up the photogenerated current.

The homojunction structures of Fig. 4.2 are suitable for absorber materials which have diffusion lengths  $L_{n,p}$  such that  $L_{n,p} \ll 1/\alpha$  but drift lengths  $L_\xi$  which are of the order of, or greater than,  $1/\alpha$ . In this homojunction configuration the electric field of the barrier region acts directly to collect photogenerated carriers. The configuration of Fig. 4.2b is seen to be much more effective than that of Fig. 4.2a in this situation.

To examine more closely the generation of the photocurrent as well as to examine the sources of carrier loss in a homojunction structure, we shall focus on homojunctions cells of the type seen in Fig. 4.1. This type is shown in Fig. 4.6 in the form of a *p* on *n* (*p*-*n*) cell under illumination.

When light impinges on the homojunction solar cell structure of Fig. 4.6a, photogenerated carriers are created in the delocalized bands. If we focus on the top layer and follow the photogenerated minority carriers (electrons), we see that they immediately become subject to bulk recombination (process 1 of Fig. 4.6a). Further, those electrons from the top layer which are unfortunate enough to arrive at the left top-surface ohmic contact<sup>†</sup> are lost to recombination through processes 2 and 3, but those that arrive at the barrier region can be swept out to the right of the figure by the barrier electrostatic field. Some of these fortunate electrons from the top layer cross the barrier region without recombining (process 4), subsequently cross the base layer without recombining in the bulk (process 5), and even cross into the right ohmic contact without being lost (processes 6 and 7). Electrons from the top layer, which succeed in avoiding the loss mechanisms provided by processes 1–7, are a component of the current  $I$  flowing through the external circuit. Figure 4.6a shows that, to increase this contribution of photogenerated electrons from the top layer, it is necessary to reduce the detrimental effects of processes 1–7.

An additional component of  $I$  is seen to arise from electrons photogenerated in the barrier region and subsequently swept out by the barrier electric field before recombining. To contribute to  $I$ , these must then cross the base and right ohmic contact without recombining. A final contribution arises from those photogenerated electrons, created in the base, which

<sup>†</sup> From Fig. 4.3 it is seen that the actual ohmic contact (the grids) covers only part of the front surface to allow the penetration of light into solar cell structures using metal grid fingers. Hence, the left boundary in Fig. 4.6a is a composite structure, in general. We will refer to it as the top-surface ohmic contact or simply top-surface.

succeed in arriving at the right interface and, subsequently, cross into the right ohmic contact. To enhance the current contribution from photo-generated electrons created in the barrier region and in the base region, it is clear that processes 4–7 of Fig. 4.6a must be minimized. We have made these arguments in terms of electrons; the corresponding arguments also follow for holes.

By comparing Figs. 4.6a and 4.6b, it is seen that the check valve of Fig. 1.1 is the built-in, high electric field of the barrier region. It acts as a sink to pull photogenerated electrons away from loss mechanisms 1–3, and it sets photogenerated electrons in motion through the barrier and base regions (where they still may be lost to processes 4–7). It also pulls photogenerated holes away from loss mechanisms 5–7 and sets them in motion across the barrier and emitter regions.

It is the loss mechanisms 1–7 of Fig. 4.6a (together with such problems as series resistance arising from contacts or bulk resistance) that determine the shape of the current–voltage ( $I$ – $V$ ) characteristic of a cell. In particular, these loss mechanisms effect the short-circuit current  $I_{sc}$  and they establish the open-circuit voltage  $V_{oc}$  since this is the voltage necessary to reduce the barrier electric field enough, and necessary to drive the electron and hole quasi-Fermi levels apart sufficiently, to ensure that all the photogenerated electrons (and holes) are lost internally in the cell through processes 1–7. It follows that the more effective are processes 1–7 in reducing the photo-carrier populations, the more the open-circuit voltage  $V_{oc}$  will be reduced. Note that for the device of Fig. 4.6a, under illumination, the left contact is positive with respect to the right contact for any point on the  $I$ – $V$  characteristic of Fig. 2.25, and the upper bound on this voltage developed by the cell structure under illumination is  $V_{oc}$ .

Let us take an even closer look at these various components of the current  $I$  flowing in Fig. 4.6. This time we shall become a bit more specific and assume that our solar cell has a one-dimensional structure. Since the minority-carrier electrons in the top layer will have their number density greatly increased in the top layer due to the illumination and, since both the barrier region and the left top-surface ohmic contact are sinks for these carriers, it is clear that there can be a substantial electron number density gradient  $dn/dx$  in this top layer under light.

Because the barrier and left top-surface ohmic contact are both sinks for photogenerated electrons, this gradient will change sign somewhere in the top layer. In the region where  $dn/dx < 0$ , an electron diffusion current will exist which is carrying electrons to the high electrostatic field region of the barrier of Fig. 4.6a. To increase this advantageous supply of photo-generated electrons from the top layer, which are diffusing to the barrier, we want to move the plane for which  $dn/dx = 0$  farther to the left and we want

to assure that electrons to the right of this plane can reach the barrier without suffering bulk recombination (process 1 of the figure). Hence, to improve cell performance we would like to reduce substantially the strength of the sink at the top-surface ohmic contact and we want to increase the distance electrons diffuse without suffering recombination in the top layer. A measure of the strength of the sink at the left top-surface ohmic contact is given by  $S_n$ , the minority-carrier surface recombination speed of Eq. (3.63), which is a phenomenological quantity characterizing this left boundary (loss processes 2 and 3 of the figure); and, of course, a measure of the distance an electron can diffuse in the top layer without recombining is given by  $L_n$ , the diffusion length of Eq. (3.1).

Since we are neglecting electron drift in the top layer at this point, the value of the advantageous electron current density emanating from this layer at  $x = 0$  is given by the diffusion component of Eq. (2.62)<sup>†</sup>; viz.,

$$J_n(x = 0)|_{\text{dif}} = eD_n(dn/dx)|_{x=0} \quad (4.1)$$

In the configuration of Fig. 4.6a we rely on photogeneration in the top layer and on this component of  $J_n$  to collect the photogenerated electrons from the top layer.

We must now ask ourselves if this expression for the diffusion component of  $J_n$  is indeed the total electron current density at  $x = 0$ . Are we justified in neglecting the drift component of Eq. (2.62)? In exploring this question we admit that for the majority-carrier holes in the top layer of Fig. 4.6a, both drift and diffusion are probably important; i.e., from Eq. (2.66) we expect that  $e\mu_p p\xi$  may be of the order of  $eD_p dp/dx$  in the top layer.<sup>‡</sup> It would also seem reasonable that  $eD_n dn/dx$  would be of the order of  $eD_p dp/dx$  since  $dp/dx \approx dn/dx$  should hold in the top layer of a lifetime semiconductor (see Section 2.9). It follows that we expect  $|e\mu_n n\xi| \ll |eD_n dn/dx|$  so long as  $n \ll p$  in the top layer of Fig. 4.6a. We conclude that Eq. (4.1) should satisfactorily give  $J_n(0)$ , the total electron current density at  $x = 0$ , for lifetime semiconductors when  $n \ll p$ . However, this result would not hold for concentrator cells. Under concentration (with  $p \approx n$ ), even in lifetime semiconductors, drift currents can also be important in the top layer of structures as simple as Fig. 4.6a. We discuss this latter point in some detail in Section 4.2.2.2.

Returning to the mainstream of our discussion, we know that some fraction of  $J_n(x = 0)$  coming out of the top layer will be successful in crossing the rest of the structure and contributing to the total current density  $J$ . In addition, we know that there will be contributions to the total current

<sup>†</sup> We neglect at this point any variations in the electron temperature  $T_e$  or hole temperature  $T_h$  which may be present in the cell under illumination.

<sup>‡</sup> This is basically due to the fact that, although  $\xi$  may be very small in the top layer, the  $p\xi$  product can be large.

density  $J$  coming from photogenerated electrons created in the barrier and base regions. We properly account for these additional contributions to  $J$  as well as account for the loss of some of  $J_n|_{x=0}$  across the barrier and base by simply noting that the net result of all these effects must be equal to  $J_p|_{x=0}$  since

$$J = J_n|_{x=0} + J_p|_{x=0} \quad (4.2)$$

gives the total current density at the plane  $x = 0$ . In this one-dimensional structure,  $J$  is a constant which will be negative for Fig. 4.6.

It follows from Fig. 4.6a that

$$J_p|_{x=0} = -e \int_0^w G_L dx + e \int_0^w R dx + J_p \Big|_{x=w} \quad (4.3)$$

As a result Eq. (4.2) becomes

$$J = J_n \Big|_{x=0} - e \int_0^w G_L dx + e \int_0^w R dx + J_p \Big|_{x=w} \quad (4.4)$$

which says that the total current density  $J$  flowing under illumination, when the device is developing some total voltage  $V$ , can be interpreted as arising from the net flow of electrons out of the  $p$ -type region, the net rate of generation of carriers in the barrier region, and the net flow of holes out of the  $n$ -type region. Equation (4.4) is a precise statement involving no restrictions other than the assumption of a one-dimensional structure for simplicity. Note that  $J_n|_{x=0}$  and  $J_p|_{x=w}$  are negative under illumination for Fig. 4.6.

Viewed from the perspective of Eq. (4.4) it is seen that the conclusions we have drawn concerning electrons in the top layer of Fig. 4.6a can now be applied to holes in the base. Specifically, it is seen that the diffusion of holes out of the base toward the sink provided by high electrostatic field region of the barrier is crucial to device performance for structures of the form of Fig. 4.6a. It follows that the strength of the right ohmic contact as a sink for holes in the structure of Fig. 4.6a must be reduced to enhance performance, and the hole diffusion length must be as long as possible. However, it also follows from our previous arguments concerning the role of drift that even for a lifetime semiconductor used in the simple configuration of Fig. 4.6a, drift currents in the base can be important for concentrator cells.

From Eq. (4.4) it is seen that the contribution to  $J$  coming from the barrier region depends on (a) the total number of photogenerated carriers per second per area produced in the region; (b) the net recombination in the region; and (c)  $W$ , the width of the region. For materials with small diffusion lengths, one could rely more in such materials on the photocarriers produced directly in the high-field barrier region itself. If this approach were taken to extremes, we would want  $W$  as large as possible and we

would want the electric field in the barrier as large as possible while striving to reduce the net recombination in the barrier region. From our analysis of  $p-n$  junction barriers in Section 3.4.2.1, it follows that the barrier can be made wider by reducing the doping density in that region. This leads to the use of  $p$ -type-intrinsic- $n$ -type ( $p-i-n$ ) homojunction solar cell structures<sup>†</sup> such as that seen in Fig. 4.2 in materials which have poor diffusion lengths [16]. In configurations such as Fig. 4.2 we need not rely that much on photo-generation (and collection) in the top and base layers. Consequently these can be made very narrow.

Most of this qualitative analysis of homojunction solar cell operation has been based on assuming the absorber is a single-crystal lifetime semiconductor; however, the features described are of general validity, although care must be exercised in deciding the relative importance of diffusion and drift for a specific material and specific illumination conditions. The general operating features which have been discussed are not dependent on whether or not the carrier transport is in localized or delocalized states. The discussions have assumed the photogenerated carriers are electrons and holes, but this same qualitative analysis is applicable if the photogenerated carriers are polarons. If the photogenerated carriers are excitons, it is clear that we must rely on their diffusion to the barrier region, and on their production in the barrier region. The latter contribution may be increased by utilizing a  $p-i-n$  configuration. In any case, excitons must be separated in the high-field barrier region to produce the charged particles (electrons and holes) of a current.

#### 4.2.1.2 Design Considerations

Based on our understanding of  $p-n$  homojunction solar cell operation developed in the last section, we can begin refining the cell structure. Looking back at the simple homojunction devices shown in Figs. 4.1 and 4.2, we can now see that these are far from optimum configurations. For example, rather than the ohmic contacts seen in these figures, the devices should have selective-ohmic contacts as discussed in Section 3.6.3 and Fig. 3.23. The left top-surface ohmic contact of Fig. 4.1, for example, should block holes (ideally  $S_p = 0$ ); the right ohmic contact should block electrons (ideally  $S_n = 0$ ).

As we have seen, one type of selective-ohmic contact that could be used for the left top-surface ohmic contact would be the high-low (HL) junction; i.e., if the  $n$  layer of Fig. 4.1 were to be modified such that an  $n^+$  layer existed adjacent to the top surface, the resulting  $n^+-n$  structure would

<sup>†</sup> In practice this intrinsic  $i$  layer is approximated by either a high resistivity  $p$  layer denoted as a  $\pi$  layer or a high resistivity  $n$  layer denoted as a  $v$  layer.

produce an electrostatic field that reflects minority-carrier electrons away from the top-surface ohmic contact. However, this structure would provide an excellent ohmic contact for majority electrons when used in conjunction with gridding. Devices with this HL junction in the top layer have been termed high-low emitter (H-L-E) cells [17].

Another approach to the top-surface ohmic contact would be to passivate the semiconductor surface between the grids by using an insulator layer as discussed in Section 3.4.5. These layers could also be used to introduce fixed charge (Section 3.4.5) which, if it has the correct sign, can set up an electrostatic field adjacent to the top surface to reflect minority carriers away from the left boundary of Figs. 4.1 and 4.2. Such devices have been made for structures of the form of Fig. 4.1: Silicon *p*-*n* structures have been fabricated using a thermal oxide on the top surface to obtain an oxide-charge-induced front-surface field (FSF) cell [17]. In the particular FSF cell of Ref. [17]  $Q_{\text{fix}} > 0$  and the top layer is *n*-type.

Selective-ohmic contacts should be used at the back contact also. From Section 3.6.3 and Fig. 3.23 it is seen that a variety of such contacts is conceptually possible: Choosing a high-low junction for the right boundary of the base layer in Figs. 4.1 and 4.2 results in the common selective-ohmic contact structure which is termed the back-surface field (BSF) solar cell.

As we have discussed, homojunction solar cell structures of the type seen in Fig. 4.1 rely on diffusion of photogenerated minority carriers to the high-field barrier region for photovoltaic action. However, it is possible to supplement this diffusion in the top and base layers by building in drift fields in these regions. This approach is attractive for materials which have poor diffusion lengths. Built-in drift fields can be designed into a cell to ensure that drift will aid diffusion by (a) incorporating doping variations into the top and base layers (setting up electrostatic drift fields [18–20]) or (b) incorporating electron affinity variations, hole affinity variations, or band effective-densities-of-states variations into the top and base layers (setting up effective drift fields [21]). An alternative design approach for the situation where the material has poor diffusion lengths is, of course, the *p*-*i*-*n* configuration of Fig. 4.2.

As we saw in the preceding section, the bucking current opposing the photocurrent flows because of processes 1–7 in Fig. 4.6a. Frequently, processes 1 and 5 (bulk recombination in the top and base layers, respectively) dominate in homojunctions of the form seen in Fig. 4.6a. Focusing on these loss mechanisms, it follows from Section 2.6 that the formulation for the net bulk recombination  $\mathcal{R}$  occurring through process 1 of Fig. 4.6a, for example, may be written as

$$\mathcal{R} = (n - n_{p0})/\tau_n \quad (4.5)$$

independent of whether the actual recombination mechanism is radiative recombination, Auger recombination, or S-R-H recombination. We will use Eq. (4.5) to aid in the consideration of cell design by noting that if the electron quasi-Fermi level  $E_{Fn}$  at some point in the top layer is measured from its thermodynamic equilibrium position, Eq. (4.5) may be rewritten as

$$\mathcal{R} = n_{p0}(e^{E_{Fn}/kT} - 1)/\tau_n \quad (4.6)$$

This expression for the number of electrons lost in the top layer per second per unit volume through process 1 is proportional to the equilibrium number density of electrons  $n_{p0}$  and inversely proportional to the electron lifetime  $\tau_n$ .

Equation (4.6) immediately suggests that the top layer (and by extension the base layer) in Fig. 4.6a should be heavily doped to reduce the strength of the bulk recombination loss mechanism, which would in turn reduce the bucking current and increase  $V_{oc}$ . Equation (4.6) suggests heavy doping is advantageous since

$$n_{p0} = n_i^2/N_A \quad (4.7)$$

where this particular expression for  $n_{p0}$  is valid for nondegenerate materials only (see Section 2.7). Heavy doping seems especially advantageous for the top layer provided the top surface is passivated (HLE or FSF cell) since the layer could then be made thinner (moving the barrier which separates photogenerated carriers closer to the plane of entry for the light and allowing better use of higher energy photons) while retaining an acceptable resistance to lateral flow of majority carriers to the grids.

Unfortunately, there are a number of complications which arise when the design approach of using heavily doped top and base layers is put into practice. First, when heavy doping is employed there is band edge tailing [22], which can be looked upon as a narrowing of the band gap [23]. From Eq. (4.7) it is seen that this means a given  $N_A$  leads to a larger  $n_{p0}$  than expected since  $n_i$  has increased with the gap narrowing. However, if the Fermi-level rises to within a few  $kT$  of a band edge due to heavy doping Eq. (4.7) itself is not valid (see Section 2.7) since Fermi-Dirac statistics now must be used to compute  $n_{p0}$ . When proper account is taken of the need for Fermi-Dirac statistics the effects of band-edge tailing and band-gap narrowing are still present but found to be less severe:  $n_{p0}$  is somewhat smaller for a given doping and assumed degree of band gap narrowing than Eq. (4.7) would predict [24, 25].

Further complications arise with using heavily doped regions to reduce processes 1 and 5 of Fig. 4.6a when one considers that the  $\tau_n$  appearing in Eq. (4.5) will also vary with doping. If the recombination mechanism is Shockley-Read-Hall recombination, it is seen from Eq. (2.29) that an

increased trap density  $N_T$  will reduce  $\tau_n$ . Increased trap densities may result due to damage incurred with heavy doping especially in heavily diffused top layers [26]. However, by comparing Eqs. (2.13), (2.19a), (2.19b), and (2.29) it may be inferred that Auger recombination will become the dominant mechanism for processes 1 and 5 at some value of increasing doping density. This must occur since  $\tau^A$  varies inversely with the square of the doping density for heavy doping [27, 28]. Experimentally, it has been found that the threshold for the onset of this domination by Auger recombination is  $N_A \simeq 2 \times 10^{18} \text{ cm}^{-3}$  and  $N_D \simeq 5 \times 10^{18} \text{ cm}^{-3}$  in silicon [29]. Because  $\tau$  eventually varies as the reciprocal of the square of the doping density, the advantage of heavy doping, first suggested by Eq. (4.6), must become limited due to Auger recombination independent of other effects such as band-edge tailing. As a result of these several effects (band-gap narrowing, Fermi-Dirac statistics, defects created by heavy doping, and Auger recombination) it has been experimentally observed in silicon that the increase in  $V_{oc}$ , expected from Eq. (4.6) with increased doping density, begins to saturate for doping densities  $\gtrsim 10^{17} \text{ cm}^{-3}$  [30, 31].

At this point we change the perspective being used to view the  $p-n$  homojunction solar cell and look at it from the point of view of Eq. (2.100). This approach allows us to focus on the Dember potential and conductivity modulation. So far, these effects have not specifically entered into our qualitative discussion of device operation and cell design.

Using Eq. (2.100) we note that regions which have  $d(\Delta n)/dx > 0$  in Fig. 4.6a make a detrimental contribution<sup>†</sup> to the open-circuit voltage  $V_{oc}$ , and regions which have  $d(\Delta n)/dx < 0$  make an advantageous contribution to  $V_{oc}$ ; similarly, regions for which  $d(\Delta p)/dx > 0$  are advantageous, and regions for which  $d(\Delta p)/dx < 0$  are disadvantageous. Frequently, it is argued that these Dember contributions apparent from the perspective of Eq. (2.100) are not significant in solar cell structures. In general, this argument must be viewed with care. It is based on the assumption that  $\Delta n \simeq \Delta p$  in the top and base layers (lifetime semiconductor) and on the assumption that the carrier mobilities are nearly equal. However, carrier mobilities may differ by orders of magnitude. This can occur, for example, if one carrier type exists in delocalized states and the other exists in localized states. It is also clear that even in quasi-neutral regions  $\Delta n$  certainly need not equal  $\Delta p$  (or  $\Delta p_j$ , if there is carrier transport in the conduction band and in some  $j$ th group of localized states, for example) in materials such as amorphous solids.

These Dember terms will make contributions of varying degrees depending on cell design and cell material. For example, we can reduce the

<sup>†</sup>The structure for which Eq. (2.100) was derived is such that, under light, the right side develops a voltage which is negative with respect to the left side; the same is true for the device of Fig. 4.6.

contribution from  $d(\Delta n)/dx > 0$  in the top layer of Fig. 4.6a by reducing the strength of the minority-carrier sink at the top-surface ohmic contact by using a selective-ohmic contact or by otherwise passivating this left boundary. Hence, from this perspective, one advantage of a selective-ohmic contact at the left boundary of the top layer would be to reduce a disadvantageous Dember contribution. It is also apparent that materials can be selected for  $p-n$  solar cell structures with the objective of increasing advantageous Dember contributions.

Again returning to Eq. (2.100), it is seen that photovoltaic action results from conductivity modulation under illumination in the field regions. This is how the principal source of photovoltaic action in the device—the depleted, high field barrier region—manifests itself in this perspective.

Any effect such as diffusion, drift electrostatic fields, effective drift fields, selective-ohmic contacts, and reflecting fields at boundaries which will enhance the photogenerated carrier population in a depleted barrier region by directing carriers there, will enhance the conductivity modulation and, hence, device response.

From Eq. (2.100) it may also be seen that drift electrostatic fields, fields at selective-ohmic contacts, reflecting fields, and effective drift fields can make an additional primary contribution to photovoltaic action, if they exist in regions of conductivity modulation. This can be of importance in concentrator applications and even under one sun conditions for devices which exhibit pronounced photoconductivity [32].

## 4.2.2 Device Analysis Concepts

### 4.2.2.1 Mathematical System

We are now at the point where we can begin to analyze homojunction solar cell behavior in detail, which means we need the full system of equations developed in Chapter 2. Using these equations we shall be able to compute  $J-V$  characteristics and efficiencies. For convenience the equations are repeated, omitting the terms involving effective forces. We limit ourselves to one-dimensional structures.

We recall from Chapter 2 that the current density  $J$  flowing when a homojunction solar cell is developing a voltage  $V$  under illumination must be the sum of contributions given by

$$J = J_n + J_p + \sum_i J_{Li} \quad (4.8)$$

and the voltage  $V$  must be given by

$$V = \int_{\text{structure}} (\xi - \xi_0) dx \quad (4.9)$$

Here  $J_n$ , the current density developed in the conduction band, is given by

$$J_n = en\mu_n\xi + eD_n dn/dx + eD_n^T dT_e/dx \quad (4.10)$$

or equivalently

$$J_n = en\mu_n dE_{Fn}/dx - en\mu_n S_n dT_e/dx \quad (4.11)$$

and  $J_p$ , the current density developed in the valance band, is given by

$$J_p = ep\mu_p\xi - eD_p dp/dx - eD_p^T dT_h/dx \quad (4.12)$$

or equivalently

$$J_p = ep\mu_p dE_{Fp}/dx - ep\mu_p S_p dT_h/dx \quad (4.13)$$

As discussed in Chapter 2, similar expressions hold for the current density  $J_{Li}$  developed by carriers in the  $i$ th localized level; i.e.,

$$J_{Li} = en_i\mu_{ni}\xi + eD_{ni} dn_i/dx + eD_{ni}^T dT_{ei}/dx \quad (4.14)$$

The electrostatic field  $\xi$  appearing in these equations is related in turn to the band populations ( $n$  and  $p$ ) and the localized-state populations according to Poisson's equation; viz.,

$$d\xi/dx = (e/\epsilon_s)(p - n + \dots) \quad (4.15)$$

Here the implied terms allow for any charge residing in localized states.

We have from Chapter 2 a final set of equations which relate gradients in the current densities to photogeneration and net recombination. These are the continuity equations

$$dJ_n/dx = e \left[ \mathcal{R}_n - \int G_n^S(x, \lambda) d\lambda \right] \quad (4.16)$$

$$dJ_p/dx = e \left[ -\mathcal{R}_p + \int G_p^S(x, \lambda) d\lambda \right] \quad (4.17)$$

and

$$dJ_{Li}/dx = e \left[ \mathcal{R}_{Li} - \int G_{Li}^S(x, \lambda) d\lambda \right] \quad (4.18)$$

The quantity  $G_n^S$  gives the rate of production of electrons per volume in the conduction band at point  $x$  due to absorption of illumination of wavelength  $\lambda$ . The  $G_p^S$  and  $G_{Li}^S$  are corresponding quantities for the valence band and the  $i$ th localized level as discussed in Chapter 2. The quantity  $\mathcal{R}_n$  models the net recombination-thermal-generation rate per volume for electrons in the conduction band. It contains the kinetics involved in electron transfer in and out of the conduction band due to thermally induced communication with localized states or due to thermally induced communication with the

valence band. The  $\mathcal{R}_p$  and  $\mathcal{R}_{Li}$  are corresponding quantities for the valence band and the  $i$ th level, respectively.

To obtain a feel for this mathematical system, let us consider a material which has just one localized level. For a homojunction structure fabricated using this material, Eqs. (4.10), (4.11), and (4.14)–(4.18) constitute a set of seven equations which, together with boundary conditions, must be solved in general to obtain  $\Delta n = \Delta n(x)$ ,  $\Delta p = \Delta p(x)$ , etc. Unfortunately, examination of this set of seven equations shows that it is not complete since there are 10 unknowns. To complete the set, one has two choices: neglect variations in the carrier temperatures, or add the three equations dealing with the energy balance for each population as discussed in Section 2.7.3.2.

Regardless of whether the set of equations is closed by neglecting temperature variations or by adding the energy balance equations, the completed mathematical system (set of equations plus boundary conditions) must be solved to yield  $\Delta n = \Delta n(x)$ ,  $\Delta p = \Delta p(x)$ ,  $\xi = \xi(x)$ , etc. These functions can be used in Eqs. (4.10), (4.12), (4.14), and then in Eq. (4.8) to give  $J$  with  $V$  determined by Eq. (4.9). Alternatively, the approach of Eq. (2.103) can be used to obtain  $J = J(V)$ ; i.e., the light  $J$ – $V$  characteristic can be obtained by using the functions  $\Delta n = \Delta n(x)$ ,  $\Delta p = \Delta p(x)$ , etc. in expressions of the form

$$\begin{aligned} V = & - \int_0^L \left( \frac{e\mu_n \Delta n + e\mu_p \Delta p}{\sigma} \right) \xi_0 dx \\ & + kT \int_0^L \frac{1}{\sigma} \left( e\mu_p \frac{d \Delta p}{dx} - e\mu_n \frac{d \Delta n}{dx} \right) dx + J \int_0^L \frac{dx}{\sigma} \end{aligned} \quad (4.19)$$

where the particular expression seen in Eq. (4.19) assumes that only the conduction band and valence band carriers are mobile.

The mathematical system which must be solved in order to evaluate homojunction solar cell behavior is quite formidable. This system is seen to involve a set of coupled, nonlinear differential equations. From the optimist's point of view such a system can be looked upon as a rich source of a broad range of physical phenomena which can take on varying degrees of importance depending on material parameters, illumination levels, and device structure.

#### 4.2.2.2 Range of Physical Phenomena

Some indication of the broad range of behavior lurking in this mathematical system will be demonstrated by discussing several distinct situations. The extreme situations which will be discussed are transport involving (a) minority-carrier diffusion, (b) ambipolar diffusion, and (c) space-charge limited currents.

(1) *Minority-carrier-Diffusion* We begin by considering a homojunction structure fabricated using a lifetime semiconductor (see Section 2.9). For definitiveness, we assume a homojunction structure with a *p*-type emitter region such as that seen in Fig. 4.6a. Assuming there are no built-in fields in the emitter and base,  $\Delta n \sim \Delta p$  in these regions for a lifetime semiconductor under illumination. It follows from Eq. (4.15) that any electric field in these regions would be expected to be small under illumination.

Focusing on the emitter layer, for example, we can say that even though  $\xi$  is small, the term  $ep\mu_p\xi$  may be significant in Eq. (4.12) in this region of a cell since  $p$  is large. However, as we argued earlier in Section 4.2.1.1, the term  $en\mu_n\xi$  in Eq. (4.10) differs by a factor  $n/p$  from the corresponding drift term in Eq. (4.12) but the diffusion terms are comparable. Therefore, for low levels of illumination in the *p* region ( $n \ll p$ ), we expect<sup>†</sup>

$$J_n = eD_n dn/dx \quad (4.20)$$

Using Eq. (4.20) and noting from Section 2.6 that all the models for band-to-band net recombination-generation in the quasi-neutral *p* region may be written as

$$\mathcal{R}_n = \Delta n/\tau_n \quad (4.21)$$

where  $\tau_n$  is a constant for low-level illumination ( $n \ll p$ ), allows the continuity equation for electrons in a *p* region to be expressed as a linear second-order differential equation; viz.,

$$\frac{dn^2}{dx^2} - \frac{n - n_{p0}}{L_n^2} = -\left(\frac{1}{D_n}\right) \int G_n^S(x, \lambda) d\lambda \quad (4.22)$$

Here  $L_n$  is the diffusion length defined by Eq. (3.1) and the right-hand side is some known function of  $x$ . Equation (4.22) (together with boundary conditions) gives the  $n = n(x)$  we needed in Eq. (4.1) to evaluate the diffusion current coming out of a *p*-type emitter.

Equations (4.20)–(4.22) apply to any quasi-neutral *p*-type region in a solar cell structure under low-level illumination. It follows that the corresponding equations for a quasi-neutral *n*-type region under low-level illumination are

$$J_p = -eD_p dp/dx \quad (4.23)$$

$$\mathcal{R}_p = \Delta p/\tau_p \quad (4.24)$$

and

$$\frac{d^2p}{dx^2} - \frac{p - p_{n0}}{L_p^2} = -\left(\frac{1}{D_p}\right) \int G_p^S(x, \lambda) d\lambda \quad (4.25)$$

<sup>†</sup> We neglect any variations in carrier temperature in this section.

where  $L_p$  is hole diffusion length and the right-hand side of Eq. (4.25) is some known function of  $x$ . Both Eqs. (4.22) and (4.25) are linear differential equations since  $\tau_{n,p}$  (and, therefore,  $L_n$  and  $L_p$ ) are independent of minority-carrier number density in this regime of behavior.

Equation (4.22) states that the electron distribution in any quasi-neutral  $p$ -region of a cell under low-level illumination is dictated by diffusion, recombination, and photogeneration. Equation (4.25) makes the corresponding statement for holes in a quasi-neutral  $n$  region of a cell under low-level illumination. Equation (4.22) (plus boundary conditions) can give us  $\Delta n = \Delta n(x)$  and, therefore,  $\Delta p$  since  $\Delta p \sim \Delta n$  for a quasi-neutral  $p$  layer of a cell structure; and Eq. (4.25) can give us  $\Delta p = \Delta p(x)$  and, therefore,  $\Delta n$  since  $\Delta n \sim \Delta p$  in a quasi-neutral  $n$  layer of a cell structure. This looks like a promising approach to a complete analysis in appropriate situations, but we postpone pursuing it until Section 4.2.3. At this point we are interested in gaining more insight into the physical phenomena built into the mathematical system presented in Section 4.2.2.1.

(2) *Ambipolar Diffusion* Let us continue to assume we have a homojunction structure fabricated using a lifetime semiconductor, but let us relax the restriction that limited use to regimes of behavior where  $n \ll p$  or  $p \ll n$ . That is, we consider levels of illumination such that  $n \sim p$ , as would occur under light concentration or in intrinsic regions without concentration. In the absence of built-in electric fields, it still follows that  $\Delta n \sim \Delta p$  in this material; consequently, any field in quasi-neutral regions present under illumination should still be small. Unfortunately, the fact that the electrostatic field is small does not help us to get at the physics dictating the number-density distributions in these quasi-neutral regions, since  $n \sim p$  and the drift terms in both Eqs. (4.10) and (4.12) are now important. It follows that neither Eq. (4.22) nor Eq. (4.25) is appropriate for obtaining  $\Delta n = \Delta n(x)$  or  $\Delta p = \Delta p(x)$ .

However, we can glean insight into the physics controlling the number densities in quasi-neutral regions of cells in this regime of behavior by undertaking some algebraic manipulation. By substituting Eq. (4.10) into Eq. (4.16) and by substituting Eq. (4.12) into Eq. (4.17), we obtain

$$\mu_n \xi \frac{dn}{dx} + \mu_n n \frac{d\xi}{dx} + D_n \frac{dn^2}{dx^2} - \mathcal{R}_n = - \int G_n^S(x, \lambda) d\lambda \quad (4.26)$$

and

$$-\mu_p \xi \frac{dp}{dx} - \mu_p p \frac{d\xi}{dx} + D_p \frac{dp^2}{dx^2} - \mathcal{R}_p = - \int G_p^S(x, \lambda) d\lambda \quad (4.27)$$

which are the continuity equations which replace Eqs. (4.22) and (4.25), respectively. Poisson's equation [Eq. (4.15)] is now seen to be involved in

setting up the number-density distributions through the factors  $d\xi/dx$  and  $\xi$ .

If we multiply Eq. (4.26) by  $\mu_p p$  and Eq. (4.27) by  $\mu_n n$  and add, the result is

$$\begin{aligned} & (\mu_p \mu_n p - \mu_p \mu_n n) \xi \frac{dn}{dx} + (\mu_p D_n p + \mu_n D_p n) \frac{dn^2}{dx^2} - (\mu_p \mathcal{R}_n + \mu_n \mathcal{R}_p) \\ & = - \left[ \mu_p p \int G_n^S(x, \lambda) d\lambda + \mu_n n \int G_p^S(x, \lambda) d\lambda \right] \end{aligned} \quad (4.28)$$

which makes use of the fact that  $\Delta n \sim \Delta p$  for lifetime semiconductors in the cell regions under discussion, and that  $\xi_0 = 0$  has been assumed in these regions.

If the role played by localized states in the absorption of light is negligible, then  $G_n^S = G_p^S = G^S$ . With this stipulation and the constraint that carrier transport in localized states is negligible, it follows that  $\mathcal{R}_n = \mathcal{R}_p = \mathcal{R}$ , independent of the actual kinetics involved.<sup>\*</sup> For such a material Eq. (4.28) becomes

$$\mu^* \xi \frac{dn}{dx} + D^* \frac{dn^2}{dx^2} - \frac{n - n_0}{\tau} = - \int G^S(x, \lambda) d\lambda \quad (4.29)$$

Here  $n_0$  denotes the electron density in thermodynamic equilibrium,  $\mu^*$  is the ambipolar mobility defined by [33]

$$\mu^* = \mu_n \mu_n (p - n) / (\mu_p p + \mu_n n) \quad (4.30)$$

and  $D^*$  is the ambipolar diffusivity (or diffusion coefficient) defined by [33]

$$D^* = D_p D_n (p + n) / (D_p p + D_n n) \quad (4.31)$$

Equation (4.29) utilizes the fact the  $\mathcal{R}$  can be written as

$$\mathcal{R} = \Delta n / \tau \quad (4.32)$$

which is valid when  $\Delta n \simeq \Delta p$  as follows from the discussion in Section 2.6. Equation (4.32) differs from Eq. (4.21) in that  $\tau$  is no longer a constant in general [see Eqs. (2.13), (2.19) and (2.29)]. Since  $n \sim p$  in the situation under consideration,  $\tau$  is used in Eq. (4.32) without a subscript.

In  $p$ - and  $n$ -type quasi-neutral regions under high irradiance, we expect  $n/p \rightarrow 1$ . In intrinsic, or nearly intrinsic, quasi-neutral regions under even low illumination we expect  $n/p \rightarrow 1$ . Consequently, for the situations under consideration, we find that Eq. (4.29) becomes

$$\frac{dn^2}{dx^2} - \frac{n - n_0}{L^{*2}} = - \left( \frac{1}{D^*} \right) G^S(x, \lambda) d\lambda \quad (4.33)$$

\* In such a material in steady state, a net loss of electrons from the conduction band, for example, can only occur to the valence band, since the populations of any localized states are fixed and these localized states experience no influx of carriers due to transport or light.

where  $L^*$  is the ambipolar diffusion length [33]. We note that this same equation will result for the hole number density  $p$ .

Surprisingly, Eq. (4.33) states that the carrier distributions [ $n = n(x)$  or  $p = p(x)$ ] in the cell quasi-neutral regions are again shaped by diffusion, but now the mechanism is ambipolar diffusion.<sup>†</sup> If  $\tau$  were a constant in Eq. (4.33), the carriers would have the same distribution as would be predicted by Eq. (4.22) or (4.25). In general,  $\tau$  is not a constant in the regime of behavior under consideration. This has interesting ramifications; i.e., in the regime of behavior where Eq. (4.22) or (4.25) are appropriate, doubling the intensity of illumination will double the number density at a given point. However, in the regime of behavior described by Eq. (4.33), the dependence of the number density at a point on intensity of illumination may be sublinear, since  $\tau$  decreases with  $n$  and  $p$  for radiative [Eq. (2.13)] and Auger [Eq. (2.19)] recombination.

The solution to Eq. (4.33) can be used in Eq. (4.1) to compute, for example, the diffusion component of the electron current coming out of a *p*-type emitter such as those seen in Figs. 4.1 and 4.2. This would not be the total current density  $J_n$  in this case since the drift component would also be significant. We postpone further discussion of a complete analysis in this situation until Section 4.2.4.

(3) *Space-charge Limited Currents* Another limiting class of behavior built into the system of equations presented in Section 4.2.2.1 is space-charge limited transport. To discuss this phenomenon we consider the case where a homojunction solar cell is fabricated using a relaxation semiconductor (see Section 2.9).

In such a material the carrier lifetimes are much less than the dielectric relaxation time; consequently,  $n$  need not equal  $p$  anywhere in a cell structure under illumination. The implication is that strong electric fields can develop throughout a cell. In this regime of behavior neither Eq. (4.22), (4.25), nor (4.29) is applicable. If drift dominates over diffusion, the pertinent continuity equations for the regions where this occurs are

$$\mu_n \xi dn/dx + \mu_n n d\xi/dx - \mathcal{R}_n = - \int G_n^S(x, \lambda) d\lambda \quad (4.34)$$

and

$$-\mu_p \xi dp/dx - \mu_p p d\xi/dx - \mathcal{R}_p = - \int G_p^S(x, \lambda) d\lambda \quad (4.35)$$

<sup>†</sup> Ambipolar diffusion may be thought of as carriers diffusing in a coupled manner due to the presence of a self-generated electric field tying the hole and electron motion together.

which together with Poisson's equation, and the models for the  $\mathcal{R}_n$  and  $\mathcal{R}_p$ , must be solved to yield  $\Delta n = \Delta n(x)$ ,  $\Delta p = \Delta p(x)$ , and  $\xi = \xi(x)$ . The kinetics involved in  $\mathcal{R}_n$  and  $\mathcal{R}_p$  can become dependent on  $\xi$  in the presence of traps and a strong electric field. In fact, it is through  $\mathcal{R}_n$  and  $\mathcal{R}_p$  that the Poole-Frenkel and Poole effects discussed in Section 2.7 can enter into the system of equations presented in Section 4.2.2.1

### 4.2.3 Analysis of a Simple $p$ - $n$ Homojunction Structure

Having defined the mathematical system necessary for homojunction analysis, we can now consider determining the current-voltage characteristic of a cell. However, being aware of the broad range of physical phenomena that can be involved in solar cells, we shall begin cautiously and bring our analytical tools to bear on the simple  $n$ - $p$  homojunction structure seen in Fig. 4.7. This basic cell is assumed to be fabricated using a single-crystal lifetime semiconductor. The configuration contains no drift fields, and any selective-ohmic contacts which may be present will be handled with effective-carrier recombination speeds at  $x = -d$  and  $x = L + W$ . The level of illumination is assumed to be such that  $n \ll p$  in  $p$ -type regions and  $p \ll n$  in  $n$ -type regions.

For this one-dimensional structure the current density is a constant which may be evaluated at any point. We choose  $x = 0$ ; hence,

$$J = J_p(0) + J_n(0) \quad (4.36)$$

Under the assumed conditions,  $J_p(0)$  is a diffusion current given by

$$J_p(0) = -eD_p(dp/dx)_{x=0} \quad (4.37)$$

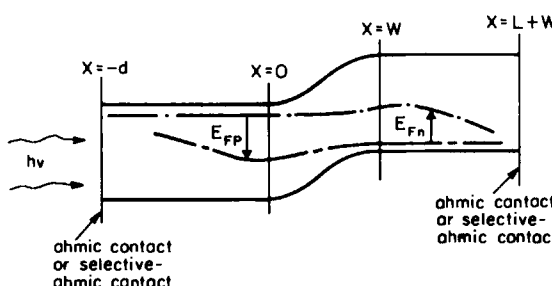


Fig. 4.7 An  $n$ - $p$  homojunction cell under illumination. The quasi-Fermi level variations shown are dictated by  $J_n = en\mu_n dE_{Fn}/dx$  and  $J_p = -ep\mu_p dE_{Fp}/dx$ . The minus sign appearing in this second expression arises here since  $E_{Fp}$  is now being measured as shown in the figure.

where  $p = p(x)$  satisfies

$$\frac{d^2p}{dx^2} - \frac{p - p_{n0}}{L^2} + \frac{\Phi_0 \alpha}{D_p} e^{-\alpha(x+d)} = 0 \quad (4.38)$$

which follows from Eq. (2.31) and the discussion in Section 4.2.2.2. We assume here illumination of a single wavelength. Superposition gives the response to a spectrum. Superposition is valid since Eq. (4.38) and the boundary conditions about to be developed constitute a linear mathematical system.

The function  $p = p(x)$  is subject to the boundary conditions

$$\left. \frac{dp}{dx} \right|_{x=-d} = \frac{S_p}{D_p} [p(-d) - p_{n0}] \quad (4.39)$$

at  $x = -d$  and

$$p(0) = p_{n0} e^{E_{Fp}(0)/kT} \quad (4.40)$$

at  $x = 0$ . The former follows from the discussion of ohmic contact modeling found in Section 3.6.2 and the latter from the definition of the hole quasi-Fermi level. Here  $E_{Fp}$  is measured down from its thermodynamic equilibrium position in the gap of the top layer as seen in Fig. 4.7. The mathematics expressed in Eqs. (4.38)–(4.40) model photogeneration in the top layer and the effects of processes 1–3 of Fig. 4.6a.

We can relate  $J_n(0)$  of Eq. (4.36) to  $J_n(W)$ . This is advantageous since we can assume a priori that  $J_n(W)$  is a diffusion current which is consistent with the treatment of  $J_p(0)$ . The relation between  $J_n(0)$  and  $J_n(W)$  is simply

$$J_n(0) = J_n(W) + e\Phi_0 e^{-\alpha d} (1 - e^{-\alpha W}) - e \int_0^W \mathcal{R} dx \quad (4.41)$$

neglecting effects of any localized states on light generation and on recombination (i.e.,  $\mathcal{R}_n = \mathcal{R}_p = \mathcal{R}$ ). The term  $J_n(W)$  is given by

$$J_n(W) = eD_n \left. dn/dx \right|_{x=W} \quad (4.42)$$

The term  $e\Phi_0 e^{-\alpha d} (1 - e^{-\alpha W})$  represents the production of photocarriers in the space-charge region, whereas the term  $\int_0^W \mathcal{R} dx$  models net recombination in the space-charge region (process 4 of Fig. 4.6a).

Equation (4.42) necessitates determining  $n = n(x)$  for  $L + W \geq x \geq W$ . With the assumption that electron transport in the base is dominated by diffusion, the needed  $n = n(x)$  satisfies

$$\frac{d^2n}{dx^2} - \frac{n - n_{p0}}{L_n^2} + \frac{\Phi_0 \alpha}{D_n} e^{-\alpha(x+d)} = 0 \quad (4.43)$$

with  $n(x)$  subject to

$$\left. \frac{dn}{dx} \right|_{x=L+W} = - \frac{S_N}{D_N} [n(L + W) - n_{p0}] \quad (4.44)$$

and

$$n(W) = n_{p0} e^{E_{Fn}(W)/kT} \quad (4.45)$$

We note that Eqs. (4.43)–(4.45) model photogeneration in the base layer and loss processes corresponding to 5–7 of Fig. 4.6a.

Combining Eqs. (4.36), (4.37), (4.41), and (4.42) gives

$$J = -eD_p \left. \frac{dp}{dx} \right|_{x=0} + eD_n \left. \frac{dn}{dx} \right|_{x=W} + e\Phi_0 e^{-\alpha d} (1 - e^{-\alpha W}) - e \int_0^W \mathcal{R} dx \quad (4.46)$$

Using  $p = p(x)$ , as determined by Eqs. (4.38)–(4.40), and  $n = n(x)$ , as determined by Eqs. (4.43)–(4.45), to evaluate the derivatives in Eq. (4.46), we are well on the way to determining the function  $J = J(V)$  for this cell. What remains is to relate  $E_{Fp}(0)$  and  $E_{Fn}(W)$  to  $V$  and to relate the space-charge recombination component of Eq. (4.46) to  $V$ .

The first task presenting itself now is to relate  $E_{Fp}(0)$  and  $E_{Fn}(W)$  to the voltage  $V$  developed by the cell. To do this we assume the quasi-Fermi levels are flat across the barrier region although, according to Eqs. (4.11) and (4.13), they must have some slope as seen in Fig. 4.7. The assumption of flat quasi-Fermi levels across the interface is termed the quasi-equilibrium assumption. It has been extensively discussed in the literature [35–38] and we shall explore it in some depth in our treatment of heterojunctions in Section 5.2.3.1. With the quasi-equilibrium assumption the statements

$$n(W)/n(0) = e^{-(V_{bi} - V_j)/kT} \quad (4.47)$$

and

$$p(0)/p(W) = e^{-(V_{bi} - V_j)/kT} \quad (4.48)$$

follow from Fig. 4.7, where  $V_j$  is the change in the band-bending over the barrier region when the structure is biased by illumination or an external voltage. Since  $x = 0$  and  $x = W$  are the borders of the quasi-neutral regions of the lifetime semiconductor, we may write two additional conditions; viz.,

$$n(W) - n_{p0}(W) = p(W) - p_{p0}(W) \quad (4.49)$$

and

$$n(0) - n_{n0}(0) = p(0) - p_{n0}(0) \quad (4.50)$$

For the regime of behavior we are considering,  $p \ll n$  in quasi-neutral  $n$  regions and  $n \ll p$  in quasi-neutral  $p$  regions. This situation is frequently

termed low-level injection. For low-level injection the set of equations given by Eqs. (4.47)–(4.50) may be solved to yield

$$n(W) = n_{p0}(W)e^{V_j/kT} \quad (4.51)$$

and

$$p(0) = p_{n0}(0)e^{V_j/kT} \quad (4.52)$$

which allow us to note that

$$E_{Fn}(W) = V_j \quad (4.53a)$$

and

$$E_{Fp}(0) = V_j \quad (4.53b)$$

The voltage  $V_j$  may be replaced by the voltage  $V$  across the cell terminals if there is no additional voltage developed at selective-ohmic contacts and if series resistance losses can be neglected.

Having related  $E_{Fn}(W)$  and  $E_{Fp}(0)$  to  $V$ , it remains to evaluate the integral  $\int_0^W \mathcal{R} dx$  appearing in Eq. (4.46) and to relate it to the cell voltage  $V$ . Since  $0 \leq x \leq W$  is certainly not a quasi-neutral region, we are not justified in assuming  $\Delta n \simeq \Delta p$ ; hence, formulations which express  $\mathcal{R}$  in terms of a carrier lifetime such as Eqs. (4.21), (4.24), or (4.32) are not appropriate. We must use the general expressions for  $\mathcal{R}$  found in Section 2.6. Assuming that the net thermal generation recombination in the space-charge region is controlled by the S–R–H processes, we get a specific form for  $\mathcal{R}$  and can write

$$\int_0^W \mathcal{R} dx = \int_0^W \int_0^{E_v} \left( \frac{A_{1p}^L A_{1n}^L g_T(x, E_T) dE_T}{A_{1p}^L p + A_{1p}^L p_1 + A_{1n}^L n + A_{1n}^L n_1} \right) (np - n_i^2) dx \quad (4.54)$$

as follows from Eq. (2.28). Here  $g_T(x, E_T)$  is the density of gap states of energy  $E_T$  per volume per energy at some point  $x$  in the space-charge region; the energy  $E_T$  is being measured from the position of the valence band edge at this point  $x$ .

Since we are invoking the quasi-equilibrium assumption in the present analysis ( $E_{Fn}$  and  $E_{Fp}$  assumed flat across the space-charge region) and since we have established from Eqs. (4.53) that the quasi-Fermi levels in the space-charge region are split apart by the amount  $V_j$  for the illumination conditions being considered ( $n \gg p$  in the top layer and  $p \gg n$  in the base layer of Fig. 4.7), it follows that the  $np$  product in Eq. (4.54) is independent of position; viz.,

$$n(x)p(x) = N_c N_v e^{-E_v/kT} e^{(E_{Fn} - E_{Fp})/kT} = n_i^2 e^{V_j/kT} \quad (4.55)$$

With the aid of Eq. (4.55), Eq. (4.54) may be rewritten as

$$\int_0^W \mathcal{R} dx = n_i^2 \left[ \int_0^W \int_0^{E_g} \left\{ \frac{A_{1p}^L A_{1n}^L g_T(x, E_T) dE_T}{A_{1p}^L p + A_{1p}^L p_1 + A_{1n}^L n + A_{1n}^L n_1} \right\} dx \right] [e^{V_j/kT} - 1] \quad (4.56)$$

which for  $V_j > kT$  becomes

$$\int_0^W \mathcal{R} dx = n_i^2 \left[ \int_0^W \int_0^{E_g} \left\{ \frac{A_{1p}^L A_{1n}^L g_T(x, E_T) dE_T}{A_{1p}^L p + A_{1p}^L p_1 + A_{1n}^L n + A_{1n}^L n_1} \right\} dx \right] e^{V_j/kT} \quad (4.57)$$

Again we point out that  $V_j$  equals the cell voltage  $V$  unless there is additional voltage developed at selective-ohmic contacts or series resistance losses.

Examination of the quantity in the brackets in Eq. (4.57), which we term  $\gamma$ , shows that its only dependence on  $V_j$ , the voltage developed across the barrier region, occurs through the  $p$  and  $n$  terms seen in its denominator. This latter point is important since it means that

$$\gamma \equiv \int_0^W \int_0^{E_g} \left\{ \frac{A_{1p}^L A_{1n}^L g_T(x, E_T) dE_T}{A_{1p}^L p + A_{1p}^L p_1 + A_{1n}^L n + A_{1n}^L n_1} \right\} dx \quad (4.58)$$

decreases as  $V_j$  increases; i.e., as the quasi-Fermi levels are forced farther apart in the space-charge regions of Fig. 4.7, the carrier populations  $n$  and  $p$  increase forcing  $\gamma$  to decrease.

Put succinctly,  $\int_0^W \mathcal{R} dx$  does not vary as  $\exp(V_j/kT)$  which a first glance at Eq. (4.57) might suggest but, rather,  $\int_0^W \mathcal{R} dx$  must have a weaker dependence on  $V_j$ . We have established this conclusion without any a priori assumptions regarding the energy or spatial distribution of the recombination centers. The fact that the dependence of  $\int_0^W \mathcal{R} dx$  on  $V_j$  is weaker than  $\exp(V_j/kT)$  is often acknowledged by writing

$$\int_0^W \mathcal{R} dx \propto [e^{V_j/n_R kT} - 1]$$

or

$$e \int_0^W \mathcal{R} dx = J_{RB} [e^{V_j/n_R kT} - 1] \quad (4.59)$$

The  $n$ -factor  $n_R$  must be greater than or equal to unity. It is not, in general, limited by an upper bound of 2, as is often asserted. The prefactor  $J_{RB}$  will have a relatively weak dependence on bias arising through  $W$  (see Section 3.4.2.1).

If (a) the spatial distribution of recombination centers is fairly uniform across the space-charge region, (b) the energy distribution of recombination

centers is fairly uniform across the gap (or is nonzero just in the middle of the gap), and (c) the recombination center parameters ( $A_{1n}^L$  and  $A_{1p}^L$ ) are equal and fairly independent of  $E_T$ , then  $\gamma$  can be approximated by [33, 34]

$$\gamma \simeq (A_1^L N_T / 2n_i) e^{-V_j / 2kT} \quad (4.60)$$

where  $N_T$  is the number of recombination centers per volume within  $\sim 2kT$  of the mid-gap. For this situation  $\int_0^W \mathcal{R} dx$  becomes ( $V_j > kT$ )

$$\int_0^W \mathcal{R} dx \simeq \frac{WA_1^L N_T n_i}{2} e^{V_j / 2kT} \quad (4.61)$$

which follows from Eqs. (4.57), (4.58), and (4.60). Comparison of Eq. (4.61) with (4.59) shows that  $n_R$  is a constant in this case and equal to 2 for  $V_j > kT$ . The comparison shows that  $J_{RB} = (eWA_1^L N_T n_i)/2$  in this case.

It is important to note from Eq. (4.56) that this overall approach to evaluating  $\int_0^W \mathcal{R} dx$ , based on using the assumption of quasi-equilibrium and Eqs. (4.53), neglects photocarrier loss in the space-charge region (process 4 of Fig. 4.6a) under short-circuit conditions (with  $V_j = V = 0$ ). Clearly there is a loss of photogenerated carriers through process 4 of Fig. 4.6a when  $V = 0$ , but expressions based on Eq. (4.56) do not account for it. Expressions based on Eq. (4.56) do account for recombination in the space-charge region (the process 4 we are trying to model) if  $V \neq 0$ .

Following the recipe already outlined for evaluating the terms of Eq. (4.46) gives our goal  $J = J(V)$ . The resulting expression may be written as

$$\begin{aligned} J = & e\Phi_0 \left\{ \left[ \frac{\beta_2^2}{\beta_2^2 - \beta_1^2} \right] \left[ \frac{(\beta_3 \beta_1 / \beta_2) + 1}{\beta_3 \sinh \beta_1 + \cosh \beta_1} \right] \right. \\ & - \left[ \frac{\beta_2^2 e^{-\beta_2}}{\beta_2^2 - \beta_1^2} \right] \left[ \left( \frac{\beta_3 \cosh \beta_1 + \sinh \beta_1}{\beta_3 \sinh \beta_1 + \cosh \beta_1} \right) \left( \frac{\beta_1}{\beta_2} \right) + 1 \right] \Big\}_{top} \\ & + e\Phi_0 \left\{ \left\{ 1 - e^{-\beta_4} \right\} e^{-\beta_2} \right\}_{barrier} \\ & + e\Phi_0 \left\{ \left[ \frac{\beta_6^2 e^{-\beta_2} e^{-\beta_4} e^{-\beta_6}}{\beta_6^2 - \beta_5^2} \right] \left[ \frac{(\beta_7 \beta_5 / \beta_6) - 1}{\beta_7 \sinh \beta_5 + \cosh \beta_5} \right] \right. \\ & + \left[ \frac{\beta_6^2 e^{-\beta_2} e^{-\beta_4}}{\beta_6^2 - \beta_5^2} \right] \left[ 1 - \left( \frac{\beta_5}{\beta_6} \right) \left( \frac{\beta_7 \cosh \beta_5 + \sinh \beta_5}{\beta_7 \sinh \beta_5 + \cosh \beta_5} \right) \right] \Big\}_{base} \\ & - \left\{ \frac{eD_p p_{no}}{L_p} (e^{V/kT} - 1) \right\} \left\{ \frac{\beta_3 \cosh \beta_1 + \sinh \beta_1}{\beta_3 \sinh \beta_1 + \cosh \beta_1} \right\}_{top} - J_{RB} \{ e^{V/n_R kT} - 1 \}_{barrier} \\ & - \left\{ \frac{eD_n n_{po}}{L_n} (e^{V/kT} - 1) \right\} \left\{ \frac{\beta_7 \cosh \beta_5 + \sinh \beta_5}{\beta_7 \sinh \beta_5 + \cosh \beta_5} \right\}_{base} \end{aligned} \quad (4.62)$$

where  $V_j = V$  has been assumed.

TABLE 4.1

Dimensionless  $\beta$  Numbers for  $n-p$  Homojunction Cell

$\beta$ Number	Definition	Physical significance
$\beta_1$	$d/L_p$	Ratio of top layer width to top layer minority-carrier diffusion length
$\beta_2$	$d\alpha$	Ratio of top layer width to absorption length
$\beta_3$	$L_p S_p / D_p$	Ratio of top-surface minority-carrier recombination velocity $S_p$ to top-layer minority-carrier diffusion velocity $D_p / L_p$
$\beta_4$	$W\alpha$	Ratio of space-charge region width to absorption length
$\beta_5$	$L/L_n$	Ratio of base layer width to base layer minority-carrier diffusion length
$\beta_6$	$L\alpha$	Ratio of base layer width to absorption length
$\beta_7$	$L_n S_n / D_n$	Ratio of back-surface minority-carrier recombination velocity $S_n$ to base-layer minority-carrier diffusion velocity $D_n / L_n$

Use is made in Eq. (4.62) of seven dimensionless numbers,  $\beta_1$ ,  $\beta_2$ , etc. which are convenient and which show the interplay and importance of specific combinations of cell characteristic lengths and material properties. These  $\beta$  numbers appearing in Eq. (4.62) are defined in Table 4.1. Each is seen to be either a ratio of lengths or a ratio of carrier speeds. For specific values of  $e\Phi_0$ ,  $eD_p p_{n0} / L_p$ , and  $eD_n n_{p0} / L_n$  (each of which has the units of a current density) performance of a  $p-n$  homojunction solar cell is seen to be optimized by varying the  $\beta$  numbers until the best efficiency is attained. We note from Eq. (4.62) that  $\beta_1 = \beta_2$  or  $\beta_5 = \beta_6$  represents a special case which necessitates reexamining the form of the solutions to Eqs. (4.38) and (4.43). These special cases have been considered by Wolf [39]. They represent no new physical phenomena; the mathematical complications they introduce are discussed in Ref. [39].

Equation (4.62) is seen to be of the form  $J = J_{ph} - J_{bk}(V)$ . The photocurrent  $J_{ph}$  is easily identified since it is zero if  $\Phi_0 = 0$ ;  $J_{ph}$  is seen essentially to be equal to  $J_{sc}$  in this case<sup>†</sup> and it has three components. These arise, as labeled, from the top layer, the space-charge layer, and the base layer. There are three components of the bucking current  $J_{bk}(V)$  in Eq. (4.62); each of these is independent of  $\Phi_0$  for this structure and they arise, as labeled, from the top layer, the space-charge layer, and the base layer. The bucking current developed in the top layer may be interpreted as a recombination-diffusion controlled current as may the bucking current developed in the base. The bucking-current component arising from the barrier region is a recombination current.

The effects of the top-layer loss processes 1–3 of Fig. 4.6a are present in the top layer contribution to  $J_{ph}$  in Eq. (4.62) through  $L_p$  (characterizing

<sup>†</sup>  $J_{ph}$  is not strictly independent of  $V$  even for the simple cell of Fig. 4.7, since  $\beta_4 = W\alpha$  and the space-charge width  $W$  varies with voltage developed.

hole diffusion and recombination) and  $S_p$ ; these loss processes 1–3 are seen to cause the top-layer bucking-current component. Similarly, the effects of the base-layer loss processes 5–7 of Fig. 4.6a are present in the base layer contribution to  $J_{ph}$  in Eq. (4.62) through  $L_n$  and  $S_n$ ; these loss processes 5–7 are seen to cause the base layer bucking-current component. Process 4 of Fig. 4.6a has been modeled by  $J_{RB}(\exp[V/n_R kT] - 1)$  in Eq. (4.62) which essentially means its presence has only been accounted for in the bucking current due to the approximation of Eq. (4.56).

In the short-circuit condition it is seen that  $J = J_{sc}$ . When the device is open circuited, the solar cell biases itself until the bucking current (which is coming from processes 1–7 of Fig. 4.6) balances  $J_{ph}$ . Since the mathematical system [Eqs. (4.38)–(4.40) and (4.43)–(4.45), plus Eqs. (4.53)–(4.59)] producing Eq. (4.62) is linearized, it is no surprise that the resulting  $J = J(V)$  is essentially of the form  $J = J_{sc} - J_{bk}(V)$ ; i.e., it is a superposition of the short-circuit current  $J_{sc}$  and the dark-diode current  $J_{bk}(V)$  developed by the structure viewed as a diode under a forward bias  $V$ .

Let us now use Eq. (4.62) to design an optimum homojunction configuration. By optimum we mean a cell that yields the highest efficiency  $\eta$  (where  $\eta = (J_{mp} V_{mp})/P_{in}$ ) for a specified value of the incoming power per area  $P_{in}$ . We begin with the premise that to optimize  $\eta$ , we want to enhance the photocurrent  $J_{ph}$  and reduce the bucking current  $J_{bk}$  as much as possible.

Considering the top layer, it follows from Eq. (4.62) that

$$J_{sc|top} = e\Phi_0 \left\{ \left[ \frac{\beta_2^2}{\beta_2^2 - \beta_1^2} \right] \left[ \frac{(\beta_3 \beta_1 / \beta_2) + 1}{\beta_3 \sinh \beta_1 + \cosh \beta_1} \right] - \left[ \frac{\beta_2^2 e^{-\beta_2}}{\beta_2^2 - \beta_1^2} \right] \left[ \left( \frac{\beta_3 \cosh \beta_1 + \sinh \beta_1}{\beta_3 \sinh \beta_1 + \cosh \beta_1} \right) \left( \frac{\beta_1}{\beta_2} \right) + 1 \right] \right\} \quad (4.63)$$

This photocurrent contribution is seen to approach its largest value for

$$\beta_1 \rightarrow 0 \quad (4.64)$$

$$\beta_3 \rightarrow 0 \quad (4.65)$$

in which case

$$J_{sc|top} \rightarrow e\Phi_0(1 - e^{-\beta_2}) \quad (4.66)$$

Equation (4.66) says all the photogenerated carriers created in such an optimized top layer are collected.

The corresponding top-layer contribution to  $J_{bk}$  is seen from Eq. (4.62) to be such that

$$J_{bk|top} \approx \left( \frac{eD_p p_{n0}}{L_p} \right) (\beta_1 + \beta_3) (e^{V/kT} - 1) \quad (4.67)$$

for  $\beta_1, \beta_3 \rightarrow 0$ .

From this analysis of the top layer, the following design criteria can be stated: The homojunction structure seen in Fig. 4.7 comes closer to achieving optimum performance, the closer

$$d/L_p \rightarrow 0 \quad (4.68)$$

and the closer

$$L_p S_p / D_p \rightarrow 0 \quad (4.69)$$

These quantify conclusions we reached in Section 4.2.1. Conditions (4.68) and (4.69) must be achieved together with  $(eD_p p_{n0}/L_p)$  being as small as possible, which suggests that the top layer should be heavily doped. These guidelines lead to the emitter region of Fig. 4.7 giving an enhanced spectral response<sup>†</sup> and a reduced bucking current. Of course, these conclusions are based on an analysis that assumes (a)  $p \ll n$  (low-level injection), (b) the absorber is a lifetime semiconductor, (c) flat quasi-Fermi levels across the barrier region (quasi-equilibrium), and (d) neglects the band gap narrowing and enhanced recombination that accompanies heavy doping.

For the base layer it follows from Eq. (4.62) that

$$\begin{aligned} J_{sc}|_{\text{base}} = e\Phi_0 & \left\{ \left[ \frac{\beta_6^2 e^{-\beta_2} e^{-\beta_4}}{\beta_6^2 - \beta_5^2} \right] \left[ 1 - \left( \frac{\beta_5}{\beta_6} \right) \left( \frac{\beta_7 \cosh \beta_5 \sinh \beta_5}{\beta_7 \sinh \beta_5 + \cosh \beta_5} \right) \right] \right. \\ & \left. + \left[ \frac{\beta_6^2 e^{-\beta_2} e^{-\beta_4} e^{-\beta_6}}{\beta_6^2 - \beta_5^2} \right] \left[ \frac{(\beta_7 \beta_5 / \beta_6) - 1}{\beta_7 \sinh \beta_5 + \cosh \beta_5} \right] \right\} \end{aligned} \quad (4.70)$$

This photocurrent contribution is seen to approach its largest value for

$$\beta_5 \rightarrow 0 \quad (4.71)$$

$$\beta_7 \rightarrow 0 \quad (4.72)$$

in which case

$$J_{sc}|_{\text{base}} \rightarrow e\Phi_0 (e^{-\beta_2} e^{-\beta_4}) (1 - e^{-\beta_6}) \quad (4.73)$$

<sup>†</sup> The spectral response SR is defined as being the short-circuit current collected for a given number of photons per second of energy  $h\nu$  impinging on (external SR) or entering into (internal SR) a solar cell structure. The quantity SR, which is also known as the collection efficiency at each wavelength or as the quantum efficiency, is obviously such that  $\text{SR} = \text{SR}(\lambda)$ . If  $\Phi_0(\lambda)$  is the photon flux density for photons of wavelength ( $\lambda$ ) just inside the top surface of a solar cell structure, then the internal spectral response may be written as

$$\text{SR} = J_{sc}(\lambda) / (e\Phi_0)$$

The overall collection efficiency  $Q$  of Eq. (3.67) may be expressed in terms of SR; viz.,

$$Q = \left[ \int_0^{\lambda(E_g)} \text{SR}(\lambda) \phi(\lambda) d\lambda \right] / \left[ \int_0^{\lambda(E_g)} \phi(\lambda) d\lambda \right]$$

where  $\Phi_0 = \phi(\lambda) \Delta\lambda$ .

Equation (4.73) represents the largest contribution to  $J_{sc}$  physically possible from the base<sup>†</sup>: All the light entering and being absorbed in the base is being converted into collected photocarriers giving SR = 1 if  $\beta_6 \rightarrow 0$ . The corresponding base-layer contribution to  $J_{bk}$  is seen from Eq. (4.62) to be such that

$$J_{bk}|_{\text{base}} \approx [eD_n n_{p0}/L_n](\beta_5 + \beta_7)(e^{V/kT} - 1) \quad (4.74)$$

for  $\beta_5, \beta_7 \rightarrow 0$ .

This analysis of the base region permits design criteria to be stated: A homojunction structure comes closer to optimum performance the closer

$$L/L_n \rightarrow 0 \quad (4.75)$$

$$L_n S_n / D_n \rightarrow 0 \quad (4.76)$$

and [from Eq. (4.73)] the closer

$$L\alpha \rightarrow \infty \quad (4.77)$$

Conditions (4.75)–(4.77) must be achieved together with  $(eD_n n_{p0}/L_n)$  being as small as possible. This suggests that it is also advantageous to heavily dope the base layer, but the base diffusion length must be large.

The specific requirement on the base diffusion length necessitates elaboration. For the top layer there is no restriction on  $\alpha d$ . In the optimum design, any light not absorbed in the top layer passes through the barrier to the base. The top layer thickness  $d$  is picked consistent with condition (4.68). There is no specific constraint on the top-layer diffusion length except that  $L_p S_p / D_p$  and  $eD_p p_{n0}/L_p$  be small. In the base, the situation is slightly different. To make full use of the light, it cannot be allowed to leave the base. Hence, Eqs. (4.77) shows that ideally  $L \gg 1/\alpha$ ; i.e.,  $\alpha$  imposes a constraint on the base width  $L$ . From Eqs. (4.75) and (4.77) it is seen that this imposes a constraint on  $L_n$ ; i.e.,  $L_n$  must be large compared to  $1/\alpha$ .

In summary, this analysis gives, as design criteria for the base for optimum performance of the  $p-n$  homojunction cell,<sup>‡</sup>

$$L_n > L > 1/\alpha \quad (4.78)$$

and

$$L_n S_n / D_n \rightarrow 0 \quad (4.79)$$

<sup>†</sup> From the point of view of Eq. (4.62), the barrier region presents no problems in designing an optimum contribution from the barrier  $J_{sc}$  component. Whatever the  $\beta_4$  selected, there is a 100% contribution of the photocarriers to  $J_{sc}$ . The barrier region should be designed, however, to minimize the bucking-recombination current of this region. Of course,  $\beta_4$  will actually be determined by the doping and doping profiles selected for the top and base. As we pointed out earlier, the 100% collection in the barrier region is due to the model used for the barrier-region recombination integral; i.e., Eq. (4.56).

<sup>‡</sup> Of course, achieving optical reflection at the back surface can relieve the constraint that  $L > 1/\alpha$ .

together with minimizing  $(eD_n n_{p0}/L_n)$ . Equation (4.78) quantitatively makes the point that was discussed so extensively in Section 3.2: Strong absorbers are very advantageous since they require less material and shorter diffusion lengths to be effective. Equations (4.78) and (4.79) also make the point that very strong absorbers permit shorter  $L_n$  values, enabling condition (4.79) to be more closely achieved. Equation (4.79) shows that low back-surface recombination speed is necessary in an optimum device. Physically, condition (4.79) is saying that the back contact must make it difficult for the photogenerated minority-carriers to leak out there and consequently, a selective-ohmic contact is needed.

The overall device design criteria developed here in our elementary analysis allows device performance to approach optimum. We must keep in mind, however, that these criteria have been developed for the ideal single-crystal lifetime semiconductor of Fig. 4.7 and that they are the result of an analysis that incorporates a number of assumptions.

Efficiency  $\eta$ , short-circuit current  $J_{sc}$ , and open-circuit voltage  $V_{oc}$  computed on the basis of Eq. (4.62) are presented in Figs. 4.8 and 4.9 for the case of AM1 illumination of a single-crystal  $n-p$  silicon cell of the form seen in Fig. 4.7. The evaluation neglects the barrier-region recombination term of  $J_{bk}$  in Eq. (4.62) and uses the idealization that  $S_n = S_p = 0$ . Series resistance is also neglected and  $V = V_f$  is used [40]. However, the experimentally observed dependence of the minority-carrier lifetime on doping density for S-R-H recombination and the control of the minority-carrier lifetime by Auger recombination for higher doping levels are included through the fit of Fig. 4.10. Any band-gap narrowing effects in Si are

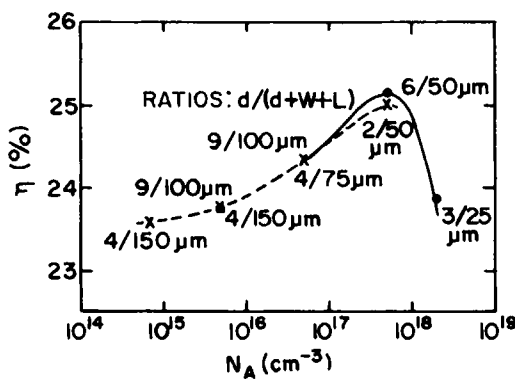


Fig. 4.8 Plot of the efficiencies obtained for idealized structures ( $S_n = S_p = 0$ ) for various base majority-carrier concentrations  $N_A$ . The dimensionless ratios of front-region donor to base-region acceptor concentrations  $N_D/N_A$  and of junction depth to cell thickness  $d/(d + W + L)$  are parameters.  $N_D/N_A = 1$  (—) and  $N_D/N_A = 10$  (---). (After Ref. [40]; © IEEE 1980, with permission.)

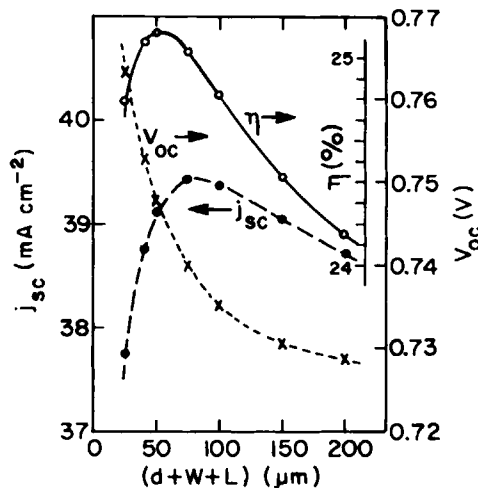


Fig. 4.9 Dependence of  $J_{sc}$ ,  $V_{oc}$ , and  $\eta$  on cell thickness for  $S_n = S_p = 0$ ,  $N_D = 5 \times 10^{17}$  on  $N_A = 5 \times 10^{17}$ ,  $d = 4 \mu\text{m}$  (After Ref. [40], with permission © IEEE 1980.)

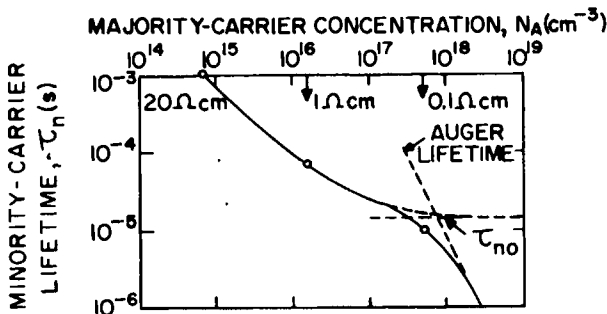


Fig. 4.10 The minority-carrier lifetime versus majority-carrier concentration relationship used for  $p$ -type silicon. This  $\tau_n = \tau_n(N_A)$  used to obtain plots of Figs. 4.8 and 4.9. For  $n$ -type silicon the Auger cutoff is shifted slightly toward lower concentrations. Otherwise,  $\tau_p$  was taken as identical to  $\tau_n$ . The three circles indicate data points from which the solid curve was extrapolated and interpolated to the Auger regime. (After Ref. [40], with permission © IEEE 1980.)

ignored, but the experimentally observed variation of carrier mobilities with doping density is also included [40]. Figures 4.8 and 4.9 are based on the assumption that a back-surface reflector with 100% internal reflection is present at  $x = W + L$  in Fig. 4.7, which introduces an additional generating term

$$(\Phi_0 \alpha / D_p) e^{-\alpha(d + W + L)} e^{-x(W + L - x)}$$

into Eq. (4.43) and a corresponding additional term into Eqs. (4.38) and (4.41) [40].

#### 4.2.4 Analysis of a $p-n$ Homojunction Structure under Concentration

When a solar cell structure is under concentration, the device is operating in a regime<sup>†</sup> where  $p$  and  $n$  can become of the same order of magnitude. As a consequence, ambipolar effects which are discussed in Section 4.2.2.2, can become important as can the fact that carrier lifetimes may be carrier-concentration dependent. Equations (4.38) and (4.43) are no longer valid for predicting the number densities as a function of position, and a further complication is that the boundary conditions given by Eqs. (4.53a) and (4.53b) are no longer valid. Since the mathematical system can become nonlinear, one must also question the use of superposition. All of this means that determining  $J = J(V)$  has become more difficult.

Considering the problem of proper boundary conditions, we note that, even if quasi-equilibrium is still valid, the expressions for the  $n(W)$  and  $p(0)$  of Fig. 4.7, which result from Eqs. (4.47)–(4.50), now must be written as

$$n(W) = (N_A B^2 + N_D B)/(1 - B^2) \quad (4.80)$$

and

$$p(0) = (N_D B^2 + N_A B)/(1 - B^2) \quad (4.81)$$

with  $B \equiv \exp[-(V_{bi} - V_j)/kT]$ . Consequently,  $E_{Fn}(W) \neq V_j$  and  $E_{Fp}(0) \neq V_j$  even with the flat quasi-Fermi levels of the quasi-equilibrium assumption. One may also question the applicability of the boundary conditions given by Eqs. (4.39) and (4.44) since these can be recognized to be linearized expressions analogous to Eq. (4.21). The correct, nonlinear boundary conditions for ohmic or selective-ohmic contacts would depend on the transport mechanisms at such interfaces; i.e.,  $S_{n,p}$  is no longer a constant.

Several approaches to the analysis of  $p-n$  homojunction cells under concentration have been undertaken [41, 42]. Some of these use a numerical analysis [41] of the set of governing equations of Section 4.2.2 while the others [42] use the ambipolar continuity equation [Eq. (4.33)] to determine the number densities, and then use an expression equivalent to Eq. (4.19) to compute  $V_{oc}$ . Both approaches have predicted  $V_{oc} \sim 0.77$  V and  $J_{sc} \sim 20$  A/cm<sup>2</sup> for single-crystal Si under 500 suns.

#### 4.2.5 Analysis of a $p-i-n$ Homojunction Structure

Whether under concentration or not, there can be regions of the  $p-i-n$  solar cell where  $p$  and  $n$  can be of the same order of magnitude. Consequently, ambipolar effects and carrier-concentration-dependent lifetimes may become important at any level of illumination. The applicability of boundary conditions of the form of Eqs. (4.39), (4.44), (4.53a), and

<sup>†</sup> Commonly called the high-level injection regime.

(4.53b) must also be questioned. Further, the quasi-equilibrium assumption is not valid across an *i* layer and the approach of Eq. (4.56) to  $\int_0^W \mathcal{R} dx$  cannot be justified.

To avoid these problems, numerical approaches to the full system of equations presented in Section 4.2.2.1 have been undertaken for *p-i-n* cells. These numerical treatments of single-crystal cells of the type seen in Fig. 4.2a use the complete, nonlinear expression for S-R-H recombination given by Eq. (2.28); i.e. [43],

$$\mathcal{R}^L = (np - n_i^2) / [\tau_p^*(n + n_i) + \tau_n^*(p + n_i)] \quad (4.82)$$

where  $\tau_n^* \equiv 1/A_{1n}^L N_T$  and  $\tau_p^* \equiv 1/A_{1p}^L N_T$ . This full expression, which assumes a single recombination level at mid-gap, correctly accounts for the fact that the S-R-H lifetime can be carrier-concentration dependent. A similar, nonlinearized expression assuming S-R-H recombination at the top and back boundaries of the cell has been used in some treatments for the boundary conditions needed at those planes. That is,  $J_n$  at the top surface and  $J_p$  at the back surface of Fig. 4.2a are specified by [43]

$$|J_{n,p}| = eS_0 \frac{np - n_i^2}{n + n_i + p + p_i} \quad (4.83)$$

where  $S_0$  is a surface recombination velocity. Equation (4.83) is obtained from Eq. (3.62).

Bulk Auger recombination which is in parallel with the bulk S-R-H path of Eq. (4.82) has been accounted for in numerical analyses of *p-i-n* single-crystal cells by approximating the expressions for processes *A* and *B* of Section 2.6.1.2 with the form [43]

$$\mathcal{R}^A = \gamma_n(n^2 p - n_0^2 p_0) + \gamma_p(p^2 n - p_0^2 n_0) \quad (4.84)$$

For example,  $\gamma_n = 2.8 \times 10^{-31}$  cm<sup>6</sup>/sec and  $\gamma_p = 0.99 \times 10^{-31}$  cm<sup>6</sup>/sec are the values used for these Auger coefficients for silicon [44].

Some numerical analyses have also accounted for hot-carrier effects and the dependence of mobility on carrier concentration in semiconductors. For example, in the analysis of *p-i-n* structures in silicon, the models [43]

$$\mu_p = 470 \left[ 1 + \left( \frac{(pn)^{1/2}}{4 \times 10^{17}} \right)^{0.6} \right]^{-1} \left[ 1 + \left( \frac{\xi}{1.8 \times 10^4} \right)^{1.21} \right]^{-1/1.21} \quad (4.85)$$

and

$$\mu_n = 1400 \left[ 1 + \left( \frac{(pn)^{1/2}}{6.5 \times 10^{16}} \right)^{0.6} \right]^{-1} \left[ 1 + \left( \frac{\xi}{7.24 \times 10^3} \right)^{1.3} \right]^{-1/1.3} \quad (4.86)$$

have been used where  $\mu_p$  and  $\mu_n$  are in cm<sup>2</sup>/V-sec.

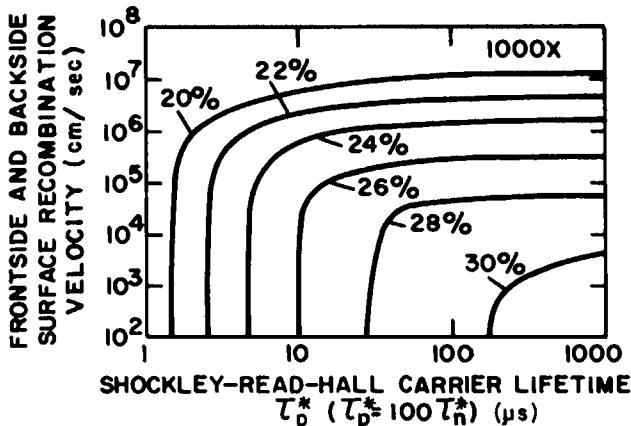


Fig. 4.11 Contour plot of  $p-i-n$  solar cell efficiency at  $T = 300^\circ\text{ K}$  in AM1 sunlight concentrated 1000 times. The assumption  $\tau_p = 100\tau_n$  is used. (After Ref. [43], with permission © IEEE 1980.)

Efficiency results from a numerical analysis for  $p-i-n$  structures of the form of Fig. 4.2a in Si are presented in Fig. 4.11. It is seen in Fig. 4.11 that conversion efficiency  $\eta \geq 30\%$  is theoretically possible with the structure of Fig. 4.2a using single-crystal silicon at 1000 suns. This particular numerical analysis incorporated the phenomena modeled by Eqs. (4.82)–(4.86). The importance of Auger recombination with increased concentration is indicated for this device by Fig. 4.12. The behavior depicted is due to the lifetime dependence on carrier concentration appearing in Eqs. (2.19a) and (2.19b).

#### 4.2.6 Comments on a General Analysis

It should be clear from the preceding analyses of homojunction solar cells that analytical solutions for device  $J-V$  characteristics under light can only be obtained when a number of assumptions can be made and justified. Numerical approaches allow for the relaxation of these assumptions; however, numerical approaches still require decisions on the models to be used to represent the boundary conditions needed at ohmic contacts, decisions on whether hot-electron effects are pertinent, and decisions on whether band-edge tailing and other heavy doping effects are important.

Inhomogeneities in material parameters, which may advertently or inadvertently arise, must also be considered in general cell analyses. For example, it has been pointed out that diffused  $p^+-n$  or  $n^+-p$  cell structures with narrow emitter regions can have strong, unintentional, built-in electric fields in the top layer, due to the shape of the diffusion profile, which must

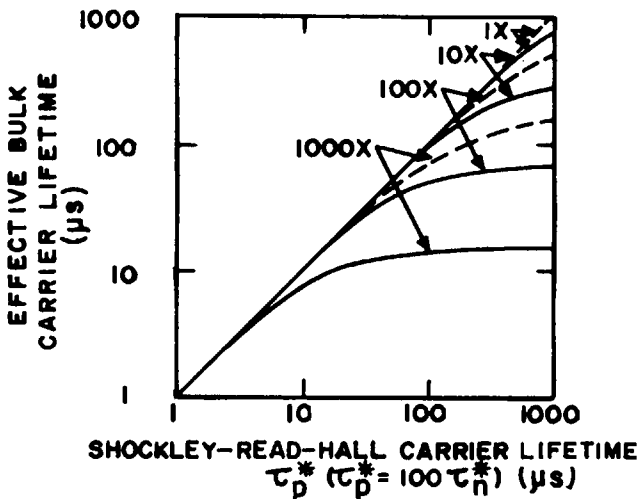


Fig. 4.12 Effective bulk carrier lifetime, defined by  $1/\tau_{\text{eff}} = (1/\tau_{\text{S-R-H}} + 1/\tau_A)$ , in  $p-i-n$  solar cell under open-circuit (—) and at maximum power point (---) for a frontside and backside surface recombination speed of 100 cm/sec. Degradation in the effective bulk lifetime is most severe at 1000 suns, where the bulk carrier concentration is highest and Auger recombination losses are the greatest. (After Ref. [43], with permission © IEEE 1980.)

be considered in cell analysis [28]. The built-in electrostatic field that can exist in a diffused  $n^+$  emitter region in thermodynamic equilibrium is obtained by setting  $J_n = 0$  in Eq. (2.61) and by assuming  $n \approx N_D$ ; viz.,

$$\xi_0 = \left[ -kT \frac{d}{dx} \ln N_D(x) + \frac{d\chi}{dx} + kT \frac{d}{dx} \ln N_c(x) \right] \quad (4.87)$$

This field  $\xi_0$  is set up to counter any electron effective drift fields and any doping gradient existing in thermodynamic equilibrium as the equation demonstrates. The  $d\chi/dx$  and  $d(\ln N_c)/dx$  terms are present, since heavy doping may affect the affinity and band-effective density of states.

All the preceding specific situations which we analyzed were for cells fabricated using single-crystal semiconductors. If polycrystalline absorbers are considered, the boundary conditions become more involved since transport at the grain-boundary interface must be modeled and, in general, the analysis becomes three-dimensional as seen in Fig. 4.13. If semiconductors with significant localized state densities in the gap throughout the material are considered (such as  $a\text{-Si}$ ), the possibility that part of the transport of carriers takes place in these states must be assessed. It may also be necessary to consider, in this case, the effects of the kinetics associated with the communication between localized states and the bands. Excitons and polarons may also play an important role in some materials.

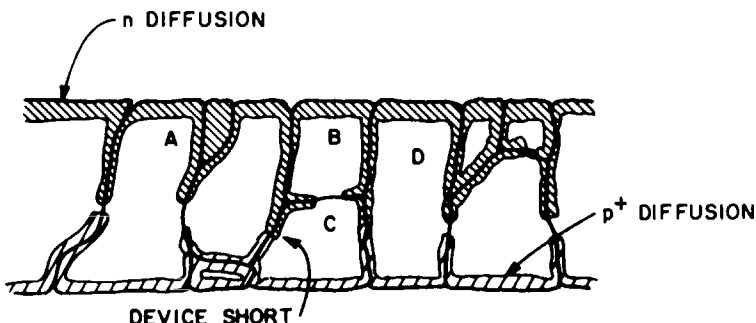


Fig. 4.13 Shown is  $p$ -type polycrystalline material. A back-ohmic contact has been formed by a  $p^+$  diffusion; a front barrier region by an  $n$  diffusion. As is seen, grain-boundary penetration of the doping may occur. Device shorting can occur. Materials and processing must be designed to avoid the detrimental effects. Device analysis is seen to be a complicated three-dimensional problem.

### 4.3 HOMOJUNCTION CELL CONFIGURATIONS AND PERFORMANCE

#### 4.3.1 Single-Crystal Devices

##### 4.3.1.1 Without Concentration

Single-crystal  $p-n$  homojunction solar cell structures have evolved into sophisticated, efficient devices. The more efficient devices use various combinations of selective-ohmic contacts, passivation, texturing, and internal reflection. Some typical  $p-n$  homojunction cell configurations are seen in Fig. 4.14.

The device seen in Fig. 4.14a is of the form  $p^+-n-n^+$  ( $n^+-p-p^+$ ). This particular design approaches the problem of the carrier sink provided by the front surface, by moving the check valve (the barrier) as close to the top surface as possible, which means that the top layer must be heavily doped to reduce lateral series resistance. As we have noted, heavy doping can introduce a whole class of new problems, and its use must be carefully scrutinized. In the particular configuration of Fig. 4.14a, an effort to reduce the recombination speed  $S_n$  at the top surface has been made by introducing an insulator-semiconductor interface between the grid fingers. As we have seen in Section 4.2.3, the approach of a very narrow, heavily doped emitter need not be adhered to, if the top surface can be passivated such that  $S_n \approx 0$  and if  $L_n \gtrsim d$ . In Fig. 4.14a the  $p^+-n-n^+$  ( $n^+-p-p^+$ ) structure has a selective-ohmic contact to the base layer formed by the HL junction. This BSF configuration reduces the effective minority-carrier surface recom-

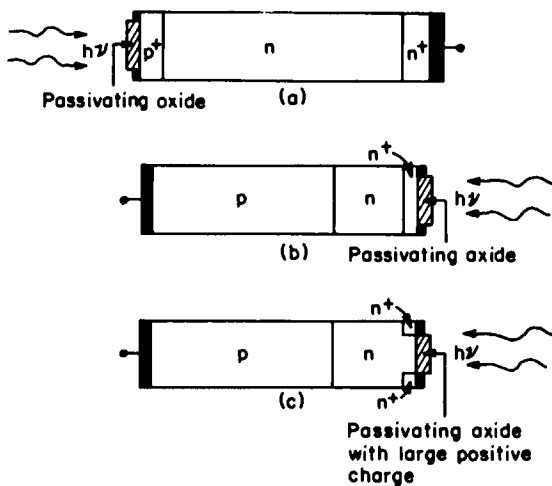


Fig. 4.14 Some  $p-n$  homojunction cell configurations. (a) A  $p^+-n-n^+$  BSF structure; (b) an  $n^+-n-p$  FSF structure; and (c) an  $n^+-n-p$  structure which uses an oxide to induce the FSF.

bination speed at the back of the base layer. Again, the size and doping level of the heavily doped layer used to form this selective-ohmic contact must be carefully scrutinized.

Devices of the BSF form have yielded efficiencies (single-crystal) approaching the 19–20% range for silicon [5], and efficiencies (single-crystal) approaching ~21% for GaAs under terrestrial conditions [11]. Generally it has been found that cells of this form have their  $V_{oc}$  values limited by recombination current in the top or in the HL junction regions, or limited by surface recombination at the front-surface ohmic contact, provided the base minority-carrier lifetime is sufficiently long [17].

Figure 4.14b represents a device class of the form  $n^+-n-p^+$  (or  $p^+-p-n^+$ ) where the  $n^+-n$  ( $p^+-p$ ) region is the top layer. As shown, a passivating layer may or may not be used between the grids on the top surface. The HL junction in the top layer produces a selective-ohmic contact at the front-surface ohmic contact. The advantageous effect of this emitter HL junction may be augmented by the passivation of the top surface and further augmented if a  $Q_{fix}$  of the proper sign is present in any passivating insulator layer. The presence of  $Q_{fix}$  of the proper sign would, of course, further enhance the formation of a reflecting field at the top surface between grids. HLE-BSF  $p-n$  cells combining elements of Figs. 4.14a and 4.14b have efficiencies under terrestrial conditions that are up to ~20% for silicon devices [5].

The device class represented in Fig. 4.14c has top layer HL junctions only under the grids and passivation between the grids. Structures such as this,

fabricated using silicon with a *p*-type base, have employed a passivating oxide thermally grown on the silicon ( $Q_{\text{fix}} > 0$ ) to produce passivation of the top surface and to induce a minority-carrier reflecting field in the *n*-type top layer. As seen in Fig. 4.14c the heavily doped  $n^+$  region is confined to lying just below the grids. With such small, heavily doped regions, a reflecting minority-carrier field, and a passivated front surface it is not surprising that the bucking current is suppressed in these oxide-charge-induced-high-low-emitter (OCI-HLE) cells and that they have given the highest  $V_{\text{oc}}$  values reported to date for Si *p-n* cells under terrestrial conditions ( $V_{\text{oc}} = 0.647$  V at 25°C) [45].

All of the efficiencies quoted so far in this section have been obtained using "electronic grade" semiconductors (material quality comparable to that used in the microelectronics industry). However, results for some single-crystal *p-n* homojunction devices fabricated with potentially low-cost silicon produced by metallurgical techniques are among the data seen in Table 4.2. These cells have used structures belonging to the classes seen in Fig. 4.14 ( $n^+ - p - p^+$  or  $p^+ - n - n^+$ ).

Some *p-n* homojunction single-crystal structures fabricated with materials other than Si and GaAs use elements of the design features seen in Fig. 4.14. Others have not evolved far enough to employ these and are simply *p-n* or *n-p* devices. Among the more efficient single-crystal structures which use semiconductors other than Si and GaAs are the InP cell ( $\eta = 6.7\%$  at 70 mW/cm<sup>2</sup>) [46] and the CdTe cell ( $\eta = 6\%$  for 77.2 mW/cm<sup>2</sup>) [47, 48].

Homojunction solar cells in configurations other than simple *p-n* structures and other than the more sophisticated structures seen in Fig. 4.14 have also been developed. Among these are the heterostructure and hete-

TABLE 4.2  
*Some Homojunction Cells Using Photovoltaic Materials Produced by Potentially Low-cost Metallurgical Techniques*

Material <sup>a</sup>	Technique	Cell configuration used for evaluation	AM1 (%) efficiency	Reference
Si(SC)	Edge-defined film-fed growth	<i>p-n</i> homojunction	12	49
Si(SC)	Dendritic web growth	<i>p-n</i> homojunction	14	50
Si(P)	Ribbon to ribbon	<i>p-n</i> homojunction	12	51
Si(P)	Ribbon against drop	<i>p-n</i> homojunction	6.9	52, 53
Si(P)	Dip coating	<i>p-n</i> homojunction	9.5	54
Si(P)	Casting <sup>b</sup>	<i>p-n</i> homojunction	16	55
Si(P)	Casting <sup>b</sup>	<i>p-n</i> homojunction	~12	56

<sup>a</sup> SC, essentially single crystal; P, polycrystalline.

<sup>b</sup> Obtained with sheets cut from bricks. The goal is to cast sheets [55].

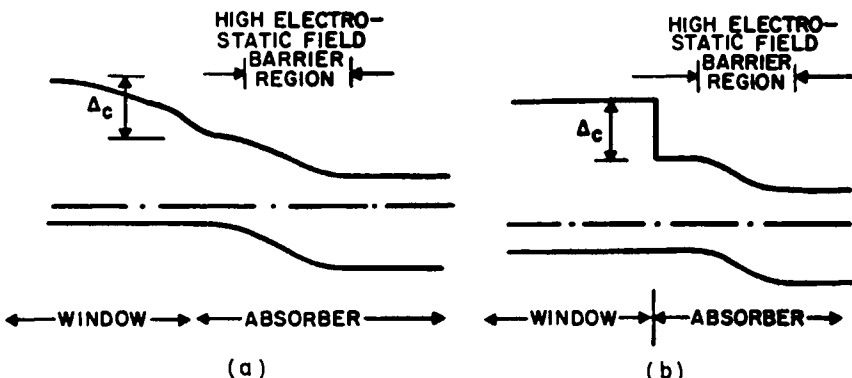


Figure 4.15 Homojunction solar cell structures using a graded gap region: (a) a gradual grading which is frequently termed a heterostructure, and (b) an abrupt grading which is frequently termed a heteroface cell. It is probably clearer to apply the terminology "heteroface" to both situations.

roface cells seen in Fig. 4.15, the front-surface field (FSF) interdigitated-back (IBC) cell (Fig. 4.16), and tandem-junction (TJ) cells (Fig. 4.16).

Heterostructure cells (Fig. 4.15a) use a graded-gap window layer adjacent to the top surface to reduce top-surface recombination and a  $p-n$  homojunction for the principal barrier region. Heteroface cells (Fig. 4.15b) differ only in that the transition to the window layer is abrupt. In both cases the window layer serves as a selective-ohmic contact. A heteroface cell ( $(p)\text{Ga}_x\text{Al}_{1-x}\text{As}/(p)\text{GaAs}/(n)\text{GaAs}$  has yielded  $\eta = 22\%$  under one sun conditions [12].

The FSF-IBC variation of the  $p-n$  homojunction solar cell has an electrostatic field built into the region labeled "surface" in Fig. 4.16. This is done either by establishing a HL junction in that region or by inducing a field by having the proper  $Q_{fix}$  in a passivating layer on the top surface.

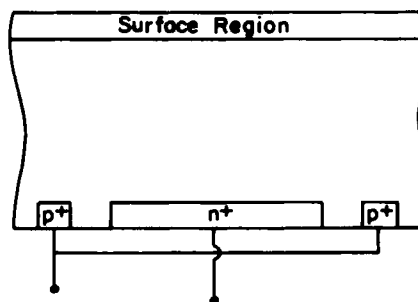


Fig. 4.16 A unified view of the front-surface field (FSF) interdigitated-back contact (IBC) cell and the tandem-junction (TJ) cell. The bulk region is  $p$ -type.

This front-surface field reflects photogenerated carriers away from the top surface. Contact to the region generating the photocarriers (the  $p$  region of Fig. 4.16) is made by interdigitated ohmic contacts at the back (the  $p^+$  regions of Fig. 4.16). The charge-separating depleted barrier region is provided by interdigitated  $n$ -type regions at the back (the  $n^+$  regions of Fig. 4.16). This structure avoids the loss of light incurred in conventional cells which have the collecting grids on the top surface. A potential advantage may exist for FSF-IBC cells in concentrated sunlight applications. This is because the possible lower series resistance inherent in this structure may result in a superior fill factor [17].

A tandem-junction (TJ) solar cell configuration may also be visualized with the aid of Fig. 4.16. In this case the region labeled "surface" in the figure is doped oppositely to the doping of the region generating photocarriers. For the device of Fig. 4.16 this means that this region labeled "surface" is  $n$ -type. The TJ cell can be operated in one of two modes [57]: The surface  $n$  region of Fig. 4.16 can be contacted allowing this barrier region to collect along with the back-surface barrier regions; alternatively, the surface  $n$  region can be allowed to float, and the surface junction will bias itself into forward bias under illumination to an extent necessary to have no net current ( $J_n + J_p$ ) crossing at the surface  $n$  region- $p$  region interface of Fig. 4.16. Unfortunately, this does not mean this surface layer fully protects minority carriers from the top surface since there is no assurance  $J_n = 0$  in this case. As with the other structures described by Fig. 4.16 the potential of using the TJ device without front grids is attractive. One sun conversion efficiencies for TJ cells (operated in the second mode) of  $\eta = 16.4\%$  at AM1 have been obtained for single-crystal Si [57].

#### 4.3.1.2 With Concentration

A number of single-crystal  $p-n$  homojunction photovoltaic converters have been examined for concentrator systems. Among them are (a) tandem-junction devices such as that seen in Fig. 4.16, (b) vertical multiple-junction devices such as that of Fig. 4.17, (c) beam-splitting photovoltaic converters such as that of Fig. 4.18a, and (d) cascade multijunction photovoltaic converters such as that of Fig. 4.18b.

The tandem-junction device of Fig. 4.16 is attractive because there is no grid shadowing necessary (if operated in the second mode discussed in Section 4.3.1.2), and because it offers the possibility of low series resistance, which is an important consideration in concentrator (high current density) applications [17]. Devices of this type have been fabricated and operated in concentrators. Concentrator TJ single-crystal Si converters of the form seen in Fig. 4.16, in which the cells are operated in the second mode with the surface junction floating, have produced  $\eta \approx 17\%$  at 20 suns [57].

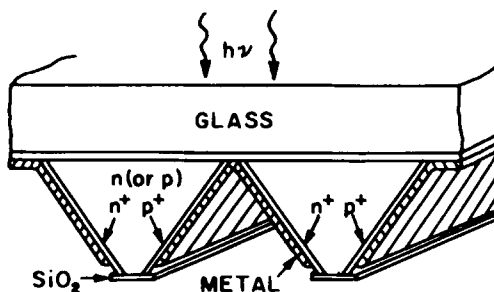


Fig. 4.17 A vertical multijunction (VMJ) type of solar cell structure.

Another  $p-n$  junction configuration which has the potential for inherently less severe series resistance problems, and which does not need contacting grids on the top surface is the vertical multijunction (VMJ) cell. This class of  $p-n$  homojunction solar cell has the charge-separating depleted barrier parallel to, or at some angle to, the incoming light. In the version seen in Fig. 4.17 the basic unit of the cell is defined by the  $p^+-n$  (or  $p$ )- $n^+$  structure which is repeated over and over. These basic units are optically in parallel

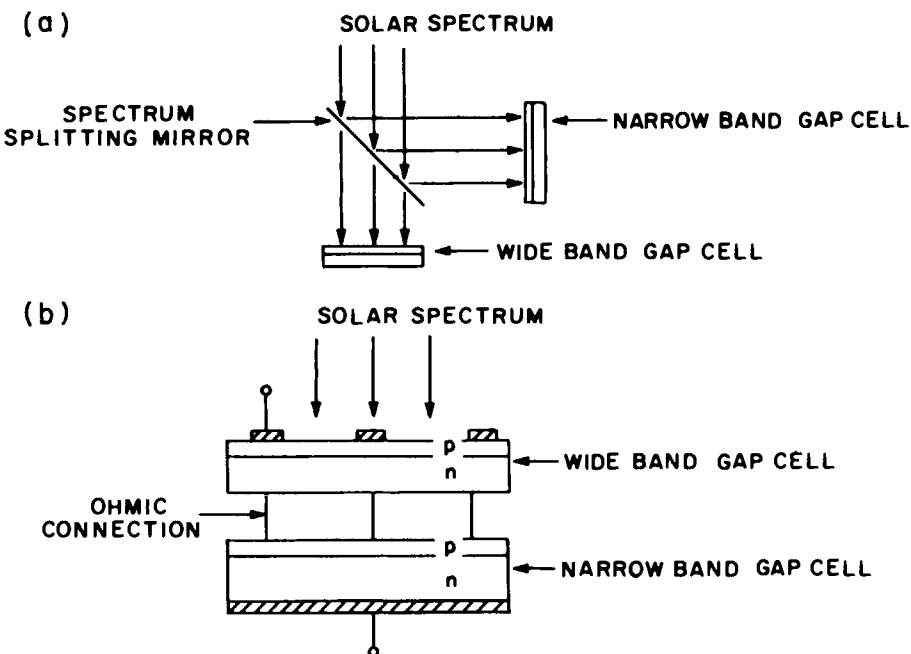


Fig. 4.18 Two approaches to high-efficiency photovoltaic concentrator systems: (a) spectrum splitting and (b) cascade cell.

but electrically in series. We note that each unit must be bound by ohmic contacts to allow the voltages developed under light to add. We also note that, since these devices have their barrier regions parallel to, or at least at an angle to, the incoming light, we expect that their long wavelength spectral response should be very good. This would give the VMJ device good radiation tolerance and, in fact, it was for this reason that the structure was originally proposed for space applications.

Numerical analyses of silicon single-crystal VMJ cells designed for concentrator applications has led to predictions of efficiencies as high as  $\eta = 24\%$  at 100 suns [58, 59]. Actual efficiencies of  $\eta \simeq 20\%$  (600 suns at 28°C) have been reported [5].

In concentrator systems the energy waste resulting from the loss of photons with  $h\nu < E_g$  and the energy waste resulting from the loss of some of the energy of those photons with  $h\nu > E_g$  are obviously amplified. Two ways of reducing this energy waste have been suggested [60]: One (spectrum splitting) is to divide, physically, the spectrum into two or more wavelength ranges and to match these spectra to different cells (Fig. 4.18a); the other (cascade cells) is to mount the cells in optical tandem so that each cell absorbs the light above its band gap and transmits the remaining light to the next cell (Fig. 4.18b).

Modeling of a two-junction spectrum splitting approach indicates that efficiencies above 35% near ambient temperatures are achievable from series-connected cells as well as from cells operated separately at their maximum-power points. The spectrum splitting approach has been explored experimentally and has proven effective. For example, a two-junction spectrum splitting system (Fig. 4.18a), using a single-crystal Si *p-n* homojunction for the narrow band-gap cell and a single crystal  $\text{Ga}_x\text{Al}_{1-x}$  heterostructure (see Fig. 4.15) for the wide band-gap cell, has yielded  $\eta = 28\%$  for a concentration of 150 suns [60].

The second approach to obtaining a better match between the solar spectrum and concentrator photovoltaic converters is seen in Fig. 4.18b. This is the cascade converter which has cells optically and electrically in series. The ohmic connection seen schematically in the two cell version of Fig. 4.18b, in reality, is an interface region which must optically, electrically, and thermally couple the cells. It follows from the general insight provided by Eq. (2.100) that this interfacial *n-p* region of the figure cannot be photoconductive. If it were, the photovoltage developed at the interfacial *n-p* region would oppose that developed in the *p-n* regions of the cells.

One approach to the required, interfacial ohmic connection regions has been to use a tunnel junction which ideally passes any current required with no change in the carrier populations. This approach, as seen in Fig. 4.19, is

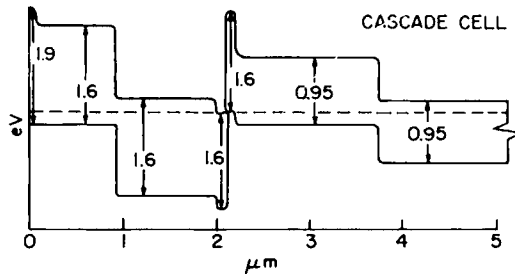


Fig. 4.19 Energy band diagram for cascade cell. A tunnel junction ohmic connection is seen at  $x = 2\mu\text{m}$ .

complicated since it necessitates high doping ( $\gtrsim 10^{18} \text{ cm}^{-3}$ ), narrow-layer thicknesses ( $\sim 0.1 \text{ nm}$ ), and low dopant diffusion coefficients (to maintain the integrity of the tunnel junction during subsequent device processing). A second type of interfacial ohmic connection region, avoiding the need for creating a tunnel junction, can be produced by separately fabricating optimized top and bottom cells and then subsequently bonding them together. The coupling material can be a transparent, thermal and electrical conductor; thermal or laser fusion can be used for the bonding.

A theoretical study of cascade cell structures has shown that the maximum ideal efficiencies that can be expected at 1000 suns, with the cells at 300°K, are 50% for two cells, 56% for three cells, and 72% for 36 cells [61]. This prediction was made using AM1.5 for the spectrum. It represents an upper bound on efficiency since it is based on assuming (a) all solar photons with  $h\nu > E_g$  generate electron–hole pairs, and (b) only loss mechanisms 1, 4, and 5 of Fig. 4.6a are present. Further, loss mechanisms 1, 4, and 5 are assumed to occur only through radiative recombination. We note that bulk interband radiative recombination will always be present in a cell since it represents the converse process to bulk, interband optical absorption as discussed in Section 2.6.1.1.

Numerical modeling, which makes a realistic assessment of all the loss mechanisms present schematically in Fig. 4.6, for a two junction, cascade converter, has shown that the top cell should have  $E_g \approx 1.6 \text{ eV}$  and the bottom cell should have  $E_g \approx 0.95 \text{ eV}$  as seen in Fig. 4.19 (the actual value of the gaps varies with concentration and operating temperature). This modeling has predicted that AM0, one sun efficiencies of  $\eta \gtrsim 30\%$  should be achievable for such a two-cell cascade structure [62]. Experimentally, the two-cell cascade structure seen in Fig. 4.19, using tunnel junctions for the ohmic connection, has achieved  $\eta \simeq 17\%$  with  $V_{oc} = 2.05 \text{ V}$  (AM1 at one sun).

TABLE 4.3  
*Some Homojunction Cells Using Thin Film Photovoltaic Materials*

Thin film material <sup>a</sup> under evaluation	Substrate	Growth or deposition technique	Cell configuration used for evaluation	Best AM1 efficiency reported (%)	Reference
Si(P)	Wacker poly silicon	Chemical transport	<i>p-n</i> homojunction	>10	63
Si(P)	Metallurgical silicon	Chemical transport	<i>p-n</i> homojunction	9.5–10.6	63, 64
CuInS <sub>2</sub> (P)	Metallized substrate	Vacuum evaporation	<i>p-n</i> homojunction	3.6	65
CuInSe <sub>2</sub> (P)	Metallized substrate	Vacuum evaporation	<i>p-n</i> homojunction	3	66

<sup>a</sup> P, polycrystalline.

### 4.3.2 Polycrystalline Devices

Polycrystalline *p-n* homojunction solar cell devices have been fabricated using a number of inorganic and organic polycrystalline semiconductors. Results for some of the more efficient cells are summarized in Tables 4.2 and 4.3. At this stage of the development of these devices, little or no attempt has been made yet to optimize their geometry and doping as discussed in Section 4.2 or to introduce minority-carrier blocking contacts at the top and back surfaces. As discussed in Chapter 3, in a fully optimized *p-n* homojunction solar cell fabricated with polycrystalline material, one must also optimize the grain-boundary properties and doping. Several of these *p-n* homojunction structures appear to be achieving some degree of this optimization [67]. To achieve the best possible performance on polycrystalline material, one must also consider how grain size affects efficiency. In this regard there are special problems that can arise with *p-n* homojunctions since there usually will be various degrees of junction penetration down the grain boundaries as seen in Fig. 4.13 [55]. This can be disadvantageous, for example, in the base of the shorting seen in Fig. 4.13. It can be advantageous, if controlled; i.e., the back *p*<sup>+</sup> fingers present in Fig. 4.13 could enhance collection.

### 4.3.3 Amorphous Devices

The most effective homojunction solar cells employing amorphous absorbers have been *p-i-n* devices fabricated with amorphous silicon [68–70]. These *p-i-n* amorphous silicon devices have the band diagrams seen in Fig.

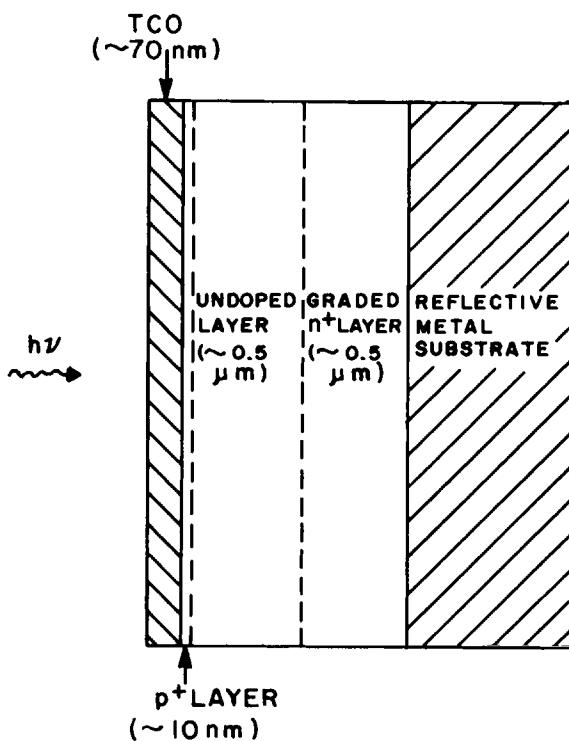


Fig. 4.20 Schematic of an amorphous silicon  $p$ - $i$ - $n$  cell on a metal substrate (TCO is a transparent-conductive oxide). (After Ref. [68], with permission.)

4.2 and a physical configuration typified by Fig. 4.20. A thin  $p$ - $i$ - $n$  configuration is used to collect photocarriers in amorphous silicon because the material is a very strong absorber and its diffusion lengths are in a range  $\lesssim 400\text{\AA}$  necessitating the reliance on drift [68]. Efficiencies of configurations such as the one seen in Fig. 4.20 have been  $\eta \geq 6\%$  under terrestrial illumination; however, it has been estimated that efficiencies of over 20% are possible in optimized  $a$ -Si devices [68].

An interesting approach to the use of amorphous materials has been to employ them in multilayered  $p$ - $i$ - $n$  absorbers such as that seen in Fig. 4.21 [70]. This has the advantage of increasing the region in the absorber which has a large drift electrostatic field for collection as may be noted from Figs. 4.21b and 4.21c. The approach is similar to the cascade photovoltaic converters discussed in Section 4.3.1.2, in that the cells are optically and electrically in series; however, it differs in that an attempt may or may not be made to vary the band gap of successive units. Since light traverses

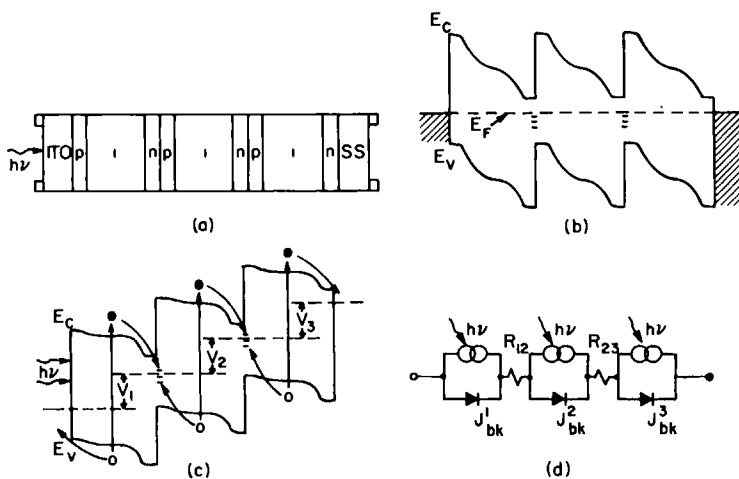


Fig. 4.21 Schematic illustration of (a) the structure, (b) the band diagram in the dark, (c) the band diagram under illumination, and (d) the equivalent circuit of a layered  $p$ - $i$ - $n$  multilayered absorber.

through the sequence of cells seen in the figure and since they are electrically in series, the successive units must be tailored to insure that they each give the same current, as must also be the case for cascade converters. This requirement is easily explained with the aid of Fig. 4.21d: any unit whose current is below the others would have to reduce its bucking current  $J_{bk}$ , and consequently voltage, to try to catch up. This unit may even have to reverse bias itself in its efforts to get in line with the other cells. Consequently, voltage is lost and, if the unit is reverse biased, it becomes a power sink.

Just as in the case of cascade photovoltaic converters, an ohmic connection is needed between the units of a multilayered  $p$ - $i$ - $n$  absorber. To ensure that the total  $V_{oc}$  produced by a multilayered cell is not reduced due to opposing photovoltages developed in these interfacing ohmic connections, they can not be photoconductive; or, put another way, they ideally should pass any current required without any change in carrier populations.

Two of the several approaches [70, 71] that have been successful for  $a$ -Si in producing interfacing regions with the correct properties have been (a) to fabricate  $n^+$ - $p^+$  tunnel junction interfaces which ideally achieve  $\Delta\sigma/\sigma \approx 0$ , and (b) to create regions of high recombination in the interfacing ohmic connections which force  $\Delta\sigma/\sigma \approx 0$  as seen in Fig. 4.21c.

Light  $J$ - $V$  characteristics (corresponding to Fig. 2.25) for two-layer multilayered  $a$ -Si  $p$ - $i$ - $n$  converters using tunnel junction ohmic connections are seen in Fig. 4.22. The difference in the shape of the  $J$ - $V$  characteristics

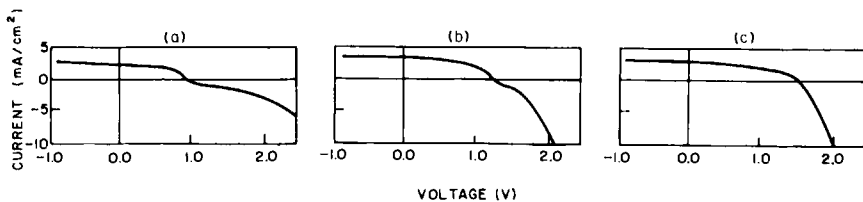


Fig. 4.22 Light  $J$ - $V$  characteristics (AM1) of two-layer multilayered a-Si photovoltaic converters. The different tunnel-junction structures used as the ohmic connections approach ideal behavior to varying degrees, giving the differences in the characteristics seen in the power quadrant. The tunnel junction of (a) is  $n^+ - p^+$ , that of (b) is  $n^+ - \text{Pt-SiO}_x - p^+$ , and that of (c) is  $n^+ - \text{Ti/Pt-SiO}_x - p^+$ . (After Ref. [71], with permission.)

in the power quadrant for the three converters can be attributed to the degree to which the tunnel junctions used approach ideal behavior. The three devices of this example gave (a)  $V_{\text{oc}} = 0.96$  V, (b)  $V_{\text{oc}} = 1.26$  V, and (c)  $V_{\text{oc}} = 1.57$  V [71]. Five-layer multilayered a-Si  $p-i-n$  converters using high recombination ohmic connections have achieved voltages as high as  $V_{\text{oc}} = 2.4$  V [70].

#### 4.4 NOTES FOR THE EXPERIMENTALIST

In summary, when the principal source of photovoltaic action in a solar energy converter is the barrier region of a  $p-n$  or  $p-i-n$  homojunction, the converter is termed a  $p-n$  or  $p-i-n$  homojunction solar cell. Additional photovoltaic action can also arise in such a cell from two sources: (a) modification, due to the presence of light, of the conductivity in regions of effective forces (varying material properties) or in regions of electrostatic forces outside the homojunction barrier, and (b) the Dember effect.

The band bending, or built-in potential energy  $V_{\text{bi}}$ , in the barrier region establishes an upper bound on the barrier, and consequently, principal contribution to  $V_{\text{oc}}$ . This band bending is caused by the differences in the  $n$  side and  $p$  side work functions and must always be

$$V_{\text{bi}} = \phi_p - \phi_n \quad (4.88)$$

The total band bending must be given by (4.88), but the shape of the barrier (i.e., the rate at which the bands bend as a function of position) will depend strongly on (a) the role of mobile carriers in developing charge, (b) the doping densities as a function of position, and (c) the presence of any other localized states in the gap of the semiconductor. These factors influence the origins and spatial dependence of the electrostatic field which, through Eq. (3.3), produces  $V_{\text{bi}}$ .

The built-in potential energy of a homojunction often is measurable using capacitance techniques. Deducing its value necessitates a priori assumptions concerning the origins and spatial dependence of the barrier-region electrostatic field. From such a set of assumptions,  $C$  (the capacitance per area) can be predicted as a function of bias  $V$  and frequency  $v$ . If experimentally obtained  $C = C(V, v)$  data agree with the predicted model, self-consistency is obtained and barrier parameters, such as  $V_{bi}$ , may be extracted. If the experimental  $C = C(V, v)$  does not agree with that predicted, the original set of assumptions is varied until self-consistency is obtained.

For example, (a) if the depletion assumption is made for the depleted space-charge region, (b) if the dopants are fully ionized and have a step function distribution (abrupt junction), and (c) if the presence of any other localized gap states can be neglected, then a model for  $C = C(V, v)$  is obtained which is of the form [72]

$$C = \frac{e\epsilon}{2} \left[ \left( \frac{N_A N_D}{N_A + N_D} \right) \left( \frac{1}{V_{bi} - V} \right) \right]^{1/2} \quad (4.89)$$

for reverse ( $V < 0$ ) bias. We note that this equation predicts that the capacitance in reverse bias will show no dispersion with frequency and it predicts that a plot of  $1/C^2$  versus bias is a straight line with intercept  $V_{bi}$ . If experimental  $C = C(V, v)$  data agree with this model, a self-consistent picture of the barrier region is obtained.

As another example, we note that if the same set of assumptions are made, but the doping is linearly graded from *n*-type to *p*-type,  $C$  is again independent of  $v$  for reverse bias; however, it is now given by [72]

$$C = \left[ \frac{ea\epsilon^2}{12} \left( \frac{1}{V_{bi} - V} \right) \right]^{1/3} \quad (4.90)$$

where  $a \equiv |d(N_D - N_A)/dx|$  characterizes the linear grading. If experimental  $C = C(V, v)$  data agree with this model, a self-consistent model of the barrier results. In this case a plot of  $1/C^3$  is a straight line with intercept  $V_{bi}$ .

In general, the dependence of the capacitance on voltage is related to the shape of the barrier region. Dependence of the capacitance on frequency is related to the role of mobile minority carriers and localized states in the gap (lying deeper than donor or acceptor levels) in developing the space-charge region. The function  $C = C(V, v)$  can show significant dispersion, for example, in amorphous materials where charge moving in and out of localized states can be important in developing the barrier charge [73].

It must be stressed that  $V_{bi}$  is only an upper limit to the barrier contribution to  $V_{oc}$ . The actual value of  $V_{oc}$  that is obtained depends on the kinetics taking place in the cell, under illumination. If we look at Fig. 4.6,

we see that  $V_{oc}$ —as well as  $J_{sc}$  and, in fact, the whole shape<sup>†</sup> of the light  $J$ – $V$  characteristic—is determined by the interplay between photogeneration, transport, and the loss processes 1–7 of the figure.

The current–voltage ( $J$ – $V$ ) characteristic of a  $p$ – $n$  homojunction solar cell such as that of Fig. 4.6 can always be written as

$$J = \int_{-d}^{W+L} G_L dx - \int_{-d}^{W+L} R dx - J_{sr}(-d) - J_{sr}(L + W) \quad (4.92)$$

which is an application of Eqs. (4.16)–(4.18) in integral form. The term  $\int_{-d}^{W+L} G_L dx$  accounts for the photogeneration of electron–hole pairs in the structure. The term  $\int_{-d}^{W+L} R dx$  accounts for bulk recombination through loss mechanisms labeled 1, 4, and 5 in the figure; the current density  $J_{sr}(-d)$  represents loss mechanisms 2 and 3 occurring at the top surface, whereas the current density  $J_{sr}(L + W)$  represents loss mechanisms 6 and 7 occurring at the back surface.

As we have seen, it is often convenient to break Eq. (4.92) into the form

$$J = J_{ph}(\Phi_0, V) - J_{bk}(\Phi_0, V) \quad (4.93)$$

where  $J_{ph}$  is the photocurrent and  $J_{bk}$  is the bucking current. Even though both  $J_{ph}$  and  $J_{bk}$  may, in general, depend on the photon flux density  $\Phi_0$  and bias  $V$ , a unique  $J_{ph}$  and  $J_{bk}$  can always be mathematically defined since  $J_{ph} \rightarrow 0$  as  $\Phi_0 \rightarrow 0$  and  $J_{bk} \rightarrow 0$  as  $V \rightarrow 0$ .

The quantity  $J_{ph}(\Phi_0, 0)$  is the short-circuit current density arising from photons of wavelength  $\lambda$ ; i.e., it is the photocurrent collected when  $V = 0$ . As a practical matter, the incoming flux density  $\Phi_0$  will have a band width  $\Delta\lambda$  in wavelength such that  $\Phi_0 = \phi(\lambda)\Delta\lambda$ . Hence, a spectral response can be assigned to the range  $\lambda$  to  $\lambda + \Delta\lambda$  by

$$SR(\lambda) = J_{ph}(\Phi_0, 0)/e\Phi_0 \quad (4.94)$$

It follows that the total short-circuit current density  $J_{sc}$  of a cell responding to a spectrum of incoming photons would be

$$J_{sc} = e \int_{\text{spectrum}} SR(\lambda)\phi(\lambda) d\lambda \quad (4.95)$$

In terms of the overall collection efficiency  $Q$  introduced in Chapter 3, this same  $J_{sc}$  may be written as

$$J_{sc} = eQ N_{ph}(E_g) \quad (4.96)$$

<sup>†</sup> A convenient measure of the shape of the  $J$ – $V$  characteristic under illumination is the fill factor FF, where

$$\text{FF} \equiv (V_{mp} J_{mp})/(V_{oc} J_{sc}) \quad ^*(4.91)$$

where we defined  $N_{ph}(E_g)$  as being the number of photons in a spectrum with energies  $> E_g$ .

The quantity  $Q$  and the more detailed quantity  $SR = SR(\lambda)$  are determined by transport in the cell and by loss processes 1–7 for Fig. 4.6a. Hence, they may be used to obtain information on the loss mechanisms. For example, information in the spatial variation of the losses in a cell can be extracted from  $SR = SR(\lambda)$  since different wavelengths penetrate different distances into a cell structure [74].

The quantity  $J_{bk}(0,V)$  is what we have termed the dark  $J$ – $V$  characteristic. This  $J_{bk}(0,V)$  is determined by transport in the cell, and loss processes 1–7 of Fig. 4.6a. Hence, it too, may be used to obtain information on the transport and the loss processes; i.e., the functional dependence of  $J_{bk}(0,V)$  on bias  $V$  and temperature  $T$  can be used to determine the role of S–R–H and Auger recombination, surface recombination, ambipolar diffusion, space-charge limited currents, etc. [75–77].

A straightforward technique to determine if  $J_{ph}$  of Eq. (4.93) is a function of voltage in a specific cell structure is to reverse bias the device under illumination to determine if the amount of collected photocurrent varies. Another technique to determine if  $J_{ph}$  depends on  $V$ , and to determine if  $J_{bk}$  depends on  $\Phi_0$ , is to plot  $J_{sc}$  versus  $V_{oc}$  by varying the level of illumination and to compare the curve obtained with the dark characteristic  $J = J_{bk}(0,V)$ . If they coincide, Eq. (4.93) can be rewritten as

$$J = J_{sc} - J_{bk}(V) \quad (4.97)$$

which is the functional form that resulted from the detailed analysis of Section 4.2.3. Superposition is valid when Eq. (4.97) is valid and the simple equivalent circuit seen for a cell in Fig. 4.21d is appropriate.

Up to this point we have generally neglected series and shunt resistance. Equation (2.103) shows that bulk series resistance will always affect cell characteristics to some degree. Added to this source of series resistance is resistance arising from contacts and gridding. A number of experimental techniques exist to assess the importance of series and shunt resistance in a cell structure and excellent discussions can be found in the literature [77, 78].

## REFERENCES

1. R. S. Ohl, U.S. Patent 2,402,662 (1941).
2. D. M. Chapin, C. S. Fuller, and G. L. Pearson, *J. Appl. Phys.* **25**, 676 (1954).
3. D. A. Jenny, J. J. Loferski, and P. Rappaport, *Phys. Rev.* **10**, 1208 (1956).
4. H. W. Brandhorst, *Proc. Int. Conf. Solid State Devices, 8th, Tokyo, 1976*. *Jpn. J. Appl. Phys.* **16**, 399 (1977).
5. H. J. Hovel, *Tech. Dig.-Int. Electron Devices Meet.*, p. 3. IEEE, New York, 1979.
6. J. Lindmayer and J. F. Allison, *Conf. Rec. IEEE Photovoltaic Spec. Conf. 9th* p. 83. IEEE, New York, 1972.

7. J. Mandelkorn and J. Lamneck, *Conf. Rec. IEEE Photovoltaic Spec. Conf.*, 9th, p. 66. IEEE, New York, 1972.
8. J. G. Hyenas, J. F. Allison, R. A. Arndt, and A. Muelenberg, *Proc. Int. Conf. Photovoltaic Power Generation 1974*, p. 487.
9. J. Scott-Monck, C. Gay, P. Stella, and F. Uno. High Efficiency Solar Panel (HESP), AFAPL-TR-77-36. U.S. Air Force (Jul. 1977).
10. J. Scott-Monck, *Conf. Rec. IEEE Photovoltaic Spec. Conf.*, 13th p. 421. IEEE, New York, 1978.
11. J. C. C. Fan, C. O. Bozler, and R. C. Chapman, *Appl. Phys. Lett.* **32**, 390 (1978).
12. J. Woodall and H. Hovel, *Appl. Phys. Lett.* **30**, 492 (1977).
13. L. L. Kazmerski and G. A. Sanborn, *J. Appl. Phys.* **48**, 3178 (1977).
14. L. L. Kazmerski, *Ternary Compounds 1977 Conf. Ser.-Inst. Phys.* **35**, 217 (1977).
15. W. E. Spear, P. G. LeComber, S. Kinmond, and M. H. Brodsky, *Appl. Phys. Lett.* **28**, 105 (1976).
16. D. E. Carlson, *Int. Conf. Amorphous Liq. Semicond.* 8th, Harvard Univ., Cambridge, Massachusetts, August 27-31, 1979.
17. F. A. Lindholm and J. G. Fossum, *Tech. Dig. Int. Electron Devices Meet.* p. 304. IEEE, New York, 1979.
18. A. G. Jordan and A. G. Milnes, *IRE Trans. Electron Devices* **ED-7**, 242 (1960).
19. B. Dale and F. P. Smith, *J. Appl. Phys.* **32**, 1377 (1961).
20. M. Wolf, *Proc. IEEE* **51**, 674 (1963).
21. S. J. Fonash, *CRC Crit. Rev. Solid State Mater. Sci.* **9**, 107-209 (1980).
22. E. O. Kane, *Phys. Rev.* **131**, 79 (1963).
23. F. A. Lindholm, A. Neugroschel, C. T. Sah, M. P. Godlewski, and H. W. Brandhorst, *Conf. Rec. IEEE Photovoltaic Spec. Conf.*, 12th p. 1. IEEE, New York, 1976.
24. M. A. Shbib, F. A. Lindholm, and F. Therez, *IEEE Trans. Electron Devices* **ED-26**, 959 (1979).
25. P. M. Dunbar and J. R. Hauser, *Solid-State Electron.* **20**, 697 (1977).
26. J. Lindmayer and J. F. Allison, *COMSAT Tech. Rev.* **3**, 1 (1973).
27. D. Redfield, *Appl. Phys. Lett.*, **33**, 531 (1978); **35**, 182 (1979).
28. D. Redfield, *IEEE Trans. Electron Devices* **ED-27**, 766 (1980).
29. J. Dziewior and W. Schmid, *Appl. Phys. Lett.* **31**, 346 (1977).
30. P. A. Iles and S. I. Soclof, *Conf. Rec. IEEE Photovoltaic Spec. Conf.*, 11th pp. 19-24. IEEE, New York, 1975.
31. H. Fischer and W. Pschunder, *Conf. Rec. IEEE Photovoltaic Spec. Conf.*, 11th pp. 25-31. IEEE, New York, 1975.
32. S. J. Fonash and S. Ashok, *Appl. Phys. Lett.* **35**, 535 (1979).
33. A. K. Jonscher, "Principles of Semiconductor Device Operation." Bell, London, 1960.
34. H. J. Hovel, in "Semiconductors and Semimetals" (R. K. Willardson and A. C. Beer, eds.), Vol. 11, Solar Cells. Academic Press, New York, 1976.
35. O. von Roos, *J. Appl. Phys.* **48**, 5389 (1977).
36. H. Guckel, D. C. Thomas, and A. Demirkol, *J. Appl. Phys.* **50**, 4477 (1979).
37. F. Berz, *J. Appl. Phys.* **50**, 4479 (1979).
38. O. von Roos, *J. Appl. Phys.* **50**, 4482 (1979).
39. M. Wolf, *Proc. IRE* **48**, 1246 (1960).
40. M. Wolf, *IEEE Trans. Electron Devices* **ED-27**, 751 (1980).
41. J. G. Fossum, E. L. Burgess, and F. A. Lindholm, *Solid-State Electron.* **21**, 729 (1978).
42. C-Y. Wu and W-Z. Shen, *Solid-State Electron.* **23**, 209 (1980).
43. T. I. Chappell, *IEEE Trans. Electron Devices* **ED-27**, 760 (1980).
44. J. Dziewior and W. Schmid, *Appl. Phys. Lett.* **31**, 346 (1977).
45. A. Neugroschel, F. A. Lindholm, S. C. Pao, and J. G. Fossum, *Appl. Phys. Lett.* **33**, 168 (1978).

46. V. V. Galavanov, R. M. Kundukhov, and D. N. Nasledov, *Sov. Phys.—Solid State (Engl. Trans.)* **8**, 2723 (1967).
47. G. P. Naumov and O. V. Nikolaeva, *Sov. Phys.—Solid State (Engl. Trans.)* **3**, 2718 (1961).
48. J. Mimila-Arroyo A. Bouazzi, and G. Cohen-Solal, *Rev. Phys. Appl.* **12**, 423 (1977).
49. Large Area Si Sheet By EFG, Proj. Rep. ERDA-JPL-954355-77/4. Mobile-Tyco Solar Corp. (Dec. 1977).
50. R. G. Seidensticker, R. H. Hopkins, J. P. McHugh, C. S. Duncan, P. D. Blais, J. R. Davis, Jr., and A. Rohatgi, *Conf. Rec. IEEE Photovoltaic Spec. Conf., 13th* p. 358. IEEE, New York, 1978.
51. A. Baghadadi, R. W. Gurtler, R. Legge, R. J. Ellis, and B. Sopori, *Conf. Rec. IEEE Photovoltaic Spec. Conf., 13th* p. 363. IEEE, New York, 1978.
52. C. Belouet, J. Hervo, R. Martres, Ngo Tech Phuoc, and M. Pertus, *Conf. Rec. IEEE Photovoltaic Spec. Conf., 13th* p. 131. IEEE, New York, 1978.
53. E. Fabre, Y. Baudet, and S. Makram Ebeid, *Conf. Rec. IEEE Photovoltaic Spec. Conf., 13th* p. 1101. IEEE, New York, 1978.
54. J. D. Zook, S. B. Schuldt, R. B. Maciolek, and J. D. Heaps, *Conf. Rec. IEEE Photovoltaic Spec. Conf., 13th* p. 472. IEEE, New York, 1978.
55. J. Lindmayer, *Conf. Rec. IEEE Photovoltaic Spec. Conf., 13th* p. 1096. IEEE, New York, 1978.
56. H. Fisher and W. Pschunder, *IEEE Trans. Electron Devices* **ED-24**, 438 (1977).
57. W. Matzen, S. Chiang, and B. Carbajal, *IEEE Trans. Electron Devices* **ED-26**, 1365 (1979).
58. H. J. Hovel, *IBM J. Res. Dev.* **22**, 112 (1978).
59. T. I. Chappell, *IEEE Trans. Electron Devices* **ED-26**, 1091 (1979).
60. See, e.g., N. S. Alvi, C. E. Backus, and G. W. Masden, *Conf. Rec. IEEE Photovoltaic Spec. Conf., 12th* p. 948. IEEE, New York, 1979; E. D. Jackson, *Conf. Use Solar Energy* **5**, 122. Univ. Arizona Press, Tucson, 1958; M. Wolf, *Proc. IRE* **48**, 1246 (1960); L. W. James, *Tech. Dig.-Int. Electron Devices Meet. 1975* p. 87. IEEE, New York, 1975; J. J. Loferski, *Conf. Rec. IEEE Photovoltaic Spec. Conf., 12th* p. 957. IEEE, New York, 1976.
61. C. H. Henry, *J. Appl. Phys.* **51**, 4494 (1980).
62. S. M. Bedair, S. B. Phatak, and J. R. Hauser, *IEEE Trans. Electron Devices* **ED-27**, 822 (1980).
63. P. H. Robinson, R. V. D'Aiello, D. Richman, and B. W. Faughnan, *Conf. Rec. IEEE Photovoltaic Spec. Conf., 13th* p. 1111. IEEE, New York, 1978.
64. T. L. Chu, S. S. Chu, E. D. Stokes, C. L. Lin, and R. Abderrassoul, *Conf. Rec. IEEE Photovoltaic Spec. Conf., 13th* p. 1106. IEEE, New York, 1978.
65. L. L. Kasmerski and G. A. Sanborn, *J. Appl. Phys.* **48**, 3178 (1977).
66. L. L. Kasmerski, *Ternary Compounds 1977, Conf. Ser.-Inst. Phys.* **35**, 217 (1977).
67. L. M. Fraas, *J. Appl. Phys.* **49**, 871 (1978).
68. D. E. Carlson, *Int. Conf. Amorphous Liq. Semicond.*, 8th. Harvard Univ. Cambridge, Massachusetts, Aug. 27-31, 1979.
69. H. Okamoto, Y. Nitta, T. Adachi, and Y. Hamakawa, *Surf. Sci.* **98**, 505 (1980).
70. Y. Hamakawa, H. Okamoto, and Y. Nitta, *Appl. Phys. Lett.* **35**, 187 (1979).
71. J. Hanak, *J. Non-Cryst. Solids* **35-36**, 755 (1980).
72. S. M. Sze, "Physics of Semiconductor Devices." Wiley (Interscience), New York, 1969.
73. J. Singh and M. H. Cohen, *J. Appl. Phys.* **51**, 413 (1980).
74. E. C. Douglas and R. V. D'Aiello, *IEEE Trans. Electron Devices* **ED-27**, 792 (1980).
75. G. F. J. Garlick and A. H. Kachare, *Appl. Phys. Lett.* **36**, 911 (1980).
76. J. G. Fossum, R. D. Nasby, and S. C. Pao, *IEEE Trans. Electron Devices* **ED-27**, 785 (1980).
77. R. N. Hall, *Solid-State Electron.* **24**, 595 (1981).
78. M. Wolf and H. Rauschenbach, *Adv. Energy Convers.* **3**, 455 (1963).

## CHAPTER 5

# Semiconductor-Semiconductor Heterojunction Cells

### 5.1 INTRODUCTION

Semiconductor-semiconductor heterojunction solar cells, together with their variant, semiconductor-insulator-semiconductor heterojunction solar cells, are the subject of this chapter. The basic features characterizing this class of solar cell are seen in Fig. 5.1. These features are the following: (1) two different semiconductors are used to form a metallurgical interface (which may be gradual or abrupt), and (2) the metallurgical interface occurs in the principal barrier region. We note that heteroface solar cells, both graded and abrupt (see Fig. 4.15), have been discussed in Chapter 4 since those devices have a *p-n* homojunction as the principal source of photovoltaic action.

Semiconductor-semiconductor and semiconductor-insulator-semiconductor solar cells can be of the form absorber-absorber (photogenerated, electron-hole pairs created in both semiconductors), or they can be of the form window-absorber (photogenerated, electron-hole pairs created in just one semiconductor). They are either isotype heterojunctions such as the example of Fig. 5.1a or they are anisotype heterojunctions such as the example of Fig. 5.1b.

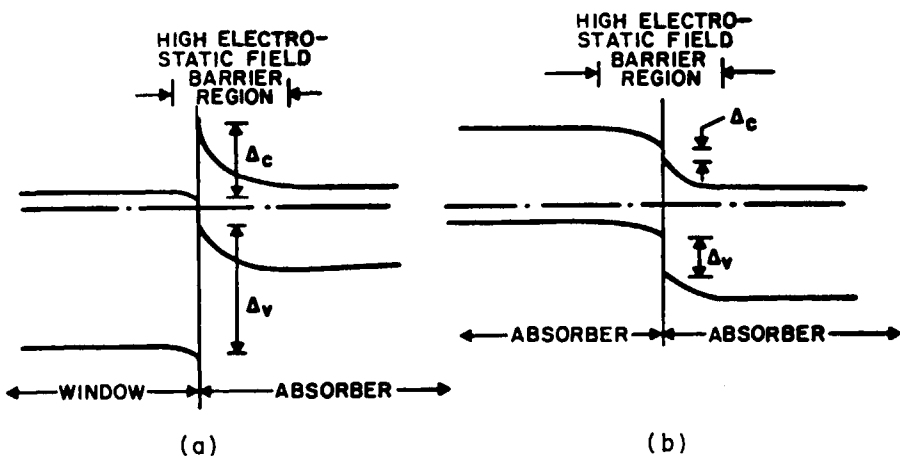


Fig. 5.1 Semiconductor-semiconductor heterojunction solar cell configurations: (a) an *n-n* isotype junction and (b) a *p-n* anisotype junction. Junctions can be of the form window-absorber or absorber-absorber.

Efforts to develop the heterojunction solar cell date from the work on the  $(p)\text{Cu}_2\text{S}/(n)\text{CdS}$  materials system reported by Reynolds in 1954 [1]. Reynolds found that certain types of copper contacts to single-crystal CdS gave open-circuit voltages of 0.45 V and short-circuit currents of  $15 \text{ mA/cm}^2$  in direct sunlight. Although it was first believed that a barrier at a Cu/CdS interface gave the photovoltaic action in this cell [2], it was later established that the principal barrier in efficient devices arises at a  $\text{Cu}_2\text{S}/\text{CdS}$  heterojunction [3]. In 1956, Carlson *et al.* [4] made the first polycrystalline  $\text{Cu}_2\text{S}/\text{CdS}$  solar cells which today have developed into thin-film devices that can achieve  $\eta \gtrsim 10\%$  [5] in terrestrial sunlight.

In the 1960s there was considerable interest in semiconductor-semiconductor heterojunctions for microelectronics applications which led to the consideration of semiconductor pairs other than  $\text{Cu}_2\text{S}/\text{CdS}$  for solar cell applications. During this period, heterojunctions involving III-V semiconductors were explored which resulted in devices such as an 8% efficient  $(p)\text{GaP}/(n)\text{GaAs}$  device [6]. Heterojunctions involving II-VI semiconductors other than CdS were also explored which led to devices such as the 6% efficient I-VI/II-VI structure composed of  $(p)\text{Cu}_{2-x}\text{Te}/(n)\text{CdTe}$  [7].

With the 1970s came rapid advances in heterojunction device technology producing solar cells such as the single-crystal III-V heterojunction solar cell  $(n)\text{AlAs}/(p)\text{GaAs}$  with  $\eta = 18.5\%$  (AM1.3) [8], the single-crystal II-VI/III-V structure  $(n)\text{CdS}/(p)\text{InP}$  with  $\eta = 13.5\%$  (AM2) [9], and the single-crystal II-VI/I-III-VI<sub>2</sub> cell  $(n)\text{CdS}/(p)\text{CuInSe}_2$  with  $\eta = 12\%$  ( $92 \text{ mW/cm}^2$ ) [10]. Today heterojunction solar cells involving inorganic and organic

materials in crystalline, polycrystalline, and amorphous forms are in various stages of research and development.

## 5.2 HETEROJUNCTION SOLAR CELL DEVICE PHYSICS

### 5.2.1 Qualitative Discussion

#### 5.2.1.1 General Features

As we noted, the hallmark of a semiconductor-semiconductor or semiconductor-insulator-semiconductor heterojunction solar cell is that two chemically different semiconductors are employed and their metallurgical junction, which may be gradual or abrupt, occurs in the main barrier region of the cell. The barrier region is usually an electrostatic field region but, in principle, it could be an effective force field region. In fact, the barrier region must always include an effective force field due to the variations in electron and hole affinities and due to the variations in band-effective densities of states inherent to this device class.

The use of two chemically different semiconductors, which is a characteristic feature of this type of solar cell, introduces a new set of problems not encountered in homojunctions such as chemical compatibility and stability, reproducibility of the chemical and physical interface, and, in the case of crystalline and polycrystalline materials, lattice compatibility at the metallurgical junction. On the basis of the list of new problems inherent to heterojunction cells one might question the interest in these devices. However, there is a strong interest which stems from two features: (a) heterojunctions allow the use of semiconductors which can only be doped either *n*-type or *p*-type and have attractive properties (and perhaps, attractive cost considerations); and (b) heterojunctions of the form window-absorber which can be used to form structures that shield carriers from top-surface or back-surface recombination sinks.

One might also expect that heterojunctions should display a third advantageous feature: it might appear that these cells should be capable of higher efficiencies than homojunction cells due to a better match to the solar spectrum. Put succinctly, there are now two band gaps to match to the solar spectrum. To explore this possibility we consider Fig. 5.2 which shows a homojunction cell (Fig. 5.2a) and a heterojunction cell (Fig. 5.2b) under illumination. We will assume that the base layer is the same semiconductor of energy gap  $E_g$  in both the homojunction and the heterojunction and that the Fermi level positions with respect to the band edges,  $V_n$  and  $V_p$ , are the same in both structures.

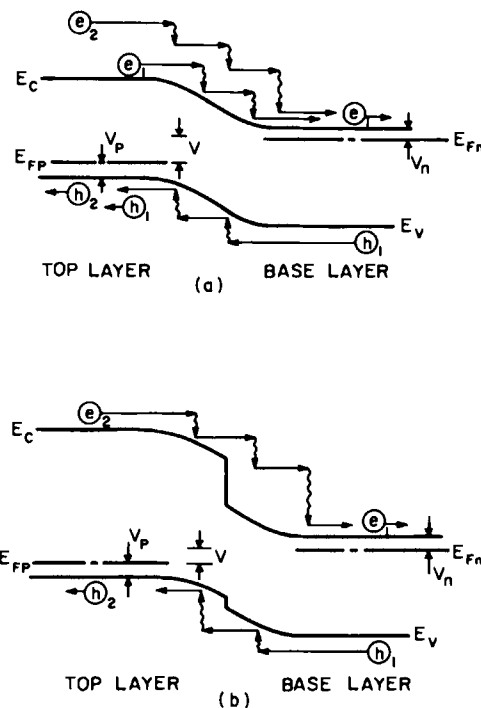


Fig. 5.2 Electron-hole pairs created by photons of energy  $h\nu_1$  and  $h\nu_2$  ( $h\nu_2 > h\nu_1$ ) in a (a) homojunction structure and in a (b) heterojunction structure. Pairs labeled with the subscript 1 are created by the absorption of  $h\nu_1$ ; pairs labeled with subscript 2 are created by the absorption of  $h\nu_2$ . Photons of energies  $h\nu_1$  and  $h\nu_2$  create electron-hole pairs throughout the homojunction cell; however, the higher energy photons ( $h\nu_2$ ) tend to be absorbed closer to the top surface since their absorption coefficient is higher (see Fig. 2.13). In the heterojunction the photons of lower energy are absorbed only in the base layer.

In the homojunction cell it is seen that photons of energy  $h\nu_1$ , where we have chosen  $h\nu_1 \approx E_g$ , create electron-hole pairs labeled with the subscript 1. If we follow an electron of one of these pairs that was created on the left side of the junction we see that this electron loses energy as it crosses the barrier until it fits into the electron distribution dictated by the electron temperature  $T_e$  and electrochemical potential  $E_{Fn}$  existing to the right of the barrier region. This lost energy is converted into heat and is unavailable for work in an external load. When the homojunction cell is developing some voltage  $V$ , as indicated by the split of the electrochemical potentials in Fig. 5.2a, the loss of energy available to do work is seen from the figure to be unavoidable. Figure 5.2a shows that electrons created by photons of energy

$h\nu_2$ , where  $h\nu_2 > E_g$ , waste even more energy. To reduce all this loss of available energy in the homojunction cell, it is seen from the figure that the electrochemical potentials (Fermi levels) on either side of the junction must be split farther apart (increased  $V$  and increased free energy) for a given value of the net current produced. Put another way, the bucking current at a given voltage must be reduced. Of course, we realized this in Chapter 4 when we explored many approaches for reducing the bucking current in a homojunction configuration.

Is there anything to be gained in the struggle to reduce this inherent loss of useful energy by going to heterojunction configurations; i.e., is there a third advantage to heterojunctions? This question can be answered with the help of Fig. 5.2b which shows a heterojunction whose top layer has a gap  $E_g \approx h\nu_2$  and whose base layer has the same gap as the homojunction of Fig. 5.2a; i.e.,  $E_g \approx h\nu_1$ . When the heterojunction is developing the same bias  $V$  as the homojunction, the inherent loss of available energy is seen to be exactly the same for the same  $V_p$ ,  $V_n$ , and  $E_g$ . There is no advantage to the heterojunction in this respect. Once again, to reduce the inherent loss of available energy, it is seen that the electrochemical potentials on either side of the junction must be split farther apart (increased  $V$ ) for a given value of the net current. Once again we realize that to reduce the inherent loss, the bucking current at a given voltage must be reduced; as we shall see, the lower bound to the bucking current for the heterojunction of Fig. 5.2b is the same as the lower bound for the homojunction of Fig. 5.2a.

Consequently, a single heterojunction cell does not offer any basic advantage over a single homojunction cell in dealing with the problem of wasted available energy (reduced free energy) as seen in Fig. 5.2. Two advantages remain: (a) heterojunctions do allow the use of semiconductors which have only one doping type, and (b) they do allow the use of window-absorber structures. The problem of wasting energy available in higher energy photons of the solar spectrum must be handled by the spectrum splitting, cascade, and tandem cell approaches discussed in Chapter 4.

We now examine in some detail what happens when light impinges on a heterojunction solar cell and creates itinerant electrons and holes as seen in Fig. 5.3. If we follow the photogenerated carriers, we see that they immediately become subject to the carrier loss mechanisms of (a) bulk recombination (loss mechanisms 1 and 5 of the figure), (b) recombination in the barrier region (mechanism 4), (c) recombination at the top contact (mechanisms 2 and 3), and (d) recombination at the back contact (mechanisms 6 and 7). For heterojunctions, there is the additional loss mechanism (process 8) arising from interface recombination through localized states situated at the metallurgical junction.

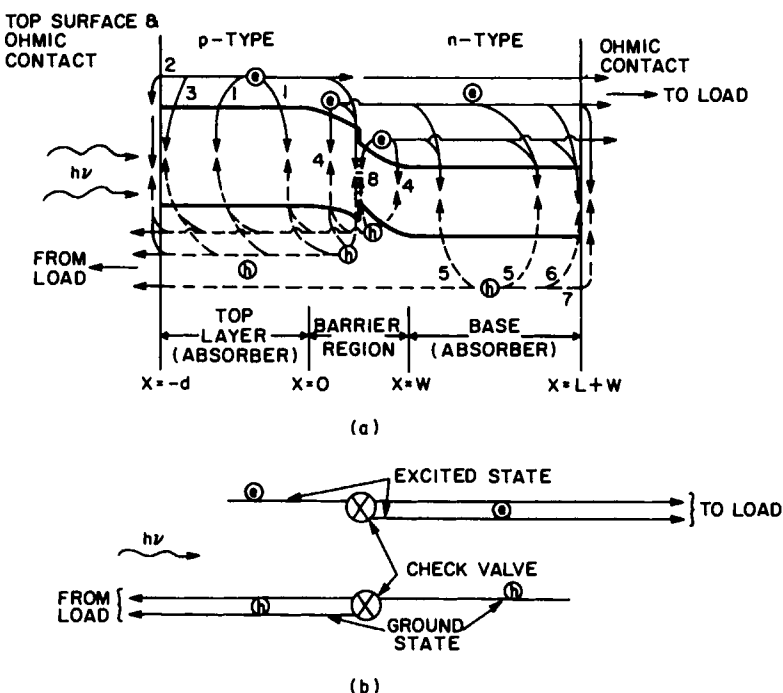


Fig. 5.3 (a) A *p* on *n* (*p-n*) heterojunction of the form absorber-absorber. (b) This device in terms of the generalized representation of Chapter 1. Paths (processes) 1-8 are all loss mechanisms: paths 1, 4, and 5 are bulk recombination; paths 2, 3, 6, and 7 are losses at the top-surface ohmic contact and base-layer ohmic contact; and path 8, the unique feature of heterojunctions, is the interface-states recombination path. The check valve is the high-field barrier region.

Expressed quantitatively, the net current density  $J$  crossing at  $x = L + W$  under illumination<sup>†</sup> may be written as

$$J = e \int_{-d}^{L+W} G_L(x) dx - e \int_{-d}^{L+W} \mathcal{R}(x) dx - J_{sr}(-d) - J_{sr}(L+W) - J_{ir} \quad (5.1)$$

which represents an application of Eqs. (4.16)-(4.18) in their integral form. In Eq. (5.1) the  $J_{sr}(-d)$  accounts for the electrons (and consequently holes) lost at the top surface through loss mechanisms 2 and 3,  $J_{sr}(L+W)$  accounts for the holes (and consequently electrons) lost at the back surface through mechanisms 6 and 7, and  $J_{ir}$  accounts for the interface recom-

<sup>†</sup> Which is the same as the net current density at any plane in the cell since a one-dimensional structure is assumed.

bination loss through mechanism 8. Loss mechanisms 1, 4, and 5 are accounted for by the integral  $\int \mathcal{R}(x) dx$ ;  $\int G_L(x) dx$  is the total optical generation in the structure.

In the example of Fig. 5.3 the high electrostatic field of the barrier region reduces the detrimental effects of the four loss terms of Eq. (5.1) and it gives a directed motion to the carriers. Specifically, the job of the high electric field of the barrier is (a) to act as a sink drawing photogenerated carriers away from loss mechanisms at the top and back surfaces, in the bulk of the top, and in the bulk of the base layer, and (b) to sweep photogenerated carriers past the loss mechanisms in the space-charge region and at the metallurgical junction. This check-valve action of the barrier region is seen in the generalized schematic of Fig. 5.3b.

Loss mechanisms 1–7 of Fig. 5.3, together with loss mechanism 8 which is unique to heterojunctions, determine the shape of the light  $J$ – $V$  characteristic of a solar cell. They determine the short-circuit current density  $J_{sc}$  and the open-circuit voltage  $V_{oc}$ . In fact,  $V_{oc}$  is just the voltage necessary to reduce the barrier electric field, and to drive the electron and hole quasi-Fermi levels apart sufficiently to ensure that all the photogenerated carriers  $\int G_L dx$  are internally shorted out through paths 1–8. The stronger are paths 1–8, the more the open-circuit voltage will be reduced. The open-circuit voltage developed under illumination by the device seen in Fig. 5.3 would be such that the right side of the structure would be negative with respect to the left side.

At this point we return to a remark made earlier: The all-important barrier region in a solar cell is not limited to being an electrostatic field region in a heterojunction structure. We recall from Eq. (2.62) that the total force  $F_e$  acting on a conduction-band electron in a region of varying properties is

$$F_e = -e \left[ \xi - \frac{d\chi}{dx} - kT_e \frac{d \ln N_c}{dx} \right] \quad (5.2a)$$

where  $\xi$  is the electric force field and  $\xi'_n = [-d\chi/dx - kT_e d \ln N_c / dx]$  is the effective force field acting on the electron. As shown in Chapter 2, Eq. (5.2a) may be rewritten in the form

$$F_e = -e \left[ \frac{dE_c}{dx} - kT_e \frac{d \ln N_c}{dx} \right] \quad (5.2b)$$

Comparison of Eqs. (5.2a) and (5.2b) allows one to note that a barrier in the conduction band of a heterojunction [a region where  $E_c = E_c(x)$ ] arises from some combination of electrostatic and effective forces.

Similarly, we recall from Eq. (2.66) that the total force  $F_h$  acting on a valence-band hole in a region of varying material properties is

$$F_h = e \left[ \xi - \frac{d}{dx}(\chi + E_g) + kT_h \frac{d \ln N_v}{dx} \right] \quad (5.3a)$$

where  $\xi$  is the electrostatic force field and

$$\xi'_p = \left[ -\frac{d}{dx}(\chi + E_g) + kT_h \frac{d \ln N_v}{dx} \right]$$

is the effective force field acting on the hole. Equation (5.3a) may also be cast in the form

$$F_h = e \left[ \frac{dE_v}{dx} + kT_h \frac{d \ln N_v}{dx} \right] \quad (5.3b)$$

as follows from Chapter 2. Comparison of Eqs. (5.3a) and (5.3b) shows that the barrier in the valence band of a heterojunction is similarly not limited to electrostatic origins.

Equations (5.2) and (5.3) establish that effective forces are always present in heterojunctions and that, in principle, there can be heterojunction structures where the field in the barrier region arises solely from the effective force terms of Eqs. (5.2) and (5.3). As an example, the reader is referred to Fig. 5.4 which depicts a pair of semiconductors which give rise to an effective force field but no electrostatic field at their junction. As seen in Fig. 5.4a, before contact, both materials 1 and 2 have the same electrochemical potential when measured with respect to a common reference energy (the vacuum level); i.e., both semiconductors have the same work function. Consequently, when a junction is formed between these materials as seen in Fig. 5.4b, there is no electrostatic field created at the interface—provided we idealize and neglect charging of any interface states present. There are, however, effective fields at the interface which are such that the effective force on electrons acts as a sink for electrons photogenerated in the top layer, and tends to sweep them to the right in the figure; the effective force on holes acts as a sink for holes photogenerated in the base layer and tends to sweep them to the left in the figure. The effective force fields of the barrier seen in Fig. 5.4b are serving as the check valve of Fig. 5.3b.

Generally, heterojunction solar cells are constructed with depleted, electrostatic field regions present and these serve as the principal source of photovoltaic action. Photovoltaic action arising from effective forces in the barrier region adds to (or subtracts from) the photovoltaic action arising from electrostatic fields. Conceptually, this means that the heterojunction

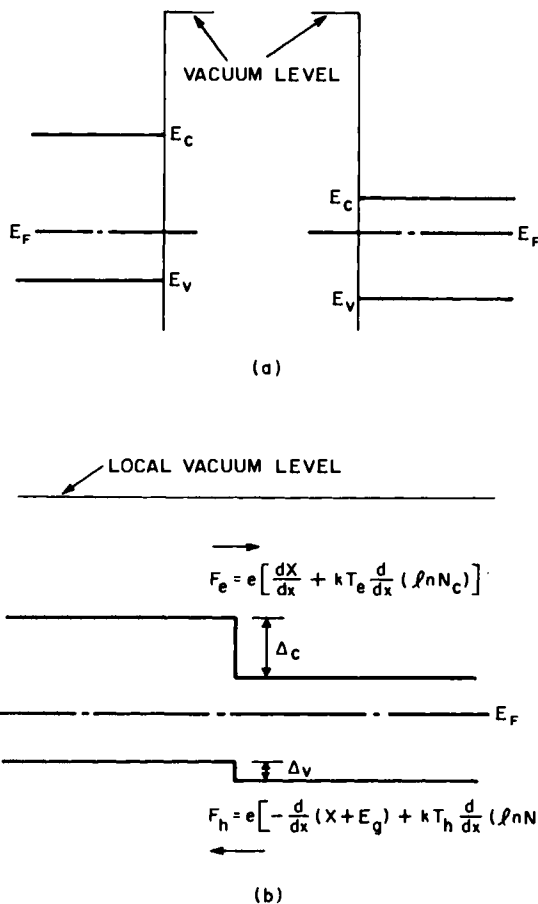


Fig. 5.4 (a) Heterojunction composed of two semiconductors which are such that (b) the barrier region has no electrostatic field present. The effective forces collect photogenerated minority carriers and give rise to photovoltaic action.

solar cell does offer an advantage not previously mentioned: the upper bound on the open-circuit voltage available in a heterojunction can be larger than that of a homojunction for the case when both structures have the same built-in potential. In principle, this could be used advantageously in concentrator systems.

#### 5.2.1.2 Design Considerations

All the design approaches discussed in Section 4.2.1.2 for homojunctions can be applied to minimize the effects of the loss terms  $\int_{-a}^{L+W} \mathcal{R}(x) dx$ ,

$J_{sr}(-d)$ , and  $J_{sr}(L + W)$  appearing in Eq. (5.1). For example, for a *p*-type top layer the integrand in  $\int_{-d}^{L+W} \mathcal{R}(x) dx$  is of the form<sup>†</sup>

$$\mathcal{R} = n_{p0}(e^{E_{Fn}/kT} - 1)/\tau_n \quad (5.4)$$

which follows from Section 2.6. As with homojunctions, it would appear from Eq. (5.4) that going to heavily doped layers would be advantageous since this would decrease  $n_{p0}$ . However, as with homojunctions, this approach is not without its limits; i.e., (a)  $\tau_n$  can become limited by Auger recombination, (b) defects introduced by heavy doping can reduce  $\tau_n$  if recombination is still in the S-R-H regime, (c) concentration effects can modulate  $\tau_n$ , and (d) band-edge tailing can occur (see Sections 2.6 and 4.2.1.2). The advantages of heterojunction structures can be brought to bear on the problem of bulk recombination: The top layer in our example can be made a window semiconductor ( $E_g \gtrsim 2.5$  eV) which appreciably reduces the strength of path 1 since

$$n_{p0} \propto e^{-E_g/kT} \quad (5.5)$$

The term  $J_{sr}(-d)$ , which accounts for carrier-loss paths 2 and 3 at the top surface in Fig. 5.3, can be reduced by using the approach of selective-ohmic contacts as discussed in Section 3.6 and Fig. 3.23, and as used so effectively in homojunction structures (see Chapter 4). However, a potential advantage of the heterojunction solar cell again shows up: By making the top layer a window semiconductor, the loss paths at the top surface can be reduced in strength without recourse to selective-ohmic contacts. This follows from Eq. (3.62), which allows us to write

$$J_{sr}(-d) = en_{p0}S_n(e^{E_{Fn}/kT} - 1) \quad (5.6)$$

where  $E_{Fn}$  is the position of the electron quasi-Fermi level in the top layer, measured from its thermodynamic equilibrium position in that layer, and  $n_{p0}$  obeys Eq. (5.5).

If the top layer is made a window semiconductor, then the base layer is the principal contributor to  $\int G_L(x) dx$  of Eq. (5.1) and the loss term  $J_{sr}(L + W)$ , which accounts for loss paths 6 and 7 of Fig. 5.3, can be handled by employing selective-ohmic contacts at the back of the base layer. Alternatively, the choice may be made to use the wide-gap semiconductor as the base layer.

In summary, the use of window-absorber heterojunction solar cell devices is attractive since it leads to reduced bulk recombination in the layer that is chosen to be the wide-gap material. Also, this layer can be heavily

<sup>†</sup> We note the  $E_{Fn}$  in Eq. (5.4) is being measured from the position of  $E_F$  in the *p*-type top layer in thermodynamic equilibrium.

doped to reduce series resistance without the deleterious lifetime effects encountered in heavily doped layers in homojunctions. When a heavily doped window layer is the top layer of the cell, one can use a simple, relatively widely spaced grid pattern for current collection at the top surface. The use of window-absorber heterojunction solar cell devices is also very attractive since it leads to reduced surface recombination for the window layer without the necessity of a selective-ohmic contact. These advantages of heterojunctions are only potentially available, however. A great deal of care must be exercised to ensure that the advantages gained by going to a heterojunction cell structure are not offset by losses incurred due to the existence of the new loss path  $J_{ir}$  present at the metallurgical interface, and by difficulties in forming a properly shaped, reproducible barrier at the junction.

The occurrence of interface states at the metallurgical junction through which the recombination current  $J_{ir}$  can flow and in which charge may be stored (modifying barrier shape) is seen from Fig. 5.5 to be a basic feature of heterojunctions which exists even if no defects are created by mechanisms such as cross diffusion. Generally speaking there is some lattice mismatch whenever two different crystalline or polycrystalline semiconductors are interfaced, and the manner in which the mismatch is accommodated

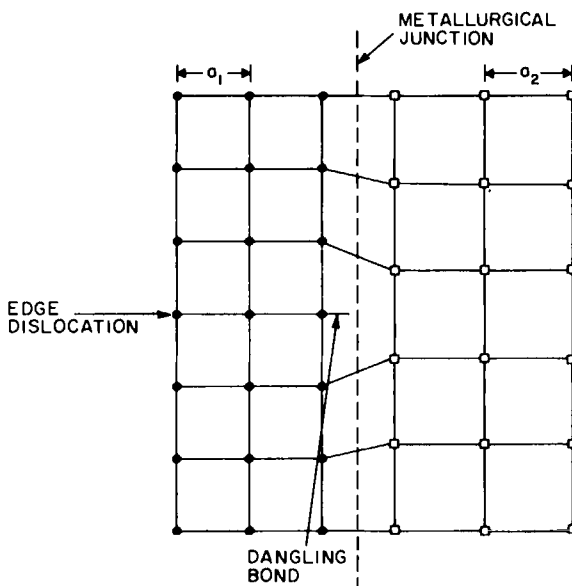


Fig. 5.5 Cross section perpendicular to the idealized junction plane of a heterojunction between two simple cubic crystals with lattice constants  $a_1$  and  $a_2$ .

establishes the interface strain field<sup>†</sup> and the concentration and nature of the metallurgical defects at the interface [11, 12]. Initially, as a crystalline or polycrystalline material is grown or deposited on a crystalline or polycrystalline substrate, the lattice mismatch is accommodated elastically until a critical thickness is reached, whereupon it becomes energetically favorable to accommodate the strain plastically and dislocations are generated at the interface as seen in Fig. 5.5 [13]. The ends of these dislocations are defined by the dangling bonds seen in the figure which give rise to the previously mentioned localized, interface states in the energy gap.

The question of the number of interface states per area  $N_i$  expected to be available to carry  $J_{ir}$  and expected to be available to store charge, has been addressed by several groups [14, 15]. Their results allow  $N_i$  due to dislocations to be estimated from [13-16]

$$N_i \approx \Delta a/a^3 \quad (5.7)$$

where  $\Delta a$  is the difference in the lattice constant in the plane of the junction and  $a$  is the average lattice constant in the plane of the junction. On the basis of Eq. (5.7) one can determine that a lattice mismatch of just 1% can produce  $10^{13}$  localized states per  $\text{cm}^2$  through which  $J_{ir}$  can flow and in which, in principle, charge may be stored leading to modifications of the heterojunction barrier. As we shall see in Section 5.2.3.2, a localized state density of  $10^{13} \text{ cm}^{-2}$  can hurt solar cell performance significantly. Equation (5.7), while illuminating due to its simplicity, is only an estimate based on assuming an abrupt metallurgical junction, complete plastic relaxation of the misfit strain, and the oversimplification of pure edge dislocations as seen in Fig. 5.5 [13].

One might be tempted to turn to amorphous materials as a means of avoiding these interface states arising from lattice mismatch. However, amorphous materials, rather than having only localized gap states at the interface, have localized gap states throughout the structure. If there is an advantage to this approach, it has to lie in the possibility that the bulk localized states of the amorphous material may be more easily modified and passivated than interface states, or in the possibility that the amorphous material can offer some improved property (such as the high absorption coefficient of  $a\text{-Si}$ ) plus reduced cost.

On the basis of this discussion so far, it would appear safe to say that heterojunction solar cells using crystalline and polycrystalline semiconductors must be designed with lattice mismatch which is not more than a

<sup>†</sup> The picture is further complicated by the fact that a difference in thermal expansion often exists between the materials that form a heterojunction. Even if two semiconductors have a good lattice match at room temperature, there may be mismatch at the temperature at which the junction is fabricated. The converse is also possible.

TABLE 5.1  
*Lattice Mismatch and Solar Conversion Efficiency for Several Heterojunctions*

Junction <sup>a</sup>	Lattice mismatch (%)	Efficiency (%) <sup>b</sup>	Reference
(p)Cu <sub>2</sub> S/(n)CdS	4.6	9.15	5
(n)CdS/(p)InP	0.3	14.4	9, 17
(n)CdS/(p)CdTe	9.7	8.0	18
(n)ZnO/(p)CdTe	29.1	~3.0	19

<sup>a</sup> First material listed is top layer.

<sup>b</sup> All approximately for terrestrial sunlight.

fraction of a percent. However, there are heterojunctions which function as photovoltaic devices yet have substantial lattice mismatch (Table 5.1). The question now is, what are the additional factors which modify and perhaps, in some cases, overshadow the influence of the interfacial lattice mismatch problem? It appears that there are a number of additional factors which affect the physical and chemical nature of the interface formed in a heterojunction solar cell. Among them are the tying up of dangling bonds, compensation, interdiffusion, formation of intermediary layers (including alloying and compound formation), and formation of oxide layers.

Dangling bonds, seen in Fig. 5.5, need not all be electrically active as recombination centers. Instead, a great deal of tying up or passivation of dangling bonds can take place. The result in some materials systems can be that only a small fraction of the dangling bonds function as active recombination centers which carry  $J_{ir}$  [20].

Figure 5.6 shows one possibility. The dangling bonds seen in Fig. 5.5 at the ends of the dislocations are assumed acceptorlike and are shown in Fig. 5.6 having trapped electrons which cause them to be negatively charged sites. However, in this figure, the trapped negative charge is bound by ion interstitials (positively charged donor sites) located adjacent to the dislocations. The result in this case is that the negative charge is tied up or fixed by the presence of the positive ion and this fixed occupation of the dangling

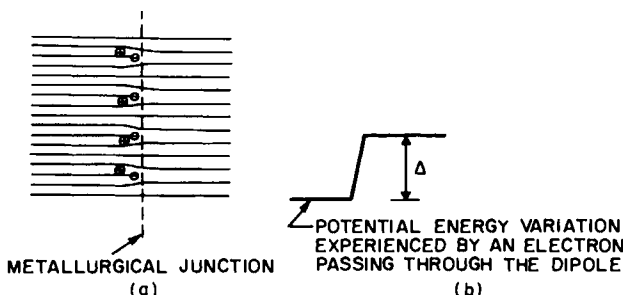


Fig. 5.6 (a) Schematic representation of a compensated version of the interface seen in Fig. 5.5. (b) The permanent dipole contribution resulting from the structure seen in (a).

bond prevents it from serving as a conduit for  $J_{ir}$ . The particular mechanism assumed has created a permanent interfacial dipole with its own potential energy contribution  $\Delta$  as seen in Fig. 5.6b. The effect of interface dipoles such as this on barrier formation was discussed in Section 3.4. As a result, we know that Eq. (3.13), which computes the built-in potential for an anisotype heterojunction, must be modified to

$$V_{bi1} + V_{bi2} - \Delta = \phi_{p2} - \phi_{n1} \quad (5.8)$$

for Fig. 5.6.

When dangling bonds are tied up at a heterojunction interface, there is no guarantee that a macroscopic dipole such as that seen in Fig. 5.6 will occur. The tying up of the bond could simply nullify the ability of the bond to result in a net charge at the interface; i.e., nullify the ability of the bond (localized state) to act as a unipole. The point is that when dangling bonds are tied up and consequently have a fixed charge occupation, they no longer function as recombination centers. Hence, they have become electrically inactive and cannot carry  $J_{ir}$ .

The possibility for the chemical modification and passivation of dangling bonds at the interface of some materials systems is substantiated by the fact that accumulation and precipitation of impurities in lattice mismatch regions has been reported [21], and by the data seen in Fig. 3.20 which demonstrates the modification of dangling bonds in the context of the grain-boundary (lattice mismatch) regions of polycrystalline material. The tying up of dangling bonds also seems quite possible when one realizes that the various constituents of the two chemically different semiconductors involved in a heterojunction can cross diffuse across the idealized junction plane seen in Fig. 5.5 and bond with chemically active species at the junction.

When it is recalled that the precise criterion for thermodynamic equilibrium across an interface is that the electrochemical potentials of every species that can pass back and forth across the interface must be equal [22], one realizes that there is a strong impetus for atoms and ions as well as electrons and holes to be exchanged across a heterojunction interface. The degree to which this exchange takes place depends on the mobility of the species in question, the temperature, etc. One may argue cross diffusion takes place in homojunctions where various species used in doping can cross diffuse and, of course, it does. However, in homojunctions the concentrations at the source layers of the potentially diffusing species exist at levels of  $\sim 10^{15}$  to  $10^{18} \text{ cm}^{-3}$ , whereas in heterojunctions the concentration at the source layers of the potentially diffusing species exist at levels of  $10^{22} \text{ cm}^{-3}$ . The strong gradients driving cross diffusion in heterojunctions imply that cross diffusion should be involved in phenomena other than just its possible role in the tying up of dangling bonds at heterojunctions. We now explore this point further.

Depending on the fabrication procedure used to form a heterojunction and the materials involved, cross diffusion has been found to give rise to compensation in some materials systems which may partially offset the effects of bulk doping in a portion of the depletion region of a heterojunction [13, 23–25]. Cross diffusion can result in an increase as well as decrease in the interface state density  $N_i$ . It has also been found that cross diffusion can cause the formation of intermediary or third-phase layers with composition, and consequently optical and electrical properties, different from either of the two constitutive semiconductors [13, 23–25]. These intermediary layers<sup>†</sup> may exist due to chemical compound formation or to alloying. It has been suggested that these intermediary layers may be advantageous in some cases and may serve to lessen the lattice mismatch problems [25].

As a result of this discussion we have come to realize that a number of materials-related effects can be present at heterojunctions. We have noted that the union of chemically and physically dissimilar materials in a heterojunction can result in interface states due to lattice mismatch, cross diffusion, vacancies, etc. These interface states can give rise to the detrimental recombination current  $J_{ir}$  and can give rise to unipoles or permanent dipoles that modify the barrier shape from that expected on the basis of doping and work-function difference. We have also noted that cross diffusion can lead to the tying up of dangling bonds, the modification of bulk doping due to compensation in the barrier region, and intermediary layer formation. The degree to which these various effects are important depends not only on the materials involved but on the processing used to form the heterojunction. We now focus in more detail on how these various materials-related phenomena can affect the photovoltaic action of a heterojunction solar cell.

Equation (2.100) in the form of Eq. (2.100b), will be found useful in this discussion. For convenience we rewrite this equation here:

$$\begin{aligned} V_{oc} = & - \int_0^L \left( \frac{e\mu_n \Delta n}{\sigma} \right) \left( \frac{dE_c}{dx} \right) dx - \int_0^L \left( \frac{e\mu_p \Delta p}{\sigma} \right) \left( \frac{dE_v}{dx} \right) dx \\ & + kT \int_0^L \frac{1}{\sigma} \left( e\mu_p \frac{d}{dx} \Delta p - e\mu_n \frac{d}{dx} \Delta n \right) dx \\ & - kT \int_0^L \left[ \frac{e\mu_p \Delta p}{\sigma} \frac{d}{dx} \ln N_v - \frac{e\mu_n \Delta n}{\sigma} \frac{d}{dx} \ln N_c \right] dx \end{aligned} \quad (5.9)$$

<sup>†</sup> When an intermediary layer between two semiconductors in a heterojunction solar cell has a wide energy gap, it may be thought of as an insulator, and the structure is referred to as an S-I-S solar cell. Such structures may result for some materials systems due to cross diffusion or they can arise due to the purposeful or inadvertent formation of oxide layers at the interface during fabrication.

We recall from Chapter 2 that it is obtained from Eq. (2.100a) by using

$$dE_c/dx = \xi_0 - d\chi/dx \quad (5.10)$$

and

$$dE_v/dx = \xi_0 - d(E_g + \chi)/dx \quad (5.11)$$

Disregarding the Dember term and the photovoltage arising from variations in the band-effective densities of states, Eq. (5.9) underscores that it is the variation of the conduction-band edge  $E_c$  and the valence-band edge  $E_v$  across a junction region, exhibiting photoconductivity, that gives rise to the photovoltaic action of a heterojunction.

We demonstrate the point that the materials-related phenomena unique to heterojunctions can greatly influence cell performance by using Fig. 5.7. We will show that these materials-related phenomena can each have varying degrees of importance depending on the fabrication procedures used to form the junction. We note that Fig. 5.7a shows two semiconductors, one of work function  $\phi_{p2}$  and the other of work function  $\phi_{n1}$  before contact. Figures 5.7b–5.7e show some of the various barrier shapes [i.e., possible variations of  $E_c$  and  $E_v$  with position] that can result when the two semiconductors form nominally the same heterojunction. It follows from Eq. (5.9) that differences in the barrier shapes seen in Figs. 5.7 b–e mean different photovoltaic performance can be expected in cases b to e.

We now explore more closely how all the different barrier shapes seen as examples in Figs. 5.7b–e can arise from junctions between the two semiconductors of Fig. 5.7a. To make things simpler we shall assume that the bulk doping in the barrier regions is the same in all the cases seen in Fig. 5.7. However, it should be clear that different processing could lead to various degrees of compensation, further increasing the variety of barrier shapes available to what we originally thought was a well-defined heterojunction between semiconductors 1 and 2 of Fig. 5.7a. For ease in deciphering Fig. 5.7 we recall from Chapter 2 that the built-in potential at a junction is always equal to the total change in the local vacuum level across the junction. We also recall from Chapter 2 that the electrostatic field  $\xi_0$  is always given by the gradient of the local vacuum level.

If the two semiconductors of Fig. 5.7a form an abrupt heterojunction free from interface states, interface dipoles, cross diffusion, and intermediary layers, the idealized situation of Fig. 5.7b, which is termed the Anderson model [26], occurs. The variation of  $E_c$  and  $E_v$  across the interface [i.e., the barrier in the conduction band and the barrier in the valence band] can be seen from Eqs. (5.10) and (5.11) always to consist of two sources in heterojunctions. These are easily distinguishable in this case: (a) the variation in electron and hole affinities [the  $d\chi/dx$  and  $d(\chi + E_g)/dx$  terms of

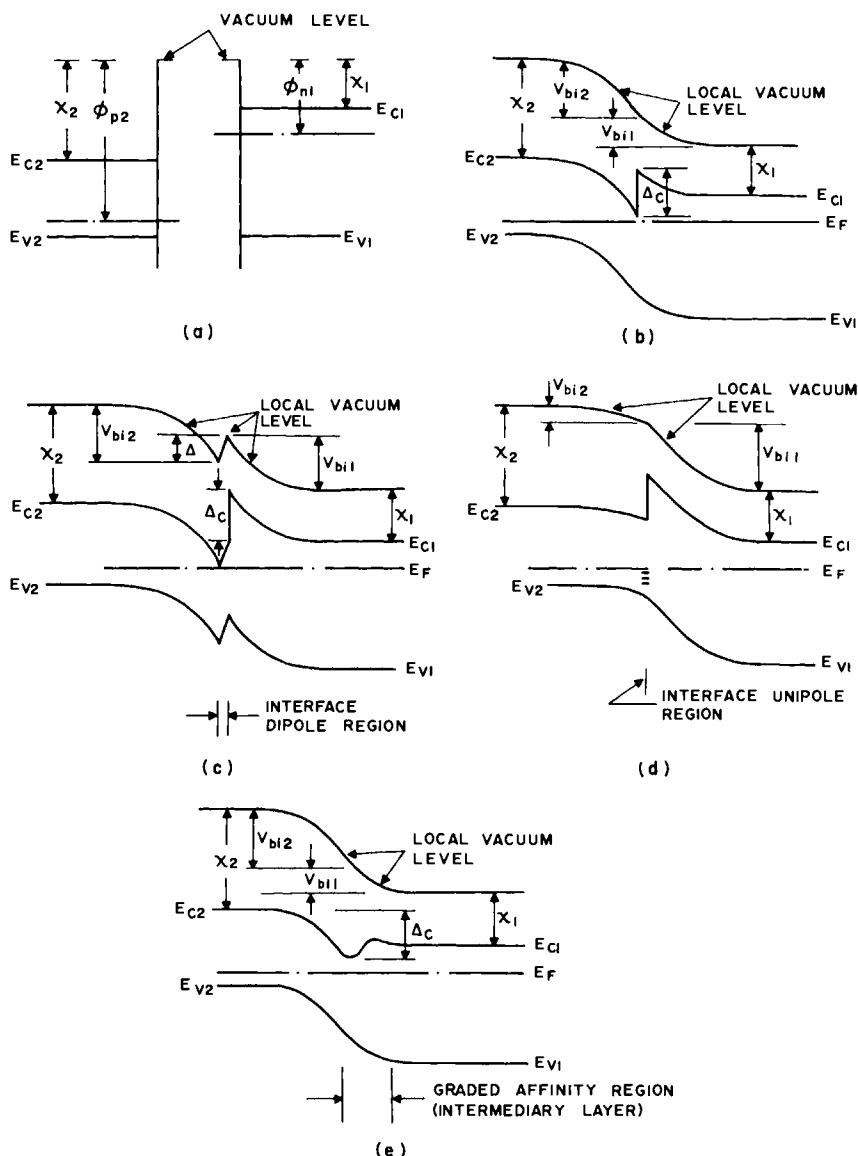


Fig. 5.7 (a) The energy band scheme for two semiconductors before contact, depicted with respect to the same reference energy. (b)-(e) The energy band schemes possible after contact: (b) ideal (Anderson) heterojunction; (c) junction with permanent interface dipole oriented to increase barrier; (d) junction with negative charge build-up in interface states; and (e) junction with graded electron affinity region. The figure demonstrates that various barrier shapes [ $E_c = E_c(x)$  and  $E_v = E_v(x)$ ] can exist in what is nominally the same heterojunction. For simplicity a pair of semiconductors have been chosen for which  $\Delta_v = 0$ .

Eqs. (5.10) and (5.11)] giving rise to effective forces at the plane of discontinuity, and (b) the built-in potential [the  $\xi_0$  terms of Eqs. (5.10) and (5.11)] giving rise to electrostatic forces throughout the barrier region. The quantities  $\Delta_c$  and  $\Delta_v$  appearing in the figure are defined by Eqs. (3.14) and (3.15); i.e., the total variation in the electron affinity is

$$\Delta_c = (\chi_2 - \chi_1) \quad (5.12)$$

and the total variation in the hole affinity is

$$\Delta_v = \chi_2 + E_{g2} - \chi_1 - E_{g1} \quad (5.13)$$

The built-in potential variation is given by Eq. (3.13); i.e.,

$$V_{bi1} + V_{bi2} = \phi_{p2} - \phi_{n1} \quad (5.14)$$

We note from Eq. (5.13) that  $\Delta_v = 0$  for this particular pair of semiconductors. We also note from Fig. 5.7b and Eq. (5.9) that this particular pair of semiconductors has a disadvantageous spike in the conduction band due to the electron affinity change which detracts from the open-circuit voltage. Equivalently, the spike hinders the collection of photocurrent coming out of the *p*-type semiconductor and reduces the open-circuit voltage.

Figure 5.7c shows the same two semiconductors again in an abrupt heterojunction configuration but, in this case, an interface permanent dipole (see Fig. 5.6) is assumed present as a result of the particular processing used. The variation in  $E_c$  and  $E_v$  across the junction arising from the electron and hole affinity changes must be the same as that found in the Anderson model. Since this is an abrupt junction, electron and hole affinity changes are again limited to the plane of the junction; i.e., sharp discontinuities  $\Delta_c$  and  $\Delta_v$  in the band edges at the plane of the junction. However, the presence of the dipole modifies the electrostatic field such that the variation of the band edges in thermodynamic equilibrium in semiconductor 2 which we term  $V_{bi2}$  and the corresponding quantity in semiconductor 1 which we term  $V_{bi1}$  must obey a modified Eq. (5.14) given by Eq. (5.8). Equation (5.9) shows that the change in barrier shape from Fig. 5.7b to Fig. 5.7c can affect cell performance.

Figure 5.7d represents still another possibility: The same two semiconductors are again fabricated into an abrupt junction but, instead of a permanent dipole being present, there are interface states which cause recombination and which give rise to unipoles whose population can change with illumination and bias (i.e., there is a variable charge stored in the interface states). The variation in the band edges in Fig. 5.7d due to the electron and hole affinity changes are the same as Figs. 5.7b and 5.7c, and this source of variation is assumed once again to be limited to the plane of

the abrupt junction. The total variation of the band edges due to electrostatic forces ( $V_{bi1} + V_{bi2}$ ) is again given by Eq. (5.14) in this case. However, the actual variation in semiconductor 1 or 2 will be different from Fig. 5.7b due to the interface charge as follows from the analysis of Section 3.4.3.1. It follows from Eq. (5.9) that this change in the shape of the barrier as well as the possible direct influence of the loss mechanism of interface state recombination can affect cell performance.

Figure 5.7e shows the barrier shape that can be present in a heterojunction formed from the same two semiconductors of Fig. 5.7a when processing gives rise to a graded intermediary layer. Although  $\Delta_c$  must be given by Eq. (5.12) for all these structures in Fig. 5.7,  $\Delta_c$  occurs in Fig. 5.7e over a graded affinity region. That is, this is not an abrupt junction but rather it is assumed that there is an intermediary layer present over which  $\chi$  varies monotonically from  $\chi_2$  to  $\chi_1$ . Because the electrostatic field term  $\xi$  and this effective field term  $d\chi/dx$  have opposite signs for any junction between the semiconductors of Fig. 5.7a, it follows from Eq. (5.10) that these two force fields oppose one another in all the cases seen in Fig. 5.7; because this occurs over a finite region in the nonabrupt case of Fig. 5.7e, the variation in  $E_c$  through the barrier region is seen to be reduced. Put succinctly, part of  $V_{bi1} + V_{bi2}$  is always offset for the conduction band edge by  $\Delta_c$  for the semiconductors of this figure. In Fig. 5.7e this occurs across the whole barrier. The result is that there is less of a barrier in the conduction band in Fig. 5.7e, and  $dE_c/dx$  in Eq. (5.10) is reduced over the whole junction region [27, 28]. It follows from Eq. (5.9) that this reduction of the variation of  $E_c$  in the strongly photoconductive region of the heterojunction will have a significant influence on the performance of this heterojunction as a solar cell. Of course, for pairs of semiconductors which do not exhibit the spike in  $E_c$  seen in the Anderson model, one does not have to worry that processing variations may lead to something like Fig. 5.7e since  $\xi$  and  $d\chi/dx$  in Eq. (5.10) will always add when the Anderson model shows no spike.

In conclusion, our qualitative discussions have shown that heterojunction solar cells offer potential design advantages over homojunctions, but it has become apparent that heterojunctions introduce a whole new set of problems at the metallurgical junction. These range from the occurrence of localized states, which can give rise to unipoles or interface dipoles that modify barrier shape and can act as a sink for photogenerated carriers, to cross diffusion and intermediary layer effects which can modify barrier shape and also influence interface recombination. Together, these effects can lead to a barrier shape and photovoltaic performance that are very dependent on the details of device fabrication. The control of all these problems unique to heterojunctions must be considered when choosing semiconductor pairs and fabrication procedures for solar cell structures.

### 5.2.2 Device Analysis Concepts

The mathematical system which can be used to quantify these effects we have just discussed and which can be used to determine heterojunction performance is that developed in Chapter 2. This mathematical system has been summarized in Section 4.2.2.1 for homojunctions. The summary must be slightly modified in the case of heterojunctions to account for the presence of effective forces.

For example, considering carriers in the conduction and valence bands,  $J_n$  must be modified to

$$J_n = en\mu_n[\zeta - d\chi/dx - kT_e d(\ln N_c)/dx] + eD_n dn/dx + eD_n^T dT_e/dx \quad (5.15)$$

which still retains the form

$$J_n = en\mu_n dE_{Fn}/dx - en\mu_n S_n dT_e/dx \quad (5.16)$$

when expressed in terms of the electron quasi-Fermi level instead of electrostatic fields and effective fields. Similarly,  $J_p$  must be modified to

$$J_p = ep\mu_p[\zeta - d(\chi + E_g)/dx + kT_h d(\ln N_v)/dx] - eD_p dp/dx - eD_p^T dT_h/dx \quad (5.17)$$

which still retains the form

$$J_p = ep\mu_p dE_{Fp}/dx - ep\mu_p S_p dT_h/dx \quad (5.18)$$

when expressed in terms of the hole quasi-Fermi level instead of electrostatic fields and effective fields.

Just as in the case of homojunctions, there is a wide variety of physical phenomena built into this mathematical system. The variety of the phenomena present allow bulk transport in the semiconductor regions of a heterojunction to be controlled by minority-carrier diffusion, ambipolar diffusion, space-charge limited currents, etc. Of course, transport in the bulk regions is in series with transport at the interface giving heterojunctions an even broader range of possible behavior as we shall see.

In the case of homojunctions we found that a fully linearized version of the mathematical system (differential equations plus boundary conditions accounting for interface transport) could be justified in certain cases. Homojunction analysis based on this linearized mathematical system gave a light  $J-V$  characteristic of the form

$$J = J_{sc} - J_{bk}(V) \quad (5.19)$$

However, we shall find that Eq. (5.19) is not valid at all for many heterojunction solar cell devices. Figure 5.8 presents one example: this gives experimental dark and light  $J-V$  characteristics for a  $\text{Cu}_2\text{S}/\text{CdS}$  cell that display a crossover which is inconsistent with Eq. (5.19) [29].

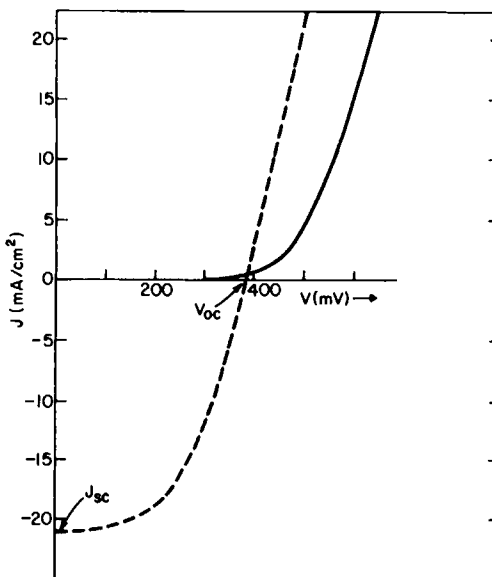


Fig. 5.8 Light (---) and dark (—)  $J$ - $V$  for a  $\text{Cu}_2\text{S}/\text{CdS}$  heterojunction solar cell structure. It is evident that a  $J$ - $V$  model of the form of Eq. (5.19) is not valid. (After Ref. [29].)

In the case of many heterojunctions it is found that, at best, we shall be able to use a partially linearized version of the mathematical system in our modeling. The basic origins of these complications in a number of heterojunctions are the interface-caused effects we discussed in the preceding section; however, using the partially linearized mathematical system we shall be able to incorporate many of these effects into the analysis and we shall find [see Eq. (5.56)] that the  $J$ - $V$  characteristic under illumination can be written as

$$J = J_{\text{ph}}(\Phi_0, V) - J_{\text{bk}}(\Phi_0, V) \quad (5.20)$$

Here the bucking current  $J_{\text{bk}}$  under illumination at a voltage  $V$  may not be the same as the dark current at the same voltage and the photocurrent  $J_{\text{ph}}$  may be a function of voltage. Equation (5.20), which is found useful in interpreting the behavior of many heterojunctions, is developed in the next section.

We point out that Eq. (5.20), as well as Eq. (5.19), are exactly equivalent to Eq. (5.1). The latter is the very general expression, valid under all conditions, that we found useful in our qualitative discussions. We note, however, that  $\int G_L(x) dx$  could only equal  $J_{\text{ph}}$  or  $J_{\text{sc}}$ , if the spectral response SR were identically unity for all wavelengths absorbed in the structure.

### 5.2.3 Analysis of Anisotype Semiconductor-Semiconductor Structures

#### 5.2.3.1 Analysis

We shall limit ourselves to abrupt semiconductor-semiconductor heterojunction structures in this section in order to obtain a tractable analytical solution to predict device characteristics. Heterojunctions with graded intermediary layers (Fig. 5.7e) generally necessitate numerical techniques to obtain device  $J-V$  characteristics and performance data [30]. Abrupt heterojunctions of the form semiconductor-insulator-semiconductor (S-I-S) will be discussed in Sections 5.2.5 and 5.2.6. Further, in this section we restrict ourselves to the advantageous heterojunction solar cell configuration of the form window-absorber; it will also be assumed that electrons and holes have the same temperature as the lattice in the analysis.

Figure 5.9 gives the band diagrams for two abrupt, anisotype heterojunctions of the form window-absorber. The devices are shown under illumination and, as a consequence, a voltage  $V$  is being developed. A portion  $V_1$

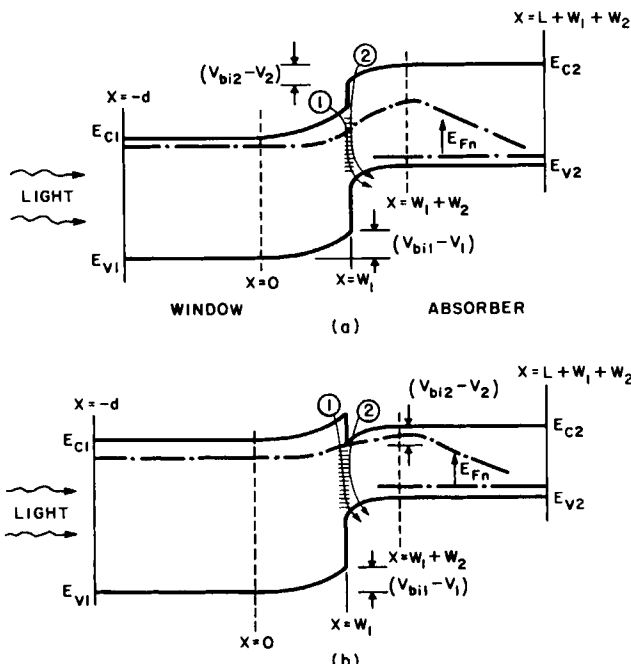


Fig. 5.9 Schematic of two possible window-absorber  $p-n$  heterojunction solar cell configurations. Configuration (b) has an interface spike in the conduction band. In both junctions, interface recombination can occur through paths 1 and 2.

of this voltage is developed in the window semiconductor; the remainder  $V_2$  (where  $V = V_1 + V_2$ ) is developed in the absorber semiconductor as shown. Our objective is to find the current density  $J$  being produced at a voltage  $V$  under these conditions.

If the absorber materials of Fig. 5.9 are lifetime semiconductors that contain no drift fields<sup>†</sup> and if the level of illumination is such that  $n \ll p$  in the absorbers, then the functional form of the electron number density  $n = n(x)$  for the quasi-neutral region  $L + W_1 + W_2 \geq x \geq W_1 + W_2$  is controlled by photogeneration, recombination, and diffusion; and the electron current density  $J_n$  in the quasi-neutral region is due to simple diffusion. Consequently,  $n = n(x)$  must satisfy

$$\frac{d^2n}{dx^2} - \frac{n - n_{p0}}{L_n^2} + \frac{\Phi_0}{D_n} \propto e^{-\alpha(x-W_1)} = 0 \quad (5.21)$$

and  $J_n$  is given by

$$J_n = eD_n dn/dx \quad (5.22)$$

for  $L + W_1 + W_2 \geq x \geq W_1 + W_2$ . The reasons behind all the provisos needed to write Eqs. (5.21) and (5.22) were discussed at length in Section 4.2.2.2; hence, the limitation of the analysis follows from that discussion. We recognize that Eqs. (5.21) and (5.22) are the same equations that arise for homojunctions, under the same set of stipulations, because we have confined the effective forces to the plane of the junction ( $x = W_1$ ). In limiting ourselves to heterojunctions which fulfill these stipulations, we have gained linear expressions for the function  $n = n(x)$  and the current density  $J_n$  which are readily solvable and yet will give us insight into device performance.

Our strategy for determining the function  $J = J(V)$  is now apparent: The current density  $J$  is a constant with position in the one-dimensional structures of Fig. 5.9 which may be evaluated from the sum  $J_p(W_1 + W_2) + J_n(W_1 + W_2)$ . The component  $J_n(W_1 + W_2)$  is a simple diffusion current which can be evaluated from Eq. (5.22) and  $J_p(W_1 + W_2)$  is a majority-carrier current which can be related back to the transport properties of the metallurgical junction and, if necessary, to the transport properties of the  $n$ -type semiconductor. To proceed with this strategy, it is necessary to solve Eq. (5.21) subject to boundary conditions at  $x = W_1 + W_2$  and  $x = L + W_1 + W_2$  to determine the function  $n = n(x)$  which can be used in Eq. (5.22) to give  $J_n(W_1 + W_2)$ .

<sup>†</sup> A constant drift field can be handled with ease analytically as shown by Wolf [31]. Its incorporation into the analysis to be presented here is straightforward. Its physical effect, is only to aid diffusion since  $n \ll p$  is assumed here; i.e., there is no appreciable photoconductivity in the region which might incorporate a drift field.

To account for the possibility that there is a selective-ohmic contact at  $x = L + W_1 + W_2$ , the boundary condition on  $n(x)$  at that plane shall be written as

$$\frac{dn}{dx}|_{L+W_1+W_2} = -\frac{S_n}{D_n} [n(L + W_1 + W_2) - n_{p0}] \quad (5.23)$$

whereas the boundary condition at  $x = W_1 + W_2$  shall be written as

$$n|_{W_1+W_2} = n_{p0} \exp[E_{Fn}(W_1 + W_2)/kT] \quad (5.24)$$

Here  $n_{p0}$  is our usual notation for the thermodynamic equilibrium number density of electrons in the absorber of Fig. 5.9 and  $E_{Fn}(x)$  is the electron quasi-Fermi level measured from its thermodynamic equilibrium value in the absorber. By using Eq. (5.24) we avoid any a priori assumption that the minority-carrier quasi-Fermi level is flat across the junction. As we shall see, if we were to assume a priori that  $E_{Fn}$  were flat across the barrier region and metallurgical junction, we would be ignoring many of the important effects of interface states and the barrier shape [32-34].

Equation (5.21) is readily solved, subject to the boundary conditions of Eqs. (5.23) and (5.24), as was done in the analogous situation of Section 4.2.3. When the resulting expression for  $n = n(x)$  is used to compute  $J_n(W_1 + W_2)$ , it is found to be of the form

$$J_n(W_1 + W_2) = J_L - J_{\text{dif}} \{\exp[E_{Fn}(W_1 + W_2)/kT] - 1\} \quad (5.25)$$

where  $J_L$  is the photocurrent of electrons diffusing out of the quasi-neutral region of the absorber and  $J_{\text{dif}} \{\exp[E_{Fn}(W_1 + W_2)/kT] - 1\}$  is an opposing current component arising from electron diffusion-recombination in the quasi-neutral region of the absorber.

The quantity  $J_L$  appearing in Eq. (5.25) is found to be given by

$$J_L = e\Phi_0 \left\{ \left[ \frac{\beta_6^2 e^{-\beta_4} e^{-\beta_6}}{\beta_6^2 - \beta_5^2} \right] \left[ \frac{(\beta_7 \beta_5 / \beta_6) - 1}{\beta_7 \sinh \beta_5 + \cosh \beta_5} \right] \right. \\ \left. + \left[ \frac{\beta_6^2 e^{-\beta_4}}{\beta_6^2 - \beta_5^2} \right] \left[ 1 - \left( \frac{\beta_5}{\beta_6} \right) \left( \frac{\beta_7 \cosh \beta_5 + \sinh \beta_5}{\beta_7 \sinh \beta_5 + \cosh \beta_5} \right) \right] \right\} \quad (5.26)$$

and the quantity  $J_{\text{dif}}$  is found to be given by

$$J_{\text{dif}} = \left[ \frac{eD_n n_{p0}}{L_n} \right] \left[ \frac{\beta_7 \cosh \beta_5 + \sinh \beta_5}{\beta_7 \sinh \beta_5 + \cosh \beta_5} \right] \quad (5.27a)$$

Equation (5.27a) may be conveniently expressed as

$$J_{\text{dif}} = \Theta_B (eD_n n_{p0} / L_n) \quad (5.27b)$$

where the definition of  $\Theta_B$  follows from Eq. (5.27a).

The dimensionless  $\beta$  numbers appearing in Eqs. (5.26) and (5.27) are the same as the  $\beta$  numbers used in the homojunction cell analysis of Chapter 4 with one exception: the dimensionless number  $\beta_4$  is now defined by

$$\beta_4 = W_1 \alpha \quad (5.28)$$

since there is no absorption in the window layer. The function  $\Theta_B$  appearing in Eq. (5.27b) is plotted in Fig. 5.10 as a function of  $\beta_5$  with  $\beta_7$  as a parameter. The range of  $\beta_7$  is chosen by letting the back recombination speed  $S_n$  vary between 0 and  $10^5$  cm/sec and by letting the diffusion speed  $D_n/L_n$  have values  $\gtrsim 10^2$  cm/sec. The lower limit on the diffusion speed is that value expected in "good" single-crystal materials; larger diffusion speeds are expected for polycrystalline and amorphous materials.

We realized in Section 5.2.1.2 that the effects of interface states, the influence of the barrier shape, etc. can all be very important in determining heterojunction solar cell performance. However, if we write the current density  $J$  developed under illumination as we have presently determined it, the result is

$$J = J_p(W_1 + W_2) + J_L - J_{\text{dif}} \{ \exp[E_{\text{Fn}}(W_1 + W_2)/kT] - 1 \} \quad (5.29)$$

Looking at Eqs. (5.26), (5.27), and (5.29), we note that the expected interface effects are not apparent. However, they will come into focus as we begin to

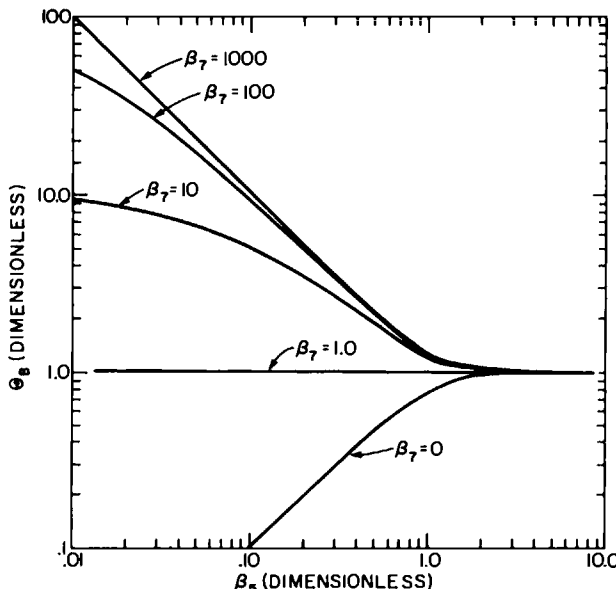


Fig. 5.10. The dimensionless factor  $\Theta_B$  versus  $\beta_5$  with  $\beta_7$  as a parameter for a representative range of values of  $\beta_5$  and  $\beta_7$ . The values chosen span from crystalline to amorphous materials.  $\beta_5 = L/L_n$ ;  $\beta_7 = (S_n)/(D_n/L_n)$ , TS;  $\beta_7 = (S_n)/(D_n/I_n)$ .

see how the values of  $E_{Fn}(W_1 + W_2)$  and  $J_p(W_1 + W_2)$  are determined by the interface properties.

Our first objective will be to work back toward the interface to relate the electron quasi-Fermi level at the edge of the quasi-neutral region  $E_{Fn}(W_1 + W_2)$  to its value  $E_{Fn}(W_1^+)$  just to the right of the metallurgical junction. This can be done using Eq. (5.16), which we employ in the form<sup>†</sup>  $J_n = e\mu_n n(dE_{Fn}/dx)$ , where

$$n = n_{p0} e^{\psi_2/kT} e^{E_{Fn}/kT} \quad (5.30)$$

Equation (5.30) follows from Eq. (2.54). The  $\psi_2$  appearing in this equation locates the band edges in the band-bending (barrier) region of the absorber with respect to their position in the bulk of the absorber. The quantity  $\psi_2$  is measured positively down whereas  $E_{Fn}$  is measured positively up from its thermodynamic equilibrium position in the absorber bulk.

Neglecting recombination and photogeneration in the barrier region<sup>‡</sup> of the absorber allows  $E_{Fn}(W_1^+)$  to be related to  $E_{Fn}(W_1 + W_2)$  by straightforward integration of Eq. (5.16) across the barrier with  $n = n(\psi_2)$  given by Eq. (5.30); viz. [32-34],

$$\begin{aligned} J_L - J_{\text{dif}}\{e^{E_{Fn}(W_1 + W_2)/kT} - 1\} &= J_{\text{sweep}}^{2n}\{e^{E_{Fn}(W_1 + W_2)/kT} - 1\} \\ &\quad - J_{\text{sweep}}^{2n}\{e^{E_{Fn}(W_1^+)/kT} - 1\} \end{aligned} \quad (5.31a)$$

This may be rearranged into the form

$$[e^{E_{Fn}(W_1 + W_2)/kT} - 1] = \frac{J_L}{J_{\text{dif}} + J_{\text{sweep}}^{2n}} + \frac{J_{\text{sweep}}^{2n}}{J_{\text{dif}} + J_{\text{sweep}}^{2n}} [e^{E_{Fn}(W_1^+)/kT} - 1] \quad (5.31b)$$

Here we have introduced the definition

$$J_{\text{sweep}}^{2n} \equiv \frac{en_{p0}\mu_n kT}{\int_{W_1^+}^{W_1 + W_2} e^{-\psi_2/kT} dx} \quad (5.32)$$

It is pointed out that it is not necessary to neglect recombination and generation in the depletion layer to proceed with this analysis. We do it here only because we want to focus on the role of the interface. The reader is referred to Section 6.2.3.

The quantity  $J_{\text{sweep}}^{2n}$  is a measure of the ease with which electrons cross the barrier region  $W_2 + W_1 \geq x \geq W_1$  in the absorber as indicated by the subscripts employed. The superscripts are an effort to try to keep track of

<sup>†</sup> We assume that the carriers suffer enough collisions in the region  $W_1 + W_2 > x > W_1$  to make these expressions developed in Chapter 2 valid.

<sup>‡</sup> We neglect recombination in the depletion region by arguing that we shall lump all its effects at the interface  $x = W_1$ . However, neither recombination nor generation in the depletion layer need be ignored (see Section 6.2.3).

the fact that this quantity applies to electrons in semiconductor 2 (the absorber of Fig. 5.9). As seen from Eq. (5.32),  $J_{\text{sweep}}^{2n}$  depends on the shape of the conduction-band barrier  $E_c = E_c(x)$  in the absorber; consequently, it is generally expected to be bias dependent.

Digressing for a moment, we note that Eq. (5.31a) says that  $E_{Fn}(W_1 + W_2)$  is larger than  $E_{Fn}(W_1^+)$  since  $J_L > J_{\text{dif}}\{e^{E_{Fn}(W_1 + W_2)/kT} - 1\}$ . We anticipated this in our sketch of  $E_{Fn} = E_{Fn}(x)$  in Fig. 5.9. However, if

$$J_{\text{sweep}}^{2n} \gg J_{\text{dif}} \quad (5.33)$$

then Eq. (5.31) becomes

$$e^{E_{Fn}(W_1 + W_2)/kT} = \frac{J_L}{J_{\text{sweep}}^{2n}} + e^{E_{Fn}(W_1^+)/kT} \quad (5.34)$$

The significance of Eq. 5.33 can be seen by substituting Eq. (5.34) into our statement for the total current, Eq. (5.29). When the substitution is made, Eq. (5.29) becomes

$$J = J_p(W_1 + W_2) + J_L - J_L \left( \frac{J_{\text{dif}}}{J_{\text{sweep}}^{2n}} \right) - J_{\text{dif}}\{\exp[E_{Fn}(W_1^+)/kT] - 1\} \quad (5.35)$$

Except for a correction term  $J_L(J_{\text{dif}}/J_{\text{sweep}}^{2n})$ , which is negligible since we are assuming Eq. (5.33) applies, Eq. (5.35) is exactly what we would have obtained had we assumed a priori that  $E_{Fn}$  was flat across the band-bending (barrier) region in the absorber. Put succinctly, Eq. (5.33) is the criterion which must be fulfilled in the region  $W_2 + W_1 \geq x \geq W_1$  for  $E_{Fn}$  to be flat across this region. We assumed flat quasi-Fermi levels across barrier regions in Section 4.2.3 in our treatment of homojunctions. Here we have outlined rigorous criteria [the criterion for holes in a homojunction would follow by extension of Eq. (5.33)] for the validity of the assumption.

Returning to our objective, the general expression relating  $E_{Fn}(W_1 + W_2)$  to  $E_{Fn}(W_1^+)$  given by Eq. (5.31) can be used in Eq. (5.29) resulting in a characteristic, under illumination, of the form [32–34]

$$\begin{aligned} J = J_p(W_1 + W_2) + J_L &\left( \frac{J_{\text{sweep}}^{2n}}{J_{\text{dif}} + J_{\text{sweep}}^{2n}} \right) \\ &- J_{\text{dif}} \left( \frac{J_{\text{sweep}}^{2n}}{J_{\text{dif}} + J_{\text{sweep}}^{2n}} \right) \{\exp[E_{Fn}(W_1^+)/kT] - 1\} \end{aligned} \quad (5.36)$$

Equation (5.36) underscores the fact that Eq. (5.33) must be obeyed or, equivalently,  $E_{Fn}$  must be flat across the absorber-barrier region, if all of  $J_L$  generated in the quasi-neutral region is to reach  $x = W_1^+$ . If electrons do not easily cross  $W_2 + W_1 \geq x \geq W_1$  in the absorber [i.e., if Eq. (5.33) is not

obeyed], then part of  $J_L$  is lost because the bucking current increases, as Eq. (5.29) shows and as indicated by the hump in  $E_{Fn}$  in Fig. 5.9.

Turning now to the objective of relating  $J_p(W_1 + W_2)$  to interface properties, we note that [33]

$$\begin{aligned} J_p(W_1 + W_2) = & \frac{eA_{1p}^{IL}A_{1n}^{IL}N_1^{II}}{A_{1p}^{IL}p(W_1^+) + A_{1p}^{IL}p_1^{II} + A_{1n}^{IL}n(W_1^+) + A_{1n}^{IL}n_1^{II}} [n(W_1^+)p(W_1^+) - n_{ip}^2] \\ & - \frac{eA_{1p}^{IL}A_{1n}^{IL}N_1^I}{A_{1p}^{IL}p(W_1^+) + A_{1p}^{IL}p_1^I + A_{1n}^{IL}n(W_1^-) + A_{1n}^{IL}n_1^I} [n(W_1^-)p(W_1^+)] \\ & - n_{n0}e^{-V_{bi1}/kT}p_{p0}e^{-V_{bi2}/kT}] \end{aligned} \quad (5.37)$$

This equation states that  $J_p(W_1 + W_2)$  flows solely to supply holes for S-R-H recombination through path 2 (first term) and through path 1 (second term). There are no holes coming from the window or injected into the window due to its large gap. The terms of Eq. (5.37) are similar to Eq. (3.62), which was developed in our general discussion of transport at interfaces. We note that the second term of Eq. (5.37) is driven by the difference between  $n(W_1^-)p(W_1^+)$  under operating conditions and its value in thermodynamic equilibrium.

Defining a current density  $J_r^2$ , which characterizes recombination through path 2, as the subscript and superscript indicate, by<sup>†</sup>

$$J_r^2 = \frac{eA_{1p}^{IL}A_{1n}^{IL}N_1^{II}p_{p0}n_{p0}}{A_{1p}^{IL}(W_1^+) + A_{1p}^{IL}p_1^{II} + A_{1n}^{IL}n(W_1^+) + A_{1n}^{IL}n_1^{II}} \quad (5.38)$$

and defining a corresponding quantity for path 1 by<sup>†</sup>

$$J_r^1 = \frac{eA_{1p}^{IL}A_{1n}^{IL}N_1^I n_{n0} e^{-V_{bi1}/kT} p_{p0} e^{-V_{bi2}/kT}}{A_{1p}^{IL}p(W_1^+) + A_{1p}^{IL}p_1^I + A_{1n}^{IL}n(W_1^-) + A_{1n}^{IL}n_1^I} \quad (5.39)$$

we can rewrite Eq. (5.37) as

$$J_p(W_1 + W_2) = -J_r^2(e^{E_{Fn}(W_1^+)/kT} - 1) - J_r^1(e^{E_{Fn}(W_1^-)/kT} - 1) \quad (5.40)$$

Equation (5.40) makes use of

$$n(W_1^+) = n_{p0}e^{V_{bi2}/kT}e^{-V_2/kT}e^{E_{Fn}(W_1^+)/kT} \quad (5.41)$$

$$n(W_1^-) = n_{n0}e^{-V_{bi1}/kT}e^{-V_2/kT}e^{E_{Fn}(W_1^-)/kT} \quad (5.42)$$

<sup>†</sup> There are actually a series of terms such as Eq. (5.38) for  $J_r^2$  and such as Eq. (5.39) for  $J_r^1$ ; however, it is the localized states in mid-gap which contribute the most to these sums. For  $J_r^1$  mid-gap is defined as  $(E_{c1} + E_{v2})/2$  whereas it is  $(E_{c2} + E_{v1})/2$  for  $J_r^2$ .

and

$$p(W_1^+) = p_{p0} e^{-V_{bi2}/kT} e^{V_2/kT} \quad (5.43)$$

The last of these equations assumes  $E_{Fn}$  is flat across the barrier region in the absorber; i.e., the  $p$ -type absorber is able to keep up with the demand for holes for recombination at the interface.

Substituting Eq. (5.40) into Eq. (5.36), we obtain

$$\begin{aligned} J &= J_L \left( \frac{J_{sweep}^{2n}}{J_{dif} + J_{sweep}^{2n}} \right) - J_r^1 (e^{E_{Fn}(W_1^-)/kT} - 1) - J_r^2 (e^{E_{Fn}(W_1^+)/kT} - 1) \\ &\quad - J_{dif} \left( \frac{J_{sweep}^{2n}}{J_{dif} + J_{sweep}^{2n}} \right) (e^{E_{Fn}(W_1^+)/kT} - 1) \end{aligned} \quad (5.44)$$

The influence of the metallurgical-junction localized states and the influence of the barrier shape on heterojunction solar cell performance are certainly coming into focus in Eq. (5.44). However, before we become too elated over our success, we must realize that Eq. (5.44) still contains  $E_{Fn}(W_1^+)$  and  $E_{Fn}(W_1^-)$  which are unknown. What we really want for assessing heterojunction performance is a function of the form  $J = J(V)$ . Clearly  $E_{Fn}(W_1^+)$  and  $E_{Fn}(W_1^-)$  must be related to  $V$ .

Our scheme for relating  $E_{Fn}(W_1^+)$  and  $E_{Fn}(W_1^-)$  to the voltage developed by the cell is the following: We shall relate  $E_{Fn}(W_1^+)$  to  $E_{Fn}(W_1^-)$  on the left side of the metallurgical junction and then we shall relate  $E_{Fn}(W_1^-)$  to  $E_{Fn}(0)$ . Since we are assuming the majority-carrier number densities are not significantly perturbed in the quasi-neutral regions, it follows that  $E_{Fn}(0)$  is  $V$ .

As follows from our discussion in Section 3.5, electrons in the conduction band of the absorber at  $x = W_1^+$  can cross into the window by thermionic emission at  $x = W_1$  or, in the case of Fig. 5.9b, they can also use the parallel path of tunneling through the spike seen in the conduction band [35–38]. We shall assume thermionic emission is the dominant mechanism for now. Hence, electrons in the absorber conduction band at  $x = W_1^+$  are being emitted into the window semiconductor conduction band; electrons in the window conduction band at  $x = W_1^-$  are being emitted into the absorber conduction band. Consequently, the net current density at  $x = W_1$  resulting from this exchange can be deduced from Eq. (3.59); it is of the form [33–36]

$$J_{th} [\exp(E_{Fn}(W_1^+)/kT) \exp(-V_2/kT) - \exp(E_{Fn}(W_1^-)/kT) \exp(-V_2/kT)].$$

As used here,  $J_{th}$  is a constant, at a given temperature, for a specific absorber–window pair [33–36]. We shall discuss this factor  $J_{th}$  extensively in Section 5.2.3.2.

The net electron current density at  $x = W_1$  must carry the electrons coming out of the absorber; hence

$$\begin{aligned} J_{\text{th}} \exp(-V_2/kT) &\{\exp[E_{Fn}(W_1^+)/kT] - \exp[E_{Fn}(W_1^-)/kT]\} \\ &= J_L \left( \frac{J_{\text{sweep}}^{2n}}{J_{\text{dif}} + J_{\text{sweep}}^{2n}} \right) - J_r^2 (e^{E_{Fn}(W_1^+)/kT} - 1) \\ &\quad - J_{\text{dif}} \left( \frac{J_{\text{sweep}}^{2n}}{J_{\text{dif}} + J_{\text{sweep}}^{2n}} \right) (e^{E_{Fn}(W_1^+)/kT} - 1) \end{aligned} \quad (5.45)$$

This equation may be rearranged to give [32-34]

$$(e^{E_{Fn}(W_1^+)/kT} - 1) = \frac{[J_{\text{th}} e^{-V_2/kT} (e^{E_{Fn}(W_1^-)/kT} - 1) + J_L (J_{\text{sweep}}^{2n} / (J_{\text{dif}} + J_{\text{sweep}}^{2n}))]}{[J_{\text{th}} e^{-V_2/kT} + J_r^2 + J_{\text{dif}} (J_{\text{sweep}}^{2n} / (J_{\text{dif}} + J_{\text{sweep}}^{2n}))]} \quad (5.46)$$

Equation (5.46) tells us how the electron quasi-Fermi levels  $E_{Fn}(W_1^-)$  and  $E_{Fn}(W_1^+)$  on either side of the metallurgical junction are related. This applies under illumination when the current density  $J$  is being developed by the cell.

With Eqs. (5.46) and (5.44), the current density flowing through the cell, under illumination can be written as [32-34]

$$\begin{aligned} J &= J_L \left[ \frac{J_{\text{sweep}}^{2n}}{J_{\text{dif}} + J_{\text{sweep}}^{2n}} \right] \\ &\times \left[ \frac{J_{\text{th}} e^{-V_2/kT}}{J_{\text{th}} e^{-V_2/kT} + J_r^2 + J_{\text{dif}} \left( \frac{J_{\text{sweep}}^{2n}}{J_{\text{dif}} + J_{\text{sweep}}^{2n}} \right)} \right] - J_r^2 (e^{E_{Fn}(W_1^-)/kT} - 1) \\ &- J_r^2 \left[ \frac{J_{\text{th}} e^{-V_2/kT}}{J_{\text{th}} e^{-V_2/kT} + J_r^2 + J_{\text{dif}} \left( \frac{J_{\text{sweep}}^{2n}}{J_{\text{dif}} + J_{\text{sweep}}^{2n}} \right)} \right] [e^{E_{Fn}(W_1^-)/kT} - 1] \\ &- J_{\text{dif}} \left[ \frac{J_{\text{sweep}}^{2n}}{J_{\text{dif}} + J_{\text{sweep}}^{2n}} \right] \\ &\times \left[ \frac{J_{\text{th}} e^{-V_2/kT}}{J_{\text{th}} e^{-V_2/kT} + J_r^2 + J_{\text{dif}} \left( \frac{J_{\text{sweep}}^{2n}}{J_{\text{dif}} + J_{\text{sweep}}^{2n}} \right)} \right] [e^{E_{Fn}(W_1^-)/kT} - 1] \end{aligned} \quad (5.47)$$

Equation (5.47) depends only on  $e^{E_{Fn}(W_1^-)/kT}$  as we wanted, but it is unwieldy; let us introduce notation that will simplify its writing and yet

give us further insight into the operation of heterojunction solar cells. To do this we introduce a set of junction transport factors [32–41] whose value lies between zero and one. These transport factors are defined by

$$F_{2n} \equiv \frac{J_{\text{sweep}}^{2n}}{J_{\text{dif}} + J_{\text{sweep}}^{2n}} \quad (0 \leq F_{2n} \leq 1) \quad (5.48)$$

which quantifies the interplay between the tendency of an electron to be swept across the band-bending region of the absorber and its tendency to diffuse away from the junction and by

$$F_1 \equiv \frac{J_{\text{th}} e^{-V_2/kT}}{J_{\text{th}} e^{-V_2/kT} + J_r^2 + J_{\text{dif}} \left( \frac{J_{\text{sweep}}^{2n}}{J_{\text{dif}} + J_{\text{sweep}}^{2n}} \right)} \quad (0 \leq F_1 \leq 1) \quad (5.49)$$

which quantifies the interplay between the tendency of an electron to be emitted over the barrier at  $x = W_1$  and its tendency to recombine through path 2 or back-diffuse away [32–34]. With these definitions Eq. (5.47) becomes

$$\begin{aligned} J = & F_{2n} F_1 J_L - J_r^1 (e^{E_{Fn}(W_1^-)/kT} - 1) - F_1 J_r^2 (e^{E_{Fn}(W_1^-)/kT} - 1) \\ & - F_{2n} F_1 J_{\text{dif}} (e^{E_{Fn}(W_1^-)/kT} - 1) \end{aligned} \quad (5.50)$$

Comparison of Eq. (5.50) with Eq. (5.44) is very useful because it gives us a firm criterion for determining if the disadvantageous situation of an electron quasi-Fermi level change across the plane  $x = W_1$  (the metallurgical junction) occurs. The comparison shows that for  $E_{Fn}(W_1^-)$  to equal  $E_{Fn}(W_1^+)$ , it must be true that

$$J_{\text{th}} e^{-V_2/kT} \gg \left[ J_r^2 + J_{\text{dif}} \left( \frac{J_{\text{sweep}}^{2n}}{J_{\text{dif}} + J_{\text{sweep}}^{2n}} \right) \right] \quad (5.51)$$

This says simply that thermionic emission at  $x = W_1$  must dominate over interface-state recombination and diffusion for  $E_{Fn}(W_1^-)$  to equal  $E_{Fn}(W_1^+)$ . If condition (5.51) is not obeyed, part of  $J_L$  is lost since  $F_1$  does not have its optimum value of unity as is seen from Eq. (5.49). This loss in  $J_L$  is incurred because Eq. (5.45) shows that  $E_{Fn}(W_1^+)$  is bigger than  $E_{Fn}(W_1^-)$  and additional loss occurs now because of bucking current flows due to electrons backing up at  $x = W_1^+$  leading to their recombining through path 2 or back-diffusing away.

So far, our analysis has shown quantitatively how the shape of the barrier in the absorber (through  $J_{\text{sweep}}^{2n}$ ), the interface-state recombination (through  $J_r^1$  and  $J_r^2$ ), and the transport across the barrier at the metallurgical junction (through  $J_{\text{th}}$ ) can influence heterojunction performance. If we now relate  $E_{Fn}(W_1^-)$  to  $V$  and convert Eq. (5.50) into  $J = J(V)$ , we shall complete our

analysis and pick up the term, which we shall call  $J_{\text{sweep}}^{1n}$ , quantifying the effect of the shape of the barrier in the window semiconductor.

We relate  $E_{Fn}(W_1^-)$  to  $V$  by using

$$J_n = e\mu_n n dE_{Fn}/dx \quad (5.52)$$

and

$$n = n_{n0} e^{-V/kT} e^{-\psi_1/kT} e^{E_{Fn}/kT} \quad (5.53)$$

Here  $E_{Fn}$  is measured just as it was for Eq. (5.30) and  $\psi_1$  locates the conduction-band edge in the band-bending (barrier) region of the window with respect to its position in the bulk of the window. This  $\psi_1$  is measured positively up in Fig. 5.9. If recombination is neglected in the barrier,<sup>†</sup> then  $J_n$  of Eq. (5.52) is the constant  $J$ , the total current density, since there is no photogeneration in this region. Consequently, Eq. (5.52) may be integrated easily, using Eq. (5.53), to yield

$$e^{E_{Fn}(W_1^-)/kT} - 1 = (J/J_{\text{sweep}}^{1n}) + e^{V/kT} - 1 \quad (5.54)$$

where

$$J_{\text{sweep}}^{1n} \equiv e\mu_{n1} n_{n0} e^{-V/kT} kT \left/ \int_0^{W_1} e^{\psi_1/kT} dx \right. \quad (5.55)$$

The quantity  $J_{\text{sweep}}^{1n}$  has the same physical meaning as  $J_{\text{sweep}}^{2n}$  introduced earlier; i.e.,  $J_{\text{sweep}}^{1n}$  accounts for the influence of the shape of that part of the barrier which is in the window.

Equations (5.50) and (5.54) allow us to achieve our objective  $J = J(V)$ , after some algebraic manipulation [32-34]. Using the interface transport factors, this relationship between the current density  $J$  and the voltage  $V$  is

$$\begin{aligned} J &= F_{1n} F_{2n} F_I J_L - F_{1n} J_r^1 (e^{V/kT} - 1) - F_{1n} F_I J_r^2 (e^{V/kT} - 1) \\ &\quad - F_{1n} F_{2n} F_I J_{\text{dif}} (e^{V/kT} - 1) \end{aligned} \quad (5.56)$$

This is the long-pursued expression for the  $J-V$  characteristic of a heterojunction solar cell. It differs from Eq. (5.50) in that  $e^{E_{Fn}(W_1^-)/kT}$  has been replaced with  $e^{V/kT}$ , and in the appearance of a new transport factor  $F_{1n}$  defined by

$$F_{1n} \equiv \frac{J_{\text{sweep}}^{1n}}{J_r^1 + F_I J_r^2 + F_{2n} F_I J_{\text{dif}} + J_{\text{sweep}}^{1n}} \quad (0 \leq F_{1n} \leq 1) \quad (5.57)$$

It is important to realize that the transport factors in Eq. (5.56) can be functions of voltage developed and illumination although all are  $0 \leq F \leq 1$ .

<sup>†</sup> This is a very reasonable assumption since the window is a wide-gap semiconductor.

It is also important to note that the prefactors  $J_r^1$  and  $J_r^2$  can also be functions of voltage and illumination. The dependence on illumination can arise since light may change localized state populations and the barrier shape.

### 5.2.3.2 Discussion

The current-voltage ( $J-V$ ) characteristic of a heterojunction solar cell given by Eq. (5.56) represents an optimistic assessment which only considers interface recombination through paths 1 and 2 and bulk diffusion-recombination as the sources of the bucking current. There can be other parallel paths of bucking current flow such as space-charge region recombination current and interface multistep tunneling (see Fig. 3.21) [36–39]. Even so, Eq. (5.56) predicts that a heterojunction can only achieve performance that is, at best, as good as that of an equivalent homojunction solar cell. By equivalent homojunction we mean one composed of the absorber semiconductor and one whose emitter photocurrent is negligible and whose emitter bucking current has been suppressed.<sup>†</sup> Thus, Eq. (5.56) shows analytically that the heterojunctions of Fig. 5.9 have the potential of removing the problems associated with suppressing the emitter bucking current of a homojunction; but, as can be seen from the equation, there are a great deal of potential problems associated with the metallurgical junction which may cause the advantage of a heterojunction solar cell to be lost. Of course, heterojunctions always have the advantage of allowing semiconductors which cannot be doped both  $n$  and  $p$  to be used, and they may offer advantages under concentration (not included in our analysis) as discussed in Section 5.2.1.2.

We note that Eq. (5.56) is of the form indicated in Eq. (5.20) where the photocurrent density is

$$J_{ph}(\Phi_0, V) = (F_{1n} F_{2n} F_l) J_L \quad (5.58)$$

and the bucking current density is

$$\begin{aligned} J_{bk}(\Phi_0, V) = & F_{1n} J_r^1 (e^{V/kT} - 1) + (F_{1n} F_l) J_r^2 (e^{V/kT} - 1) \\ & + (F_{1n} F_{2n} F_l) J_{dif} (e^{V/kT} - 1) \end{aligned} \quad (5.59)$$

Equation (5.59) may also be written as

$$J_{bk} = J_{bk}|_1 + J_{bk}|_2 + J_{bk}|_{dif} \quad (5.60)$$

<sup>†</sup> To give the same performance as the equivalent homojunction, the heterojunction must have  $J_r^1 = 0$  and  $J_r^2 = 0$  and  $F_{1n} = F_{2n} = F_l = 1$ . Forcing these transport factors equal to unity is the same as saying  $E_{Fn}$  is flat across the entire junction.

where

$$J_{bk}|_1 = F_{1n} J_r^1 (e^{V/kT} - 1) \quad (5.61)$$

$$J_{bk}|_2 = F_{1n} F_1 J_r^2 (e^{V/kT} - 1) \quad (5.62)$$

and

$$J_{bk|dif} = F_{1n} F_{2n} F_1 J_{dif} (e^{V/kT} - 1) \quad (5.63)$$

are the three components of the bucking current.

The photocurrent term [Eq. (5.58)] of the  $J-V$  characteristic is proportional to  $\Phi_0$ . It can also be seen to be a function of the voltage  $V$  developed in the cell through the transport factors. The photocurrent density is constant and always equal to the short-circuit current density  $J_{sc}$  only if the transport factors  $F_{1n}$ ,  $F_{2n}$ , and  $F_1$  are identically equal to one. The bucking-current term [Eq. (5.59)] of the  $J-V$  characteristic is explicitly a function of voltage through the diode factor ( $e^{V/kT} - 1$ ) and implicitly a function of voltage through the transport factors and the interface recombination. It, too, can be a function of illumination as mentioned.

On the basis of the explicit dependence on voltage seen in Eq. (5.59), one might expect plots of  $\ln J_{bk}$  versus voltage to be straight lines for  $V > kT$ . However, due to the interaction of the voltage dependence of the diode factor ( $e^{V/kT} - 1$ ) and the voltage dependence in the transport factors and in the interface-recombination prefactors  $J_r^1$  and  $J_r^2$ , plots of  $\ln J_{bk}$  versus voltage can actually differ appreciably from straight lines for  $V > kT$ . This can occur even without the addition of the possible parallel path of bucking current provided by multistep tunneling and without the further complication of including tunneling in the prefactor  $J_{th}$  for junctions with spikes (Fig. 5.9b). Due to the possible influence of light on the barrier shape and on localized state populations, the transport factors and recombination prefactors in Eq. (5.59) may be different in the dark and under illumination. This implies that the dark  $J-V$  characteristic (the so-called diode characteristic) of a heterojunction solar cell and  $J_{bk}$  versus  $V$  under illumination need not be identical.

We now explore the transport factors and the interface transport in some detail. We shall group this examination into (1) the transport factor  $F_{2n}$ , (2) the interface recombination prefactor  $J_r^2$ , (3) the thermionic emission prefactor  $J_{th}$ , (4) the transport factor  $F_1$ , (5) the interface recombination prefactor  $J_r^1$ , and (6) the transport factor  $F_{1n}$ .

(1) *The Transport Factor  $F_{2n}$*  If the transport factor  $F_{2n}$  has its upper bound value ( $F_{2n} = 1$ ),  $E_{Fn}$  is flat across that part of the band-bending region which lies in the absorber. Put physically,  $F_{2n} = 1$  means that this

part of the band-bending region, which lies in the absorber, is acting as an effective sink for photogenerated carriers diffusing out of the quasi-neutral region of the absorber. To determine the dependence of  $F_{2n}$  on material parameters and to make sure that in optimizing  $F_{2n}$ , we do not detrimentally affect  $J_L$  or  $J_{dif}$ , we now closely examine this transport factor.

It follows from Eq. (5.48) that the key to  $F_{2n}$  lies in the term  $J_{sweep}^{2n}$  and it follows from Eq. (5.32) that the key to  $J_{sweep}^{2n}$  lies in evaluating the integral  $\int_{W_1}^{W_1 + W_2} e^{-\psi_2/kT} dx$ . If we use the approximation given by Eq. (3.17) to establish spatial dependence of  $\psi_2$ , we find

$$\psi_2 = (eN_A/2\varepsilon_2)(x - W_1)^2 - (eN_A W_2/\varepsilon_2)(x - W_1) + V_{bi2} - V_2 \quad (5.64)$$

which results in [33]

$$\int_{W_1}^{W_1 + W_2} e^{-\psi_2/kT} dx = \frac{\pi^{1/2}}{2} L_{D2} \operatorname{erf} \left\{ \left[ \frac{V_{bi2} - V_2}{kT} \right]^{1/2} \right\} \quad (5.65)$$

where  $L_{D2}$  is the extrinsic Debye length for material 2 [defined in Eq. (3.37) for  $n$ -type material]. The quantity  $L_{D2}$  is shown as a function of doping density in Fig. 5.11.

By using Eq. (5.65),  $J_{sweep}^{2n}$  may be expressed as

$$J_{sweep}^{2n} = \left( \frac{2}{\pi^{1/2}} \right) \left( e n_{p0} \mu_{n2} \frac{kT}{L_{D2}} \right) \operatorname{erf} \left[ \left( \frac{V_{bi2} - V_2}{kT} \right)^{1/2} \right] \quad (5.66)$$

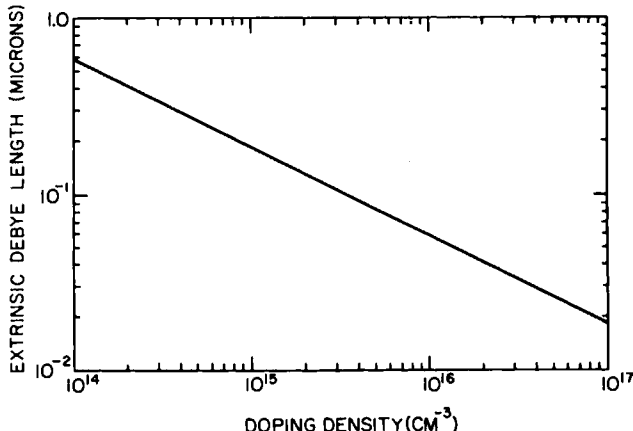


Fig. 5.11 Extrinsic Debye length [defined in Eq. (3.37)]  $L_{D2}$  versus doping density  $N_A$ . A temperature of 300°K and a relative dielectric constant of 12 have been assumed.  $L_{D2} = [2\varepsilon_s kT/eN_A]^{1/2}$ .

which allows  $F_{2n}$  to be written, with the help of Eq. (5.27B), as

$$F_{2n} = \left\{ \frac{L_{D2}}{L_n} \Theta_B \operatorname{erf} \left[ \left( \frac{V_{bi2} - V_2}{kT} \right)^{1/2} \right] + 1 \right\}^{-1} \quad (5.67)$$

Since the error function is positive and always  $\leq 1.0$ , it follows that whether or not  $F_{2n}$  is unity depends on the ratio  $(\Theta_B L_{D2})/L_n$ . In fact, it is seen from Eq. (5.67) that we would like this ratio to be  $\ll 1$ . Striving for this goal does not detrimentally affect  $J_L$  or  $J_{dif}$  as may be determined from Eqs. (5.26) and (5.27).

It follows from Fig. 5.11 that the Debye length appearing in Eq. (5.67) is such that  $L_{D2} < 1 \mu\text{m}$  for doping levels normally encountered in this region of a solar cell. For "good" single-crystal absorber semiconductors,  $L_n$  values as high as of the order of  $100 \mu\text{m}$  are possible [42]. For properly designed absorbers (material and back-contact)  $\Theta_B \leq 1.0$  is attainable as follows from Fig. 5.10 and Section 4.2.3. Consequently,  $F_{2n} = 1.0$  is expected for single-crystal materials. This means  $J_{sweep}^{2n}$  dominates  $J_{dif}$  and, equivalently, the quasi-Fermi level  $E_{Fn}$  is flat across that part of the barrier which lies solely in the absorber. In this case, the region  $W_1 \leq x \leq W_1 + W_2$  is acting as a very effective sink for photogenerated minority carriers coming out of the absorber base.

Looking at the other extreme in materials, we see that diffusion lengths can be small in some amorphous semiconductors. For example,  $L_p \lesssim 4 \times 10^{-2} \mu\text{m}$  is reported for some hydrogenated *a*-Si [43]. The representative value of  $\Theta_B$  for amorphous materials may be estimated from Fig. 5.10 by noting that  $\beta_5 = L/L_n$  will be  $\geq 1.0$  for this class of semiconductors since  $L/L_n \gtrsim 1/\alpha L_n$  is a necessity and  $1/\alpha \simeq 1.0 \mu\text{m}$  for *a*-Si, for example [43]. As a result, we find  $\Theta_B \simeq 1.0$  for amorphous absorbers is expected. Based on these approximations, it is seen from Eq. (5.67) that  $F_{2n} < 1.0$  (i.e.,  $J_{dif} \gtrsim J_{sweep}^{2n}$ ) is a possibility for amorphous absorber heterojunctions designed such that the photogenerated current is collected by the barrier acting as a sink for diffusion. Given that  $J_L$  itself can fall far short of its potential value due to poor diffusion lengths in the quasi-neutral region, it becomes apparent that heterojunction cell designs that rely on drift alone to collect the photocarriers may be the best approach for some amorphous absorber cells; i.e., *p-i-n* type heterojunctions analogous to the *p-i-n* homojunctions first discussed in Section 4.2.1 are probably the better *p-n* heterojunction structure when amorphous absorbers with poor diffusion lengths are employed.

In cases where  $F_{2n}$  is not identically equal to unity, it may be voltage dependent due to the presence of the error function. The factor  $F_{2n}$  can be illumination dependent because light changes the localized state populations and, consequently,  $L_{D2}$  and the barrier shape.

(2) *The Interface Recombination Prefactor  $J_r^2$*  The recombination path 2 of Fig. 5.9 has been characterized in this analysis by the prefactor  $J_r^2$  appearing in Eq. (5.56). To examine  $J_r^2$  we begin with its definition [Eq. (5.38)] which may be rearranged into the form

$$J_r^2 = \left[ n_{ip} (e\langle v \rangle \Omega_2 N_1^{II}) \right] \left/ \left\{ \exp \left( \frac{E_{g2}}{2kT} - \frac{V_p}{kT} - \frac{V_{bi2}}{kT} + \frac{V_2}{kT} \right) + 2 \right. \right. \\ \left. \left. + \exp \left[ - \left( \frac{E_{g2}}{2kT} - \frac{V_p}{kT} - \frac{V_{bi2}}{kT} + \frac{V_2}{kT} \right) \right] \exp \left[ \frac{E_{Fn}(W_1^+)}{kT} \right] \right\} \right] \quad (5.68)$$

Here  $n_{ip}$  is the intrinsic number density and  $E_{g2}$  is the gap of the absorber;  $V_p$  is our usual parameter for locating the Fermi level in thermodynamic equilibrium with respect to the valence-band edge in the absorber. Equation (5.68) assumes for convenience equal thermal velocities  $\langle v \rangle$  and equal capture cross section  $\Omega_2$  for holes and electrons (see Section 2.6.1.3) in addition to assuming  $N_c = N_v$ . Use is also made of the fact that the most effective recombination centers for Eq. (5.38) are those localized states in the middle of the gap.

It follows from Eq. (5.68) that the upper bound on  $J_r^2$  is such that

$$J_r^2 \leq e\langle v \rangle \Omega_2 N_1^{II} (n_{ip}/4) \quad (5.69)$$

A plot of  $[(J_r^2)/(e\langle v \rangle \Omega_2 N_1^{II} n_{ip})]$  versus  $[(E_{g2}/2kT) - (V_p/kT) - (V_{bi2}/kT)]$ , which is pertinent to thermodynamic equilibrium [ $V_2 = E_{Fn}(W_1^+) = 0$ ], is presented in Fig. 5.12. It shows that  $J_r^2$  peaks very sharply to the value given in Eq. (5.69).

It is now possible to examine the behavior of the prefactor  $J_r^2$  when the cell is under illumination and developing voltage by using Eqs. (5.68) and (5.69) and Fig. 5.12. To begin, we note that Fig. 5.12 and Eq. (5.68) show that there are three ranges of behavior for  $J_r^2$  in thermodynamic equilibrium. These are defined as follows:

*Case I*

$$J_r^2 \simeq p_{p0} e^{-V_{bi2}/kT} [e\langle v \rangle \Omega_2 N_1^{II}] \quad (5.70)$$

*Case II*

$$J_r^2 \simeq (n_{ip}/4) [e\langle v \rangle \Omega_2 N_1^{II}] \quad (5.71)$$

*Case III*

$$J_r^2 \simeq n_{p0} e^{V_{bi2}/kT} [e\langle v \rangle \Omega_2 N_1^{II}] \quad (5.72)$$

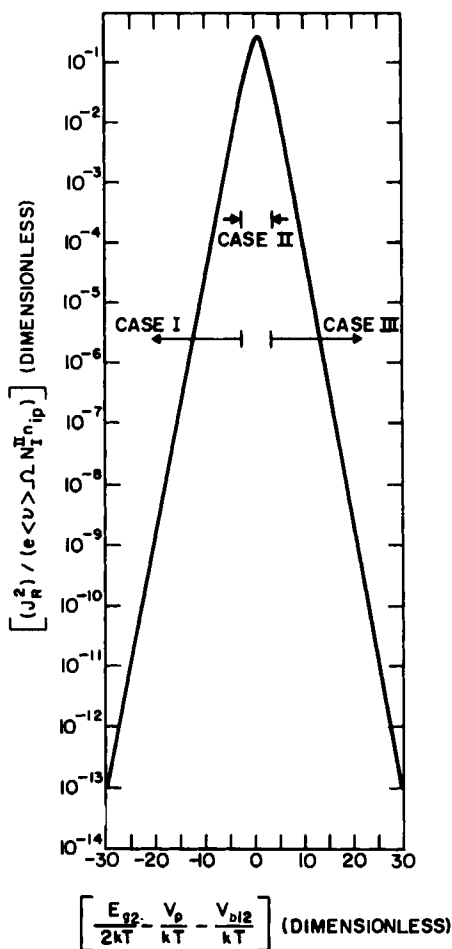


Fig. 5.12 The prefactor  $J_r^2$ , characterizing recombination through path 2 at the interface of Fig. 5.9, versus  $(E_{g2}/2kT - V_p/kT - V_{b12}/kT)$ . In this plot  $J_r^2$  has been normalized by dividing its maximum value by  $e < v > \Omega_2 N_1^H n_{ip}$ . The same curve is obtained for a normalized  $J_r^1$  versus  $(G/2kT - V_p/kT - V_{b12}/kT)$ ; see text.

These three regimes of behavior are denoted in Fig. 5.12. They correspond to the Fermi level at  $x = W_1^+$  being in the top of the absorber gap (case I), being at the middle of the absorber gap (case II), and being in the bottom of the absorber gap (case III) in thermodynamic equilibrium. It is clear in Fig. 5.12 that  $J_r^2$  for both cases I and III is much smaller than  $J_r^2$  for case II. In case I, holes control  $J_r^2$ ; in case II, both carriers control  $J_r^2$ ; and in case III, electrons control  $J_r^2$ .

Now what happens to  $J_r^2$  when the cell is under illumination and a voltage is developed? If the heterojunction is such that it may be categorized as case II in thermodynamic equilibrium, then

$$J_r^2 = (n_{ip}/4)[e\langle v \rangle \Omega_2 N_i^{II}][4/(e^{V_2/kT} + 2 + e^{V_1/kT})] \quad (5.73)$$

where we have assumed  $E_{Fn}(W_1^+) = V$  as it should be in a solar cell structure. This says that if the Fermi level is at mid-gap of the absorber at  $x = W_1$  in thermodynamic equilibrium, then the component of the bucking current  $J_{bk}|_2$  due to path 2 is seen from Eq. (5.59) to be<sup>†</sup>

$$J_{bk}|_2 = (n_{ip}/4)[e\langle v \rangle \Omega_2 N_i^{II}][4e^{V/kT}/(e^{V_2/kT} + e^{V_1/kT})] \quad (5.74)$$

for  $V > kT$ . An  $n$  factor may be introduced by requiring that the expression

$$J_{bk}|_2 = n_{ip}[e\langle v \rangle \Omega_2 N_i^{II}]e^{V/nkT} \quad (5.75)$$

and Eq. (5.74) be identical. It is seen from Eqs. (5.74) and (5.75) that the  $n$  factor of Eq. (5.75) is  $\geq 1.0$  and is a function of voltage since  $V_1 = V_1(V)$  and  $V_2 = V_2(V)$ , in general [44]. These functions  $V_1 = V_1(V)$  and  $V_2 = V_2(V)$  can be as simple as those given by Eqs. (3.24) and (3.25), valid when the interface-state populations do not vary with  $V$ , or as complex as those given by Eq. (3.25) and (3.27), valid when the interface-state populations do vary with  $V$ .

Plots of  $J_{bk}|_2$  versus  $V$  for case II are presented in Fig. 5.13. The figure shows this component of a heterojunction solar cell  $J-V$  characteristic for two of the infinite sets of  $V_1 = V_1(V)$  and  $V_2 = V_2(V)$  possible in case II. These two examples are (a) the voltage is developed entirely in the absorber ( $V_1 = 0$ ,  $V_2 = V$ ) and (b) the voltage is developed equally in the absorber and window ( $V_1 = V_2 = V/2$ ). For situation (a) the  $n$  factor is infinite<sup>‡</sup> and the slope of the  $J_{bk}|_2$  is not temperature dependent; for situation (b) the  $n$  factor is 2 and the slope of the  $\ln J_{bk}|_2$  versus voltage is  $1/(2kT)$ . The curves of Fig. 5.13 for case II are based on an intrinsic number density of  $n_{ip} = 10^{10} \text{ cm}^{-3}$ , a thermal velocity of  $\langle v \rangle = 10^7 \text{ cm/sec}$ , a capture cross section of  $\Omega_2 = 4 \times 10^{-16} \text{ cm}^2$  (using the geometrical cross section of an atom), and an  $N_i^{II}$  arising from a lattice mismatch of 1% [see Eq. (5.7)].

For heterojunctions where case I or III exists in the absorber at  $x = W_1^+$  in thermodynamic equilibrium, we see that Eq. (5.68) may be written as

$$J_r^2 = n_{p0}e^{V_{bi2}/kT}[e\langle v \rangle \Omega_2 N_i^{II}][e^{V_2/kT} + (n_{p0}e^{V_{bi2}/kT}/p_{p0}e^{-V_{bi2}/kT})e^{V_1/kT}]^{-1} \quad (5.76)$$

<sup>†</sup> Since  $E_{Fn}(W_1^+) = V$  is assumed here,  $F_{1n} = F_1 = 1$  is also being assumed. One implies the other.

<sup>‡</sup> The  $n$  factor for a recombination current at the interface need not always equal 2, as this discussion and Fig. 5.13 demonstrates.

This says that, if the Fermi level at zero bias is in the top of the gap (case I) or in the bottom of the gap (case III) of the adsorber at  $x = W_1$ , then the component of the bucking current  $J_{bk}|_2$  due to path 2 takes the form

$$J_{bk}|_2 = n_{p0} e^{V_{bi2}/kT} [e \langle v \rangle \Omega_2 N_1^{II}] \left[ \frac{e^{V/kT}}{e^{V_2/kT} + (n_{p0} e^{V_{bi2}/kT} / p_{p0} e^{-V_{bi2}/kT}) e^{V_1/kT}} \right] \quad (5.77)$$

for  $V > kT$ . In Eqs. (5.76) and (5.77),  $n_{p0} e^{V_{bi2}/kT} \gg n_{ip}$  and  $p_{p0} e^{-V_{bi2}/kT} \ll n_{ip}$  for case I, whereas  $n_{p0} e^{V_{bi2}/kT} \ll n_{ip}$  and  $p_{p0} e^{-V_{bi2}/kT} \gg n_{ip}$  for case III.

Plots of  $\ln J_{bk}|_2$  versus  $V$  for cases I and III are also presented in Fig. 5.13. For case I, two possible situations are assumed: (c) the voltage is developed entirely in the absorber ( $V_1 = 0$ ,  $V_2 = V$ ), and (d) the voltage is developed equally in the absorber and window ( $V_1 = V_2 = V/2$ ). For case III two possible situations are assumed: (e) the voltage is developed entirely in the window ( $V_1 = V$ ,  $V_2 = 0$ ), and (f) the voltage is developed equally in the

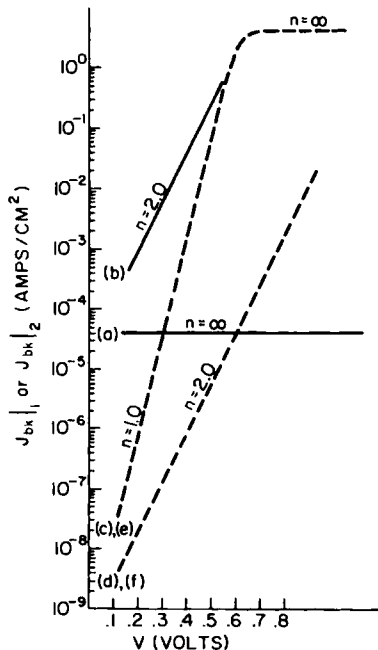


Fig. 5.13 Plots of  $J_{bk}|_1$  and  $J_{bk}|_2$  versus voltage for  $n_{ip} = 10^{10} \text{ cm}^{-3}$ ,  $\langle v \rangle = 10^7 \text{ cm/sec}$ ,  $\Omega = 4 \times 10^{-6} \text{ cm}^2$ , and a 1% lattice mismatch. Case II behavior: (a)  $V_1 = 0$  and  $V_2 = V$ ; (b)  $V_1 = V_2 = V/2$ . Case I behavior: (c)  $V_1 = 0$  and  $V_2 = V$ ; (d)  $V_1 = V_2 = V/2$ . Case III behavior: (e)  $V_1 = V$  and  $V_2 = 0$ ; (f)  $V_1 = V_2 = V/2$ . Dividing these curves by  $e^{V/kT}$  gives the voltage dependence of the prefactor  $J_t^1$  or  $J_t^2$  for  $V > kT$ .

absorber and window ( $V_1 = V_2 = V/2$ ). The curves shown are based on  $V_p + V_{\text{bi}2} - E_{g2}/2 = 0.3$  (Fermi level is 0.3 eV above mid-gap at  $x = W_1^+$  at zero bias) for case I and on  $V_p + V_{\text{bi}2} - E_{g2}/2 = -0.3$  (Fermi level is 0.3 eV below mid-gap at  $x = W_1^+$  at zero bias) for case III.

Curve (c) of case I in Fig. 5.13 is seen from Eq. (5.77) to obey

$$J_{\text{bk}}|_2 = p_{p0} e^{-V_{\text{bi}2}/kT} [e \langle v \rangle \Omega_2 N_1^{\text{II}}] e^{V/kT} \quad (5.78)$$

for  $V > kT$ , until a voltage is reached such that

$$V = 2V_p + 2V_{\text{bi}2} - E_{g2} \quad (5.79)$$

For voltages such that  $V > 2V_p + 2V_{\text{bi}2} - E_{g2}$ , which means for  $V > 0.6$  eV for the parameters being employed, curve (c) obeys

$$J_{\text{bk}}|_2 = n_{p0} e^{V_{\text{bi}2}/kT} [e \langle v \rangle \Omega_2 N_1^{\text{II}}] \quad (5.80)$$

as follows from Eq. (5.77). Curve (d), on the other hand, obeys one expression for the whole range of voltages  $>kT$ ; viz.,

$$J_{\text{bk}}|_2 = p_{p0} e^{-V_{\text{bi}2}/kT} [e \langle v \rangle \Omega_2 N_1^{\text{II}}] e^{V/2kT} \quad (5.81)$$

For the simple expressions assumed for the functions  $V_1 = V_1(V)$  and  $V_2 = V_2(V)$  for curve (c) of case I, which are  $V_1 = 0$  and  $V_2 = V$ , the  $n$  factor seen in Fig. 5.13 has a region of behavior where  $n = 1$  [holes, which control recombination in this region of curve (c), are increasing in population according to  $e^{V/kT}$ ] and a region of behavior where  $n = \infty$  [electrons, which control recombination in this region of curve (c), have a fixed population at  $x = W_1^+$ , since  $V_2 = V$ ]. For the simple expressions assumed for the function  $V_1 = V_1(V)$  and  $V_2 = V_2(V)$  for curve (d) of case I, which are  $V_1 = V/2$  and  $V_2 = V/2$ , the  $n$  factor seen in Fig. 5.13 is 2.0. This holds for all  $V > kT$  since holes control recombination for the whole of curve (d) and both hole and electron populations increase according to  $e^{V/2kT}$ . Much more complicated functional relationships are possible [44] for  $V_1 = V_1(V)$  and  $V_2 = V_2(V)$  as follows from Eqs. (3.24)–(3.27); these could lead to  $n$  factors for case I that are functions of voltage.

Curve (e) of case III in Fig. 5.13 is seen from Eq. (5.77) to obey

$$J_{\text{bk}}|_2 = n_{p0} e^{V_{\text{bi}2}/kT} [e \langle v \rangle \Omega_2 N_1^{\text{II}}] e^{V/kT} \quad (5.82)$$

for  $V > kT$ , until a voltage is reached where

$$V = E_{g2} - 2V_p - 2V_{\text{bi}2} \quad (5.83)$$

For voltages exceeding the value given by Eq. (5.83), the recombination current for curve (e), case III, is

$$J_{\text{bk}}|_2 = p_{p0} e^{-V_{\text{bi}2}/kT} [e \langle v \rangle \Omega_2 N_1^{\text{II}}] \quad (5.84)$$

With the parameters being used for this example of case III behavior, Eq. (5.84) applies for  $V > 0.6$  eV. For the situation of curve (f),  $J_{bk|2}$  obeys

$$J_{bk|2} = n_{p0} e^{V_{bi2}/kT} [e\langle v \rangle \Omega_2 N_1^H] e^{V/2kT} \quad (5.85)$$

for the entire range  $V > kT$ . It is seen from Fig. 5.13 that curve (e) is the same as curve (c) and curve (f) is the same as curve (d), since the case I examples have the Fermi level 0.3 eV above, and the case III examples have the Fermi level 0.3 eV below, the absorber mid-gap at  $x = W_1^+$  in thermodynamic equilibrium or zero bias conditions for the examples chosen.

As a result of this discussion, we can draw several conclusions regarding the recombination current  $J_{bk|2}$  flowing through path 2:

(a) The recombination current  $J_{bk|2}$  need not have an  $n$  factor of 2. In fact, Fig. 5.13 shows that  $n$  factors from 1 to  $\infty$  are possible for this current. The  $n$  factor can be a function of  $V$ ; the functional form of  $n = n(V)$  depends on the Fermi-level position at zero bias and on  $V_1 = V_1(V)$  and  $V_2 = V_2(V)$ .

(b) The current density  $J_{bk|2}$  can determine  $V_{oc}$ . That is,  $J_{ph}$  values are of the order of tens of mA/cm<sup>2</sup> at AM1 and  $J_{bk|2}$  can be of, or exceed, that order of magnitude for  $V \lesssim E_g$  as seen in Fig. 5.13.

(c) To reduce the strength of  $J_{bk|2}$  it is seen from Fig. 5.13 that several courses of action appear feasible. One is to design the heterojunction solar cells so that  $E_{Fn}(W_1)$  is at the absorber mid-gap in thermodynamic equilibrium and the cell voltage is developed entirely in the absorber. However, this is not an acceptable solution, since it limits  $V_{oc}$  to  $E_{g2}/2$ . The best course is to have  $E_{Fn}(W_1)$  as far as possible from the absorber mid-gap in thermodynamic equilibrium and to have, if possible,  $V_1 = V_1(V)$  and  $V_2 = V_2(V)$  such that there is some splitting of the cell voltage between absorber and window.

(d) It is important to note that the current density  $J_{bk|2}$  can be reduced by increasing the absorber gap  $E_{g2}$  only for case II and case III situations.

(e) In heterojunction solar cell analysis it is frequently assumed that interface recombination currents such as that flowing through path 2 of Fig. 5.9 can be written as

$$J_{bk|2} = eN_c S_i e^{-\phi'/kT} e^{V/kT} \quad (5.86)$$

(valid for  $V > kT$ ) where  $S_i$ , the interface recombination speed, is a constant given by [16, 39–41]

$$S_i = \langle v \rangle \Omega_2 N_1^H \quad (5.87)$$

and  $\phi'$ , the activation energy, is a constant given by [16, 39–41]

$$\phi' = E_{g2}/2 - V_p - V_{bi2} \quad (5.88)$$

However, it follows from Eqs. (5.74)–(5.85) that this model is not always valid. Put simply, it is not always possible to write  $J_{bk|2}$  in the form of Eq.

(3.63) since the carrier limiting the recombination is not always that which is the minority carrier in the bulk absorber. In fact, we see that the carrier controlling the process can change with  $V$ . For situations examined in Fig. 5.13, the model of Eqs. (5.86)–(5.88) holds only for the first section of curve (e) of case III. The validity of the model given by Eq. (5.86)–(5.88) depends on two things: the position of  $E_F$  at  $x = W_1^+$  in thermodynamic equilibrium or zero bias and the functional forms of  $V_1 = V_1(V)$  and  $V_2 = V_2(V)$ .

(3) *Thermionic Emission Prefactor  $J_{th}$*  Assuming electrons conserve total energy and transverse momentum as they cross over the conduction-band barrier at the metallurgical junction ( $x = W_1$  of Fig. 5.9) allows the prefactor  $J_{th}$  to be expressed as [35]

$$J_{th} = \left[ \frac{2e}{\hbar(2\pi)^3} e^{-\phi/kT} \int_0^\infty e^{-E_T/kT} \left[ \iint_S dk_y dk_z \right] dE_T \right] \quad (5.89a)$$

This equation may be cast into the form

$$J_{th} = A^* T^2 e^{-\phi/kT} \quad (5.89b)$$

Here  $A^*$  is an effective Richardson constant defined in terms of the integrals in Eq. (5.89a). Equations (5.89) are valid for crystalline and polycrystalline heterojunction solar cells.

In this formulation for  $J_{th}$  the  $yz$  plane has been chosen as the plane of the junction; hence the  $\mathbf{k}$  space integration involves  $k_y$  and  $k_z$  integrations. These are over an area  $S$  defined as the mutual region of overlap (or some subregion thereof, as discussed in Ref. [35]) of the shadow onto the  $yz$  plane of an energy surface of the absorber and of the shadow onto the  $yz$  plane of the corresponding surface (same total energy) of the window [35]. The overlapping of these shadows, for a given total energy, represents conservation of momentum in the plane of the junction. Examples are seen in Fig. 5.14. The energy  $E_T$  appearing in Eq. (5.89) is measured from the top of

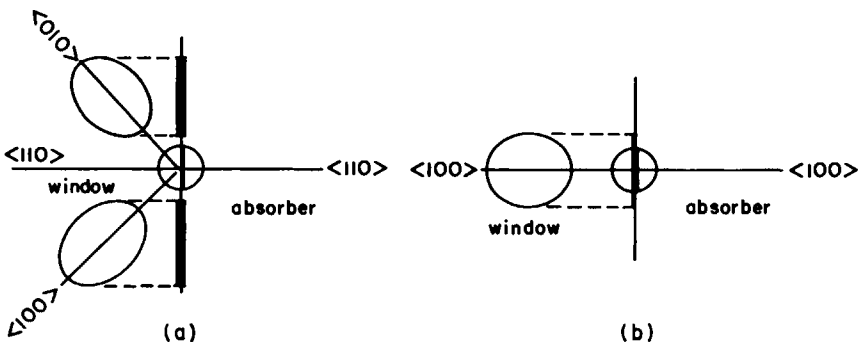


Fig. 5.14 The energy surface projections for (a) a (100) junction and (b) a (110) junction.

the barrier at  $x = W_1$ ; i.e., it is measured from  $\phi_A = E_{g2} - V_p - V_{bi2}$  for Fig. 5.9a and from  $\phi_B = E_{g2} - V_p - V_{bi2} + \chi_2 - \chi_1$  for Fig. 5.9b where  $\phi_A$  and  $\phi_B$  are the two possible values for the  $\phi$  appearing in Eq. (5.89).

Equation (5.89) expresses the commonly recognized observation that spikes are disadvantageous to photocurrent collection [45, 46]. For Fig. 5.9b the  $\phi$  in Eq. (5.89) is increased by  $\chi_2 - \chi_1$  for given values of  $E_{g2}$ ,  $V_{bi2}$ , and  $V_p$ . Thus the presence of the spike seen in the conduction band in Fig. 5.9b greatly reduces the effectiveness of this over-the-barrier channel of flow. This causes backed-up photogenerated electrons [ $E_{Fn}(W_1^+)$  must increase] to short out through interface recombination path 2, if present, or to back-diffuse away from the junction [33-35].

Equation (5.89) allows another interface effect to be pointed out: band structure can also be very important in determining the effectiveness of this conservative, over-the-barrier channel in carrying photogenerated electrons [35]. That is, the  $S$  overlap region of integration may yield very different values depending on the semiconductors under consideration and depending on the crystallographic plane of the junction. This has implications for crystalline and polycrystalline  $p-n$  heterojunction solar cell design and evaluation.

To demonstrate this point, consider a junction (Fig. 5.9a) between two semiconductors with cubic structure. Let the absorber have constant energy surfaces for the conduction band which are spherical and centered at  $\Gamma$  in the Brillouin zone (see Chapter 2). Let the window semiconductor have constant energy surfaces which are ellipsoids (with transverse effective mass  $m_T$  and longitudinal effective mass  $m_L$ ) located in  $k$  space along the  $\langle 100 \rangle$  axes at  $X$  in the Brillouin zone (see Chapter 2). For a  $(100)$  junction between these two materials, a surface of energy  $E_T$  in the absorber projects onto the  $(100)$  plane an area of  $2\pi m_S E_T / \hbar^2$ , where  $m_S$  is the effective mass for these spherical constant energy surfaces. From Fig. 5.9 it is seen that the corresponding energy (determined by conservation of total energy) in the window semiconductor, measured from the conduction-band edge, is  $E_T + \chi_1 - \chi_2$ . There are six ellipsoids with this energy; however, only those along the  $[100]$  axis have projections on the  $(100)$  junction plane which overlap the  $E_T$  surface of the absorber. These project an area of  $2\pi m_T (E_T + \chi_1 - \chi_2) / \hbar^2$ , where  $m_T$  is the transverse effective mass of the ellipsoids. The smaller of these projected areas dictates the  $S$  in Eq. (5.89). For the sake of argument, we assume  $m_S \lesssim m_T$ ; hence  $S = 2\pi m_S E_T / \hbar^2$  and  $J_{th}(100)$  is

$$J_{th}(100) = [4e\pi(kT)^2 m_S / h^3] \exp[-(E_{g2} - V_p - V_{bi2})/kT] \quad (5.90)$$

which gives a Richardson's constant of  $A^* = 4e\pi k^2 m_S / h^3$  from Eq. (5.89). For other values of the  $m_S/m_T$  ratio,  $S$ ,  $A^*$ , and  $J_{th}(100)$  can readily be calculated.

Suppose we now consider a (110) junction between these two semiconductors. Again the absorber projects a circle for the  $E_T$  surface as seen in Fig. 5.14. The surfaces of corresponding energy ( $E_T + \chi_1 - \chi_2$ ) in the window semiconductor are each seen to project an ellipse onto the (110) junction plane. From the geometry of Fig. 5.14 it is seen that  $E_{Tm}$ , the minimum value of  $E_T$  (measured in eV) for which overlap is possible, is determined, using  $m_0$  as the free electron mass, by

$$\left( e(E_{Tm}) \left( \frac{m_s}{m_0} \right) \right)^{1/2} + \left( e(E_{Tm} + \chi_1 - \chi_2) \left( \frac{m_L + m_T}{2m_0} \right) \right)^{1/2} = \hbar \left( \frac{\pi}{a} \right) \left( \frac{1}{m_0} \right)^{1/2} \quad (5.91)$$

With a representative lattice parameter value  $a = 4 \text{ \AA}$ , the right-hand side of Eq. (5.91) can be evaluated. As a result, the condition of Eq. (5.91) becomes

$$(E_{Tm})^{1/2} \left( \frac{m_s}{m_0} \right)^{1/2} + (E_{Tm} + \chi_1 - \chi_2)^{1/2} \left( \frac{m_L + m_T}{2m_0} \right)^{1/2} = (4.7)^{1/2} \quad (5.92)$$

It is clear from Eq. (5.92) that  $E_{Tm}$  can be of the order of electron volts. Only for  $E_T \geq E_{Tm}$  is the  $S$  overlap area nonzero in this example. Hence the lower limit on the  $E_T$  integration becomes  $E_{Tm}$  in Eq. (5.89). The consequence of this is that  $J_{th}(110) \ll J_{th}(100)$  in the situation considered or, equivalently,  $A^*(110) \ll A^*(100)$  using Eq. (5.89b).

Several conclusions can be reached regarding the prefactor  $J_{th}$  as a result of this discussion:

(a) For heterojunctions where electrons cross over the barrier at the metallurgical junction via transitions that conserve total energy and transverse momentum, the band structure of the constituents of crystalline and polycrystalline materials can strongly affect  $J_{th}$  due to thermionic emission.

(b) In some heterojunction solar cell structures, phonon emission or absorption may be required at  $x = W_1$  to allow electrons to shift from the band structure of the absorber to the band structure of the window semiconductor, since conservative processes as described by Eq. (5.89) cannot support the photocurrent [35].

(c) In heterojunctions with spikes (see Fig. 5.9b),  $J_{th}$  due to thermionic emission is reduced by  $e^{-(\chi_2 - \chi_1)/kT}$ . In such situations a parallel path of current flow due to tunneling through the spike may dominate [37, 38, 47].

(4) *Transport Factor  $F_I$*  To focus on the competition among the various transport processes available to an electron at  $x = W_1$ , it will be assumed that  $F_{2n} = 1$  allowing Eq. (5.49) to be written as

$$F_I = J_{th} e^{-V_2/kT} / (J_{th} e^{-V_2/kT} + J_r^2 + J_{dif}) \quad (5.93)$$

The question to be addressed now is the following: Under what condition does the inequality  $(J_r^2 + J_{\text{dif}}) < J_{\text{th}} e^{-V_2/kT}$  hold, where this inequality is the requirement for unimpeded collection of the photocurrent across the metallurgical junction? In answering this question we shall limit ourselves to the advantageous configuration provided by heterojunctions of the type seen in Fig. 5.9a.

First we determine the role played by  $J_{\text{dif}}$  in Eq. (5.93) by comparing  $J_{\text{th}}$ , using Eq. (5.89b), and  $J_{\text{dif}}$ , using Eq. (5.27b). Since it was established earlier that  $\Theta_B \lesssim 1$  is expected in solar cell structures, it follows that  $J_{\text{dif}}$  will be negligible if

$$A^* T^2 > (eD_n/L_n)N_c \quad (5.94)$$

where  $N_c$  is the effective density of states for the conduction band. Taking  $N_c = 10^{19} \text{ cm}^{-3}$  and the diffusion velocity  $D_n/L_n \lesssim 10^4 \text{ cm/sec}$  (expected to be the upper limit for crystalline as well as amorphous materials), it is seen that the inequality expressed in Eq. (5.94) holds, if  $A^*$  is of the order of  $120 \text{ A}/(\text{cm} \cdot {}^\circ\text{K})^2$ , which is the value that comes from Eq. (5.90) with  $m_s$  equal to the free electron mass. Even if  $A^*$  were reduced by two orders of magnitude due to lack of overlap of the energy surface shadows, inequality (5.94) would still be expected to hold [34]. Consequently our examination of  $F_1$  reduces to considering

$$F_1 = J_{\text{th}} e^{-V_2/kT} / (J_{\text{th}} e^{-V_2/kT} + J_r^2) \quad (5.95)$$

That is, the competition at  $x = W_1$  is between electrons going across  $x = W_1$  or being lost to recombination through path 2.

It may be seen from Eqs. (5.68) and (5.89b) that Eq. (5.95) for  $F_1$  can be written, after some algebraic manipulation, as<sup>†</sup>

$$F_1 = \left[ 1 + \left( \frac{N_c e \langle v \rangle \Omega_2 N_1^{\text{II}}}{A^* T^2} \right) \times \left( \frac{\exp\left(\frac{V_2}{kT}\right)}{e^{V_2/kT} + 2 \exp\left(\frac{V_p}{kT} + \frac{V_{\text{bi}2}}{kT} - \frac{E_{g2}}{2kT}\right) + \exp\left(\frac{2V_p}{kT} + \frac{2V_{\text{bi}2}}{kT} - \frac{E_{g2}}{kT}\right) \exp\left(\frac{E_{Fn}(W_1^+)}{kT} - \frac{V_2}{kT}\right)} \right)^{-1} \right]^{-1} \quad (5.96)$$

where the expression is valid for the three possible positions (cases I-III) of the Fermi level at  $x = W_1^+$  for thermodynamic equilibrium (or zero bias). Equation (5.96) indicates that the dimensionless ratio  $[(N_c e \langle v \rangle \Omega_2 N_1^{\text{II}})/A^* T^2]$  is critical in determining if  $F_1$  deviates from unity.

Plots of  $F_1$  versus  $V$  are presented in Fig. 5.15a for two case I situations, in Fig. 5.15b for two case II situations, and in Fig. 5.15c for two case III

<sup>†</sup> For simplicity we continue to assume here that  $N_c = N_v$ .

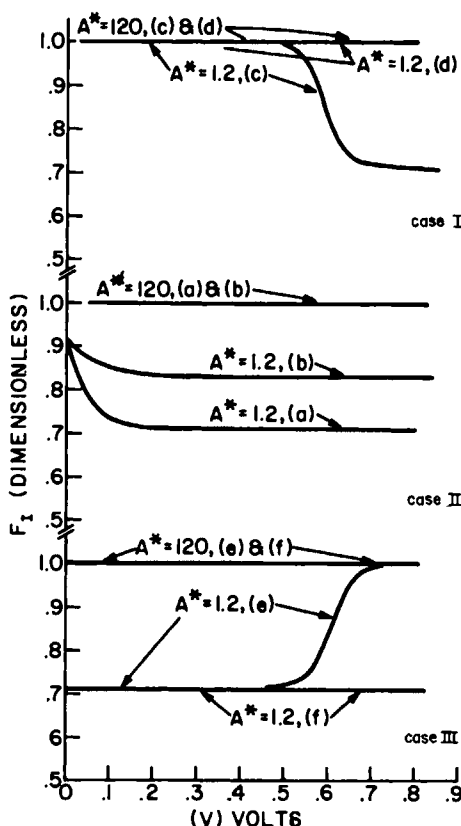


Fig. 5.15 Case I, case II, and case III.  $F_I$  versus voltage for the (a) and (b) situations of case II, the (c) and (d) situations of case I, and the (e) and (f) situations of case III. Curves show two values of  $A^*$ . Notation (a), (b), etc. refers to the set of parameters used for the corresponding curves of Fig. 5.13.

situations. One set of curves assumes  $A^* = 120 \text{ A}/(\text{cm}^{-2}\text{K})^2$  and the other uses  $A^* = 1.2 \text{ A}/(\text{cm}^{-2}\text{K})^2$ . It is assumed in Fig. 5.15 that  $E_{Fn}(W_1^+) = V$ , which is correct provided  $F_{In} = 1$  and  $F_I = 1$ . Therefore, in regions of the figure where  $F_I$  varies with voltage the curve shape shown is approximate, since  $E_{Fn}(W_1^+) \gtrsim V$  for a cell under illumination.

It can be concluded from this discussion and Fig. 5.15 that:

- (a) There is the potential for loss of photocurrent at  $x = W_1$  if

$$N_c e \langle v \rangle \Omega_2 N_I^H / A^* T^2 \gtrsim 0.05 \quad (5.97)$$

- (b) Heterojunction configurations for which the Fermi level is in the top of the absorber gap at  $x = W_1^+$  in thermodynamic equilibrium (case I) are more tolerant of low  $A^*$  values or high ( $\langle v \rangle \Omega_2 N_I^H$ ) values.

(c) The manner in which voltage is developed in a heterojunction cell [i.e.,  $V_1 = V_1(V)$  and  $V_2 = V_2(V)$ ] can affect  $J_r^1$ .

(5) *Recombination Prefactor  $J_r^1$*  The recombination current flowing through path 1 of Fig. 5.9, which represents electrons in the window semiconductor at  $x = W_1^-$  falling into holes in the absorber semiconductor at  $x = W_1^+$ , is characterized by the prefactor  $J_r^1$ . Using Eq. (5.39), the basic definition of  $J_r^1$ , and Eqs. (5.42) and (5.43) allows this prefactor to be written as

$$J_r^1 = [e\langle v \rangle \Omega_1 N_l^1] \times \left[ \frac{N_c \exp\left[-\left(\frac{G}{2kT}\right)\right]}{\exp\left(\frac{G}{2kT} - \frac{V_p}{kT} - \frac{V_{bi2}}{kT} + \frac{V_2}{kT}\right) + 2 + \exp\left[-\left(\frac{G}{2kT} - \frac{V_p}{kT} - \frac{V_{bi2}}{kT} + \frac{V_2}{kT}\right)\right] \exp\left[\frac{E_{Fn}(W_1^-)}{kT}\right]} \right] \quad (5.98)$$

which assumes the thermal velocity and capture cross sections are the same for both carriers. Further, it assumes that the effective density of states for the conduction band in the window has the same value as the effective density of states for the valence band in the absorber. Equation (5.98) uses an effective gap  $G$  defined in terms of the notation in Fig. 5.9 as

$$G = E_{c1}(W_1^-) - E_{v2}(W_1^+) \quad (5.99)$$

i.e.,  $G$  is the difference in electron volts between the window conduction-band edge at  $x = W_1^-$  and the absorber valence-band edge at  $x = W_1^+$ . Equation (5.98) also makes use of the fact that the localized states at  $x = W_1$ , which will be most effective in carrying the current flowing through path 1, will be states located half-way across the effective gap  $G$  at  $x = W_1$ .

Comparing Eq. (5.98) to Eq. (5.68) shows that they are exactly the same except that  $G$  plays the role of  $E_{g2}$  and  $N_c \exp[-(G/2kT)]$  plays the role of  $n_{ip}$  of Eq. (5.68). Consequently, Fig. 5.12 represents a plot of  $[J_r^1/(N_c e^{-G/2kT} e\langle v \rangle \Omega_1 N_l^1)]$  versus  $[(G/2 - V_p - V_{bi2})/kT]$  for thermodynamic equilibrium. When interpreting this plot in terms of  $J_r^1$  it must be realized that case I now means  $E_F$  in the top part of the effective gap, case II now means  $E_F$  in the middle of the effective gap, and case III now means  $E_F$  in the bottom part of the effective gap at thermodynamic equilibrium. The upper bound on  $J_r^1$  is seen from Eq. (5.98) and Fig. 5.12 to be

$$J_r^1 \leq e\langle v \rangle \Omega_1 N_l^1 (N_c e^{-G/2kT}/4) \quad (5.100)$$

The component of the bucking current  $J_{blk1}$  due to path 1 is seen from Eq. (5.61) to be

$$J_{blk1} = J_r^1 (e^{V/kT} - 1) \quad (5.101)$$

if  $F_{1n} = 1$ . It follows that the curves in Fig. 5.13 can be interpreted as giving this function  $J_{bk|1}(V)$  for two case I situations, two case II situations, and two case III situations with  $G$  playing the role of  $E_{g2}$  and  $N_c \exp[G/2kT]$  playing the role of  $n_{ip}$ . When these curves are used to represent  $J_{bk|1}$ , the parameters have been selected such that  $V_p + V_{bi2} - G/2 = 0.3$  for case I,  $V_p + V_{bi2} - G/2 = 0$  for case II, and  $V_p + V_{bi2} - G/2 = -0.3$  for case III.

Several conclusions emerge as a result of this discussion and Fig. 5.13:

- (a) The recombination current  $J_{bk|1}$  need not have an  $n$  factor of 2. In fact  $n$  may vary from 1 to  $\infty$ .
- (b) The current density  $J_{bk|1}$  can determine  $V_{oc}$  since this current density can be of the order of  $J_{ph}$  at AM1 for  $V \lesssim E_g$ .
- (c) To reduce the strength of  $J_{bk|1}$  it is seen from Fig. 5.13 that the best approach is to have  $E_F$ , in thermodynamic equilibrium, removed as far as possible from the middle of the effective gap at  $x = W_1$  and to have, if possible,  $V_1 = V_1(V)$  and  $V_2 = V_2(V)$  such that there is some splitting of the cell voltage between absorber and window.
- (d) It is important to note that the current density  $J_{bk|1}$  can be reduced by increasing the effective gap only for case II and case III situations.
- (e) Care must be exercised when using a model for  $J_{bk|1}$  of the form [39–41]

$$J_{bk|1} = eN_c S_i e^{-\phi'/kT} e^{V/kT} \quad (5.102)$$

(valid for  $V > kT$ ). Here  $S_i$  is taken as a constant given by [16, 39–41]

$$S_i = \langle v \rangle \Omega_1 N_i^l \quad (5.103)$$

and  $\phi'$  is taken as a constant activation energy given by [16, 39–41]

$$\phi' = G - V_p - V_{bi2} \quad (5.104)$$

It follows from Eqs. (5.98) and (5.101) and Fig. 5.13 that Eqs. (5.102)–(5.104) are not always valid. The model does hold if  $E_F$  is in the bottom of the effective gap at  $x = W_1$  at thermodynamic equilibrium and if  $V_1 = V$  and  $V_2 = 0$ .

(f) The states  $N_i^l$  do not coincide in energy with the states  $N_i^H$  unless  $G = E_{g2}$ .

(g) The strong dependence of  $J_{bk|1}$  and  $J_{bk|2}$  on the position of the Fermi level at  $x = W_1$  at zero bias suggests that crossover phenomena such as that seen in Fig. 5.8 could arise in some cases from a reshaping of the barrier due to the presence of light and consequently a repositioning of  $E_F$  in the gaps  $E_{g2}$  and  $G$  at zero bias.

(6) *Transport Factor  $F_{1n}$*  Before delving into an examination of the transport factor  $F_{1n}$  [Eq. (5.57)], an explicit expression for the integral

$\int_0^{W_1} e^{\psi_1/kT} dx$  appearing in the definition of  $J_{\text{sweep}}^{1n}$  [Eq. (5.55)] must be developed. It is seen from Fig. 5.9 that the principal contribution to this integral will come from the top of the barrier in the window semiconductor. In that region  $\psi_1$  can be approximated by

$$\psi_1 = V_{\text{bi}1} - \xi_{\text{M}1}(W_1 - x) \quad (5.105)$$

where  $\xi_{\text{M}1}$ , the maximum electrostatic field in the window material, is a function of voltage given by Eq. (3.22) with  $V_{\text{bi}1}$  replaced by  $(V_{\text{bi}1} - V_1)$ . Using Eq. (5.105) allows the integral  $\int_0^{W_1} e^{\psi_1/kT} dx$  to be evaluated; viz. [33]

$$\int_0^{W_1} \exp(\psi_1/kT) dx = \frac{kT}{\xi_{\text{M}1}} \exp[(V_{\text{bi}1} - V_1)/kT] \quad (5.106)$$

Combining Eqs. (5.27b), (5.68), (5.98), and (5.106) with Eqs. (5.55) and (5.57) permits  $F_{1n}$  to be expressed as<sup>†</sup>

$$\begin{aligned} F_{1n} = & \left[ 1 + \left\{ \left( \frac{\langle v \rangle \Omega_1 N_1^1}{\mu_{n1}} \right) \left( \frac{\varepsilon_{s1}}{2eN_D V_{\text{bi}1}} \right)^{1/2} \right\} \right. \\ & \times \left\{ \frac{\left( \frac{V_{\text{bi}1}}{V_{\text{bi}1} - V_1} \right)^{1/2} \exp \left[ \left( \frac{G}{2kT} - \frac{V_p}{kT} - \frac{V_{\text{bi}2}}{kT} + \frac{V_2}{kT} \right) \right]}{\exp \left[ \left( \frac{G}{2kT} - \frac{V_p}{kT} - \frac{V_{\text{bi}2}}{kT} + \frac{V_2}{kT} \right) \right] + 2 + \exp \left[ - \left( \frac{G}{2kT} - \frac{V_p}{kT} - \frac{V_{\text{bi}2}}{kT} + \frac{V_2}{kT} \right) \right] \exp \left[ \frac{E_{Fn}(W_1^-)}{kT} \right]} \right\} \\ & + \left\{ \exp \left[ - \left( \frac{\chi_1 - \chi_2}{kT} \right) \right] \left( \frac{\langle v \rangle \Omega_2 N_1^1}{\mu_{n1}} \right) \left( \frac{\varepsilon_{s1}}{2eN_D V_{\text{bi}1}} \right)^{1/2} \right\} \\ & \times \left\{ \frac{\left( \frac{V_{\text{bi}1}}{V_{\text{bi}1} - V_1} \right)^{1/2} \exp \left[ \left( \frac{E_{g2}}{2kT} - \frac{V_p}{kT} - \frac{V_{\text{bi}2}}{kT} + \frac{V_2}{kT} \right) \right]}{\exp \left[ \left( \frac{E_{g2}}{2kT} - \frac{V_p}{kT} - \frac{V_{\text{bi}2}}{kT} + \frac{V_2}{kT} \right) \right] + 2 + \exp \left[ - \left( \frac{E_{g2}}{2kT} - \frac{V_p}{kT} - \frac{V_{\text{bi}2}}{kT} + \frac{V_2}{kT} \right) \right] \exp \left[ \frac{E_{Fn}(W_1^+)}{kT} \right]} \right\} \\ & + \left\{ \exp \left[ - \left( \frac{\chi_1 - \chi_2}{kT} \right) \right] \left( \frac{D_n}{L_n \mu_{n1}} \right) \left( \frac{\varepsilon_{s1}}{2eN_D V_{\text{bi}1}} \right)^{1/2} \left\{ \left( \frac{V_{\text{bi}1}}{V_{\text{bi}1} - V_1} \right)^{1/2} \exp \left[ - \left( \frac{V_{\text{bi}2} - V_2}{kT} \right) \right] \right\}^{-1} \right\} \end{aligned} \quad (5.107)$$

This equation uses the fact that  $G = E_{g2} - \chi_1 + \chi_2$ , assumes  $F_1 = F_{2n} = 1$  to focus on the competition among the alternatives available to an electron at  $x = W_1^-$ , and assumes  $\Theta_B = 1$ .

Equation (5.107) shows that  $F_{1n}$  would always have its upper bound value of unity except for the tendency of electrons to be lost through path 1 (first product in braces), the tendency of electrons to be lost through path 2 (second product in braces), and the tendency of electrons to back-diffuse away from the junction (third product in braces). The factors influencing the relative importance of path 1 are seen to be (a) a dimensionless number

$$R_1 \equiv (\langle v \rangle \Omega_1 N_1^1 / \mu_{n1}) (\varepsilon_{s1} / 2eN_D V_{\text{bi}1})^{1/2} \quad (5.108)$$

<sup>†</sup> We continue to assume  $N_{c1} = N_{c2} = N_{v2}$  for simplicity.

which represents the ratio of a recombination speed for path 1 to a drift speed characterizing the depletion region in the window semiconductor, and (b) the position of  $E_F$  (in thermodynamic equilibrium) with respect to the middle of the effective gap  $G$  at  $x = W_1$ . The factors influencing the relative importance of path 2 are seen from Eq. (5.107) to be (a) a dimensionless number

$$R_2 \equiv \exp \left[ -\left( \frac{\chi_1 - \chi_2}{kT} \right) \right] \left( \frac{\langle v \rangle \Omega_2 N_1^{\text{II}}}{\mu_{n1}} \right) \left( \frac{\varepsilon_{s1}}{2eN_D V_{bi1}} \right)^{1/2} \quad (5.109)$$

which represents the ratio of an effective recombination speed for path 2 to a drift speed for the window depletion region, and (b) the position of  $E_F$  (in thermodynamic equilibrium) with respect to the middle of absorber gap  $E_{g2}$ . The factor determining the relative importance of the tendency to back-diffuse away from the junction is

$$R_3 \equiv \exp \left[ -\left( \frac{\chi_1 - \chi_2}{kT} \right) \right] \left( \frac{D_n}{L_n \mu_{n1}} \right) \left( \frac{\varepsilon_{s1}}{2eN_D V_{bi1}} \right)^{1/2} \quad (5.110)$$

which is a dimensionless number representing the ratio of an effective diffusion velocity as seen by an electron at  $x = W_1^-$  to a drift velocity characterizing the window depletion region.

We limit our discussion of  $F_{1n}$  to potentially advantageous heterojunctions of the form seen in Fig. 5.9a and consider a few examples of the behavior that can be exhibited by  $F_{1n} = F_{1n}(V)$ . In these examples we use  $\Omega_1 = \Omega_2 = 4 \times 10^{-16} \text{ cm}^2$  and  $\langle v \rangle = 10^7 \text{ cm/sec}$ , as before. For the first example, we assume that the window is a crystalline semiconductor with  $\mu_{n1} = 10^3 \text{ cm}^2/\text{V-sec}$ , that the zero bias field in the window is of the order of  $10^5 \text{ V/cm}$ , and that  $N_1^I = N_1^{\text{II}} = 6 \times 10^{12} \text{ cm}^{-2}$  ( $\sim 1\%$  lattice mismatch). It follows from Eq. (5.108) that  $R_1 = 2.5 \times 10^{-4}$  and that  $R_2 < 2.5 \times 10^{-4}$ . Regardless of whether the absorber is a crystalline or an amorphous semiconductor, we expect the diffusion velocity in that material to be such that  $D_n/L_n \lesssim 10^4 \text{ cm/sec}$ . This has as its consequence the fact that  $R_3 < 10^{-4}$ . Using these values for  $R_1$ ,  $R_2$ , and  $R_3$  and evaluating  $F_{1n}$  as a function of voltage developed by the cell from Eq. (5.107) gives the curve labeled  $\alpha$  in Fig. 5.16. This same curve  $\alpha$  is obtained for any  $V_1 = V_1(V)$  and  $V_2 = V_2(V)$  for any position of  $E_F$  in the effective gap at  $x = W_1$  and in the absorber gap at  $x = W_1^+$ , and for any value of  $\chi_1 - \chi_2 \geq 0$ . Clearly the window semiconductor is very effective in collecting the photocurrent in this example.

Now we look at another extreme: the electron mobility in the window is taken to be  $10 \text{ cm}^2/\text{V-sec}$ , the zero bias field in the window is taken to be  $10^4 \text{ V/cm}$ , and  $N_1^I = N_1^{\text{II}}$  is taken to be  $6 \times 10^{13} \text{ cm}^{-2}$  (10% mismatch). From Eq. (5.108) it follows that  $R_1 = 2.5$  in this example. Since Eq. (5.109) now

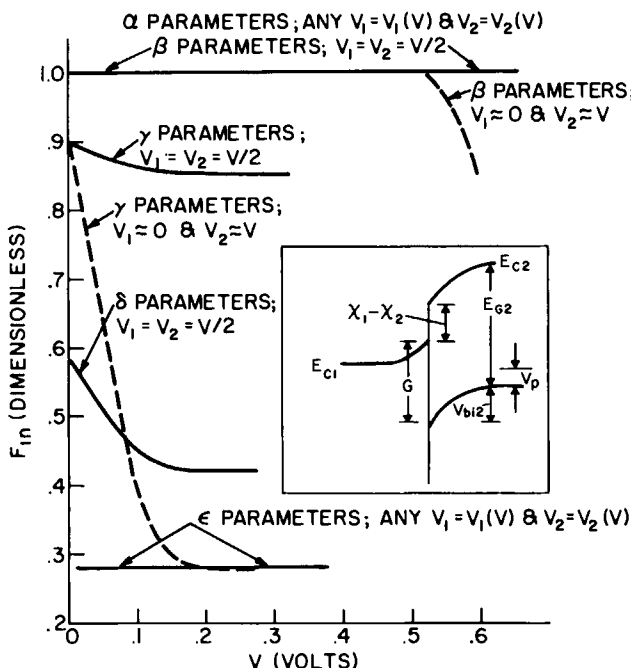


Fig. 5.16 The function  $F_{1n} = F_{1n}(V)$  characterizing photocurrent collection by the window semiconductor for several possible situations. The  $\alpha$  curve is for  $R_1 = 2.5 \times 10^{-4}$ ,  $R_2 < 2.5 \times 10^{-4}$ , and  $R_3 < 10^{-4}$ . It applies to any  $V_1 = V_1(V)$  and  $V_2 = V_2(V)$  as well as to any position of  $E_F$  at zero bias and any  $\chi_1 - \chi_2 > 0$ . The  $\beta$ ,  $\gamma$ ,  $\delta$ , and  $\epsilon$  curves apply to situations where  $R_1 = 2.5$ ,  $R_2 = 0.01$ , and  $R_3 = 5 \times 10^{-3}$  with  $\chi_1 - \chi_2 = 0.08$  eV. The  $\beta$ ,  $\gamma$ ,  $\delta$ , and  $\epsilon$  designate positions of  $E_F$  at zero bias: i.e.,  $\beta$  denotes  $(V_p + V_{bi2} - E_{g2})/2 = 0.3$  eV,  $\gamma$  denotes  $(V_p + V_{bi2} - E_{g2})/2 = 0$ ,  $\delta$  denotes  $(V_p + V_{bi2} - G)/2 = 0$ , and  $\epsilon$  denotes  $(V_p + V_{bi2} - G)/2 = -0.3$  eV. These parameters are all defined in the insert.

shows that recombination through path 2 has the potential of affecting  $F_{1n}$ . With this choice of parameters, it becomes necessary to be more specific in the calculation of  $R_2$ . Consequently, it is assumed that  $\chi_1 - \chi_2 = 0.08$  eV for our hypothetical heterojunction solar cell which leads to  $R_2 = 0.01$ . For these parameters we also obtain  $R_3 = 5 \times 10^{-3}$ . With the  $R$  values just calculated, we find that Eq. (5.107) predicts  $F_{1n}$  can be less than unity—i.e., there can be difficulty in collecting photocurrent. Whether there is difficulty depends strongly on the position of the Fermi level at  $x = W_1$  in thermodynamic equilibrium and on the splitting of the voltage developed by the cell as is shown in Fig. 5.16 with curves  $\beta$ ,  $\gamma$ ,  $\delta$ , and  $\epsilon$ .

As a result of this discussion and Fig. 5.16, several conclusions may be drawn for junctions of the form seen in Fig. 5.9a:

- For values of  $R_1$  and  $R_2 \gtrsim 0.05$ , there is the potential for loss of photocurrent due to inefficiency of the window drift field in competing with

path 1 and path 2. The detrimental effect of the loss provided by paths 1 and 2 is least for junctions where  $E_F$ , at zero bias, is above  $E_{g2}/2$  at  $x = W_1^+$ . The detrimental effect of paths 1 and 2 increases as  $E_F$ , at zero bias, is positioned successively lower in the absorber gap at  $x = W_1^+$ .

(b) It can be seen from Eq. (5.107) that the  $F_{1n}$  transport factor has the simple form [16, 39–41]

$$F_{1n} = [1 + (\langle v \rangle \Omega_1 N_1^I / \mu_{n1} \xi_{M1}) + e^{-(x_1 - x_2)/kT} (\langle v \rangle \Omega_1 N_1^H / \mu_{n1} \xi_{M1})]^{-1} \quad (5.111)$$

only if  $E_F$  at  $x = W_1$  lies below  $G/2$  at zero bias. For other possible positions of the Fermi level at  $x = W_1$ , in thermodynamic equilibrium,  $F_{1n}$  is larger than the value given by Eq. (5.111). Equation (5.111) represents a worst-case bound for  $F_{1n}$ .

(c) From Eq. (5.58) a collection function  $h(V)$  may be defined according to [13]

$$h(v) = F_{1n} F_{2n} F_1 \quad [h(V) \leq 1] \quad (5.112)$$

The behavior of this function will arise from the product of  $F_{2n}$  with  $F_1$  (Fig. 5.15) and with  $F_{1n}$  (Fig. 5.16).

#### 5.2.3.3 Summary

To summarize, this analysis of anisotype heterojunction solar cells has shown that the  $J-V$  characteristic of a window-absorber heterojunction solar cell will lead to a conversion efficiency that is poorer than—or at best equal to—that of the cell termed an equivalent homojunction (no loss in the emitter and no appreciable current generation in the emitter). The current collection in a heterojunction solar cell is influenced by the mechanism by which the electrons of the photogenerated current make their transition at the metallurgical junction from initial states in the conduction band of the absorber (*p*-type) to final states in the conduction band of the window. It is strongly influenced by the presence of recombination loss paths at the metallurgical junction, the effectiveness of collecting drift fields in the absorber and window materials, and by the position of the Fermi level at zero bias at the metallurgical junction [48–50]. The open-circuit voltage can be controlled by recombination at the interface<sup>†</sup> or by diffusion-recombination in the absorber bulk. If multistep tunneling-recombination is also present (see Fig. 3.21), a first approximation to the bucking current would be to add Eq. (3.61) to Eq. (5.56); as a consequence, multistep tunneling could then control  $V_{oc}$ . We underscore here the point made first in Chapter 3: the bucking-current mechanisms possible in

<sup>†</sup> We include recombination through paths 1 and 2 as well as recombination in the space-charge region.

heterojunctions can change from device to device and, hence, the curves of Fig. 3.25 are only a guide to absorber gap selection.

In cases where the wide gap semiconductor is not a window material but actually absorbs a significant part of the solar spectrum, the foregoing analysis would have to be modified to account for the contribution of the wider gap semiconductor to  $J_{ph}$  and to  $J_{bk}$ .

### 5.2.4 Analysis of Isotype Semiconductor-Semiconductor Heterojunction Structures

Figure 5.17 shows a  $p-p$  isotype semiconductor-semiconductor heterojunction solar cell of the form window-absorber under illumination. As with the anisotype structure, an assessment of the performance of this device will necessitate examining the  $J-V$  characteristic under illumination. We can quickly begin to write this characteristic by realizing that Eq. (5.29) applies equally well to Fig. 5.17. All the symbols have the same meaning as they did in Section 5.2.3.

It follows from Eq. (5.29) that we would like  $E_{Fn}(W_1 + W_2)$  to have the smallest value possible to reduce the strength of the bulk diffusion-recombination component of the bucking current, and it follows from Fig. 5.17 that the smallest value possible for  $E_{Fn}(W_1 + W_2)$  is  $V$ . Assuming electrons are readily swept across the region  $W_1 + W_2 > x > W_1$ , the requirement that  $E_{Fn}(W_1 + W_2) = V$ , and the requirement that photocurrent must flow across  $x = W_1$  will be achieved only if recombination path 3 of Fig. 5.17 acts as an infinite sink for electrons at  $x = W_1^+$ . We are forced to the conclusion that here is a device structure which relies on recombination

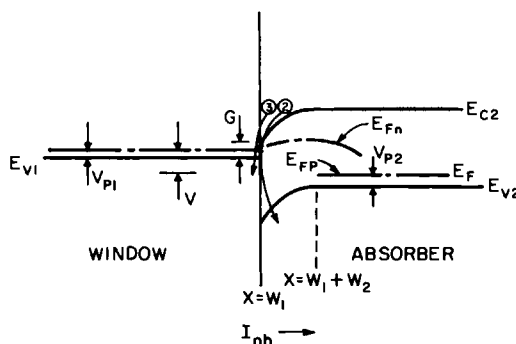


Fig. 5.17 A  $p-p$  isotype heterojunction under illumination and developing a voltage  $V$ . Recombination path 2 is the same as that of Fig. 5.9; recombination path 3, present here, was negligibly small in Fig. 5.9. The window semiconductor is degenerate.

at the metallurgical junction to carry the photogenerated current [51]. Consequently, the effective gap  $G$  at  $x = W_1$  must be as small as possible. For S-R-H recombination the  $\Omega_3 N_1^{\text{III}}$  product must be as large as possible. Note that  $\chi_1 + E_{g1} - \chi_2 \geq 0$  is needed to prevent a spike at  $x = W_1$ .

Generation and recombination in  $W_1 + W_2 > x > W_1$  can be rigorously included in  $J_p(W_1 + W_2)$  as discussed in Section 6.2.3. For algebraic simplicity, we neglect them here and attribute all recombination to the plane  $x = W_1$ . Hence ( $V > kT$ ),

$$J_p(W_1 + W_2) = -A^* T^2 e^{-(V_{p2} + V_{bi2})/kT} e^{V/kT} - J_r^2 e^{V/kT} - J_0 e^{BT} e^{AV} \quad (5.113)$$

which says that the hole current at  $x = W_1 + W_2$  flows to supply holes for (a) thermionic emission at  $x = W_1$ , (b) recombination path 2, and (c) multistep tunneling. The  $A^*$  in Eq. (5.113) is an effective Richardson's constant for holes in the absorber and the prefactor  $J_r^2$  is given by Eq. (5.68). Some typical behavior, with voltage, of the component  $J_r^2 e^{V/kT}$  is seen in Fig. 5.13. Multistep tunneling is depicted (for electrons) in Fig. 3.21; direct tunneling is not present since the barrier is assumed too wide.

Assuming path 3 is able to maintain  $E_{Fn}(W_1 + W_2) = V$  and using Eq. (5.113), we can write Eq. (5.29) as ( $V > kT$ )

$$J = J_L - A^* T^2 e^{-(V_{p2} + V_{bi2})/kT} e^{V/kT} - J_0 e^{BT} e^{AV} - J_r^2 e^{V/kT} - J_{\text{dif}} e^{V/kT} \quad (5.114)$$

Equation (5.114) shows that  $J_{\text{ph}}$  is a constant when path 3 is an effective sink [52]. It also shows that  $V_{oc}$  can be determined by thermionic emission of majority carriers, by multistep tunneling of majority carriers, by interface recombination, or by minority-carrier diffusion-recombination in this device structure [52]. Clearly, the open-circuit voltage and, hence, the efficiency will be less than, or at best equal to, that of an equivalent homojunction (whose emitter photocurrent and bucking current are negligible). Such a homojunction would only have the diffusion-recombination component of the bucking current of Eq. (5.114).

### 5.2.5 Analysis of Anisotype S-I-S Structures

Anisotype S-I-S heterojunction solar cell structures differ from the S-S devices of Fig. 5.9 in that a wide gap insulator (I) layer has been inserted between the two semiconductors. Generally, this I layer has a thickness in the range  $1 \text{ nm} \lesssim \delta \lesssim 5 \text{ nm}$  to allow collection of the photocurrent. An anisotype S-I-S configuration, corresponding to the S-S configuration of Fig. 5.9a, is seen in Fig. 5.18. Figure 5.18a shows the device in thermodynamic equilibrium; Fig. 5.18b shows the device under illumination and producing power.

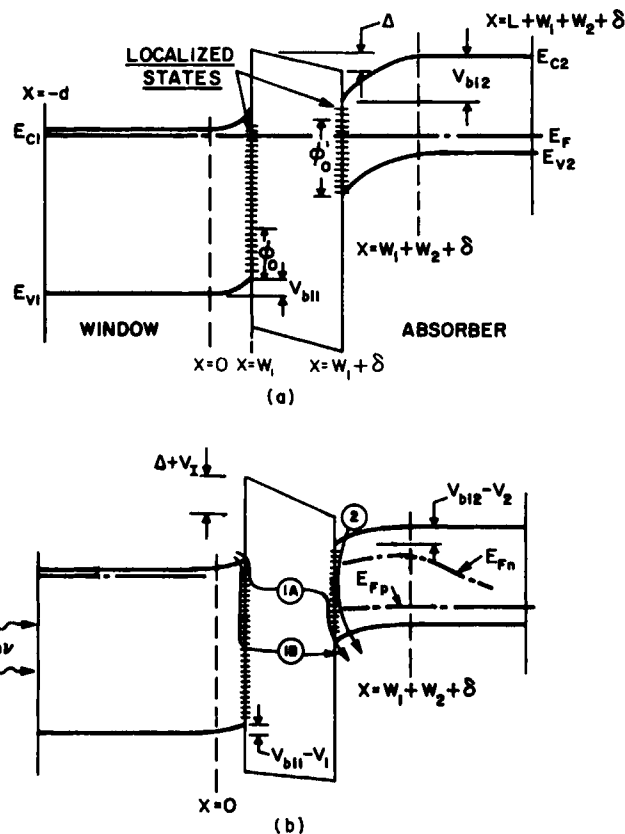


Fig. 5.18 An anisotype S-I-S heterojunction in (a) thermodynamic equilibrium and (b) under illumination. The quantity  $\phi_0$  denotes the short range neutrality level for the interface at  $x = W_1$  whereas  $\phi'_0$  denotes the same quantity at  $x = W_1 + \delta$ . The charge distribution in this particular example is such that the sense of  $\Delta$  and  $V_{bi1} + V_{bi2}$  is opposite. Regions are not to scale.

The current density  $J$  flowing in this structure when it is under illumination is a constant, independent of position. It may be evaluated at  $x = W_1 + W_2 + \delta$ ; viz.,

$$J = J_p(W_1 + W_2 + \delta) + J_n(W_1 + W_2 + \delta) \quad (5.115)$$

Using Eq. (5.25), we can immediately rewrite this as

$$J = J_p(W_1 + W_2 + \delta) + J_L - J_{\text{dif}} \{ \exp[E_{Fn}(W_1 + W_2 + \delta)/kT] - 1 \} \quad (5.116)$$

This equation is equivalent to Eq. (5.29); the only change is that the edge of the space-charge region in the absorber is now at  $x = W_1 + W_2 + \delta$  instead of at  $x = W_1 + W_2$ . By analogy to our treatment of Eq. (5.29), it follows that Eq. (5.116) can be written in a form corresponding to Eq. (5.56). Consequently, the resulting  $J = J(V)$  for this anisotype S-I-S solar cell is

$$\begin{aligned} J = & F_{1n}F_{2n}F_I J_r^1(e^{V/kT} - 1) - F_{1n}F_I J_r^2(e^{V/kT} - 1) \\ & - F_{1n}F_{2n}F_I J_{\text{dif}}(e^{V/kT} - 1) \end{aligned} \quad (5.117)$$

As in the case of the anisotype S-S solar cell,  $F_{1n}$  is defined by Eq. (5.57),  $F_I$  is defined by Eq. (5.49), and  $F_{2n}$  is defined by Eq. (5.48). The prefactor  $J_{\text{dif}}$  is again given by Eq. (5.27) and the prefactor  $J_r^2$  is again given by Eq. (5.38) with  $W_1 + \delta$  replacing  $W_1$ . However, the prefactor  $J_{\text{th}}$  must be modified from the form given in Eq. (5.89) to

$$J_{\text{th}} = \Xi A^* T^2 e^{-(E_{g2} - V_{b12} - V_{p2})/kT} \quad (5.118)$$

The quantity  $\Xi$  is a transmission probability which accounts for the fact that electrons at  $x = W_1 + \delta$  must cross the I layer to arrive at  $x = W_1$ . Expressions for  $\Xi$  have been derived in the literature by assuming that electrons cross the insulator layer by direct tunneling [53]. The prefactor  $J_r^1$  must also be modified from the form used for S-S structures since electrons passing through path 1 must now cross the I layer as seen in Fig. 5.18. The form of  $J_r^1$  will depend on which particular route (two possibilities are seen in the figure) is most effective. We avoid pursuing this further and simply choose not to specify a specific form for  $J_r^1$ .

Using Fig. 5.18 and Eq. (5.117), we can now reach several conclusions:

(a) As was the situation for the anisotype S-S solar cells of Fig. 5.9, the window- and absorber-electron affinities (since the absorber is *p*-type) of an anisotype S-I-S structure must be chosen so as to avoid a conduction-band spike. This has been done in Fig. 5.18 and assumed in Eq. (5.118).

(b) For an S-I-S structure to be an effective solar cell, it is essential that  $F_I = 1$ ; i.e., from Eq. (5.93),

$$J_{\text{th}} e^{-V_2/kT} > J_r^2 + J_{\text{dif}} \quad (5.119)$$

must hold for the photocurrent to be collected. Hence, the presence of the I layer, which modifies  $J_{\text{th}}$  through Eq. (5.118), cannot be allowed to disturb the sense of this inequality. Put physically, the fact that the electrons in the absorber conduction band must cross the I layer to be collected as the photocurrent cannot be allowed to impede them to an extent that they choose to recombine through path 2 of Fig. 5.18 or to back-diffuse away from the barrier.

(c) The use of an S-I-S configuration, rather than an S-S configuration, can be advantageous for a specific materials system, if the presence of the insulator layer significantly reduces the interface state density, and if  $J_{\text{blk}1}$  (path 1) or  $J_{\text{blk}2}$  (path 2) dominated the bucking current of the S-S structure. If the interface state density (at  $x = W_1$  and  $x = W_1 + \delta$ ) is reduced in the S-I-S device to a point where  $J_{\text{blk}1}$  and  $J_{\text{blk}2}$  are now insignificant compared to the diffusion-recombination bucking-current component, Eq. (5.117) becomes

$$J = F_{1n}F_{2n}F_I J_L - F_{1n}F_{2n}F_I J_{\text{dif}}(e^{V/kT} - 1) \quad (5.120)$$

Since  $J_L$  and  $J_{\text{dif}}(e^{V/kT} - 1)$  must be the same for these corresponding S-S and S-I-S cells, the S-I-S device will show enhanced open-circuit voltage when compared to the S-S device for this materials system. If  $F_{1n} = 1$ ,  $F_{2n} = 1$ , and  $F_I = 1$  can be maintained in the S-I-S structure, then the S-I-S cell will also have enhanced efficiency. Solar cells, whose  $J-V$  characteristic obeys Eq. (5.120), have been referred to as minority-carrier devices, since the bucking current determining  $V_{\text{oc}}$  is the diffusion-recombination of minority-carrier electrons in the base of the *p*-type absorber of Fig. 5.18 [53].

(d) On the other hand, the use of a S-I-S configuration, rather than a S-S configuration, can also be advantageous for those materials systems where the presence of the insulator layer significantly shifts the position of the Fermi level with respect to the band edges at the interface without necessarily reducing the interface state densities. Again this potential advantage only holds if  $J_{\text{blk}1}$  (path 1) or  $J_{\text{blk}2}$  (path 2) dominates the bucking current of the S-S structure.

The advantage here lies in the fact that the currents  $J_{\text{blk}1}$  and  $J_{\text{blk}2}$  can be dramatically changed by shifting the position of the Fermi level at the interface in thermodynamic equilibrium. This is demonstrated by Figs. 5.12 and 5.13. If they are suppressed below  $J_{\text{dif}}(e^{V/kT} - 1)$ , by the presence of the I layer for a given materials system, then Eq. (5.120) results, and solar cell performance is enhanced provided  $F_{1n} = 1$ ,  $F_{2n} = 1$ , and  $F_I = 1$ .

The shifting of the Fermi-level position at the interface, in thermodynamic equilibrium, can occur with the introduction of an insulator layer since now

$$V_{\text{bi}1} + V_{\text{bi}2} + \Delta = \phi_{p2} - \phi_{n1} \quad (5.121)$$

The presence of  $\Delta$ , seen in Fig. 5.18a, causes  $V_{\text{bi}1}$  and  $V_{\text{bi}2}$  to change from the values they would have in the absence of the I layer; consequently,  $E_F$  moves with respect to the band edges. In the S-I-S structure of Fig. 5.18a, negative charge resides at  $x = W_1$  and positive charge resides at  $x = W_1 + \delta$  in localized states. These sheets of charge, together with bulk charge in the window and adsorber, determine  $\Delta$  (see Section 3.4.6). The resulting  $\Delta$ , in the case of Fig. 5.18, is negative.

### 5.2.6 Analysis of Isotype S-I-S Structures

Figure 5.19 shows an isotype, semiconductor-insulator-semiconductor heterojunction under illumination. As was the case for the isotype S-S cell of Fig. 5.17, interface recombination path 3 must carry the photocurrent across the junction. An electron passing through path 3 must cross the I layer in the S-I-S structure; consequently, it has been found that the layer thickness  $\delta$  is restricted to  $1 \text{ nm} \leq \delta \leq 5 \text{ nm}$  in effective devices [53].

As with all the structures we have analyzed, we assume a one-dimensional configuration for simplicity; consequently the current density  $J$  present under illumination is a constant with position in Fig. 5.19. As has been our custom, we choose to evaluate that constant at the edge of the space-charge region in the absorber. Since the absorber in the figure is assumed to be *p*-type, the electron current density at the edge of the absorber space-charge region is given by Eq. (5.25). The requirement that this electron current must flow unimpeded through path 3 of Fig. 5.19 in an effective cell means the electron quasi-Fermi level appearing in Eq. (5.25) must be  $V$ ; hence, at the edge of the space-charge region, in the absorber,

$$J_n = J_L - J_{\text{dif}} \{ \exp V/kT - 1 \} \quad (5.122)$$

The hole current density present at the edge of the space-charge region, in the absorber, follows from Eqs. (3.59), (3.61), and (5.37); viz.,

$$J_p = -\Xi A^* T^2 e^{-(V_{p2} + V_{b12})/kT} e^{V_2/kT} - J_r^2 e^{V/kT} - \Xi' J_0 e^{BT} e^{AV_2} \quad (V > kT) \quad (5.123)$$

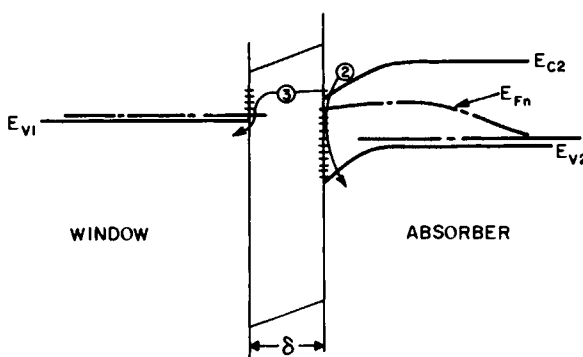


Fig. 5.19 Isotype S-I-S heterojunction under illumination. The window semiconductor in this example is degenerately doped. Recombination path 2 is present as it was in Figs. 5.9 and 5.18; however, path 1 is negligibly small here. Recombination path 3, absent in Figs. 5.9 and 5.18, is present here and in Fig. 5.17. In fact, it carries the photocurrent in isotype structures.

Here the  $\Xi$  and  $\Xi'$  are transmission probabilities which account for the fact that holes thermionically emitted from the absorber or undergoing multistep tunneling from the absorber must cross the I layer present in Fig. 5.19.

Combining Eqs. (5.122) and (5.123), we obtain the  $J = J(V)$  characteristic for an isotype S-I-S solar cell structure under illumination. The result is

$$J = J_L - \Xi A^* T^2 e^{-(V_{p2} + V_{bi2})/kT} e^{V_2/kT} - J_r^2 e^{V/kT} - \Xi' J_0 e^{BT} e^{AV_2} - J_{dif} e^{V/kT} \quad (V > kT) \quad (5.124)$$

Using Fig. 5.19 and Eq. (5.124) we can now reach several conclusions concerning isotype S-I-S solar cells:

(a) The photocurrent crosses the interface through the recombination process of path 3 seen in the figure. If path 3 does not provide an infinite sink for electrons arriving at the barrier in the absorber, then  $E_{Fn} > V$  at the edge of the absorber space-charge region; consequently, the bucking current arising from diffusion-recombination increases as does the recombination current passing through path 2.

(b) The presence of the insulator layer can significantly reduce the thermionic emission and multistep tunneling bucking currents due to the effect of the factors  $\Xi$  and  $\Xi'$  and due to the fact that these currents now depend on  $V_2$  instead of  $V$  in Eq. (5.124). If these components of the bucking current dominated in the isotype S-S heterojunction configuration, using the isotype S-I-S configuration has the potential of decreasing the bucking current for the same value of photocurrent (assuming path 3 is an infinite sink). The result can be an increased  $V_{oc}$  and efficiency.

(c) The presence of the I layer can modify the barrier shape in the semiconductors since now

$$V_{bi1} + \Delta + V_{bi2} = \phi_{p2} - \phi_{p1} \quad (5.125)$$

Here  $\Delta$  is the built-in potential developed across the insulator.

Modification of the barrier shape can affect the thermionic emission current since it depends exponentially on  $V_{bi2}$ . It can affect the recombination current, through path 2, due to the strong dependence of  $J_r^2$  on band-edge positions with respect to the Fermi level (see Figs. 5.12 and 5.13). Modifying the barrier shape can also affect the multistep tunneling component of  $J_{bk}$  due to the change in the tunnel barriers.

If any of these bucking-current components dominates in the isotype S-S heterojunction and, if the use of the isotype S-I-S heterojunction suppresses the component,  $V_{oc}$  and device efficiency increase in the S-I-S configuration.

(d) If the bucking-current component  $J_r^2 e^{V/kT}$  dominates in a S-S heterojunction and, if using the S-I-S configuration removes the localized states through which this current passes, then the S-I-S configuration has the potential of giving a higher  $V_{oc}$  and efficiency for this materials system.

### 5.3 S-S AND S-I-S HETEROJUNCTION CELL CONFIGURATIONS AND PERFORMANCE

#### 5.3.1 Single-Crystal Devices

The potential of heterojunction solar cells was made apparent in 1975 with the development of a 12.5% ( $53 \text{ mW/cm}^2$  terrestrial sunlight) single-crystal  $(n)\text{CdS}/(p)\text{InP}$  cell (AR coated) [9]. This S-S structure, subsequently improved to yield efficiencies  $\sim 15\%$  under terrestrial conditions [9], owes its performance to a number of design features. The CdS ( $E_g = 2.42 \text{ eV}$ ) serves as window semiconductor and provides a good lattice match to the strongly absorbing, direct gap semiconductor InP ( $E_g = 1.35$ ; see Fig. 2.13). Since the InP is a strong absorber, it follows from Fig. 3.3 that poorer minority-carrier lifetime and diffusion length values can be tolerated. The lattice mismatch between the (111) plane of zinc-blende InP (Fig. 2.1) and the basal plane of wurtzite CdS (Fig. 2.1) is only 0.32%, and the lattice match is good for any crystallographic orientation since the tetrahedral interatomic distances (see Fig. 2.2) are virtually identical for these two compounds. (The In-P distance is  $2.533 \text{ \AA}$  and the Cd-S distance is  $2.532 \text{ \AA}$  [54]). A further advantage of this materials system is that the electron affinities of its constituents are such that there is no spike in the conduction band at the metallurgical junction and, hence, the band diagram of Fig. 5.9a applies.

The  $(n)\text{CdS}/(p)\text{InP}$  single-crystal structure has yielded short-circuit current densities in the  $18 \text{ mA/cm}^2$  range for terrestrial conditions [9]. Using this value for  $J_{sc}$  and using Eq. (5.63), with Eq. (5.27b) for  $J_{dif}$ , we can estimate what  $V_{oc}$  should be developed by this semiconductor-semiconductor (S-S) structure, if diffusion-recombination in the absorber (InP) is dominating the bucking current. Since mobility values in the range of  $100 \text{ cm}^2/\text{V}\cdot\text{sec}$  and  $N_A$  in the range of  $10^{17} \text{ cm}^{-3}$  were reported for the absorber [9], it follows from Eq. (5.63) that  $V_{oc} \sim 0.97 \text{ V}$  would be expected for  $L_n \sim 100 \mu\text{m}$ ,<sup>†</sup> or  $V_{oc} \sim 0.85 \text{ V}$  would be expected for the more probable range of  $L_n \sim 1 \mu\text{m}$ .<sup>†</sup> Actual  $V_{oc}$  values of  $\lesssim 0.79 \text{ eV}$  were obtained from the device [9] indicating one of the other possible bucking-current components (interface recombination<sup>‡</sup> or multistep tunneling) is probably dominating. One would like to remove the interface recombination and multistep tunneling-recombination leaving the bulk diffusion-recombination (which cannot be removed) to determine  $V_{oc}$ .

<sup>†</sup> For  $L_n \lesssim 100 \mu\text{m}$   $\Theta_B$  would be expected to be  $\sim 1$  from Fig. 5.10 since  $\beta_5 \gtrsim 1$  for the InP thicknesses used. Physically this means recombination at the back surface is not important.

<sup>‡</sup> Again, we include in this term recombination at the metallurgical junction as well as adjacent to it in the space-charge region.

At about the same time as that of the emergence of the  $(n)\text{CdS}/(p)\text{InP}$  cell the second heterojunction configuration<sup>†</sup> to achieve conversion efficiencies greater than 10% was fabricated. This cell was the single-crystal  $(n)\text{CdS}/(p)\text{CuInSe}_2$  device with  $\eta = 12\%$  ( $92 \text{ mW/cm}^2$ ; AR coated) [10]. The direct gap, strongly absorbing  $\text{CuInSe}_2$  ( $E_g = 1.04 \text{ eV}$ ; see Fig. 2.13) serves as the absorber, and  $\text{CdS}$  serves as the window in this cell which has excellent lattice match between the chalcopyrite type  $\text{CuInSe}_2$  and the wurtzite  $\text{CdS}$  (lattice mismatch = 1.16%; see Table 3.1) [55]. An additional advantageous feature of this materials system is that there is no spike in the conduction band; i.e., the band diagram of Fig. 5.9a applies to this S-S heterojunction.

Another S-S heterojunction solar cell configuration based on using  $\text{CdS}$  as an optical window is the  $(n)\text{CdS}/(p)\text{CdTe}$  device which, in single-crystal form, has given  $\eta = 12\%$  [18]. Here the direct gap, strongly absorbing II-VI semiconductor  $\text{CdTe}$  ( $E_g = 1.44 \text{ eV}$ ; see Fig. 2.13) is the absorber, again giving the advantage that  $J_L$  can be collected from the bulk with relatively poor  $\tau_n$  and  $L_n$  values (see Fig. 3.3). The lattice mismatch is 9.7% (Table 3.1) and interface recombination has been found to dominate the bucking current, which means that higher  $V_{oc}$  values would be possible if this channel of bucking current flow were eliminated.

The  $(p)\text{Cu}_2\text{S}-\text{(n)}\text{CdS}$  heterojunction structure in its single-crystal form has been examined by a number of workers and efficiencies in the 5–6% range are reported under terrestrial illumination conditions [16, 32, 56–58]. This device has been intensively studied in the configuration with  $\text{Cu}_2\text{S}$  on a  $\text{CdS}$  substrate (light enters the  $\text{Cu}_2\text{S}$ ) and has been fabricated by using either the “Clevite wet process” [58], which forms the  $\text{Cu}_2\text{S}$  layer by a Cu–Cd ion exchange process, or by using the “Philips dry process” [58], which forms the  $\text{Cu}_2\text{S}$  layer by reacting evaporated  $\text{CuCl}$  with the  $\text{CdS}$  substrate. The  $\text{Cu}_2\text{S}$  is a strongly absorbing semiconductor ( $E_g = 1.2 \text{ eV}$ ; see Fig. 2.13) which, when produced as described, is nearly degenerate due to a deficiency of copper. Its interface with  $\text{CdS}$  can lead optimally to a lattice mismatch of 4% [16], but the absorber  $\text{Cu}_2\text{S}$  has been found to exhibit a rather complicated phase diagram [59] with the most important phases being chalcocite ( $\text{Cu}_2\text{S}$ ), djurleite ( $\text{Cu}_{1.96}\text{S}$ ), digenite ( $\text{Cu}_{1.8}\text{S}$ ), and covellite ( $\text{CuS}$ ). Experimentally it has been found that a stoichiometry of  $\text{Cu}/\text{S} > 1.995$  is correlated with the more efficient devices [60].

A number of slightly different band diagrams have been proposed for the  $\text{Cu}_2\text{S}/\text{CdS}$  system and the bucking current mechanism has been variously attributed to interface state recombination or to some form of multistep tunneling-recombination [3, 16, 32, 56–58]. At least part of this problem is

<sup>†</sup>We have considered the  $\text{Ga}_x\text{Al}_{1-x}\text{As}/\text{GaAs}$  cell, which achieved  $\eta > 10\%$  in 1972, as a homojunction since the principal junction is, indeed, a  $p-n$   $\text{GaAs}$  junction (see Chapter 4).

caused by the fact that different groups are actually working with differently shaped heterojunction barriers. Variations in the interface can easily be caused by the particular details of a given fabrication procedure as pointed out by Fig. 5.7. Heat treatments in various ambients have been studied thoroughly for this heterojunction and have been shown to influence the performance of the cell due to a combination of (a) the heat treatment affecting the stoichiometry of the  $\text{Cu}_2\text{S}$ , and (b) the heat treatment influencing the barrier shape and thereby influencing current collection and possibly the bucking-current mechanism [16, 32, 56–58].

The configuration has the disadvantage of placing the Fermi level at zero bias (or thermodynamic equilibrium) near the bottom of the *p*-type absorber gap at  $x = W_1$ . This position of the Fermi level at zero bias increases the susceptibility of the transport factor  $F_1$  to the details of the transfer mechanism for photogenerated electrons at  $x = W_1$  as discussed in Section 5.2.3.2(4). Also we recall that the transport factor  $F_{1n}$  has more of a potential to deviate from unity the lower  $E_F$  is positioned in the absorber gap at  $x = W_1$  at zero bias. Because of the position of  $E_F$  at  $x = W_1$ , with respect to the effective and absorber gaps, the transport factor  $F_{1n}$  is adequately represented by Eq. (5.111) for the  $\text{Cu}_2\text{S}/\text{CdS}$  cell indicating that the  $R_1$  ratio is critical to the performance of the device [16, 39–41]. From the point of view of reducing recombination through path 1, the position of the Fermi level at zero bias in this device is acceptable, although having all the voltage developed in the CdS (which is believed to occur) is not an optimum situation as follows from Part (5) Section 5.2.3.2 and Fig. 5.13.

Among III-V compound semiconductor S-S heterojunctions that have been explored in single-crystal form is the (*n*)AlAs/(*p*)GaAs materials system which is reported to have given  $\eta = 18.5\%$  (AM1.5) [8] in spite of the fact that the cell should have a spike in the conduction band as may be deduced from the affinity values given in Table 3.1. In this heterojunction solar cell, the AlAs ( $E_g = 2.1$  eV) is the wide-gap semiconductor which gives a good lattice match to the strongly absorbing, direct-gap GaAs ( $E_g = 1.42$  eV; see Fig. 2.13), which is the principal absorber. An example of another III-V heterojunction solar cell is the graded-gap (*n*) $\text{Al}_x\text{Ga}_{1-x}\text{As}/(\text{p})\text{GaAs}$  single-crystal structure ( $\eta = 13.6\%$  at AM0 [61]. Here the stoichiometry of the ternary  $\text{Al}_x\text{Ga}_{1-x}\text{As}$  is varied with position producing mainly a change in the electron affinity with position, and the result is a solar cell where the effective forces are not confined to the plane  $x = W_1$ .

Cells of this graded-gap heterojunction configuration, which have grading in the principal photovoltage-producing junction (Fig. 5.20), have several potential advantages. If properly designed, they can (a) remove recombination paths 1 and 2 of Fig. 5.9 through a gradual accommodation of the lattices, (b) enable the use of a wide gap to shield photogenerated

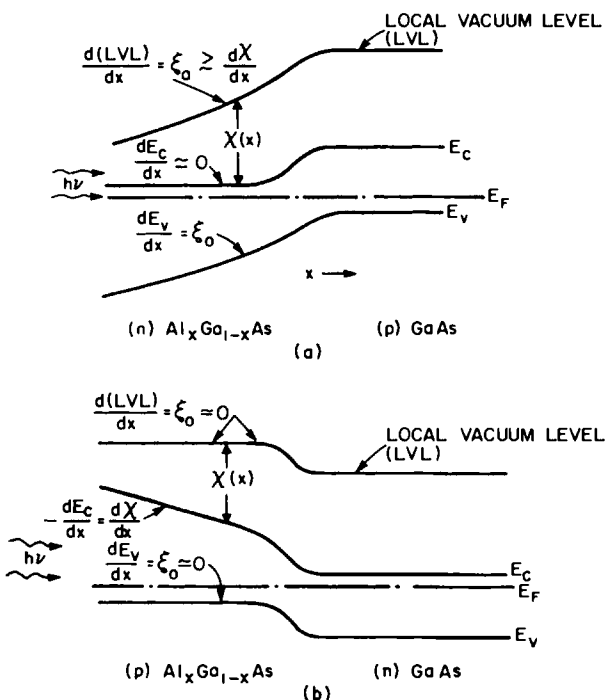


Fig. 5.20 The importance of properly using effective force fields together with the electrostatic force field is seen here. (a) The effective force acts on electrons in the opposite sense as the barrier electrostatic field as might be guessed by noting that the corresponding abrupt junction would have a spike in the conduction band. The best that can be hoped for is that an electrostatic field develops in the graded region to counter  $d\chi/dx$  and to give the advantageous shape seen for  $E_v$  in the graded region. The occurrence of such an electrostatic field would be a fortuitous situation. However, by just changing the doping as seen in (b), the effective force field acts in the same sense as the barrier electrostatic field. The effective field directly acts to send carriers toward the junction and can directly add to the photovoltage. No electrostatic field is required in the graded region of (b). The diagram neglects any change in hole affinity with Al/Ga ratio change.

carriers from the top surface, and (c) have the possibility of using effective forces directly to give photovoltaic action. The latter potential advantage arises since the effective force field coincides with at least part of the region of the cell which is photoconductive [see Eq. (2.100) or Eq. (5.9)] even under normal illumination (i.e., no concentration).

However, the aforementioned graded-gap  $(n)\text{Al}_x\text{Ga}_{1-x}\text{As}/(p)\text{GaAs}$  heterojunction cell has not produced as high efficiencies as the  $(p)\text{Al}_x\text{Ga}_{1-x}\text{As}/(p)\text{GaAs}/(n)\text{GaAs}$  heteroface, homojunction cells [61] discussed in Chapter 4. It has been suggested that the performance of the graded-gap heterojunction is reduced due to absorption in the  $\text{Al}_x\text{Ga}_{1-x}\text{As}$  layer, which is

generally thicker in the graded configuration than it is in the heteroface, *p-n* homojunction structure [46].

Another possible source of difficulty in the graded-gap (*n*)Al<sub>x</sub>Ga<sub>1-x</sub>As/(*p*)GaAs cell deserves examination. In this particular cell, varying the Al/Ga ratio causes the electron affinity to vary; varying the Al/Ga ratio also causes the hole affinity to vary but it is a smaller change which we neglect in this discussion. We can then focus on the potential source of difficulty by examining the role of the term  $d\chi/dx$ .

Looking at a band diagram for the (*n*)Al<sub>x</sub>Ga<sub>1-x</sub>As/(*p*)GaAs heterojunction cell as seen in Fig. 5.20a we note that  $d\chi/dx$  seems, at first glance, to be very advantageous in this structure since it is oriented to shield photo-generated carriers from the top surface (gap widens towards the top). However, closer examination allows us to realize that  $dE_c/dx \gtrsim 0$  is a necessity in this cell; otherwise electrons swept over the barrier are confined to the interface region. However, it is seen from Eq. (5.10) that the requirement that  $dE_c/dx \geq 0$  forces

$$\xi_0 \gtrsim d\chi/dx$$

in the graded Al<sub>x</sub>Ga<sub>1-x</sub>As region. In other words, in order for  $d\chi/dx$  not to detract from the performance of the (*n*)Al<sub>x</sub>Ga<sub>1-x</sub>As/(*p*)GaAs cell, it must be off-set by an electrostatic field  $\xi_0$  which must occur in the graded region. If the doping profile in the graded region allows such an electrostatic field to occur, then the gradient of the local vacuum level (LVL) is  $\gtrsim d\chi/dx$  as seen in Fig. 5.20a and the valence-band edge has the advantageous  $E_v = E_v(x)$  seen because, from Eq. (5.11),

$$dE_v/dx \simeq \xi_0$$

This follows since the hole affinity of Al<sub>x</sub>Ga<sub>1-x</sub>As is roughly constant.

To summarize, the effective force arising from  $d\chi/dx$  in the (*n*)Al<sub>x</sub>Ga<sub>1-x</sub>As/(*p*)GaAs cell is actually oriented in the wrong sense. It leads to a voltage that opposes the barrier photovoltage as might be guessed by noting from Table 3.1 that the corresponding (*n*)AlAs/(*p*)GaAs abrupt junction should have a spike in the conduction band at the metallurgical interface. The best that can be hoped for in the graded junction is that this effective force arising from  $d\chi/dx$  is overcome by a built-in electrostatic field in the graded-gap region. If such an electrostatic field does exist, it cancels  $d\chi/dx$ ; it also causes an advantageous gradient in the valence-band edge as seen in Fig. 5.20a which can direct minority carriers toward the junction and which can contribute directly through Eq. (5.9) to the photovoltaic action in regions of photoconductivity. The difficulty with the structure lies in being assured that the proper built-in electrostatic field does develop in the graded (*n*)Al<sub>x</sub>Ga<sub>1-x</sub>As region.

It is important to realize that a graded-gap  $(p)\text{Al}_x\text{Ga}_{1-x}\text{As}/(n)\text{GaAs}$  structure would not require the difficult condition of a compensating, electrostatic field in the graded region to be effective but, instead, would use the force arising from  $d\chi/dx$  directly. Put another way, in the  $(p)\text{Al}_x\text{Ga}_{1-x}\text{As}/(n)\text{GaAs}$  device the photovoltage arising from  $d\chi/dx$  adds to the barrier photovoltage as seen from Fig. 5.20b and Eqs. (5.9)–(5.11). Single-crystal graded-gap  $(p)\text{Al}_x\text{Ga}_{1-x}\text{As}/(n)\text{GaAs}$  heterojunction structures have been fabricated and the force arising from  $d\chi/dx$  is not only effective in directing photogenerated minority carriers toward the junction, but  $d\chi/dx$  has been proven to be capable of contributing directly to the photovoltage [62, 63] as indicated by Eq. (2.100) or (5.9). In fact, it has been found that under 1000 suns the open-circuit voltage of an  $(p)\text{Al}_x\text{Ga}_{1-x}\text{As}/(n)\text{GaAs}$  structure, with a  $p^+ - p$  selective-ohmic contact to the graded region, was 25% higher with the addition of photovoltage coming from the  $(d\chi/dx)$  component and the  $p^+ - p$  selective-ohmic contact components [62].

Up to this point all the cell structures we have discussed have been anisotype S–S heterojunctions; however, a number of configurations of the form isotype S–S, isotype S–I–S, and anisotype S–I–S have also been fabricated and evaluated as solar cell structures. Isotype  $(n-n)$   $\text{SnO}_2/\text{GaAs}$ ,  $\text{SnO}_2/\text{Ge}$ ,  $\text{SnO}_2/\text{Si}$ , and  $\text{SnO}_2/\text{GaP}$  heterojunctions have been explored by several groups [64–67]. When the oxide semiconductor (Table 3.1)  $\text{SnO}_2$  is formed by one of the various versions of hydrolysis of  $\text{SnCl}_4$  [64–66], it is found to give a heterojunction that exhibits photovoltaic activity in the case of  $(n)\text{GaAs}$ ,  $(n)\text{Ge}$ , and  $(n)\text{Si}$  and to give a junction that is ohmic on  $(n)\text{GaP}$ . When the  $\text{SnO}_2$  is deposited by  $e$ -beam, photovoltaic activity is again found using  $(n)\text{Si}$  [67]. At least in their more efficient forms these  $\text{SnO}_2$  devices, as well as similar devices using the alloy  $\text{In}_2\text{O}_3-\text{SnO}_2$ (ITO) in place of the  $\text{SnO}_2$ , probably are S–I–S heterojunctions. Isotype  $(n-n)$  devices using  $e$ -beam deposited or hydrolysis-produced  $\text{SnO}_2$  on single-crystal  $(n)\text{Si}$  have yielded  $\eta > 10\%$  (AM1) [67]; devices using spray-hydrolysis-produced ITO on single-crystal  $(n)\text{Si}$  have yielded  $\eta \approx 12\%$  (AM1) [65]. The band diagram for this latter device, as deduced from capacitance measurements, is seen in Fig. 5.21. The device is definitely an isotype S–I–S cell since an ultrathin silicon oxide was purposefully grown during fabrication.

It is important to determine the precise structure of the solar cell formed by using a specific materials system and a specific fabrication procedure. When the structure is determined (isotype S–S, isotype S–I–S, anisotype S–S, homojunction, etc.), the mechanisms controlling device performance can be established and a rationale for optimizing device design can be developed. Determining the cell structure produced by a specific materials system can sometimes be rather difficult, however. As an example, we note that the ITO/ $\text{SiO}_x/(p)\text{Si}$  cell, where the indium tin oxide is produced by

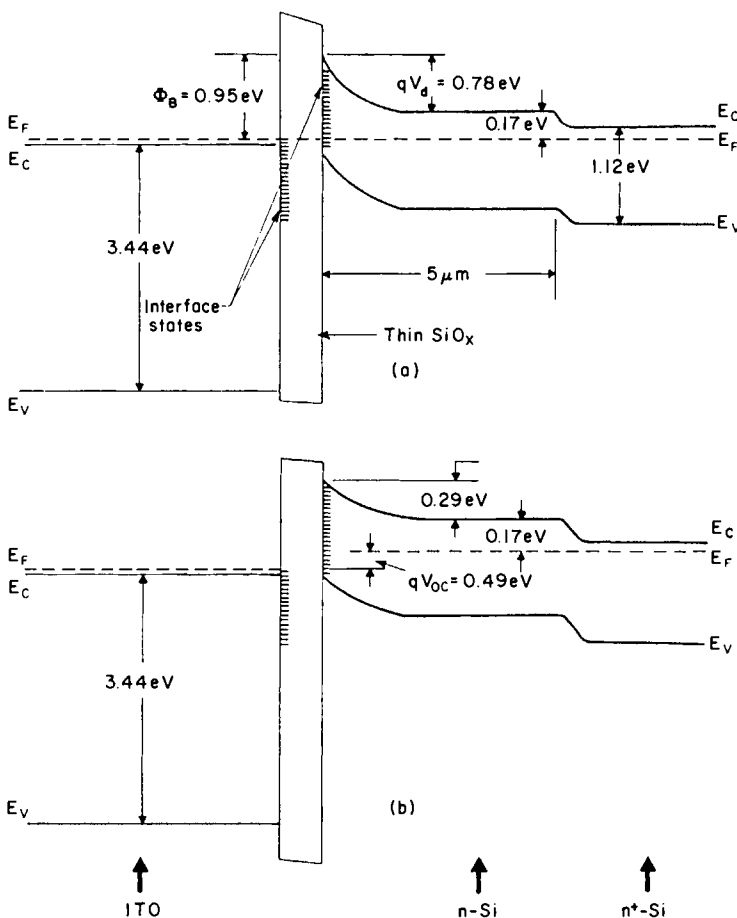


Fig. 5.21 Isotype S-I-S heterojunction band diagram as experimentally determined for the system composed of spray hydrolysis-formed indium tin oxide (ITO)/( $n$ ) silicon: (a) zero bias; (b) under illumination, open-circuit. Epitaxial silicon was used in this particular case for ease of forming the back contact although the epilayer chosen is too thin for optimum performance [65] as may be seen from Fig. 3.1.

neutral ion beam sputtering, and the  $\text{SiO}_x$  is purposefully grown during fabrication, had been considered to be an anisotype S-I-S solar cell [ $\eta \approx 14\%$  (AM1) using single-crystal Si] [68]. The fact that ion-beam sputtered ITO gave a barrier on ( $p$ )Si was considered anomalous since spray-deposited ITO gave photovoltaic action on ( $n$ )Si [and an ohmic contact on ( $p$ )Si] as we have just discussed. Although considered anomalous, the formation of a barrier by ion-beam-sputtered ITO on ( $p$ )Si was considered possible, since the electron affinity and hole affinity are a

function of composition in an alloy semiconductor and the composition of ion-beam-sputtered ITO may not be the same as that of spray-deposited ITO.

In exploring this anomalous behavior further, it has been determined that when ion-beam processing is used, a positively charged defect layer is created at the surface of (*p*)Si which causes the adjacent (*p*)Si to deplete (to shield this positive charge residing in defects). Consequently, this work indicates that the neutral ion-beam produced ITO/SiO<sub>x</sub>/(*p*)Si cell is not an anisotype S-I-S cell, but a homojunction cell of the form ITO/SiO<sub>x</sub>/(*n*)Si/(*p*)Si [69].

### 5.3.2 Polycrystalline Devices

A number of anisotype S-S devices have also been explored for application to polycrystalline materials. Table 5.2 gives efficiencies for some selected polycrystalline anisotype S-S heterojunction solar cells; all of the devices shown are thin-film structures whose total window-absorber thickness is at least less than 25  $\mu\text{m}$ . An example is the thin-film (*n*)CdS/(*p*)CuInSe<sub>2</sub> cell, fabricated entirely by vacuum evaporation and sputtering techniques, which has achieved 9.4% efficiencies under terrestrial conditions [70] as seen in the table. The actual (*n*)CdS/(*p*)CuInSe<sub>2</sub> structure is  $\sim 5 \mu\text{m}$  thick.

The II VI heterojunction (*n*)CdS/(*p*)CdTe has achieved  $\eta = 8.7\%$  (70 mW/cm<sup>2</sup>) in thin-film polycrystalline form when prepared by the combined use of chemical deposition and vacuum evaporation techniques [71]. A heterojunction between these same materials, prepared on borosilicate glass substrates by successively repeating screen printing and heating of pastes of CdS, CdTe, and C, has achieved  $\eta = 6.3\%$  [25]. The distribution of sulfur and tellurium in the junction region of the screen printed cell, which uses the carbon as a contact, is seen in Fig. 5.22 for several heat treatments. The movement of S and Te with heat treatments is apparent; the existence of a continuously varying, optimally configured CdS<sub>1-x</sub>Te<sub>x</sub> layer is believed

TABLE 5.2  
*Some Polycrystalline Anisotype S-S Heterojunction Cells*

Structure (window/absorber)	Efficiency (%)	Light conditions (mW/cm <sup>2</sup> )	Reference
( <i>n</i> )CdS/( <i>p</i> )InP	5.7	74	9
( <i>n</i> )CdS/( <i>p</i> )CuInSe <sub>2</sub>	9.4	Terrestrial	70
( <i>n</i> )CdS/( <i>p</i> )CdTe	$\sim 10$	70	71
( <i>n</i> )CdS/( <i>p</i> )Cu <sub>2</sub> S	9.15	88	5
( <i>n</i> )Zn <sub>x</sub> Cd <sub>1-x</sub> S/( <i>p</i> )Cu <sub>2</sub> S	8.7	87	72
( <i>p</i> )ZnTe/( <i>n</i> )CdSe	$\sim 2$	87	73

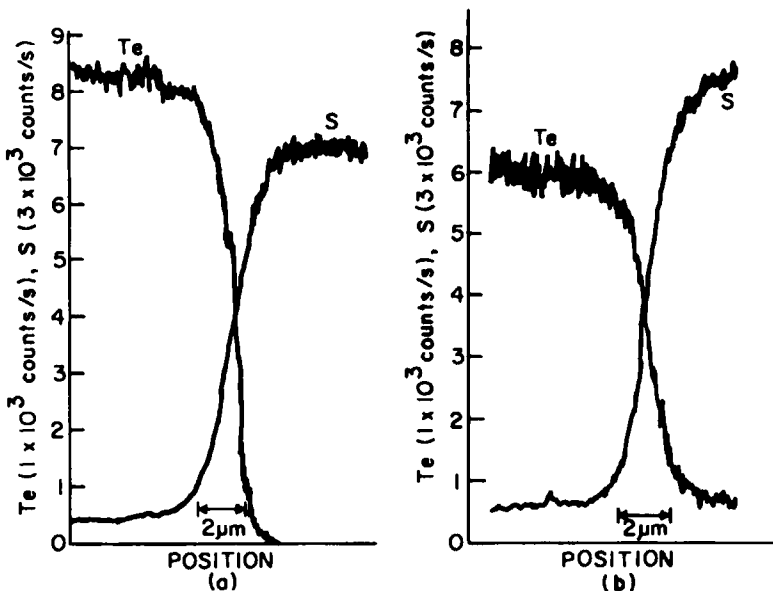


Fig. 5.22 Distribution of S and Te in the junction region of the CdS/CdTe solar cell with the carbon electrode, (a) after heat treatment at 200°C for 10 min in N<sub>2</sub> atmosphere, and (b) after additional heat treatment at 400°C for 10 min in N<sub>2</sub> atmosphere. (After Ref. [25], with permission.)

to contribute to the reduction of lattice mismatch in this cell and to contribute to efficiency [25].

The first thin-film heterojunction solar cell, (n)CdS/(p)Cu<sub>2</sub>S, remains one of the more efficient polycrystalline devices. As noted in Table 5.2, devices with  $\eta = 9.15\%$  (88 mW/cm<sup>2</sup>) have been produced [5]. Although CdS/Cu<sub>2</sub>S cells have been fabricated by a number of techniques [74], the procedure employed in the most efficient cells has been to vapor-deposit CdS onto a Zn plated Cu foil, to form the absorbing, degenerate (p)Cu<sub>2</sub>S by Cu–Cd ion exchange in a cuprous-ion solution (which gives  $\sim 1000 \text{ \AA}$  of a heavily textured, light-trapping Cu<sub>2</sub>S layer), to evaporate a highly transmitting ( $\sim 96\%$ ) Au grid as the top electrical contact, and to vapor deposit SiO<sub>x</sub> as the AR coating [5, 75].

The bucking current of this thin-film (n)CdS/(p)Cu<sub>2</sub>S device, which has a band diagram similar to that of Fig. 5.9a, has been shown to be dominated by the interface recombination current  $J_{\text{blk}}|_1$  of Eq. (5.60) [5, 16, 75]. Hence, the device is not operating at the bulk diffusion–recombination limit for the bucking current [term  $J_{\text{blk,dif}}$  of Eq. (5.60)]<sup>†</sup> and, in principle, the open-circuit

<sup>†</sup> We note from Eq. (5.60) that, even if we could eliminate interface recombination, junction region recombination, and multistep tunneling, we are always left with the bulk diffusion–recombination component of  $J_{\text{blk}}$ .

voltage can be improved. The factor  $R_1$ , given by Eq. (5.108), has been shown to be very important for current collection in the heterojunction, since Eq. (5.111) holds for  $F_{1n}$ ; and significant voltage dependence of  $J_{pb}$ , arising through the presence of the window electrostatic field  $\xi_{M1}$  term in Eq. (5.111), has been demonstrated [40, 41]. Because of the dependence on  $\xi_{M1}$ ,  $F_{1n}$  can be affected by cross diffusion of Cu into the CdS since Cu introduces acceptor levels that modify the barrier shape in the optical window material and, hence, modify  $\xi_{M1}$  [40, 41]. As with the corresponding single-crystal heterojunction, the stoichiometry of the  $\text{Cu}_2\text{S}$  layer also affects cell performance [74, 75].

Polycrystalline  $(n)\text{CdS}/(p)\text{Cu}_2\text{S}$  cells optimally have a lattice mismatch of 4% (varies depending on the copper sulfide phases present [74]). If the ternary  $\text{Zn}_x\text{Cd}_{1-x}\text{S}$  ( $3.6 \geq E_g \geq 2.42$  eV depending on  $X$ ) is used as the window in place of CdS, a better lattice match to  $\text{Cu}_2\text{S}$  is possible by adjustment of  $X$  and, hence, by adjustment of the lattice structure of the  $\text{Zn}_x\text{Cd}_{1-x}\text{S}$  [12, 46]. Experimentally, the polycrystalline  $(n)\text{Zn}_x\text{Cd}_{1-x}\text{S}/(p)\text{Cu}_2\text{S}$  heterojunction is found to give a higher  $V_{oc}$  than the corresponding  $(n)\text{CdS}/(p)\text{Cu}_2\text{S}$  cell. This is anticipated since a band diagram similar to Fig. 5.9a (with the  $p$ -type absorber  $\text{Cu}_2\text{S}$  being degenerate) is believed to apply and, as a consequence,  $J_{bk|1}$  of Eq. (5.60) should be reduced in the  $(n)\text{Zn}_x\text{Cd}_{1-x}\text{S}/(p)\text{Cu}_2\text{S}$  device due to the reduction in  $N_1^I$  expected with the better lattice match. It can also be pointed out that  $J_{bk|1}$  in the  $(n)\text{Zn}_x\text{Cd}_{1-x}\text{S}/(p)\text{Cu}_2\text{S}$  cell can be reduced for another reason: Eq. (5.102) applies because of the position of  $E_F$  at zero bias at  $x = W_1$ , and because  $V_1 \approx V$  and  $V_2 \approx 0$ ; therefore  $\text{Zn}_x\text{Cd}_{1-x}\text{S}$ , which has an electron affinity that decreases with increasing  $X$ , will result in a larger effective gap  $G$  than will similarly doped CdS. As seen from Eq. (5.102), a larger  $G$  value will result in a reduced  $J_{bk|1}$ .

The affinity of  $\text{Zn}_x\text{Cd}_{1-x}\text{S}$  can become less than that of  $\text{Cu}_2\text{S}$  (see Table 3.1). The result can be a disadvantageous spike in the conduction band at  $x = W_1$  and difficulty in the collection of photocurrent. It has been noted that the short-circuit currents in some  $(n)\text{Zn}_x\text{Cd}_{1-x}\text{S}/(p)\text{Cu}_2\text{S}$  cells have been lower than expected [16, 72]. However,  $(n)\text{Zn}_x\text{Cd}_{1-x}\text{S}/(p)\text{Cu}_2\text{S}$  cells with  $\eta = 10\%$  ( $87 \text{ mW/cm}^2$ ) have been achieved [72].

Another heterojunction structure with potential for thin-film solar cells would appear to be CdSe-ZnTe devices since the lattice mismatch is very small (0.35%) [73]. The CdSe ( $E_g = 1.70$  eV) serves as the absorber and the ZnTe ( $E_g = 2.26$  eV) serves as the optical window; since CdSe has an electron affinity of 4.95 eV and ZnTe has an electron affinity of 3.53 eV (Table 3.1), the heterojunction solar cell structure must be  $(p)\text{ZnTe}/(n)\text{CdSe}$  to avoid a conduction-band spike. As seen from Table 5.2, polycrystalline devices of this type have yielded efficiencies of  $\eta \sim 2\%$  ( $87 \text{ mW/cm}^2$ ) [73].

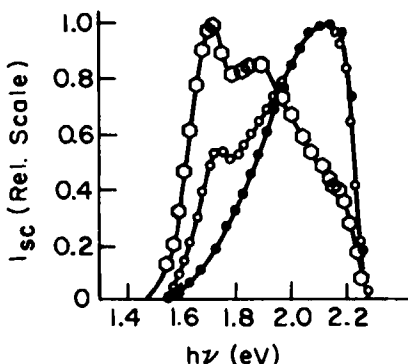


Fig. 5.23 Spectral response of short-circuit current for three (*n*) CdSe/(*p*) ZnTe cells prepared with different substrate temperatures. In order of increasing magnitude of the 1.72-eV peak, the curves are for  $T_s = 502^\circ\text{C}$ ,  $T_s = 565^\circ\text{C}$ , and  $T_s = 591^\circ\text{C}$ . (After Ref. [73], with permission.)

The spectral response SR for three (*p*)ZnTe/(*n*)CdSe cells are seen in Fig. 5.23; each cell employed different substrate temperatures during CdSe deposition. These data underscore a point made in Section 5.2.1: the barrier shape in nominally the same heterojunction structures can be a strong function of device processing.

### 5.3.3 Amorphous Devices

All-amorphous, thin-film heterojunctions have been fabricated and examined for photovoltaic response. For example, photovoltaic action has been observed in an anisotype structure in the form of an amorphous (*p*)SiC:H/(*i*)Si:H/(*n*)Si:H junction; the resulting AM1 conversion efficiency was greater than 7.1% [76]. It would be expected that *p-i-n* type heterojunction structures, principally using drift to collect photocarriers, would be the more effective solar cell configuration in those amorphous materials with poor diffusion lengths.

## 5.4 NOTES FOR THE EXPERIMENTALIST

In choosing semiconductor pairs for heterojunctions, physical compatibility (lattice match, thermal expansion) and chemical compatibility must be considered. In addition, if the absorber in an anisotype (S-S or S-I-S) junction is *p*-type, the electron affinity of the absorber must be less than or equal to the electron affinity of the window so that a conduction-band spike will not occur. If the absorber in an anisotype (S-S or S-I-S) junction is *n*-type, the hole affinity of the absorber must be greater than or equal to the hole affinity of the window in order to avoid a valence-band spike. These restrictions on the electron and hole affinities do not pertain to

isotype heterojunctions since the photocurrent must cross the metallurgical junction by interface recombination in this device class. Instead, a new set of guidelines apply: for  $n-n$  isotype (S-S or S-I-S) heterojunctions, the window electron affinity should have a value close to that of the absorber hole affinity to reduce the effective gap  $G$  (optimally the window electron affinity  $\gtrsim$  the absorber hole affinity); for  $p-p$  isotype (S-S or S-I-S) heterojunctions, the window hole affinity should have a value close to that of the absorber electron affinity to reduce the effective gap  $G$  (optimally the window hole affinity  $\lesssim$  the absorber electron affinity). Unfortunately, there is a complication that arises when performing these assessments of semiconductor affinities: the relationship between experimental affinity data such as that seen in Table 3.1 and the actual magnitude of the band discontinuities is not a straightforward one [77]. However, the data of Table 3.1 provide a convenient starting point.

When one is considering the usefulness of a semiconductor pair in a heterojunction solar cell structure, the Anderson model, although an idealization, is extremely helpful; however, the actual band diagram that may apply to a heterojunction formed from a given pair of materials may be considerably different from that predicted by the Anderson model, as pointed out by Fig. 5.7. In fact, the band diagram that may apply can vary with processing as implied by Figs. 5.22 and 5.23. Processing variations can cause differences in cross diffusion, intermediary layer formation, and interface state density (interface unipoles and dipoles).

An extreme example of the influence of processing on cell structure is the ITO-Si system discussed in Section 5.3.1. Another example of the role of processing is provided by the rf sputtered indium-tin-oxide (ITO)-InP system. Initially this materials system was thought to result in an  $(n)$ ITO/ $(p)$ InP anisotype S-S heterojunction [78]. Efficiencies of  $\sim 14\%$  displayed by the cell were surprising, however, due to the large lattice mismatch present between ITO and InP. Subsequent investigation has shown that the device produced by rf sputtering ITO on  $(p)$ InP is not a S-S heterojunction at all; rather, the resulting configuration is a homojunction cell of the form  $(n^+)$ ITO/ $(n)$ InP/ $(p)$ InP. It has been shown that substantial Sn diffusion into the InP, resulting in the  $n$ -type doping of a layer that was originally  $p$ -type InP, can occur to form the homojunction, if the InP temperature during rf sputtering is  $250^\circ\text{C}$  or more [79]. It has also been shown that a  $\sim 1\ \mu\text{m}$ -thick  $n$ -type InP layer can be created by damage incurred during rf sputter-deposition on room-temperature heat-sunk InP even without impurity out-diffusion from the ITO [80]; i.e., damage induced by rf sputtering (in addition to cross diffusion) can produce a homojunction structure in this materials system.

Verifying the form of the junction and the transport mechanisms operative in a solar cell are necessary if fundamental operation limitations are to be understood. As was the case for homojunctions, spectral response and capacitance measurements are important, nondestructive tools for studying heterojunction barrier regions [3, 65, 80]. Plots of  $J_{sc}$  versus  $V_{oc}$  and dark-diode characteristics are also important [3, 81-84]. These data, especially when obtained at different temperatures, allow the transport mechanisms operative in a cell to be determined by comparing experimentally obtained voltage, temperature, and illumination dependence with that predicted theoretically in the discussions of Sections 5.2.2-5.2.6.

## REFERENCES

1. D. D. Reynolds, G. Leies, L. L. Antes, and R. E. Marburger, *Phys. Rev.* **96**, 533 (1954).
2. R. Williams and R. H. Bube, *J. Appl. Phys.* **6**, 968 (1960).
3. R. H. Bube, *Heterojunctions for Thin Film Solar Cells* in "Solar Materials Science" (L. Murr, ed.). Academic Press, New York, 1980.
4. A. E. Carlson, Research on Semiconductor Films, WADC Tech. Rep. 56-62. Clevite Corp., 1956.
5. A. M. Barnett, J. A. Bragagnolo, R. Hall, J. E. Phillips, and J. D. Meakin, *Conf. Rec. IEEE Photovoltaic Spec. Conf.*, 13th p. 419. IEEE, New York, 1978.
6. Z. Alferov, N. Zimogorova, M. Trukan, and V. Tuchkevich, *Sov. Phys.—Solid State (Engl. Trans.)* **7**, 990 (1965).
7. D. A. Cusano, *Solid-State Electron.* **6**, 217 (1963); *Rev. Phys. Appl.* **1**, 195 (1966).
8. W. Johnston, Jr., and W. Callahan, *Appl. Phys. Lett.* **28**, 150 (1976).
9. S. Wagner, J. L. Shay, K. J. Bachmann, and E. Buehler, *Appl. Phys. Lett.* **26**, 229 (1975); M. Bettini, K. J. Bachmann, and J. L. Shay, *J. Appl. Phys.* **49**, 865 (1978).
10. J. L. Shay, S. Wagner, and H. Kasper, *Appl. Phys. Lett.* **27**, 89 (1975).
11. W. G. Oldham and A. G. Milnes, *Solid-State Electron.* **7**, 153 (1964).
12. K. W. Boer, *J. Appl. Phys.* **50**, 5356 (1979).
13. A. L. Fahrenbruch and J. Aranovich, *Heterojunction Phenomena and Interfacial Defects in Photovoltaic Converters* in "Solar Energy Conversion: Solid-State Physics Aspects" (B. O. Seraphin, ed.), Vol. 31, Topics in Applied Physics, p. 257. Springer-Verlag, Berlin and New York, 1979.
14. D. B. Holt, *J. Phys. Chem. Solids* **27**, 1053 (1966).
15. H. Kressel, *J. Electron. Mater.* **4**, 1081 (1975).
16. A. M. Barnett and A. Rothwarf, *IEEE Trans. Electron Devices* **ED-27**, 615 (1980).
17. A. Yoshikawa and Y. Sakai, *Solid-State Electron.* **20**, 133 (1977).
18. K. Yamaguchi, N. Nakayama, H. Matsumoto, and S. Ikegami, *Jpn. J. Appl. Phys.* **16**, 1203 (1977).
19. A. L. Fahrenbruch, J. Aranovich, F. Courreges, T. Chynoweth, and R. H. Bube, *Conf. Rec. IEEE Photovoltaic Spec. Conf.*, 13th p. 281. IEEE, New York, 1978.
20. T. L. Tansley, *Heterojunction Properties in Semiconductors and Semimetals* (R. K. Willardson and A. C. Beer, eds.), Vol. 7, p. 294. Academic Press, New York, 1971.
21. H. Kasano and S. Hosoki, *J. Appl. Phys.* **46**, 394 (1975).
22. T. O'M. Bockris and A. K. N. Reddy, "Modern Electrochemistry," Vols. 1 and 2. Plenum, New York, 1977.

23. C. C. Wang, M. H. Kalisher, J. M. Tracy, J. E. Clarke, and J. T. Longo, *Solid-State Electron.* **21**, 625 (1978).
24. F. Buch, A. L. Fahrenbruch, and R. H. Bube, *J. Appl. Phys.* **48**, 1596 (1977).
25. N. Nakayama, H. Matsumoto, A. Nakano, S. Ikegami, H. Uda, and T. Yamasita, *Jpn. J. Appl. Phys.* **19**, 703 (1980).
26. R. L. Anderson, *Solid-State Electron.* **5**, 341 (1962).
27. W. G. Oldham and A. G. Milnes, *Solid-State Electron.* **6**, 121 (1963).
28. D. T. Cheung, S. Y. Chiang, and G. L. Pearson, *Solid-State Electron.* **18**, 263 (1975).
29. J. F. Jordan, Thin Film Cu<sub>2</sub>S/CdS Solar Cells by Chemical Spraying, Final Rep. Contr. Ex-76-C643579. Dept Energy, Washington, D.C., 1978.
30. J. E. Sutherland and J. R. Hauser, *IEEE Trans. Electron Devices* **ED-24**, 363 (1977).
31. M. Wolf, *Proc. IEEE* **51**, 674 (1963).
32. T. S. Te Velde, *Solid-State Electron.* **16**, 1305 (1973).
33. S. J. Fonash, *J. Appl. Phys.* **51**, 2115 (1980).
34. S. J. Fonash and S. Ashok, *Conf. Rec. IEEE Photovoltaic Spec. Conf.*, 14th p. 591. IEEE, New York, 1980.
35. S. J. Fonash, *Solid-State Electron.* **22**, 907 (1979).
36. L. L. Chang, *Solid-State Electron.* **8**, 721 (1965).
37. T. L. Tansley, *Phys. Status Solidi* **18**, 105 (1966).
38. A. R. Riben and D. L. Feucht, *Solid-State Electron.* **9**, 1055 (1966).
39. A. Rothwarf, NSF Rep. NSF-RANN AER 75-15858, pp. 9-50.
40. A. Rothwarf and A. M. Barnett, *IEEE Trans. Electron Devices* **ED-24**, 381 (1977).
41. A. Rothwarf, J. Phillips, and N. Convers-Wyeth, *Conf. Rec. IEEE Photovoltaic Spec. Conf.*, 13th pp. 399-405. IEEE, New York, 1978.
42. H. J. Hovel, in "Semiconductors and Semimetals" (R. K. Willardson and A. C. Beer, eds.), Vol. 11, Solar Cells. Academic Press, New York, 1975.
43. D. L. Staebler, *Int. Conf. Amorphous Liq. Semicond.*, 8th, Harvard Univ., Aug. 27-31, 1979.
44. H. C. Card, *J. Appl. Phys.* **50**, 2822 (1979).
45. S. Wagner, J. L. Shay, K. J. Bachmann, and E. Buehler, *Appl. Phys. Lett.* **26**, 229 (1975).
46. D. L. Feucht, *J. Vac. Sci. Technol.* **14**, 57 (1977).
47. T. L. Tansley and S. J. T. Owen, *IEEE Trans. Electron Devices* **ED-23**, 1123 (1976).
48. J. Donnelly and A. Milnes, *Int. J. Electron.* **20**, 295 (1966).
49. A. DeVos, *Energy Convers.* **16**, 67 (1976).
50. A. DeVos and H. J. Pauwels, *IEEE Trans. Electron Devices* **ED-24**, 388 (1977).
51. S. Ashok, P. P. Sharma, and S. J. Fonash, *IEEE Trans. Electron Devices* **ED-27**, 725 (1980).
52. H. J. Pauwels, *Solid-State Electron.* **22**, 988 (1979).
53. J. Shewchun, J. DuBow, A. Myszkowski, and R. Singh, *J. Appl. Phys.* **49**, 855 (1978).
54. J. C. Phillips, "Bonds and Bands in Semiconductors." Academic Press, New York, 1973.
55. L. L. Kazmerski, F. R. White, M. S. Ayyagari, Y. J. Juang, and R. P. Patterson, *J. Vac. Sci. Technol.* **14**, 65 (1977).
56. P. F. Lindquist and R. H. Bube, *J. Electrochem. Soc.: Solid State Sci. Technol.* **119**, 936 (1972).
57. F. A. Shirland and P. Rai-Choudhury, *Rep. Prog. Phys.* **41**, 1839 (1978).
58. K. W. Boer and A. Rothwarf, *Prog. Solid State Chem.* **10**, 71 (1975); *Annu. Rev. Mater. Sci.* **6**, 303 (1976).
59. E. H. Roseboom, *Econ. Geol.* **61**, 641 (1966).
60. W. Palz, et. al., *Conf. Rec. IEEE Photovoltaic Spec. Conf.*, 9th p. 97. IEEE, New York, 1973.
61. J. A. Hutchby, R. Sahai, and J. S. Harris, *Tech. Dig.-Int. Electron Devices Meet.*, Washington, D.C., p. 93. IEEE, New York, 1975.

62. A. Berkeliiev, A. S. Volkov, A. N. Imenkov, A. L. Lipko, N. Nazarov, B. S. Suleimenov, B. V. Tsarenkov, and Yu. P. Yakovlev, *Fiz. Tekh. Poluprovodn.* **13**, 938 (1979) [*Sov. Phys.—Semicond. (Engl. Transl.)* **13**, 549 (1979)].
63. O. A. Tokalin, *Fiz. Tekh. Poluprovodn.* **13**, 2071 (1979) [*Sov. Phys.—Semicond. (Engl. Transl.)* **13**, 1211 (1979)].
64. J. C. Manifacier and L. Szepessy, *Appl. Phys. Lett.* **31**, 459 (1977).
65. S. Ashok, P. P. Sharma, and S. J. Fonash, *IEEE Trans. Electron Devices* **ED-27**, 725 (1980).
66. E. Y. Wang and R. N. Legge, *IEEE Trans. Electron Devices* **ED-25**, 800 (1978); *Conf. Rec. IEEE Photovoltaic Spec. Conf., 12th* p. 967. IEEE, New York, 1976.
67. T. Feng, C. Fishman, and A. K. Ghosh, *Conf. Rec. IEEE Photovoltaic Spec. Conf., 13th* p. 519. IEEE, New York, 1978; *Appl. Phys. Lett.* **34**, 198 (1978).
68. D. E. Burk, J. B. DuBow, and J. R. Sites, *Appl. Phys. Lett.* **29**, 494 (1976); A. P. Genis, P. A. Smith, C. Osterwald, R. Singh, and J. DuBow, *IEEE Electron Device Lett.* **EDL-1**, 143 (1980).
69. S. Ashok, S. J. Fonash, R. Singh, P. Wiley, *IEEE Electron Device Lett.* **EDL-2**, 184 (1981).
70. *Electronics* **53**, (18), p. 43 (Aug. 14, 1980).
71. H. Uda, H. Taniguchi, M. Yoshida, and T. Yamashita, *Jpn. J. Appl. Phys.* **17**, 585 (1978).
72. R. B. Hall, R. W. Birkmire, J. E. Phillips, and J. D. Meakin, *Appl. Phys. Lett.* **38**, (July, 1981).
73. F. Buch, A. L. Fahrenbruch, and R. H. Bube, *Appl. Phys. Lett.* **28**, 593 (1976).
74. M. Savelli and J. Bougnot, Problems of the Cu<sub>2</sub>S/CdS Cell, in "Solar Energy Conversion: Solid-State Physics Aspects" (B. O. Seraphin, ed.), Vol. 31, Topics in Applied Physics. Springer-Verlag, Berlin and New York, 1979.
75. J. A. Bragagnolo, A. M. Barnett, J. E. Phillips, R. B. Hall, A. Rothwarf, and J. D. Meakin, *IEEE Trans. Electron Devices* **ED-27**, 645 (1980).
76. Y. Tawada, H. Okamoto, and Y. Hamakawa, *Appl. Phys. Lett.* **39**, 237 (1981).
77. H. Kroemer, *CRC Crit. Rev. Solid State Mater. Sci.* **5**, 555 (1975); W. R. Frensel and H. Kroemer, *Phys. Rev. B: Solid State* **16**, 2642 (1977).
78. K. S. Sree Harsha, K. J. Bachmann, P. H. Schmidt, E. G. Spencer, and F. A. Thiel, *Appl. Phys. Lett.* **30**, 645 (1977).
79. K. J. Bachmann, H. Schreiber, Jr., W. Sinclair, P. Schmidt, F. Thiel, E. Spencer, G. Pasteur, W. Feldmann, and K. S. Sree Harsha, *J. Appl. Phys.* **50**, 3441 (1979).
80. Ming-Jong Tsai, A. L. Fahrenbruch, and R. H. Bube, *J. Appl. Phys.* **51**, 2696 (1980).
81. N. Nakayama, *Jpn. J. Appl. Phys.* **8**, 450 (1969).
82. H. Luquet, G. M. Moussalli, J. Bougnot, M. Perotin, and M. Savelli, *Rev. Phys. Appl.* **14**, 245 (1979).
83. R. Moorthy, L. Partain, D. Okubo, and D. Henderson, *Tech. Dig.-Int. Electron Devices Meet., Washington, D.C.* p. 442. IEEE, New York, 1979.
84. S. Kar, S. Ashok, and S. Fonash, *J. Appl. Phys.* **51**, 3417 (1980).

## CHAPTER 6

# Surface-Barrier Solar Cells

### 6.1 INTRODUCTION

All surface-barrier solar cells have the common feature that only one semiconductor, in one doping type, is employed and the principal source of photovoltaic action is a depleted barrier region at the surface of this semiconductor. There are basically two types of surface-barrier cells which can be distinguished by the materials system used to form the surface barrier: one type is the all-solid-state cell and the other is the electrolyte-solid cell. The all-solid-state cell uses a metal-semiconductor (M-S) or metal-insulator-semiconductor (M-I-S) configuration, whereas the electrolyte-solid cell uses a liquid-semiconductor configuration. The M-S and M-I-S devices are often referred to as Schottky-barrier type cells and the liquid-semiconductor devices are referred to as electrochemical photovoltaic cells (EPC).

The lineage of surface-barrier solar cells can be traced back to the electrolyte-solid structures used by Becquerel [1] in 1839 in the first reported studies of photovoltaic action. Investigation of the solid state, surface-barrier cell begins with the Cu-Cu<sub>2</sub>O structure which was shown to be photosensitive by Hallwachs [2] in 1904, and which was developed into a photovoltaic device by 1927 [3]. By the 1930s, Cu-Cu<sub>2</sub>O metal-

semiconductor, surface-barrier devices were in production and were being used for applications such as photometry and light control. At this stage of their development, solar conversion efficiencies of  $\eta \lesssim 1\%$  had been achieved in solid-state surface-barrier photovoltaic devices [2].

During the early 1950s, surface-barrier photovoltaic structures were quickly eclipsed by the emerging  $p-n$  homojunction solar cell technology just as Schottky-barrier diodes were quickly surpassed by  $p-n$  junction diodes during this time. By 1970–1972 Schottky-barrier solar cells had only evolved to  $\eta \lesssim 6\%$  for single-crystal Si M-S devices and to  $\eta \lesssim 9\%$  for single-crystal GaAs M-S devices (terrestrial conditions) [4], whereas liquid-semiconductor (EPC) solar cells of the period were unstable devices with efficiencies which had yet to reach 1% under terrestrial sunlight [5–7].

In the case of the Schottky-barrier devices, the cause of these relatively low conversion efficiencies rested in the basic physics governing the operation of M-S cells: the bucking current of an M-S cell is dominated by thermionic emission of the majority carriers since this component is generally found to be orders of magnitude larger, for a given bias, than the minority carrier, bulk diffusion–recombination bucking-current component [see Fig. 6.7)]. This bulk diffusion–recombination component, overshadowed in the M-S cell, ideally dominates the bucking current in a  $p-n$  homojunction solar cell as we saw in Chapter 4. Hence  $V_{oc}$  is expected to be lower for a M-S cell than for the corresponding  $p-n$  homojunction device fabricated with the same semiconductor. Even though  $J_{sc}$  can be the same for both structures, solar energy conversion efficiency suffers in the M-S configuration due to the low  $V_{oc}$  values.

In the case of the liquid-semiconductor (EPC) devices, the cause of the poor stability and extremely low conversion efficiencies was simply that the oxidation–reduction couple–solvent systems (see Section 3.4.7) used to form the barrier in the semiconductor and used to collect the photocurrent were not serving as an efficient sink for photogenerated minority carriers swept to the liquid–semiconductor interface. Since the photocarriers were not being effectively siphoned off at the semiconductor surface, they were recombining, back-diffusing away, or participating in photodecomposition of the semiconductor electrode, resulting in the very poor conversion efficiencies and instability observed.

In the early to mid-1970s there were several developments which led to rapid improvement of the surface-barrier class of solar cells. For the all-solid-state cells, the turning point occurred in 1972 when it was found experimentally that the open-circuit voltage of an Al/(p)Si M-S solar cell could be substantially increased by fabricating the structure such that there is an insulating  $\text{SiO}_x$  layer between the Al and the  $p$ -type silicon [8]. This development ushered in the surface-barrier photovoltaic device which we

now term the metal-insulator-semiconductor (M-I-S) solar cell. The M-I-S solar cell employs the I layer to suppress the thermionic emission bucking current which limits performance in the M-S configuration. The result is an increase in  $V_{oc}$  which can be designed to occur without impeding collection of the photocurrent. Other groups showed experimentally that the M-I-S surface-barrier configuration could be used with *n*-type silicon [9], with III-V compound semiconductors (*n*)GaAs [4, 10], and could be developed to suppress totally the majority-carrier bucking current [11]. The latter work demonstrated that the relatively simple M-I-S solar cell structure, produced with potentially low-temperature processing, could yield the efficiencies and performance of a *p-n* homojunction solar cell. By the end of the decade, M-I-S inversion layer devices (M-I-S type structures) had been developed for single-crystal (*p*) silicon to a point where  $\eta = 16\%$  (AM1) had been achieved [12, 13] and M-I-S structures fabricated with single-crystal (*n*)GaAs had been developed to a point where  $\eta = 17\%$  (AM1) had been achieved [14].

For liquid-semiconductor surface-barrier solar cells, the turning point in their development was the report in 1976 that a liquid-(*n*)CdS device had been stabilized and conversion efficiencies in the 1–2% range had been achieved by using a polychalcogenide<sup>†</sup> electrolyte [15, 16]. The particular oxidation-reduction (redox) couple used in this work was the sulfide-polysulfide ( $S^{2-}/S_n^{2-}$ ) couple in an aqueous solution. Its success lay in the fact that this couple causes a barrier at the surface of CdS and, most importantly, the couple serves as an efficient sink for photogenerated holes swept to the liquid-(*n*)CdS interface by the semiconductor surface barrier. By choosing redox couples favorably located in energy with respect to the surface positions of the semiconductor band edges, or by modifying the kinetics governing electron transfer between the semiconductor and redox couple, or by doing both, liquid-semiconductor surface-barrier solar cells had achieved stable terrestrial solar conversion efficiencies as high as  $\eta = 12\%$  (polyselenide electrolyte-(*n*)GaAs) [17] by the end of the 1970s.

Today, surface-barrier solar cell configurations (metal-semiconductor, metal-insulator-semiconductor, and liquid-semiconductor junctions) are being used with a wide variety of amorphous, polycrystalline, and crystalline organic and inorganic semiconductors. This interest stems from the fact that surface-barrier devices are the simplest and potentially least expensive of solar cell structures. Also barrier formation in surface-barrier devices is a low-temperature process; e.g., in EPC devices it is achieved simply by immersing a semiconductor into an electrolyte. Because barrier formation can be accomplished at low temperatures without danger of affecting the

<sup>†</sup> Chalcogens are the group VIA elements O, S, Se, and Te.

bulk absorber properties, and because only one semiconductor is involved in these structures, surface-barrier solar cells are particularly advantageous in assessing the potential of new absorber materials.

## 6.2 SURFACE-BARRIER SOLAR CELL DEVICE PHYSICS

### 6.2.1 Qualitative Discussion

#### 6.2.1.1 General Features

The basic feature of all surface-barrier solar cells is that the principal source of photovoltaic action is a depleted, space-charge region existing at the semiconductor (absorber) surface as seen in Fig. 6.1. The three types of surface-barrier cells (M-S, M-I-S, and EPC) differ only in the materials system used to the left of  $x = 0$  in Fig. 6.1 to form the barrier and to collect photogenerated carriers.

As was the case for the other two broad classes of solar cell structures (homojunctions and semiconductor-semiconductor heterojunctions), surface-barrier solar cells can be designed either to use diffusion to bring photogenerated minority carriers to a relatively narrow barrier region, or cell structures can be designed to use drift directly to collect photogenerated carriers (these two extreme approaches to photocurrent collection were discussed in general terms in Section 3.2). The surface-barrier cell of Fig. 6.1a is suitable for absorbers that have diffusion lengths  $L_{n,p}$  which are of the order of, or greater than, the absorption length  $1/\alpha$ , whereas the surface-barrier cell of Fig. 6.1b is suitable for absorbers that have diffusion lengths such that  $L_{n,p} \ll 1/\alpha$  but drift lengths which are of the order of, or greater than,  $1/\alpha$ .

To investigate more closely the generation of the photocurrent as well as the sources of carrier loss in surface-barrier devices, we examine the surface-barrier structure seen under illumination in Fig. 6.2. This structure, which could be an M-S, M-I-S, or EPC cell, is seen to have electron-hole pairs created in the absorber by the impinging light. Focusing on the minority-carrier holes, it is seen that they are subject to (a) recombination at the ohmic contact (which can be minimized by the use of selective-ohmic contacts—see Section 3.6.3), (b) recombination in the bulk and space-charge regions, (c) interface recombination, and (d) recombination in the barrier-forming material. Those minority carriers which survive all the loss mechanisms are collected by the barrier former (a metal, a metal-insulator, or a redox couple). Consequently they constitute the photocurrent which does work in an external load.

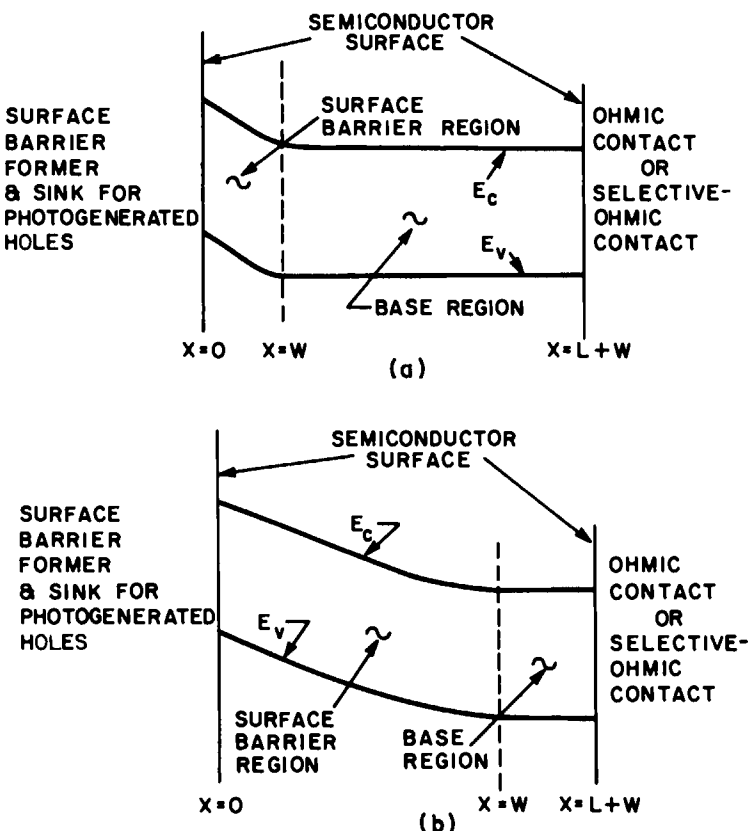


Fig. 6.1 Common features of all surface-barrier solar cells are shown assuming an *n*-type semiconductor. (a), (b) A surface barrier exists in the semiconductor (absorber). This barrier is the result of a metal-semiconductor (M-S), a metal-insulator-semiconductor (M-I-S), or a liquid-semiconductor (EPC) junction. (a) Diffusion is being relied on to bring minority carriers into the barrier region for collection. (b) Drift is being used directly to collect photogenerated carriers; in (b) the base (quasi-neutral region) width may be zero.

Photogenerated holes may be collected by the barrier former simply by being emitted from the valence band at  $x = 0$  in Fig. 6.2. These carriers are collected by the metal in M-S and M-I-S cells and by the redox couple in EPC cells (due to oxidation of the reduced species and the subsequent motion to the left of the resulting oxidized ion). Photogenerated holes may also be collected by the barrier former via the path labeled 6 in the figure. In metal-semiconductor and metal-insulator-semiconductor cells on *n*-type material, process 6 represents localization, at the interface, of photo-generated minority-carrier holes and their subsequent tunneling into the metal. In liquid-semiconductor cells, process 6 represents the localization of

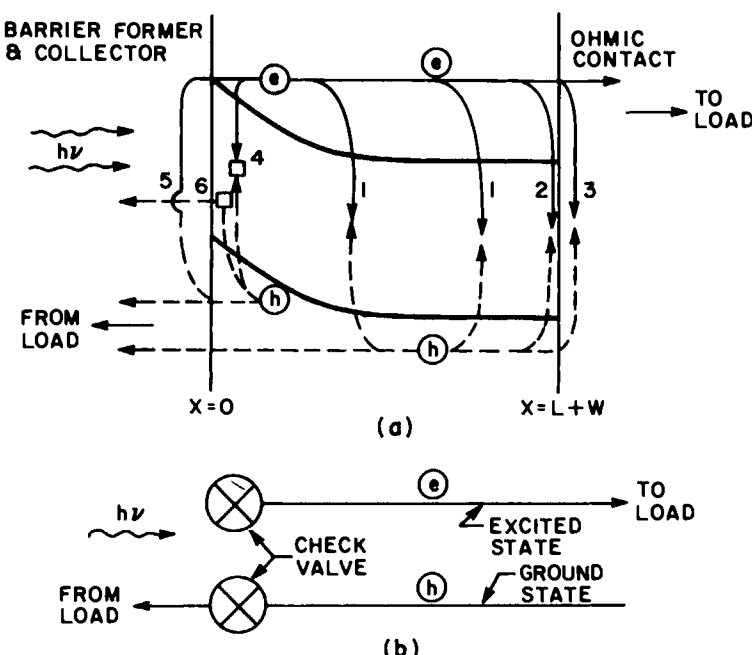
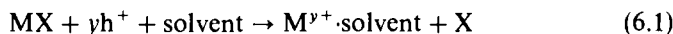


Fig. 6.2 (a) A surface-barrier solar cell structure under illumination; (b) The device in terms of the generalized representation of Chapter 1. The processes labeled 1–5 are all mechanisms by which photogenerated carriers are lost. Process 1 is space-charge and base-layer recombination, processes 2 and 3 are losses at the ohmic contact, process 4 is interface recombination, and process 5 is majority-carrier emission (giving minority-carrier loss as seen). Process 6 represents the localization of photogenerated minority carriers at the semiconductor surface. In metal-semiconductor (M-S) and metal-insulator-semiconductor (M-I-S) cells, this localized carrier can tunnel into the metal giving photocurrent collection. In liquid-semiconductor (EPC) cells this localized carrier could be transferred to the redox couple in solution giving photocurrent collection. Of course, photocurrent collection also takes place directly from the valence band as seen.

a photogenerated hole at the semiconductor surface (for the  $n$ -type semiconductor of Fig. 6.2) and the subsequent oxidation of the reduced species in solution. The transfer of the electron from the reduced species to the interface state occupied by a hole gives continuity of current and the resulting oxidized entity in solution carries the current to the left in the figure.

Unfortunately, the arrival of photogenerated holes at the surface of the  $n$ -type semiconductor of Fig. 6.2 can also produce broken bonds. This can lead to photodecomposition of the semiconductor electrode in EPC surface-barrier cells. The photodecomposition takes place according to



where the semiconductor is MX. As can be seen, photodecomposition also results in collection of the photocurrent since  $M^{y+}$  continues to carry the positive charge of the  $y$  holes to the left in Fig. 6.2 but this photocurrent produces destruction of the semiconductor surface. The collection of photocurrent by this mechanism of photodecomposition, which exists in parallel with collection by the redox couple from the valence band or from interface states, must be suppressed in any successful, stable EPC cell.

Since the arrival of photogenerated holes at the semiconductor surface in Fig. 6.2 always has the possibility of producing broken semiconductor bonds, electrochemical reactions such as the process leading to photodecomposition of the semiconductor in liquid-semiconductor junctions are possible in M-S and M-I-S cells (as well as in other all-solid-state solar cell structures) [18, 19]; however, these processes are much more destructive in the EPC cell due to the increased ability of ions to move in and out of the liquid-semiconductor interface. In all-solid-state devices the ions are relatively frozen in their positions.

#### *6.2.1.2 General Design Considerations for Surface-Barrier Cells*

The considerations involved in designing the absorber base of a surface-barrier cell are the same as those which arise for homojunctions as well as S-S and S-I-S heterojunctions. Reduction of photogenerated carrier loss in the absorber (process 1 of Fig. 6.2) and photogenerated carrier loss at the ohmic contact (processes 2 and 3) are approached in the same manner for surface-barrier cells as for homojunctions and heterojunctions. Bulk, absorber recombination, in principle, can be reduced by using heavy doping, and the ohmic contact loss can be reduced by using selective-ohmic contacts. The use of heavy doping in the absorber has the same problems we encountered in other solar cell structures: the minority-carrier lifetime ( $\tau_p$  for the example of Fig. 6.2) can become limited by Auger recombination, defects introduced by heavy doping can reduce  $\tau_p$  if recombination is still in the S-R-H regime, carrier concentration effects can modulate  $\tau_p$ , and band-edge tailing can occur as discussed in Sections 2.6 and 4.2.1.2.

Although the problems of absorber design are the same for all surface-barrier cells and, indeed, are the same as those of any solar cell, many of the problems of barrier formation can be quite different due to the differences in the materials systems used as barrier formers. Before we individually discuss the all-solid-state cell (Section 6.2.1.3) and the electrolyte-solid cell (Section 6.2.1.4), we list four common design objectives which must be considered when choosing the materials system that will create the surface barrier. These design objectives common to all surface-barrier cells are the following: (1) the materials system forming the barrier must not significantly

absorb the impinging light, if used in the configuration where the light first impinges on the barrier, (2) the materials system forming the barrier must produce a built-in potential  $V_{bi}$  in the semiconductor which approaches the gap energy of the semiconductor for efficient carrier collection and for the highest possible upper bound on  $V_{oc}$ , (3) the materials system forming the barrier must be an effective collector of photocurrent, and (4) the materials system forming the surface barrier must be chemically compatible with the semiconductor.

#### 6.2.1.3 Design Considerations for M-S and M-I-S Cells

The M-S and M-I-S surface-barrier cells provide the unique design advantage of being an all-solid-state configuration that employs only one semiconductor. They also provide the possibility of potentially low-cost, low-temperature processing for barrier formation. In addition, the spectral response of an M-S or M-I-S cell is potentially better than that of a homojunction because losses associated with the front-ohmic contact as well as the bulk of an emitter semiconductor layer have been eliminated. As we encountered in a similar situation with window-absorber heterojunctions, these potential advantages may be outweighed by new problems inherent in the M-S and M-I-S structures.

The advantages of ease of barrier formation and of not having the loss mechanisms associated with the emitter layer of a homojunction can be offset for two reasons. One is the presence of the additional source of carrier losses due to localized gap states arising at or near the metallurgical interface at  $x = 0$  (process 4 of Fig. 6.2). As discussed in Section 3.4.4, these interface states giving rise to process 4 can be intrinsically present (intrinsic interface states due to the termination of the semiconductor lattice) or can be present as a result of the act of forming the barrier (i.e., dislocations, cross diffusion, vacancies).

The second reason that the potential advantages of an M-S or M-I-S surface-barrier structure may be lost lies in what we have termed process 5 in Fig. 6.2. This represents thermionic emission of majority carriers at  $x = 0$ . The majority carriers emitted over the barrier at  $x = 0$  contribute to the loss of photogenerated carriers, since they negate part of the photocurrent as seen in the figure. As we have mentioned, majority-carrier thermionic emission current is usually the dominant loss mechanism in metal-semiconductor cells and consequently, the one determining  $V_{oc}$ .

At this point we must examine more closely why thermionic emission of majority carriers is so important in metal-semiconductor and metal-insulator-semiconductor surface-barrier solar cells and ask why thermionic emission leads to low  $V_{oc}$  values. Recalling the analysis of Section 5.2.3.1, we realize that over-the-barrier transport certainly is involved in the loss

mechanisms of homojunctions and heterojunctions; however, in those structures a loss path consists of over-the-barrier transport in series with recombination and bulk diffusion-recombination. The latter usually are found to be rate-limiting steps<sup>†</sup> in the path. For example, with a metal to the left of  $x = 0$  in Fig. 6.2, the rate-limiting step for loss path 5 is thermionic emission over the barrier; but, if a semiconductor were to the left of  $x = 0$  in the figure, the rate-limiting step for carriers to pass through loss path 5 would probably be recombination or diffusion-recombination in the hypothetical semiconductor existing to the left of  $x = 0$ . This implies that thermionic emission is usually not expected to be the rate-limiting step when in series with recombination and recombination-diffusion because it must be able to supply larger current densities, for a given voltage, than recombination or recombination-diffusion. It follows that when thermionic emission is not in series with other loss mechanisms, but in parallel, it is expected to determine  $V_{oc}$ . This  $V_{oc}$  is generally smaller than that which would be possible, if  $V_{oc}$  were controlled by diffusion-recombination as it ideally is in homojunctions.

How can the possible detrimental features of M-S and M-I-S cells be suppressed? First, the semiconductor surface preparation and barrier formation process must be chosen so as to reduce interface recombination. Second, and usually most important, the majority-carrier thermionic emission current must be reduced. Our ultimate goal would be to completely turn off the majority-carrier thermionic emission current. As can be seen in Fig. 6.2, if the interface recombination current were suppressed and if the majority-carrier thermionic emission current were totally eliminated, the only loss mechanisms remaining would be exactly the same as those present in the base of a homojunction: i.e., space-charge recombination, minority-carrier diffusion-recombination, and back-ohmic contact losses. Consequently, device performance would be the same as that of the equivalent  $p-n$  homojunction [11, 19].

At this point we can fully appreciate the advantages of the M-I-S surface-barrier configuration. The presence of the insulator layer between the metal and the semiconductor in many cases may serve to reduce the number of localized states at the semiconductor interface and hence serve to reduce interface recombination. For example, a thin  $\text{SiO}_x$  layer (which may itself contain defects since  $x$  may not be 2) thermally grown on Si may tie up dangling bonds at the semiconductor interface, and the presence of the  $\text{SiO}_x$  may protect the silicon from the creation of defects during the metallization [20, 21].

Reducing the interface recombination is to no avail, if the dominant

<sup>†</sup> Note that the over-the-barrier process in series with  $J_{bk}|_2$  and  $J_{bk}|_{\text{dif}}$  of Eq. (5.59) is accounted for by the  $F_t$  transport factor appearing in Eqs. (5.62) and (5.63).

majority-carrier thermionic emission current is not suppressed. However, the presence of the insulator layer between the metal and the semiconductor can significantly reduce this thermionic emission current because [22] (1) the presence of the I layer can modify the charge configuration in the semiconductor and hence can be used to increase the majority-carrier thermionic emission barrier height  $\phi_B$  [see Eq. (3.60)]; (2) the presence of the I layer gives the thermionically emitted majority carriers another hurdle to cross before they reach the metal and this series process of crossing the I layer (by direct tunneling or by hopping) can severely reduce the effective thermionic emission; and (3) localized states in the I layer can charge on the passing of a photocurrent allowing significant voltage to be developed across the I layer (which, as we shall see, can lead to a reduced majority-carrier thermionic emission current for the same total voltage).

We note that the insulator layer in an M-I-S structure must reduce the majority-carrier thermionic emission current yet not interfere with the transport of minority carriers from the semiconductor to the metal. We also note that the ability of the insulator layer to modify the interface-recombination current can be strongly interrelated with its ability to modify the charge configuration, and thus the barrier, in the semiconductor.

Careful consideration must be given to the materials system used in an M-I-S cell. Just the act of inserting an I layer between the metallization and the semiconductor is not sufficient to guarantee enhanced performance over the M-S configuration even if the I layer does not interfere directly with the passage of photocurrent. An example is the Al/SiO<sub>x</sub>/(n)Si structure. Rather than being an M-I-S solar cell, this materials system makes a simple, useful ohmic contact to n-type Si. The positive charge characteristically found in thermally grown SiO<sub>x</sub> [23] together with the low work junction of Al, causes the formation of an accumulation layer at the surface in the n-type Si. This is the opposite of what is needed for photovoltaic action [24, 25]. As a general rule metals with high work functions (see Fig. 3.5) are to be used in both M-S and M-I-S structures on n-type semiconductors and the I layers which effectively introduce negative charge are to be used in M-I-S structures on n-type material. The converse holds for p-type absorbers.

Considering an n-type semiconductor for definitiveness, we summarize by noting that the M-I-S configuration can give enhanced performance over the M-S configuration, if one or more of the following occurs:

- (a) The I layer contains negative charge or its presence results in the decrease of positive charge contained in localized states at the semiconductor surface. This forces the semiconductor to deplete more, or even to invert, and thereby increases the barrier height. An increased barrier height

suppresses majority-carrier thermionic emission (usually the dominant loss mechanisms in M-S cells).

(b) The I layer attenuates the thermionically emitted majority-carrier current by the necessity of hopping or direct tunneling across the layer.

(c) The I layer supports a portion of the voltage developed by the cell. This leads to a reduced majority-carrier thermionic current, since the supply of carriers for that current is a function of the voltage developed in the semiconductor.

For an M-I-S cell to be able to approach or equal the performance of a homojunction, the I layer must also do the following:

(a) The presence of the I layer must suppress the interface-recombination current.

(b) The I layer must not impede the flow of the photocurrent (holes since we have assumed an *n*-type absorber). If direct tunneling carries the photocurrent across the I layer, the insulator is limited to being  $\lesssim 2\text{ nm}$  [11]; if the photocurrent is carried across the I layer by some hopping mechanism, it has been shown that it can be as thick as  $\sim 40\text{ nm}$  [26].

It must be pointed out that there are practical difficulties found in M-I-S solar cells. Perhaps foremost among these are chemical stability in some materials systems. Related to this is the fact that, although the presence of the insulator layer can be used to modify the semiconductor surface charge configuration and thereby increase the barrier to majority-carrier thermionic emission, this modified charge configuration can be unstable under prolonged illumination [27].

Also, M-I-S (and M-S) cells necessitate a trade-off between the sheet resistance and optical transmission properties of the thin metallization, when illumination enters the cell through this layer. The problem is more severe for some metals than others [28], but the trade-off always causes a reduction in the  $J_{sc}$  values attainable. Two solutions have been proposed for this problem: one is to use a configuration with the surface barrier at the back of the cell and the other is the M-I-S inversion layer cell [12, 13]. Of these solutions, the most successful has been the M-I-S inversion layer cell on (*p*)Si. The configuration uses an I layer containing positive charge to invert the *p*-type silicon, creating a barrier at the front silicon surface as well as a low resistance path for lateral flow of  $J_{sc}$ . The photocurrent is collected by the metal which is only located at grid fingers on the front surface. Since the metallization only exists at grid fingers, light easily enters the front. Further, thermionic emission can occur only under the grids and, in the most successful structure, it is suppressed below the bulk absorber losses due to the presence of the I layer under the grids [12, 13]. Further discussion is given in Section 6.4.1.

#### 6.2.1.4 Design Considerations for Liquid–Semiconductor Cells

Design considerations for liquid–semiconductor (EPC) cells focus on barrier formation, photocurrent collection by the redox couple, and photo-decomposition. The guidelines for barrier formation were discussed in detail in Section 3.4.7. They are the same as those used for any junction: to form a depleted space-charge region (which may even be inverted near the surface) in an *n*-type semiconductor one begins by choosing a redox couple whose electrochemical potential lies further below the vacuum level than the electrochemical potential of the semiconductor; to form a depleted space-charge region (which may even be inverted near the surface) in a *p*-type semiconductor one chooses a redox couple whose electrochemical potential lies closer to the vacuum level than the electrochemical potential of the semiconductor. Figure 3.5 shows the relative positions of the electrochemical potentials of several semiconductors and several redox couples in aqueous solution with respect to the vacuum-level reference of solid state. To locate the electrochemical potential of a redox couple with respect to the vacuum level, we introduced an effective work function  $\phi_{\text{redox}}$  in Chapter 3 which is related to the standard redox potential  $E_{\text{redox}}^0$  of electrochemistry by Eq. (3.53b).

When forming a solar cell structure on an *n*-type semiconductor, for example, it would appear that the best course of action would be to select a redox couple with as large a  $\phi_{\text{redox}}$  as possible in order to obtain as large a  $V_{\text{bi}}$  as possible. However, there are several difficulties with this approach. They are the following: (a)  $dV_{\text{bi}}/d\phi_{\text{redox}}$  need not be unity and, in fact, it has been demonstrated that  $dV_{\text{bi}}/d\phi_{\text{redox}} \approx 0$  (Fermi-level pinning) for some systems as discussed in Section 3.4.7; (b) the most probable energy for the reduced species  $E_{\text{re}}$  can be pushed too low with respect to the valence-band edge at  $x = 0$  and, as seen in Fig. 6.3, this can hinder photocurrent collection, and (c) poor positioning of the most probable energy for the reduced species  $E_{\text{re}}$  can result in photocurrent collection by the reduced species of the redox couple being unable to compete favorably with the photocurrent flowing via decomposition.

The fact that the built-in potential in a semiconductor may not be determined fully by the difference in the before-contact electrochemical potentials of the constituents of a junction is not a new idea to us. This same possibility exists in the heterojunctions with intermediary layers [see, for example, Eq. (5.8)] and in M–S and M–I–S junctions [see, for example, Eq. (3.45)]. The cause of this difficulty is, of course, interface states (intrinsic or arising from junction formation) and the presence of an interfacial layer. Also, the fact that  $E_{\text{re}}$  can be located too low with respect to  $E_v(0)$  for efficient collection of photocurrent-carrying holes in an *n*-type semiconductor is analogous to the S–S or S–I–S heterojunction case of having a

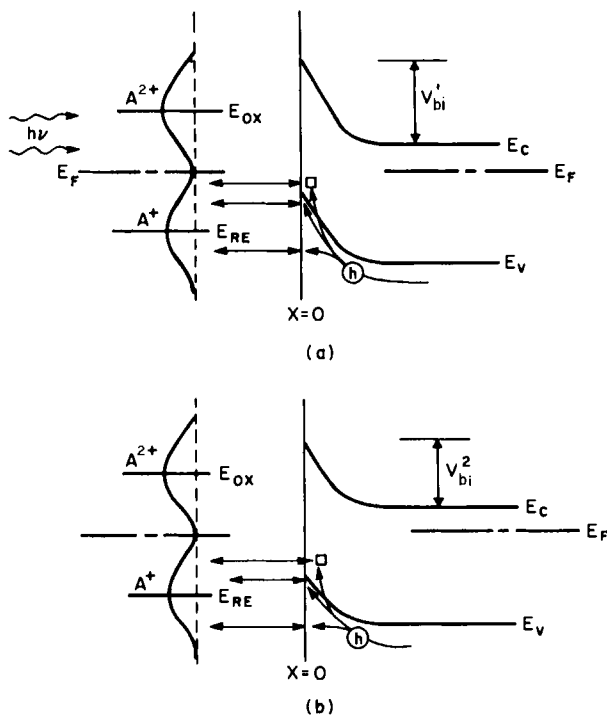


Fig. 6.3 The two liquid-semiconductor junctions under illumination are shown in the short-circuit condition; (a) redox couple effective work function  $\phi_{\text{redox}}^1$ ; (b) redox couple effective work function  $\phi_{\text{redox}}^2$ . Note that  $\phi_{\text{redox}}^1 > \phi_{\text{redox}}^2$  but the same semiconductor is used in both junctions; consequently,  $V_{\text{bi}}^1 > V_{\text{bi}}^2$ . The influence of any interface states on the distribution of the electrostatic potential has been ignored here. In (a) there are few energy levels of the reduced species opposite localized holes or holes with energies  $\approx E_v(0)$ . The configuration of (b) has many more reduced species levels opposite localized holes and holes with  $E \approx E_v(0)$ , ideally leading to better collection of the photocurrent. Note that  $A^{2+}$  levels have moved up closer to  $E_c(0)$  in (b). Unfortunately, this provides more final states for bucking-current electrons being emitted over the barrier at  $x = 0$ .

spike in the valence band when the absorber is *n*-type. We discussed this at length in Chapter 5. However, photodecomposition is a phenomenon we have ignored in our discussions of other solar cell configurations. It cannot be ignored in liquid-semiconductor junctions due to the relative ease of motion of ions in and out of the semiconductor at its surface.

To discuss this problem of decomposition, which is so important in liquid-semiconductor junctions, we follow Gerischer [29] and introduce the idea of a critical value for the minority-carrier quasi-Fermi level which we call the decomposition energy  $E_{\text{decomp}}$ . For definitiveness we consider the case of an *n*-type semiconductor: if the hole quasi-Fermi level  $E_{Fp}$  at a

liquid- $(n)$ semiconductor surface equals or lies below  $E_{\text{decomp}}$ , decomposition can occur since the holes have enough free energy to create broken semiconductor bonds at the surface [29]. Whether decomposition is appreciable depends on the rate at which the broken bonds are created and the rate at which holes are removed by the competing, nondestructive photocurrent paths seen in Fig. 6.3. Put concisely, the stability of the semiconductor essentially depends on two factors [29]: (a) the position in energy of the critical value of the hole quasi-Fermi level  $E_{\text{decomp}}$  with respect to the position at  $x = 0$  of the electron electrochemical potential of the system in thermodynamic equilibrium, and (b) the kinetics of the competing electron transfer mechanisms.<sup>†</sup> Building our approach to photodecomposition on the ideas of Gerischer we illustrate several situations with Fig. 6.4.

From Fig. 6.4 it can be seen that there are two basic possibilities at the surface of an  $n$ -type semiconductor subject to decomposition via the breaking of bonds by holes. The first situation (Fig. 6.4a) is thermodynamically unstable since the critical value of the hole quasi-Fermi level  $E_{\text{decomp}}$  lies above the Fermi level in the dark and under zero bias; consequently, the holes always have enough free energy to break bonds and appreciable decomposition can take place at the semiconductor surface. However, even under these circumstances the rate at which the semiconductor electrode decomposes (the broken bonds are created) depends on the decomposition kinetics and these could be quite slow. The second situation (Fig. 6.4b) is thermodynamically stable since the critical value of the hole quasi-Fermi level  $E_{\text{decomp}}$  lies below the Fermi level in thermodynamic equilibrium. Under illumination this liquid-semiconductor junction can be kinetically stable (the quasi-Fermi level  $E_{Fp}$  lies above  $E_{\text{decomp}}$ ), or potentially unstable (the quasi-Fermi level  $E_{Fp}$  lies at or below  $E_{\text{decomp}}$ ) as shown.

Whether the thermodynamically stable cells of Fig. 6.4b are kinetically stable or potentially unstable depends upon the effectiveness of the redox couple in siphoning off photogenerated holes from the semiconductor surface before the competing kinetics of Eq. (6.1) has a chance to create the  $M^{y+}$  ion in solution. If the collection of photogenerated holes from intermediary states (not shown in Fig. 6.4; see Fig. 6.3), of photogenerated holes with  $E \simeq E_v(0)$  in the valence band (see Fig. 6.3), and of hot-photogenerated holes in the valence band (Fig. 6.3) is fast enough to keep  $E_{Fp}$  at  $x = 0$  essentially at the level of the electrochemical potential of the redox couple, then there is no doubt that the cell of Fig. 6.4b is kinetically stable. In this case, the nondestructive photocurrent collection mechanisms are so fast that the hole free energy (quasi-Fermi level) cannot increase to a point where enough energy is available to break bonds. However, if these

<sup>†</sup> These same considerations apply to all-solid-state solar cells also and should be examined when considering long-term stability, especially at elevated temperatures.

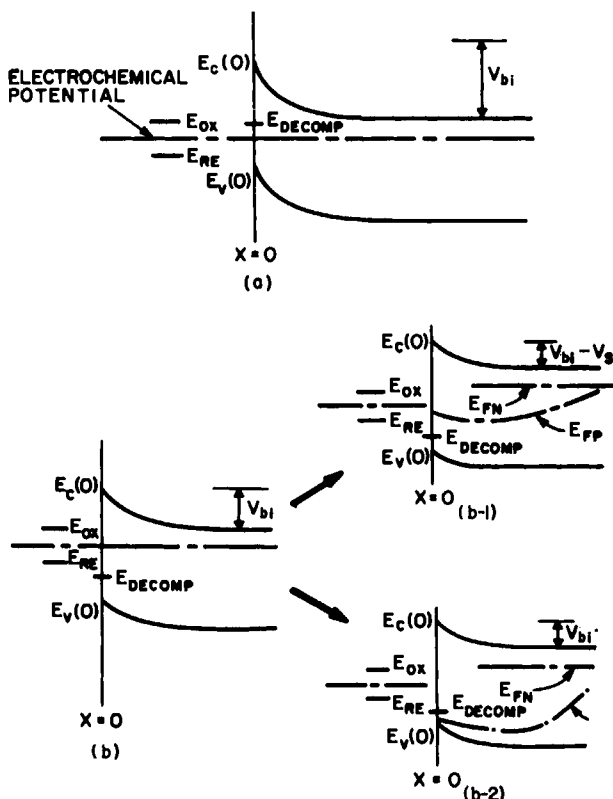


Fig. 6.4 Two classes of liquid-semiconductor junctions: (a) is inherently unstable since  $E_{decomp}$  lies above the Fermi level in the zero bias case. How unstable the junction is depends on the kinetics of the decomposition. (b) is stable in thermodynamic equilibrium: under illumination it may be kinetically stable [ $E_{fp}$  does not reach  $E_{decomp}$  as depicted in (b-1)], or potentially unstable [ $E_{fp}$  below  $E_{decomp}$  as seen in (b-2)]. In the latter case, how unstable the junction is depends on the kinetics.

nondestructive paths are not able to remove all the photogenerated holes as they arrive at  $x = 0$ , the hole population builds up at  $x = 0$ . As a result the quasi-Fermi level  $E_{fp}$  falls below the redox-electrochemical potential (the hole-free energy increases), and an effective series resistance appears in these channels of photocurrent collection. If  $E_{fp}$  falls to or below  $E_{decomp}$ , large numbers of broken bonds are now energetically possible at the semiconductor surface and a large flow of photocurrent can occur by decomposition. Even in this case decomposition may not be appreciable, if the rate of creation of broken bonds is slow.

When designing liquid-semiconductor junction solar cells it appears that the situation of Fig. 6.4b must be achieved and the configuration should fall

into the classification we have labeled kinetically stable to avoid all competition from decomposition as well as to avoid appreciable series resistance due to inefficient collection of photocurrent. One may argue that the Fig. 6.4b situation, labeled potentially kinetically unstable under illumination (enough hole free energy is available to create broken bonds), can be acceptable if the kinetics of decomposition are slow. This is not the case, however, because the change in the hole quasi-Fermi level at  $x = 0$  needed to push photogenerated holes into the reduced solution species in this case will appear as series resistance impeding the collection of photocurrent and hindering cell performance.

Given these deductions based on Fig. 6.4, it is surprising that experimental work has shown that cell designs falling into the classification of Fig. 6.4a need not be ruled out [7, 15, 29, 30]. That is, thermodynamic stability does not appear to be essential for adequately-lived liquid–semiconductor cells, provided the kinetics of photodecomposition can be made extremely slow.

We now ask the question: Why design a cell which is of the type seen in Fig. 6.4a when cells of the type seen in Fig. 6.4b, which are thermodynamically and kinetically stable, assure us of long-lived, stable performance? The answer is easily seen from Fig. 6.4b: cells of the Fig. 6.4b configuration have a built-in potential  $V_{bi}$  limited by

$$E_g - E_{decomp} \gtrsim V_{bi} + V_n \quad (6.2)$$

where  $E_{decomp}$  is being measured from the valence-band edge. Unless  $E_{decomp} \lesssim 0$ , which generally is not the case [30], the open-circuit voltage which can be achieved by an EPC device using an *n*-type semiconductor is limited by Eq. (6.2), if thermodynamic stability is to be guaranteed. It is clearly advantageous to use a configuration which gives the largest  $V_{bi}$  possible (Fig. 6.4a), if photodecomposition can be reduced to an insignificant level.

Turning to the specifics of selecting a redox couple for an *n*-type semiconductor, we consider two cases (Note  $\Delta_G \simeq 0$  for the redox concentrations of interest.) (a)  $dV_{bi}/d\phi_{redox} = 1$  [ $\Delta_H = \Delta_I = 0$  in Eq. (3.54a)] and (b)  $dV_{bi}/d\phi_{redox} \neq 1$  [ $\Delta_H \neq 0, \Delta_I \neq 0$  in Eq. (3.54a)]. If case (a) applies and if thermodynamic stability is desired (Fig. 6.4b), then it is necessary for

$$\phi_{redox} \lesssim E_g + \chi - E_{decomp} \quad (6.3)$$

To ensure stability under illumination, there must be significant overlap in energy of the reduced species levels with the levels in the semiconductor serving as a conduit for photogenerated carriers (localized states and minority-carrier valence-band levels in Fig. 6.3). There must also be rapid kinetics governing the charge exchange between these levels. If case (a)

applies and the control of photodecomposition strictly by kinetics is to be used (Fig. 6.4a), then  $\phi_{\text{redox}}$  has no upper bound equivalent to Eq. (6.3). However, it follows that significant overlap in energy of the reduced species levels with the localized and valence-band levels of the semiconductor must be maintained (Fig. 6.3), as must very rapid charge exchange kinetics. This restriction of significant overlap puts an effective upper bound on  $\phi_{\text{redox}}$  which depends on the reorganization energy  $\lambda$  (and on the interface state configuration, if significant photocurrent collection occurs through localized states).

If case (b) applies and if thermodynamic stability is desired, then it is necessary to select the redox couple such that

$$\phi_{\text{redox}} \lesssim E_g + \chi - E_{\text{decomp}} + \Delta_H + \Delta_I \quad (6.4)$$

To ensure stability under illumination, initial- and final-state overlap in energy and rapid kinetics must exist. If case (b) applies and the control of photodecomposition is strictly by kinetics, then  $\phi_{\text{redox}}$  has no upper bound equivalent to Eq. (6.4). However, it follows that initial- and final-state overlap in energy and very rapid kinetics are a necessity. The restriction of significant overlap puts an effective upper bound on  $\phi_{\text{redox}}$  which depends on  $\lambda$  (and on the interface state configuration, if significant photocurrent collection occurs through localized states).

The chemical nature of the redox couple, the specific solvent utilized, and surface treatments all can affect  $\Delta_H$  and  $\Delta_I$ ; consequently, these factors can strongly influence the thermodynamic stability of the surface of a given semiconductor through Eq. (6.4). Whether the approach of Fig. 6.4a or 6.4b is taken, the chemical nature of the redox couple, the solvent used, and surface treatments all can strongly affect the kinetics of photocurrent collection from interface states and the kinetics of photocurrent collection from the minority-carrier band. The kinetics of photodecomposition can also be modified by these same factors [31].

In conclusion, we note an important distinction between the situation of Figs. 6.4a and 6.4b. If a cell is of the form seen in Fig. 6.4a, the kinetics of photodecomposition must be made as slow as possible and the kinetics of nondestructive photocurrent collection must be made as rapid as possible. On the other hand, if a cell is of the form seen in Fig. 6.4b, consideration need only be given to the kinetics of photocurrent collection. Again this process must be made as rapid as possible.

### 6.2.2 Device Analysis Concepts

It is important to realize that the physics governing the response of the absorber region  $0 < x \leq L + W$  seen in the surface-barrier cells of Fig. 6.1 is

the same as it would be for any solar cell. Consequently, the mathematical description of light absorption, carrier recombination, charge distributions, and current transport in this region of any surface-barrier cell is the same as that used for homojunctions and heterojunctions; i.e., the mathematical system developed in Chapter 2 and outlined in Section 4.2.2.1 applies to  $0 < x \leq L + W$ . Transport at  $x \approx 0$  must be discussed in terms of the interface mechanisms introduced in Section 3.5. Some reexamination and reformulation of the interface transport models will be needed in the case of EPC cells since the electron states to the left of  $x = 0$  in this particular surface-barrier cell are localized states existing on mobile ions in solution.

It can be seen from Fig. 6.2 that the  $J-V$  characteristic of a surface-barrier cell, under illumination, can always be written as

$$J = e \int_0^{L+W} G_L(x) dx - e \int_0^{L+W} \mathcal{R}(x) dx - J_{\text{maj}} - J_{\text{ir}} - J_{\text{sr}}(L + W) \quad (6.5)$$

where this equation is an application of Eqs. (4.16)–(4.18) in integral form. In Eq. (6.5),  $\int G_L(x) dx$  is the total optical generation in the absorber;  $\int \mathcal{R} dx$  represents recombination in the space-charge region and in the base of the absorber (process 1),  $J_{\text{maj}}$  represents majority-carrier current crossing at  $x = 0$  (process 5),  $J_{\text{ir}}$  accounts for the interface-recombination loss (process 4), and  $J_{\text{sr}}(L + W)$  accounts for minority-carrier (and consequently majority-carrier) loss at the back surface  $x = L + W$  processes 2 and 3). The influence of the majority-carrier current crossing at  $x = 0$  on the performance of any surface-barrier cell is clear from Eq. (6.5).

As has been the case for homojunctions and heterojunctions, we shall often find it convenient to express Eq. (6.5) as

$$J = J_{\text{ph}}(\Phi_0, V) - J_{\text{bk}}(\Phi_0, V) \quad (6.6)$$

in our analyses of surface-barrier cells. Here  $J_{\text{ph}}$  is the photocurrent and  $J_{\text{bk}}$  is the bucking current set up in the cell to oppose  $J_{\text{ph}}$ . As was the case for the other classes of solar cells, this splitting of Eq. (6.5) into  $J_{\text{ph}}$  and  $J_{\text{bk}}$  is not arbitrary. These opposing currents are uniquely defined since  $J_{\text{ph}} \rightarrow 0$  as  $\Phi_0 \rightarrow 0$  and  $J_{\text{bk}} \rightarrow 0$  as  $V \rightarrow 0$ . Just as was the case for homojunctions and heterojunctions, Eq. (6.6) reduces to

$$J = J_{\text{sc}} - J_{\text{bk}}(V) \quad (6.7)$$

if superposition is valid.

### 6.2.3 Analysis of Metal–Semiconductor Structures

The first surface-barrier solar cell we shall analyze is the all-solid-state metal–semiconductor (M–S) cell. Figure 6.5 shows an M–S solar cell

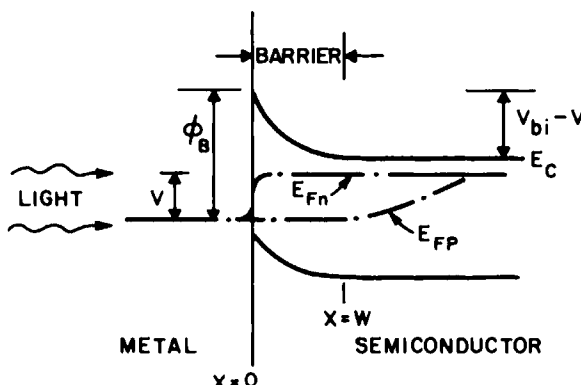


Fig. 6.5 A surface-barrier solar cell formed by a metal-semiconductor interface is shown under illumination. The cell is developing a voltage  $V$  and a current density  $J$ .

configuration with an  $n$ -type absorber. The structure is under illumination. We are keenly aware from Section 4.2.2.2 that there is a wide variety of phenomena contained in the system of equations which describe generation, recombination, charge distribution, and transport in an absorber. Consequently, we shall limit our analysis to a structure that uses a single-crystal, lifetime semiconductor (from time to time we shall extend our results to polycrystalline and amorphous materials, when appropriate) which contains no built-in drift fields in its base. The level of illumination is assumed to be such that  $p \ll n$  in the base of the absorber. Any selective-ohmic contacts which may be present at the back ( $x = W + L$ ) will be handled with an effective carrier recombination speed.

Our objective is to determine the  $J-V$  characteristic of this M-S cell to assess its efficiency, open-circuit voltage, short-circuit current, etc. Using the fact that the total current density  $J$  developed under illumination is a constant in the one-dimensional structure, we choose to evaluate it at the edge of the space-charge region ( $x = W$ ). Hence,  $J$  which we take as a positive quantity is

$$J = -[J_n(W) + J_p(W)] \quad (6.8)$$

where the minus sign arises since  $J_p(W)$ , for example, is negative if holes move to the left in Fig. 6.5.

Under the assumed conditions  $J_p(W)$  is a diffusion current given by

$$J_p(W) = -eD_p(dp/dx)_{x=W} \quad (6.9)$$

where  $p = p(x)$  satisfies

$$d^2p/dx^2 - [(p - p_{n0})/L_p^2] + (\Phi_0\alpha/D_p)e^{-\alpha(x)} = 0 \quad (6.10)$$

which follows from Eq. (4.38) and the discussion in Section 4.2.3.2. The function  $p = p(x)$  is subject to the boundary conditions

$$\frac{dp}{dx}|_{x=W+L} = -(S_p/D_p)[p(W+L) - p_{n0}] \quad (6.11)$$

at  $x = W + L$  and

$$p(W) = p_{n0} e^{E_{Fp}(W)/kT} \quad (6.12)$$

at  $x = W$ . The former follows from the discussion of ohmic-contact modeling found in Section 3.6.2 and the latter from the definition of the hole quasi-Fermi level. Here  $E_{Fp}$  is measured down from its thermodynamic equilibrium position in the gap.

Equation (6.10) is readily solved, subject to the boundary conditions of Eqs. (6.11) and (6.12). When the resulting  $p = p(x)$  is used in Eq. (6.9),  $J_p(W)$  is found to be given by

$$J_p(W) = -[J_L - J_{\text{dif}}\{\exp[E_{Fp}(W)/kT] - 1\}] \quad (6.13)$$

Here  $J_L$  is the photocurrent of holes diffusing out of the quasi-neutral base region of the absorber and  $J_{\text{dif}}\exp[E_{Fp}(W)/kT] - 1$  is the bucking current component arising from hole diffusion-recombination in the quasi-neutral base region of the absorber and from recombination at the back contact.

The quantity  $J_L$  appearing in Eq. (6.13) is a positive quantity given by

$$J_L = e\Phi_0 \left\{ \left[ \frac{\beta_6^2 e^{-\beta_4} e^{-\beta_6}}{\beta_6^2 - \beta_5^2} \right] \left[ \frac{(\beta_7 \beta_5 / \beta_6) - 1}{\beta_7 \sinh \beta_5 + \cosh \beta_5} \right] \right. \\ \left. + \left[ \frac{\beta_6^2 e^{-\beta_4}}{\beta_6^2 - \beta_5^2} \right] \left[ 1 - \left( \frac{\beta_5}{\beta_6} \right) \left( \frac{\beta_7 \cosh \beta_5 + \sinh \beta_5}{\beta_7 \sinh \beta_5 + \cosh \beta_5} \right) \right] \right\} \quad (6.14)$$

and the quantity  $J_{\text{dif}}$  is a positive quantity given by

$$J_{\text{dif}} = \left[ \frac{eD_p p_{n0}}{L_p} \right] \left[ \frac{\beta_7 \cosh \beta_5 + \sinh \beta_5}{\beta_7 \sinh \beta_5 + \cosh \beta_5} \right] \quad (6.15a)$$

Equation (6.15a) may be conveniently expressed as

$$J_{\text{dif}} = \Theta_B (eD_p p_{n0}/L_p) \quad (6.15b)$$

where the definition of  $\Theta_B$  is obtained by comparing Eqs. (6.15a) and (6.15b).

The dimensionless  $\beta$  numbers in Eqs. (6.14) and (6.15) are the same as the  $\beta$  numbers used in the homojunction cell analysis of Chapter 4 with the exception that the subscript  $p$  is interchanged with the subscript  $n$  appearing in Table 4.1. Again the dimensionless number  $\beta_4$  is defined by

$$\beta_4 \equiv W\alpha \quad (6.16)$$

The function  $\Theta_B$  used in Eq. (6.15b) is plotted in Fig. 5.10 as a function of  $\beta_s$  with  $\beta_7$  as a parameter. The range of  $\beta_7$  is chosen by letting the back-recombination speed  $S_p$  vary between 0 and  $10^5$  cm/sec and by letting the diffusion speed  $D_p/L_p$  have values  $\gtrsim 10^2$  cm/sec. The lower limit on the diffusion speed is that value expected in "good" single-crystal materials.

Writing the current density  $J$  present under illumination as we have determined it thus far gives

$$J = -J_n(W) + J_L - J_{\text{dif}} \{ \exp[E_{Fp}(W)/kT] - 1 \} \quad (6.17)$$

We shall see that the interface at  $x = 0$  exerts its influence on Eq. (6.17) through the term  $J_n(W)$ , the majority-carrier current at  $x = W$ , and through  $E_{Fp}(W)$ , the minority-carrier quasi-Fermi level at  $x = W$ . We now begin to show this. Our first task will be to work back toward the interface to relate  $E_{Fp}(W)$  to its value  $E_{Fp}(0)$ .

To relate the hole quasi-Fermi level at  $x = W$  to the hole quasi-Fermi level at  $x = 0$ , we shall need Eq. (4.13) in the form<sup>†</sup>

$$J_p = -ep\mu_p dE_{Fp}/dx \quad (6.18)$$

The sign choice in Eq. (6.18) comes about since  $E_{Fp}(x)$  is being measured positively down in Fig. 6.5. We also note that the  $p = p(x)$  appearing in Eq. (6.18), which is the hole number density distribution in the space-charge region, can be written as

$$p = p_{n0} e^{\psi/kT} e^{E_{Fp}/kT} \quad (6.19)$$

The quantity  $\psi$  in Eq. (6.19) locates the band edges in the band-bending (barrier) region of the absorber with respect to their position in the bulk of the absorber;  $\psi$  is measured positively up in the figure.

Substituting Eq. (6.19) into Eq. (6.18) and integrating across the space-charge region, we obtain

$$e^{E_{Fp}(W)/kT} = e^{E_{Fp}(0)/kT} - \frac{1}{J_{\text{sweep}}^p} \frac{\int_0^W J_p(x) e^{-\psi/kT} dx}{\int_0^W e^{-\psi/kT} dx} \quad (6.20)$$

where, analogous to the notation of Section 5.2.3, we have introduced

$$J_{\text{sweep}}^p \equiv ep_{n0}\mu_p kT / \int_0^W e^{-\psi/kT} dx \quad (6.21)$$

Remembering that  $J_p(x)$  will be negative under illumination for the coordinate system of Fig. 6.5, we note that Eq. (6.20) demonstrates that  $E_{Fp}(W)$  must be greater than or possibly equal to  $E_{Fp}(0)$ .

If  $J_p(x)$  is reasonably constant across the space-charge region (which, in this case, means it varies more slowly than exponentially), the integral

<sup>†</sup> Note that any hot-hole effects are being neglected in Eq. (6.18).

$\int_0^W J_p(x) e^{-\psi/kT} dx$  will receive its principal contribution from within the first few  $kT$  of band bending. Hence, Eq. (6.20) can be rewritten as

$$e^{E_{Fp}(W)/kT} = e^{E_{Fp}(0)/kT} - [J_p(W)/J_{\text{sweep}}^p] \quad (6.22)$$

Using Eq. (6.13), this becomes

$$e^{E_{Fp}(W)/kT} - 1 = [J_{\text{sweep}}^p/(J_{\text{sweep}}^p + J_{\text{dif}})] [e^{E_{Fp}(0)/kT} - 1] + J_L/(J_{\text{sweep}}^p + J_{\text{dif}}) \quad (6.23)$$

which, when substituted into Eq. (6.17), yields

$$J = -J_n(W) + \left[ \frac{J_{\text{sweep}}^p}{J_{\text{sweep}}^p + J_{\text{dif}}} \right] J_L - \left[ \frac{J_{\text{sweep}}^p}{J_{\text{sweep}}^p + J_{\text{dif}}} \right] \left[ J_{\text{dif}}(e^{E_{Fp}(0)/kT} - 1) \right] \quad (6.24)$$

Equation (6.24) shows the importance of the quantity  $J_{\text{sweep}}^p$  which characterizes the ability of the holes to move across the space-charge region of the barrier. If

$$J_{\text{sweep}}^p \gg J_{\text{dif}} \quad (6.25)$$

then the full photocurrent  $J_L$  coming out of the base of the absorber is collected. We also note that, if condition (6.25) is satisfied, the resulting Eq. (6.24) is exactly what we would have obtained had we assumed a priori that  $E_{Fp}$  was flat (quasi-equilibrium assumption) across the band-bending region in the absorber. Put succinctly, condition (6.25) is the criterion for the quasi-equilibrium assumption to be valid for holes in the region  $0 < x \leq W$  of Fig. 6.5.

Since our objective is the  $J-V$  characteristic of the M-S cell under illumination, a problem that now concerns us is determining how  $E_{Fp}(0)$  is related to  $V$ . However, in the M-S configuration there is no difficulty in the communication between the valence band of the semiconductor and the metal. Any ultrathin interfacial or intermediary layer present is assumed completely transparent to holes. Thus the hole population at  $x = 0$  must follow the metal carrier population; i.e., the quasi-Fermi level of holes at  $x = 0$  must be the same as the Fermi level of the metal. Consequently  $E_{Fp}(0)$ , as we are measuring it, must be equal to  $V$ . With this realization, Eq. (6.24) may be rewritten as

$$J = -J_n(W) + F_p J_L - F_p J_{\text{dif}}(e^{V/kT} - 1) \quad (6.26)$$

Analogous to our notation of Section 5.2.3, we have introduced the transport factor  $F_p$  in Eq. (6.26) where

$$F_p \equiv J_{\text{sweep}}^p/(J_{\text{sweep}}^p + J_{\text{dif}}) \quad (6.27)$$

We now must begin to relate  $J_n(W)$  in Eq. (6.26) to transport at the interface. To do that we first will need Eq. (4.11) in the form<sup>†</sup>

$$J_n = en\mu_n dE_{Fn}/dx \quad (6.28)$$

The sign choice here comes from the coordinate system of Fig. 6.5 and from measuring  $E_{Fn}$  positively up from its thermodynamic equilibrium position, in the gap, in the bulk of the absorber. We note that  $n = n(x)$  in Eq. (6.28) is given by

$$n = n_{n0} e^{-\psi/kT} e^{E_{Fn}/kT} \quad (6.29)$$

Substituting Eq. (6.29) into Eq. (6.28) and integrating across the space-charge (barrier) region results in

$$e^{E_{Fn}(0^+)/kT} = 1 - \left[ \frac{1}{J_{\text{sweep}}^n} \right] \left[ \frac{\int_{0^+}^W J_n(x) e^{\psi/kT} dx}{\int_{0^+}^W e^{\psi/kT} dx} \right] \quad (6.30)$$

Here we have introduced the definition

$$J_{\text{sweep}}^n \equiv en_{n0} \mu_n kT \left/ \int_{0^+}^W e^{\psi/kT} dx \right. \quad (6.31)$$

and have used the fact that  $E_{Fn}(W) = 0$ . The notation  $x = 0^+$  in Eq. (6.30) denotes a plane just to the right of the interface ( $x = 0$ ) in Fig. 6.5.

If  $J_n(x)$  is reasonably constant across the space-charge region (which, in this case, means it varies more slowly than exponentially), the integral  $\int_{0^+}^W J_n(x) e^{\psi/kT} dx$  is essentially determined by the contributions coming from within the first several  $kT$  of the barrier peak. Consequently, Eq. (6.30) may be rewritten as

$$e^{E_{Fn}(0^+)/kT} = 1 - [J_n(0^+)/J_{\text{sweep}}^n] \quad (6.32)$$

The majority-carrier current  $J_n(0^+)$  appearing in Eq. (6.32) can flow (a) due to emission of electrons over or through the barrier at  $x = 0$  into the metal (with a current density  $J_{ob}$ ), (b) due to the capture of electrons by localized states near the interface and then the subsequent emission of these electrons into the metal (with a current density  $J_{ls}$ ), and (c) due to interface recombination (with a current density  $J_{ir}$ ). The sum  $J_{ob} + J_{ls}$  is the  $J_{maj}$  appearing in Eq. (6.5) and, of course,  $J_{ir}$  is the  $J_{ir}$  of Eq. (6.5).

Assuming that  $J_{ob}$  involves only thermionic emission allows the use of Eq. (3.59) to model this current. The result is

$$J_{ob} = J_{th}(e^{V/kT} e^{E_{Fn}(0^+)/kT} - 1) \quad (6.33)$$

in the case of the metal-semiconductor interface where

$$J_{th} = A^* T^2 e^{-\phi_B/kT} \quad (6.34)$$

<sup>†</sup> We neglect any temperature gradient effects here.

It is important to keep in mind that  $E_{Fn}$  appearing in Eq. (6.33) is measured up positively from the position of the Fermi level in the gap of the bulk absorber.

The current density  $J_{LS}$  involves capture of conduction-band electrons by localized interface states [situated in the energy gap at some energy  $\phi_T$  below the conduction-band edge at  $x = 0$  and having a density  $N_T(m^{-2})$ ]. Hence  $J_{LS}$  may be modeled using the interface equivalent of Eq. (2.24) which describes communication between localized states and the conduction band; viz.,

$$J_{LS} = e \langle v_n \rangle \Omega_n N_T [(1 - f_T)n(0) - f_T n_1] \quad (6.35)$$

where  $f_T$  is the probability of occupancy of the localized interface states and the other quantities are defined in Section 2.6.1.3. Assuming there is excellent communication between these localized states and the metal in the M-S configuration results in  $f_T$  being a constant which is independent of illumination and cell bias; i.e., the population of the interface states in this situation follows the metal. Due to the fact that  $f_T$  is a constant in the M-S cell, it may be evaluated at thermodynamic equilibrium ( $J_{LS} = 0$ ) giving

$$J_{LS} = (e \langle v_n \rangle \Omega_n N_T) \left( \frac{e^{-\phi_B/kT} e^{-\phi_T/kT} N_c}{e^{-\phi_B/kT} + e^{-\phi_T/kT}} \right) (e^{V/kT} e^{E_{Fn}(0^+)/kT} - 1) \quad (6.36a)$$

This equation uses the fact that  $n(0) = n_{n0} e^{-V_{bi}/kT} e^{V/kT} e^{E_{Fn}(0^+)/kT}$  as is specified by Eq. (6.29). Equation (6.36a) may be rewritten in the more convenient form

$$J_{LS} = J_{surf} (e^{V/kT} e^{E_{Fn}(0^+)/kT} - 1) \quad (6.36b)$$

by introducing the prefactor  $J_{surf}$  defined by

$$J_{surf} \equiv (e \langle v_n \rangle \Omega_n N_T) \left( \frac{e^{-\phi_B/kT} e^{-\phi_T/kT} N_c}{e^{-\phi_B/kT} + e^{-\phi_T/kT}} \right) \quad (6.37)$$

The current density  $J_{ir}$  may be modeled by using the first term of Eq. (5.37); viz.,

$$J_{ir} = \left[ \frac{e A_{1p}^L A_{1n}^L N_1 n_i^2}{A_{1p}^L p(0^+) + A_{1p}^L p_1 + A_{1n}^L n(0^+) + A_{1n}^L n_1} \right] [e^{E_{Fp}(0^+)/kT} e^{E_{Fn}(0^+)/kT} - 1] \quad (6.38)$$

where appropriate changes in the notation [the absorber is *p*-type for Eq. (5.37)] have been made. Defining a prefactor  $J_r$  by

$$J_r \equiv \frac{e A_{1p}^L A_{1n}^L N_1 n_i^2}{A_{1p}^L p(0^+) + A_{1p}^L p_1 + A_{1n}^L n(0^+) + A_{1n}^L n_1} \quad (6.32)$$

allows Eq. (6.38) to be written as

$$J_{ir} = J_r (e^{V/kT} e^{E_{Fn}(0^+)/kT} - 1) \quad (6.40)$$

which uses the fact that  $E_{Fp}(0) = V$ .

One final expression is needed to relate  $J_n(W)$  to transport at the interface and that comes from applying the continuity equation for electrons in integral form; i.e.,

$$J_n(W) = J_n(0^+) - e \int_0^W G_L(x) dx + e \int_0^W \mathcal{R}(x) dx \quad (6.41)$$

We have already established that the  $J_n(0^+)$  appearing in this equation is given by

$$\begin{aligned} J_n(0^+) &= J_{\text{th}}(e^{V/kT} e^{E_{Fn}(0^+)/kT} - 1) + J_{\text{surf}}(e^{V/kT} e^{E_{Fn}(0^+)/kT} - 1) \\ &\quad + J_r(e^{V/kT} e^{E_{Fn}(0^+)/kT} - 1) \end{aligned} \quad (6.42)$$

Equations (6.32), (6.41), and (6.42) constitute a set of three equations in the three unknowns  $E_{Fn}(0^+)$ ,  $J_n(0^+)$ , and  $J_n(W)$ . This set of equations may be solved for  $J_n(W)$  by eliminating  $E_{Fn}(0^+)$  and  $J_n(0^+)$ . The result is

$$\begin{aligned} J_n(W) &= F_n J_{\text{th}}(e^{V/kT} - 1) + F_n J_{\text{surf}}(e^{V/kT} - 1) \\ &\quad + F_n J_r(e^{V/kT} - 1) - e \int_0^W G_L(x) dx + e \int_0^W \mathcal{R}(x) dx \end{aligned} \quad (6.43)$$

where the transport factor  $F_n$ , defined by

$$F_n \equiv \frac{J_{\text{sweep}}^n}{(J_{\text{sweep}}^n) + (J_{\text{th}} + J_{\text{surf}} + J_r)e^{V/kT}} \quad (6.44)$$

has been employed. This  $F_n$  is a measure of the relative ease with which electrons cross the space-charge region.

Using the model

$$e \int_0^W G_L(x) dx - e \int_0^W \mathcal{R}(x) dx = e\Phi_0(1 - e^{-\alpha W}) - J_{\text{RB}}(e^{V/n_R kT} - 1) \quad (6.45)$$

which was discussed in depth in Section 4.2.3 in Eq. (6.43), we finally get

$$\begin{aligned} J_n(W) &= F_n J_{\text{th}}(e^{V/kT} - 1) + F_n J_{\text{surf}}(e^{V/kT} - 1) \\ &\quad + F_n J_r(e^{V/kT} - 1) - e\Phi_0(1 - e^{-\alpha W}) + J_{\text{RB}}(e^{V/n_R kT} - 1) \end{aligned} \quad (6.46)$$

We are now in a position to construct the long-sought-after  $J-V$  characteristic of the solar cell structure of Fig. 6.5. This may be done by substituting Eq. (6.46) into Eq. (6.26); the result is

$$\begin{aligned} J &= J_{\text{LSC}} + F_p J_{\text{L}} - F_n J_{\text{th}}(e^{V/kT} - 1) - F_n J_{\text{surf}}(e^{V/kT} - 1) \\ &\quad - F_n J_r(e^{V/kT} - 1) - J_{\text{RB}}(e^{V/n_R kT} - 1) - F_p J_{\text{dir}}(e^{V/kT} - 1) \end{aligned} \quad (6.47)$$

which uses the notation  $J_{\text{LSC}}$  for  $e\Phi_0(1 - e^{-\alpha W})$ , the photocurrent generated in the space-charge region.

This  $J-V$  characteristic of an M-S cell is seen to be of the form of Eq. (6.6). The photocurrent is composed of contributions from the space-charge region and the base of the absorber. It will be a function of voltage if the transport factor  $F_p$  depends on voltage. The bucking current is seen to be composed of five components: the components  $J_{RB}(e^{V/nkT} - 1)$  and  $F_p J_{dif}(e^{V/kT} - 1)$  which describe loss mechanisms 1, 2, and 3 of Fig. 6.2;  $F_n J_r(e^{V/kT} - 1)$  which describes loss mechanism 4 of Fig. 6.2; and  $F_n J_{th}(e^{V/kT} - 1)$  and  $F_n J_{surf}(e^{V/kT} - 1)$  which describe loss mechanism 5. The bucking current may be a function of light intensity and wavelength, if light affects any of the prefactors or transport factors. Although only one term explicitly shows an  $n$  factor, or ideality factor, that is not unity, the other bucking current terms can effectively have voltage dependencies of the form  $e^{V/nkT}$  with  $n \neq 1$  since  $F_n$ ,  $F_p$ , and  $J_r$  all can conceivably depend on voltage.

We now ask if there are any simplifications that can be made to the  $J-V$  characteristic of Eq. (6.47) based on the capture cross sections, localized state densities, etc. that we expect in a metal-semiconductor structure. Looking at the prefactors  $J_{th}$  and  $J_{surf}$ , we note from Eqs. (6.34) and (6.37) that

$$A^* T^2 \lesssim e \langle v_n \rangle \Omega_n N_T N_c \quad (6.48)$$

is necessary, if the process of electron capture by localized states near the interface and the subsequent emission of this electron into the metal is to compete with the process of thermionic emission at the interface. Use representative values ( $T = 300^\circ\text{K}$ ,  $A^* = 120 \text{ A}/(\text{cm} - \text{K})^2$ ,  $\langle v \rangle = 10^7 \text{ cm/sec}$ , and  $N_c = 10^{19} \text{ cm}^{-3}$ ) it can be seen that the  $\Omega_n N_T$  must be of the order of unity for  $J_{surf}$  to compete against  $J_{th}$ . Since  $N_T$ , the number of interface sites at the semiconductor surface, is limited to being of the order of the two-thirds power of the bulk atomic number density, it follows that  $N_T \lesssim 10^{14} \text{ cm}^{-2}$ . Also, we assume  $\Omega_n$  is limited by the cross-sectional area of an atom; i.e.,  $\Omega_n \lesssim 10^{-16} \text{ cm}^2$ . Consequently, we do not expect condition (6.48) to be met and, as a result,  $J_{surf}$  may be set equal to zero in Eq. (6.47) for an M-S solar cell structure.

What about loss process 4 of Fig. 6.2 (characterized by the prefactor  $J_r$ ); is it at least as important as process 5 (which we have reduced to being characterized only by the prefactor  $J_{th}$ ) in a M-S configuration? If loss process 4 is dominated by process 5, then from Eq. (6.47)

$$J_{th} > J_r \quad (6.49)$$

Using Eqs. (6.39) and (5.76), this condition may be rewritten as

$$A^* T^2 e^{-\phi_B/kT} > p_{n0} e^{V_{bi}/kT} (e \langle v \rangle \Omega_l N_l) \left( e^{V/kT} + \frac{p_{n0} e^{V_{bi}/kT}}{n_{n0} e^{-V_{bi}/kT}} \right)^{-1} \quad (6.50)$$

Note that Eq. (5.76) has been modified in that  $n$  and  $p$  have been interchanged, since we are dealing with an  $n$ -type absorber in Fig. 6.5.

It may be seen from Eq. (5.76) and Fig. 5.12 that

$$p_{n0} e^{V_{bi}/kT} (e \langle v \rangle \Omega_l N_l) \left( e^{V/kT} + \frac{p_{n0} e^{V_{bi}/kT}}{n_{n0} e^{-V_{bi}/kT}} \right)^{-1} \lesssim N_c e^{-\phi_B/kT} (e \langle v \rangle \Omega_l N_l) \quad (6.51)$$

is always true<sup>†</sup> for any value of the barrier height (for any position of the Fermi level in the gap at  $x = 0$  in thermodynamic equilibrium). Consequently, this allows us to simplify the condition of (6.50) to

$$A^* T^2 > e \langle v \rangle \Omega_l N_l N_c \quad (6.52)$$

The condition expressed in (6.52) looks the same as that expressed in (6.48). However, there is an important distinction:  $\Omega_l$  is the capture cross section for defects (traps) lying near, but not necessarily at, the semiconductor surface of a density  $N_l$  (effective number per area) and these defects serve as a conduit for interband transitions (process 4 of Fig. 6.2).

Using  $T = 300 \text{ }^\circ\text{K}$ ,  $A^* = 120 \text{ A}/(\text{cm} - \text{K})^2$ ,  $\langle v \rangle = 10^7 \text{ cm/sec}$ , and  $N_c = 10^{19} \text{ cm}^{-3}$ , it is apparent that the  $\Omega_l N_l$  must be of the order of unity for  $J_r$  to compete with  $J_{th}$ . Since we expect  $\Omega_l \lesssim 10^{-16} \text{ cm}^2$ , this means  $N_l \lesssim 10^{16} \text{ cm}^{-2}$  must occur in materials systems where  $J_r$  is important in the M-S configuration. If the defects giving rise to  $N_l$  are a product of the act of forming the barrier, it is conceivable that they could exist over  $\sim 100 \text{ nm}$ . However, for  $N_l = 10^{16} \text{ cm}^{-2}$  it would be necessary for every tenth atom in this 100-nm layer to serve as a conduit for  $J_r$ . Since this seems excessive, we conclude that  $J_r$  probably can also be set equal to zero in Eq. (6.47) for metal-semiconductor solar cells.

As a result of a very thorough examination of the loss mechanisms and transport in a metal-semiconductor solar cell structure we arrived at Eq. (6.47). By looking at the relative importance of several of the bucking-current terms in Eq. (6.47), we now see that this general expression can be reduced to

$$\begin{aligned} J = J_{LSC} + F_p J_L - F_n J_{th} (e^{V/kT} - 1) \\ - J_{RB} (e^{V/n_R kT} - 1) - F_p J_{dif} (e^{V/kT} - 1) \end{aligned} \quad (6.53)$$

for M-S solar cell structures. It is important to realize that this simplification occurs because the thermionic emission current is so large in the M-S configuration.

<sup>†</sup> We assume that  $N_c$  and  $N_v$  are of the same order of magnitude here.

Several conclusions can be drawn concerning the operation of the M-S solar cell using Eq. (6.53):

(a) The photocurrent of a metal-semiconductor solar cell will be the same as that coming from the base of a *p-n* homojunction cell fabricated from the same semiconductor provide the M-S device has an identical back-contact structure. This neglects absorption in the emitter of the *p-n* device, and the problems of reflection and absorption associated with the metal layer of the M-S device.

(b) The transport factor  $F_p$ , which is such that  $0 \leq F_p \leq 1$ , must be unity to collect all the photocurrent coming out of the bulk region of the absorber. Using Eqs. (6.21) and (6.27) plus the results of the discussion leading to Eq. (5.67) allows us to write this transport factor as

$$F_p = \left\{ \frac{L_D}{L_p} \Theta_B \left[ \operatorname{erf} \left( \frac{V_{bi} - V}{kT} \right)^{1/2} \right] + 1 \right\}^{-1} \quad (6.54)$$

Equation (5.67) is modified as seen because the absorber under discussion in Section 5.2.3.2 is *p*-type.

Since the error function is positive and always  $\leq 1$ , it follows that whether or not  $F_p$  is unity depends on the ratio  $(L_D \Theta_B)/L_p$  where  $L_D$  is the Debye length. The Debye length is seen from Fig. 5.11 to be such that  $L_{D2} < 1 \mu\text{m}$ . For "good" single-crystal absorbers  $L_p$  values as high as of the order of  $100 \mu\text{m}$  or more are possible and for properly designed absorbers (material and back-contact)  $\Theta_B \leq 1.0$  is attainable as follows from Fig. 5.10 and Section 4.2.3. Consequently,  $F_p = 1.0$  is expected for single-crystal materials. This means  $J_{\text{sweep}}^p$  dominates  $J_{\text{dif}}$  and, equivalently, the quasi-Fermi level  $E_{F_p}$  is flat across the space-charge region.

Looking at the other extreme, we recall that diffusion lengths can be small in some amorphous semiconductors. For example, we have noted  $L_p \approx 4 \times 10^{-2} \mu\text{m}$  is reported for some hydrogenated *a-Si*. The representative value of  $\Theta_B$  for amorphous materials may be estimated from Fig. 5.10 by noting that  $\beta_5 = L/L_p$  will be  $\geq 1.0$  for this class of semiconductors since  $L/L_p \geq 1/\alpha L_p$  is a necessity and  $1/\alpha \approx 1.0 \mu\text{m}$  for *a-Si*, for example. As a result we find  $\Theta_B \approx 1.0$  for amorphous absorbers is expected. Based on these approximations, it is seen from Eq. (6.54) that  $F_p < 1.0$  (i.e.,  $J_{\text{dif}} \gtrsim J_{\text{sweep}}^p$ ) can be a possibility for M-S cells using some amorphous absorbers. Given the added fact that  $J_L$  itself can fall far short of its potential in amorphous materials with poor diffusion lengths in the quasi-neutral region, it becomes apparent that metal-semiconductor cell designs that rely on drift alone to collect the photocarriers may be the best approach for some amorphous

absorber cells; i.e., M-i-n (or M-i-p) type cells analogous to the p-i-n homojunctions discussed in Section 4.2.1 are probably the better M-S structure when amorphous absorbers with poor diffusion lengths are employed.

In cases where  $F_p$  is not identically equal to unity it may be voltage dependent due to the presence of the error function. The factor  $F_p$  can be illumination dependent through the presence of light changing the effective doping density and, consequently, changing  $L_D$  and  $V_{bi}$ .

(c) The transport factor  $F_n$  only enters into Eq. (6.53) through the product  $F_n J_{th}$ . Writing out this product it is seen that it may be expressed as

$$F_n J_{th} = \frac{en_{n0}\mu_n\xi_M e^{-V_{bi}/kT} A*T^2 e^{-\phi_B/kT}}{en_{n0}\mu_n\xi_M e^{-V_{bi}/kT} + A*T^2 e^{-\phi_B/kT}} \quad (6.55)$$

where use has been made of Eq. (5.106) with appropriate notation changes. The quantity  $\xi_M$  in Eq. (6.55) is the maximum field in the space-charge region for some bias V. Equation (6.55) may be rearranged into the form

$$F_n J_{th} = \frac{A*T^2 e^{-\phi_B/kT}}{1 + (A*T^2/eN_c\mu_n\xi_M)} \quad (6.56)$$

From Eq. (6.53) and (6.56) it can be seen that the bucking-current component arising from thermionic emission over the barrier at  $x = 0$  can be written as

$$F_n J_{th}(e^{V/kT} - 1) = \left[ \frac{A*T^2 e^{-\phi_B/kT}}{1 + (A*T^2/eN_c\mu_n\xi_M)} \right] (e^{V/kT} - 1) \quad (6.57)$$

The form of the prefactor on the right hand side of Eq. (6.57) stresses that the thermionic emission of the electrons is in series with drift and diffusion of these electrons across the space-charge region. The latter transport processes come in through  $F_n$ . It should be noted that the drift and diffusion transport represented in Eq. (6.57) is that of electrons not bulk minority-carrier holes.

The bucking-current model of Eq. (6.57) is often referred to as the thermionic emission-diffusion model. It has been discussed extensively in the literature [32-34]. In M-S solar cells using absorbers with low mobilities, this bucking-current component reduces to

$$F_n J_{th}(e^{V/kT} - 1) = [eN_c\mu_n\xi_M e^{-\phi_B/kT}] (e^{V/kT} - 1) \quad (6.58)$$

which says that the crossing of the space-charge region is the rate-limiting step for loss process 5 of Fig. 6.2. In M-S solar cells using absorbers with high mobilities, this bucking-current component reduces to

$$F_n J_{th}(e^{V/kT} - 1) = [A*T^2 e^{-\phi_B/kT}] (e^{V/kT} - 1) \quad (6.59)$$

which says that thermionic emission is the rate-limiting step for process 5. As an example of the application of these models we note that the limiting case given by Eq. (6.58) is used for this bucking-current component in M-S devices made using some amorphous Si [35], whereas the limiting case given by Eq. (6.59) is used in M-S devices made using single-crystal Si.

(d) The majority-carrier bucking-current component  $F_n J_{th}(e^{V/kT} - 1)$  generally dominates (by orders of magnitude) over the minority-carrier diffusion-recombination component  $F_p J_{dif}(e^{V/kT} - 1)$  of Eq. (6.53)—see Fig. 6.7. Hence,  $F_n J_{th}(e^{V/kT} - 1)$  determines the open-circuit voltage of an M-S solar cell. As a result, the open-circuit voltage and, consequently, the efficiency of an M-S solar cell are less than that of a *p-n* homojunction device fabricated using the same semiconductor. In the latter device the bucking current  $F_p J_{dif}(e^{V/kT} - 1)$  would ideally dominate as discussed in Chapter 4.

#### 6.2.4 Analysis of Metal–Insulator–Semiconductor Structures

Fortunately, the physical phenomena taking place in the absorber of any surface-barrier cell under illumination are the same whether the device is an M-S, M-I-S, or EPC structure. This will enable us to take advantage of much of the analysis developed for M-S devices (Section 6.2.3) in our discussion of M-I-S solar cell structures.

Figure 6.6 depicts an M-I-S solar cell structure under illumination. The absorber shown is an *n*-type material. Since we are aware from Section 4.2.2.2 of the wide variety of physical phenomena contained in the equations describing the absorber under illumination, we will again limit ourselves in this analysis to an absorber which is a single-crystal lifetime semiconductor. However, from time to time we shall extend our conclusions to polycrystalline and amorphous materials, when appropriate. The base of the absorber will be assumed to contain no drift fields and will be assumed subject to a level of illumination such that  $p \ll n$ . Any selective-ohmic contacts, which may be present at the back ( $x = W + L + \delta$ ), will be treated by using an effective carrier recombination speed.

To obtain the *J-V* characteristic of the M-I-S solar cell seen in Fig. 6.6, we note that the current density *J* developed under illumination is a constant. We choose to evaluate this constant at the edge of the space-charge region ( $x = W + \delta$ ) as is our custom; viz.,

$$J = -[J_n(W + \delta) + J_p(W + \delta)] \quad (6.60)$$

The minus sign arises from the fact that  $J_p(W + \delta)$ , for example, is negative, if holes move to the left in Fig. 6.6, and from the fact that we have always chosen *J* to be a positive quantity when a cell is producing power.

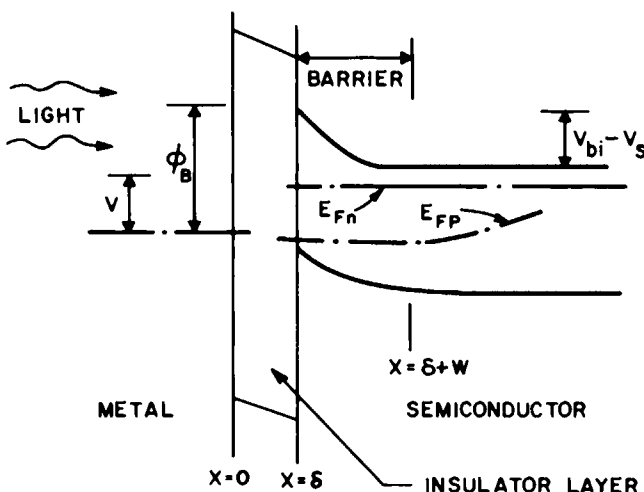


Fig. 6.6 A surface-barrier solar cell formed by a metal-insulator-semiconductor interface structure is shown under illumination. The cell is developing a voltage  $V$  and a current density  $J$ . In general,  $V = V_s + V_1$ , where  $V_s$  is the voltage developed in the semiconductor and  $V_1$  is the voltage developed across the insulator layer. Note that the value of  $\phi_B$ , the semiconductor barrier height, need not be the same when the device is developing a voltage as it is in thermodynamic equilibrium in the M-I-S configuration. In the text  $\phi_B = V_{bi} + V_n$ ; i.e.,  $\phi_B$  is only used for the thermodynamic equilibrium value.

Since the physical phenomena taking place in the absorber of this M-I-S structure are the same as those of an M-S structure, Eq. (6.13) is valid for  $J_p(W + \delta)$ . Equation (6.23) is also valid allowing us to write immediately that

$$J = -J_n(W + \delta) + F_p J_L - F_p J_{dif}(e^{E_{Fp}(\delta)/kT} - 1) \quad (6.61)$$

Note that  $x = W$  in Eq. (6.23) becomes  $x = W + \delta$  in Eq. (6.61) and  $x = 0$  in Eq. (6.23) becomes  $x = \delta$  in Eq. (6.61). The quantity  $F_p$  is the transport factor defined by Eq. (6.27). Also note that  $E_{Fp}(\delta)$  equals  $V$  only if the hole collection processes (see Fig. 6.2) are effective enough in the M-I-S structure to allow the hole population at  $x = \delta$  to follow the metal. Since  $E_{Fp}(\delta) \geq V$  is required if the holes are to move from the semiconductor (at  $x = \delta$ ) across the I layer into the metal, it is clear from Eq. (6.61) that  $E_{Fp}(\delta) = V$  (i.e., excellent hole communication across the I layer) is necessary for optimum M-I-S solar cell performance (for an  $n$ -type absorber). We shall return to this point [see Eq. (6.70) and related discussion].

The results of Section 6.2.3 may be used to evaluate the current density  $J_n(W + \delta)$ . Once again we may use the idea of continuity (Eq. 6.41) to write

$$J_n(W + \delta) = J_n(\delta) - J_{LSC} + J_{RB}(e^{V/n_R kT} - 1) \quad (6.62)$$

where

$$\begin{aligned} J_n(\delta) = & \Xi_{ob} J_{th}^n [e^{V_s/kT} e^{E_{Fn}(\delta)/kT} - e^{-V_1/kT}] \\ & + J_{surf} [e^{-\phi_B/kT} + e^{-\phi_T/kT}] [(1 - f_T) e^{\phi_T/kT} e^{V_s/kT} e^{E_{Fn}(\delta)/kT} - f_T e^{\phi_B/kT}] \\ & + J_r [e^{E_{Fp}(\delta)/kT} e^{E_{Fn}(\delta)/kT} - 1] \end{aligned} \quad (6.63)$$

In addition, the quantity  $E_{Fn}(\delta)$  appearing in Eq. (6.63) may be related back to  $J_n(\delta)$  by using a modified Eq. (6.32); viz.,

$$e^{E_{Fn}(\delta)/kT} = 1 - (J_n(\delta)/J_{sweep}^n) \quad (6.64)$$

The first term of the right-hand side of Eq. (6.63) represents thermionic emission of electrons over the barrier at  $x = \delta$ . The expression is modified from that of Eq. (6.33) for two reasons [22]: (a) electrons emitted at  $x = \delta$  must cross the I layer by direct tunneling or hopping (hence the need for the transmission probability  $\Xi_{ob}$ ) and (b) part of the voltage produced by the cell may be developed across the I layer [hence  $V_s$ , the voltage developed in the semiconductor, modifies the band bending to the right of  $x = \delta$  in Fig. 6.6 and  $V_1$ , the voltage developed across the insulator, modifies the band bending to the left of  $x = \delta$ ; see Eq. (3.59)].

The second term on the right-hand side of Eq. (6.63) represents the capture of conduction-band electrons at  $x = \delta$  by interface states and the subsequent emission of those captured electrons into the metal. It follows directly from Eq. (6.35) but differs from Eq. (6.36) for two reasons: (a)  $f_T$  need not follow the metal since the emitted electrons must cross the I layer, and (b) the band-bending change in the semiconductor in the M-I-S configuration is  $V_s$ .

The third term of the right-hand side in Eq. (6.63) is the band-to-band interface recombination (through defects arising from the act of forming the barrier). This expression is the same as Eq. (6.38) with  $x = \delta$  replacing  $x = 0$ . We note once again that  $E_{Fp}(\delta)$  only equals  $V$  in an optimally designed M-I-S device ( $n$ -type absorber).

In Section 6.2.3, the system of equations corresponding to Eqs. (6.62)–(6.64) had three unknowns which could easily be determined as functions of voltage. At first glance it would appear that Eqs. (6.62)–(6.64) also have only three unknowns [ $J_n(W + \delta)$ ,  $J_n(\delta)$ , and  $E_{Fn}(\delta)$ ] which can be determined as functions of voltage  $V$ . However, closer examination reveals that this system of equations in the M-I-S case has additional unknowns. These are seen to be  $V_s$ ,  $V_1$ ,  $f_T$ , and  $E_{Fp}(\delta)$ . Clearly, four addition relations are needed in the M-I-S case to determine our objective which is  $J_n(W + \delta)$  as a function of voltage for use in Eq. (6.61).

One additional relation is provided by the fact that

$$V = V_s + V_1 \quad (6.65)$$

in an M-I-S configuration [22]. Another comes from our being able to define an  $n$  factor such that [36]

$$V_s = V/n \quad (6.66)$$

which also means that  $V_i = V[(n - 1)/n]$ . In general, the quantity  $n$  is a function of voltage; to actually evaluate this  $n$  one must turn to electrostatics as Eq. (4.9) indicates. The reader is referred to the literature for further discussions of this point [22, 36]. For our purposes we shall assume here that the  $n$  is known. In practical situations it is determined experimentally.

A third additional relation can be developed from an expression for the emission of electrons, from the localized states at the semiconductor surface, across the I layer to the metal. This expression is [37]

$$J_{LS} = (eN_t/\tau_T)\Xi_{LS}(f_T - f_M) \quad (6.67)$$

where  $\tau_T$  is a time constant characteristic of the interface state potential and  $\Xi_{LS}$  is the transmission probability for electron transport across the I layer. For M-S devices, we were able to argue in Section 6.2.3 that  $f_T = f_M$ . That is not necessarily the case here. From Fig. 6.6 it can be seen that  $f_M$ , the probability of occupancy for the levels in the metal which have the same energy as the interface states, is given by

$$f_M = [1 + \exp + (\phi_B - \phi_T + V_i)/kT]^{-1} \quad (6.68)$$

Using Eq. (6.68) and the fact that  $J_{LS}$ , as given by Eq. (6.67), must equal  $J_{LS}$  as determined by the net capture of conduction-band electrons by the interface states allows us to write the required third relation:

$$(eN_t/\tau_T)\Xi_{LS}[f_T - (1 + e^{(\phi_B + V_i - \phi_T)/kT})^{-1}] = J_{surf}[e^{-\phi_B/kT} + e^{-\phi_T/kT}][(1 - f_T)e^{\phi_T/kT}e^{V_s/kT}e^{E_{Fn}(\delta)/kT} - f_Te^{\phi_B/kT}] \quad (6.69)$$

The fourth additional relation is obtained from a model for the collection of holes at  $x = \delta$ . This model says that the hole current collected from  $x = \delta$  is given by  $\Xi_{ph}J_{th}^p[\exp(V_i/kT) - \exp(E_{Fp}(\delta)/kT)\exp-(V_s/kT)]$  which is essentially the same approach used to discuss electron collection at  $x = W_1$  for the  $p$ -type absorbers of Fig. 5.9. The prefactor  $J_{th}^p$  (characterizing thermionic emission of holes at  $x = \delta$ ) is different from the  $J_{th}^n$  (characterizing thermionic emission of electrons at  $x = \delta$ ) appearing in Eq. (6.63). Also,  $\Xi_{ph}$  is different from  $\Xi_{ob}$  since  $\Xi_{ph}$  is the transmission probability for holes traversing the I layer in Fig. 6.6. With this model we can write the fourth relationship required to determine  $J_n(\delta + W)$ ; viz.,

$$\begin{aligned} \Xi_{ph}J_{th}^p[\exp(V_i/kT) - \exp(E_{Fp}(\delta)/kT)\exp-(V_s/kT)] &= -J_{LSC} \\ &- F_p J_L + F_p J_{dif}[\exp(E_{Fp}(\delta)/kT) - 1] \\ &+ J_r[\exp(E_{Fp}(\delta)/kT)\exp(E_{Fn}(\delta)/kT) - 1] \\ &+ J_{RB}[\exp(V/n_R kT) - 1] \end{aligned} \quad (6.70)$$

Note the if  $\Xi_{ph} J_{th}^p$  is large compared to  $F_p J_{LSC} + J_L$  then Eq. (6.70) says that  $E_{Fp}(\delta) = V$  which is what we assumed in the case of M-S solar cell devices.

Equations (6.62)–(6.66), (6.69), and (6.70) can now, in principle, be solved to determine  $J_n(W + \delta)$  and  $E_{Fp}(\delta)$  as functions of voltage. The resulting expressions can then be used in Eq. (6.61) to give a very general  $J-V$  characteristic for an M-I-S solar cell structure under illumination. From a practical standpoint the way to approach this set of equations is to solve it numerically. When the result is combined with Eq. (6.61), a numerical  $J-V$  characteristic is obtained [38].

Rather than use a numerical approach we shall make some assumptions which will allow this set of equations to be simplified considerably. These assumptions are valid for many materials systems and they give a straightforward analytical expression for the  $J-V$  characteristic of an effective M-I-S solar cell which brings the device operation into focus. These assumptions are the following: (a)  $J_{sweep}^n > J_n(\delta)$  [electron quasi-Fermi level is flat across the space-charge region resulting in  $E_{Fn}(\delta) = 0$ ], (b)  $F_p = 1$  [hole quasi-Fermi level is flat across the space-charge region], (c)  $E_{Fp}(\delta) = V$  [as must be the case in any efficient M-I-S solar cell], and (d)  $J_{LS} \ll J_{ob}$  [this is plausible from the discussion of Section 6.2.3 since both  $J_{LS}$  and  $J_{ob}$  are reduced in the M-I-S configuration due to the necessity of tunneling across the I layer].

With these assumptions, Eqs. (6.61)–(6.63), (6.65), and (6.66) may be combined to give [22]

$$J = J_{LSC} + J_L - \Xi_{ob} A^* T^2 e^{-\phi_B/kT} [e^{V/nkT} - e^{-(n-1)V/nkT}] - J_r [e^{V/kT} - 1] \\ - J_{RB} [e^{V/n_R kT} - 1] - J_{dif} [e^{V/kT} - 1] \quad (6.71)$$

The quantity ( $J_{LSC} + J_L$ ) is the photocurrent. The other four terms are all the components of the bucking current; i.e., the majority-carrier over-the-barrier component (first expressed in the form seen in Eq. (6.71) by Strikha [39]), interface-recombination, space-charge-recombination, and bulk-diffusion-recombination. Since, in general,  $J_r = J_r(V)$ , each of the bucking-current terms can have an  $n$ -factor different from unity except for the bulk-diffusion-recombination term.

On the basis of our analysis, a number of conclusions can be drawn concerning the operation of M-I-S solar cells:

(a) The majority-carrier thermionic emission current, which usually dominates the bucking current in the M-S solar cell configuration, can potentially be suppressed in the M-I-S configuration. We have said that there are three reasons for this. The three reasons can be seen in the mathematics of Eq. (6.71). They are [22] (1) the presence of the I layer can introduce fixed charge or can modify the charge configuration in interface

states leading to an increased barrier height  $\phi_B$ , in properly chosen materials systems, (2) the presence of the I layer can suppress the majority-carrier thermionic emission current due to the presence of the transmission probability  $\Xi_{ob}$ , and (3) localized states at the semiconductor-insulator interface or in the I layer can charge on the passing of a current allowing a significant voltage to be developed across the insulator and leading to an  $n$  factor for the majority-carrier thermionic emission current which is  $n > 1$ .

It can be seen from Eq. (6.71) that any combination of these three effects will reduce the majority-carrier bucking-current component for a given voltage and, since this thermionic emission current usually dominates the bucking current, any combination of these effects will increase the open-circuit voltage and cell efficiency. This latter statement assumes that  $E_{Fp}(\delta) = V$  is attained in the M-I-S configuration.

The fact that the majority-carrier thermionic emission bucking-current component usually dominates over the minority-carrier diffusion-recombination bucking-current component of Eq. (6.71) in an M-S structure is seen in Fig. 6.7. Curve 1 of the figure typifies the majority-carrier thermionic emission bucking currents expected in a GaAs M-S solar cell; curve 5 typifies the minority-carrier diffusion-recombination bucking currents expected.

Figure 6.7 also shows how the thermionic emission current can be suppressed by the presence of  $N_{fix}$  ( $\text{cm}^{-2}$ ) fixed charge sites at or near the insulator-semiconductor interface in the M-I-S configuration. If this charge is properly chosen (i.e., negative charge for an  $n$ -type semiconductor), the semiconductor is forced to shield the insulator charge in the M-I-S configuration by increasing the band bending in the semiconductor space-charge region. This increased polarization in the semiconductor means an increased  $\phi_B$  and, as curves 2-4 of Fig. 6.7 show, a reduced thermionic emission current. That is, as  $\phi_B$  increases the thermionic emission current moves successively through the positions of curves 1-4, etc. If the thermionic emission current is suppressed below curve 5, it is negligible compared to the minority-carrier diffusion-recombination bucking current.

Figure 6.8 demonstrates how the I layer can suppress the thermionic emission component of Eq. (6.71) due to the presence of the transmission probability  $\Xi_{ob}$ . For the thermionic emission bucking-current component curves seen in this figure, the  $n$  factor is taken to be unity and the insulator is assumed not to introduce any charge<sup>†</sup> in order to focus on the effect of  $\Xi_{ob}$ . To calculate the transmission probability for these curves, direct tunneling has been assumed and a standard approximation for calculating

<sup>†</sup> Note that  $\phi_B$  does change for curve 4. This occurs since the flux lines originating in the semiconductor (we assumed no charge resides in the insulator here) must cross a wider I layer as  $\delta$  increases. This increases  $\Delta$ , decreases  $V_{bi}$  since  $\Delta + V_{bi}$  must be constant, and reduces  $\phi_B$  since  $\phi_B = V_{bi} + V_n$ .

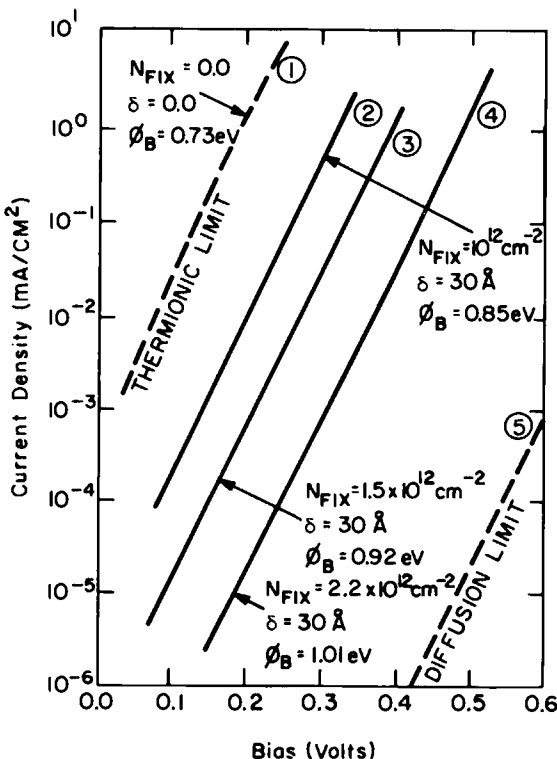


Fig. 6.7 Dark  $J$ - $V$  characteristics are seen to be dominated by thermionic emission in the M-S ( $\delta = 0$ ) configuration. However, the M-I-S configuration ( $\delta \neq 0$ ) with properly chosen fixed charge in the insulator, can reduce this thermionic emission current toward the diffusion limit by increasing the barrier height  $\phi_B$ . The fixed charge in the insulator  $Q_{\text{fix}}$  has been assumed to be negative, which is advantageous for an *n*-type semiconductor. It is assumed located at the insulator-semiconductor interface. Note that  $Q_{\text{fix}} = eN_{\text{fix}}$ . Both  $\Xi_{\text{ob}}$  and  $n$  are assumed to be unity here to focus on the effect of  $\phi_B$ .

tunneling probabilities has been used to evaluate  $\Xi_{\text{ob}}$  [22]. The curves show that, when direct tunneling is the transport mode by which thermionically emitted electrons cross the I layer, this bucking-current component is reduced roughly one order of magnitude for every four angstroms of additional insulator layer. Consequently, the thermionic emission bucking current moves from curve 1 for the M-S configuration to curves 2–4, etc. as the insulator thickness increases and the tunneling probability decreases. If the thermionic emission current is suppressed below curve 5 of the figure, the open-circuit voltage is determined by the diffusion-recombination component of Eq. (6.71), provided the interface and space-charge region recombination bucking-current terms can be neglected.

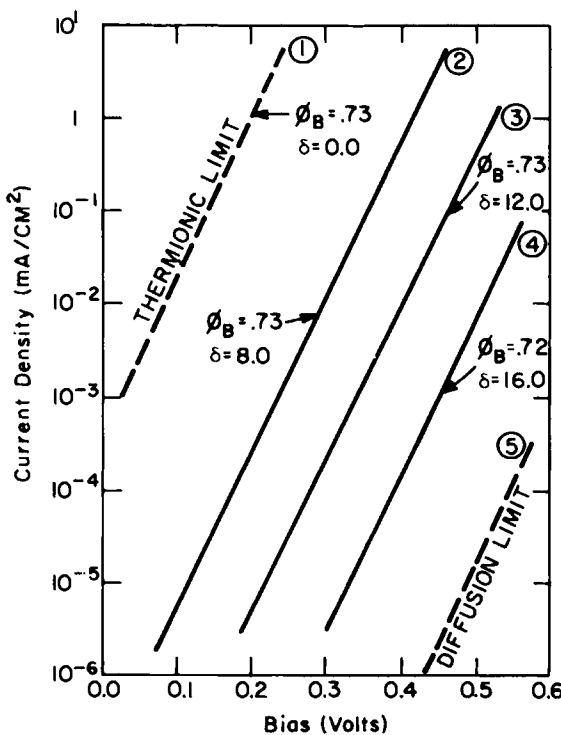


Fig. 6.8 Transport control by direct tunneling. In this case the ideality factor  $n$  is set equal to unity and the presence of charge in the insulator is neglected to focus on  $\Xi_{ob}$ , the transmission coefficient. Since  $\Xi_{ob}$  is assumed to be the result of direct tunneling here, it is seen to decrease by one order of magnitude for roughly every four angstroms of additional I layer thickness. The curves shown are for parameters appropriate to GaAs and  $\phi_M = 4.80$ .

Figure 6.9 focuses on the third possible effect that can be introduced by the presence of the I layer in the M-I-S configuration; namely, the charging of localized states at or near the insulator-semiconductor interface on the passing of a current [22]. To concentrate on this effect  $\Xi_{ob} = 1$  is used and  $\phi_B$  is held constant in the figure. Several  $n = n(V)$  functions, which have been calculated from electrostatics [22], are used in the  $J_{ob}$  term of Eq. (6.71). As can be seen, this charging of localized states on the passing of a current, which results in  $n > 1$ , causes a suppression of the thermionic emission process. Curves 1-3 represent successively higher localized state densities. The higher the state density, the more trapped charge and the larger  $V_1$  (and thus the larger  $n$ ) for a given current density [22].

(b) If  $A^*T^2 > eN_c\mu_n\xi_M$ , where  $\xi_M$  is the maximum electrostatic field in the space-charge region, then majority-carrier diffusion-drift and not

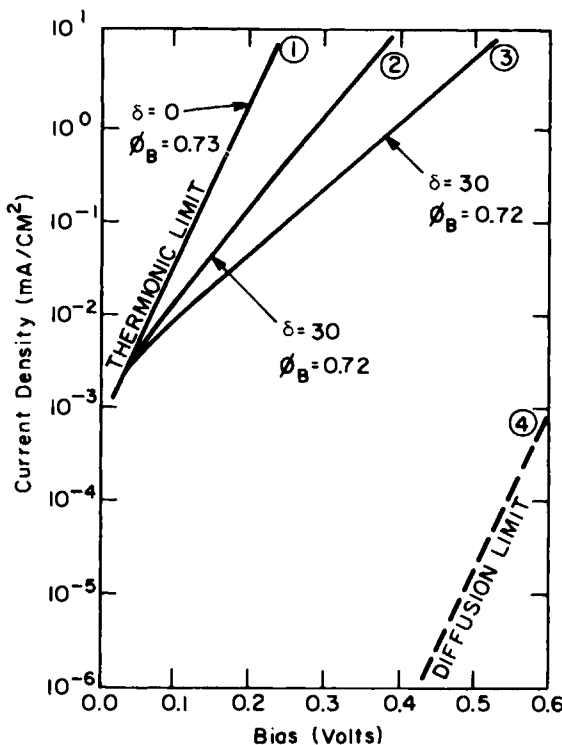


Fig. 6.9 The dark  $J$ - $V$  characteristics resulting from the presence of the charging of localized states on the passing of a current. No tunneling control or  $Q_{fix}$  is present, enabling the effects of an ideality factor  $n > 1$  to be seen.

thermionic emission becomes the rate-limiting step for the majority-carrier bucking current. In that case  $eN_c\mu_m\zeta_M$  replaces  $A^*T^2$  in Eq. (6.71) as follows from the detailed discussion in Section 6.2.3. This replacement becomes necessary in M-I-S structures using low-mobility solids such as some amorphous Si M-I-S devices.

(c) If multistep tunneling is present in an M-I-S configuration then a term of the form of Eq. (3.61) (valid for  $V > kT$ ) must be added to Eq. (6.71).

(d) It can be seen from Eq. (6.71) that, if the majority-carrier bucking current can be suppressed and if the interface and space-charge region recombination currents can be suppressed, then the bucking current of an M-I-S device is the same as that of an ideal  $p$ - $n$  junction (with no emitter bucking current) [22, 38]. That is, the bucking current in an M-I-S device can never drop below the diffusion limit seen in Figs. 6.7-6.9. Devices in which the bucking current has been forced to this limit have been given the

name minority-carrier M-I-S devices in the literature [38]; the fact that such devices can be fabricated has been demonstrated experimentally [40].

(e) A high barrier height is beneficial since it acts to suppress the majority-carrier thermionic emission bucking current. It is also beneficial because higher  $\phi_B$  values give higher  $J_{th}^p$  values. As can be seen from Eq. (6.70), if  $J_{th}^p$  is large, the advantageous situation of  $E_{Fp}(\delta) = V$  is more apt to be achieved in an M-I-S device. A high  $\phi_B$  value implies a high  $J_{th}^p$  value since

$$J_{th}^p = A^* T^2 e^{-(E_K - \phi_B)/kT} \quad (6.72)$$

as may be inferred from Part 3 of Section 5.2.3.2.

(f) As we have seen, increasing  $\phi_B$  reduces the majority-carrier bucking current and simultaneously helps in the collection of  $J_{ph}$ . The effect of the charging of localized states at or near the insulator-semiconductor interface on the passing of a current (causing  $n > 1$ ) reduces the majority-carrier bucking current also, and does not interfere with the collection of  $J_{ph}$ .

On the other hand, using the I layer as a tunneling barrier to suppress the majority-carrier bucking current through  $\Xi_{ob}$  has its drawbacks since the I layer may also significantly suppress the collection of  $J_{ph}$ . Conceptually one could envision I layers designed to avoid this. For example, if the insulator valence-band edge in Fig. 6.6 were moved up to, or above, the semiconductor valence-band edge, electrons would still find it difficult to tunnel across the I layer, but holes would now be relatively unimpeded [22].

### 6.2.5 Analysis of Liquid-Semiconductor Structures

Once again we note that the physical phenomena taking place in the absorber of any surface barrier cell under illumination are the same whether the device is an M-S, M-I-S, or EPC device. Using that fact, we will borrow extensively from Sections 6.2.3 and 6.2.4 in this analysis of EPC solar cells.

Figure 6.10 shows a liquid-semiconductor solar cell structure under illumination. The current density  $J$  being produced is a constant for a given voltage developed and for a given illumination level. As is our custom, we begin by evaluating this constant at the edge of the semiconductor space-charge region ( $x = W$ ); viz.,

$$J = -[J_n(W) + J_p(W)] \quad (6.73)$$

If we make the same assumptions about the absorber as we did in Sections 6.2.3 and 6.2.4 (i.e., the absorber is a lifetime semiconductor and the illumination level is such that  $p \ll n$  in the base), then we can immediately note that  $J_p(W)$  in Eq. (6.73) is flowing by diffusion. Consequently, Eq. (6.13) is again appropriate for  $J_p(W)$ . Further, by applying the continuity

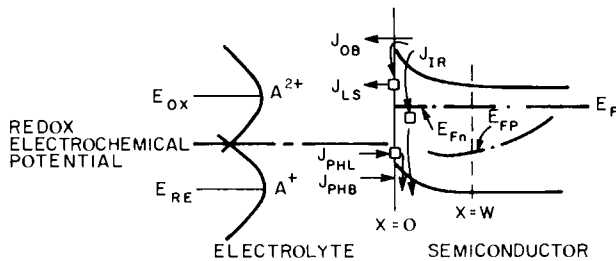


Fig. 6.10 Liquid-semiconductor solar cell under illumination.

equation for electrons [Eq. (4.16)] in integral form to the space-charge region of the absorber ( $0 < x \leq W$ ) and by using the notation of Fig. 6.10, we can write that the  $J_n(W)$  of Eq. (6.73) is given by

$$J_n(W) = J_{ob} + J_{LS} + J_{ir} + e \int_0^W \mathcal{H}(x) dx - e \int_0^W G_L(x) dx \quad (6.74)$$

Combining Eqs. (6.13) and (6.74) with Eq. (6.73), and using Eq. (6.45) to model  $e \int_0^W \mathcal{H}(x) dx - e \int_0^W G_L(x) dx$ , we can rewrite  $J$  as

$$\begin{aligned} J = & J_{LSC} + J_L - J_{ob} - J_{LS} - J_{ir} \\ & - J_{RB}(e^{V/n_R kT} - 1) - J_{dif}(e^{E_{Fp}(W)/kT} - 1) \end{aligned} \quad (6.75)$$

As has been our practice, we continue to measure  $E_{Fp}$  positively down from the Fermi-level position in the bulk. Since Eq. (6.23) is valid, Eq. (6.75) can be expressed in the form

$$\begin{aligned} J = & J_{LSC} + F_p J_L - J_{ob} - J_{LS} - J_{ir} \\ & - J_{RB}(e^{V/n_R kT} - 1) - F_p J_{dif}(e^{E_{Fp}(0)/kT} - 1) \end{aligned} \quad (6.76)$$

where  $F_p$  is the hole transport factor first introduced in Section 6.2.3. If we knew the dependence of  $J_{ob}$ ,  $J_{LS}$ , and  $J_{ir}$  on  $E_{Fn}(0)$  and  $E_{Fp}(0)$ , and if we knew the relationship between  $E_{Fn}(0)$  and  $V$  and  $E_{Fp}(0)$  and  $V$ , Eq. (6.76) would give us our goal  $J = (V)$ .

We begin to develop a model for the bucking-current density  $J_{ob}$  by noting that it is caused by the emission of electrons from the conduction band at  $x = 0$  into the empty, localized electron states provided by the oxidized species  $A^{2+}$  in the liquid. However,  $J_{ob}$  cannot be modeled by an approach based on Eq. (6.33) since it is not a current arising from electron transitions from delocalized states to delocalized states; rather,  $J_{ob}$  in EPC devices arises from electrons going from delocalized states in the semiconductor to localized states existing on ions in solution. Hence, to model  $J_{ob}$  in EPC devices we shall turn to an approach developed by Gerischer [41, 42].

Using the notation of Section 3.4.7, we note that

$$N^{\text{ox}}(0^-)(4\pi\lambda kT)^{-1/2} \exp(-[E + E_c(0) - E_{\text{ox}}]^2/(4\lambda kT))$$

is a measure of the number of localized, empty levels of energy  $E$  available per volume in the liquid adjacent to the surface; similarly

$$N^{\text{re}}(0^-)(4\pi\lambda kT)^{-1/2} \exp(-[E + E_c(0) - E_{\text{re}}]^2/(4\lambda kT))$$

is a measure of the number of localized, occupied levels of energy  $E$  present per volume in the liquid adjacent to the surface.<sup>†</sup> We also note that

$$g(E) \exp(-[E + V_{\text{bi}} + V_n - V_s - E_{F_n}(0)]/kT) dE$$

gives the number of electrons in the conduction band at  $x = 0$  with energies between  $E$  and  $E + dE$ , and

$$g(E)[1 + \exp(-[E + V_{\text{bi}} + V_n - V_s - E_{F_n}(0)]/kT)]^{-1} dE$$

gives the number of unoccupied states in the conduction band at  $x = 0$  with energies between  $E$  and  $E + dE$ . Here  $g(E)$  is the density of states function for the conduction band. As has been our practice,  $E_{F_n}$  is measured positively up from the position of  $E_F$  in the bulk. In these last two expressions  $V_s$  represents the change in band bending which occurs in the semiconductor when the EPC device is under illumination and developing a voltage  $V$ . In all four of these expressions the variable energy  $E$  is measured positively up from the position of the semiconductor conduction-band edge at  $x = 0$ .

The particle current of electrons emitted from the semiconductor at  $x = 0$  into the oxidized species in solution is expected to be proportional to the product of the number of available electrons at  $x = 0$  in the semiconductor and the number of empty, available oxidized levels in solution; viz. [41, 42],

$$\frac{N^{\text{ox}}(0^-)}{(4\pi\lambda kT)^{1/2}} \int_0^\infty v^{\text{so}}(E) g(E) \exp(-[E + V_{\text{bi}} + V_n - V_s - E_{F_n}(0)]/kT) \\ \exp(-[E + E_c(0) - E_{\text{ox}}]^2/4\lambda kT) dE$$

This sum is over all energies in the conduction band which are greater than  $E_c(0)$ . Implicit in this expression is the assumption that the transfer process conserves energy [43]. We shall limit all non-conservative transitions to path  $J_{1S}$  seen in Fig. 6.10. It follows that the particle current of electrons

<sup>†</sup> Some doubt has been raised concerning the validity of these two distributions [43]. However, no alternative distributions have been shown to be valid or, for that matter, proposed. In view of this, we shall follow common practice and use these functions [44].

emitted from the reduced species in solution back into the conduction band at  $x = 0$  is expected to be of the form

$$\frac{N^{re}(0^-)}{(4\pi\lambda kT)^{1/2}} \int_0^\infty v^{rs}(E)g(E)[1 + \exp(-[E + V_{bi} + V_n - V_s - E_{Fn}(0)/kT])^{-1} \\ \exp(-[E + E_c(0) - E_{re}]^2/4\lambda kT) dE$$

As a result,  $J_{ob}$  is given by [41, 42]

$$J_{ob} = \frac{e}{(4\pi\lambda kT)^{1/2}} \left[ N^{ox}(0^-) \int_0^\infty v^{so}(E)g(E)e^{-\phi_B/kT} e^{-(E - V_s - E_{Fn}(0))/kT} e^{-(E + E_c(0) - E_{ox})^2/(4\lambda kT)} dE \right. \\ \left. - N^{re}(0^-) \int_0^\infty v^{rs}(E)g(E)[1 + e^{-\phi_B/kT} e^{-(E - V_s - E_{Fn}(0))/kT}]^{-1} \right. \\ \left. \times e^{-(E + E_c(0) - E_{re})^2/(4\lambda kT)} dE \right] \quad (6.77)$$

The quantity  $v^{so}(E)$  in Eq. (6.77) characterizes the transition of an electron of energy  $E$  from the semiconductor to the oxidized species;  $v^{rs}(E)$  characterizes the transition of an electron of energy  $E$  from the reduced species to the semiconductor. The barrier height  $\phi_B$  is the same parameter encountered in our discussion of M-S and M-I-S devices; i.e.,  $\phi_B = V_{bi} + V_n$ .

In thermodynamic equilibrium  $J_{ob}$  must be zero. With this fact and the principle of detailed balance, Eq. (6.77) can be manipulated to show that  $v^{so}(E) = v^{rs}(E) = v^{ob}(E)$  [41]. The simplification allows Eq. (6.77) to be rewritten in the form

$$J_{ob} = \frac{e}{(4\pi\lambda kT)^{1/2}} \left[ N^{ox}(0^-) \int_0^\infty v^{ob}g(E)[e^{-\phi_B/kT} e^{-(E - V_s - E_{Fn}(0))/kT}] \right. \\ \left. \times [e^{-(E + E_c(0) - E_{ox})^2/(4\lambda kT)}] dE \right. \\ \left. - N^{re}(0^-) \int_0^\infty v^{ob}g(E)[1 + e^{-\phi_B/kT} e^{-(E - V_s - E_{Fn}(0))/kT}]^{-1} \right. \\ \left. \times [e^{-(E + E_c(0) - E_{re})^2/(4\lambda kT)}] dE \right] \quad (6.78a)$$

Algebraic manipulation shows that Eq. (6.78a) can also be put into the form

$$J_{ob} = ee^{-\phi_B/kT} \int_0^\infty v^{ob}(E)D(E)g(E)\{[e^{-(E - V_s - E_{Fn}(0))/kT}][1 + e^{-(E + \phi_B + V_t)/kT}]^{-1} \\ - [1 + e^{-\phi_B/kT} e^{-(E - V_s - E_{Fn}(0))/kT}]^{-1}[e^{-(E + V_t)/kT}]\} dE \quad (6.78b)$$

if we use the definition [41, 44]

$$D(E) \equiv \frac{N^{\text{ox}}(0^-)}{(4\pi\lambda kT)^{1/2}} \exp[-(E + \Delta_{\text{ox}} + V_l)^2/(4\lambda kT)] \\ + \frac{N^{\text{re}}(0^-)}{(4\pi\lambda kT)^{1/2}} \exp[-(E + \Delta_{\text{re}} + V_l)^2/(4\lambda kT)] \quad (6.79)$$

While Eq. (6.78a) is a general statement, Eq. (6.78b) is limited to situations where  $N^{\text{ox}}(0^-) = N_0^{\text{ox}}$  and  $N^{\text{re}}(0^-) = N_0^{\text{re}}$  since these values for the redox concentrations at  $x = 0^-$  are assumed in using  $D(E)$  [41, 44]. In a solar cell structure one would hope to have  $N^{\text{ox}}(0^-) = N_0^{\text{ox}}$  and  $N^{\text{re}}(0^-) = N_0^{\text{re}}$ ; i.e. one would hope that the redox couple concentrations do not vary significantly from those of thermodynamic equilibrium. This is equivalent to a negligible voltage drop in the solution.

Two new quantities have been introduced in Eq. (6.79). These are

$$\Delta_{\text{ox}} \equiv [E_c(0) - E_{\text{ox}}]_{\text{thermodynamic equilibrium}} \quad (6.80)$$

and

$$\Delta_{\text{re}} \equiv [E_c(0) - E_{\text{re}}]_{\text{thermodynamic equilibrium}} \quad (6.81)$$

As can be seen from Fig. 6.10,  $\Delta_{\text{ox}}$  locates the position of the conduction band at  $x = 0$  with respect to the most probable energy  $E_{\text{ox}}$  for an empty level in solution (in thermodynamic equilibrium);  $\Delta_{\text{re}}$  locates the position of the conduction band edge at  $x = 0$  with respect to the most probable energy  $E_{\text{re}}$  for an occupied level in solution (in thermodynamic equilibrium).

The  $V_s$  and  $V_l$  appearing Eqs. (6.78) are such that

$$V = V_s + V_l \quad (6.82)$$

where  $V$  is the total voltage developed by the cell. The quantity  $V_s$  is the change in the band bending in the semiconductor, and  $V_l$  is the change in the electrostatic potential energy developed across the Helmholtz layer and across any interfacial layer present under illumination. Clearly  $V_l$  is very similar to the  $V_l$  developed across the I layer in M-I-S devices except that in EPC devices  $V_l$  has the additional possibility of being developed, at least in part, across the Helmholtz layer. We can relate  $V_s$  and  $V_l$  to  $V$  by defining an  $n$  factor for EPC devices; viz.,

$$V_s = \left(\frac{1}{n}\right)V \quad (6.83)$$

$$V_l = \left(\frac{n-1}{n}\right)V \quad (6.84)$$

This  $n$  factor, as was the case for M-I-S cells, is determined by electrostatics (see Section 6.2.4). We shall assume  $n = n(V)$  is known.

Although the expression for  $J_{ob}$  given in Eq. (6.78b) is not of general validity since it assumes  $N^{ox}(0^-) = N_0^{ox}$  and  $N^{re}(0^-) = N_0^{re}$ , it is useful for making several points. First of all it underscores the strong dependence of  $J_{ob}$  on the barrier height  $\phi_B$ . Secondly, it can be written as

$$J_{ob} = e e^{-\phi_B/kT} \left[ \int_0^\infty v^{ob}(E) D(E) g(E) e^{-E/kT} dE \right] [e^{V_s/kT} e^{E_{Fn}(0)/kT} - e^{-V_t/kT}] \quad (6.85)$$

if  $E + \phi_B + V_t > kT$  and  $\phi_B + E - V_s - E_{Fn}(0) > kT$  (as we expect). The similarity between Eq. (6.85) and the majority-carrier over-the-barrier term of Eq. (6.63) is striking. On the basis of that similarity, one might be tempted to define a “Richardson’s constant”  $B^*$  for the majority-carrier bucking current in an EPC cell according to

$$B^* = \frac{e}{T^2} \left[ \int_0^\infty v^{ob}(E) D(E) g(E) e^{-E/kT} dE \right] \quad (6.86)$$

However, this is not a true Richardson’s constant, as may be seen by comparing this expression with Eq. (5.89). This  $B^*$  for an EPC device depends on the rearrangement energy  $\lambda$ , on the concentration of oxidized and reduced species, on the positions of  $E_{ox}$  and  $E_{re}$ , and on  $V_t$ ; a true Richardson’s constant simply depends on the carrier effective mass values in the semiconductor as Eq. (5.90) shows; i.e., it is a property of the semiconductor alone. However, Eq. (6.86) is a convenient short hand. In that spirit we will use  $B^*$  allowing us to write

$$J_{ob} = B^* T^2 e^{-\phi_B/kT} (e^{V_s/kT} e^{E_{Fn}(0)/kT} - e^{-V_t/kT}) \quad (6.87)$$

If  $N^{ox}(0^-) = N_0^{ox}$  and  $N^{re}(0^-) = N_0^{re}$ , then Eq. (6.87) may be used in constructing  $J = J(V)$  from Eq. (6.76); if these constraints on the redox couple concentrations are relaxed, Eq. (6.78a) must be used.

We now need to develop an expression for the current density  $J_{LS}$  appearing in Eq. (6.76). Fortunately the model used for the  $J_{LS}$  component of Eq. (6.63) is also valid for EPC devices; i.e.,

$$J_{LS} = J_{surf} [e^{-\phi_B/kT} + e^{-\phi_T/kT}] \\ \times [(1 - f_T) e^{\phi_T/kT} e^{V_s/kT} e^{E_{Fn}(0)/kT} - f_T e^{\phi_B/kT}] \quad (6.88)$$

The fact that Eq. (6.88) is valid for the liquid–semiconductor interface is quite understandable since it expresses  $J_{LS}$  in terms of the capture and emission going on between the conduction band at  $x = 0$  and localized states at the surface.

An expression is also needed for the second step in this current path; i.e., a model is needed for the net emission of electrons from the localized

interface states to the localized states situated on the ions in solution. The current density arising due to electrons making the transition from interface states to states on the oxidized species should be proportional to the product of the density of filled interface states and the density of oxidized levels; i.e., it should be of the form

$$\frac{e}{(4\pi\lambda kT)^{1/2}} v_T^{RL} N^{ox}(0^-) N_T f_T \exp[-(\Delta_{ox} - \phi_T + V_l)^2/4\lambda kT] \Delta E_T$$

This assumes that this part of the two-stage process giving  $J_{LS}$  is conservative and assumes that the interface states involved have energies in the range  $E_T$  to  $E_T + \Delta E_T$ . A broader range of interface state energies would necessitate an integration over  $E_T$ . Using the same argument, the current density due to the converse process (electrons going from the reduced species to the interface states) should be of the form

$$\frac{e}{(4\pi\lambda kT)^{1/2}} v_T^{LR} N^{re}(0^-) N_T (1 - f_T) \exp[-(\Delta_{re} - \phi_T + V_l)^2/4\lambda kT] \Delta E_T$$

The first of these expressions makes use of the fact that  $E_T - E_{ox} = \Delta_{ox} - \phi_T + V_l$  and the second makes use of the fact that  $E_T - E_{re} = \Delta_{re} - \phi_T + V_l$  where  $\phi_T$  locates the interface state level with respect to  $E_c(0)$ . It follows that the difference in these two current densities gives  $J_{LS}$ ; viz.,

$$J_{LS} = \frac{eN_T}{(4\pi\lambda kT)^{1/2}} [v_T^{RL} N^{ox}(0^-) f_T \exp[-(\Delta_{ox} - \phi_T + V_l)^2/4\lambda kT] - v_T^{LR} N^{re}(0^-) (1 - f_T) \exp[-(\Delta_{re} - \phi_T + V_l)^2/4\lambda kT]] \Delta E_T \quad (6.89)$$

Since it can be shown that  $v_T^{RL} = v_T^{LR} = v_T$  [41], our expression for  $J_{LS}$  can be written as

$$J_{LS} = \frac{eN_T v_T \Delta E_T}{(4\pi\lambda kT)^{1/2}} [N^{ox}(0^-) f_T \exp[-(\Delta_{ox} - \phi_T + V_l)^2/4\lambda kT] - N^{re}(0^-) (1 - f_T) \exp[-(\Delta_{re} - \phi_T + V_l)^2/4\lambda kT]] \quad (6.90)$$

This equation is of general validity and may be used together with Eq. (6.88) to construct the  $J_{LS}$  component of  $J = J(V)$ .

If we limit ourselves to cases where  $N^{ox}(0^-) = N_0^{ox}$  and  $N^{re}(0^-) = N_0^{re}$ , then we can define a  $D(-\phi_T)$  according to

$$D(-\phi_T) = \frac{N^{ox}(0^-)}{(4\pi\lambda kT)^{1/2}} \exp[-(\Delta_{ox} - \phi_T + V_l)^2/(4\lambda kT)] + \frac{N^{re}(0^-)}{(4\pi\lambda kT)^{1/2}} \exp[-(\Delta_{re} - \phi_T + V_l)^2/(4\pi\lambda kT)] \quad (6.91)$$

and write

$$J_{LS} = eN_T D(-\phi_T) v_T \Delta E_T \left[ f_T - \left( \frac{1}{1 + e^{(V_l + \phi_B - \phi_T)/kT}} \right) \right] \quad (6.92)$$

This equation, together with Eq. (6.88), characterizes the current  $J_{LS}$  if  $N^{ox}(0^-) = N_0^{ox}$  and  $N^{re}(0^-) = N_0^{re}$ ; these two equations can be used to construct the  $J_{LS}$  component of  $J = J(V)$  as in Eq. (6.76).

A final point can be made concerning Eq. (6.92): it is very similar to Eq. (6.67) developed in our discussion of M-I-S solar cells. This becomes especially apparent if one defines an  $f_{redox} \equiv [1 + e^{(V_I + \phi_B - \phi_T)/kT}]^{-1}$ . However, it must be kept in mind that, although the mathematical forms of these expressions are similar the physics being modeled is different. Note that the coefficient  $(eN_T\Xi_{LS}/\tau_T)$  in Eq. (6.67) depends only on interface state and I layer properties. The coefficient in Eq. (6.92) may include tunneling through an interfacial layer and interface properties but it also includes  $\lambda$ , the solvation or rearrangement energy of the redox couple, the redox couple concentrations, and the redox couple level distributions.

We turn now to the current density component in Eq. (6.76) which has yet to be modeled; that term is the bucking-current component  $J_{ir}$ . Since it is flowing through defects in the semiconductor at and near the surface (created in the act of forming the barrier), it is governed by the same equation that was used for this current density in M-S and M-I-S devices (Eq. (6.38)); hence,

$$J_{ir} = J_r [e^{E_{Fp}(0)/kT} e^{E_{Fn}(0)/kT} - 1] \quad (6.93)$$

The prefactor  $J_r$  is defined by Eq. (6.39).

Before we can say that we have generated the necessary set of equations that will permit  $J = J(V)$  to be determined from Eq. (6.76), two final tasks remain. One is to relate  $E_{Fn}(0)$ , the electron quasi-Fermi level at  $x = 0$ , to the electron current flowing at the interface. This task is easily accomplished since Eq. (6.64) is valid; consequently,

$$e^{E_{Fn}(0)/kT} = 1 - \frac{J_{ob} + J_{LS} + J_{ir}}{J_{sweep}^n} \quad (6.94)$$

The second task is to determine  $E_{Fp}(0)$ , the hole quasi-Fermi level at  $x = 0$ . Since it is known experimentally that the reduced species in at least some materials systems can have difficulty in collecting the photogenerated holes arriving at  $x = 0$ , one cannot assume a priori that  $E_{Fp}(0) = V$  (excellent communication between the valence band and the redox couple); rather, it will be necessary to develop models for the photocurrent collection paths  $J_{PHL}$  and  $J_{PHB}$  seen in Fig. 6.10. These expressions for  $J_{PHL}$  and  $J_{PHB}$  will determine  $E_{Fp}(0)$  since we have the constraint that

$$\begin{aligned} J_{PHL} + J_{PHB} &= -J_{LSC} - F_p J_L + J_r (e^{E_{Fp}(0)/kT} e^{E_{Fn}(0)/kT} - 1) \\ &\quad + J_{RB}(e^{V/n_R kT} - 1) + F_p J_{dif} [e^{E_{Fp}(0)/kT} - 1] \end{aligned} \quad (6.95)$$

The current density  $J_{\text{PHL}}$  flows via a two step process: first a hole is captured by the intermediary states seen in Fig. 6.10; then the hole is subsequently emitted from the localized state of the intermediary to a localized state on the reduced species in solution. This path can be important in the collection of photocurrent in EPC cells since a higher number of reduced states could overlap the energy of the intermediary level than overlap the energy of the band edge  $E_g(0)$ .

The first step in the flow of  $J_{\text{PHL}}$  is modeled by the valence-band analog of Eq. (6.35); viz.,

$$J_{\text{PHL}} = -e \langle v_p \rangle \Omega_p N_i [f_i p(0) - (1 - f_i)p_1] \quad (6.96)$$

Here the minus sign arises because of the coordinate system choice of Fig. 6.10. The intermediary states involved in carrying  $J_{\text{PHL}}$  have a density  $N_i(\text{cm}^{-2})$ , are located  $\phi_i$  above  $E_g(0)$  in the gap, and have a probability of occupancy equal to  $f_i$ . By using the definition

$$J_{\text{surf}}^i \equiv (e \langle v_p \rangle \Omega_p N_i N_v) (e^{-(E_g - \phi_B)/kT} e^{-\phi_i/kT}) \quad (6.97)$$

this current  $J_{\text{PHL}}$  can be written as

$$J_{\text{PHL}} = J_{\text{surf}}^i [(1 - f_i) e^{(E_g - \phi_B)/kT} - f_i e^{\phi_i/kT} e^{-V_s/kT} e^{E_{FP}(0)/kT}] \quad (6.98)$$

The second step in the flow of  $J_{\text{PHL}}$  is modeled by the hole emission analog of Eq. (6.90); viz.,

$$\begin{aligned} J_{\text{PHL}} = & \frac{-eN_i v_i \Delta E_i}{(4\pi\lambda kT)^{1/2}} [N^{\text{re}}(0^-)(1 - f_i) \exp[-(\Delta_{\text{re}} - E_g + V_l + \phi_i)^2/4\lambda kT] \\ & - N^{\text{ox}}(0^-)f_i \exp[-(\Delta_{\text{ox}} - E_g + V_l + \phi_i)^2/4\lambda kT]] \end{aligned} \quad (6.99\text{a})$$

Equation (6.99a) is of general validity. If the function  $D(E)$  is used with  $E = -E_g + \phi_i$ , then Eq. 6.99a may be rewritten as

$$\begin{aligned} J_{\text{PHL}} = & -eN_i D(-E_g + \phi_i)v_i \Delta E_i \{[1 - f_i][1 + \exp(\phi_B - E_g + \phi_i + V_l)/kT]^{-1} \\ & - [f_i][1 + \exp[-(\phi_B - E_g + \phi_i + V_l)/kT]]^{-1}\} \end{aligned} \quad (6.99\text{b})$$

This latter form is limited to cases where

$$N^{\text{ox}}(0^-) = N_0^{\text{ox}}$$

and

$$N^{\text{re}}(0^-) = N_0^{\text{re}}$$

since it uses the function  $D(E)$ . In both forms of Eq. 6.99,  $v_i$  characterizes the hole transfer back and forth with the redox couple. It has been assumed that the intermediary states involved in this process are found in an energy

range  $E_i$  to  $E_i + \Delta E_i$ . If they are over a broad range in energy instead, an integration over  $E_i$  is necessary in Eq. (6.99) as it would be in Eq. (6.98). Note that, if  $J_{\text{surf}}^i \rightarrow \infty$  and  $v_i \rightarrow \infty$  (excellent communication through these intermediary states), Eqs. (6.98) and (6.99) show that  $E_{\text{Fp}}(0) = V$ .

We shall assume that the current density  $J_{\text{PHB}}$  collected directly from the valence band involves transitions which conserve energy. This permits us to obtain an expression for  $J_{\text{PHB}}$  by extending Eqs. (6.99) to the situation of a band. The general statement (analogous to Eq. 6.99a) valid for any concentration of the redox couple is

$$\begin{aligned} J_{\text{PHB}} = & \frac{-e}{(4\pi\lambda kT)^{1/2}} \int_0^\infty v^{\text{PHB}}(E) g(E) \\ & \times \left\{ N^{\text{re}}(0^-) \left[ 1 + \exp\left(\frac{E_g - \phi_B + E + V_s - E_{\text{Fp}}(0)}{kT}\right) \right]^{-1} \right. \\ & \times \exp[-(\Delta_{\text{re}} + V_i - E_g - E)^2/4\lambda kT] \\ & - N^{\text{ox}}(0^-) \left[ 1 + \exp\left(-\frac{E_g - \phi_B + E + V_s - E_{\text{Fp}}(0)}{kT}\right) \right]^{-1} \\ & \left. \times \exp[-(\Delta_{\text{ox}} + V_i - E_g - E)^2/4\lambda kT] \right\} dE \end{aligned} \quad (6.100a)$$

The alternative statement, limited to cases where

$$N^{\text{ox}}(0^-) = N_0^{\text{ox}}$$

and

$$N^{\text{re}}(0^-) = N_0^{\text{re}}$$

since it uses the function  $D(E)$ , is

$$\begin{aligned} J_{\text{PHB}} = & -e \int_0^\infty v^{\text{PHB}}(E) D(-E_g - E) g(E) \\ & \times \left\{ \left[ 1 + \exp\left(\frac{E_g - \phi_B + E + V_s - E_{\text{Fp}}(0)}{kT}\right) \right]^{-1} \right. \\ & \times [1 + \exp(\phi_B - E_g - E + V_i)/kT]^{-1} \\ & - \left[ 1 + \exp\left(-\frac{E_g - \phi_B + E + V_s - E_{\text{Fp}}(0)}{kT}\right) \right]^{-1} \\ & \left. \times [1 + \exp(-(\phi_B - E_g - E + V_i)/kT)]^{-1} \right\} dE \end{aligned} \quad (6.100b)$$

If  $v^{\text{PHB}} \rightarrow \infty$  (excellent direct communication), it can be seen from Eqs. (6.100) that  $E_{\text{Fp}}(0)$  must equal  $V$ . The formulation of Eqs. (6.100) accounts for the collection of all the holes arriving at  $x = 0$  no matter what their energy in the valence band. It does not, however, consider hot-hole effects since it assumes that the holes at  $x = 0$  have been thermalized to the same temperature  $T$  that exists in the bulk absorber (see Section 2.7.3.2). The suggestion has been made that hot-hole effects (in the case of Fig. 6.10) may be important in EPC devices [45, 46].

Equations (6.83), (6.84), (6.87), (6.88), (6.90), (6.93)–(6.95), and (6.98)–(6.100) constitute a set of eleven equations which may be used to determine the eleven unknowns ( $J_{\text{ob}}$ ,  $J_{\text{LS}}$ ,  $J_{\text{ir}}$ ,  $J_{\text{PHL}}$ ,  $J_{\text{PHB}}$ ,  $V_s$ ,  $V_i$ ,  $E_{\text{Fp}}(0)$ ,  $E_{\text{Fn}}(0)$ ,  $f_T$ , and  $f_i$ ) in terms of the voltage  $V$  developed by the cell, and in terms of the illumination intensity. If the voltage dependence of  $J_{\text{ob}}$ ,  $J_{\text{LS}}$ ,  $J_{\text{ir}}$ , and  $E_{\text{Fp}}(0)$  determined by solving this set of equations is inserted into Eq. (6.76), the result is our goal: the  $J$ – $V$  characteristic of a liquid–semiconductor solar cell under illumination.

If a specific liquid–semiconductor configuration is to be used effectively as a solar cell, there cannot be an appreciable photocurrent flowing via photodecomposition. Therefore, this current component of an EPC solar cell (discussed in Section 6.2.1.4) has been neglected in the analysis. Aside from this point, the analysis has been very general. We have allowed for the possibility that (a) hole collection ( $n$ -type absorber) may be a problem [ $E_{\text{Fp}}(0)$  was not forced equal to  $V$ ], (b) hole collection may proceed via intermediary states (due to better energy overlap with the distribution of levels of the reduced species), and (c)  $J_{\text{LS}}$  may be a significant component of the bucking current (due to overlap with the distribution of levels of the oxidized species). Unfortunately including these important aspects of EPC device physics means that our set of eleven equations cannot be simplified (as we did with a comparable set of equations in the case of M–I–S devices) and we will not be able to write Eq. (6.76) as an explicit function of voltage and illumination intensity. We will have to solve the set of eleven equations numerically and use the numerically determined  $J_{\text{ob}}$ ,  $J_{\text{LS}}$ ,  $J_{\text{ir}}$ , and  $E_{\text{Fp}}(0)$  in Eq. (6.76).

Actually, there is one more aspect of the analysis of EPC solar cells that must be taken into consideration. As we have noted, it is not necessarily true that  $N^{\text{re}}(0^-) = N_0^{\text{re}}$  (where  $N_0^{\text{re}}$  is the concentration of reduced species in thermodynamic equilibrium) nor is it necessarily true that  $N^{\text{ox}}(0^-) = N_0^{\text{ox}}$  (where  $N_0^{\text{ox}}$  is the concentration of oxidized species in thermodynamic equilibrium) when a current of density  $J$  is flowing. If

$$N^{\text{re}}(0^-) \neq N_0^{\text{re}}$$

and

$$N^{\text{ox}}(0^-) \neq N_0^{\text{ox}}$$

then our set of equations contains thirteen unknowns. In that case  $N^{re}(0^-)$  and  $N^{ox}(0^-)$  must be determined from diffusion models for the transport of oxidized and reduced species in solution; viz., [47]

$$J = eK_D(N^{ox}(0^-) - N_0^{ox}) \quad (6.101)$$

and

$$J = eK_D(N_0^{re} - N^{re}(0^-)) \quad (6.102)$$

where  $N_0^{ox}$  is assumed to be valid for the oxidized species concentration and  $N_0^{re}$  is assumed to be valid for the reduced species concentration away from the interface and where  $K_D$  is a measure of the ease of ion transport in the liquid. The  $J$  obtained from Eq. (6.76) for a specific  $V$  by solving the set of eleven equations for assumed  $N^{ox}(0^-)$  and  $N^{re}(0^-)$  must be consistent with the  $J$  given by Eqs. (6.101) and (6.102) for the same ion concentrations at the interface. If it is not,  $N^{ox}(0^-)$  and  $N^{re}(0^-)$  are varied until self-consistency is obtained.

The procedure outlined in this section, when followed, generates  $J-V$  characteristics such as those seen in Figs. 6.11–6.14 [47]. The curves seen in these figures were obtained using the parameter values listed in Table 6.1.

From this analysis, and the sample  $J-V$  characteristics seen in Figs. 6.11–6.14, it can be concluded that the performance of an EPC device is strongly controlled by the position and distribution of redox couple levels and by interface properties. However, no matter what the shape of the  $J-V$  characteristic of a liquid–semiconductor solar cell, it must always fit inside the envelope characteristic generated by

$$J = J_{LSC} + F_p J_L - F_p J_{dif}[\exp(V/kT) - 1] \quad (6.103)$$

This equation follows from Eq. (6.76) since, at least conceptually,  $J_{ob}$ ,  $J_{LS}$ ,  $J_{ir}$ , and  $J_{RB}$  can all be suppressed to a point where they are negligible compared to the diffusion–recombination bucking-current term, but the diffusion–recombination bucking-current term can never be reduced below  $F_p J_{dif}[\exp(V/kT) - 1]$ . Using the terminology applied to M–I–S cells, an EPC device obeying Eq. (6.103) would be a minority-carrier cell at the diffusion limit.

Provided the constraint  $V_{oc} \lesssim V_{bi}$  of electrostatics is not violated, Eq. (6.103) gives the upper bound that can be expected for  $V_{oc}$  for a liquid–semiconductor solar cell. Assuming  $F_p = 1$ , writing  $J_{dif} = eN_v V_D \exp[-(E_g - V_n)/kT]$  (assuming  $\Theta_B = 1$ ), and computing  $J_{LSC} + J_L$  versus  $E_g$  by using Fig. 1.3 (AM2) and a quantum efficiency of unity allows the kinetic upper bound on  $V_{oc}$  predicted by Eq. (6.103) to be plotted in Fig. 6.15 as a function of the EPC absorber gap  $E_g$ . Curve 1 is plotted for a diffusion velocity attainable in very good single-crystal material ( $V_D = 10^2$  cm/sec) whereas curve 2 is plotted for the more typical value ( $V_D = 10^4$  cm/sec). The largest electrostatic upper bound possible ( $V_{oc} = E_g$ )

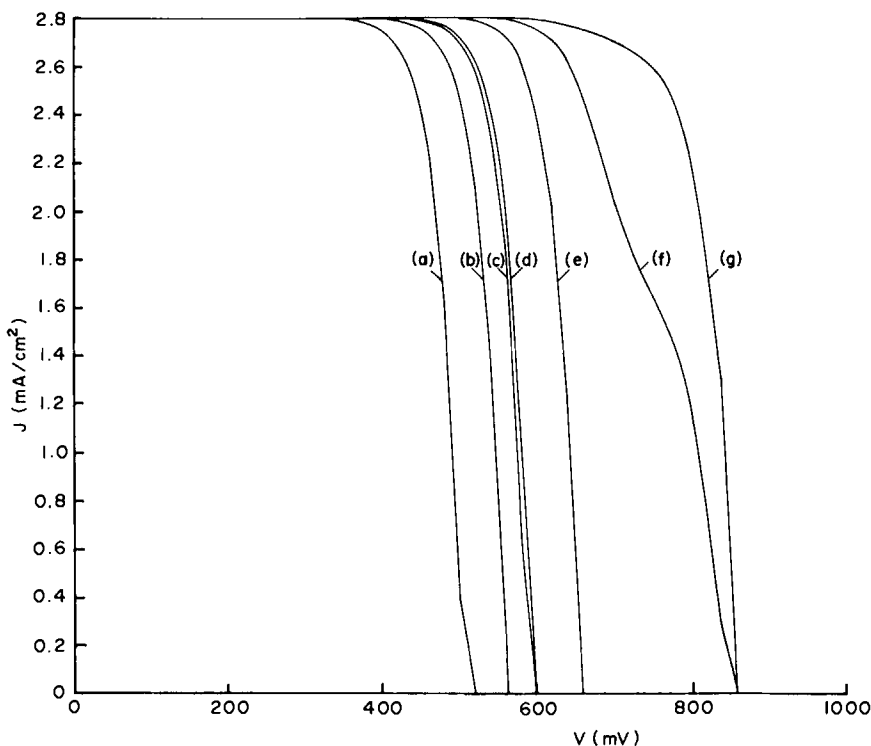


Fig. 6.11 Numerical evaluation of Eq. (6.76) for the parameters seen in Table 6.1. The interface recombination current density denoted by  $J_{ir}$  in Eq. (6.76) dominates the bucking current for curves (a) and (b). The density of the interface states (the  $N_i$  of Table 6.1) has been decreased for curves (c) and (d) to a level where the  $J_{ob}$  and  $J_{LS}$  bucking-current components of Eq. (6.76) now dominate for the parameters selected. For these curves it is actually the component  $J_{LS}$  which predominates.

With  $N_i$  held at the value it has for curve (d), curves (e)–(g) represent successive reductions of the capture cross sections involved in the flow of  $J_{ob}$  and  $J_{LS}$ . These capture cross sections have been decreased for curve (g) to a level where now the minority-carrier diffusion bucking component of Eq. (6.76) dominates. Curve (f) owes its unique slope to a change-over from the bucking current being dominated by  $J_{LS}$  for low voltages to the bucking current being dominated by  $J_{ob}$  for high voltages. Variation of the capture cross sections in the ion-electron interaction is through  $v_T$  and  $v^{ob}$ .

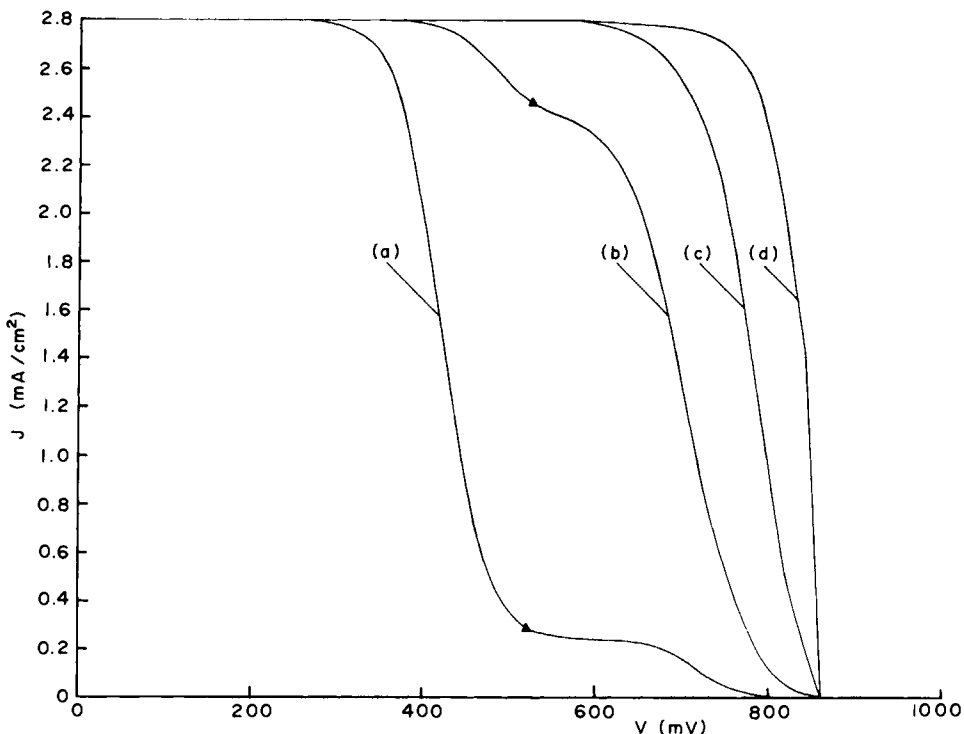


Fig. 6.12 Numerical evaluation of Eq. (6.76) for the parameters seen in Table 6.1. As can be seen by comparing the parameters used for Fig. 6.11 and this figure, the bucking current in this evaluation is dominated by the minority-carrier (hole) diffusion component of Eq. (6.76).

The extremely poor fill factor displayed by curve (a) is due to poor collection of holes through paths  $J_{PHL}$  and  $J_{PHB}$  of Fig. 6.10. As can be seen from Table 6.1, this poor collection is caused by the low capture cross sections assumed for these paths. As these capture cross sections are increased (curves (b)–(d)), the fill factor is seen to be dramatically improved. Collection of the photocurrent is found to be by  $J_{PHL}$  for curves (a) and (b) up to the triangle seen on these curves. After the triangle, collection is by  $J_{PHB}$ . Collection is found to be dominated by  $J_{PHB}$  for all of curves (c) and (d). Curve (d) is the envelope characteristic discussed in the text and given by Eq. (6.103). The sum  $J_{LSC} + F_p J_L$  in Eq. (6.76) was set equal to  $2.8 \text{ mA/cm}^2$  in these computations. Variation of the capture cross-sections in the ion-hole interaction is through  $v_i$  and  $v^{PHB}$ .

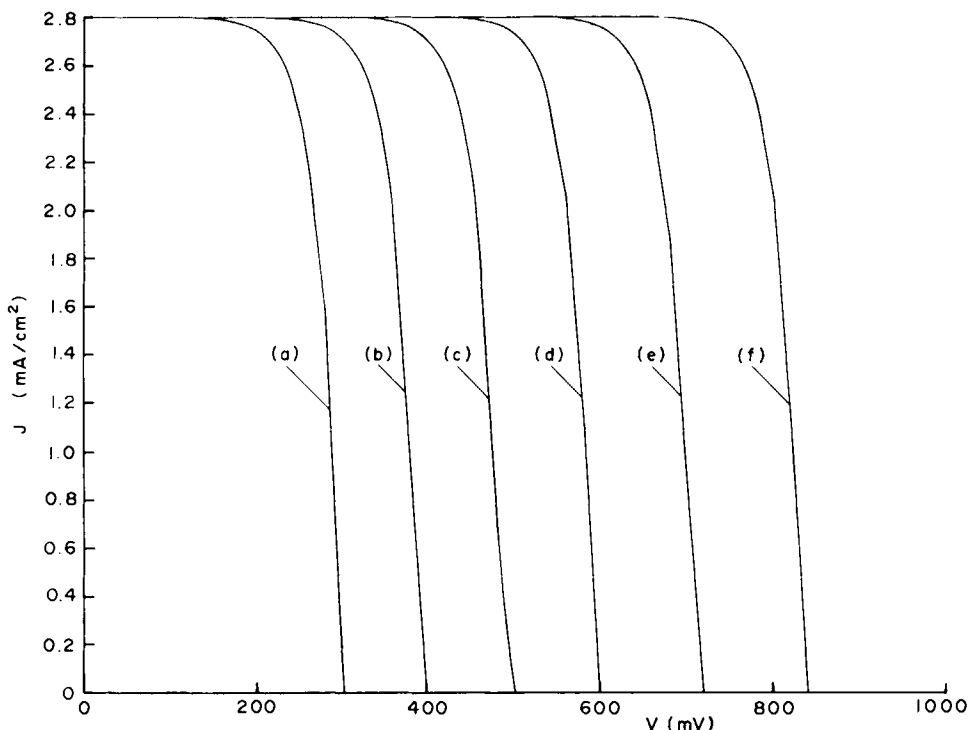


Fig. 6.13 Numerical evaluation of Eq. (6.76) for the parameters seen in Table 6.1. The bucking-current component  $J_{ir}$ , which arises from interface recombination, is negligible for these curves. The dominant bucking-current mechanism is formed by components  $J_{ob}$  and  $J_{Ls}$ . As the standard redox potential  $E_{redox}$  is systematically varied through curves (a)–(f), the cell performance is seen to increase; i.e., as the “work function”  $\phi_{redox}$  is increased by changing only the standard potential there is a monotonic increase seen in  $V_{oc}$ .

Curve (d) of this figure is identical to curve (d) of Fig. 6.11; both have their bucking currents controlled by electron emission into oxidized levels in solution. Curves (e) and (f) of this figure give better performance than curve (d) because  $\phi_{redox}$  has been further increased due to a change in the standard potential. This further increase in  $\phi_{redox}$  enhances  $V_{bi}$  which decreases the electron supply at  $x = 0$  and reduces the number of isoenergetic oxidized levels available to these electrons. The latter occurs because the distribution of oxidized levels seen in Fig. 6.10 shifts to a lower energy. Both effects act to reduce the electron-emission bucking current. The sum  $J_{LSC} + F_p J_L$  in Eq. (6.76) was set equal to 2.8 mA/cm<sup>2</sup> in these computations.

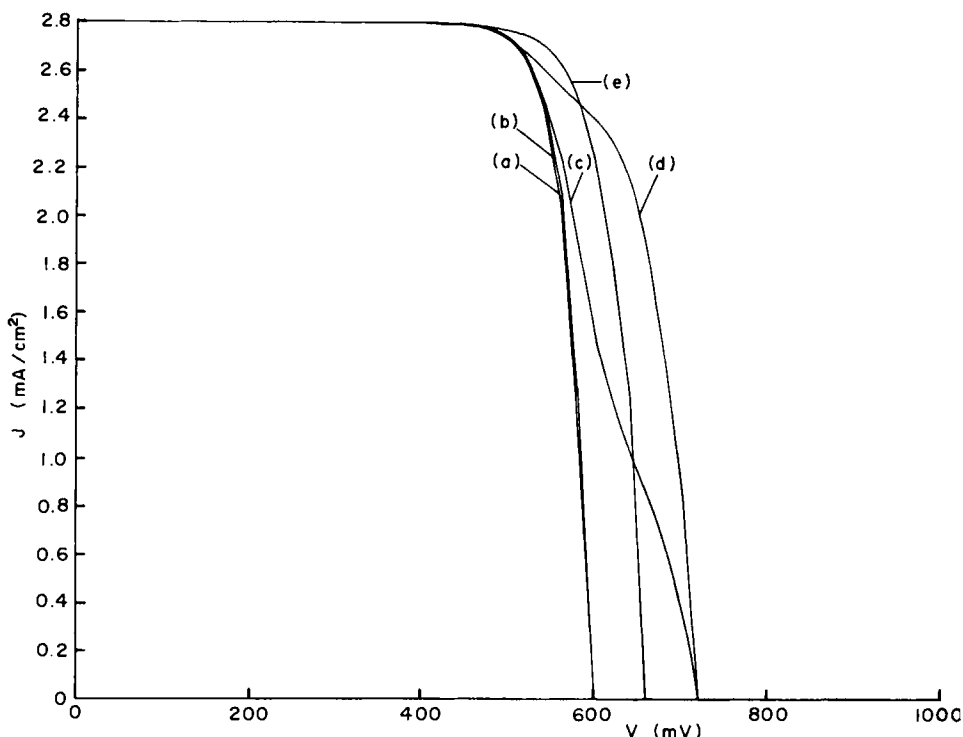


Fig. 6.14 Numerical evaluation of Eq. (6.76) for the parameters seen in Table 6.1. The bucking-current component  $J_{ir}$ , which arises from interface recombination, is negligible for these curves. Curves (a) and (b) of the figure are essentially identical to curve (d) in Figs. 6.11 and 6.13; the bucking current is controlled by electron emission into oxidized levels in solution. As the concentration of oxidized species in solution is systematically lowered (see Table 6.1), the  $J$ - $V$  behavior is seen to deviate from that of curves (a) and (b); however, the bucking current is controlled by electron emission into oxidized levels for all these curves. If the concentration of oxidized species is lowered and the concentration of reduced species is kept constant as done here, two effects occur: the redox couple "work function"  $\phi_{\text{redox}}$  decreases causing  $V_{bi}$  to decrease and the number of oxidized levels decreases, although their distribution in energy does not shift. The first effect increases the supply of electrons available for emission into oxidized levels. Hence it tends to decrease  $V_{oc}$ . The second effect reduces the emission current since final states are removed. Hence it tends to increase  $V_{oc}$ . The interplay between these two effects is seen in the figure. The sum  $J_{LSC} + F_p J_L$  in Eq. (6.76) was set equal to  $2.8 \text{ mA}/\text{cm}^2$  in these computations.

TABLE 6.1

*Parameters Used to Generate J-V Characteristics in Figs. 6.11-6.14.*  
*(In all cases the semiconductor is assumed to be n-type GaAs with  $N_D = 4.5 \times 10^{17} \text{ cm}^{-3}$ ;  $V_i$  is assumed to be zero;*  
 *$\lambda$  is assumed to be 0.55 eV; and  $K_D$  is assumed to be 0.036 cm/sec)*

Figure and curve	$N_i$ (cm <sup>-2</sup> )	$\phi_i$ (eV)	$\Delta E_i$ (eV)	$V_i$ (cm <sup>3</sup> /sec) <sup>a</sup>	$V_{\text{PHB}}$ (cm <sup>4</sup> -eV/sec)	$N_T$ (cm <sup>-2</sup> )	$\phi_T$ (eV)	$\Delta E_T$ (eV)	$V_T$ (cm <sup>3</sup> /sec) <sup>b</sup>	$V^{\text{orb}}$ (cm <sup>4</sup> -eV/sec)	$N_i$ (cm <sup>-3</sup> ) <sup>c</sup>	$E_{\text{edox}}$ (eV)	$N_{\text{ox}}$ (moles)	$N^{\text{re}}$ (moles)	$V_{\text{bi}}$ (eV) <sup>d</sup>	
6.11 a	$6.5 \times 10^{12}$	0.2	0.032	$1 \times 10^{-14}$	$1 \times 10^{-14}$	$9.8 \times 10^{11}$	0.28	0.022	$1 \times 10^{-14}$	$1.2 \times 10^{12}$	5.0	3.0	1.53	0.93		
b																
c																
d																
e																
f	$6.5 \times 10^{12}$	0.2	0.032	$1 \times 10^{-14}$	$1 \times 10^{-14}$	$9.8 \times 10^{11}$	0.28	0.022	$1 \times 10^{-14}$	$1.2 \times 10^{11}$	5.0	3.0	1.53	0.93		
g	$6.5 \times 10^{12}$	0.2	0.032	$1 \times 10^{-14}$	$1 \times 10^{-14}$	$9.8 \times 10^{11}$	0.28	0.022	$1 \times 10^{-16}$	$1.2 \times 10^9$	5.0	3.0	1.53	0.93		
6.12 a	$6.5 \times 10^{12}$	0.2	0.032	$1 \times 10^{-17}$	$1 \times 10^{-17}$	$9.8 \times 10^{11}$	0.28	0.022	$1 \times 10^{-17}$	$1.2 \times 10^9$	5.0	3.0	1.53	0.93		
b																
c																
d	$6.5 \times 10^{12}$	0.2	0.032	$1 \times 10^{-14}$	$1 \times 10^{-14}$	$9.8 \times 10^{11}$	0.28	0.022	$1 \times 10^{-18}$	$1.2 \times 10^8$	5.0	3.0	1.53	0.93		
6.13 a	$6.5 \times 10^{12}$	0.2	0.032	$1 \times 10^{-14}$	$1 \times 10^{-14}$	$9.8 \times 10^{11}$	0.28	0.022	$1 \times 10^{-14}$	$1.2 \times 10^8$	4.7	3.0	1.53	0.63		
b																
c																
d																
e																
f	$6.5 \times 10^{12}$	0.2	0.032	$1 \times 10^{-14}$	$1 \times 10^{-14}$	$9.8 \times 10^{11}$	0.28	0.022	$1 \times 10^{-14}$	$1.2 \times 10^8$	5.0	3.0	1.53	0.93		
6.14 a	$6.5 \times 10^{12}$	0.2	0.032	$1 \times 10^{-14}$	$1 \times 10^{-14}$	$9.8 \times 10^{11}$	0.28	0.022	$1 \times 10^{-14}$	$1.2 \times 10^8$	5.0	5.1	3.0	1.53	1.13	
b																
c																
d																
e	$6.5 \times 10^{12}$	0.2	0.032	$1 \times 10^{-14}$	$1 \times 10^{-14}$	$9.8 \times 10^{11}$	0.28	0.022	$1 \times 10^{-14}$	$1.2 \times 10^8$	5.0	0.001	1.53	0.73		

<sup>a</sup>  $\Omega_p$  for the path  $J_{\text{PHB}}$  is taken to be  $10^{-16} \text{ cm}^{-2}$ .

<sup>b</sup>  $\Omega_x$  for the path  $J_{\text{LS}}$  is taken to be  $10^{-16} \text{ cm}^{-2}$ .

<sup>c</sup> The states through which  $J_{\text{ir}}$  is flowing are taken to be at mid-gap.

<sup>d</sup> Computed from Eq. (3.54) by neglecting  $\Delta_{\text{I}}$ ,  $\Delta_G$ , and  $\Delta_H$ .

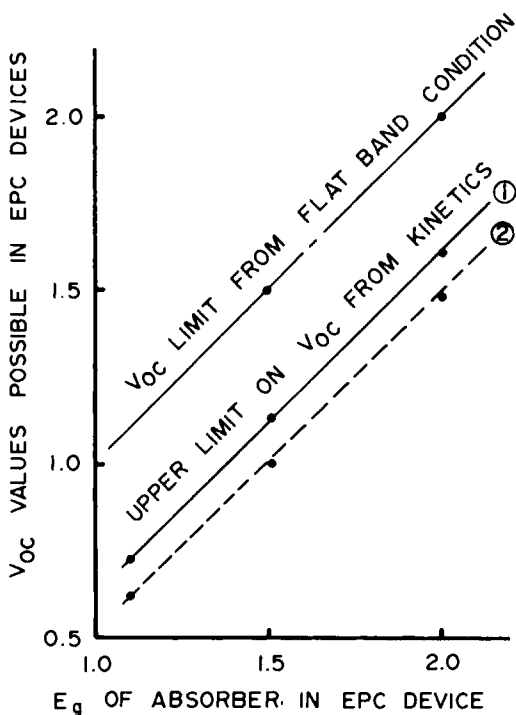


Fig. 6.15 Any EPC solar cell which achieves a  $V_{oc}$  value above curve 1 at AM1 must have an electrochemical process taking place in series with the photovoltaic effect. Curve 1 is obtained using an optimum value of the hole diffusion speed. Such a value ( $V_D = 10^2$  cm/sec) can be attained in very good single-crystal materials. Curve 2 is obtained using a more typical value ( $V_D = 10^4$  cm/sec). Both curves assume the bulk Fermi level is 0.15 eV from the majority-carrier band. The curve labeled " $V_{oc}$  limit from flat band condition" comes from the less restrictive condition that  $V_{oc} \leq V_{bi}$ .

is also shown. Note that if a measured  $V_{oc}$  value lies above curve 1 in the figure, there must be an electrochemical process present which is in series with the photovoltaic effect.

### 6.3 SURFACE-BARRIER SOLAR CELL CONFIGURATIONS AND PERFORMANCE

#### 6.3.1 M-S and M-I-S Devices

For the reasons pointed out qualitatively in Section 6.2.1 and quantitatively in Section 6.2.3, metal-semiconductor (M-S) solar cells give poor conversion efficiencies. For example, the best reported efficiency under

simulated terrestrial light for Au/(n)GaAs M-S solar cells is  $\eta = 10\%$  using single-crystal GaAs [10]. In the M-I-S configuration the same single-crystal GaAs yields efficiencies of 17% due to partial suppression of the majority-carrier over-the-barrier current [14]. However, because it is particularly simple and because it involves low temperature processing, the M-S configuration is still very useful in evaluating the photovoltaic behavior of materials.

The M-I-S configuration has proven effective in increasing the efficiency over that of the M-S configuration for a number of materials systems. As noted, it has been very successfully employed with single-crystal GaAs. It has also led to better efficiencies than the M-S cell when used with polycrystalline GaAs ( $\eta \approx 6\%$  at AM1 for the M-I-S cell) [48, 49]. In the case of another III-V semiconductor (InP) cells fabricated using anodized InP to form the I layer have exhibited a reduction of the dark diode current by three orders of magnitude and an increase in  $\phi_B$  of  $\sim 0.3$  eV when compared to M-S structures fabricated on the same single-crystal InP. Although current transport in the M-I-S device on InP was still found to be dominated by majority-carrier (electrons) thermionic emission, the partial suppression of this bucking current in the M-I-S configuration increased the AM1 efficiency from 3.5% (M-S) to 6% (M-I-S). It was also found  $V_{oc}$  could be increased to 0.46 V in the M-I-S structure without any reduction in  $I_{sc}$  [50].

The M-I-S configuration has also been successful with both *n*- and *p*-type Si. Cells with AM1 efficiencies over 13% have been demonstrated on single-crystal material [51, 52]. The high  $V_{oc}$  values attainable on *p*-type Si strongly suggests that the diffusion limit (see Figs. 6.7-6.9) can be achieved; i.e., the bucking current can be made that of an ideal *p-n* homojunction cell. Indeed, it has been established that the majority-carrier bucking current can be totally suppressed in certain Al/SiO<sub>x</sub>/(*p*)Si devices and they do operate at the minority-carrier diffusion limit [40] (see in Figs. 6.7-6.9 for GaAs devices).

In practice, the attainment of high short-circuit currents is a problem in M-S and M-I-S cells due to the high absorption and reflectivity of the barrier metal. Even with extremely thin metallizations ( $\sim 5$  nm), which necessitate efforts to overcome the sheet resistance problem, only moderate one sun AM1 values of  $J_{sc}$  have been reported. For example, for silicon the best  $J_{sc}$  values attained for single-crystal material under these conditions have been in the range of 26 to 28 mA/cm<sup>2</sup> [53, 54] which is well below the potential  $J_{sc}$  values for Si seen in Fig. 3.1. In using such thin metallizations one exposes the barrier region to possible degradation. The degradation can arise due to chemical interaction with ambients; this can be controlled by encapsulation. A more insidious form of degradation has been found in at least one structure: it has been demonstrated that photons of wavelengths  $\lesssim 450$  nm cause unstable operation of Al/SiO<sub>x</sub>/(*p*)Si devices and this

instability increases the thinner the metallization (more of these photons get through the metallization). Apparently photons of these wavelengths modify the charge configuration in the insulator leading to a reduction of the originally high barrier  $\phi_B$  of the Al/SiO<sub>x</sub>/(p)Si materials system [27].

To avoid the problems of metal absorption and reflectivity and the problems of ultrathin metallizations, one could turn to back-illuminated (back-wall) M-I-S solar cell structures. It has been shown theoretically that this approach can give performance comparable front-illuminated devices [55-58] and it allows the use of thick metallizations. Another approach is that of the metal-insulator-semiconductor inversion layer (M-I-S-I-L) solar cell. This structure is shown in Fig. 6.16 for p-type single-crystal silicon. The oxide layer and ultrathin I layer are the source of fixed charge (positive in the case of Fig. 6.16) which causes the semiconductor to develop charge of opposite polarity. If the fixed charge is of the proper sign and of a sufficient density to cause the semiconductor to invert, a situation has been achieved where there is now a strong electric field and a highly conducting channel (for electrons in Fig. 6.16) at the semiconductor surface. Since the oxide and ultrathin I layer are the source of the charge which causes the band bending in the semiconductor and since electrons can easily move laterally in the inversion layer, the metallization is only needed in the grid pattern seen in the figure for collection. Except for the area covered by the grid, the M-I-S-I-L cell successfully avoids the problem of high metal absorption and reflectivity.

As with any M-I-S configuration, the M-I-S-I-L uses the I layer (a) to be the source of charge (together with the thicker oxide layer seen in Fig. 6.16) for increasing the band bending in the semiconductor, (b) to act as a

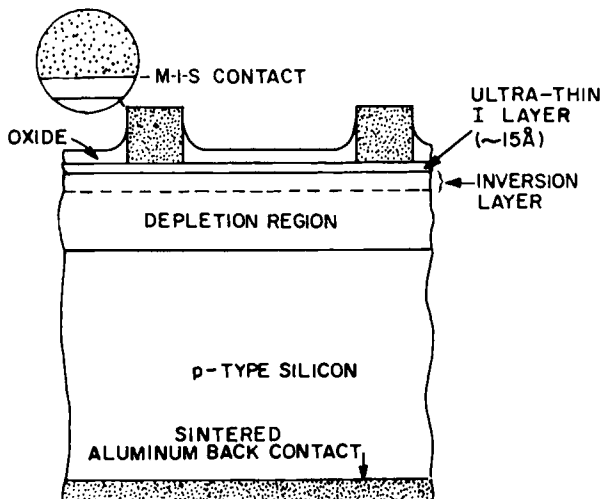


Fig. 6.16 M-I-S inversion layer solar cell configuration. Device shown has been fabricated using single-crystal p-type silicon.

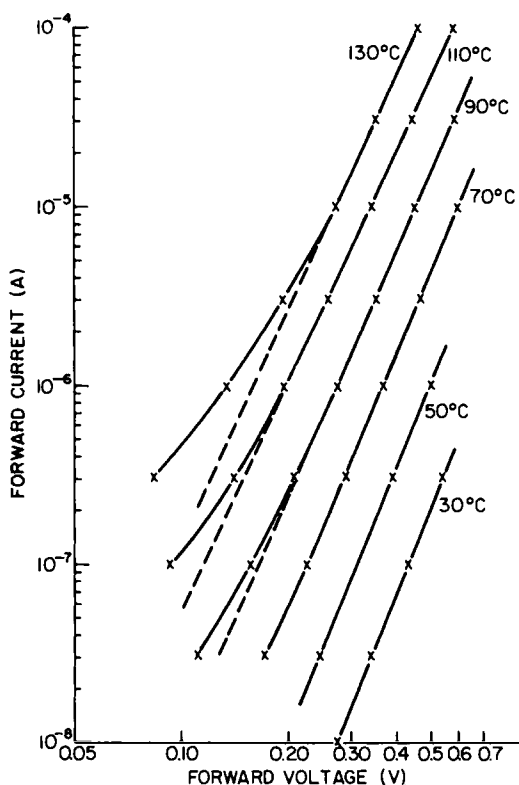


Fig. 6.17 Dark-diode characteristics at different temperatures for a  $Pd/a\text{-SiH}_x$  structure. For this particular alloy and configuration the dark characteristics have the form of a space-charge-limited current.

transport barrier for majority carriers (under the metallizations), and (c) to develop perhaps some of the voltage. In addition, the M-I-S-I-L cell suppresses the majority over-the-barrier bucking current by its geometry since this current can only flow beneath the metallizations.

In the case of Si the ultrathin I layer seen in Fig. 6.16 has usually been a thermally grown  $\text{SiO}_x$  layer. The thicker oxide layer has been fabricated using processes as diverse as evaporating  $\text{SiO}$  [59] and spinning-on tantalum oxide [60]. Both the evaporated  $\text{SiO}$  and the spin-on tantalum oxide have achieved sufficient positive charge to cause strong inversion in  $p\text{-Si}$ . In the former case  $\eta = 15\%$  has been realized [59], whereas in the latter case  $\eta \geq 16\%$  has been realized [60] with single-crystal silicon.

Conventional front wall M-S and M-I-S structures have proven very effective in evaluating and developing new materials. This has been especially true in the case of amorphous silicon and several organic materials.

The M-S device structure has yielded  $\eta = 5.5\%$  (AM1) when used with some  $a\text{-SiH}_x$  alloys [61] whereas the M-I-S device structure has given  $\eta = 4.8\%$  for  $a\text{-SiH}_x$  [62] (AM1) and  $\eta = 6.3\%$  for  $a\text{-SiH}_x\text{F}_y$  [63]. Usually the bucking current in these M-S and M-I-S configurations on  $a\text{-Si}$  is believed to be over-the-barrier majority-carrier current which has been modeled by Eq. (6.58) for these particular  $a\text{-Si}$  due to poor mobilities [61–63]. Evidence has been presented showing that, for some  $a\text{-Si}$  alloys, space-charge (bulk) limited current may be an important current flow mechanism at least for dark diode behavior; this mechanism may not be important under light due to the photoconductivity of many  $a\text{-Si}$  materials. If a current is space-charged limited, then [64]

$$I = AV^M \quad (6.104)$$

This behavior is seen in Fig. 6.17 for the dark diode characteristics of an M-S solar cell device on an  $a\text{-Si}$  alloy [64].

In the case of organic materials, M-I-S device structures have been particularly effective. In the late 1970s AM1 efficiencies of  $\sim 0.7\%$  were reported for large area ( $\sim 1\text{ cm}^2$ ) M-I-S cells of the form Al/Al<sub>2</sub>O<sub>3</sub>/merocyanine dye [65]. This efficiency was about a factor of 50 higher than previously obtained solar-cell efficiencies for organic materials subject to light of this intensity and spectral content. By the early 1980s the efficiency had been increased to  $\sim 2\%$  (AM2) by varying the merocyanine molecular configuration [66]. The bucking current of these cells is believed to be controlled by the thermionic emission component. A very interesting aspect of these cells is that their photocurrent is composed of excitons [65, 66].

### 6.3.2 Liquid–Semiconductor Devices

Liquid–semiconductor surface-barrier solar cell structures have been fabricated in front-wall (light passes through liquid) and in back-wall (light enters absorber first) configurations. Although most work, including the results seen in Table 6.2, has been done using front-wall cells, the back-wall

TABLE 6.2

Some Semiconductor–Electrolyte Solar Cell Results

Semiconductor–redox couple <sup>a</sup>	Efficiency (%)	Light conditions	Reference
(n)GaAs/Se <sup>2-</sup> –Se <sub>2</sub> <sup>2-</sup>	8.8	AM2	67
(n)GaAs (Ru surface treatment)/Se <sup>2-</sup> –Se <sub>2</sub> <sup>2-</sup>	12.0	$\sim 100\text{ mW/cm}^2$	17
(n)CdSe (polycrystalline)/S <sup>2-</sup> –S <sub>n</sub> <sup>2-</sup>	5.1	AM2	68
(n)CdSe/S <sup>2-</sup> –S <sub>n</sub> <sup>2-</sup>	7.5	AM2	68
(p)InP/V <sup>2+</sup> –V <sup>3+</sup>	11.5	$89.5\text{ mW/cm}^2$	69

<sup>a</sup> Solvent used in all cases here is water.

configuration must be used when the electrolyte absorbs significantly. Table 6.2 lists some performance data for EPC devices. Each of these particular cells uses water as the solvent for the redox couple; cells using other solvents have also been successful. The devices listed in this table have been reported to be stable.

#### 6.4 NOTES FOR THE EXPERIMENTALIST

##### 6.4.1 M-S and M-I-S Devices

Data, such as that seen in Fig. 3.5, are an extremely useful starting place in choosing a metal to use with a specific absorber in an M-S or M-I-S solar cell work function. Ideally the built-in potential that must be set up in the absorber can be predicted by the difference between the metal work function and the semiconductor work function [Eq. (3.30)]. Hence, metals with large work functions should be used with *n*-type semiconductors and metals with low work functions should be used with *p*-type materials. Unfortunately, the data of Fig. 3.5 are just a starting place for predicting the built-in potential. As we discussed in Section 3.4.4, even in nominally intimate M-S configurations there can be interfacial or intermediary layers which means that, in reality, the built-in potential in the semiconductor plus any potential developed across an interfacial or intermediary layer must equal the work function difference [Eq. (3.45)]. The potential developed across an interfacial or intermediary layer can be significant since localized charge can reside at or near the layer-semiconductor interface due to the presence of intrinsic interface states or of states arising from the act of forming the barrier (vacancies, cross diffusion, chemical interaction, etc.).

Although the data of Fig. 3.5 provide a convenient guideline for the initial selection of the metal to be used with a specific semiconductor, the actual built-in potential (or barrier height) that will be obtained using a metal picked on the basis of Fig. 3.5 will depend on semiconductor surface preparation, the chemical properties of the metal and of the semiconductor, the tendency of the materials-system components to cross diffuse, and the method of metallization (*e*-beam, evaporation, sputtering, electroless deposition, etc.).

In the case of the M-I-S configuration there is now a purposefully inserted I layer between the metal and the semiconductor. The data of Fig. 3.5 provide the same convenient starting place for picking the metal to use with a specific semiconductor but it is clear that it is the built-in potential in the semiconductor plus the potential across the I layer which must equal the work function difference. If one wants an M-I-S device with the same barrier height as the corresponding M-S device, then the I layer cannot

introduce charge or modify the charge configuration at the semiconductor surface. If one wants to increase the barrier height in a semiconductor by using the M-I-S configuration, one wants an I layer that develops negative charge in the case of an *n*-type semiconductor or positive charge in the case of a *p*-type semiconductor [70].

The charge that will reside in an I layer will depend on the semiconductor, the method of introducing the I layer (thermally grown oxide [9], anodized oxide [71], sputtered insulator [9], evaporated insulator, etc.) the metal, and the method of metallization. Chemical properties are important because the I layer in an M-I-S structure can be thought of as redefining the chemical nature of the semiconductor surface which affects interface states and charge. Fabrication procedures are important since they can cause different defects, in which charge can reside, in the I layer and at or near the I layer-semiconductor interface.

The choice of what metal to use in an M-S or M-I-S solar cell involves additional consideration, if the front-wall configuration is employed. Obviously the metal should have relatively low reflectivity and absorption and it should have a relatively low resistivity. The latter is necessary to avoid excessive series resistance. Experimentally, it is found that these properties vary significantly from metal to metal and with thickness for ultrathin metal films [28].

The problem of reflectivity can be approached by using AR coatings and, if necessary texturing. The problem of absorption can be reduced by using ultrathin metallizations, but as the film thickness decreases, sheet resistance increases necessitating a trade off. Also, as we have discussed, devices are more prone to degradation the thinner the metallization. There is a further complication: ultrathin metal films nucleate and grow differently on different surfaces. Hence, ultrathin films ( $\lesssim 150 \text{ \AA}$ ) of silver, for example, have different sheet resistivities and absorption properties for a given nominal thickness when deposited on bare Si than they do when deposited on an ultrathin ( $\lesssim 30 \text{ \AA}$ ),  $\text{SiO}_x$  layer thermally grown on Si [72].

#### 6.4.2 Liquid-Semiconductor Devices

As in the case of M-S and M-I-S solar cells, data such as that of Fig. 3.5 are an extremely useful starting place when deciding what material combinations to employ in an EPC device. In choosing a redox couple for a specific absorber, one is guided by the idealization that the built-in potential set up in an absorber is equal to the difference between the redox couple work function and the work function of the semiconductor. Hence, it is not surprising that Table 6.2 shows that the vanadium couple (low work function in Fig. 3.5) works well with (*p*)InP.

However, we know from our discussion in Sections 3.4.7 and 6.2.1.4 that, in reality, the built-in potential in the absorber probably is not simply given by the difference between the work functions; rather the built-in potential in the absorber is related to the difference between the work functions through Eq. (3.54). As with M-S and M-I-S devices, charge residing in intrinsic interface states or residing in defects created in the act of forming the barrier can significantly affect the built-in potential in the presence of the Helmholtz layer and interfacial or intermediary layers.

If a redox couple is appropriate on the basis of its ability to form an acceptable barrier, there are other criteria that must be met. Primary among these is the fact that the couple must provide fast collection of photogenerated minority carriers. This means that the couples must have fast electron transfer kinetics and (for an *n*-type absorber) the reduced species levels must overlap in energy with the valence band or with some intermediary state acting as a conduit for the photocurrent. Fast in this context means kinetics which are sufficient to prevent holes (*n*-type absorber) from building up at the interface where they can participate in recombination, back-diffuse away, or cause photodecomposition. In addition, the couple cannot chemically react with the semiconductor, it must be stable under illumination, and must be soluble enough in the liquid being used to sustain the current density produced by the absorber [Eqs. (6.101) and (6.102)].

A final note of caution is needed for EPC cells: one must always realize the significance of Eq. (6.103) when dealing with these devices. Put succinctly: if a  $V_{oc}$  value is obtained from a device that significantly lies above curve 1 in Fig. 6.15, then the device has an electrochemical effect in series with the photovoltaic activity.

## REFERENCES

1. E. Becquerel, *Compt. Rend.* **9**, 561 (1839).
2. M. Wolf, *Proc. Power Sources Symp.*, 25th, May 23–25, 1972 p. 120.
3. L. O. Grondahl, *Rev. Mod. Phys.* **5**, 141 (1933).
4. R. J. Stirn and Y.-C. M. Yeh, *Conf. Rec. IEEE Photovoltaic Spec. Conf.*, 10th p. 15. IEEE, New York, 1973; Y.-C. M. Yeh and R. J. Stirn, *Conf. Rec. IEEE Photovoltaic Spec. Conf.*, 11th p. 391. IEEE, New York, 1975.
5. N. N. Winogradoff and H. K. Kessler, U.S. Patent 3,271,198 (1966).
6. W. W. Anderson and Y. G. Chai, *Energy Convers.* **15**, 85 (1976).
7. A. J. Nozik, *Philos. Trans. R. Soc. London, Ser. A* **295**, 453 (1980).
8. E. J. Charlson, A. B. Shak, and J. C. Lien, *Int. Electron Devices Meet. Washington, D.C.* IEEE, New York, 1972.
9. S. Shevenock, S. Fonash, and J. Geneczko, *Tech. Dig.-Int. Electron Devices Meet. Washington, D.C.* p. 211. IEEE, New York, 1975.

10. R. J. Stirn and Y.-C. M. Yeh, *Conf. Rec. IEEE Photovoltaic Spec. Conf.*, 11th p. 437. IEEE, New York, 1975; R. J. Stirn and Y.-C. M. Yeh, *Appl. Phys. Lett.* **27**, 95 (1975).
11. J. Shewchun, M. A. Green, and F. D. King, *Solid-State Electron.* **17**, 563 (1974); J. Shewchun, R. Singh, and M. A. Green, *J. Appl. Phys.* **48**, 765 (1977).
12. R. E. Thomas, R. B. North, and C. E. Norman, *IEEE Electron Device Lett.* **EDL-1**, 79 (1980).
13. M. A. Green, R. B. Godfrey, M. R. Willison, and A. W. Blakers, *Conf. Rec. IEEE Photovoltaic Spec. Conf.*, 14th p. 684. IEEE, New York, 1980.
14. Y.-C. M. Yeh and R. J. Stirn, *Appl. Phys. Lett.* **33**, 401 (1978); Y.-C. M. Yeh, F. P. Ernest, and R. J. Stirn, *Conf. Rec. IEEE Photovoltaic Spec. Conf.*, 13th p. 966. IEEE, New York, 1978.
15. A. B. Ellis, S. W. Kaiser, and M. S. Wrighton, *J. Am. Chem. Soc.* **98**, 1635 (1976).
16. B. Miller and A. Heller, *Nature* **262**, 680 (1976).
17. B. A. Parkinson, A. Heller, and B. Miller, *Appl. Phys. Lett.* **33**, 521 (1978).
18. E. H. Nicollian and A. K. Sinha, Effects of Interfacial Reactions on the Electrical Characteristics of M-S Contacts in "Thin Films—Interdiffusion and Reactions" (J. M. Poate, K. N. Tu, and J. W. Mayer, eds.), p. 481. Wiley, New York, 1979.
19. S. J. Fonash, *Thin Solid Films* **36**, 387 (1976).
20. J. P. Ponpon and P. Siffert, *Conf. Rec. IEEE Photovoltaic Spec. Conf.*, 13th p. 639. IEEE, New York, 1978.
21. W. E. Spicer, I. Lindau, P. Skeath, C. Y. Su, and P. Chye, *Phys. Rev. Lett.* **44**, 420 (1980).
22. S. J. Fonash, *J. Appl. Phys.* **46**, 1286 (1975); **47**, 3597 (1976).
23. A. Goetzberger, E. Klausmann, and M. J. Schulz, *CRC Crit. Rev. Solid State Sci.* **00**, 1 (1976).
24. J. R. Szedon, T. A. Temofonte, T. W. O'Keeffe, H. C. Dickey, S. J. Fonash, and T. E. Sullivan, Heterojunction Single-Crystal Si Photovoltaic Solar Cells, Rep. DOE Contract EY-76-C-03-1282 (1979).
25. N. G. Tarr, D. L. Pulfrey, and P. A. Iles, *J. Appl. Phys.* **51**, 3926 (1980).
26. R. J. Stirn, High Efficiency Thin Film GaAs Solar Cells, Rep. 5030-255, Contract ERDA/NASA EG-77-A-29-1074. ERDA (Sept. 1978).
27. J. K. Kleta and D. L. Pulfrey, *IEEE Electron Device Lett.* **EDL-1**, 107 (1980).
28. H. J. Hovel, *J. Appl. Phys.* **47**, 4968 (1976).
29. H. Gerischer and W. Mindt, *Electrochim. Acta* **13**, 1329 (1968); H. Gerischer, Semiconductor Electrochemistry, in "Physical Chemistry, An Advanced Treatise" (H. Eyring, D. Henderson, and W. Jost, eds.), Vol. 9A, Electrochemistry. Academic Press, New York, 1970; H. Gerischer, *J. Vac. Sci. Technol.* **15**, 1422 (1978).
30. A. Heller and B. Miller, *Electrochim. Acta* **25**, 29 (1980).
31. M. Wrighton, R. G. Austin, A. B. Bocarsly, J. M. Bolts, O. Haas, K. D. Legg, L. Nadjo, and M. C. Palazzotto, *J. Am. Chem. Soc.* **100**, 1602 (1978).
32. W. Schultz, *Z. Phys.* **138**, 598 (1954).
33. B. R. Gossick, *Solid-State Electron.* **6**, 445 (1963).
34. C. R. Crowell and S. M. Sze, *Solid-State Electron.* **9**, 1035 (1966).
35. C. R. Wronski, D. E. Carlson, and R. E. Daniel, *Appl. Phys. Lett.* **29**, 602 (1976).
36. S. J. Fonash, *Conf. Rec. IEEE Photovoltaic Spec. Conf.*, 11th p. 376. IEEE, New York, 1975.
37. L. B. Freeman and W. E. Dahlke, *Solid-State Electron.* **13**, 1483 (1970).
38. M. A. Green, F. D. King, and J. Shewchun, *Solid-State Electron.* **17**, 551 (1974).
39. V. I. Strikha, *Radio Eng. Electron. Phys. (Engl. Transl.)* **4**, 552 (1964).
40. N. G. Tarr and D. L. Pulfrey, *Appl. Phys. Lett.* **34**, 295 (1979).
41. H. Gerischer, *Z. Phys. Chem. (Wiesbaden)* **26**, 223 (1960); **27**, 48 (1961).

42. R. Memming, *Electroanal. Chem.* **11**, 1 (1979).
43. C. B. Duke, *Proc. Electrochem. Soc. Ext. Abstr.* **79-1**, 833 (1979).
44. S. R. Morrison, "Electrochemistry at Semiconductor and Oxidized Metal Electrodes." Plenum, New York, 1980.
45. F. Williams and A. J. Nozik, *Nature (London)* **271**, 137 (1978).
46. A. J. Nozik, D. S. Boudreux, R. R. Chance, and F. Williams, *Adv. Chem. Ser.* **184**, 155 (1980).
47. S. J. Fonash, M. Rose, K. Corby, and J. Jordan, Final Report, Solar Energy Research Institute, Contract XP-9-8002-10 (1981).
48. K. P. Pande, D. H. Reep, S. K. Shastry, A. S. Weiner, J. M. Borrego, and S. K. Ghandhi, *IEEE Trans. Electron Devices* **ED-27**, 635 (1980).
49. S. S. Chu, T. L. Chu, and Y. Ti Lee, *IEEE Trans. Electron Devices* **ED-27**, 640 (1980).
50. K. P. Pande, *IEEE Trans. Electron Devices* **ED-27**, 631 (1980).
51. W. A. Anderson, G. Rajeswaran, K. Rajkanan, and G. Hoeft, *IEEE Electron Device Lett.* **EDL-1**, 128 (1980).
52. J. Shewchun, D. Burk, and M. B. Spitzer, *IEEE Trans. Electron Devices* **ED-27**, 705 (1980).
53. E. Fabre, J. Michel, and Y. Baudet, *Conf. Rec. IEEE Photovoltaic Spec. Conf.*, 12th p. 904. IEEE, New York, 1976.
54. W. A. Anderson, A. E. Delahoy, J. K. Kim, S. H. Hyland, and S. K. Dey, *Appl. Phys. Lett.* **33**, 588 (1978).
55. P. Basu and H. Baha, *Phys. Status Solidi A* **37**, 625 (1976).
56. K. Bhattacharya, P. Basu, and H. Saha, *Phys. Status Solidi A* **41**, 317 (1977).
57. R. J. Soukup and L. A. Akers, *J. Appl. Phys.* **49**, 4031 (1978).
58. G. S. R. Krishna Murthy, V. V. Kapadin, V. J. Ras, and A. P. B. Sinha, *Phys. Status Solidi A* **57**, 691 (1980).
59. R. B. Godfrey and M. A. Green, *Appl. Phys. Lett.* **33**, 637 (1978).
60. R. E. Thomas, C. E. Norman, and R. B. North, *Conf. Rec. IEEE Photovoltaic Spec. Conf.*, 14th p. 1350. IEEE, New York, 1980.
61. D. E. Carlson and C. R. Wronski, *J. Electron. Mater.* **6**, 95 (1977).
62. J. I. B. Wilson, J. McGill, and S. Kimmond, *Nature (London)* **272**, 152 (1978).
63. A. Madan, J. McGill, W. Czubatyj, J. Yang, and S. R. Ovshinsky, *Appl. Phys. Lett.* **37**, 826 (1980).
64. S. Ashok, P. Lester, and S. J. Fonash, *IEEE Electron Device Lett.* **EDL-1**, 200 (1980).
65. A. K. Ghosh and T. Feng, *J. Appl. Phys.* **49**, 5982 (1978).
66. G. A. Chamberlain and P. J. Cooney, *Nature (London)* **289**, 45 (1981).
67. A. Heller, ed., "Semiconductor Liquid-Junction Solar Cells," Vol. 77-3. Electrochem. Soc., Princeton, New Jersey, 1977.
68. B. Miller, A. Heller, M. Robbins, S. Menezes, K. C. Chang, and J. Thomson, Jr. *J. Electrochem. Soc.* **124**, 1019 (1977).
69. A. Heller, B. Miller, and F. Thiel, *Appl. Phys. Lett.* **38**, 282 (1981).
70. R. Childs, J. Fortuna, J. Geneszko, and S. J. Fonash, *Conf. Rec. IEEE Photovoltaic Spec. Conf.*, 12th p. 862. IEEE, New York, 1976.
71. P. C. Mathur, J. D. Arora, H. L. Hartnagel, *IEEE Trans. Electron Devices* **ED-28**, 69 (1981).
72. S. J. Fonash, G. Fishkorn, and T. E. Sullivan, Nat. Bur. Stand. (US), Spec. Publ. 400-58, p. 63. Nat. Bur. Stand., Washington, D.C., 1979.

# Index

## A

Abrupt junction, 204, 208–219  
Absorbers, *see also* Semiconductors, 69–75, 125, 127–130, 164  
Absorption coefficient, *see also* Optical properties, 26–29, 37, 70, 163  
Absorption edge, 25–28  
Absorption length, 70–74  
Acceptors, 18  
Accumulation, 88, 122  
Adiabatic principle, 14  
Affinity, *see* Electron affinity, Hole affinity  
Air Mass X (AMX) spectra, 3  
Ambipolar diffusion, 151–154, 166, 206  
Ambipolar diffusivity, 152  
Ambipolar mobility, 152  
Amorphous solids, 9–11, 125  
    absorption edge, 27  
    conductivity, 50  
    current density, 48, 53  
    diffusion length, 222, 289  
    by glow discharge, 126  
    localized gap states, 20, 198  
        extrinsic, 20  
        intrinsic, 20  
    mobility, 48, 50  
    mobility gap, 20–21  
    optical gap, 27–28  
    in *p-i-n* structures, 179  
    presence of hydrogen, 126  
Anderson heterojunction model, 92, 202, 258  
Antireflection coatings, 69–70  
Auger recombination, *see also* Recombination, 32–34

## B

Back surface field, 135–137, 170–171  
Back surface reflector, 136–137  
Band edge tailing, 145–146  
Band gap, *see also* Gap, 15–18  
Band-to-band transition, 27  
Barrier formation, 75–85  
Barrier height, 181, 202–203, 229–230, 243, 284, 296, 300, 305  
Base layer, 137–147

Beam-splitting, 176  
Bloch one-electron states, 19  
Boltzmann approximation, 39  
Boltzmann transport equation, 40  
Born–Oppenheimer principle, 14  
Bose–Einstein statistics, 11  
Brillouin zone, 12  
Bucking current, 127–128, 159–163, 183–184, 207, 219–220, 279, 290–291, 295–300, 311–315  
Built-in effective fields, *see* Effective force field  
Built-in electrostatic fields, *see* Electrostatic field  
Built-in potential, 89–112, 181, 200–204, 271, 273, 311, 317, 322–324  
    limit to  $V_{oc}$ , 61, 181, 311, 317  
    measuring, 182  
Built-in potential energy, *see* Built-in potential  
Built-in voltage, *see* Built-in potential  
Bulk recombination, *see also* Recombination, 139, 141, 145, 196

## C

Capacitance, 182  
Carrier concentration, 38–39, 43, 47  
Carrier lifetime, 145, 166, 169  
    Auger recombination, 33–34  
    radiative recombination, 31–32  
    S-R-H recombination, 36  
Cascade multijunction cell, 175–177  
Chalcogenides, 76  
Chalcopyrites, 78–81  
Charge density, 85, 88, 100  
Check valve, 1, 138, 170, 192–194  
Collection efficiency, 128, 183  
Collection function, 239  
Collision time, *see also* Scattering time, 42  
Concentration of sunlight, 141, 166–168, 174  
Concentrator cells, 141, 174–178  
Conduction band, 15, 38, 43, 193  
    spike, 204, 230  
Conductivity, *see also* Resistivity, 43–46, 48–52, 114  
Continuity, 47, 148

- Crystalline solids, 7–9  
 lattice, 7–8  
 long range order, 7  
 multiparticle states, 21  
 phonon dispersion relationship, 12  
 single particle states, 15–20  
 unit cell, 7
- Current density, 38, 44–47, 48–49
- Current transport,  
 across grain boundaries, 114  
 across insulating layer, 243  
 diffusion, 73, 91, 142, 155, 209  
 drift, 73  
 effect of band structure, 230–231  
 electrochemical photovoltaic cells, 279  
 junction transport factors, 217–222, 286–287  
 loss mechanisms, 138–144, 156, 159–161, 183  
 heterojunction, 191, 196, 236  
 homojunction, 138–140, 183, 190–191, 196  
 surface-barrier cells, 263–265  
 S–I–S structure, 245–246  
 transmission probability, 243, 246
- Current transport mechanisms, 44–49, 116–120  
 in bulk delocalized states, 43–47  
 in bulk localized states, 48–49  
 hopping, 49–50  
 interfacial, 116–120  
 Poole–Frenkel, 51–52  
 space-charge limited currents, 65, 153, 320–321
- Current–voltage characteristics, 128, 182–183, 218–220, 279
- Curve factor, *see* Fill factor
- D**
- Dangling bonds, *see also* Surface states, Interface states, 89, 126, 198–200  
 Debye length, 100  
 versus doping, 221
- Decomposition, 267–268, 273–278
- Degenerate materials, 40
- Delocalized states, 15–21, 139
- Dember potential, 61–63, 85, 146
- Depleted regions, 122, 125
- Dielectric relaxation time, 65–66
- Diffusion,  
 ambipolar, *see also* Ambipolar diffusivity, mobility, 151–153, 166  
 majority carrier, 290–291, 298–299  
 minority carrier, 141–142, 150–151, 208–210, 280–281, 292, 301
- Diffusion coefficient, 45, 46, 53
- Diffusion length, 72, 142  
 base layer, 163  
 top layer, 163
- Diode ideality factor, *see* n-factor
- Diode quality factor, *see* n-factor
- Direct gap, 16, 26–27
- Dislocations, 197–199
- Donors, 18
- Doping, *see also* Heavy doping effects, 125–127, 145–146, 164–165, 181, 196
- Drift field, 144, 209
- Drift length, 73
- E**
- Effective force field, 61–63, 82–85, 120, 138, 193–194, 202
- Effective mass, 15
- Efficiency, 57, 128–129, 161, 168  
 ultimate, 129–130  
 versus band gap, 128–130
- Electrochemical photovoltaic cells, *see also* Liquid–semiconductor (EPC) solar cells  
 bucking current, 301  
 current–voltage characteristics, 311  
 decomposition energy, 274  
 open circuit voltage, 277, 317  
 performance data, 321  
 photodecomposition, 267, 274–278  
 reorganization energy, 107–108, 278  
 series resistance, 277
- Electrochemical potential, *see also* Fermi level, 82, 191
- Electrolyte, 107
- Electron affinity, 17, 41, 60, 63, 258  
 data, 76–83
- Electron current density, *see also* Current density, 38, 43–45, 58, 141
- Electrostatic field, 57–59, 61–63, 75, 82–85  
 heterojunction, 92–98, 194, 204  
 homojunction, 89–91, 137, 169  
 liquid–semiconductor (EPC), 107–110  
 M–I–S, 104–106  
 M–S, 100, 120–122  
 S–I–S, 104–106
- Emitter, *see* Top layer
- Encapsulants, 69–70
- Energy levels, 14–23  
 delocalized, 15–21  
 localized, 18–21  
 multiparticle in amorphous solids, 23  
 multiparticle in crystalline solids, 21–23  
 single particle in amorphous solids, 20

- single particle in crystalline solids, 15–20
- EPC devices, *see* Liquid–semiconductor (EPC) solar cells
- Equivalent circuit, 180
- Excitons, 14, 21–22, 54, 143, 169
- F**
- Fermi–Dirac statistics, 145
- Fermi function, 38
- Fermi level, *see also* Electrochemical potential, 38–46, 82, 84
- Fermi level pinning, 96, 110, 112–113, 273
- Field emission, 119
- Fill factor, 183
- Franz–Keldysh effect, 28–29
- Front surface field, 144, 172–174
- G**
- Gap, 15–18
- data, 76–83
  - direct, 16, 26–27
  - indirect, 16, 26–27
  - mobility, 20–21, 28
  - optical, 28
  - optimum, 127–130
- Generation-recombination, *see* Recombination-generation, 30–37
- Gouy layer, 109
- Graded gap structures, 98, 173, 249–251
- Grain boundaries, 110–115
- Grids, 135, 272, 319–320
- H**
- Heat flux, 54
- Heavy doping effects, 145–146, 196
- Helmholtz layer, 109
- Heteroface, 173
- Heterojunction, 92–97
- abrupt, 203, 208–219
  - Anderson model, 92, 203
  - anisotype, 92–97, 187, 239, 252
  - barrier region, 92–98, 189, 193
  - barrier shapes, 202–203
  - isotype, 97
  - $p-i-n$  configuration, 257
- Heterojunction solar cells, 121, 187–261
- advantages, 189, 219
  - AlAs/GaAs, 188, 249, 251
  - Al<sub>x</sub> Ga<sub>1-x</sub> As/GaAs, 249–252
  - amorphous materials, 257
  - anisotype cells, 208–240, 241–244
  - cause of photovoltaic action, 201–205
- CdS/CdTe, 248, 254
- CdS/CuInSe<sub>2</sub>, 248, 254
- CdS/InP, 247
- CdSe/ZnTe, 256
- cross diffusion effects, 201, 203
- Cu<sub>2</sub>S/CdS, 188, 206, 248, 255–256
- history, 187–189
- intermediary layer, 205, 249
- isotype cells, 240–241, 245–246
- $p-i-n$  devices, 257
- polycrystalline materials, 254–257
- S–I–S structure and advantages, 121, 241–246, 244
- using indium-tin oxide, 252–254, 258
- using SnO<sub>2</sub>, 252
- window-absorber, 196–197, 208–219
- Zn<sub>x</sub>Cd<sub>1-x</sub>S cells, 256
- Heterostructure, 173
- High–Low junction, *see also* Homojunction, Selective-ohmic contacts, 91, 143
- Hole affinity, 17, 60, 258
- Hole current density, *see also* Current density, 38, 46–47, 58, 245
- Homojunction, 89–91, 121
- anisotype, 89–91
  - isotype (high–low), 91
  - $p-i-n$  configuration, 134, 166–168, 222
- Homojunction solar cells, 121, 133–186
- amorphous materials, 137, 178–181
  - back surface field, 135, 144, 170
  - black cell, 135
  - CuInS<sub>2</sub>, 137, 178
  - CuInSe<sub>2</sub>, 137, 178
  - front surface field, 144, 172
  - GaAs, 137, 173
  - heteroface, 172
  - heterostructure, 172
  - history, 133–137
  - interdigitated back, 173
  - optimum, 162–164
  - $p-i-n$ , 134, 166–168, 179–181
  - polycrystalline materials, 178
  - silicon, 136
  - tandem-junction, 174
  - violet cell, 135
- Hopping conduction, 25, 49–50, 243, 246
- Hot carrier effects, 55–56, 167
- in electrochemical photovoltaic cells, 310
- I**
- Ideality factor, *see* n-factor
- Indirect gap, 16, 26–27

Insulating layer, *see also* Interfacial layer, 104, 241–246  
advantages in M–I–S structure, 270–272, 295  
charge build up, 271  
current transport, 243  
localized states, 271  
modification of barrier shape, 243, 246  
in ohmic contact, 271  
thickness in M–I–S cells, 269–272  
thickness in S–I–S cells, 245  
Insulators, 15, 65  
Interface recombination, 192–193, 197–198, 208, 214, 223–229, 234–235, 240–241, 245–246, 265–279, 285–288, 312  
Interface states, 86  
heterojunctions, 94–97, 197  
liquid–semiconductor, 110, 273, 278, 305–307, 312–315, 324  
M–S and M–I–S, 102–103, 125, 269–270  
origins, 197–203  
population, 102, 285  
Interfaces, 75–119  
transport mechanisms, 116–119  
types, 85–115  
Interface strain field, 198  
Interfacial layer, *see also* Insulating layer, 102, 242–245  
Inversion layer cell  
M–I–S, 272, 319–320  
Inversion layers, 99–101, 106

**K**

**K**-space, 12

**L**

Lattice mismatch, 197–200  
Lifetime, *see* Carrier lifetime  
Lifetime semiconductor, 65  
Liquid–semiconductor (EPC) solar cells, 273–278, 300–317, 321–322, 323–324  
CdSe/S<sub>n</sub><sup>2+</sup>–S<sub>n</sub><sup>2-</sup>, 321  
GaAs/Se<sup>2+</sup>–Se<sub>2</sub><sup>2-</sup>, 321  
history, 262–265  
InP/V<sup>2+</sup>–V<sup>3+</sup>, 321  
polycrystalline materials, 321  
Localized states, 18–21, 53, 111, 114, 125–127, 169, 198  
acceptor state, 18  
donor state, 18  
Loss mechanisms, 138–141, 191–193, 265–278  
Low level injection, 157

**M**

Maximum power point, 57, 128  
Metal–insulator–semiconductor junction, 104–106  
Metal–semiconductor junction, 98–103  
Bardeen model, 102  
Mott–Schottky model, 101  
Miller indices, 9  
Minority carriers, 73, 140  
diffusion, 144, 150–151, 206  
injection, 120  
lifetime, *see* Carrier lifetime  
sinks, 75, 138–140  
M–I–S solar cells, 121, 269–272, 291–300  
Al/SiO<sub>x</sub>/Si devices, 263, 318  
amorphous materials, 321  
Au/I/GaAs, 318  
Au/I/InP, 318  
history, 262–265  
inversion layer cell, 319–320  
Mobility, 44, 46, 49–50  
concentration effects, 167  
hot carrier effects, 167  
Mobility gap, 20–21  
M–S solar cells, 121, 269–272, 279–291  
Al/Si devices, 263  
amorphous materials, 321  
Au/GaAs, 318  
Cu/Cu<sub>2</sub>O devices, 262–263  
history, 262–265  
Multistep tunneling processes, 118–119, 220, 241, 246

**N**

n-factor, 128–129  
from interface layer voltage split, EPC, 304  
M–I–S, 293–294  
from interface recombination, 226–228, 234–235  
from space-charge recombination, 158  
Neutrality energy, 103, 106, 111, 112

**O**

Ohmic contact, 120–124, 155, 166, 176, 265  
high–low junction, 91, 143, 170–172  
selective-ohmic contact, 123–124, 136, 143, 166  
Open circuit voltage, 57  
sources, 56–63  
Optical generation, *see also* Absorption coefficient, 37

**O**ptical properties, *see also* Absorption  
 coefficient, 23–30  
 absorption processes, 23–28  
 excitons, 25, 28  
 free carrier absorption, 23, 25  
 interband transitions, 24–29  
 localized state involvement, 25, 27–28  
 phonon absorption, 24  
**O**rganic solids, 11, 19, 28–29, 62, 82–83, 321  
**O**xidation–reduction couple, *see also* Redox couple, 107–110  
**O**xide semiconductors, 80–83

**P**

Phonon emission, 34, 231  
**P**honons, 11  
 in amorphous solids, 13–14  
 in crystalline solids, 12–13  
 Photoconductivity,  
 effect on transport, 320  
 relation to photovoltaics, 60–63  
 Photocurrent, 159–163, 183–184, 207, 219–220, 233, 238–239, 265–278, 288–289, 295, 300, 307–317  
 basic collection methods, 71–74  
 Photodecomposition, 267–268, 273–278  
 Photogenerated carriers, 139–143, 154–160, 190–195, 265–278  
 Photogeneration, *see also* Absorption coefficient, 37  
 Photons, 1–3  
 photon spectra, 3  
 Photosynthesis, 1–2  
 Photovoltaic action, 56–63  
 from Dember effect, 61–62  
 from effective force fields, 60, 63  
 from electrostatic fields, 56–61  
 Photovoltaic energy conversion, 1–2  
 $p-i-n$  cells, *see also* Homojunction solar cells, Heterojunction solar cells, 166–168, 179–181, 222  
 $p-n$  cells, *see* Homojunction solar cells, Heterojunction solar cells  
 Poisson's equation, 64, 111  
 Polarons, 14, 22–23, 54, 169  
 Polycrystalline materials, 7–9  
 carrier transport, 114, 169  
 grain boundary, 7, 110  
 grains, 7  
 resistivity, 113–114  
 Poole effect, 52  
 Poole–Frenkel effect, 52  
 Potential energy, 83, 87, 89

**Q**

Quasi-equilibrium assumption, 156, 213  
 Quasi-Fermi levels, 40–53, 210–218  
 Quasi-neutral regions, 157

**R**

Radiative recombination, *see also* Recombination, 30–32  
 Rearrangement energy: *see* Reorganization energy  
 Reciprocal space, 12  
 Recombination, 30–36  
 Auger, 32–34, 146, 164, 167–168, 184  
 interface, *see also* Interface recombination, Surface recombination, 192–193, 197–198, 214, 223–229, 234–235, 265–270, 285–288, 293, 307, 312  
 radiative, 30–32  
 Shockley–Read–Hall, 34–36, 123, 145, 157, 164, 167, 184, 214, 241  
 surface, *see also* Interface recombination, 120, 123, 138–143  
 Recombination center, 36, 115, 158  
 Recombination-generation, *see also* Recombination, 30–36  
 Redox couple, 107–110, 273–278, 323–324  
 distribution of electron energy levels, 107–108  
 effective work function, 84, 108, 273  
 electrochemical potentials, 84, 108–110, 273  
 surface concentration, 310–311  
 Redox potential, 84, 108–110  
 Relaxation semiconductor, 65  
 Reorganization energy, 107–108, 278  
 Resistance,  
 series, 158, 184  
 shunt, 184  
 Resistivity, *see also* Conductivity, 72, 113  
 Ribbon–grown materials, 172  
 Richardson constant, 117, 229–231  
 applicability to EPC cells, 305

**S**

Scattering time, 42, 49  
 Schottky-barrier devices, *see also* Metal–semiconductor junction, M–S solar cells, 98–103, 263  
 Schottky-barrier height, 102, 105  
 Schubweg, *see also* Drift length, 73  
 Seebeck coefficient, 44–46, 53  
 Selective-ohmic contacts, *see also* Ohmic contact, 123–124, 143–144

- Semiconductor, 15–18  
 electronic grade, 172  
 lifetime, 65, 146  
 low cost fabrication of, 172  
 properties, 26, 27, 29, 76–83, 84  
 relaxation, 65
- Semiconductor–electrolyte interface, *see also*  
 Liquid–semiconductor (EPC) solar cells, 86, 107–110
- Semiconductor grain–grain boundary interface,  
*see also* Grain boundaries, 86, 110–115
- Semiconductor–insulator interface, 86, 104
- Semiconductor–insulator–metal interface, *see also*  
 Metal–insulator–semiconductor junction, 86, 104–105
- Semiconductor–insulator–semiconductor interface, *see also* Semiconductor–insulator–semiconductor junctions, 86, 104, 106
- Semiconductor–insulator–semiconductor junctions, 104, 106
- Semiconductor–liquid (EPC) solar cells, *see also*  
 Liquid–semiconductor (EPC) solar cells
- Semiconductor–liquid junction, *see also*  
 Liquid–semiconductor (EPC) solar cells, 86, 107–110
- Semiconductor–metal interface, *see also*  
 Metal–semiconductor junction, 86
- Semiconductor–semiconductor heterojunction, *see also* Heterojunction, 86, 92–98
- Semiconductor–semiconductor homojunction, *see also* Homojunction, 86, 89–91
- Semiconductor–vacuum interface, 86–89
- Semi-insulator, 65
- Series resistance, 70–71  
 causes, 64, 184  
 measurement, 184
- Shockley–Read–Hall recombination, *see also*  
 Recombination, 34–36
- Short circuit current, 57, 71, 127, 140, 161, 183, 193, 206–207, 229–239, 318–319
- Shunt conductance, 184
- S-I-S solar cells, 121, 241–246
- Solar irradiance, 3
- Solar spectrum, 2–3
- Soret coefficient, 45–46
- Space-charge limited current, 65, 153–154, 206, 320–321
- Space-charge region, 82, 87, 155–156, 182, 245, 265–268  
 band bending, 83–112  
*recombination, see also Recombination, 157–159*
- Spectral response, 162, 183, 257, 269
- Spectrum splitting, 175–176
- Standard redox potential, *see also Redox potential*, 108–110
- Superposition, 65, 206–207
- Surface-barrier solar cells, *see also* M–S, M–I–S, Liquid–semiconductor (EPC) solar cells, 262–326  
 history, 262–265
- Surface recombination, 120, 123, 138–143
- Surface recombination velocity, 123, 141
- Surface states, *see also* Interface states, 87, 89
- T**
- Tandem junction cells, 173
- Texturing, 136
- Thermal conduction, 54
- Thermal diffusion coefficient, 45–46
- Thermal expansion, 76–83, 198
- Thermally enhanced field emission, 118
- Thermionic emission, 117–118, 215, 231, 241  
 bucking current, 296–298  
 majority carrier, 269–271  
 minority carrier, 215–217, 229–231
- Thermoelectric effects, 44–46, 53
- Thermoelectric power, *see also* Seebeck coefficient, 44
- Top layer, 137–147
- Transport factors, 217–222, 231–239
- Trapping, 36, 119–120
- Traps, 36
- Tunneling,  
 by field emission, 119  
 in heterojunction cells, 220, 239–240, 243, 246  
 in M–I–S cells, 293  
 by multistep processes, 118–119, 220, 239–241  
 in S–I–S cells, 243, 246  
 by thermally enhanced field emission, 118
- V**
- Valence band, 15, 46–47
- Vertical multiple junction, 175
- Voltage,  
 open circuit, 57–60, 140, 146, 182, 193
- W**
- Wave vector, 15
- Window materials, 69, 75, 196–197
- Work function, 83, 181